Automated rock mass characterisation using 3-D terrestrial laser scanning

Proefschrift

ter verkrijging van de graad van doctor
aan de Technische Universiteit Delft,
op gezag van de Rector Magnificus prof. ir. K.C.A.M. Luyben,
voorzitter van het College voor Promoties,
in het openbaar te verdedigen op
vrijdag 11 juni 2010 om 12:30 uur

door Siefko SLOB
mijnbouwkundig ingenieur

geboren te Nickerie, Suriname

Dit proefschrift is goedgekeurd door de promotoren:

Prof. dr. A.K. Turner
Prof. dr. J. Bruining

Copromotor:

Dr. H.R.G.K. Hack

Samenstelling promotiecommissie:

Rector Magnificus	Voorzitter
Prof. dr. A.K. Turner	Colorado School of Mines, promotor
Prof. dr. J. Bruining	Technische Universiteit Delft, promotor
Dr. H.R.G.K. Hack	ITC, Universiteit Twente, copromotor
Prof. dr. S.R. Hencher	Leeds University, Halcrow Group Limited.
Prof. dr. J.D. Nieuwenhuis	Technische Universiteit Delft
Prof. dr. ir. A.A.A. Molenaar	Technische Universiteit Delft
Prof. dr. ir. G. Vosselman	ITC, Universiteit Twente

Het onderzoek is gefinancieerd door het International Institute for Geo-information Science and Earth Observation (ITC) in het kader van het interne onderzoeksprogramma HiRES3D.

ISBN 978-90-9025364-0
ITC dissertation number 172
First edition

Printed by Wöhrmann Print Service, Zutphen, The Netherlands

Dedicated to Malou and Francesca

Acknowledgements

Only in retrospect I realise how many people have helped me with my research. During the research I often thought I was completely on my own, but this has always been very far from the truth, on my own I would never have been able to finish this book.

First of all, I want to thank my supervisors, Keith Turner and Robert Hack. They have always been the driving forces as well as the critics that are so essential in accomplishing a successful research. I especially want to thank Keith for his relentless enthusiasm and Robert for his continuous faith and support in what I was doing.

I took me so long to finish my thesis that Keith eventually lost his promotion rights at TU Delft after the five years that he has left the TU. Therefore many thanks go out to Hans Bruining for gladly taking up the responsibility of secondary promotor next to Keith.

I would also like to thank ITC for providing the necessary funding and time that allowed me to carry out the research next to my other responsibilities. In that respect I want to thank Martin Hale as Head of Research who has always been very supportive and facilitating. I also want to thank Freek van der Meer, as Head of the ESA department to give me the same support and freedom as Robert did.

I am also very grateful to John Kemeny, who spend his sabbatical in Delft at a crucial period in my research. John is one of the pioneers in the field of laser scanning for rock surveying and I owe a great deal to John sharing his knowledge and the secrets behind the early versions of his software SplitFX. I am also grateful that John brought his laser scanner during the field campaign in Spain in 2004, this resulted in the data that formed the basis of this study.

I have had tremendous help from several MSc students from TU Delft and ITC in investigating some fundamental issues within this research. Bas Vos did great work on block size distribution analyses and gathered lots of scan line data in Spain in the beginning of the research. Bart van Knapen has done excellent work on the surface reconstruction and fuzzy k-means clustering, and gathered most of the field data that has been used in this study. Zillur Rahman and Ephrem Tesfamariam did also very good MSc research on determining roughness of discontinuity planes, which is a research topic that still needs to be investigated further.

I want to thank Johannes Riegl for inviting me to their office in Austria to show me the principles and possibilities of 3-D terrestrial laser scanning. I am also very grateful to Jürgen Nussbaum from Riegl to come all the way over to Belgium to scan some impressive rock faces in the Ardennes. I also want to thank Willem van Spanje and his company DelftTech for their explanation and demonstration of 3-D laser scanning at the start of my research. This made me convinced that laser scanning was the way to go.

For the rest, I want to thank my former colleagues from ITC for their support, interest and supportive criticisms; first of all, thanks go out to my colleagues from the former Engineering Geology section in Delft: Marco Huisman, Niek Rengers, Jan Rupke, Rob Soeters and Wolter Zigterman. I also want to thank all the "new colleagues" I gained when we moved from Delft to Enschede to the ESA department. There are too many to list here, but I want to thank all of them for the warm welcome I received. I want to thank George Vosselman in particular for patiently explaining me the principles behind point cloud segmentation. I also want to thank Benno Masselink for making some of the illustrations.

But most of all, I am so grateful to Malou, for her patience and support during the difficult times and all the days I have been so pre-occupied with my thesis. I spend so many long hours at home writing and editing, which I could have spend with you. And of course, thank you my dear Francesca. Your wonderful arrival gave me the inspiration to finish the job.

Summary

Automated rock mass characterisation using 3-D terrestrial laser scanning

The research that is presented in this thesis investigates the possibility of using point cloud data from 3-D terrestrial laser scanning as a basis to characterise discontinuities in exposed rock massed in an automated way. Examples of discontinuities are bedding planes, joints, fractures and schistocity. Discontinuities divide the rock mass in separate intact rock blocks. The characterisation of the discontinuities in the rock mass is of importance, since they determine to a large extend the geomechanical behaviour of the entire discontinuous rock mass. The conventional way of characterising discontinuities is by manual survey, i.e. geological compass and measuring tape. With the compass the orientation of a discontinuity (dip direction and dip angle) is measured. Orientations are usually plotted in a stereonet in order to identify discontinuity sets. With a measuring tape, discontinuity spacing and persistence is determined. The spacings are usually linked to sets and defined in term of (normal) set spacing. The conventional field methods are simple and effective, but biased, time-consuming and hazardous. Alternatives to the conventional methods for surveying rock faces are two different remote sensing methods: 3-D terrestrial laser scanning and photogrammetry. Both methods yield a detailed 3-D model of the exposed rock face in the form of a point cloud. Laser scanning and photogrammetry both have their advantages and disadvantages. However, the operational advantages and the larger accuracy and resolution that is attainable, makes laser scanning a more attractive field method and is therefore selected as the data acquisition method in this study.

The detailed 3-D point cloud data generated by laser scanning does not yet provide the information on the character of the discontinuities. Various dedicated field and computer methods have recently been developed for deriving discontinuity information from point cloud data. However, these methods make use of a highly interactive approach, which require the user to manually derive the information. This study concentrates on the development and application of different data processing methods to automate the derival of information on discontinuity orientation, discontinuity sets and normal set spacing. The automation of the information extraction process will have an important operational advantage and will reduce the bias that is again introduced by manual interaction. Here, two different approaches are followed: the first approach makes use of the reconstruction of the original rock surface trough interpolation of the point cloud data and the second approach makes use of direct segmentation of the original point cloud data.

Within the surface reconstruction approach two methods are used, referred to as Method 1 and Method 2. Method 1 is developed in Matlab, specifically for the purpose of this study. It is compared with Method 2, which is recently developed software; called Split Fx. Method 1 uses a parametric surface reconstruction. This gives a realistic 3-D virtual reconstruction of the original rock surface. Method 2 uses a 2-D gridding approach to reconstruct the rock face. Both methods yield a virtual rock surface that consists of a mesh, made up of triangles (facets). Each triangle in the mesh is defined in terms of dip angle and dip direction similar to the way orientations of discontinuities are described. The Matlab-based method first plots the poles of all the mesh facets in a stereoplot to determine possible sets. The sets are identified with fuzzy k-means clustering. Neighbouring facets that belong to the same set are subsequently merged into discontinuity planes. The Split-Fx software uses a different approach and joins neighbouring facets into planes whose pole-vector difference is below a user-specified threshold value. The poles of the joined planes are subsequently plotted in a stereonet to identify the sets.

Within the point cloud segmentation approach two methods are used, referred to as Method 3 and Method 4. Method 3 is developed entirely in Matlab specifically for this study. This mehod It is compared with Method 4, which is recently developed software called PCM (Point Cloud Mapper), originally used for processing air-borne lidar data. The key element of both methods is that the original point cloud data is utilised. The methods only work if the point cloud data is spatially structured. This assists the recurrent spatial search through the point cloud. Both methods also use a region-growing strategy. This strategy clusters points through the selection of a random seed points around which, step-by-step, additional points are sought that fall on the same plane geometry. The difference is that Method 3 uses Principal Component Analysis and

Method 4 uses 3-D Hough transform in combination with Least-squares evaluation in order to determine whether points fall on the same plane.

All four data processing methods that are used in this research yield the same basic information, which is a list of discontinuity planes with their most important geometric properties: dip direction and dip angle (orientation). Other information like plane dimension and the plane equation parameters are given as well. In order to derive normal set spacing, the plane orientations need to be clustered to discontinuity sets with fuzzy k-mean clustering. This is not required for Method 1, since this method already has a discontinuity clustering incorporated. The only input required for fuzzy k-means clustering by the user is the number of sets. Once all planes are classified to their individual sets, it is possible to compute normal set spacing with the plane equation parameter d (distance to origin).

The methods are tested and compared on two terrestrial laser scan data sets from Catalonia, Spain. One data set is of an exposure with Carboniferous Slates and the other data set is of an exposure with a Carboniferous Meta-Sandstone. Both rock exposures contain well-developed discontinuities, with contain at least 3 discontinuity sets. The rock faces were scanned with an Optech Ilris 3-D terrestrial laser scanner, one of the first generation of laser scanners. The rock faces were surveyed from a similar distance, with a similar data density. The exposures were also surveyed with conventional techniques, i.e. scanline survey and a rapid face mapping to allow a verification of the laser-based results to be made.

The main conclusion of this research is that it is possible to automate the derivation of discontinuity orientation and spacing information with all four data processing method. Point cloud segmentation is however, the most preferred approach, since it does not require prior surface reconstruction, is therefore faster, and is not strongly influenced by vegetation and other noise in the data. Point cloud segmentation uses the original point cloud, so there is no data loss, which is unavoidable with a surface reconstruction approach. The verification of the data processing with the manually acquired methods is hard to achieve since the methods are fundamentally different in nature and cover different areas in the rock face. However, specifically selected planes show pole-vector differences between the orientations of the laser data and the (manual) compass, that are generally very small, except for Method 1.The large amount of orientation data that can be derived from the point cloud data require a clustering technique, such as fuzzy k-mean clustering, in order to derive discontinuity set information in an automated way. The orientation data from all four methods are successfully clustered to the same amount of sets at each test site. However, comparison of the set clustering results does not show a good match between all sets. The main sets however, do correlate well, but the smaller sets (with fewer planes, i.e. poles) do not always match. The (normal set) spacing data are comparable between the various data-based methods, but do not show a clear correlation with the spacing statistics derived from the manual survey.

Siefko Slob, April 2010

Samenvatting

Automatische gesteentemassa karakterisatie met behulp van 3-D terrestrische laserscanning

Het onderzoek dat is gepresenteerd in dit proefschrift onderzoekt de mogelijkheid van het gebruik van punten wolk gegevens van 3-D terrestrische laser scanning als basis voor het karakteriseren van discontinuïteiten in gesteenteontsluitingen op een geautomatiseerde manier. Voorbeelden van discontinuïteiten zijn gelaagdheden, diaklazen, breuken en schistositeit. Discontinuïteiten verdelen een gesteentemassa in afzonderlijke intacte gesteenteblokken. De karakterisering van de discontinuïteiten in de gesteentemassa is van belang, omdat zij in grote mate aan het geomechanische gedrag van de gehele gesteentemassa bijdragen. De conventionele manier van het karakteriseren van discontinuïteiten is door handmatige metingen, dwz met geologische kompas en meetlint. Met het kompas wordt de richting van een discontinuïteit (hellingsrichting en hellingshoek) gemeten. Oriëntaties worden meestal uitgezet in een stereonet om discontinuïteit sets te herkennen en te bepalen. Met een meetlint wordt de afstand tussen afzonderlijke discontinuïteitsvlakken en de persistentie van individuele vlakken bepaald. De afstanden tussen vlakken zijn meestal gekoppeld aan de sets en gedefinieerd in termen van orthogonale set spatiëring. Deze conventionele meetmethoden zijn eenvoudig en doeltreffend, maar zijn veelal bevooroordeeld, tijdrovend en gevaarlijk. Alternatieven voor de traditionele methoden zijn twee verschillende teledetectie methoden: 3-D (terrestrisch) laser scannen en fotogrammetrie. Beide methoden leveren een gedetailleerde 3-D-model van het ontsloten gesteente in de vorm van een punten wolk. Laser scanning en fotogrammetrie hebben allebei hun voordelen en nadelen. Echter, de operationele voordelen en de grotere nauwkeurigheid en resolutie die kan worden bereikt, maakt laser scanning een aantrekkelijker methode en dit is dan ook gekozen als de data-acquisitie-methode in deze studie.

De gedetailleerde 3-D-punten wolk gegevens die zijn gegenereerd door laser scanning leveren nog niet direct informatie op over de aard van de discontinuïteiten in het gesteente. Diverse speciale veld- en computer methoden zijn in het recente verleden al ontwikkeld voor het afleiden van discontinuïteit informatie vanuit puntenwolken. Echter, deze methoden maken gebruik van een zeer interactieve benadering, die van de gebruiker vereist om handmatig de informatie af te leiden. Het onderzoek dat is beschreven in dit proefschrift concentreert zich op de ontwikkeling en toepassing van verschillende methoden om de verwerking van gegevens uit 3-D laser scanners te automatiseren om daaruit informatie over de discontinuïteit oriëntaties, discontinuïteit sets en orthogonale (set) spatiëring te generen. De automatisering van dit informatie-extractie proces zal een belangrijke operationele voordelen bieden. In dit onderzoek zijn twee verschillende benaderingen gevolgd: de eerste maakt gebruik van de reconstructie van het oorspronkelijke gesteente oppervlak via interpolatie van de puntenwolk en de tweede benadering maak gebruik van rechtstreekse segmentatie van de oorspronkelijke puntenwolk.

Binnen de aanpak via oppervlakte reconstructie, worden weer twee methoden gebruikt,: Methode 1 en Methode 2. Methode 1 is ontwikkeld in Matlab, specifiek voor het doel van deze studie. Het is vergeleken met Methode 2, die gebruikt maakt recent ontwikkelde software; genaamd SplitFx. Methode 1 maakt gebruik van een parametrische oppervlakte reconstructie. Dit geeft een realistische 3-D virtuele reconstructie van het oorspronkelijke gesteente oppervlak. Methode 2 maakt gebruik van een 2-D-gridding aanpak voor de reconstructie van de gesteentewand. Beide methoden leveren een virtueel gesteente oppervlak dat bestaat uit een maastructuur, opgebouwd uit driehoeken (facetten). Elke driehoek in de maas wordt gedefinieerd in termen van hellingshoek en hellingsrichting vergelijkbaar met de manier waarop oriëntaties van discontinuïteiten worden beschreven. De Matlab-gebaseerde methode plot de normaal vectoren van elk individueel facet van de 3-D maas in een stereoplot de sets te bepalen. De sets worden geïdentificeerd met *fuzzy k-means* clustering. Aangrenzende facetten die behoren tot dezelfde set worden vervolgens samengevoegd tot individuele discontinuïteit vlakken. De Split-Fx-software gebruikt een andere benadering en bundelt aangrenzende facetten in lagen, waarvan het normaal-vector verschil lager is dan door de gebruiker opgegeven drempelwaarde. De normaal vectoren van de gevonden vlakken worden vervolgens uitgezet in een stereonet om de sets te bepalen.

Binnen de puntenwolk segmentatie aanpak worden eveneens twee methoden gebruikt: Methode 3 en Methode 4. Methode 3 is volledig ontwikkeld in Matlab speciaal voor dit onderzoek. Deze Methode is vergeleken met Methode 4, de tevens recent ontwikkelde software genaamd PCM (*Point Cloud Mapper*), die oorspronkelijk bedoelt is voor de verwerking van de *airborne* lidar gegevens. Het belangrijkste element van beide methoden is dat de oorspronkelijke puntenwolk wordt gebruikt. Deze segmentatie methoden werken alleen als de puntenwolk ruimtelijk is gestructureerd. Dit helpt het ruimtelijke zoeken binnen de puntwolk, wat essentieel voor de data verwerking. Beide methoden maken ook gebruik maken van een zgn *region-growing* strategie. Deze strategie clustert punten door middel van de selectie van een willekeurige beginpunt, waarna, stap-voor-stap, extra punten worden gezocht die op hetzelfde geometrische vlak liggen. Het verschil tussen de methoden is dat methode 3 gebruik maakt van Hoofdcomponentenanalyse en Methode 4 van 3-D *Hough* transformatie in combinatie met de kleinste kwadraten evaluatie om te bepalen of de punten op hetzelfde vlak liggen.

Alle vier de dataverwerkingmethoden die gebruikt worden in dit onderzoek leveren dezelfde basisinformatie, te weten: een lijst van discontinuïteit vlakken met hun belangrijkste geometrische eigenschappen: hellingsrichting en hellingshoek (oriëntatie). Andere informatie zoals de vlak dimensies en de parameters die de vergelijking van het vlak definieren, worden tevens gegeven. Om de orthogonal set afstanden te bepalen, worden de gevonden vlakken geclusterd tot discontinuïteit sets en wel met behulp van *fuzzy k-means* clustering. Dit is niet vereist voor Methode 1, omdat voor deze methode al een discontinuïteit clustering is opgenomen. De enige inbreng die nodig is voor *fuzzy k-means* clustering door de gebruiker is het opgeven van het aantal sets. Zodra alle vlakken zijn ingedeeld naar hun individuele set, is het mogelijk om de orthogonale afstanden te bepalen met de parameter d van de vergelijking van het vlak, welke de afstand tot de oorsprong van het gekozen coordinaat stelsel weergeeft. De methoden zijn getest en vergeleken op twee terrestrische laserscan metingen in Catalonië, Spanje. Een meting is van een ontsluiting bestaande uit Leisteen en de andere meting is van een ontsluiting met een Meta-Zandsteen. Beide onstluitingen bestaan uit gesteenten uit het Carboon. Beide ontsluitingen bevatten tevens goed ontwikkelde discontinuïteiten, met ten minste 3 discontinuïteit sets. De gesteentewanden werden gescand met een Optech Ilris terristrische 3-D laser scanner, een van de eerste generatie laserscanners. De gesteentewanden waren opgemeten van een gelijkwaardige afstand, met een vergelijkbare gegevensdichtheid. De ontsluitingen zijn ook in detail beschreven met conventionele technieken, te weten een *scanline survey* en een soort van *rapid face mapping* om een verificatie van de resultaten van de laser data mogelijk te maken.

De belangrijkste conclusie van dit onderzoek is dat het inderdaad mogelijk is om het genereren van discontinuïteit informatie met alle vier de dataverwerkingsmethoden te automatiseren. Puntenwolk segmentering is echter de meest geprefereerde aanpak, aangezien zij niet vooraf een oppervlak reconstructie vereist. Deze aanpak is dus sneller, en wordt ook niet sterk beïnvloed door de vegetatie en andere ruis in de gegevens. Puntenwolk segmentatie gebruikt de oorspronkelijke puntenwolk, er is dus geen verlies van gegevens, wat met de oppervlakte reconstructie methode wel het geval is. De verificatie van de verwerking van gegevens met het conventionele (handmatige) meetmethoden is moeilijk te bereiken aangezien de methoden fundamenteel verschillend van aard zijn en betrekking hebben op verschillende gebieden in de ontsloten gesteentewand. Echter, voor een aantal speciaal geselecteerde vlakken is aangetoond dat er zeer kleine verschillen zijn tussen de oriëntaties van de laser gegevens en het (handmatige) kompasmetingen, behalve voor methode 1.

De grote hoeveelheid gegevens die kan worden afgeleid uit de puntenwolk vereisen een clustering techniek, zoals de *fuzzy k-means* clustering, om de set informatie op een geautomatiseerde manier te herleiden. De oriëntaties uit alle vier de methoden zijn met succes geclusterd tot dezelfde hoeveelheid sets. Echter, wanneer de set clustering resultaten blijkt worden vergeleken blijkt niet een goede match tussen alle sets te worden gevonden. De belangrijkste sets correleren wel goed, maar de kleinere sets (met minder polen) komen niet altijd overeen. De (orthogonale) set spatiëringen van de verschillende dataverwerkingsmethoden zijn vergelijkbaar , maar met de informatie die is afgeleid van de conventionele (handmatige) metingen blijkt geen duidelijke correlatie.

Siefko Slob, april 2010

Table of contents

1 Introduction

1.1 Scope

Engineering works placed in or on rock invariably require a proper characterisation of the rock mass. An economic and safe design of an engineering structure critically depends upon an understanding of the interaction of the structure with the rock mass. Mostly, volumes of rock contain a wide range of 'planes of weakness' at all scales, each with a statistical distribution of spacing and orientation (Goodman, 1989). In rock engineering, these planes of weakness are generally referred to as 'discontinuities'. These discontinuity planes divide the volume of rock into a framework of blocks. This arrangement of blocks of intact rock and discontinuity planes is then referred to as 'discontinuous rock mass' (Hack, 1998).

When dealing with discontinuous rock masses, the properties of the discontinuities in the rock becomes of prime importance, since they will determine, to a large extent, the mechanical behaviour of the rock mass (Bieniawski, 1989). Discontinuities are also important in permeability studies for hydrological or petroleum reservoir modelling, since fluids may flow many times faster through discontinuity networks than through intact rock. Discontinuities basically make the rock mass weaker, more deformable and highly anisotropic (Goodman, 1989). The presence of these discontinuity planes reduces the shear strength parallel to the planes and the tensile strength (often to essentially zero) perpendicular to them. Therefore, whether based on empirical, analytical, or numerical methods, discontinuity characterisation plays a fundamental role in the engineering design of man-made structures placed in or on rock masses (ISRM, 1978).

The properties of discontinuities can be classified into geometrical and non-geometrical properties. The non-geometrical properties are related to mechanical behaviour of the infill material of discontinuities and the (shear) strength of the intact rock adjacent to the discontinuity. The geometrical properties control the three-dimensional fabric of the discontinuous rock mass. As previously noted, the discontinuities also often produce a strong directional weakness, or anisotropy, exhibited by the rock mass, and this pattern of anisotropy is largely determined by the geometrical properties of the discontinuities, particularly their orientation. An important observation is that discontinuities almost never occur in a completely random fashion, but show trends that result from the geological processes involved in their formation (Price, 1966). In rock engineering it is generally accepted that the orientations of the planes of weakness cluster around one, or more frequently a few, 'discontinuity sets' or families with a preferred orientation (Goodman, 1989). Consequently, the identification of these 'sets' forms an important part of the characterisation process. In engineering practice, the important geometrical properties of discontinuities, and discontinuity sets, are:

- Orientation: the dip direction and dip angle of a discontinuity plane
- Spacing: the (perpendicular) distance between planes with similar orientation or belonging to the same discontinuity set
- Roughness: the large- and small scale irregularities of the plane's surface
- Persistence: the three-dimensional extent or continuation of a single discontinuity plane or set in a pre-defined rock mass volume

These properties are usuallly measured by hand or estimated in exposed rock masses. A survey of natural or man-made rock exposures provides one of the best field methods of characterising rock

masses. By mere visual inspection of an exposed rock mass experienced engineering geologists can rapidly assess, in reasonably good qualitative terms, the probable mechanical behaviour of the rock mass. However, in order to assess the mechanical behaviour of the rock mass quantitatively, as input to the design of the engineering works, it is essential that the rock mass properties are described and measured in an objective and effective way with sufficient detail and accuracy.

Over the years, standard techniques and methods have been developed to manually survey a rock exposure. In 1978, the International Society of Rock Mechanics (ISRM) (published its suggested methods for the quantitative description of discontinuities in rock masses (ISRM, 1978). This publication outlines the minimum scope for the quantitative description of discontinuities. Subsequently, more detailed survey methods have been described by Priest and Hudson (1981) and Priest (1993). These publications define additional procedures used to determine discontinuity properties in the field in a more structured way by using scan line surveys and cell mapping techniques. However, in practice, it is often more effective to gather discontinuity information not by detailed scanline surveys, but using engineering judgment. An experienced engineering geologist can recognise very quickly the main discontinuity sets in an exposed rock mass. By measuring the orientation of a representative discontinuity plane for a particular set, a relatively good indication of the average orientation of this discontinuity set can be found very quickly. In a similar fashion, spacing, roughness and persistence, and (shearing) history characteristics of the different sets can be estimated. This approach is incorporated in the Slope Stability Probability Classification (SSPC) System developed by Hack (1998).

1.2 Problem definition

In practice there are serious difficulties and objections to the application of the standard manual field survey techniques described above. The geometric properties of discontinuities may be measured in the field with simple tools, such as the geologic compass, clinometer, and measuring tape, see Figure 1.1. Although these tools are effective, there are many errors introduced in the use of these tools, not only due to their limited accuracy, but particularly due to human bias.

Common disadvantages in the use of manual field survey techniques are:

- Erroneous data are introduced due to sampling and procedural difficulties. For instance, the choice of sampling method, instrument error, human bias and, particularly, human blunders; all can affect the accuracy and representivity of the data.
- Safety risks are often considerable. Often field measurements have to be carried out at slopes where quarrying, tunnelling, or mining operations are underway, or along busy transportation routes. The potential for mass movement or rock fall is always present at the base of slopes, and even a small piece of rock that drops from large height can be fatal.
- Direct access to rock faces is often difficult or impossible. Dense vegetation, slope deposits or fences may hamper the physical access.
- Higher parts of the slope are impossible to reach without rock climbing equipment or scaffolding.

Apart from these practical problems, manual field survey methods are also time-consuming, labour-intensive and therefore costly. Furthermore, discontinuity properties often vary a great deal throughout the rock mass, even within a small volume. Thus, a large amount of data is required to accurately describe or calculate the mechanical behaviour of a discontinuous rock mass.

In recent years, a number of computer programs have been developed to numerically model rock mass properties in three dimensions, for instance the three-dimensional distinct element code 3-DEC (Itasca, 2006). However, these programs depend upon detailed input data that are beyond the capability of manual field survey methods to provide. For instance, in numerical distinct element modelling programs, information on each individual discontinuity plane should ideally be incorporated. If information on individual discontinuity planes is not available, at least a statistically

sound representation of the geometric properties of the identified discontinuity sets should be used, which, in turn, calls for large datasets

In conclusion, the manual survey techniques fall short of the large demands that new modelling techniques require of the input data. Safety and economic considerations are also becoming increasingly important and manual surveys are increasingly recognised as too hazardous and uneconomical to be carried out on a routine basis.

Figure 1.1. This photograph illustrates the conventional way of measuring discontinuity orientation, with a geological compass. Simple, effective, but labour-intensive, hazardous and often biased.

1.3 Research rationale

The use of remote sensing techniques offers a logical alternative to manual survey of rock faces, since remote sensing avoids the dangerous and ineffective physical contact with the rock slope. Methods that can derive orientations of discontinuity planes using analogue photogrammetry were first used in the 1960's (Linkwitz, 1963; Savage, 1965; Rengers, 1967). More recently, computer-based applications have been developed that make use of digital photogrammetric techniques to create 3-D models of rock faces (Roberts and Poropat, 2000; Fasching et al., 2001). However, even these digital applications require time-consuming data processing to arrive at the final 3-D model and still require manual outlining of discontinuity surfaces to calculate orientations. With photogrammetric techniques, it is usually necessary to measure several control points within the scene to arrive at a geometrically correct 3-D model. The first publication that described the idea to

use a laser range finder, in the form of a reflectorless total station[1], to measure fracture orientations was by Feng et al. (2001). Although good results were obtained, the number of data points that could be acquired with this method was limited and the manual operation of the total station still required a large amount of time and effort on-site.

The recent development by different manufacturers of three-dimensional terrestrial laser scanners created new possibilities (Slob et al., 2002). The main advantage of three-dimensional laser scanning is that it allows the very rapid generation of a very detailed and accurate three-dimensional geometric representation of exposed rock faces. The geometric representation is in the form of a very dense three-dimensional point dataset, a so-called *point cloud*.

The main rationale behind this research is that there is potentially a large amount of highly accurate information on the geometric properties of discontinuities stored in this very dense point cloud data. The main research question therefore is: how can the critical geometric information on discontinuities be extracted from the point cloud data, and can this be done in a fast and automated manner?

1.4 Research objective

The main research objective is to develop, test and validate computer-based methods to derive geometric properties of discontinuities from point cloud data generated by three-dimensional terrestrial laser scanners. The focus of this research will be on the automated extraction of information on discontinuity orientations, discontinuity sets, set spacings, and roughness of discontinuity surfaces

The ultimate goal is the development of techniques that will eventually replace the traditional manual rock mass survey techniques. The new automated techniques naturally form the basis for improved 3-D modelling of rock masses and supersede the inaccurate and biased, hazardous and time-consuming, conventional methods, using compass-clinometer and measuring tape.

1.5 Methodology

The methodology of this research consists of the following elements:

- Review existing discontinuity characterisation techniques. Evaluate traditional manual survey techniques, existing remote sensing techniques, and state-of-the-art methods, and efforts in these fields.
- Review 3-D terrestrial laser scanning as a remote sensing technique. Evaluate the principles or laser scanning, the data quality aspects, and operational issues, specifically for rock slope scanning. Investigate the advantages and disadvantages of terrestrial laser scanning with respect to other data acquisition techniques.
- Acquire laser scan data from various rock slopes using different models of laser scanners. Discontinuity information, using traditional survey techniques, is acquired from a selection of the scanned slopes in order to compare and validate the results.
- Review the various existing point cloud data processing and analysis techniques. Select the most promising techniques and develop, adopt, test, and validate the techniques with the point cloud data so that discontinuity information can be generated, accurately and preferably in an automated manner.

[1] A total station is an optical instrument used in surveying. It is a combination of an electronic theodolite (for measuring survey angles) and an electronic distance measuring device.

1.6 Thesis outline

This thesis consists of 10 Chapters:

Chapter 2 is about rock mass discontinuities. The chapter discusses the different types of discontinuities that are recognised, particularly in relation to the way they are created. It gives an evaluation of the properties of discontinuities, which are important in terms of geo-mechanical behaviour of the rock mass.

Chapter 3 elaborates further on the scope of this research. It summarises why discontinuity characterisation is so important and the present difficulties and limitations with the existing (manual) characterisation methods. Existing remote sensing methods for geometrical discontinuity characterisation are also discussed.

Chapter 4 introduces three-dimensional terrestrial laser scanning as a survey technique. This chapter focuses on the data quality aspects and discusses the practical application of terrestrial laser scanning to rock face characterisation.

Chapter 5 discusses field data acquisition. It has two parts: field surveys for acquiring laser scan data and the use of standard field techniques during field survey for getting the discontinuity information. These topics are illustrated by field data acquisition activities conducted as part of this research.

Chapter 6 introduces the different point cloud data processing and handling techniques. This chapter describes the theoretical background of the three approaches that are used in this research for the automated extraction of discontinuities and for the computation of the orientations of extracted discontinuities. The two approaches are: a top-down approach in the form of surface reconstruction and bottom-up approach using point cloud segmenation. These approaches are further elaborated in Chapters 7 and 8.

Chapter 7 explains the development and evaluation of the surface reconstruction approach. Here two methods for surface reconstruction are used: a 2-D gridding method and a 3-D parametric surface method. Both methods generate discontinuity orientation and spacing information. The methods are illustrated by two case studies first described in Chapter 4. At each case study location, manual field measurements collected as part of this study are used to provide verification of the point cloud analyses. The case studies used in this chapter are also used in the chapter 8, so that a comparison can be made between the different methods.

Chapter 8 explains the development and evaluation of the segmentation approach. Two methods also are used by this approach: a Principal Component Analysis and a 3-D Hough transformation. This segmentation approach is illustrated by the two case studies described in Chapter 4, and the same manual field measurements are used to provide verification. As in Chapter 6, both point cloud data analysis methods result in orientation and spacing information of the scanned rock face, which are compared.

Chapter 9 discusses the subsequent processing of the segmented point cloud data generated with the method described in Chapter 8. This post-processing reduces the segmented data to a table that lists information on each of the recognised discontinuity planes, similar to the output of the two surface reconstruction methods that are explained in Chapter 7.

Chapter 10 provides a summary of this research in the form of conclusions and recommendations for further research in this field. The practical application of the methods developed and researched in this study is discussed.

2 Discontinuities: types, origin and properties

2.1 Introduction

The research presented in this thesis concentrates on the characterisation of “planes of weakness” in rock, also referred to as “mechanical discontinuities” or simply “discontinuities”. This chapter summarises the major categories of mechanical discontinuities and discusses their origin. The chapter starts by discussing the relationships between stress regimes and the origin and orientation of discontinuities in rock masses. This information is particularly relevant to clarify how joints are formed. It also translates into important geological consequences that are relevant to the topics of this research. The chapter finalises by discussing the geometrical and non-geometrical properties of discontinuities that are used to determine the overall geo-mechanical behaviour of rock masses. The characterisation of geometrical properties is further discussed in the next Chapter 3.

2.2 The importance of discontinuities

Evaluation of the engineering properties of a rock mass requires more knowledge than simply the strength properties of intact rock specimens. A rock mass is typically more heterogeneous and anisotropic than intact rock. Discontinuities, including joints, faults, bedding planes in sedimentary rocks, and foliations in metamorphic rocks, are the primary cause of the heterogeneity and anisotropic character of rock masses.

This research has concentrated on identifying “planes of weakness” in rock masses. Most of these “planes of weakness” are “mechanical discontinuities” as defined by Goodman (1989). Mechanical discontinuities are planar breaks in the continuity of the intact rock material resulting in lower shear strength along the plane or lower tensile strength perpendicular to the plane, compared to the surrounding intact rock material (Hack, 2003; ISRM, 1981).

However, some rocks contain inherent inhomogeneity caused by discontinuities in the rock fabric that exhibit negligible differences in mechanical characteristics compared to the surrounding intact rock. These are normally denoted as “integral discontinuities” and may be formed by bands of different mineralogical or chemical content, or due to a difference in the orientation of the minerals. For example, foliation in gneisses is caused by segregation of minerals into distinct bands and yet the various bands exhibit almost identical gross mechanical properties. In some sedimentary rocks integral discontinuities, caused by changes in grain size or mineral content, may be observed with intervals of millimeters, but without mechanical changes. Only at certain much larger intervals, at scales of several centimeters, or tens of centimeters, are found bedding planes that provide separations into a sequence of strata, thereby providing mechanical discontinuity.

Integral discontinuities may become mechanical discontinuities due to weathering or changes in the stress environment (see Figure 2.1). Weathering processes can cause alteration or dissolution of specific minerals that form the integral discontinuity and thus can create a mechanical discontinuity. For example the weathering of some sedimentary rocks causes the breakdown of initially fairly thick strata into thin fragments. Similarly, some metamorphic rocks, especially schists and slates, can develop marked mechanical discontinuities due to the weathering of their internally aligned mineral grains. Stress release is often an attributing factor for weathering on outcropping rock faces since it permits the integral discontinuities to physically disconnect. On the other hand, mechanical

discontinuities can sometimes become integral discontinuities when mineralisation or cementation of the mechanical discontinuity occurs.
In most locations, rocks have been subjected to various forces that have resulted in their displacement and distortion. Forces acting over extended periods of time can produce spectacular permanent deformations, such as large-scale folds. In other cases, the forces and the resulting deformation may be more modest, but the fracture strength of the rock materials may have been exceeded, producing a variety of mechanical discontinuities. In all cases, the style of the resulting deformation depends upon interactions among a number of physical and chemical factors, including:

- The severity of the deforming forces,
- The degree to which the rocks are subjected to confining pressures,
- Temperature,
- The rate at which the deforming forces are applied,
- The rate at which the deformation proceeds,
- The presence and pressure of pore fluids, and
- The composition of the rock, and of the pore fluids.

Assessment of these discontinuities, including their classification by type and origin, as well as evaluation of their properties, requires knowledge and understanding of the basic concepts of the mechanical properties of materials, especially the reaction of brittle materials, such as rocks, to variations in stress and strain.

Figure 2.1. An example of integral bedding discontinuities that become mechanical discontinuities due to a combination of stress relief and weathering (solution). This is a man-made slope in Lower Muschelkalk (Triassic) Limestones, beside road T322, near the town of Colldejou (Photo: W. Verwaal, 2001).

2.3 Mechanical properties of rock material

2.3.1 Response of intact rock to stress

Most Intact rocks respond to stress in a relatively complex manner. Rocks deform as an *elastic* material at low confining stresses, low temperatures, and with very low strain rates – the response to the applied stress is instantaneous, the strain is recoverable, and there is a linear relationship between stress and strain (Figure 2.2):

$$\sigma = \varepsilon \cdot E \qquad [1]$$

Where:

- σ is stress,
- ε is strain, and
- E is Young's modulus (or: Modulus of elasticity, a constant)

However, in many mining, tunneling and quarrying situations, intact rock materials behave in a slightly more complex manner. When the rock is initially stressed, there is an instantaneous elastic response, but then the strain continues for an extended period of time at an exponentially decreasing rate. When the loading stress is removed, the same sequence occurs in the opposite direction, and ultimately all the strain is recovered (Figure 2.3). This combination of *elastic* and *inelastic* behaviour is of considerable importance to many engineering and rock mechanics applications.

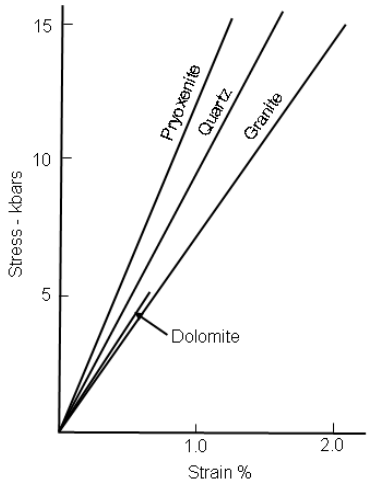

Figure 2.2. Elastic stress-strain curves for several rock types

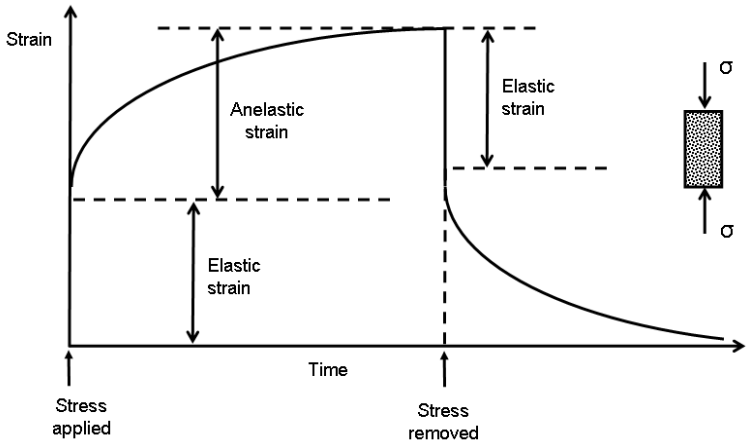

Figure 2.3. Complex elastic-anelastic behaviour of an axially loaded rock specimen. (Hobbs et al., 1976, Figure 1.27)

Over long periods of geological time, rocks often undergo permanent deformations – the rocks remain in a strained state after the stress is removed. At the low confining stresses and temperatures encountered at or near the Earth's surface, most intact rocks can withstand only fairly modest tensile stresses. They thus exhibit *brittle behaviour* – that is the rocks fractures and developes discontinuities. However, high temperatures and large confining stresses exist at deeper levels within the Earth's crust, and under these conditions rocks deform with a *ductile behaviour*, especially if strain rates are not very large. Ductile deformation allows the rock material to strain in a smoothly varying manner throughout its mass – this produces changes to the internal crystalline

properties of the rock materials, resulting in foliations and lineations in metamorphic rocks. At a larger scale, structural geologic features such as folds and domes or basins may be formed without the rocks entirely losing their internal cohesive strength.
Each particular type of rock passes through a transition between what is definitely brittle behaviour to what is definitely ductile behaviour. This *brittle-ductile transition* is controlled by the response of the rock's component minerals to temperature, confining stress, and strain rates. Extensive laboratory experiments have established the brittle-ductile response pattern for many different rock types (Figure 2.4).

Figure 2.4 also illustrates how fractures may be oriented with respect to principal stress directions in brittle and increasingly ductile materials. Very brittle materials, those that have a very low ability to resist tensile stress, typically form *"extensional fractures*" that are oriented parallel to the maximum principal stress σ_1 (and perpendicular to the minimum principal stress σ_3). This result is illustrated in the left column of Figure 2.4, and is commonly observed when rocks specimens in the laboratory are loaded uniaxially, with very low confining pressures.

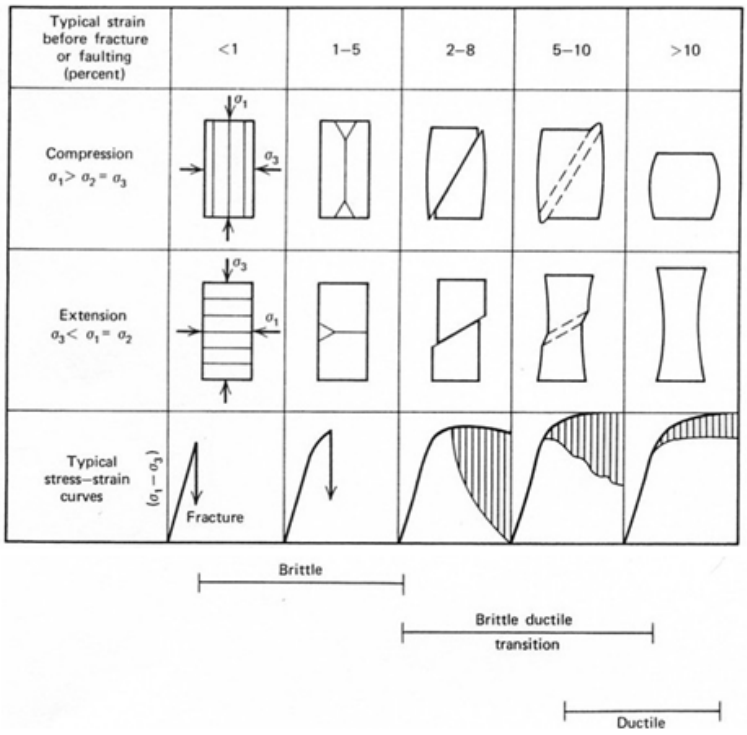

Figure 2.4. Spectrum of behaviour illustrating the brittle ductile transition for a typical rock. The shape of a rock specimen, and the manner of specimen deformation is illustrated for typical compression and extension experiments. The shape of the stress-strain curve for each case is also shown. The hatched area in the stress-strain curves shows the difference between typical brittle and ductile failure (After Griggs & Handin, 1960).

As rock specimens are tested with increasing confining pressures, they begin to behave in a more ductile fashion, as illustrated in the next two columns of Figure 2.4. Initially, the extension fractures continue to be formed, but also smaller inclined "*shear fractures*" begin to be observed. At higher confining pressures, the extension fractures are entirely replaced by inclined shear fractures. At even higher confining pressures the relatively narrow and discrete shear fracture planes become wider "*shear zones*." Ultimately, the zones become diffused throughout the volume of the specimen and completely ductile deformation occurs, as shown in the rightmost column of Figure 2.4.

2.3.2 Mohr-Coulomb failure criterion

The Mohr-Coulomb theory applies to materials whose compressive strength far exceeds their tensile strength; hence it is applicable to intact rock. The Mohr-Coulomb theory describes,

mathematically, the response of rock to shear stress as well as normal stress. The Mohr-Coulomb failure criterion defines a linear envelope obtained from a plot of the shear strength of a material versus the applied normal stress. This relation is expressed as:

$$\tau_f = c + \sigma_n \cdot \tan(\phi) \qquad [2]$$

Where:

- τ_f is the shear stress at failure,
- σ_n is the normal stress at failure,
- c is the intercept of the failure envelope with the τ axis (cohesion), and
- φ is the slope of the failure envelope (angle of internal friction, in degrees).

Figure 2.5 shows how a simple compressive stress regime with $\sigma_1 > \sigma_3$ can cause development of a shear failure plane inclined at an angle β to σ_3. The Mohr-Coulomb failure criterion that relates to this situation is shown in a Mohr circle diagram (Figure 2.6).

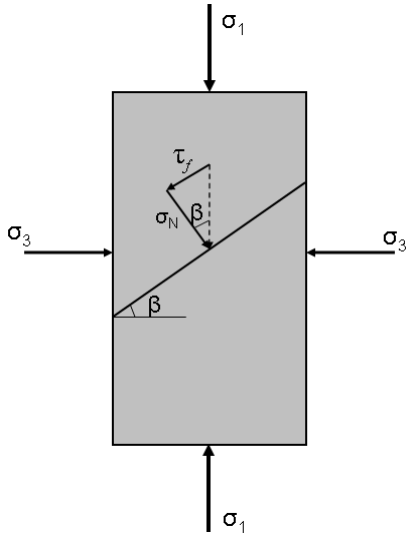

Figure 2.5. Compressive stress regime acting to cause development of a shear failure plane inclined at an angle β to σ_3.

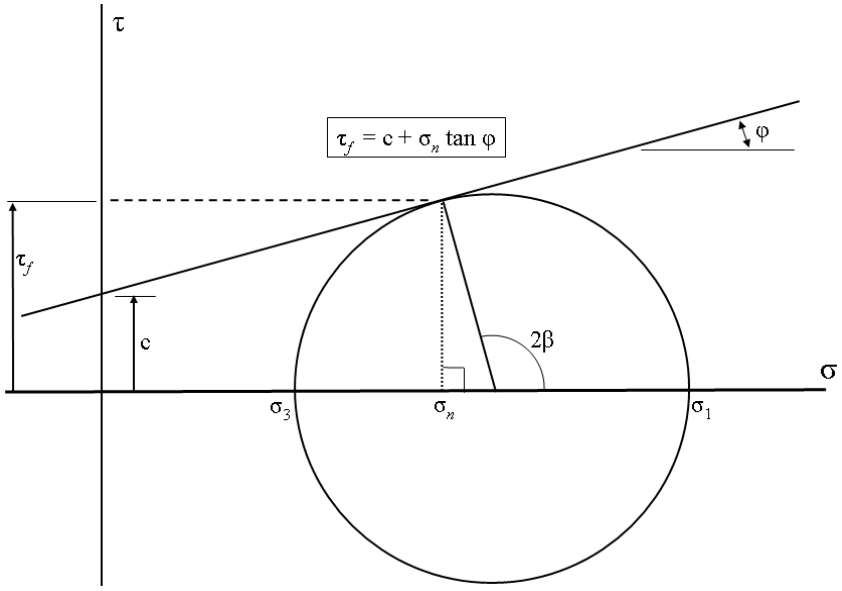

Figure 2.6. Mohr-Coulomb circle diagram, showing the rupture, or failure, envelope.

Contrary to what might be expected, at failure neither the shear stress (τ_f), nor the normal stress (σ_n), are at their individual maximum values. Stresses may not be resolved as though they were vector quantities. As shown by Figure 2.7A, if any potential failure plane is inclined so that its normal makes an angle θ with the applied force, then the area of the plane over which the normal stress is applied increases as the angle θ increases. Therefore the normal stress σ_n and the shear stress τ_n deviate from the normal and shear forces as shown by Figure 2.7B and Figure 2.7C.

The Mohr circle diagram graphically accommodates the relationships shown in Figure 2.6 and thus identifies the orientation of the shear fracture. By simple geometrical inspection of the Mohr circle diagram, it can be seen that the angle 2β equals $90^o + \varphi$; thus $\beta = 45^o + \varphi/2$. Because φ for many rock materials at relatively low confining pressures (i.e. at near surface conditions) is approximately 30^o, then $\beta = 45^o + 15^o = 60^o$, and thus we often find "*conjugate sets*" of "*shear joints*" oriented to the principal stress directions as shown in Figure 2.8.

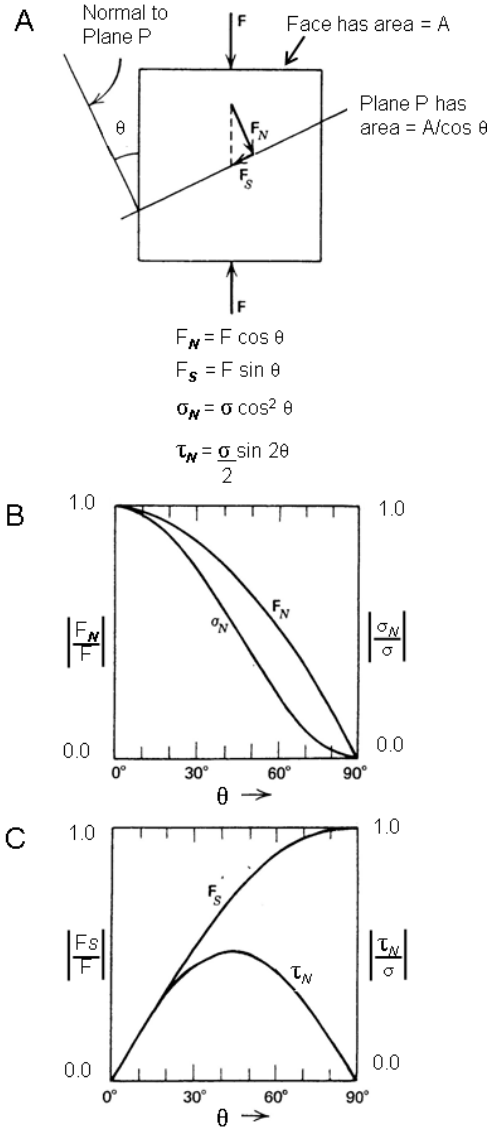

Figure 2.7. Comparison of the resolution of forces and stresses on planes inclined to a principal force (or stress) direction. The orientation of the critical shear failure plane occurs where the ratio of τ_n/σ_n is at a maximum – this occurs where neither the shear stress (τ_n), nor the normal stress (σ_n), are at their individual maximum values. (Adapted from Hobbs et al., 1976, Figure 1.2)

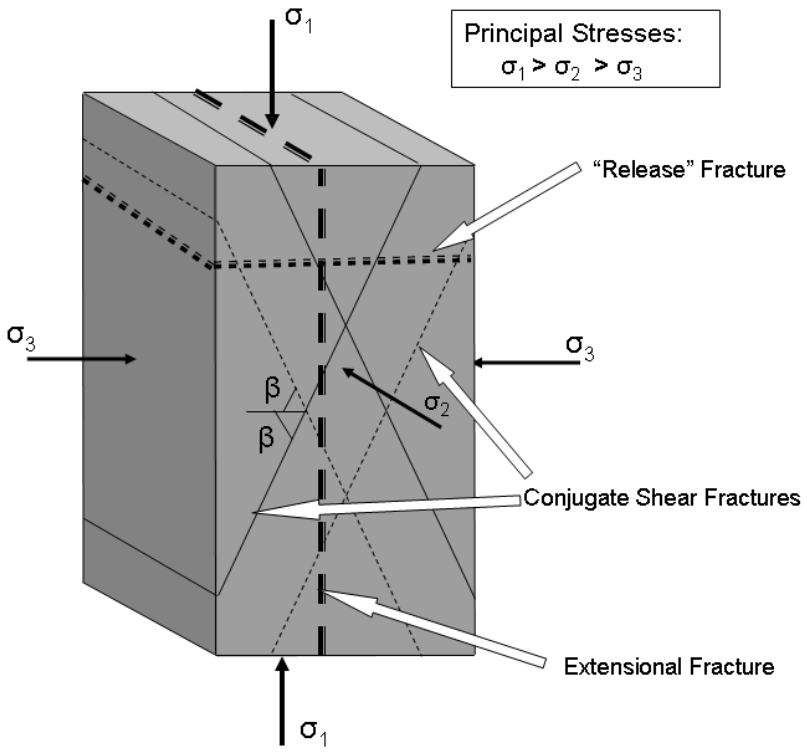

Figure 2.8. Idealized orientation of fractures developed in a three-dimensional stress field with σ_1 as the major principal stress, σ_2 as the intermediate principal stress, and σ_3 as the minor principal stress. Extensional fractures may develop in the σ_1-σ_2 plane, and "release" fractures may develop in the σ_2-σ_3 plane upon the removal of the σ_1 stress regime. However, the development of conjugate sets of shear fractures is the frequent outcome for average levels of confining stresses in many rock types. The intersections of the conjugate shears are oriented along the σ_2 principal stress axis.

2.3.3 Griffith Failure criterion

The Mohr-Coulomb failure criterion is completely empirical, but nevertheless has proved to be a very useful approach that expresses the inter-relationships observed during experiments conducted on several commonly encountered materials – mainly soils and granular aggregates or rocks.

Griffith (1920) suggested that the strength of any brittle material was controlled by the presence of very small "microcracks" that averaged 1μm in size. These "Griffith cracks" were entirely hypothetical until the advent of electron microscopy, which revealed the existence of internal crystal lattice defects and other minor flaws in tock materials. Griffith showed that very high tensile stresses would develop at the tips of such flaws. These high stress levels can lead to the propagation of the microcracks, to their inter-connection, and ultimately to the development of through-going shear fractures.

While the Mohr-Coulomb failure criterion uses a failure envelope defined by a pair of straight lines (Figure 2.9); the Griffith failure criterion results in a non-linear failure envelope (Figure 2.10). The Griffith failure criterion can be expressed as:

$$\tau = 4\tau_0^2 + 4\tau_0 \cdot \sigma_n \qquad [3]$$

Where:

- τ is shear stress,
- τ_0 is uniaxial tensile strength of the material, and
- σ_n is normal stress

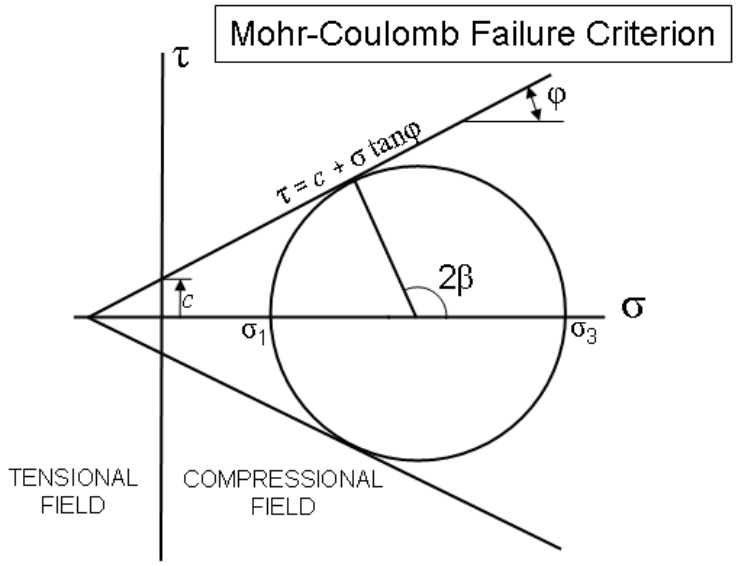

Figure 2.9. The Mohr-Coulomb Failure Criterion illustrated. Compare with Figure 2.10 below.

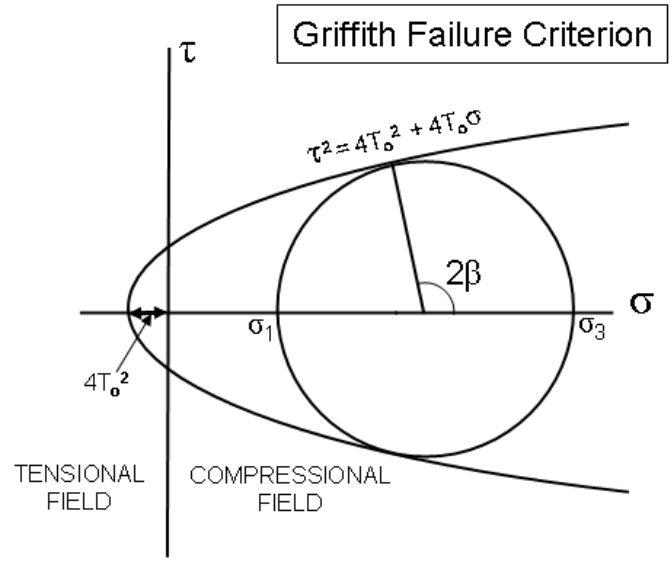

Figure 2.10. The Griffith Failure Criterion illustrated. Compare with Figure 2.9 above.

This defines a parabola, and thus the Griffith failure envelope is sometimes called the “parabolic failure envelope”. Further discussion of the derivation of the Griffith failure criterion and various extensions to this theory is beyond the scope of this thesis. There is a large amount of published material, summarised in Paterson and Wong (2005).

The Griffith failure criterion, rather than the more commonly used Mohr-Coulomb criterion, appears to more closely match many experimental results conducted on rock materials. Figure 2.11 shows some typical experimental strength tests on rocks under increasing confining stresses. An important consequence of the non-linear shape of the failure envelope is that the size of the 2β angle decreases as confining stresses (σ_1 and σ_3) increase. Figure 2.11 shows three test results: Test A has σ_3 acting as a tensile stress, Test B is under low confining stress, while Test C is under high confining stress. The three sample diagrams included in Figure 2.11 show the idealized shape of the conjugate shear failures in each tested specimen. The angle between the conjugate shears increases as the confining stress levels increase. This demonstrates how careful observation of discontinuity orientations in the field may yield important information about past stress regimes.

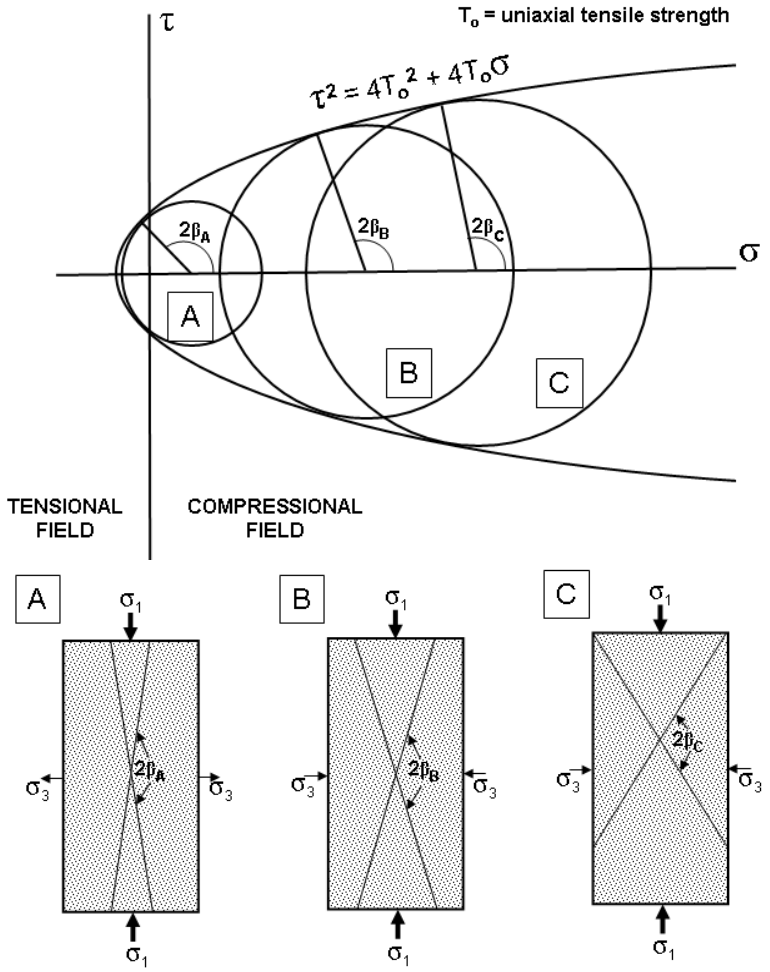

Figure 2.11. Typical experimental strength tests on rocks under increasing confining stresses. Three tests are shown: (A) has σ_3 acting as a tensile stress, (B) is under low confining stress, and (C) is under high confining stress. The three sample diagrams above show the idealized shape of the conjugate shear failures in each specimen. The angle between the conjugate shears increases as the confining stress levels increase.

2.4 Geological consequences of discontinuity development

The above discussions concerning the relationships between stress regimes and the origin and orientation of discontinuities in rock masses translate into several important geological consequences that are relevant to the topic of this research:

- Near the surface of the Earth, one of the three principal stresses (σ_1, σ_2, or σ_3) will be vertical. Anderson (1951) noted that rock surfaces exposed to the surface of the Earth must have zero shear stress, because shear stresses generated by wind or water movements are negligible compared to shear stresses generated by tectonic forces. Thus only three possible stress regimes must dominate at or close to the Earth's surface. Either the $\sigma_2\sigma_3$ plane, the $\sigma_1\sigma_2$ plane, or the $\sigma_1\sigma_3$ plane must lie parallel to the Earth's surface. As shown in Figure 2.12, in the first case (with the $\sigma_2\sigma_3$ plane horizontal, or parallel to the surface of the Earth) the major principal stress (σ_1) is oriented normal to the surface of the Earth, and *normal faults* may form. In the second case (with the $\sigma_1\sigma_3$ plane horizontal, or parallel to the surface of the Earth) the intermediate principal stress (σ_2) is oriented normal to the surface of the Earth, and *strike-slip faults* may form. In the third case (with the $\sigma_1\sigma_2$ plane horizontal, or parallel to the surface of the Earth) the least principal stress (σ_3) is oriented normal to the surface of the Earth, and *reverse-*

or *thrust faults* may form. Distributions of minor mechanical discontinuities, such as joints, will also be related to these dominant stress regimes.

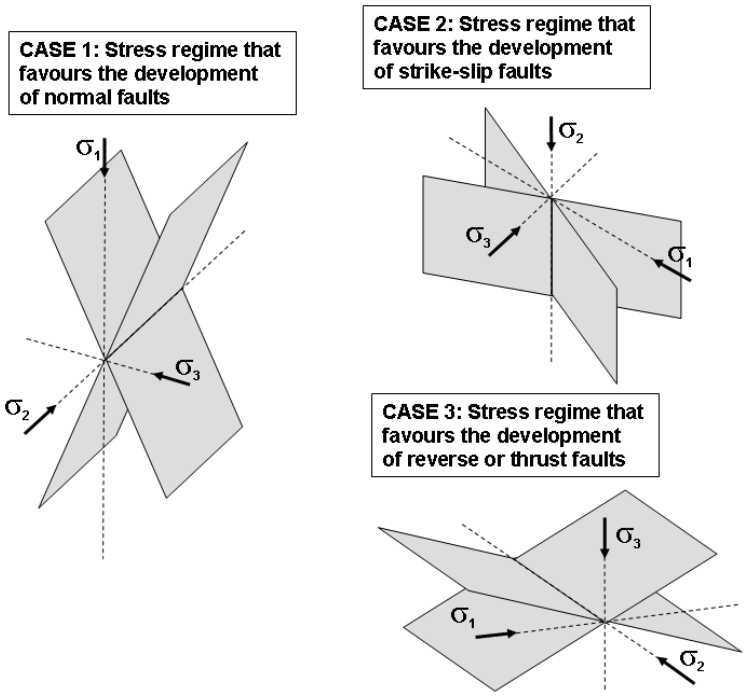

Figure 2.12. Dominant stress regimes at or near the surface of the Earth (Anderson, 1951)

- Discontinuity development may be affected locally by inherent anisotropy in the rock material, or by pre-existing discontinuities. The development and orientation of discontinuities will not always be as described by the idealized conditions discusses previously. Pre-existing discontinuities may cause local re-orientations of the stress regime. Preferred orientations of minerals within a rock matrix, or the existence of pre-existing discontinuities may favour the development of only one orientation of the conjugate shear planes. The presence of bedding planes in sedimentary strata often affects the orientation and spacing of joints.

- Burial history of the rocks will be reflected mostly in the number and types of mechanical discontinuities observed. Deep burial results in higher confining stresses, and elevated temperatures, and thus rocks are more likely to pass through the brittle-ductile transition. Thus metamorphic rocks are likely to exhibit preferential orientations of minerals – producing foliation and marked anisotropic strength characteristics (see Section 2.4.7). Joints and mechanical discontinuities dominate in the more near-surface environments. The types of joints found in relatively undeformed, flat-lying, sedimentary strata are different than those found in folded sedimentary rocks, and discontinuities found in igneous and metamorphic rocks also have distinct orientations, origins, and characteristics.

- The stability of exposed rock cliffs, natural or man-made, depends to a great extent on the number and orientation of the mechanical discontinuities. Figure 2.13 demonstrates the very different characteristics of a rock mass that has a single dominant mechanical discontinuity, compared to a rock mass that has three well-defined orientations of discontinuities.

- The stability of exposed rock faces is thus dependent on the rock type, and the number, orientation, and characteristics of the dominant discontinuities. Intersections of discontinuities with different orientations result in rock blocks of characteristic sizes and shapes. However, it should be also recognized that a single mechanical discontinuity, or even a very few discontinuities, oriented in particularly unfavourable attitudes may be the cause of major rock-slope instability or engineering geological concerns.

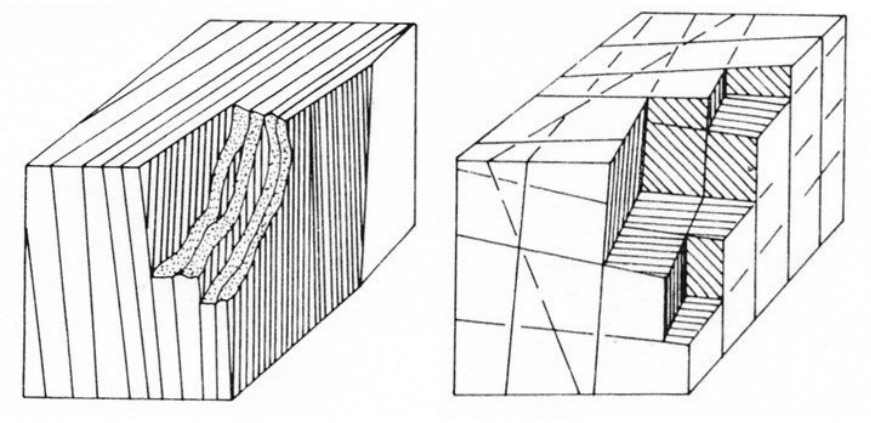

Figure 2.13. Effect of the number of joint sets on the mechanical behaviour and appearance of a rock mass (Bell, 1983, after: Barton, 1978)

2.5 Geological definitions of discontinuities

Geologists have an extensive suite of definitions to describe the various discontinuities found in rock masses. The following sections summarize the important definitions.

2.5.1 Bedding planes

Bedding planes separate successive layers of sedimentary or stratified rock. The orientations of all bedding planes in sedimentary or stratified rocks are initially (near) horizontal[2]. Of course, due to tectonics, the bedding planes in sedimentary rock may eventually have any orientation due to tilting, folding or faulting. Bedding planes result from a change in sedimentary material and/or sedimentation rate during deposition of the sediment. They frequently represent periods of non-sedimentation or even erosion. The spacing between successive planes may thus have any interval, ranging from millimetres to several metres or even in the order to tens of metres. Normally, bedding planes form a well-defined discontinuity set with large lateral persistence. Figure 2.1 illustrates a typical exposure of bedding planes in limestone observed within the study area in Spain.

2.5.2 Joints

The geological term “joint” refers to a mechanical discontinuity in the rock where there has been no lateral movement in the plane of the fracture (up, down or sideways). Joints form due to the inherent weakness of rock materials to withstand tensile stresses – rock is a brittle material. As discussed in Section 2.3, mechanical discontinuities, and hence joints, form in specific orientations within stress fields. Thus, joints generally are not found in random orientations, but in a small number of distinct “joint sets” (Figure 2.16). The spacing between joints forming a joint set is often quite regular, and is related to the mechanical properties of the rock material and the presence of pre-existing mechanical discontinuities such as the thickness of beds in sedimentary rocks (Ladeira & Price, 1981).

The stress regime that causes joints may have several origins. The most ubiquitous stress fields result from regional deformations of the Earth’s crust caused by earth tides that flex the crust in slight but measurable ways, and by movements of the continental plates due to the so-called “tectonic forces.” Loading during deep burial may also produce volumetric changes in the rock materials and later removal of this load by uplift and erosion may result in joint formation as the rock mass expands. Rocks that are formed from high-temperature liquid melts may undergo volumetric contraction during subsequent cooling, and this can produce joints. Therefore, geologists often classify joints by the geological processes responsible for their formation:

[2] The exception is cross bedding which are inclined sedimentary structures that can occur in river and wind-blown deposits.

- **Cooling:** Intrusive igneous rocks that are allowed to cool very slowly are generally massive, with very few, widely-spaced joints. But the rapid cooling of extrusive igneous rocks that form lava flows or dikes and sills causes regular polygonal jointing. Hexagonal columns are commonly observed in basaltic lava flows (Figure 2.15). The joints are oriented to form columns perpendicular to the thickness of the flow or sill or dike. This reflects the isotropic stresses that form in the plane of the flow as the material contracts on cooling.

- **Unloading or Exfoliation:** When uplift and erosion removes the overlying rocks, thereby reducing the compressive load, the rock material tends to expand. Joints related to uplift will have orientations reflecting the principal stresses during the uplift. Care needs to be taken attempting to understand past tectonic stresses to discriminate, if possible, between tectonic and unloading joints. Exfoliation joints are special cases of unloading joints that are formed at, and parallel to, the current land surface, often in rocks of high compressive strength (Figure 2.14). Despite their occurrence in many different locations and rock types, the cause of exfoliation joints remains a subject of debate among geologists. The most commonly accepted causes include:

  - removal of overburden and rebound,
  - thermo-elastic strain due to heating and cooling of exposed rock surfaces,
  - chemical weathering causing expansion of mineral grains within the rock fabric, and
  - large compressive stresses parallel to the land surface causing extensional fractures.

  Regardless of their cause, exfoliation of joints are often important to geological engineering as they may influence slope stability and can create significant leakage at dam sites.

- **Tectonic:** Tectonic joints are formed during deformation episodes whenever the differential stress is high enough to induce tensile failure of the rock, irrespective of the tectonic regime. They will often form at the same time as faults. Additional localised jointing may be generated in a relatively small area near a fault. Rawnsley et al. (1992) consider the situation when a fault plane acts as a free surface contained within an elastic body. In this situation, the fault plane induces a rotation of the principal stress axes to become either perpendicular or parallel to the fault. The free surface model seems to explain the metre-scale curvature of joints that can be observed near existing joints. Movements of ice sheets or (large) slope movements can also create tectonic stresses that result in regular jointing. As defined in Section 2.3, tectonic joints may form as (a) conjugate shears, (b) extensional joints, and (c) release joints (see Figure 2.8). Thus, measurement and analysis of tectonic joint patterns can be useful in analyzing the tectonic history of an area because of the information they give on stress orientations at the time of formation (Engelder & Geiser, 1980).

2.5.3 Joints within folded rocks

The orientations and characteristics of joints found within folded rock sequences are more varied than those described in Section 2.5.2. This is largely a consequence of the more varied and complex stress regime history recorded by the joints. Some joints may pre-date the folding, and thus represent various tectonic or other joint origins discussed in section 2.5.2.

Folding is a product of perhaps a different stress regime, or a series of stress regimes, and in any case is likely to introduce additional joints. Some of these new joints may reflect fractures introduced by bending or flexure of the rock strata. In other cases however, particularly in the case of regional metamorphism, strongly directed stresses in conjunction with elevated temperatures produce “foliations”, including mechanical discontinuities defined as “cleavage” or “schistosity”, as minerals re-crystallize or re-orient themselves to establish stability within the induced directed stress regime (see Section 2.5.7). Additional joints may develop parallel to these foliation planes.

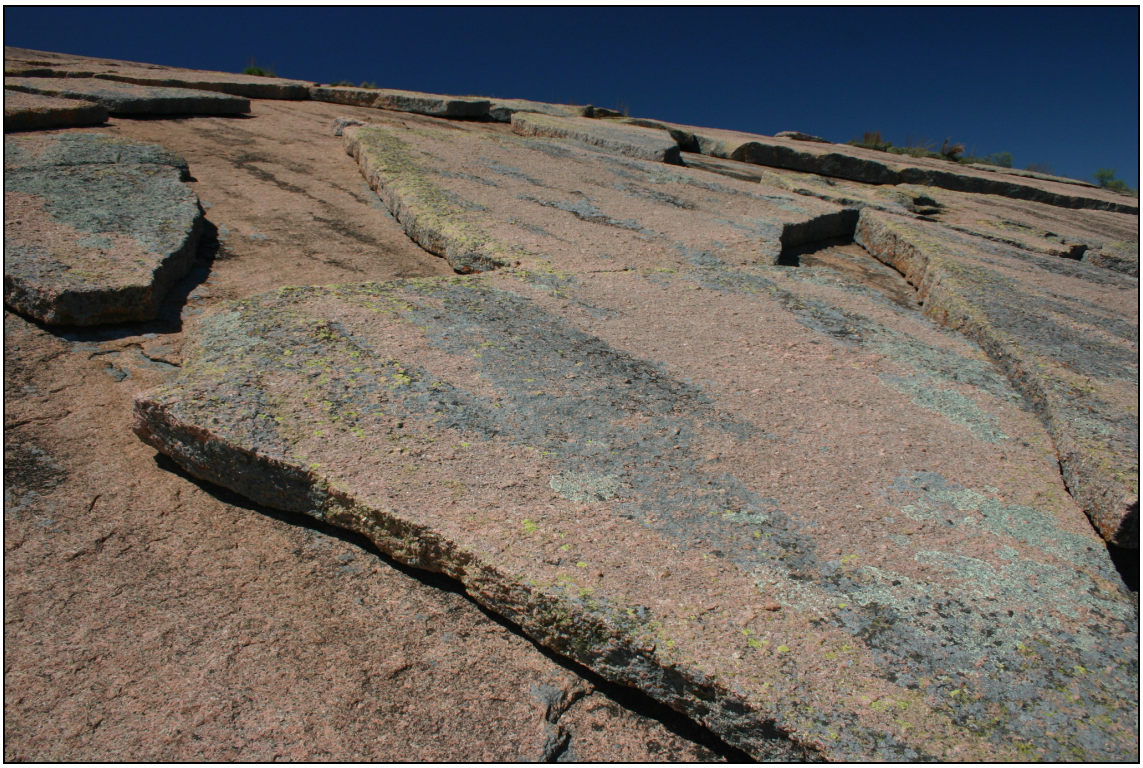

Figure 2.14. Exfoliation joints in granite at Enchanted Rock State Natural Area, Texas, USA. Detached blocks have moved along the joint plane. (Photo: Wikipedia, Wing-Chi Poon, 02/04/2005).

Figure 2.15. Hexagonal jointing due to cooling of basaltic lava flow, Giant's Causeway, County Antrim, Nothern Ireland. (Photo: Wikipedia, 01/09/2005)

Figure 2.16. Well-developed joint sets at St Mary's Chapel, Caithness, Scotland. (Photo: Wikipedia, Mike Norton, 30/04/2008)

Because of this complex stress history, geologists have adopted a relatively complex naming convention for joints in regions with folded rocks. Full details are beyond the scope of this thesis, but can be obtained in any of several structural geology reference sources, such as Hobbs et al. (1976). The system relies on establishing a set of three orthogonal axes (a, b, and c) that are related to the fold geometry – the b-axis is always parallel to the fold axis and the c-axis is oriented normal to the bedding. Thus the axis orientations vary depending on the location within the fold (see Figure 2.17A). Joints are then named based on their relationship to these axes. For example, joints found perpendicular to the fold axis (in the ac-plane) are called "cross joints". Joints parallel to the fold axis (in the bc-plane) are called "longitudinal joints" or "radial joints". As shown in Figure 2.17B at least four major types of joints can be often found in folded rock sequences. Some, such as the "radial joints" may be directly related to the bending of the layers; while other paired joint sets may predate the folding (labelled "2" in Figure 2.17B), and some paired joint sets may reflect the stress regime at the time of folding (labelled "4" in Figure 2.17B).

2.5.4 Joints in igneous intrusions

The development of joints in large igneous intrusions (batholiths) has been the subject of much intensive study over a long period of time (Cloos, 1923). It is believed that most joints and minor faults in batholiths were caused by a continuation of the stress regime responsible for the emplacement of the igneous rock materials. Four types of joints are recognized (Figure 2.18). "Cross joints" lie at right angles to the flow directions and tend to radiate from the center of the intrusion. Joints that strike parallel to the flow directions and are steeply dipping are known as "longitudinal joints." "Diagonal joints" are developed oriented at considerable angles (such as 45º) to

the flow lines. In addition, flat-lying joints may be developed during emplacement (“primary flat-lying joints”) or later, in which case they are termed “secondary flat-lying joints.” Pegmatites or aplite dike intrusions may fill many of these joint systems. Normal and thrust faults and shear zones are common around the margins of large intrusions.

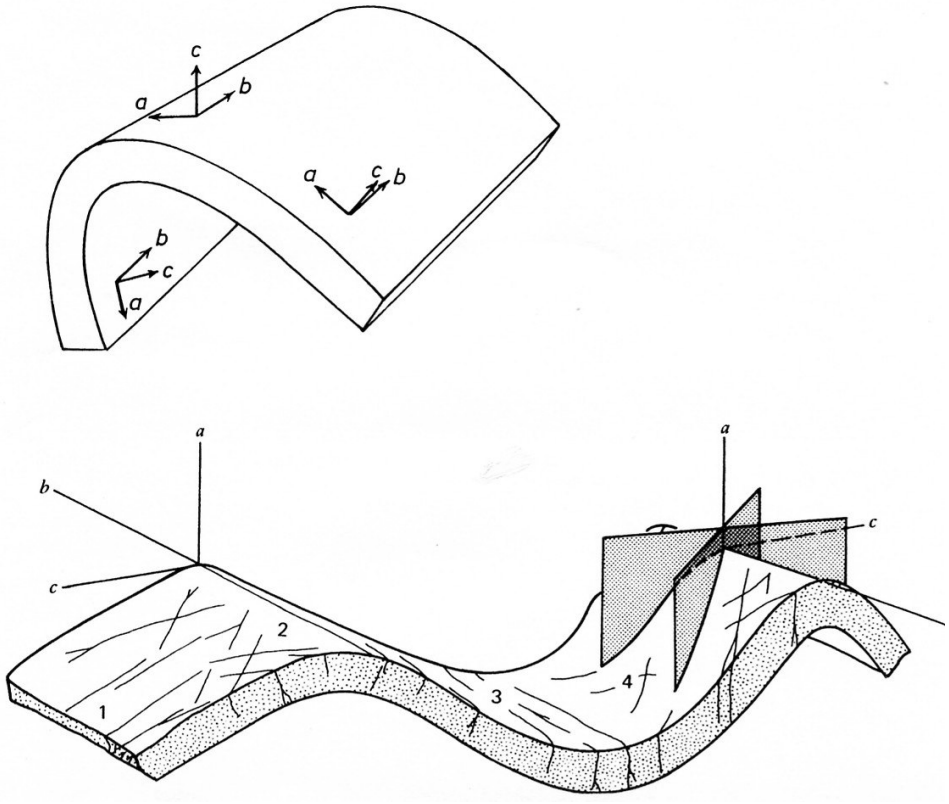

Figure 2.17. Joints in folded rocks. (Above) The orthogonal axes a, b, and c defined in folded sequences. (Below) Joint sets defined: 1 – “cross joints; 2 – paired joint set that predates folding deformation; 3 – “longitudinal” or “radial” joints; 4 – paired joint set related to folding stress regime (Hobbs, et al., 1976, Figure 7.4).

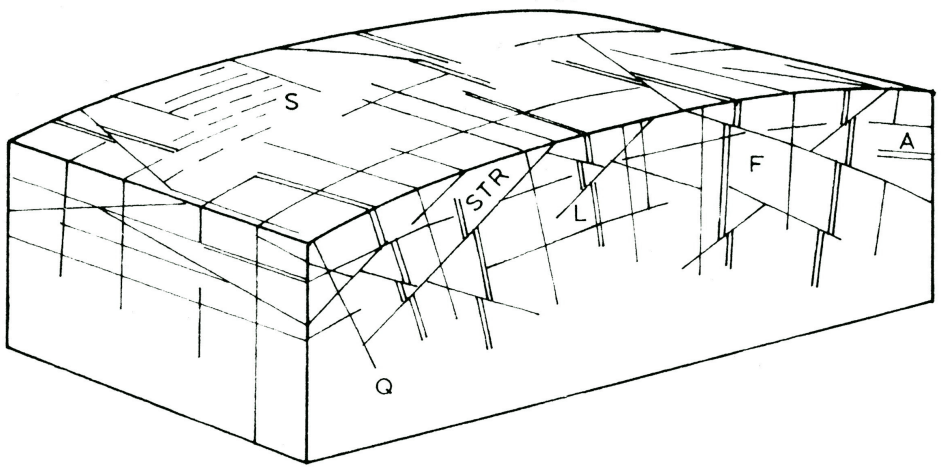

Figure 2.18. Block diagram showing the typical discontinuity structures found in a batholith. Q = cross joints, S = longitudinal joints, L = flat-lying joints, STR = planes of stretching, F = linear flow structures, A = aplite dikes (Bell, 1983, Figure 1.7; modified after Balk, 1938)

2.5.5 Faults

Faults frequently offset all other discontinuities through significant relative movement on either side of the fault. Faults may occur in a larger exposure or engineering site, but mostly as an individual phenomenon. Geologists classify faults according to their style of movement. *Normal faults* have an inclined fault plane and have experienced dominantly vertical movements – the rock located above

the fault plane (on the "hanging wall") has moved down with respect to the rock located below the fault plane (on the "foot wall"). *Thrust* or *reverse faults* have the opposite sense of movement to normal faults – the rock located on the "hanging wall" has risen up over the material on the "foot wall." Reverse faults generally have relatively steeply inclined fault planes. If the fault plane has a very low inclination, or is essentially horizontal, then the fault is referred to as a "thrust fault." Some major thrust faults, associated with large mountain ranges, have displaced rocks laterally for considerable distances, and in these cases, older rocks have overridden younger rocks. If the motion along the fault plane is predominantly sideways, the term *strike-slip fault* is used. Refer back to Figure 2.12 to see how these three major classes of fault are related to the three dominant stress regimes that Anderson (1951) demonstrated as occurring at or near the surface of the Earth.

2.5.6 Shear zones

Shear zones are parallel layers of sheared rock. Rocks deformed by folding often contain shear zones due to interlayer slip and minor fault generation. As illustrated by Figure 2.4 and discussed in Section 2.3.3, shear zones are characteristic of rocks undergoing the brittle-ductile transition. Shear zones are usually spaced more widely than joint or bedding planes and are characterised in thickness by several millimetres to as much as a meter of soft or friable materials (Goodman, 1989).

2.5.7 Foliation

These planes of weakness occur normally in metamorphic rocks and sometimes in igneous rocks. They are formed by the preferred orientation and growth of minerals under the influence of an increase of or change in (directional) stress and temperature. Two types of foliation discontinuity can be distinguished – cleavage and schistosity:

- **Cleavage** produces closely spaced, systematically oriented, planar and parallel layers that are formed by fine-grained platy minerals such as chlorite, oriented such that the maximum dimensions of the minerals are perpendicular to the direction of maximum stress. Cleavage is pronounced in metamorphic rock types named "Slate" and "Phyllite". Cleavage orientation is related to the stress regime and thus is usually discordant to the orientation of any original bedding of the former sedimentary rocks. Both slate and phyllite are metamorphosed shale. While the cleavage surfaces of slate are generally dull, those of phyllite have a silky sheen due to the presence of tiny mica crystals. The cleavage surfaces of phyllite are not as planar as slate, but are commonly rippled.

- **Schistosity** is the layering developed in a coarse-grained, crystalline rock due to the parallel arrangement of platy minerals, such as muscovite and biotite. Schistosity is prominent in the metamorphic rock type named "Schist". Schistocity can form planar, but usually strongly undulating or even folded discontinuity planes formed by the alignment of platy minerals. The spacing is small, but generally larger than the spacing of slatey cleavage (in the order of cm's).

In contrast to the mechanical discontinuities demonstrated by cleavage and schistosity, the foliation developed in the metamorphic rock type known as "Gneiss" does not produce a mechanical discontinuity, merely an "integral discontinuity." In Gneiss, mineral banding formed by lenses or bands of granular minerals alternating with those platy or elongated minerals does not create mechanical discontinuities since the banded minerals strongly interlock.

2.5.8 Fractures

Frequently, the terms "fractures" and "joints" are used interchangeably. However, in this thesis, fractures are defined as rock planes that are created after or during excavation of the rock mass by tensile failure or shearing of intact rock. Two types of fractures can be distinguished based on the type of failure mechanism that creates them:

- **Man-made fracture planes** that are generated by blasting, mechanical hammering or any other mechanical excavation. These fractures are generally non-persistent and occur in a random manner due to breakage of intact rock blocks caused by the large stress variation of the various excavation processes. These man-made fracture planes may break through natural rock bridges and will thus be similar to the fractures described below. Blasting can sometimes be recognised by radial fracture patterns.

- **Fractures through rock bridges**. A rock bridge is the intact piece of rock that exists between two coplanar or non-coplanar discontinuities. At least one of the two discontinuities is a non-persistent plane. Rock bridges occur at a number of different scales and with a variety of geometries (Kemeny, 2005). The actual fracture planes through the rock bridges are only exposed in the rock face after failure of a rock bridge and the rock block that is thus dislodged is subsequently removed. Small fractures through rock bridges separating coplanar discontinuities may be hard to recognise, since they lie in the same plane. The larger fractures through rock bridges between non-coplanar discontinuities can be mapped as separate fractures and can often be recognised by a rough undulating surface. The importance of rock bridges has been recognised by Einstein et al. (1983), Einstein (1993), Savilahti et al. (1990), Shen (1993), Sjoberg (1996) and Goodman and Kieffer (2000). The time-dependent failure of rock bridges is thought to be one of the key processes controlling the longer-term stability of rock excavations (Kemeny, 2003; 2005).

2.6 Properties of discontinuities

Discontinuities influence the construction of engineered facilities located on or within rock masses. Consequently, the identification and evaluation of the characteristics of discontinuities is required. Typically, discontinuities within rock masses are assessed by evaluating their:

1. Orientation,
2. Joint set spacing
3. Surface roughness,
4. Continuity or persistence,
5. Thickness and nature of infilling material,
6. Degree and amount of surface weathering
7. Bonding of discontinuity surfaces by cementation or mineralisation
8. Separation of discontinuity surfaces by karstification

In addition, the presence, or absence, of water within discontinuities is often of critical importance. Water may exist under considerable pressure in some discontinuities; in such cases, increased instabilities of excavations can be expected, and additional expenses will be required to manage the water volumes being discharged. In the following sections, the properties of discontinuities are discussed under two categories – “geometrical properties” and “non-geometrical properties.”

2.6.1 Geometrical properties

Geometrical properties control the three-dimensional fabric of the discontinuous rock mass, and thus strongly influence its overall mechanical behaviour. The following geometrical properties can be defined:

- Orientation: The dip direction and dip angle of the discontinuity planes. The orientation as a property by itself does not influence the mechanical behaviour of a rock mass. However, the orientation becomes very important in relation to the geometry of an excavation, since it will largely control the stability. Discontinuity orientations generally occur in preferred sets. The number of sets and their respective preferred orientation influence the mechanical behaviour of

a rock mass in combination with the set spacing discussed below. This subject is discussed further in Section 3.2.1

- Joint set spacing: The distance between subsequent discontinuities or average spacing between discontinuities from the same set. This spacing, particularly in combination with discontinuity orientation, controls the block size and -shape distribution of the rock blocks that make the discontinuous rock mass, and is therefore greatly responsible for the overall mechanical behaviour of the rock mass. For instance, a densely fractured rock mass with small spacing and four joint sets shows an entirely different mechanical behaviour compared to a massive rock mass with a large joint spacing and only one or two joint sets (see for example Figure 2.13). The block size and shape determines also the quality of dimension stones and other construction materials that can be mined. This subject is discussed further in Section 3.2.2.

- Surface roughness: The roughness of the discontinuity surface, large-scale as well as small-scale. The large-scale roughness influences the amount of interlocking between the rock blocks in the discontinuous rock mass. The small-scale roughness influences the (local) shear strength of discontinuity planes. For instance, an undulating or stepped discontinuity surface has a larger shearing resistance than a smooth and planar surface. This subject is discussed further in Section 3.2.3.

- Continuity or Persistence: The distance over which a discontinuity plane continues. Non-persistent planes terminate within intact rock or abut against another discontuinity plane. The amount of persistence - in combination with (set) spacing and orientation - determines whether individual rock blocks will actually be formed in the discontinuous rock mass, because rock blocks are only formed when discontinuities intersect. Non-persistent discontinuities result in fewer intersections than fully persistent discontinuities. The structural geological history of a rock mass can be important to the persistence of joints. Earlier joints tend to be long and continuous (persistent), while later joints abut against them and are therefore shorter (Rawnsley et al., 1990). This subject is discussed further in Section 3.2.4.

2.6.2 Non-geometrical properties

The non-geometrical properties are related to mechanical behaviour of the infill material of discontinuities and the (shear) strength of the intact rock adjacent to the discontinuity. In this way, the non-geomechanical properties primarily control the shearing resistance of discontinuity surfaces and thus influence the geomechanical behaviour of a discontinuous rock mass. The following non-geometrical properties can be defined:

- Infill material: Particularly near the surface, openings that are created by the discontinuity may be filled in with clay or other material; either flushed in by water or formed in-situ through weathering. This material generally has a low shear resistance and thus decreases the friction resistance along the discontinuity. The effect of the infill material depends on its material properties, but also on the thickness of the infill, particularly in relation with the surface roughness amplitude of the discontinuity walls (Papaliangas et al., 1993).

- Degree and amount of surface weathering: Weathering causes alteration in the mineralogical composition of the material in the intact rock adjacent to the discontinuity. This alteration generally results in a weakening of the intact strength of the rock or the generation of clay minerals. These processes, especially when they act concurrently, lower the shear strength of a discontinuity. A special case of weathering is the dissolution of $CaCO_3$ in argillaceous limestone, which will leave clay as a weathering product. This clay can also fill the discontinuity opening, thus reducing the shear strength. A continued dissolution will result in the creation of voids. This process is called karstification (see also the item below).

- Karstification (Karst): This is a process of dissolution of calcium carbonate ($CaCO_3$) minerals in limestone by water. Karst mostly starts along discontinuities where the flow of groundwater is concentrated. Karst results in the creation of voids and therefore loss of contact between the discontinuity walls, which results in loss of shear strength.

- Cementation or mineralisation: The openings created by the discontinuity allow mineralisation to take place of specific dissolved minerals in the groundwater, such as quartz, calcite or gypsum. This mineralisation may eventually fill the entire opening. The opening may also be filled by a combination of minerals that, when hardened act as cement. Both mineralisation and cementation bond the opposite walls of the discontinuity. The cement or minerals in the opening increase the shearing resistance of the discontinuity depending on the type of mineral and the strength of the cementation. Often the infill itself has shear strength similar, or even higher than the intact rock material. In this case the discontinuity ceases to be a mechanical discontinuity and becomes an integral discontinuity (see also Section 2.1).

The non-geometrical properties are mostly only relevant in rock masses that are presently, or have in the past been located near to the earth's surface. Only near the earth's surface, the described processes are able to take place, controlled by the influx of surface and ground water. The processes are concentrated initially on (near) vertical or open discontinuities (mostly joints), since the influx of water here is least hindered[3].

2.7 Discussion and conclusions

Discontinuities are formed by different large-scale geological processes, such as: sedimentation, uplift, tectonics, cooling, volcanism, unloading, faulting, shearing and metamorphism. In this Chapter the following discontinuity groups are identified:

- Bedding planes
- Joints
- Faults
- Shears
- Foliation
- Fractures

The formation of fractures is, according to the definition given in this thesis, the only type of discontinuity that is not formed by any of the geological processes given above, but through human action (blasting or excavation) or slope failures.

The formation of joints is primarily controlled by the stresses and strains that have developed within the rock throughout its geologic history. This chapter explained the various behaviours of intact rock, ranging from brittle to ductile, which depends on the rock type but also the pressure and temperature conditions. These different behaviours lead to different failure mechanisms, which again result in differently oriented joints sets, depending on the existing stress regime, i.e. the orientation of the three principal stress vectors σ_1, σ_2 and σ_3.

The discussions concerning the relationships between stress regimes and the origin and orientation of discontinuities in rock masses translate into several important geological consequences that are important to the topics of this research:

[3] Weathering zones around faults (sometimes for 100's of meters wide) may however exist at depth of over 2000 m. Pers. comment. Dr. H.R.G.K. Hack, 24-04-2009. Therefore non-geometric properties may be relevant at large depths as well.

1. Near the surface of the Earth, one of the three principal stresses (σ_1, σ_2, or σ_3) will be vertical.
2. Discontinuity development may be affected locally by inherent anisotropy in the rock material, or by pre-existing discontinuities.
3. Burial history of the rocks will be reflected in the number and types of mechanical discontinuities observed.
4. The stability of exposed rock cliffs, natural or man-made, depends to a very great extent on the number and orientation of the mechanical discontinuities.
5. The stability of exposed rock faces is thus dependent on the rock type, and the number, orientation, and characteristics of the dominant discontinuities.

The difference between mechanical and integral discontinuities is also explained. Integral discontinuities can turn into mechanical discontinuities and in some instances mechanical discontinuities can become integral discontinuities Mechanical discontinuities determine for a large part the geo-mechanical behaviour of discontinuous rock masses. In order to quantify this geo-mechanical behaviour, the mechanical discontinuities need to be characterised. Discontinuities can be characterised by a number of properties, which have been discussed in this chapter. A distinction is made between geometric and non-geometric properties, which are listed below:

Geometric properties:
- Orientation
- Joint set spacing
- Roughness
- Persistence

Non-geometric properties:
- Infill
- Cementation or mineralisation
- Weathering
- Karstification

The non-geometric properties are generally very difficult to measure or quantify. The geometrical properties of discontinuities however, by their very nature, are well suited to be measured and quantified. The research presented in this thesis concentrates on the characterisation of these geometrical properties. The following Chapter discusses various techniques, both conventional and state-of-the-art, that already exist for determining the geometrical properties.

3 Characterisation of the geometric properties of discontinuities

3.1 Introduction

This chapter introduces the theoretical and practical aspects of geometric characterisation of discontinuities within the field of rock mass characterisation. The conventional (manual) field methods for measuring and assessing the geometric properties of discontinuities are reviewed and discussed. In this chapter, remote sensing is proposed as the most logical alternative to conventional field methods. An overview of the possible remote sensing techniques for surveying rock faces is provided. The methods are narrowed down to two different methods: laser scanning and photogrammetry. Finally, methods for presenting and visualising discontinuity parameters are given and the most important statistical discontinuity orientation data analysis methods are presented.

3.2 Geometric discontinuity properties

The conventional way of rock mass characterisation in field exposures by a field (engineering) geologist consist of a series of manual measurement and the recording of qualitative observations about the rock mass. For an engineering design these measurements and descriptions are later analysed and used in rock mass classification systems. As described in the previous chapter, discontinuities play a major role in rock mass characterisation. Particularly the geometric properties orientation, spacing, roughness and persistence play a key role. The following sections introduce the field method to derive these properties.

3.2.1 Orientation

Orientation is the most important geometric property, since it determines the anisotropy in the mechanical behaviour of the discontinuous rock mass. Orientation is often recorded in terms of *strike* and *dip angle* or *plunge*. The strike of a discontinuity plane is a line representing the intersection of the plane with the horizontal and is usually recorded as bearing in terms of east or west of north, e.g.: N40ºW. This notation in terms of strike is elaborate and prone to error, since the strike has two bearings and the correct one has to be selected. It is more convenient to record the orientation of a discontinuity in terms of the *dip direction* (azimuth) and *dip angle*. The dip direction is the line perpendicular to the strike and is measured clockwise from the true north, ranging between 0º (for north), 180º (for south) up to 360º (north again).

The dip angle is the maximum declination of the plane with respect to the horizontal and is measured in degrees between 0º (horizontal plane) and 90º (vertical plane). For instance, the orientation of a plane with dip direction of 320º and dip angle of 30 º is uniquely recorded as 320/30. A truly horizontal plane does not have a dip direction (the orientation is noted as 000/00) and a truly vertical plane has in principle two dip directions (for instance 210/90 and 030/90). The orientation of a plane can also be uniquely defined by the *trend* and *plunge* of the normal vector or *pole* to the plane. Measured orientations can be plotted using hemispherical projections, which will assist in the recognition of discontinuity sets (see Section 3.7.2).

The geologic compass and clinometer (often combined) are used to measure the orientations of discontinuity planes (Figure 3.1). The difficulty with the conventional compass is that the dip direction and dip angle can only be accurately read to the nearest degree in ideal situations. An

additional problem is the placement of the compass and inclinometer on a representative section of a discontinuity plane. If the plane is curved or undulating, a single measurement will not be representative because it will be influenced by the roughness. The size of the lid of the Clar or Freiberger geological compass[4]- shown in Figure 3.3, that is mostly used as the base for the orientation measurement is rather small (about 10x10 cm) and thus much influenced by the roughness of the plane (as shown in Figure 3.1). A solution is to use a larger base, such as an aluminium plate or the cover of a notebook, to average out the effect of the roughness. A small level device (bubble) is standard on the Freiberger compass. This levelling device is helpful for finding the correct dip and direction azimuth orientations and prevents the user from measuring an incorrect apparent dip.

For other compasses that do not have a level device, one is supposed to search for the steepest dip, measure and mark the orientation, and then to measure the orientation. This normally does not result in additional errors, if properly done. However, even with a levelling device, nearly horizontal discontinuities are difficult to measure accurately, since it becomes increasingly difficult to level the compass-clinometer properly. Near-horizontal discontinuity sets therefore often exhibit a larger orientation scatter than do sets that are more inclined. This is largely due to the inclusion of incorrect apparent orientations. In some instances, discontinuities are encountered that are not well exposed, i.e., with surfaces not sufficiently large to place the lid of the geological compass. To measure these orientations, the discontinuity plane can be projected with the help of a plate or board. The orientation can then be read with the compass-clinometer placed against the plate or board. Again, this will introduce an error, since it is very hard to keep the plate accurately parallel to the discontinuity.

3.2.2 Spacing

The distance between discontinuities, generally referred to as '*spacing*', determines, to a great extent, the block size distribution and therefore greatly influences the overall mechanical properties of the discontinuous rock mass. A very densely fractured rock, i.e., a rock mass with very small blocks in the order of centimetres, behaves in a completely different manner than a rock mass that is virtually massive, or with blocks sized in the order of metres, even if the materials are the same. Discontinuity spacing data for the dominant sets is required to perform for instance an in-situ block size analysis of the rock mass (Roberts and Poropat, 2000), which can be used to determine *blastability* and *excavatability* (see also Section 3.3).

Spacing is normally measured by a measuring tape. Accurate distance measurements can be made with a measuring tape, if they are done properly. As not all planes of the same set are exactly parallel, and since there are different ways of measuring spacing, different types of spacing have been defined. Large errors are introduced if the spacing definitions are not properly applied. Three types of discontinuity spacing can be distinguished (Priest, 1993):

- Total spacing: This is the distance between a pair of adjacent discontinuities measured along a specified line, e.g., a scanline (see Figure 3.4). Total spacing gives only an indication of the amount of fracturing in a rock mass. However, since the total spacing is measured along a single (scan) line, there is much bias and there is no relation to the spacing of individual discontinuity sets.
- Set spacing: This is the distance between a pair of adjacent discontinuities, from the same set, along a specified line, e.g., a scanline (see Figure 3.5). The average of all set spacings is the *mean set spacing*. There is no correction for the orientation of the scanline. Thus, the spacing for a set that is oriented almost parallel to the scanline is greatly over-estimated.

[4] In Europe the Clar or Freiberger compass is mostly used. In North-America, the use of the Brunton compass is more commonplace. The traditional Brunton Pocket Transit compass has no possibility of measuring dip and strike simultaneously. However, the Brunton Geo-Transit (see Figure 3.2) has, like the Freiberger compass, an inclinometer built in the hinge of the lid, which can be used directly for reading the dip angle.

– Normal set spacing: This is the distance between a pair of adjacent discontinuities, from the same set, perpendicular to the average orientation in that set (see Figure 3.6). The average of all normal set spacings is the *mean normal set spacing*. Normal set spacing and mean normal set spacing are good indicators of the block shape and size distribution in the rock mass and can be used as input to rock classification systems and numerical modelling programs.

Figure 3.1. This photograph shows how the orientation of a discontinuity plane is measured with a geologic compass. A notebook is used here as a base for the compass to even out irregularities at the rock surface. One can easily see that carrying out a measurement higher than a person's eye level is becoming difficult.

Figure 3.2. Brunton Geo-Transit. This type differs from the "normal" Brunton that is has an inclinometer built in the hinge of the lid. Often used by North-American geologists.

Figure 3.3. Freiberger geologic compass. Developed by Dr. Clar and therefore also referred to as "Clar" compass. This type of compass is mostly used by European geologists.

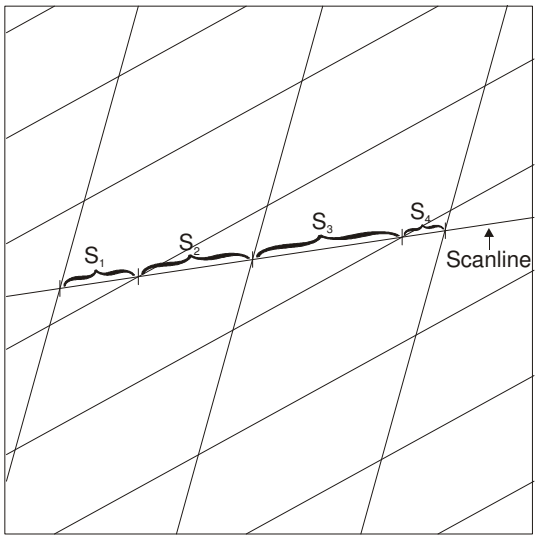

Figure 3.4. This diagram illustrates the definition of total spacing along a scanline.

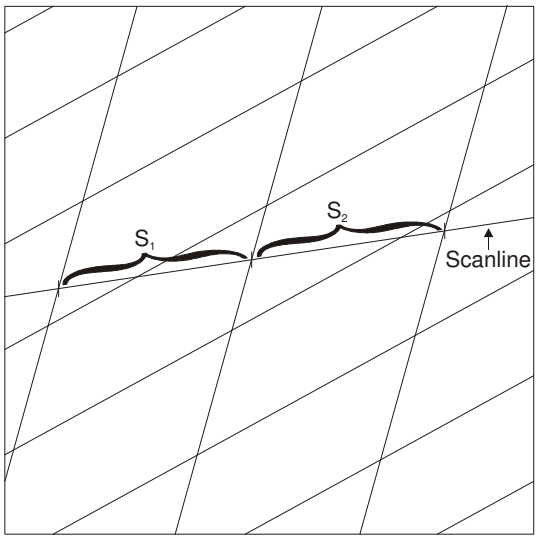

Figure 3.5. This diagram illustrates the definition of set spacing along a scanline.

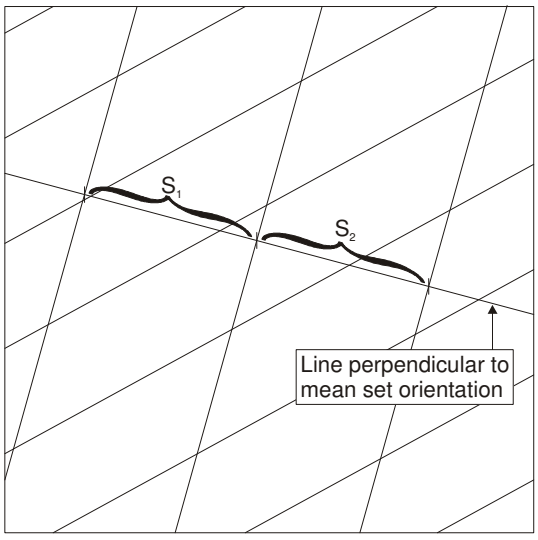

Figure 3.6. This diagram illustrates the definition of normal set spacing along a line that runs parallel to the mean normal vector of a set. Usually, the normal set spacing is not measured along a scanline but derived from the set spacing through correction of the scanline orientation with respect to the set normal orientation.

3.2.3 Roughness

The shear strength of discontinuities depends greatly upon their roughness (Rengers, 1970). Surface irregularities on the discontinuity planes produce the discontinuity roughness. Patton (1966) recognized that the asperity of a discontinuity surface occurs as either, or both, first-order (waviness) and second-order (unevenness) roughness. For small surfaces, the contribution of roughness to the shear strength can be established directly with a shear box test. The problem with larger surfaces is that it is virtually impossible to carry out shear tests in the laboratory or in the field. In such situations, the shear strength has to be derived from the roughness that we can measure in-situ in the field. By following the *'bi-linear shear criterion'* (Patton, 1966), the shear strength can be determined using the friction angle of the intact rock material and the geometry of the discontinuity roughness profiles The bi-linear shear strength criterion is a simple method to analyse the natural irregularities from discontinuity surfaces. In short, the bi-linear shear criterion states that during small displacements the shear behaviour of a discontinuous rock surface is primarily controlled by second-order asperities, while first-order asperities govern the shearing behaviour for large displacements (see Figure 3.7).

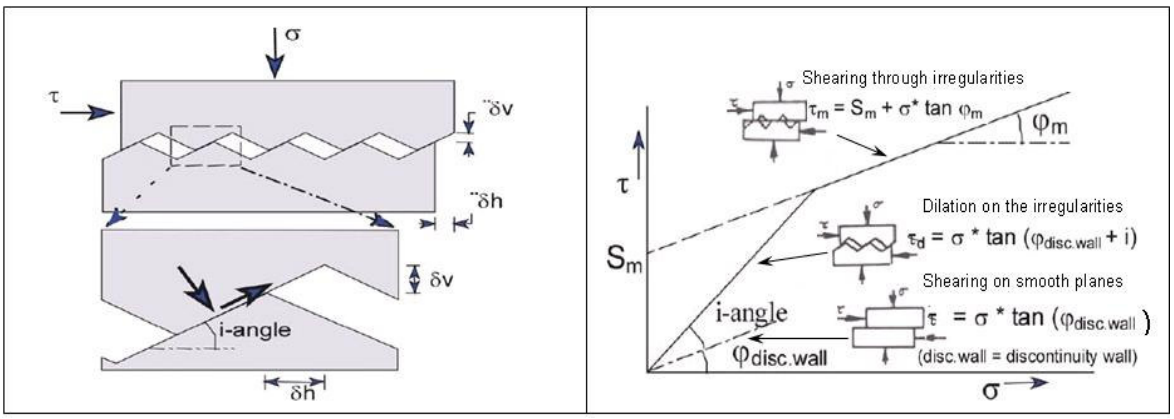

Figure 3.7. Simplified bilinear shear criterion for a discontinuity with a regular set of triangular shaped asperities (Patton, 1966 modified by Hack, 2003). The three different equations and parameters are explained below.

For small displacements the shear strength is governed by second order (small-scale) asperities in the following way:

For shearing on smooth planes: $$\tau = \sigma \cdot \tan(\varphi_{disc\ wall})$$ [4]

For shearing governed by dilation: $$\tau_d = \sigma \cdot \tan(\varphi_{disc\ wall} + i)$$ [5]

For large displacements, the shear strength is governed by the first order (large-scale) asperities in the following way:

$$\tau_m = \sigma \cdot \tan(\varphi_m)$$ [6]

Where:

- σ is the normal stress acting on the discontinuity plane.
- τ is the shear strength
- φ is the angle of friction along the discontinuity
- $\varphi_{disc.wall}$ is the angle of friction of the intact rock material in the discontinuity wall
- i is the angle of roughness
- δv is the dilatency
- S_m is the cohesion of the intact rock material in the discontinuity wall

The angle of friction ($\varphi_{disc.wall}$) along the discontinuity is a material constant depending on the texture, type of material, structure, micro-roughness, and degree of interlocking of the discontinuity

surface at the micro scale. The roughness that contributes dilatancy (opening in the direction perpendicular to the shear plane) of the discontinuity (i.e. δ_v) is not included in $\varphi_{disc.wall}$. The roughness that contributes dilatancy of the discontinuity is described by the angle of roughness (i). The steepness of the roughness which is represented by triangular asperities in this example and the normal stress (σ) across the discontinuity determines whether the asperities will break or if they will be overridden. After the asperities are shared off (beak) or non fitting, the shear strength (τ_m) of the discontinuity wall is described by the discontinuous rock material parameters such as cohesion (S_m) and friction (φ_m). If there is no gluing or bonding agent between the walls of the discontinuity, the cohesion is described as 'apparent cohesion'. If any bonding agent is present, it may provide 'real cohesion'. The parameters (S_m, and φ_m) are normally not the same as the cohesion and angle of (internal) friction (φ) of the intact rock material as described by the 'Mohr-Coulomb failure criterion'. Due to, for example, weathering along discontinuities, the material properties in the discontinuity wall are generally not the same as that of the intact rock mass.

Over the years, various methods have been developed to determine roughness and roughness profiles. The fact that there are so many different methods demonstrates that it is very difficult to decisively capture "roughness" as a parameter. It falls outside the scope of this thesis to elaborate extensively on each method. Therefore the different methods are merely listed below, with references to sources where more information can be found. Two main categories of roughness measurements are recognised;

- Roughness measurement methods that attempt to re-create the actual roughness profile (contact- and non-contact methods), and
- Roughness assessment methods that attempt to derive roughness information indirectly and qualitatively (observational methods).

3.2.3.1 Contact methods

The following roughness measurement methods attempt to measure the roughness at different scales and different dimensions using various mechanical tools that require an actual physical contact with the discontinuity surface:

- Mechanical profiling (Fecker and Rengers, 1971; ISRM, 1978; Weissbach, 1978)
- Compass and disc-clinometer (Fecker and Rengers, 1971)
- Shadow profilometry (Maerz, et al., 1990)
- Straight edge (Stimpson, 1982)
- Tangent plane and connected pin sampling (Harrison and Rasouli, 2001)

3.2.3.2 Non-contact measurements

These methods are in fact all remote sensing methods that attempt to measure roughness at different scales and different dimensions without requiring physical contact with the discontinuity surface.:

- Photogrammetry (ISRM, 1978; Wickens and Barton, 1971)
- Image processing (Galante et al., 1991)
- Fibre optic probe, and He-Ne laser beam (Yilbas and Hasmi, 1998)
- Interferometry topometric sensor (Grasselli and Egger, 2000)
- Laser scanning (Fardin et al., 2004; Hong et al., 2006, Rahman et al., 2006; Feng et al., 2003)
- Electronic stylus profilometers (Grima, 1994; Kerstiens, 1999)

3.2.3.3 Qualitative (observational) methods

Because the following methods are the most simple to use in the field, they are in practice the most widely used and are incorporated into some of the commonly applied Rock Mass Classification systems. These observational methods essentially require a mere visual comparison of the

discontinuity in the field with a number of standard roughness profiles. Some of the methods distinguish between large-scale and small-scale roughness as well.

- Join Roughness Coefficient (JRC) Method (Barton and Choubey, 1977)
- International Society for Rock Mechanics (ISRM) suggested Methods (ISRM, 1978)
- Laubscher's Roughness Curves (Laubscher, 1990)
- Sliding criterion (Hack and Price, 1995). This is also used in the Slope Stability Probability Classification (SSPC) System (Hack, 1998; Hack et al., 2003)

3.2.4 Persistence

Persistence defines the continuation of a discontinuity in different directions. In terms of persistence, three discontinuity classes can be distinguished (Hack, 1998 and ISRM, 1981):

- Persistent discontinuities: These planes are observed to continue in all directions within the exposed rock face.
- Abutting discontinuities: These planes terminate against at least one other discontinuity plane.
- Non-persistent discontinuities: These planes terminate within the intact rock.

The persistence of discontinuities greatly influences the mechanical behaviour of rock masses. Blocks on either side of a non-persistent discontinuity are not likely to move unless the discontinuity extends and breaks through intact rock. This type of failure is called a *rock bridge failure* (see also Section 2.5.8). Blocks on both sides of abutting discontinuities are also restricted in their movement unless the abutting side of the discontinuity can shear through intact rock or if at least one side of the plane is day-lighting or persistent. Blocks on both sides of persistent discontinuities can shear if the shearing resistance of the discontinuity plane is exceeded.

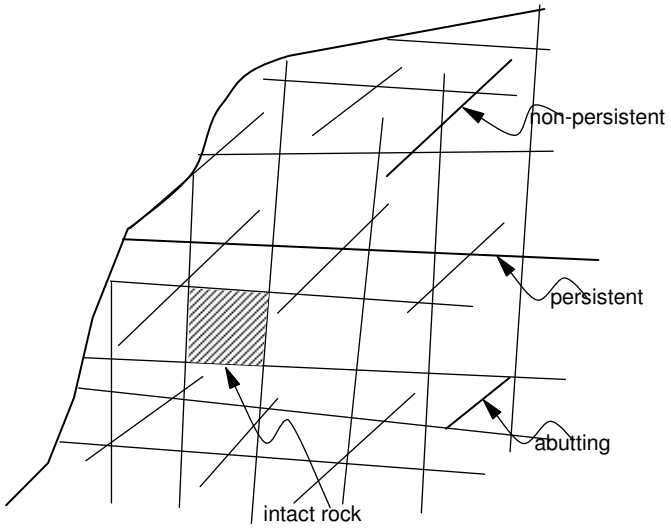

Figure 3.8. Diagram illustrating the various types of persistence.

In practice, persistence is very difficult to determine. In scanline surveys the persistence is recorded as a 1-dimensional factor, i.e. (semi-) trace length (Section 3.5.1 describes scanline surveys). It is often hard to follow the trace fully, since the entire trace may not always be well developed or exposed in rock face. Persistence should reflect the three-dimensional extent of a discontinuity plane. The three-dimensional extent is, in practice, even more difficult to determine, since mostly only a single trace or small part of the plane is exposed in a single rock face.

Even in large rock exposures, it is mostly very hard to determine whether a discontinuity is truly persistent or non-persistent, since it shows only a limited extend of the rock mass. Mostly, when persistence is described, it is in terms of outcrop-scale. Thus, if a discontinuity can be traced

throughout the exposure and no abutting or termination is observed, the discontinuity can be called persistent with a distance of at least the dimension of the exposure. If the trace terminates or abuts it can be called non-persistent and its distance can be measured.

Hack (1998) suggests measuring or estimating the persistence in the dip direction as well as in the strike direction, so that at least the 2-dimensional extent can be derived. Persistence is clearly a scale-related property. If a smaller volume of rock is considered, almost all discontinuities can be considered persistent, while viewed on a larger scale some or all discontinuities may become to a certain degree non-persistent.

Many of the earlier analyses assumed that all discontinuities are fully persistent, i.e., they extend infinitely in all directions. This clearly simplifies computations, particularly in distinct element modelling and block analysis (Goodman and Shi, 1985). However, particularly when dealing with larger rock volumes or larger excavations, persistence becomes a very important parameter to incorporate. In some of the more recent studies and applications, persistence has been incorporated as the probability that a given plane cuts any intersecting block in stochastically generated discontinuity models (Kalenchuk et al., 2006; Golder, 2004). Non-persistent or abutting discontinuities generally do not govern the mechanical behaviour of a rock mass. Most near-surface rock masses already contain so many persistent discontinuities that the behaviour of the rock mass is nearly always fully governed by these. Thus, in common practice, when examining near-surface rock masses, non-persistent and abutting discontinuities are mostly ignored. However, more sophisticated rock slope stability analyses are beginning to address the probability of rock bridge failures caused by the extension of non-persistent discontinuities (Kemeny, 2003).

3.3 The value of geometric discontinuity characterisation

Chapter 1 stated that the geometric characterisation of discontinuities in a rock mass is of prime importance in rock mass characterisation. The main objective of the geometric characterisation is in fact to create a three-dimensional rock block model that defines the mechanical fabric of the discontinuous rock mass. This fabric can be envisaged as number of intact rock blocks with different shapes and sizes that interlock and are separated by the discontinuities. Goodman and Chi (1985) used the block model as the key to a new approach to rock mechanics, named *'block theory.'* Block theory formalises procedures to design underground and surface excavations in discontinuous rock masses. A statistical parameter that is derived from the block model, the *in-situ block size or volume distribution*[5], can arguably be used as a parameter for determining the homogeneity of rock masses (Vos, 2002).

The block theory of Goodman and Shi initiated a new field of study in rock mechanics based on the relationships of in-situ block size distributions. In-situ block size distribution is an important factor in the *blastability* and *excavatability* of discontinuous rock masses. It also affects the resulting block size distribution after excavation, and thus it is an important consideration in evaluating material handling options. Wang et al. (1990, 1991 and 2003), Lu and Latham (1996), Maerz (1996) and Maerz and Germain (1996) undertook much work on the relationship between block size distribution and blasting. Further reference to this approach can be found in Lu (1997), Lu and Latham (1998) and Lu and Latham (1999a; 1999b; 1999c). Block-generating computer applications were also developed by Lu and Latham in the form of the program BLOCKS, and by Baroudi et al. (1990) in the form of the program RESOBLOK. Block theory is for instance implemented in the three-dimensional distinct element code 3-DEC (Itasca, 2006). Other applications of block size or volume distributions for excavatability analyses are described by Hadjigeorgiou and Poulin (1998), and for rock mass permeability estimation are described by Xu and Cojean (1988) and by the computer program 'FRACMAN' developed by Golder Associates (2004). Vos (2002) developed a system

[5] The Block Size Distribution is the curve that is produced when plotting the percentage passing sieve against the volumes of the blocks. The percentage passing sieve is defined by using imaginary sieves with certain sieve sizes, and calculating for each sieve size what percentage of the blocks would be able to pass the sieve (Vos, 2002).

where the shape of the blocks can be classified. Also Kalenchuk et al. (2006) developed a block shape characterisation method that classifies blocks from a three-dimensional block model in a block shape diagram.

The difficulty with all these approaches is that the three-dimensional block model can never actually be 'seen' and will always remain a 'model' in the sense that it is based on a limited number of observations that have been extrapolated in three-dimensional space. The observations are normally done in an exposed rock face, a tunnel wall, a trench, in a borehole, or sometimes on a geophysical section. In any case, the accuracy, reliability, and uncertainty of a three-dimensional rock block model are strongly related to the quality and quantity of the input data.

3.4 Use of discontinuity information by characterisation and classification systems

Since discontinuities obviously play an important role in the geomechanical behaviour of a discontinuous rock mass, the characterisation and classification of discontinuities are incorporated in most rock mass characterisation and classification systems. Rock mass characterisation systems assist in describing the rock mass in standard terms. Two main systems are used: the British Standard (BS 5930:1999) and the ISRM Basic Geotechnical Description (ISRM, 1981). The British Standard system provides a qualitative system for describing discontinuities in terms of type, e.g. joints, faults, or bedding fractures. Additionally, the dimensions and shapes of blocks these discontinuities form in the rock mass can be described in a standardised way. With respect to the geometric discontinuity properties, the ISRM Basic Geotechnical Description (ISRM, 1981) merely recommends the description of the discontinuity spacing. The more extensive ISRM "Suggested methods for rock and discontinuity characterization, testing and monitoring" (ISRM, 1978(a); 1978(b); 1981) recommends a quantitative description of the discontinuity properties, but does not provide formalised standards for doing this.

Rock mass classification systems were created mainly to provide an empirical procedure to recommend support systems for tunnels and underground excavations. The systems were developed primarily empirically by establishing the parameters of importance, giving each parameter a numerical value and weighting. These classification systems were an alternative to realistic deterministic or analytical stability calculations for tunnels in discontinuous rocks which, at that time, were nearly impossible to carry out (Hack, 1998). Although originally designed for underground excavations, some of the rock mass classification systems have been used for evaluating surface excavations and slopes, either directly or in modified form (Romana, 1985). Hack (1998) developed the Slope Stability Probability Classification (SSPC) system primarily for the design of slopes in (discontinuous) rock masses and soil.

Today, with more advanced computing power and modelling software, numerical computations have become more feasible. Nevertheless, rock mass classifications have been successfully used all over the world and they are likely to be used in the future.

Three of the most widely used rock mass classification systems are briefly discussed below. Each description demonstrates how the geometric properties of discontinuities are incorporated, shows how the geometric properties, such as orientation and spacing, influence the final rating that is used in the design of underground and surface excavations and their support and stabilisation.

3.4.1 RQD index classification systems

Discontinuity information from boreholes is often recorded in the form of Rock Quality Designation or RQD. The RQD was originally developed as a rock mass classification system. Today it is mainly used as a characterization parameter or as an input parameter for other classification systems (see below). The RQD is a quantitative index based on assessment of core recovery. RQD is applied to cores with a diameter of at least 42 mm and a length of at least 2 m. Core recovery is computed by

summing only those pieces that are longer than 100 mm; the RQD is recorded as a percentage, as follows (Deere, 1964):

$$RQD\,\% = \frac{\Sigma\ length\ of\ core\ in\ pieces \geq 100\ mm}{Length\ of\ run} \cdot 100\% \qquad [7]$$

The RQD is to a large extent determined by the fracture density, which is related to the number of discontinuity sets encountered by the borehole and the discontinuity spacing in the direction of the borehole axis. However, the RQD value is also greatly influenced by various other factors, including drilling equipment, core handling, strength of the rock material, and the homogeneity of the intact rock. However, the most important factor is the orientation of the borehole with respect to the orientation and spacing of the discontinuities. There are several (empirical) correction formulas developed to correct the RQD in order to determine the in-situ, or orientation-independent, value of RQD.

3.4.2 Q-System

RQD is used as one of the input parameters in the (empirical) Rock Mass Quality classification system. The system is also called NGI–classification or Q-rating system (Barton et al., 1974). The Q-values range between 0.00006 (for exceptionally poor rock) and 2666 (for exceptionally good rock) and should plot on a logarithmic scale. The system was developed to rate rock mass quality in the vicinity of tunnels with the purpose of designing excavation and support for tunnels and underground excavations. In this system size parameters are chosen to describe the rock mass according to Equation [8]:

$$Q = \frac{RQD}{J_n} \cdot \frac{J_r}{J_a} \cdot \frac{J_w}{SRF} \qquad [8]$$

Where:

- J_w/SRF is an expression related to inter-block stress
- J_r/J_a is an expression related to inter-block shear strength or mobility
- RQD/J_n is an expression related to block size

The factor RQD/J_n is understandably related to the geometric fabric of the discontinuous rock mass. RQD has already been defined; J_n is the Joint set number. The Joint set number is a number that relates to the number and spacing of discontinuity sets that are present, or to the degree of 'fracturing' of the rock mass. The value of J_n ranges from 0.5 to 1.0 for a massive rock with no or few joints, to a value of 9 for a rock mass with three joint sets to a maximum value of 20 for a crushed or earth-like rock mass.

The other factor (J_w/SRF) is based on stress conditions in the rock mass: J_w is the joint water reduction factor and SRF is the Stress Reduction Factor, depending on the intact rock strength and stress environment. The third factor (J_r/J_a) is a measure for the shear strength along the discontinuities: J_r is related to the related to discontinuity roughness and J_a to weathering (alteration) of the discontinuity surfaces.

3.4.3 Rock Mass Rating

The RMR, also called the Geomechanics classification system was developed by the South African Council of Scientific and Industrial Research (CSIR) and proposed by Bieniawski (1976 and 1989). Bieniawski developed a weighted rating system based on the algebraic sum of six rock mass properties:

$$RMR = R_s + RQD + R_{dj} + R_{cj} + R_w + R_{oj} \qquad [9]$$

Where:

- Rs is strength of intact rock material (rating from 0 to 15)
- RQD is Rock Quality Designation

- R_{dj} is spacing of joints (rating 5 to 30)
- R_{cj} is condition of joints (rating 0 to 25)
- R_w is groundwater conditions (rating 0 to 10)
- R_{oj} is joint orientation (rating 0 to -12)

In this classification system, geometric properties of discontinuities play a very important role; the RQD, the joint spacing (R_{dj}), and joint orientation (R_{oj}) are three geometric input parameters.

3.5 Current manual methods for collecting discontinuity data

The two most widely applied methods for recording discontinuity data from exposed rock masses are scanline mapping and cell mapping (Priest and Hudson, 1981; Priest, 1993). Scanline survey is a one-dimensional line mapping technique. Cell mapping is a two-dimensional area mapping technique. Both techniques provide a structured way to map and record discontinuities, such that the three-dimensional geometric fabric can be reconstructed. Both techniques rely mainly on the measurement of discontinuity orientation and position at the exposed rock face using simple equipment such as a geological compass, clinometer, and measuring tape.

3.5.1 Scanline mapping

Scanline mapping or *line sampling* is a one-dimensional discontinuity mapping technique. The method consists of an imaginary or physical line placed or drawn on the exposed rock face. Discontinuity planes or traces of discontinuities that intersect this line are recorded with their properties and their position of intersect. Scanline mapping provide sufficiently detailed information on the individual discontinuities in each set that can be used in a probabilistic design (Priest and Hudson, 1981; ISRM, 1981; Kulatilake, 1993). This technique has been described and discussed by a number of authors including Windsor & Robertson (1994), La Pointe & Hudson (1985), Villaescusa (1992), and Priest (1993). However, there is currently no universally accepted standard for scanline sampling.

In practice, a measuring tape of 2 to 30 metres is usually stretched at various orientations along a rock face. If possible, the face and scanline, including appropriate scale, should be photographed before the sampling process is started. Once the scanline is established the surveyor works systematically along the tape recording the position and parameters of every discontinuity that intersects it. The length of the scanline should be chosen according to the average block size of the rock mass. A densely fracture rock mass requires a smaller scanline than a massive rock mass. According to Priest and Hudson (1976) the length of the scanline should be at least fifty times the mean discontinuity spacing in order to estimate the frequency of discontinuities to a reasonable degree of precision. Priest (1993) recommends that the scanline should contain between 150 and 350 discontinuities, of which about 50% should have at least one end visible. This has implications on the minimum size of a rock exposure that can accurately be characterised with this method.

The orientations of the scanlines are chosen in such a way that as many discontinuities as possible are intersected in order to minimise orientation sampling bias. Sampling bias is introduced when the scanline is nearly parallel to the intersecting discontinuity surface; this results in under-sampling of these discontinuities. Corrections have been devised to compensate for directional bias (Terzaghi, 1965; Robertson, 1970) but these do not aid the identification of sets that intersect the scanline at low angles (<10°). The orientation sampling bias also affects the mean spacing of a discontinuity set because the intersect distance along the scanline is much harder to measure for a trace that is near-parallel to the scanline, thus creating a larger inaccuracy in the spacing measurements.

Therefore, in order to minimise the orientation sampling bias and related spacing error, the scanlines should preferably be chosen perpendicular to the main discontinuity set(s). In practice however, a scanline orientation is chosen so that it provides the easiest access. Normally it is recommended to measure at least three scanlines at right angles from each other (Priest, 1993); for

example, one horizontally with the easiest access along the base of the slope and two or more vertical scanlines. The discontinuities or entire discontuinity sets that are possibly missed with the horizontal scanline will thus be recorded with the vertical scanlines. The problem with vertical scanlines is that the higher discontinuity intersects are often very hard to reach, which makes it difficult to measure their properties. Further scanlines should preferable be set up on a second rock face, approximately at right angles to the first. Errors may arise from sampling a single rock face because those discontinuity sets that have an orientation nearly parallel to the face will be under-represented. The features that are commonly recorded in a scanline survey include the following (Clayton et al., 1995):

- Intersection distance: This is the distance in metres (rounded to the nearest cm) along the scanline to the intersection point with the discontinuity. Where the face is irregular it will be necessary to project the plane of fractures not in contact with the tape onto the tape so that the position of such fractures can be accurately recorded. In highly irregular faces, this method can lead to significant errors in the determination of joint spacing.
- Orientation: This is recorded by the dip direction and the angle of dip of the discontinuities.
- Semi-trace length: This is the distance from the intersection point on the scanline to the end of the discontinuity trace. There will be two semi-trace lengths associated with each discontinuity; one above and one below for a horizontal scanline, or one to the left and one to the right for an inclined or vertical scanline.
- Termination: This defines the way each semi-trace is terminated. The scheme recommended by ISRM (1978(a);1978(b)) could, for example, be used: 'I' or '1' for a discontinuity trace that terminates in intact rock material; 'A' or '2' for a discontinuity trace that terminates at another discontinuity; and 'O' or '3' for a discontinuity whose termination is obscured or the trace extends beyond the limits of the exposure.
- Roughness: The roughness may be estimated visually using Barton's Joint Roughness coefficient (Barton, 1973) or any of the other observational methods discussed in Section 3.2.3.

The normal set spacing distribution and mean normal set spacing is usually the most important parameter to derive from the scanline data (Section 3.2.2 defined this concept). Normal set spacings can be calculated by the following steps:

1. Select all the discontinuities that belong to a set. This requires the plotting of all orientations in a stereonet (see Section 3.7.2), and either the use of spherical directional statistics (Section 3.7.3) or the use of fuzzy k-means clustering (see Section 3.7.4).
2. Sort the intersection distances of all observations from a single set.
3. Subtract each subsequent intersection distance to get the set spacings.
4. Calculate the angle that the normal of each intersected discontinuity plane makes with the scanline bearing. The cosine of this angle is the dot product of the normal and the normalised vector representing the bearing of the scanline, as determined by Equation [11], in Section 3.7.1.
5. Calculate the average of all the (cosines of the) intersection angles.
6. Correct the set spacings with the intersection angle to get the normal set spacing (simply by multiplying each set spacing with the cosine of the average intersection angle).
7. If ample observations are made, the normal set spacings can be plotted in a histogram to view the spacing distribution, otherwise the calculation of the mean normal set spacing is sufficient.

3.5.2 Cell mapping

Cell mapping or window sampling is a two-dimensional discontinuity mapping or sampling technique. This technique consists of the selection and outlining of a square window on the rock face. Only the properties of discontinuities whose traces fall (partly) within the defined exposure of the rock surface are measured and recorded. In order to minimise the sampling bias, the window should be as large as possible, such that each side of the window intersects at least 30 to 100

discontinuities (Priest, 1993). Just as with scanline mapping, preferably two mutually perpendicular rock faces (exposures) should be sampled in order to avoid under sampling of discontinuities that run nearly parallel to the rock face. However, the linear orientation sampling bias that occurs in the scanline method is removed, since all orientations are equally represented within the sampling window. Nevertheless, cell mapping provides a poor framework within which to collect orientation, frequency and surface geometry data for individual discontinuities (Clayton et al., 1995). The window is likely to contain a large number of relatively small discontinuities, making it difficult to keep track of which discontinuities have been measured and which have not. When similarly precise sampling schemes are attempted, the cell mapping process is generally more labour intensive than scanline mapping

3.5.3 Rapid face mapping

For a preliminary assessment of a rock face, it is often sufficient to undertake a more general discontinuity study. Basic information, such as the number of discontinuity sets, the average orientation per set, and the relative importance of each set, can be gathered much faster than by the scanline or cell mapping methods described earlier. According to Hack (1998), for most applications, it is sufficient to identify the main discontinuity sets in a rock mass, and then measure, or even estimate, a representative orientation and spacing for each set. In larger rock faces, it is essential to first identify the most important homogeneous rock mass units (or zones) within the exposure, and to carry out the discontinuity assessment for each unit separately. This method has the advantage of rapidly providing a reasonably accurate engineering geological mapping and assessment of the entire rock exposure. A single scanline survey or cell mapping on a rock face may require an entire day to perform properly, while rapid face mapping may require less than an hour. Also the orientation bias that is introduced by scanline mapping methods is avoided, since the entire face is considered. Line and cell mapping may completely miss very important discontinuities, or even an entire discontinuity set, since the surveys are spatially constrained to the scanline or the mapping cell.

The rapid face mapping approach forces the engineering geologist to apply his/her engineering judgment to the assessment of the exposed rock mass. Scanline and cell mapping is often so focussed on examining and measuring discontinuities in such a detailed manner that the overview is lost. The disadvantage of rapid face mapping is that it requires a great deal of field experience to accurately recognise the different engineering units and to identify the most important discontinuity sets. The rapid face mapping approach is not systematic and thus human bias may be introduced. To minimise the human bias, Hack (1998) recommends using a field form to systematically direct the mapping of a rock face. The field form provides a checklist to record the most important properties and parameters of the rock unit and rock face. However, by merely measuring the most representative orientation and spacing for each set, statistical reliability cannot be ensured and important variations in the values may be overlooked. Sometimes the dominant discontinuity sets are not immediately evident. In order to find these sets, it is then necessary to undertake statistical analysis, for which much more data is required. ISRM (1978) suggests that statistical analysis should be based on a minimum of 150 measurements. This makes the rapid face mapping method once again more time-consuming and eliminates its most important advantage.

3.6 Current remote sensing methods for collecting discontinuity data

Remote sensing offers a logical alternative to manual data acquisition methods. Remote sensing methods for collecting information of an exposed rock face can be categorised as active and passive remote sensing. Since we are mostly dealing with inclined rock exposures, that have to be surveyed in detail, the optimal way of viewing them is by using a terrestrial platform. This allows a sub-horizontal viewing line-of-sight, and a much better view of the details of the rock exposure than can be obtained from airborne platforms looking down on the exposure. Passive remote sensing makes use of a sensor that detects the reflection of (sun) light from the exposed rock face. Under this category, we can classify ‘normal’ photography for image analysis and stereo photography for

photogrammetric purposes. Active remote sensing makes use of its own source of electromagnetic energy. This energy is emitted from the location of the sensor and the reflection of the emitted energy is detected by a sensor. Under this category, we can classify terrestrial laser scanning and reflectorless total stations. Some techniques already combine both passive and active remote sensing methods in one platform. Goldenrocks (2006) provide up to this moment the most comprehensive compilation of papers that describe both laser scanning and photogrammety applications for mapping rock faces.

3.6.1 Photo analysis

3.6.1.1 Analogue photogrammetry

Photogrammetry is a three-dimensional coordinate measuring technique that uses (analogue or digital) photographs as the fundamental medium for measurement. The fundamental principle used by photogrammetry is triangulation. By taking photographs from at least two different locations, so-called "lines of sight" can be developed from each camera to points on the object. These lines of sight are mathematically intersected to produce the 3-dimensional coordinates of the points of interest.

The earliest documented efforts to gather discontinuity information with photogrammetry are by Linkwitz (1963), Savage (1965), Rengers (1967) and Wickens and Barton (1971). These attempts were based on the manual analysis of terrestrial stereo photos of rock faces using a standard stereoscope. The photos were made with a stereo camera set for short distances or a phototheodolite for larger distances. A phototheodolite is camera mounted on a theodolite with mutually parallel optical axes which makes it possible to take photos with accurately parallel camera axes at well-defined distances from each other. By measuring the orientation of the discontinuities in the stereoscopic view with a parallax bar, the actual dip and dip direction can be calculated. A useful instrument for this procedure was the use of the ITC dip-estimator (Mekel et al., 1964). These early attempts demonstrated that, with remote sensing, it is possible to gather information on discontinuities on inaccessible slopes.

With the help of more sophisticated analogue photogrammetric equipment, such as the Zeiss stereotope, it was possible to create a more accurate height model from a stereoscopic model of a series of stereo photographs. Normally used for stereo airphotography, the photogrammetric principles and equipment could also be used with terrestrial photography of near-vertical, or vertical, rock faces. The height in this case would then be the horizontal surface variations of the rock face. The orientation of the joint surfaces can subsequently be derived from the surface angles obtained from the height model. The stereoscopic model could be created using any pair of stereo photos as long as a sufficient number of control points were gathered from the terrain and slope. Another possibility is to make stereo photographs under ideal photogrammetric conditions with a phototheodolite. Using the camera calibration data (focal point, etc), the height model can be created without the ground control points.

3.6.1.2 Analytical photogrammetry

Later, combined analogue and digital systems, also referred to as analytical photogrammetric systems came on the market that could be used for terrestrial mapping, an example of which is the Zeiss Stereocord stereoplotter (Hobbie, 1979). The basic equipment of the Stereocord consists of an opto-mechanical unit for viewing and measuring stereo photo pairs, an electronic unit for counting and viewing image coordinates and a desk computer for calculating the (3-D) ground coordinates. This system also allowed the computation of distances, slopes, angles, areas and volumes. More advanced, but similar analytical systems were put on the market in the end of the 1980's, such as the Adam MPS 2 Micro stereoplotter. This system had the advantage of using photographs from normal consumer cameras and it delivered the necessary software as FORTRAN code that could be run on widely available low-cost personal computers. Hagan (1980) also

demonstrated that it is possible to derive discontinuity orientations using an analytic photogrammetric approach in underground mines.

3.6.1.3 Digital photography and image analysis for feature extraction

Recent advances in digital photography and the possibilities of digital image processing created many new applications for rock mass characterisation. Fractures and lineaments that can easily be recognised on photographs could now be delineated with computer-based image enhancement, edge detection, and other advanced digital image processing techniques (Franklin et al., 1988). The assumption here is that discontinuities will create (even in a smooth rock face) a linear depression that creates shadow, which in turn can be recognised having a lower brightness value in a grey-scaled image. This difference in brightness values of digital rock face imagery is also used by Reid (1998) and Reid and Harrison (2000) as an input for a semi-automated method for discontinuity trace detection. Auto-delineation routines based on the Hough transformation proved to be very advantageous as well (Post et al., 2001; Post, 2001). The problem is that a fracture detected on an image is still 2-D information and gives only information on the angle of the trace and not on the 3-D orientation of the discontinuity planes that formed this trace. However, Kemeny and Post (2003) have been able to develop a method to determine three-dimensional fracture orientations from two-dimensional fracture trace information. The basis for this method are mathematical relationships that can relate a joint set, with a known mean strike and dip and Fisher constant K, to the resulting trace angles on one or more rock faces. These relationships assume that the rock face is relatively flat and that the camera is perpendicular to the rock face. The actual rock faces are not flat, thus an inverse routine was developed that allows the 3-D face geometry information to be combined with the observed fracture orientations, so that the 3-D fracture orientations can be estimated from the two-dimensional trace information.

3.6.1.4 Digital photogrammetry for topographic surface modelling

With the advent of computing and imaging technology, photogrammetry has evolved from analogue to analytical to digital photogrammetry. However, the objective of digital photogrammetry is the same as with traditional photogrammetry, i.e., to establish the geometric relationship between an object and an image and derive information about the object strictly from the image. In analogue and analytical photogrammetry a very labour-intensive process was involved to manually compare the stereo photos in order to create the geometric (elevation) information. With digital photogrammetry, the process of comparing the imagery and finding similar points can be done in an automated way using image matching techniques. Image matching is the technique of searching between two image pairs for a large number of image pixels that are similar. The introduction of digital image matching greatly accelerated the extraction of the surface geometry. Finally, with the camera calibration parameters and a number of control points in the scene, the digital three-dimensional surface can be generated rapidly and precisely.

3.6.1.5 Digital photogrammetry for characterizing rock slopes

A few commercial applications utilising digital photogrammetry principles have been developed for characterising rock masses. The main examples are two Australian systems called *Sirojoint* and *Sirovision* (Roberts and Poropat, 2000; Poropat, 2001; 2006; Surpac, 2006), and the Austrian system called *Jointmetrix 3-D* (Fasching et al., 2001; Gaich et al., 2004). The development of these systems was undoubtedly triggered by the arrival of high quality and affordable digital cameras and new computing and software capabilities for the required image matching. Both systems have a common main objective of deriving discontinuity orientation information based on a 3-D (reconstructed) surface. The 3-D surface is reconstructed on the basis of a 3-D point cloud that is made with digital photogrammetric techniques. In both systems, the orientation information is generated by the end-user who has to manually identify on a 3-D virtual surface model the discontinuity surfaces (by pointing, tracing or outlining), after which the orientation is computed. A recent attempt documented by Roncella and Forlani (2005) used a photogrammetric surface model of a rock slope to extract discontinuity orientations in an automated way based on point cloud segmentation techniques, a similar technique to that applied in this thesis. Roncella and Forlani

(2005) claim that the segmentation technique will work equally well with point clouds from photogrammetry and with point cloud data generated from terrestrial laser scan surveys. Some recent successful applications of the the Sirovision photogrammetric system for rock mass characterisation are demonstrated in the publications by Haneberg et al. (2006) and Haneberg (2007, 2008).

3.6.1.6 Photo total station

A relatively new system is the photo total station system (PTSS). Zhang et al. (2004) describe the PTSS as a new surveying system that combines digital photogrammetry techniques with a total station. Compared with traditional terrestrial photogrammetry, the advantage is that ground control points in the target scene are not needed anymore, since they can be measured with the range measuring device of the total station.

3.6.2 Laser measurements

Laser ranging devices, often also referred to as *Lidar*[6] methods, have become an important new source of spatial information to the geosciences during the past decade. The most widely adopted technique employs a laser ranging device in an aircraft to very precisely measure the distance between the aircraft and the ground surface. Provided the location and attitude (pitch and yaw) of the aircraft platform are known, these measurements can be converted into highly detailed digital elevation models (DEM). GPS and inertial guidance systems can provide the required information concerning the location and attitude of the aircraft platform, and improvements in these technologies, along with improved laser systems, now provide excellent options for obtaining detailed elevation data at reasonable cost.

Over the same time period, other researchers considered the problems of adapting laser techniques to ground-based (terrestrial) surveys. The first applications involved placing a laser ranging device on a total station theodolite, thus creating the *reflectorless total station* that is further discussed in Section 3.6.2.1. Subsequently, others adapted the airborne laser scanning technologies to create a terrestrial laser scanner that could be mounted on a typical surveyor's tripod. Because these terrestrial laser scanners were stationary and maintained a constant field of view during the collection of a single set of scanned data, they could avoid the need to use the very expensive inertial directional monitoring systems. Furthermore, the location and orientation of the scanner could be determined by standard ground-survey techniques.

3.6.2.1 Laser-transit or reflectorless total station

Ilsley (1994) and Bracco Gartner and Schlager (1997) used what they called a *laser-transit* system for detailed mapping of rock slopes, for engineering geological mapping and rock face topography mapping, respectively. The laser-transit system that was used in these two studies is in fact a total surveying station, which is theodolite that uses a laser to measure the target distance. This is also called a reflectorless total station, since the laser that is used has enough energy to allow natural surfaces to reflect the laser beam.

Feng et al. (2001) took this a step further and have measured discontinuity orientations with a non-reflector total station. This study suggested that the total station offered a better alternative to collecting accurate discontinuity orientations compared to traditional compass-clinometer measurements.

Reflectorless total stations determine the orientation of a discontinuity plane on the basis of a number of individual total-station-based point measurements. The total station uses the laser to measure the distance to any target point. On the basis of the horizontal and vertical angle of the laser beam that is recorded by the total station, the three-dimensional coordinates of the target point (P_i) can be computed by the relationships shown in Equation [10]:

[6] Lidar is the acronym for Light Detection And Ranging

$$x_i = L\cos(\alpha)\sin(\theta)$$
$$y_i = L\cos(\alpha)\cos(\theta) \quad [10]$$
$$z_i = L\sin(\alpha)$$

Where:

- L is the measured distance to target Pi
- α is the vertical angle or zenith of the laserbeam (from -90 to + 90 degrees)
- θ is the horizontal angle or azimuth of the laserbeam (from 0 to 360 degrees)

If the total station is accurately referenced, i.e., if the azimuth value 0 or 360 is oriented to the North and if the total station is perfectly levelled so that a laser beam with a vertical angle of 0 degrees is perfectly horizontal, then the measurement can directly be used to compute the actual orientation of a discontinuity plane.

In theory, as will be discussed in Section 3.7.1, a minimum of 3 coordinate measurements per discontinuity plane is sufficient to compute the orientation of a discontinuity plane that is smooth and flat. Reflectorless total stations record the locations of individual points with great accuracy and, although they can be programmed to rapidly locate a series of individual points, their design is not very suitable for locating extremely large numbers of points over an entire set of discontinuities. The operational complexity of measuring discontinuity planes by manually pointing the laserbeam is very high and it will take a very long time to gather a sufficient amount of data.

From an operational point of view, 3-D terrestrial laser scanning is a better option since the manual adjustment of the bearing of the laser beam is omitted. Although terrestrial laser scanners generate much greater densities of survey points, the geometric principles of computing the geometric properties of discontinuities are the same for both data sources.

3.6.2.2 3-D terrestrial laser scanning

Three-dimensional laser scanning as a terrestrial survey technique arrived on the market as a commercial product only in the late 1990's. One of the first terrestrial laser scanners was the Cyrax scanner developed by the company Cyra. Cyra was soon acquired by Leica Geosystems that used the technology to successfully develop their own series of laser scanners. This indicated the significance of this new technology. At the same time other surveying companies, such as Riegl, Mensi, Trimble, Optech, Zoller+Fröhlich and Q-tech also developed and launched successfully their own terrestrial laser scanners. The products were so successful because a wide range of disciplines recognised the huge potential of the technology. The biggest advantages are the rapidity of the survey, and the high accuracy and high resolution of the data. Different application fields, such as architecture, the chemical industry, civil engineering, mining, and even crime scene investigators, found terrestrial laser scanning useful. The fact that it is a new technology makes the application still relatively expensive. However, since the market became so large, the technological development is very fast. This results in increasingly accurate, fast and innovative scanner models at relatively lower prices, which is very promising for the future.

The potential for rock face scanning soon became evident. Poropat (2001), Feng (2001), Slob et al. (2002, 2004), Kemeny et al. (2003), Feng and Röshoff (2004) and Lemy and Hadjigeorgiou (2004) were the first authors to publish on the derivation of discontinuity properties from scans of rock faces. Although the data used by Poropat (2001) was derived from photogrammetric survey, it was recognised that the use of laser scanning could provide a number of important advantages. Feng (2001) was the first to investigate the potential of three remote sensing methods: a reflectorless total station, photogrammetry and (phase-based) laser scanning for mapping fracture geometry. The conclusion of this study was that (phase-based) laser scanning is the most favourable technique, particularly if the technique can be combined with accurate georeferencing with a total

station. Slob et al. (2002, 2004) published on the possibility of automatic derivation of discontinuity parameters from the point cloud data.

Kemeny et al. (2003) discussed the advantages of combining laser scanning with digital imaging. The problem with laser scanning is that it is not possible to derive orientations if discontinuity planes are not well exposed on, for example, smooth rock faces or tunnel walls. The use of image analysis is highly complementary, since it is possible to derive the discontinuity traces from the imagery. By combining the two-dimensional discontinuity trace image with the 3-D laser data, three-dimensional discontinuity orientations can be computed.

3.7 Analysis of discontinuity data

Regardless of the data collection source, the collected discontinuity data must be appropriately presented to allow for evaluation and analysis. Discontinuity data can be displayed, for example, on a scale drawing or on panoramic photographs of the rock face. However, this does not allow for the quantitative assessment of orientation and spacing. Sometimes it is not possible to immediately recognise the main discontinuity sets in the field and assess their average orientations. Statistical analysis and appropriate visualisation of the discontinuity orientation data allow for the resolution of such issues.

Analytical geometry methods of analysing the orientation and placement of planar elements in 3-D space provide the basis of many graphical and statistical evaluation methods. Section 3.7.1 describes the computation of planar orientations.

When data collection depended upon manual methods involving measuring tape and compass, the total volume of measured discontinuity orientations remained modest; rarely were more than a few hundred observations collected. Also, numerical computations were tedious before computers became readily available. Thus graphical methods of reducing, summarizing, and interpreting discontinuity data became the favoured method of analysis. A rose diagram displays directional data, while also providing some statistical properties. It shows the frequency as a function of the dip direction, but is not able to show any information on the dip amount. Thus, a rose diagram is more suited to the analysis of two-dimensional directional data, such as traces of faults or lineaments. Experience has shown that a *hemispherical projection* provides a more appropriate way of presenting three-dimensional orientation data (Hoek and Bray, 1981 and Priest, 1980 and 1985). Discontinuity spacing data is generally statistically represented in the form of *histograms*. Several graphical presentation methods are described in Section 3.7.2.

With the development of new data collection methods that provide vastly greater data volumes, coupled with increased demands from the engineering community for more precise characterisations of rock mass properties, alternatives to the traditional graphical solution methods became a high priority. Statisticians had developed appropriate methods for analysing directional data in both 2-D and 3-D environments (Fisher, 1953; Mardia, 1972). These methods allowed for the characterisation of not only smooth planar discontinuities, but also more complex situations involving variations in orientation within individual sets of discontinuities. Subsequently these numerical methods were further extended to the analysis of variability through the adaptation of *fuzzy set theory* first proposed by Zadeh (1965), but not applied to the analysis of uncertainty in natural data until much later (Bezdek, 1981; Harrison, 1992). Sections 3.7.3 and 3.7.4 discuss these topics.

3.7.1 Computation of planar orientations

A minimum of 3 coordinate measurements per discontinuity plane is sufficient to compute the orientation of a discontinuity plane that is smooth and flat. The computation of the plane through three points is basic algebra and is simply the solution to the plane equation defined by Equation [11]:

$$ax + by + cz + d = 0 \quad [11]$$

Where d is the perpendicular distance of the plane to the origin. The parameters a,b and c form the normal vector n to the plane, as shown by Equation [12]:

$$\vec{n} = \begin{pmatrix} a \\ b \\ c \end{pmatrix} \quad [12]$$

If the orientation of the plane is know, the plane equation can be written in terms of its dip direction and dip angle:

$$\sin(\theta)\sin(\gamma)\ x + \cos(\theta)\sin(\gamma)\ y + \cos(\gamma)\ z + d = 0 \quad [13]$$

Where:

- θ is dip direction (or azimuth) of the plane (from 0 to 2π)
- γ is dip angle (or plunge) of the plane (from 0 to ½ π)

The way that the plane equation is formulated in Equation [13], on the basis of the three parameters *θ*, *γ* and *d*, is used later in the 3-D Hough transform for converting point cloud data from Euclidean space to a parameter space (see section 6.6.4).

Mathematically, the parameters *a, b, c* and *d* can be found by solving the system of equations through substitution of the coordinates *x, y,* and *z* of any three points *P1*, *P2* and *P3* that fall on the plane. Another way of finding the parameters to the plane equation is by determining the normal n to the plane directly through the cross product of two vectors that are spanned by the three points. Let point P1 have the coordinates *(x1, y1, z1)*, P2 *(x2, y2, z2)* and P3 *(x3, y3, z3)*. Then, as shown by Equation [14], the two vectors *r* and *s* that lie in the plane may be defined as shown below:

$$\begin{aligned} \vec{r} &= P_2 - P_1 = \begin{pmatrix} x_2 - x_1 \\ y_2 - y_1 \\ z_2 - z_1 \end{pmatrix} \\ \vec{s} &= P_3 - P_1 = \begin{pmatrix} x_3 - x_1 \\ y_3 - y_1 \\ z_3 - z_1 \end{pmatrix} \end{aligned} \quad [14]$$

Subsequently, the normal vector *n* is defined by the cross-product of vectors r and s, since the result of the cross-product is a vector that is always perpendicular to both vectors r and s. This is shown by Equation [15]:

$$\vec{n} = \begin{pmatrix} a \\ b \\ c \end{pmatrix} = \vec{r} \times \vec{s} = \begin{pmatrix} (y_2 - y_1)\cdot(z_3 - z_1) - (z_2 - z_1)\cdot(y_3 - y_1) \\ (z_3 - z_1)\cdot(x_3 - x_1) - (x_2 - x_1)\cdot(z_3 - z_1) \\ (x_2 - x_1)\cdot(y_3 - y_1) - (y_2 - y_1)\cdot(x_3 - x_1) \end{pmatrix} \quad [15]$$

Knowing the parameters a, b and c, the final parameter d is found by substituting the coordinates of any of the three points into the plane equation (see Equation [11]). The direction of the normal is defined by the right-hand rule. Knowing the normal, the orientation of the plane in degrees can be calculated accordingly:

The dip angle is:

$$\gamma = \arccos|c| \quad [16]$$

The dip direction is:

$$\theta' = \arccos\left(\frac{|b|}{\sqrt{a^2 + b^2}}\right) \quad [17]$$

Of course, there is a special situation where *a* and *b* are both zero. This is the case when the normal is pointing upwards (*c* = 1), which makes the plane horizontal. In this case there is no dip and no dip direction, i.e. the plane has by definition an orientation 000/00. In order to find the correct dip direction, the quadrant in which the dip direction falls must be established. Then the correct direction can be determined using the criteria in Table 3.1. It is assumed here that the normal is pointing upward, i.e. that c is positive. If this is not the case then the direction of the normal vector is simply reversed by multiplying with a factor -1.

If the plane is curved and rough, it is advisable to take more than three measurements to get a better representation. The computation of the best fit plane (using, for example, a least-squares method, principal component analysis, or Hough transform) to more than three points becomes computationally slightly more complicated than the example just discussed, but will result in a better estimate of the discontinuity orientations. One way of calculating the equation of the plane on the basis of more than three points is with principal component analysis. This method will be covered in Section 6.6.6.

Table 3.1. Criteria to establish in which quadrant the dip direction fall, in order to determine the actual dip direction with Equation [17].

Criteria 1	Criteria 2	Quadrant	Dip direction θ
$a \geq 0$	$b \geq 0$	I (between 0° and 90°)	$\theta = 90 - \theta'$
	$b < 0$	II (beween 90° and 180°)	$\theta = 90 + \theta'$
$a < 0$	$b < 0$	III (between 180° and 270°)	$\theta = 270 - \theta'$
	$b \geq 0$	IV (between 270° and 360°)	$\theta = 270 + \theta'$

3.7.2 Graphical presentations and descriptive statistics

3.7.2.1 Hemispherical projections

Hemispherical projection of discontinuity data is similar to the projection systems used by geographers to represent the spherical shape of the earth on a flat surface. The principle of hemispherical projections of discontinuity data is that the three-dimensional planes are represented (projected) in the form of great circles or poles on the two-dimensional projection plane using a reference sphere. The projection of a plane works as follows:

1. A reference sphere is moved such that the centre of the sphere is located on the plane. The sphere can move laterally but is not able to rotate; hence it has a fixed orientation in space.
2. In this way all the discontinuities can be represented in the same sphere in terms of orientation, independent of their position in space.
3. The intersection of the plane with the reference sphere forms a *great circle* on the sphere.
4. The great circle can then be projected using the upper or lower reference hemisphere onto the horizontal reference plane.

In engineering geological applications, the lower hemisphere projection is normally used for the presentation of data.

The dip angle and dip direction of a plane can also be represented by the normal vector to that plane. The point where the normal vector intersects the reference plane can then be projected as the *pole* to the plane. The projection can be done using a *polar projection* or an *equatorial projection*.

There are several types of spherical projections. The two main types are:

- Equal area projection or Lambert projection. This projection preserves the spatial distribution of features. This projection is suitable for statistical distribution analysis while it also allows planes and lines to be plotted, although with reduced accuracy. Angular relationships are not preserved. An equal area stereonet is also referred to as the *Schmidt net*.
- Equal angle projection or stereographic projection. This projection preserves the angular relationships between features. Similar distances in the projection plane or net correspond to similar angles in three-dimensions. The equal angle projection offers advantages when used for geometrical construction and finds applications in block theory (Goodman and Shi, 1985) and in slope stability analysis. An equal angle stereonet is also referred to as the *Wulff net*.

3.7.2.2 Hemispherical pole plots

When dealing with larger volumes of orientation data, it becomes unworkable to represent the planes in the form of great circles. In this case it becomes attractive to use the representation of the planes in the form of poles, a so-called polar plot. A polar plot is helpful in identifying discontinuity sets. Poles to discontinuity planes that are more or less parallel and thus have a similar orientation will plot in the vicinity of each other in a polar plot. Discontinuity sets may thus be identified on a polar plot as distinct clusters of poles. The difficulty lies in accurately defining the boundary and centre of clusters. With relatively small numbers of measured orientations from distinctly different sets, it is simple to identify the sets from the polar plot. There are a number of situations that make the interpretation of the plots more complex because they result in fuzzier clusters of poles. The four most important situations are:

- Random fractures[7]. These may be the result of blasting or breaking of intact rock that do not follow any pre-existing structural trend in the fabric of the rock mass.
- Curved discontinuity surfaces. Curved or undulating surfaces do not have a single pole that represents its orientation but exhibit variation that may show as an elongated cluster of poles (Bingham orientation model) in the projection. Within the exposure, bedding planes may, for example, be deformed due to tectonic activity, resulting in similarly elongated plots.
- Non-parallel sets. Some sets contain discontinuities that are not necessarily exactly parallel, but show a certain degree of deviation from the average trend.
- Orientations from different units. A rock face may contain different engineering geological rock units with distinctly different fracture patterns. If the discontinuity orientations of the various units are mixed and plotted together in the polar plot, it will become more complex to separate the sets statistically.

3.7.2.3 Graphical analysis of pole plots

Graphical analysis of the poles in the projected equal area plane may be used to identify dispersed (or 'fuzzy') clusters of discontinuity orientations. A common method is to compute the contours of pole density. Various spatial techniques have been proposed, but the most popular technique is the counting circle (Hoek and Bray 1981; Priest, 1993). This technique uses a sampling circle with a diameter whose area represents 1% of the total area of the projection plane. The circle is subsequently placed on the equal area net and the number of poles are counted and returned in terms of percentage of the total number of poles. The sampling circle can be moved over the projection plane according to a grid system or in a random manner as a floating circle. When the counting circle approaches the edge of the equal area net, the part of the circle that extends beyond the edge of the net should be continued to include the poles enclosed by this extended area on the opposite side of the net. In this way, the concentrations are correctly counted. The returned pole concentrations can then be contoured to facilitate the interpretation. The local concentrations in pole density may thus represent the average orientation of a specific discontinuity set ant the number of local peaks may represent the number of discontinuity sets.

[7] Fractures are never completely random but always follow some form of internal weakness structure.

Geologists have used these graphical analysis methods for many years. Details of the different sampling methods are given in Hoek and Bray (1981), Matherson (1983), and Priest (1993). At present there are numerous computer applications that facilitate the plotting and contouring of discontinuity data. These applications allow the use of various averaging and contouring algorithms with different selectable parameters. These computer-based methods should be used with care, since it is not always evident which algorithms and parameters are actually applied.

3.7.2.4 Spacing distribution histograms

Histograms are the optimal way of displaying spacing data. They are created by plotting the frequency of occurrence of the measured discontinuity spacing values within a series of spacing ranges. The histogram thus presents the distribution of the observed spacings for either individual discontinuity sets or for all discontinuity data. Most discontinuity sets show a tendency to follow a fractal or lognormal distribution of spacings (Hobbs, 1993). However, over small ranges of spacing, Weibull, or sometimes Negative exponential distributions may also be applicable. Priest and Hudson (1976) described and illustrated the difference between Negative exponential, Uniform and Normal distributions of spacings (see Figure 3.9). Kulatilake (1993) also mentioned the Gamma distribution to describe the distribution of discontinuity spacings.

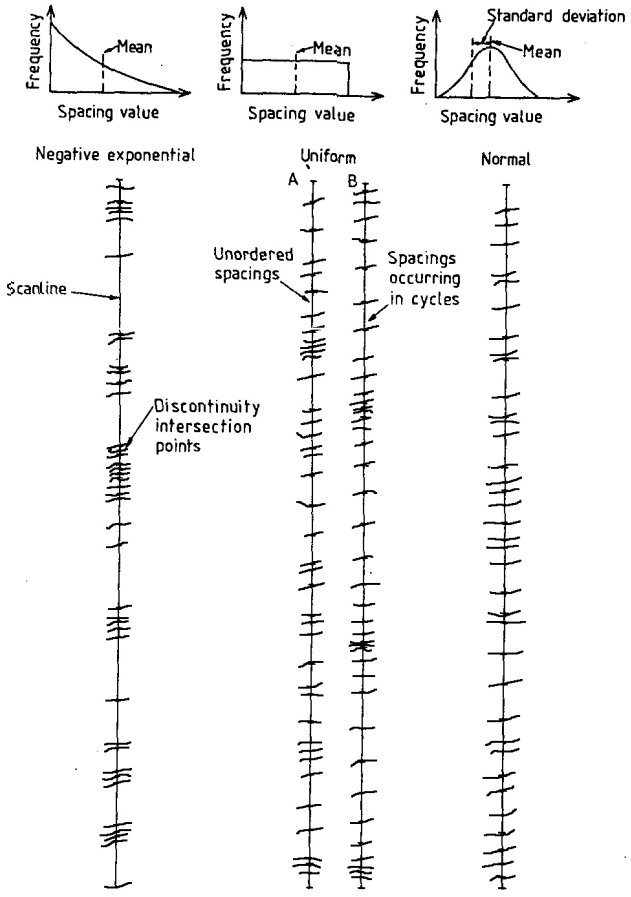

Figure 3.9. Intercepts along scanlines for negative exponential, uniform and normal spacing distributions. (from: Priest and Hudson, 1976)

In order to compute a histogram showing the spacing distribution, a sufficient number of measurements are required. At least 30 spacing measurements for each discontinuity set are necessary to make a statistically reliable estimate of the spacing distribution for that set. If a fractal dimension is to be computed, as many as 150 measurements for each discontinuity set along each scanline are required (Ehlen, 2000).

A strong negative exponential trend in the spacing data means a relative large influence of the occurrence of small discontinuity spacings. The larger spacings in the data will in this case be underrepresented in a histogram representation since the frequency of occurrence is small.

Although the occurrence is small, the relative geometric influence on the overall rock mass properties is much larger, since the large spacings will result in much larger block sizes than the small spacings would imply. In order to represent the larger spacings better, a logarithmic conversion of the spacing distances can be used with a histogram representation in the form of a logarithmic frequency distribution.

3.7.3 Spherical directional statistics

The clusters that are recognised in the hemispherical projections mostly exhibit a specific distribution character or shape. These specific shapes are called orientation models. The most common are the Fisher distribution (see Figure 3.10a) and the Bingham distribution (see Figure 3.10b).

The Fisher Distribution is the most widely used distribution for modelling 3-dimensional orientation vectors (Fisher, 1953). It describes the angular distribution of orientations with two parameters: a mean vector direction θ, and a dispersion κ; because the dispersion is assumed to be symmetric about the mean direction. As a consequence, clusters of poles following the Fisher Distribution will plot as a circular pattern on hemispherical pole plots (Figure 3.10a).

In contrast, the Bingham Distribution forms asymmetrical elliptical patterns in a hemispherical projection (Figure 3.10b). It requires additional parameters to define the elliptical pattern of the dispersion about the mean direction. The Bingham Distribution can represent the orientation of curved or wavy discontinuity surfaces (Bingham, 1964). The literature discusses additional spherical models, such as the Kent distribution (Kent, 1982) and the Watson distribution (Fisher, et al., 1987).

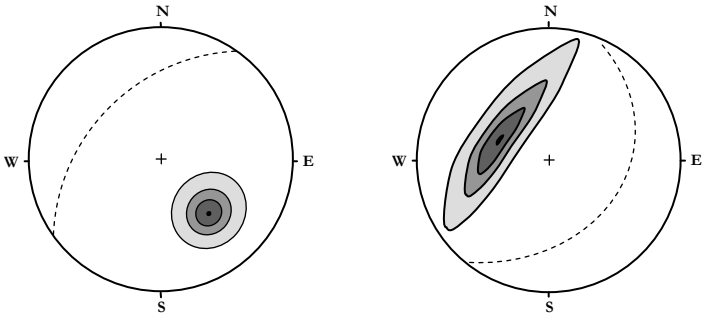

(a) Fisher distribution (b) Bingham

Figure 3.10. Two types of spherical data distributions. (a) Illustrates a typical circular Fisher Distribution. (b) Illustrates a typical Bingham Distribution, typical for undulating or curved discontinuity surfaces.

Normal statistics do not apply for the analysis of directional data. For example, computation of the mean vector orientation, and the dispersions about this mean direction, requires the use of direction cosines, or eigenvalues and eigenvectors, of the normal vectors to the discontinuity planes (see Section 3.7.4). Similarly, the angular difference between two unit (normal) vectors cannot be computed by the simple subtraction of dips and dip directions; rather the dihedral angle or pole vector difference φ between the two normal vectors n_A and n_B must be defined as shown by Equation [18]:

$$\cos(\varphi_{AB}) = \bar{n}_A \bullet \bar{n}_B \qquad [18]$$

Field measurements of discontinuity orientations are generally recorded as dip angles and dip directions. In order to carry out directional statistics computations, the dip angles and dip directions must be converted from their spherical coordinates to three-dimensional Cartesian coordinates. Using the common convention for orientations, i.e., 0 and 360 degrees define North, and assuming

that in the Cartesian coordinate system, the positive Y-axis corresponds to North and the positive X-axis corresponds to East, then the pole unit vector to a plane, directed upwards in the positive Z axis, can be converted as shown by Equation [19]:

$$\begin{aligned} x_i &= \cos D_i \sin A_i \\ y_i &= \cos D_i \cos A_i \\ z_i &= \sin D_i \end{aligned} \qquad [19]$$

Where:

- D_i is dip angle of the pole of a plane i
- A_i is dip direction of the pole of a plane i
- x_i, y_i and z_i are the direction cosines[8] of the normal vector to the *i*-th plane

Because the pole is a unit vector the following is always valid:

$$x_i^2 + y_i^2 + z_i^2 = 1 \qquad [20]$$

3.7.3.1 Resultant vector length

The mean direction of a sample of *N* unit vectors can be computed using the resultant *R,* the magnitude of the resultant vector. This is the magnitude of the vector sum of all (normalised) pole vectors in the data set and can be calculated using Equation [21]:

$$R = \sqrt{\left(\sum_{i=1}^{N} x_i\right)^2 + \left(\sum_{i=1}^{N} y_i\right)^2 + \left(\sum_{i=1}^{N} z_i\right)^2} \qquad [21]$$

The normalised form of the resultant vector, *R*, is called $\bar{R}$ and is defined by Equation [22]:

$$\bar{R} = \frac{R}{N} \qquad [22]$$

The projection of the resultant *R* to the (horizontal) XY-plane is *r*:

$$r = \sqrt{\left(\sum_{i=1}^{N} x_i\right)^2 + \left(\sum_{i=1}^{N} y_i\right)^2} \qquad [23]$$

The dip angle of the resultant *R* is the mean dip angle of the *N* samples:

$$D_R = \arccos \frac{\left|\sum_{i=1}^{N} z_i\right|}{R} \qquad [24]$$

The dip direction of the resultant *R* is the mean dip direction of the *N* samples:

$$A_{R'} = \arccos \frac{\left|\sum_{i=1}^{N} y_i\right|}{r} \qquad [25]$$

Equation [25] does not directly provide the actual dip direction, since the resulting values of $A_{R'}$ ranges between 0 and 90 degrees, while the actual dip direction ranges between 0 and 360

[8] The direction cosines are the cosines of the angles that the normal vector to a discontinuity plane makes with the *x*, *y* and *z* coordinate axes, respectively.

degrees. To determine the correct dip direction $A_{R,}$ the quadrant in which the dip direction falls must be established. Then the correct direction can be determined using the criteria in Table 3.2.

If the N unit vectors are tightly clustered around a common direction, the resultant R will approach N, since each of the input vectors have unit lengths. If the orientations are widely dispersed, R will be small. Thus, R can be used as a measure of concentration. However these values are not intuitive; since a small R value corresponds to highly dispersed orientations.

Table 3.2. Criteria to determine the Quadrant and therefore the right dip direction of the resulting vector R.

Criteria 1	Criteria 2	Quadrant	Dip direction A_R
$\sum_{i=1}^{N} x_i \geq 0$	$\sum_{i=1}^{N} y_i \geq 0$	I (between 0° and 90°)	$A_R = A_{R'}$
	$\sum_{i=1}^{N} y_i < 0$	II (beween 90° and 180°)	$A_R = 180 - A_{R'}$
$\sum_{i=1}^{N} x_i < 0$	$\sum_{i=1}^{N} y_i < 0$	III (between 180° and 270°)	$A_R = 180 + A_{R'}$
	$\sum_{i=1}^{N} y_i \geq 0$	IV (between 270° and 360°)	$A_R = 360 - A_{R'}$

3.7.3.2 Spherical variance

Most people using traditional statistics are familiar with variance, and know that the variance has small values (approaching zero) when the data have a small variation, and large values when the data are highly variable. Thus the concept of *spherical variance (s^2)* has been developed (Davis, 2002) according to the definition shown by Equation [26]:

$$s_s^2 = \frac{N - R}{N} = 1 - \bar{R} \qquad [26]$$

3.7.3.3 Fisher's constant K

By analysis of Equation [26], it can be seen that the spherical variance will range from nearly zero for tightly clustered vectors with a nearly consistent orientation, to nearly 1.0 for a set of highly variable vectors (with an R value of nearly zero). Because the spherical variance has such a small range, an alternate dispersion factor, known as the *"Fisher constant" K,* can be calculated by Equation [27]:

$$K = \frac{N - 2}{N - R} \qquad [27]$$

Where:

- K is the Fisher's constant
- N is the number of sampled poles, where $N \geq 10$

The relationship defined by Equation [27] is sufficiently accurate for "larger" K values or greater than about 10 (Davis, 2002). The Fisher constant is often used as a means to determine how well a sampled set of cluster values defines a specific discontinuity set (Mardia, 1972; Priest, 1993 and Borradaile, 2003).

By examination of Equation [27] it can be observed that a large dispersion of pole vectors produces a small resultant vector (R); thus the numerator ($N - 2$) and the denominator ($N - R \approx N$) are almost equal, and therefore Fisher's constant K is close to 1.0. In contrast, if the dispersion is small and all vectors point in approximately the same direction, then the magnitude of the resultant vector R will

be very high, approaching *N,* and the denominator will approach zero. Thus the Fisher's constant *K* will become extremely large, approaching infinity in the limit.

3.7.3.4 Principal Component Analysis

Another way of computing average orientation from a set of orientation data is by eigenvector analysis or *Principal Component Analysis* (Markland, 1974; Fisher et al., 1987). Given *N* observations, the mean orientation can be determined by calculation of the eigenvalues of the covariance matrix of the direction cosines (x_j, y_j, z_j) of the normal vectors. The covariance matrix (S) is calculated in the following way:

$$S = \begin{bmatrix} \sum_{j=1}^{N} x_j^2 & \sum_{j=1}^{N} x_j y_j & \sum_{j=1}^{N} x_j z_j \\ \sum_{j=1}^{N} x_j y_j & \sum_{j=1}^{N} y_j^2 & \sum_{j=1}^{N} y_j z_j \\ \sum_{j=1}^{N} x_j z_j & \sum_{j=1}^{N} y_j z_j & \sum_{j=1}^{N} z_j^2 \end{bmatrix} \quad [28]$$

The next step is to calculate the eigenvalues (τ_1, τ_2, τ_3) and their corresponding normalised eigenvectors ($\hat{\xi}_1, \hat{\xi}_2, \hat{\xi}_3$) from the covariance matrix. The mean orientation of the *N* observation is the eigenvector ($\hat{\xi}_3$) that is associated with the largest eigenvalue (τ_3). This is an effective way of handling orientation data, which is also used in the following section on fuzzy k-means clustering of directional data (3.7.4). The method of principal component analysis proves also to be a useful in another way, as a mathematical technique to calculate planar trends in the point cloud data. The principle component analysis is further discussed in Section 6.6.6, where also the computation of the eigenvalues and eigenvectors is demonstrated.

3.7.4 Fuzzy K-means clustering of directional data

When dealing with small amounts of directional data from well-defined discontinuity sets, the identification of these sets in a stereographic polar plot is often straightforward and intuitive and is mostly done visually where clusters can be manually outlined. However, with large amounts of directional data that is also noisy and/or show a large dispersion, it becomes much harder to objectively and accurately identify and outline potential discontinuity clusters and subsequently cluster the poles to the various sets. It becomes also very time-consuming to classify each single data point by hand. In this case it is better to resort to objective statistical data analysis techniques called *data clustering*. Data clustering partitions the data set into subsets, in this case these are the discontinuity sets. There are various ways of data clustering which fall into two general categories: *hierarchical* and *partitional* techniques. *Fuzzy k-means clustering* is a popular partitional clustering technique (Afifi et al, 2004).

Fuzzy k-means is also a data clustering technique that has successfully been applied to orientation data of discontinuities (Harrison, 1992; Hammah and Curran, 1998; 1999; 2000; Zhou and Maerz, 2002; Slob et al., 2005). Fuzzy k-means clustering classifies each orientation measurement to a pre-defined number of clusters (k). Fuzzy k-means clustering is a soft (fuzzy) clustering scheme, because it partitions the data set according to the degrees of membership assigned to each set. The degree of membership ranges from zero to one and the larger the confidence is that a pole belongs to a set, the closer the membership value reaches the value 1.

The fuzzy k-means method (sometimes also referred to as *fuzzy c-means* or *fcm*) was first conceptualised by Zadeh (1965), but it took some time to be applied to the analysis of discontinuity orientation data (Harrison, 1992). Fuzzy k-means is based on the *fuzzy set theory*, which has become a widely accepted method to account for uncertainty in data in a realistic and natural manner (Bezdek, 1981) and has successfully applied in fields like pattern recognition, image processing and neural networks (Zhou and Maerz, 2002). Hammah and Curran (1998) state that

fuzzy k-means is the optimal method for the clustering of directional data of discontinuities for rock mechanical purposes. The main reason is that is generally very difficult to delineate crisp boundaries between the discontinuity sets, since directional data from discontinuities inherently exhibit a fuzzy character. The underlying algorithms are also better suited to orientation data of discontinuities, because they are less susceptible to outliers (noise, errors and blunders) than other (hierarchical) classification methods.

In this study a modified fuzzy k-means clustering algorithm has been applied which is largely based on the method outlined by Hammah and Curran (1998). Because the orientation data is in the form of projected poles of the planes, the distance between the vector normals (for both the observations and the cluster centroids) is here computed along the unit sphere. The method applies eigenanalysis to determine the cluster centres, and contains some other modifications to enhance the performance. The largest advantage of the fuzzy k-means method is that is allows automated clustering of orientation data once the number of sets has been identified. Another advantage is the potential to use discontinuity properties, such as roughness, spacing or persistence as additional cluster attributes. The use of these attributes has the potential to improve the clustering results and can also be used as a quality control to the clustering results. In the method by Hammah and Curran (1998) the assumption is made that the pole dispersion is non-uniformly, but isotropically distributed about the mean orientation of each discontinuity set, therefore showing a Fisher's distribution. Nonetheless, non-circular (e.g. Bingham) clusters that are well separated and equally distributed with respect to each other can be classified well.
In fuzzy k-means clustering, the following objective function (J_m) is minimized (iteratively) to achieve an optimal data set partitioning (Bezdek, 1981):

$$J_m = \sum_{j=1}^{N}\sum_{i=1}^{C}(u_{ij})^m d^2(P_j, V_i) \qquad [29]$$

Where:

- C is the number of clusters
- N is the number of poles ($C \leq N$)
- $d^2(P_j, V_i)$ is the distance between projected pole P_j and the projected cluster centre V_i on a unit sphere. They are both direction cosines (see also equation [15]). In this projected (non-Euclidean) space, the sine (1-cosine) of the dihedral angle between the two normals or poles is a measure of the distance between the projected poles and can thus be used as the dissimilarity measure (Hammah & Curran, 1999):

$$d^2(P_j, V_i) = 1 - (P_j \bullet V_i)^2 \qquad [30]$$

u_{ij} is the degree of membership of data point (pole) P_j to cluster i, which is a function of the distances between this pole and the different centroids of the k clusters (Gath and Geva, 1989):

$$u_{ij} = \frac{\left[1/d^2(P_j, V_i)\right]^{1/(m-1)}}{\sum_{k=1}^{K}\left[1/d^2(P_j, V_k)\right]^{1/(m-1)}} \qquad [31]$$

m is a weighting exponent, which is often referred to as the *degree of fuzzification* that controls the "fuzziness" of the memberships. Although it should be a real number greater than 1, research has not yet resulted in an optimal value. The closer m is to 1, the harder the membership values will be (Hammah & Curran, 1999). However, $m = 2$ is thought to be the best for most applications and has often been a preferred choice for researchers (Pal and Bezdek, 1995; Bezdek, 1981; Gath & Geva, 1989).

For the calculation of cluster centres from the unit vectors or direction cosines, a mirrored vector can be used to treat antipodal (diametrically opposite) vectors (Zhou and Maerz, 2002). However,

since so many data points are involved, eigenanalysis is preferred, which avoid the need for keeping track of sign reversals involved in mirroring (Hammah and Curran, 1998). Ambiguity might take place from arbitrary distinction between antipodal vectors. For the *N* direction cosines (x_j, y_j, z_j) (note that these are not the point cloud coordinates), the mean orientation of a cluster can be calculated by determining the eigenvalues (τ_1, τ_2, τ_3) and their respective normalised eigenvectors ($\hat{\xi}_1, \hat{\xi}_2, \hat{\xi}_3$) of the following weighted orientation matrix S (Hammah and Curran, 1998):

$$S = \begin{bmatrix} \sum_{j=1}^{N} (u_{ij})^m x_j x_j & \sum_{j=1}^{N} (u_{ij})^m x_j y_j & \sum_{j=1}^{N} (u_{ij})^m x_j z_j \\ \sum_{j=1}^{N} (u_{ij})^m x_j y_j & \sum_{j=1}^{N} (u_{ij})^m y_j y_j & \sum_{j=1}^{N} (u_{ij})^m y_j z_j \\ \sum_{j=1}^{N} (u_{ij})^m x_j z_j & \sum_{j=1}^{N} (u_{ij})^m y_j z_j & \sum_{j=1}^{N} (u_{ij})^m z_j z_j \end{bmatrix} \quad [32]$$

The eigenvector $\hat{\xi}_3$ is associated with the highest eigenvalue (τ_3) that minimises the fuzzy objective function (Equation [29]) and the mean weighted vector of the group of *N* unit normal vectors can be defined according to Equation [33]:

$$\hat{V}_i = \hat{\xi}_3 \quad [33]$$

The advantage of this technique is that the eigenvalues are a direct measure of the spread and variance of the vectors in the principal directions and contains therefore important information about the shape of the cluster. The greater the ratio τ_2 / τ_1 the more elliptic the cluster shape is, following a Bingham distribution. If this ratio approaches one, its shape will be near circular or have a rotational symmetry, following a Fisher's distribution (Hammah and Curran, 1998). This characteristic can be used to outline clusters by removing measurements that contribute to large ratios and therefore result in a larger spread and variance.

The fuzzy k-means method requires an iterative procedure to arrive at the final orientation data clustering. This procedure is of course most easily implemented in a computer-aided environment in the following way:

1. Determine the number of clusters (*C*) contained in the orientation data (displayed in the form of poles in the stereo plot). This can in many cases be done visually, by the user, but the number of clusters can also be determined more objectively using cluster validity analysis (see Section 3.7.6).
2. Select the *C* initial cluster centroids, manually, randomly (using *C* random seed points from the dataset) or by certain definition, e.g. by choice of centroids that are specific distance apart from each other to ensure sufficient starting separation.
3. Calculate the distance (*d*) of the *N* observation to the *C* centroids with Equation 27.
4. Calculate the degree of membership (u_{ij}) of all *N* observations to the *K* clusters with Equation [31].
5. Calculate the new cluster centroids with the eigenanalysis of the fuzzy orientation matrix (*S*) with Equation [32].
6. Repeat the steps 3, 4 and 5, based on the cluster centroids that are calculated in the previous step. This iterative step is terminated if a certain criterion is met. For example, if the difference between the old and new degree of membership is smaller than a specific threshold value (e.g. 0.001), then terminate the iteration and use the last calculated centroids as the final values.

3.7.5 Outlier removal

The process of outlier removal in directional data can be compared with the intuitive approach that is used in the conventional visual interpretation of stereographic polar plots. Here one draws circles or delineate areas around clusters of poles that are (visually) considered to be plotting closely together. At the same time the orientations that fall outside the drawn cluster circles are thus ignored or removed and can accordingly be classified as 'outliers'. A more objective method is to use pole density contours from the projected poles. This is essentially the same process but now poles that are falling within high-density areas are classified to be more likely part of an actual joint set than poles that are plotting in low-density areas in the stereo plot. Using this process, outliers in small datasets from well-defined discontinuity sets can be removed, simply and accurately.

However, this visual outlier removal process does not have a very solid statistical basis. Also, when dealing with very large directional datasets that contain a great amount of noise and errors, it becomes much harder to draw a boundary between inliers and outliers. Therefore, it becomes important to look statistically at the data and decide on more objective grounds on the identification and removal of outliers. The fuzzy k-means clustering that is described in the previous Section (3.7.4) results in a classification of directional data to a pre-defined number of sets. But all data is classified, including inliers and outliers. For each set spherical directional statistics can be determined as described in Section 3.7.3, such as: mean orientation, Fisher's constant (K) or spherical variance (s^2). These statistical properties of each cluster or set can in turn be used to determine the outliers within the set.

The basic assumption in the outlier removal process proposed in this study is that the directional data that are closest (in terms of pole vector differences) to the mean orientation vector of the set, are more important to the set than poles that are far from the mean. This means also that a circular (Fisher) distribution has to be assumed, since there is no preference in direction, merely a measure of angular difference.

In order to implement such an outlier removal process, an interactive manual selection method or an automatic iterative method can be used. Most available orientation data handling software such as Dips (Rocscience, 2008) allow the user to interactively draw circles or areas around clusters of poles, supported by density contours in the background. The selection will immediately yield statistics, such as Fisher's κ value, so that a decision can be made on the value of the selection. The automatic iterative method developed in this study, consists of a recursive selection of poles on the basis of a step-wise decreasing (projected) pole vector distance to the mean orientation vector of the set. Every time the distance is decreased, the statistics for the new (smaller) selection of poles are evaluated. The process can be halted if certain threshold values in the cluster statistics are reached. All poles within the pole vector distance radius are then classified as inliers and the poles outside as outliers. This process is ideally suited for implementation in computer-based software. There are basically two ways how the clusters statistics can be used:

- By evaluating the absolute value of a specific statistical parameter in the new situation
- By evaluating the change (gradient) of a specific statistical parameter compared to the old situation

It is important to realise that every step involves also the re-computation of the mean cluster orientation, since by the removal of outliers in every step the mean orientation is changed as well. Particularly if the data is initially clustered with fuzzy k-means clustering, the mean orientation is very much affected by the presence of outliers. The reason is that this clustering method assigns orientation measurements based on cluster membership values (please refer back to Section 3.7.4). The original shape of the fuzzy clusters in the stereonet is also not circular, but depending on the amount sets, may be any polygonal shape. It is therefore likely that in a stereo plot the position of the mean cluster vector pole is significantly shifted from the (often-obvious) cluster centre with

high pole densities. The iterative outlier removal method that is explained above is iterating eventually towards a circular (Fisher) cluster shape. If this outlier removal is correctly done, the re-computation of mean cluster orientation should move the mean fuzzy k-mean pole vector in each step towards the centre of the highest pole density area.

The main problem is to determine what the right statistical evaluation parameters are and to select which are the appropriate threshold values. This will require proper judgement by the user, but may again introduce bias in the process. The best basis for the selection of threshold values is through the plotting of graphs of the various parameters against the pole vector distance to the cluster's mean. By looking at the variation in the values and the changes in shape of the graph, it will be easier to select the right threshold values. The statistic parameters that can be used are:

- **Eigenvalue ratio (T_1/T_2):** Woodcock (1977) and Mardia (1972) used the ratios of the three eigenvalues to analyse patterns and distinguish classes in directional data. If the objective is to find Fisher cluster boundaries, then the ratios of the two smallest eigenvalues (T_1/T_2) can be used as a measure for the uniformity of the distribution (see also Section 3.7.3.4). In other words: for a uniform distribution around the mean, the eigenvalue ratio will be moving towards 1. By plotting (T_1/T_2) versus the distance from the cluster mean, the distance at which this uniform Fisher distribution (value 1) is reached can be determined, in theory. This is only valid for a high-density circular (Fisher) distributions and an elliptical (Bingham) pole distribution will therefore not exhibit such behaviour, since the two smallest eigenvalues remain different.
- **Spherical variance (s^2):** This parameter, which is described in Section 3.7.3.2, will show a decrease in value towards 0 when the projected pole vector distance approaches the centre of the cluster (distance 0).
- **Fisher's constant (K):** This parameter, which is described in Section 3.7.3.3, will show an exponential increase in value when the projected pole vector distance approaches the centre of the cluster (distance 0).
- **Resultant Vector (R) and number of poles (N):** Both the Fisher's constant and the Spherical variance are functions of the resultant vector (R) and the number of poles (N). It may help to see any trends by plotting both the normalised resultant vector and the number of poles also as a function of distance to cluster mean. The normalised resultant vector $\bar{R}$ is expected to increase to a value of 1 towards the centre of the cluster, while the number of poles decreases during the iteration process.

The implementation of this outlier removal process, the choice of evaluation criteria and threshold values and the results are discussed in more detail in Section 7.3.4.

3.7.6 Cluster validity analysis

As explained in the previous section, the decision for the number of discontinuity sets, as input for the fuzzy k-means clustering, can be made by the user based on prior visual inspection of the polar plot of the discontinuity orientations. The result of the clustering can also be assessed visually by the user in order to confirm whether the results are as expected. If this is not the case, the fuzzy clustering can simply be repeated with a different number of clusters as input, until the results are satisfactory.

A more subjective way of determining the correct number of clusters in the dataset is with *cluster validity analysis*. Various validity methods have been proposed in literature, which are summarised and adapted for the use of discontinuity data in the paper by Hammah and Curran (2000). The different method evaluate the quality of the clustering based on the data distribution density and cluster separation and present this in the form of validity indices. The computation of the validity indices is recursively carried out for different set numbers. By plotting the various indices as a function of the number of clusters, the minimum or maximum value in the graph (depending on the type of index) is then an indication for the appropriate number of sets in the data.

Hammah and Curran (2000) discuss and modify five cluster validity analysis methods, which are listed below. The modifications to the methods are necessary since the original validity functions are based on Euclidean metric distance measurements, while the distances between the spherical orientation data is measured as projected distances on the unit sphere (please refer also to the previous Section 3.7.4). The general objective of the various cluster validity methods is to determine the separation and compactness or density of the clustered spherical data. It goes beyond the scope of this thesis to discuss the computation of the cluster indices in detail. The methods are merely listed here and one is referred to the references for more information.

1. Xie-Beni validity function (Xie and Beni, 1991).
2. Fuzzy hyper volume function (Gath and Geva, 1989).
3. Partition density function (Gath and Geva, 1989).
4. Average partition density validity functions (Gath and Geva, 1989).
5. Fukuyama-Sugeno validity function (Fukuyama and Sugeno, 1989).

Although Pal and Bezdek (1995) and Van Knapen (2005) seem to favour the use of the Xie-Beni validity function in their applications, in practise it is advisable to use all five methods concurrently to achieve the best and most objective clustering validation.

3.8 Discussion and conclusions

The geometric properties orientation, spacing, roughness and to a lesser extend persistence; are considered very important in the characterisation of rock masses. Orientation of discontinuities and the identification of sets of discontinuities are one of the key properties in determining the anisotropic behaviour of discontinuous rock masses. Orientation is relatively simply measured using the compass and clinometer. The identification of sets can be done using hemispherical or stereographic projections. Spacing between discontinuity planes or spacing within a discontinuity set can be simply measured with a measuring tape. Analysis of the spacing distributions is usually done with histogram analysis. Orientation together with spacing yields a three-dimensional block model of the rock mass. This block model, that can be generated using computer-based distinct modelling techniques, can serve in turn as an important input to the design of surface and subsurface excavations. Persistence and roughness are geometric parameters that are much harder to determine in the field. Persistence is often obscured in a rock face and therefore very hard to measure. Roughness has a strong scale-dependency and there are still no universally accepted tools to measure and quantify roughness unambiguously.

Methods for measuring the geometric properties of discontinuities with conventional manual techniques, such as compass-clinometer and measuring tape are simple and effective. The methods have successfully been used and are still one of the most important ways of characterising the geometric properties of discontinuous rock masses. However, the geometric information that is derived using manual survey may often be biased, inaccurate and sparse. Further, manual techniques are very labour-intensive and detailed mapping of rock faces is therefore often not feasible. Finally, the safety risk of working under a steep slope in often-hazardous surroundings is another reason to avoid manual survey. Remote sensing is therefore a logical alternative for manual field surveys, since physical contact with the rock exposure can be avoided. Analogue or digital photogrammetry can give good results but have as major disadvantage that the data interpretation and processing is still relative labour-intensive. The recent rapid development of three-dimensional terrestrial laser scanning offers also a great perspective for generating information on the geometric properties in a faster and more accurate way.

Orientation data of discontinuities require very specific data visualisation and analysis techniques. Normal statistics do not apply to orientation data, one has to resort to spherical statistics to calculate differences in orientation, and average orientation of a sample set of orientations. To perform these statistics, orientation information of discontinuity planes are typically converted into

their normal vectors or poles, which, in turn, are converted to direction cosines for easy of computation. Principal component analysis methods become useful for computation of statistics of large datasets.

Orientation data is typically visualised through hemispherical projections of the poles to the planes in stereographic plots. The main objective of the presentation of the data in this manner is that discontinuity sets, if present, can be recognised as clusters in the form of areas with higher point density. These areas obviously represent the poles of discontinuity planes that have similar orientation. The classification of these clusters is traditionally done visually through manual inspection and selection. A more objective and efficient way of clustering the orientation data into sets is by fuzzy k-means clustering. The identification of the number of clusters or sets is still needed as input to the fuzzy clustering, but this can too be automated using various cluster validity analysis methods.

4 Assessment of 3-D terrestrial laser scanning

4.1 Introduction

This chapter introduces three-dimensional (3-D) terrestrial laser scanning as a survey technique. It starts by providing background on the theoretical and operational aspects of terrestrial laser scanners. The two main types of laser scanners are described. The focus is on the data quality aspects, since this has considerable influence on the expected quality of the results of point-cloud analysis. The operational issues relevant to rock-face scanning are assessed. Finally, the principles of (digital) photogrammetry are discussed. Photogrammetry is the other potential remote sensing technique for geometric survey of rock faces. The advantages and disadvantages of photogrammetry are compared to terrestrial laser scanning, which, in this study, is selected as the preferred data acquisition technique.

4.2 Fundamentals of 3-D terrestrial laser scanning

3-D laser scanning is a relatively new, but already revolutionary and very successful surveying technique. Basically, three laser scanning systems exist, which differ in operating principle, resulting in important differences in range, precision and scanning time The two techniques mostly used in terrestrial surveying are the *time-based* and the *phase-based* techniques. Different naming conventions exist for both, which will be explained further on. A third type of laser scanning exists, which is the optical triangulation technique (Beraldin et al., 2000). This technique, which is mostly used indoors, generates data with a very high resolution and accuracy. However, it is not suitable for terrestrial surveying because it has a very short range and very low rate of data collection. For the purpose of scanning of rock slopes only the time-based and phase-based (terrestrial) laser scanning techniques are suited.

Whether a time-based or phase-based laser scanner is used in a survey, both yield a digital data set, which is essentially a dense “point cloud”, where each point is represented by a coordinate in 3-D space (X, Y and Z, relative to the scanner’s position). With this data, the 3-D shape of any object or geometry of a scene can be quickly determined. The most important advantage of the laser scanning method is that a very high point density can be achieved, depending of the laser scanner type and distance to the object. In any case, the shape of the surveyed object or scene can in principle be measured in three dimensions at a very high level of detail and accuracy.

4.2.1 Time-based laser scanners

Today, the most popular measurement system for laser scanners is based on the *time-of-flight* principle, which will be referred to as *time-based* scanner. This technique allows measurements of distances up to several hundreds of metres or more, under ideal circumstances. The accuracy and precision of the measured distances is in the order of 1 centimetre or better, depending on the distance to the target. The time-based scanners -or sometimes called “ranging” scanners - have a laser diode that sends a pulsed laser beam to the scanned object. The pulsed laser beam moves through a rapidly changing zenith and azimuth angle in response to the motion of a mirror inside the instrument. The pulse is diffusely reflected by the surface of the scene or object and part of the light returns to the receiver. The time that light needs to travel from the laser diode to the object surface and back is precisely measured. Knowing the speed of light, the distance from the scanner to the object and the azimuth and zenith angle of the beam, the position of each point where the beam is

reflected can be calculated to three-dimensional Cartesian space. In addition to the range and angular measurements, which are translated on-the-fly into the *X*, *Y*, *Z* coordinates, the amplitude of the returned signal is also recorded which is often referred to as *intensity* (see Section 4.3).

4.2.2 Phase-based laser scanners

The other type of laser scanner, namely phase or modulated-based systems, work in a different manner. Instead of having the light source pulsing on and off they run it constantly. The light source is modulated with a sine wave, causing the amount of light that the laser emits to vary accordingly. In similar fashion to the time-of-flight method, the signal is transmitted from the laser and reflected from the object. To determine the length measured, the phase differences between the transmitted signal and the reflected signal are compared (Greaves, 2004). The range is restricted to a maximum of seventy to one hundred metres. Accuracy and precision of the measured distances within some millimetres is possible and is in this respect better than the range-finding or time-based laser scanner. The speed of measurement is also much higher, up to 100 times faster than time-of flight laser scanners (Greaves, 2004). This allows the phase-based type of laser scanner to be used on mobile platforms for rapid surveying, for example mounted on a railway carriage inside a tunnel (Fröhlich and Mettenleiter, 2004).

4.3 Performance and specifications

Because of its great popularity, the different manufacturers are constantly developing the terrestrial laser scanning systems. In comparing the performance of the various laser scanning systems there are a number of specifications that are important. In contrast to more traditional surveying equipment, information on the specification of the various scanners with regards to precision, resolution and performance is not well specified (Fröhlich and Mettenleiter, 2004). It is therefore difficult to make here a good and objective comparison between the different laser scanner types in terms of performance. The websites of the various manufacturers describe the specifications in considerable detail, but it is hard to compare these with each other, since these tests are most likely done under different circumstances and with different objectives. The papers of Lichti et al. (2000; 2002) and the more recent papers by Lichti (2004), Fröhlich and Mettenleiter (2004) and Wehr (2005) report extensively on the performance of the various terrestrial laser scanning systems. However, a comprehensive comparative investigation and standard calibration procedure has not been developed yet. Particularly, for the specific purpose of scanning of rock faces, comprehensive testing should be carried out to select the optimal system and configuration for different scanning distances, exposure dimensions and even rock types, since these factors all have influence on the final data quality. Also the scanning environment, for instance operations at various temperatures or under dusty conditions should be incorporated. It falls outside the scope of this research to investigate this, but this is certainly a recommendation for further study.

4.3.1 Comparison of the main specification of time-based versus phase-based laser scanners.

In Table 4.1 below the main difference between time-based and phase-based laser scanners is summarised in terms of range, accuracy and scanning speed.

Table 4.1. Principal performance characteristics of time-based and phase-based terrestrial laser scanners

Measurement principle	Range (m)	Accuracy (mm)	Scanning time (pnts./second)
Time-based	< 1000	< 25	< 12000
Phase-based	< 80	< 10	< 625000

This study used time-based terrestrial laser scanners. Time-based laser scanners are, up at present, the most widely used scanners for outdoor and long-range surveys. In the following paragraphs, the performance and specifications that are discussed refer in general to time-based laser scanners. There are a number of other technical specifications to be evaluated in order to

assess the scanner's performance. Without doing a comprehensive comparison of all the specifications of the various laser scanner types the main specifications are discussed in the following sections:

4.3.2 Accuracy and precision

Unfortunately, accuracy and precision are terms that are still used interchangeable, while they represent two very different issues. The measure that is referred to is the *target coordinate* precision and accuracy since it can only be estimated at the target locations, where ground truth data is present. The values for accuracy and precision depend on the several factors, like range, physical properties and geometry of the target, which should be evaluated in calibration tests. Each manufacturer has developed their own calibration standards, which makes it difficult to compare the results. Some manufacturers even confuse accuracy and precision so care is required in interpreting the given accuracy and precision values. Tests are generally also carried out a different target ranges (e.g. at 25 and 50 metres), since the target range has an influence on the accuracy and precision. The physical properties of the target as well as the geometry of the target, has an influence as well.

In order to determine target coordinate accuracy, it is important to know to what degree the measured coordinates differs from the true coordinates. In some instances, the target's *shape accuracy* is used. Since a laser scanner generates a cloud of points, rather than comparing point-by-point it may be more relevant to determine how well (how accurate) this cloud of points represents the true target's shape. For example, a cylinder with certain well-know shape and size is chosen as a target. The cylinder has a certain centroid with *x*, *y*, *z* coordinates, and thus the accuracy with which the coordinates of the centroid of the cylinder can calculated based on the point cloud of the cylinder can then be considered *the* accuracy.

The target coordinate precision is often referred to as *modelled surface precision, repeatability* or *noise*. The precision of the target coordinate indicate to what degree repeated measurements of the same target point location differ from each other. Precision is a measure of the random variation of the measurement of a parameter often expressed as the root mean square deviation about a mean value, usually assumed the true value. This factor is important to determine to which detail the geometry of the target can be modelled. For example, in the determination of surface roughness of discontinuities, the precision or noise plays an important role.

The precision is not expected to play a large role in the determination of the orientation of discontinuity planes. In the computation of orientation of a single plane, there is a large number of point measurement that define the plane. Through averaging and least-square analysis, the effect of the precision or noise is largely removed. The accuracy of the orientation measurement however, is something that needs to be investigated in this study. The precision is expected to play an important role in the determination of (small-scale) roughness. Because when looking at roughness, the local variation in geometry will be evaluated, which will not so much be influenced by the accuracy but more by the local variation of position measurement, which has an important noise component.

4.3.3 Maximum and minimum range

The maximum range at which an object can be scanned depends not only on the specification of the equipment, but is also very much dependent on the physical properties of the material and the geometry of the surface. Obviously, the laser scanner needs to receive a reasonably strong reflected signal in order to measure distance properly. The physical properties of the material of the reflecting surface, determine how much of the laser energy is absorbed, as a function of wavelength. Also the geometric factors, such as angle of incidence and surface roughness, determine how much of the incident radiance is being scattered. The amount of energy that is reflected is again measured and recorded as intensity. There is of course a threshold distance at which no return signal can be measured, which determines the maximum range of the survey.

The maximum distance at which terrestrial laser scanner can still determine range depends on a number of factors, such as the laserbeam divergence, the frequency (colour) of the laserlight and most importantly, on the reflectance of the target. One can often see in the specification of the equipment ranges indicated for example for targets with < 80 % reflectivity and targets with less than 20 % reflectivity. Obviously the maximum range for targets with low reflectivity is much lower than targets with very high reflectivity. For phase-based laser scanners the maximum range is primarily limited by the inherent ambiguity of the method (Fröhlich and Mettenleiter, 2004). Since the range measurement is based on the phase shift of the laser signal, beyond a certain range it will not be possible to distinguish the different phase shifts from each other. It is also important to note that the time-based laser scanners have also a minimum range for which they work. The minimum range is often in order of several metres (2 to 4) metres. Therefore, for very short range surveys the time-based laser scanners are not suitable.

4.3.4 Scanning speed or sampling rate

The scanning speed is the rate at which points can be measured. The rate is give in frequency (Hz) or in points per second. The rate depends primarily on the scanning method used; phase-based laser scanning is much faster than (terrestrial) time-based laser scanning (see paragraph 4.2.2).The scanning rate is also dependent on the sampling method that is used. Some scanners take instead of single measurements multiple measurements, which are averaged, thus increasing the accuracy and precision, but obviously decreasing the sampling rate. Some laser scanners have also the option to measure the first reflection or second or last reflection, or both. This is particularly useful if there is vegetation or dust in the scan scene. Part of the laser light can be reflected by this, but parts may also continue and still reach the target. By taking the second or last reflection instead of the first one, the noise due to presence of vegetation and dust can partly be eliminated. The scanning rate is mainly restricted by the mechanical components (the rotation mechanics for the deflections mirrors[9]. The mechanics have are over the years drastically been improved, improving the scanning rates accordingly.

4.3.5 Angular resolution

The high spatial resolution with which geometry targets can be measured is one of the important features of terrestrial laser scanning. Resolution is the minimum differential measurement that can be made irrespective of accuracy or precision and is the smallest difference between two adjacent measurement values or points that can be determined. This spatial resolution is largely determined by the minimum angular resolution over which the laser beam can move vertically and horizontally. This minimum angle is called angular resolution and given in mrad, degrees or sometimes in actual spatial resolution at specific distance. Obviously, the distance to the target determines ultimately what finally the achievable spatial resolution will become. The angular resolution can be changed by the user and depending on the distance and purpose a certain spatial resolution can be selected for the survey

4.3.6 Field of view

Most of the time-based terrestrial laser scanners have a so-called camera view. The camera view is achieved by using two synchronised mirrors, one for the horizontal- and the other for the vertical beam deflection. The vertical field of view is determined by the maximum and minimum angle that the beam can be deflected in the vertical direction. The vertical field of view is often restricted not by the internal deflection mirror, but by the covering of the equipment. Some laser scanners with a restricted vertical field of view can be tilted to scan higher objects at shorter ranges. The limited horizontal field of view can be increased by rotating the entire systems over the centre axis. Most of the phase-based laser scanners however, have full 360 degrees vertical field of view which is achieved by a single rotating mirror. With a simultaneous rotation of the entire scanning system over the centre axis a full panoramic field of view is thus achieved.

[9] Time-based airborne and mobile laser scanners for instance, scan (contrary to terrestrial laser scanners) in one plane and can thus achieve a higher pulse frequency of about 300 kHz (pers. comment G. Vosselman, 24-10-2010).

4.3.7 Laser type

Most of the laser types that are used are Class 1 lasers that operate in the near infrared spectral range. Some laser scanners are Class 2 lasers that emit a green light. For Class 1 laser products the output power is below the level at which it is believed that eye damage will occur. A person receiving an eye exposure from a Class 2 laser beam will be protected from injury by their own involuntary response that causes the individual to blink and avert their head. Repeated, deliberate exposure to the laser beam may not be safe.

4.3.8 Beam divergence or spot size

The laser's beam is not a perfectly parallel beam, but will always show a certain amount of divergence with distance due to the scanner optics. For large ranges, the divergence is almost linear and specified by an angular quantity in mrad (Lichti et al. 2002). The divergence results in the spot size of the laser beam to increase with distance. The same amount of energy is thus distributed over a larger area. The target position will then also be averaged over the spot area. In case of a surface that is smooth and perpendicular to the laser beam, this will not have much influence. However, a laser beam whose angle of incidence is much larger or a laser beam that is hitting a very irregular surface, the increased spot size results in a smaller accuracy of the target position. Obviously, the smaller the laser beam divergence the better the measurements become at larger distances. In the recent development of laser scanning equipment, one of the most important aspects is in the improvement of this laserbeam divergence.

4.3.9 Scanner operation

Most laser scanners fit on a surveyor's tripod and have a regular laptop or palmtop computer attached to operate the scanner and to store the survey data. Mostly, the software used to operate the scanner is supplied by the manufacturer. Often, the scanner has a more or less advanced photo imaging system or pre-scan system that allows the user to interactively select the target area to be scanned. Based on the size and distance to the target area the user can subsequently select the appropriate scanning resolution that is best suited to the objective of the survey. Some of the software allows the user to instantly georeference the scanned point cloud data to a local or global reference grid. For this it is necessary that there are a number (minimum of three) reference objects (often strongly reflective spheres or cylinders) in the survey area for which the coordinates in the reference grid are known. The coordinates of these reference objects have to be determined with standard geodetic survey equipment. There are terrestrial laser scanners on the market that have build-in (differential) gps equipment with an electronic compass, so that the point cloud can be georeferenced without the use of other surveying tools. Similar to any other optical survey methods, there is a problem with targets that are covered or obstructed by other targets; they fall in the shadow zone of the laser scanner and can therefore not be surveyed. Also the surfaces of targets which are almost parallel to the incoming laserbeam are not properly measured or with only a limited amount of points. A solution for the shadow problem is to scan the same target from different positions and different angles. By combining the point clouds from these surveys, the shadow areas in one scan, can be complement with the measurements from the other scan. An important pre-requisite for this is that the different point clouds need to be georeferenced to the same reference grid.

4.3.10 Laser scanners combined with digital photography

The new generation of range-finding laser scanners often combine digital photography to the laser scanning survey as well. The advantage is that the actual scene is documented concurrently with the scanning survey. From the laserscan data it is not always very easy to interpret certain features in the scenes or object that has been scanned. Some laser scanners, like the Riegl Z420i scanner (Riegl, n.d.), have a calibrated high-resolution digital camera mounted on top of the laser scanner. While the scanner rotates to take the measurement, digital photos are taken as well. Since the camera is calibrated with respect to the laser scanner, it is possible to georeference the digital imagery to the point cloud data, which allows the point cloud data receive the colour information

(Red, Green, Blue values) from the photo. Also the digital image can be ortho-rectified, using the geometrical information that the point cloud data provides. The advantage of the ortho-rectified imagery is that it can directly be used for measuring or it can be used as texture mapping in 3-D digital rendering of the 3-D virtual models that are created from the point clouds.

4.4 Comparison of laserscan performance and specifications

Various terrestrial laser scanning systems are presently on the market. Both phase-based and time-based scanners are becoming more widely used throughout the world in all kinds of application. In the geosciences laser scanning is also becoming recognised as a potentially attractive survey method. At lease seven manufacturers are developing both phase-based and time-based laser scanners, of which the time-based laser scanners are more widely used. As mentioned previously, the developments in the technology is very fast and it falls outside the scope of this research to compare the performance of all laser scanners. Instead, the performance and characteristics of the two time-based laser scanners that are used in this study are summarised. In this study data from two different laser scanners are used: the Riegl LMS-420i and the Optech Ilris 3-D. In Table 4.2 the different performance parameters of the two scanners are given.

4.5 Sources of error of 3-D laserscan measurements

According to Reshetyuk (2006), there are four main sources of error in the time-based laser measurements. These are: instrumental, object-related, environmental, and methodological errors. These error sources influence each other and it is very hard to highlight the most important one.

However, instrumental error introduced by the laser scanner itself, is an important error source in laser scanner surveys. The range can be measured with a limited precision. This is related to the limited precision of the clock that measures the time difference. In addition, there is a limited precision in measurement of the rotation angle of the beam deflection. This is controlled by the mirror that makes the laser beam move vertically and horizontally along zenith and azimuth. Both deflections contribute directly to the location error. The error in the vertical direction (zenith) may be different from the error in the horizontal (azimuth) due to the different mechanics involved in the different rotations. All three errors together contribute to the accuracy and precision, or noise, associated with the location of each point in the point cloud. Due to the complexity of the equipment, individual components in the scanner may also contribute to the total error budget. These errors require a detailed understanding of the scanner design, which, for proprietary reasons are not supplied by the manufacturer.

Since terrestrial laser scanning is a reflectorless surveying technique, the results of the range measurement depend on object-reflection factors, specifically the amount of energy that is reflected by the surface being scanned. Section 4.3 explained that beam reflectance is both a function of the material and the geometric properties of the surface. Numerous benchmark studies have revealed that different materials, under different conditions (such as incidence angles, wetness, and distance) may result in slightly different range measurements. This depends also on the wavelength of the emitted laser signal. A time delay or range delay is introduced by a reduced return pulse amplitude (low intensity), compared to a full amplitude pulse (Lichti et al., 2002). The distance to the object also plays an important role, since laser-beam divergence causes the spot size to increase with distance. This results in less energy per unit of surface area being reflected and an averaging of the distance measurement over the entire spot size instead of a more specific point-wise measurement at smaller distances. The accuracy and precision of the measured target coordinates thus generally decreases with increasing survey distance.

Table 4.2. Performance and technical specifications of laser scanners used in this study

Scanner type	RIEGL LMS Z420i	Optech ILRIS 3-D
Laser wave-length & eye safety	NIR Class 1	1500 nm (NIR) Class 1
Accuracy	10 mm @ 50 m	8 mm @ 100 m
Precision-repeatability	8 mm (single shot) @ 50 m 4 mm (averaged) @ 50 m	n.a.
Minimum range	2 m	3 m
Maximum range	< 1000 m @ 80 % reflectivity,	< 1100 m @ 80% reflectivity
Maximum range	< 350 m @ 10 % reflectivity	< 400 m @ 10 % reflectivity
Horizontal field of view	0-360°	40°
Vertical field of view	80°	40°
Angular resolution	0.0025°	0.00115°
Beam divergence	0.25 mrad	0.00974°
Spot size	25 mm @ 100 m	29 mm @ 100 m
Data sample rate	8000-12000 pnts/sec	2500 pnts/sec
Additional functionality	Calibrated and definitely orientated high-resolution digital camera	Integrated digital camera (CMOS sensor)
Operational control	Standard laptop PC via TCP/IP	Handheld PDA for wireless control

Figure 4.1. Riegl LMS-Z420i scanner with mounted digital camera. In this picture, the scanner is tilted upward. Operation of the scanner is by laptop PC (not shown)

Figure 4.2. Optech Ilris 3-D scanner. On top is the PDA device for operating the scanner. The data is stored internally on a removable memory card.

Environmental aspects also influence the scanner's operations. Due to variations in the atmospheric conditions, the velocity of the laser light can change. In addition, refraction and turbulence may change the trajectory of the beam slightly. In short-range operation, the influence of atmosphere is negligible (Reshetyuk, 2006). However, laser scanners that can survey up to 1 km distance may experience significant atmospheric effects at these ranges. Of course, the platform of the scanner should be stable, and instabilities and even small vibrations may affect the position measurements, particularly at larger ranges.

Finally, there are also methodological errors introduced due to the survey method that was used. The survey points are stored in scanner coordinates, i.e. the coordinates are relative to the scanner position and do not have any relation to local or regional reference coordinate grids. There are various methods to "georeference" a point cloud, to convert the scanner coordinates into geo-referenced coordinates. This can be done using built-in GPS and electronic compass facilities, or by using a minimum of three standard reflecting target objects, which can be accurately located with geodetic survey equipment. Yet, there will always be a certain inaccuracy in the georeferencing, which adds to the total error budget. Apart from the georeferencing error, it is also possible that the chosen scanning resolution is inappropriate for the target's dimension, shape and distance, resulting in an under-sampling of the target's geometry.

4.6 Operational issues relevant to the scanning of rock faces

In general, the time-based laser scanners are popular for (long range) outdoor rock and slope surveys, while the phase-based laser scanners are more ideal for (close-range) tunnel surveys. In view of the possibilities and limitations that have been described previously, the operational issues required to assure good data quality and related issues that are relevant to the scanning of rock faces are now assessed. In this discussion, the focus is on the terrestrial laser scanning of outdoor rock exposures with time-based laser scanners, since this has most relevance to this research. The phase-based surveys, particularly the surveys for tunnels, have their specific operational issues, which fall outside the scope of this study. In general, three outdoor survey situations involving the scanning of rock exposures can be distinguished: exposures along infrastructure, exposures in open pit mines and quarries, and very large natural and man-made rock exposures.

4.6.1 Rock exposures along infrastructure

Surveys of man-made or naturally occurring rock exposures along roads, highways or railway lines are an important application of terrestrial laser scanning techniques. The height of these exposures is typically in the order of several metres to a maximum of tens of metres. Particularly for determining slope stability or generally for rock mass characterisation, these exposures are often - from a practical point or view - a logical survey target. In many cases, there is considerable choice for locating the laser scanner. The scanner can be placed on the same side of the road as the rock exposure, thus avoiding interference with passing traffic, but this location will often produce quite short scanning distances to the rock face, resulting in a relatively small scanning area. The minimum scanning distance may become an important consideration, since time-based scanners need at least 3 to 4 metres of distance to operate correctly (see Section 4.3.3). Scanning from the active road or track itself is often not feasible because the movement of the traffic will be hampered. Therefore, the most obvious location for the terrestrial laser scanner will be next to the road or track on the opposite side to the rock exposure.

With this location, depending on the width of road or railway track, the survey distance may vary between 5 and 20 metres. At these relatively short survey distances, very high scanning resolutions can be achieved with time-based laser scanners. Typically, the face of the rock exposures will trend parallel to the alignment of the road or track, which makes it relatively easy to survey. The very high parts of rock exposures may not be scanned due to the limited vertical field of view of most of the (camera-type) time-based scanners (see Section 3.2). One option is to move the laser scanner further away from the rock face to be scanned, thus increasing the scanning area within the field of

view. However, undertaking this option may not be feasible if such access is restricted by another rock slope or by a steep valley, ravine, or river or lake. This is often the case, since the rock exposure that is to be scanned is there for a reason; it was required in order to create space for the infrastructure.

In these situations, a possible solution is to scan the upper part of the rock exposure with the scanner tilted upwards. If the tilting can be set at a standard angle with a calibrated setting, the tilted scan can be easily integrated with the lower scan, even without georeferencing. However, with this procedure, the scanning of the upper portions may suffer from occlusion of important geologic details, as discussed in Section 4.6.4 and illustrated in Figure 4.3 to Figure 4.5.

If a long section along the infrastructure needs to be scanned, subsequent (overlapping) scans will be required. Also sharp corners along the road create rock exposures that require multiple scans. As long as the scans can be georeferenced, the scans can be integrated with each other relatively easily. However, from an operational point of view, the scanning procedure and developing appropriate ground-control reference points will become much more complex, since for every scan multiple target points need to be located. Some scanners have their own georeferencing system in the form of GPS and compass. These can assist in merging data produced by multiple scans into a single point cloud. The advantage of multiple (overlapping) scans is that possible shadow zone in one scan can be complemented with measurements from the other scan.

For the purpose of discontinuity analysis an absolute georeferencing of the position of the point cloud may not be necessary. Only the accurate orientation of the point cloud in terms of the horizontal plane and geographic north is necessary, since we are merely interested in orientation and geometry. For this kind of analysis, it is sufficient to orient the point cloud such that the x- or y-axis is oriented to the real north and the x-y plane is horizontal, so that the z-axis corresponds with the actual vertical.

If however the discontinuity information is to be integrated with other (georeferenced) CAD, GIS of DEM data, the complete positional georeferencing of the point cloud will become essential. Complete positional referencing is normally required if laser scans are to be collected at different times and then compared to determine if movements or deformations are occurring. Accurate positional referencing is also desirable as a check on the accuracy of multiple scans covering longer sections, to make sure that the integration of the multiple scans has not introduced systematic errors.

4.6.2 Rock exposures in open pit mines or quarries

In open pit mines and quarries, laser-scan surveys of rock slopes will be most pertinent when integrated with geodetic surveys, particularly if these laser-scan surveys are to be used to determine volumes of excavated rock by repetitive surveys. Since the geometrical lay-out of open pit mines and quarries changes rapidly, it becomes very attractive to use laser-scan surveys as a complementary technique for topographic surveying. Through laser-scan surveys of the mine or quarry from a few strategic locations, the entire geometry of the mine can be measured in a short amount of time. Suitable geodetic benchmarks and reference points are usually available, which makes it relatively simple to georeference the point-cloud data and to integrate the different scans. Subsequent scans can be used to determine changes in volumes of excavated or dumped rock material.

The man-made rock exposures in open pit mines and quarries are generally steep and inherently unstable and therefore very dangerous to access. It is not surprising that 3-D terrestrial laser scanning found its first applications in open pit surveying. Slope stability analysis, slope movement survey and rock mass characterisation are typical applications. Laser-scan surveys can also supply rock-mass characterisation information; they can, for example, aid in determining block sizes and thus for the subsequent selection of blasting or excavation techniques.

In many open pit mine and quarry situations, the scanning distances will be relatively large and long-range time-based laser scanners are the most suitable instruments. The long-range implies that relatively low scanning resolution of the rock faces will be the result. For general topographic surveying, a low scanning resolution is not a problem. For detailed rock surveying a higher scanning resolution is needed for detailed rock mas characterisation, and this will thus require additional detailed scans. These scans may need to be integrated with the scans collected at longer distances to provide a complete mine or quarry plan.

4.6.3 Scanning of very large rock faces

Very large rock faces, with dimensions in the order of several hundreds of metres in width and height, are also excellent targets for surveys with time-based terrestrial laser scanners. A large surveying distance is needed to scan these rock faces entirely. The distance between the scanner and the rock face may be of the same order of magnitude as the dimension of the rock face, perhaps a hundred metres of even several hundreds of metres. As long as the rock face has good reflective properties, it is feasible to scan these types of faces with most of the long-range time-of-flight laser scanners. However, the accuracy, precision and scanning resolution at these distances are much lower than scans of rock faces that can be scanned at much shorter range. Since it is often hard to access these large rock faces, it is difficult to place any reflective targets in the scene. Consequently, it will become very difficult to register the point cloud data that is generated from these scans accurately.

Another way of scanning larger rock faces is to make multiple sequential scans from various positions. This may be the only option if the field of view of the laser scanner is not large enough, or the distance to the rock face is too small, to capture the entire width and/or height of the face. Again, in order to merge the multiple scans, it is very desirable, even necessary, to place reflective markers in the scene, which not only complicates the operation, but may also be impossible to accomplish, considering difficulty in access to the face. There are however novel approaches to register multiple (overlapping) scans without the need for markers. This is discussed further in Section 4.6.7.

4.6.4 Horizontal and vertical sampling bias

An important issue in the survey of rock faces with laser scanning is the occurrence of sampling bias. This bias is caused by occlusion (shadowing) of the scanned rock face, which happens when the laser beam is obstructed and not able to hit the target surface. It occurs when the parts of the rock face become semi-parallel or hidden from the incoming laser beam. This bias causes discontinuity surfaces, that are parallel to the general trend of the rock face to be over-represented in the data, while discontinuity surfaces that are perpendicular to the general trend of the rock face are under-represented. The issue becomes more important in scans of highly irregular rock faces, particularly where the surveyed rock faces are high and steep or very wide. Both a vertical and horizontal sampling bias can be identified.

The vertical sampling bias occurs when a steep and high rock face is surveyed (see Figure 4.3). Upper parts of the slope can contain occlusion areas due to the larger angle of incidence of the laser beam. The consequence is that discontinuity surfaces that are dipping out of the slope (day lighting) are generally more difficult to detect. However, for slope stability analyses these discontinuities are in general the most important ones, since they may act as sliding surfaces. In addition, benched parts of the slope are more difficult to survey since the benched surfaces can be semi-parallel or even hidden from the laser beam. Some laser scanners have a limited vertical field of view, which makes it difficult to evaluate upper parts of the slope. Other laser scanners have the possibility of tilting the laser scanner itself vertically to scan higher parts of the target and thus to resolve this problem. The vertical sampling bias can be reduced by placing the laser scanner further away from the slope (see Figure 4.4) possibly in combination with placing the laser scanner on a higher platform (see Figure 4.5). In practice, it is often difficult to realise this. In case of a road cut for example, the other side of the rock face is often another rock face or a valley, which makes it

hard to set up the scanner at a larger distance from the face. An ideal situation is where another benched slope is opposite the rock face to be scanned, and so the laser scanner can be situated on one of the benches (see Figure 4.5). Other solutions, such as the construction of scaffolding, or the use of a cradle elevator, as a platform for the scanner can be considered, but this makes the survey more complex and expensive.

A horizontal sampling bias occurs when a very wide rock face is surveyed, possibly in combination with a relatively small scanning distance. The extreme left and right parts of the rock face are thus surveyed with a relatively large angle of incidence of the laser beam (see Figure 4.6), which can result in occlusion areas. If it is possible, the laser scanner should be placed at a large distance from the slope, to minimize the angle of incidence, but this result in a lower data resolution and precision. A better solution is to scan the same rock face from different angles. In this way the occlusion areas in previous scans can be surveyed. The multiple scans of the same rock face can then be merged to produce a single point cloud that minimises the occlusions (see Section 4.6.7). However, the vertical bias remains in these merged scans.

4.6.5 Influence of vegetation

Older rock faces are very often partly overgrown with plants, trees or shrubs. Of course, the presence of vegetation adversely affects the accuracy of rock face assessments, including those conducted by traditional field survey methods. However, when laser-scanning methods are employed, vegetation affects the ability of the laser beam to sample portions of the rock-face surfaces. Particularly if the vegetation is dense with large leaves, it can obstruct significant parts of the slope and creates occluded shadow zones behind it. If multiple scans are used, these shadow zones may (partly) be measured by the other scans. Even with dense vegetation, some of the laser beams may still penetrate and hit the rock surface behind the vegetation. Particularly if the second or last reflection is recorded, it may still return some reflections of the obscured rock face. When located in front of the rock face, the vegetation generally creates a “noisy” cloud of points before the actual rock face. Assessment of the point cloud data can identify these “vegetation points” and it is relatively simple to remove these manually. However, if the vegetation is really covering the rock face, without any space behind it, it becomes much harder to edit the point cloud without removing actual rock surface data. Generally the presence of vegetation has similar impacts on the final analysis of the rock face conditions regardless of the source of the data, whether by laser scanning or by conventional manual surveys. The impact of the vegetation depends of the type of analysis (see Chapter 6). Due to the inherent fuzzy character of the point cloud where vegetation exists, the presence of vegetation can be recognised and treated as noise and ignored during subsequent analysis.

4.6.6 Influence of dynamic disturbances

It is of course possible that vehicles, persons and animals pass between the laser scanner and the rock face during the scanning process. These are all considered dynamic disturbances. As long as the disturbance passes by relatively quickly (in the order of seconds or less and several times faster than the scanning time), the disturbance will produce only a few points that are located significantly in front of the rock face being studied and occur within a single or a few adjacent multiple “lines” in the final point cloud. Of course, the passing objects obstructed the scanning process for a short while, resulting is some missing points or scanned portions of the target. In the resulting point cloud, these noisy points and lines are relatively simply selected and removed since they are generally located at some distance in front of the actual rock face. Often, these dynamic disturbances are very difficult to avoid. Particularly along busy motorways, there will be a certain amount of disturbance generated. Passing vehicles generally only obstruct only the lower part of the slope, which often is not essential to the analysis. Large truck or buses, that move relatively slowly, may create larger problems since they obstruct larger areas of the slope for a longer period. Also dust, rain or snow can cause interference in the scanned scene. In principle, every particle is able to reflect the laser beam. Therefore, the application of terrestrial laser scanning is not ideal under extremely dusty, rainy or snowy conditions.

4.6.7 Registration of point cloud data

The laser scanner returns range, zenith (vertical angle) and azimuth (horizontal angle). These spherical coordinates are immediately converted by the scanner into Cartesian coordinates (x,y,z). The coordinates of the point cloud data that are thus generated are very accurate, but still relative to the scanner's own coordinate system. The origin (0,0,0) coordinate of the this coordinate system is located somewhere inside the scanner. This means that these "scanner" coordinates are not related to any existing local or global coordinates. In order to combine the point cloud data with other data from that are in a local or regional coordinate system, the point cloud data need to be registered to that coordinate system. Also if multiple scans of the same scene have to be merged these point clouds have to be registered to the same coordinate system or relative to each other.

At this time, the registration of single and multiple point clouds is considered one of the main operational problems with both laser scanning and photogrammetry (see 4.7.4.1). There are efforts to add extra components to the laser scanning equipment, such as Differential GPS, total station, levelling tools and other electronics in order to create a fully stand-alone operational tool that is able to generate fully geo-referenced point clouds (Glaesner and Cap, 2004). Trimble has very recently developed a laser scanning system that actually includes a number of these functionalities (Lemmon and Biddiscombe, 2007). These are:

- A tribrach with laser plummet to ensure that the scanner is precisely positioned on a known point.
- A mark for measuring the instrument height. The field software also corrects the instrument height measurement for the slope to obtain a true vertical measurement.
- A dual-axis compensator for leveling the instrument. The dual-axis compensator also actively corrects the horizontal and vertical angles for mislevelment to ensure that accurate measurements are obtained.
- A thread mount in the top of the scanner that allow a survey prism or GPS receiver to be placed on top of the scanner for positioning of the scanner.

These added functionalities make the operation of the scanner and the registration of the point cloud much faster and simpler. While most off-the-shelf laser scanners do not yet contain these added functionalities but, considering their great advantages, it is expected that the next generation of laser scanners will include some or most of these added features. An entirely independent surveying tool will be the result.

4.6.7.1 Conventional registration of single and multiple point clouds

In order to register an individual point cloud to a local or global coordinate system in a conventional way, a number of ground control (reference) points are needed. A minimum number of 3 points are required, but in order to determine the error in the registration a minimum of 4 control points should be used. Known points in the scan (often in the form of a number of small reflecting markers that are placed in the scene before the scan is done) have to be accurately surveyed with a theodolite or total station with reference to a local benchmark. Merging of two or more point clouds can also be done with these reflective markers, which should be visible in the overlapping areas. Through the (automatic) recognition of these markers in the various scenes, the multiple point clouds can be merged into a single point cloud. If the global coordinates of the markers are known, the entire merged point cloud is simultaneously registered to the global coordinate system as well. Some of the laser scanner software that accompanies the scanners and assists in their operation, such as the RiScan Pro software from Riegl (Riegl, n.d.), have this functionality built-in. The scanning software automatically recognises the reflective markers in the various scenes and is able to immediately register and merge the point clouds. This is done by a minimum of four retro-reflective targets per scan. The targets can be detected automatically using the signal amplitude of the data stream. To make registration even more accurate, the detected targets additionally can be scanned with higher resolution, resulting in a more precise definition of the centre of each target.

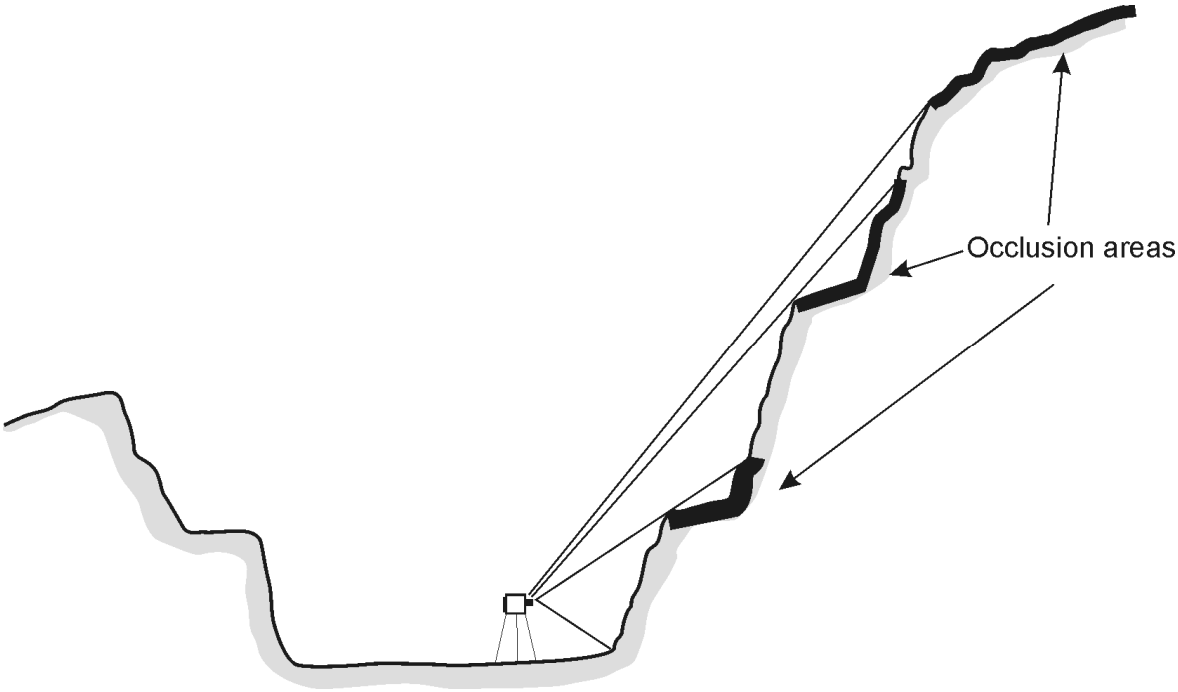

Figure 4.3. Vertical sampling bias due to occlusion (shadowing and semi-parallel surfaces). The reason is the relative small scanning distance, a low survey position and a limited vertical field of view of the laser scanner.

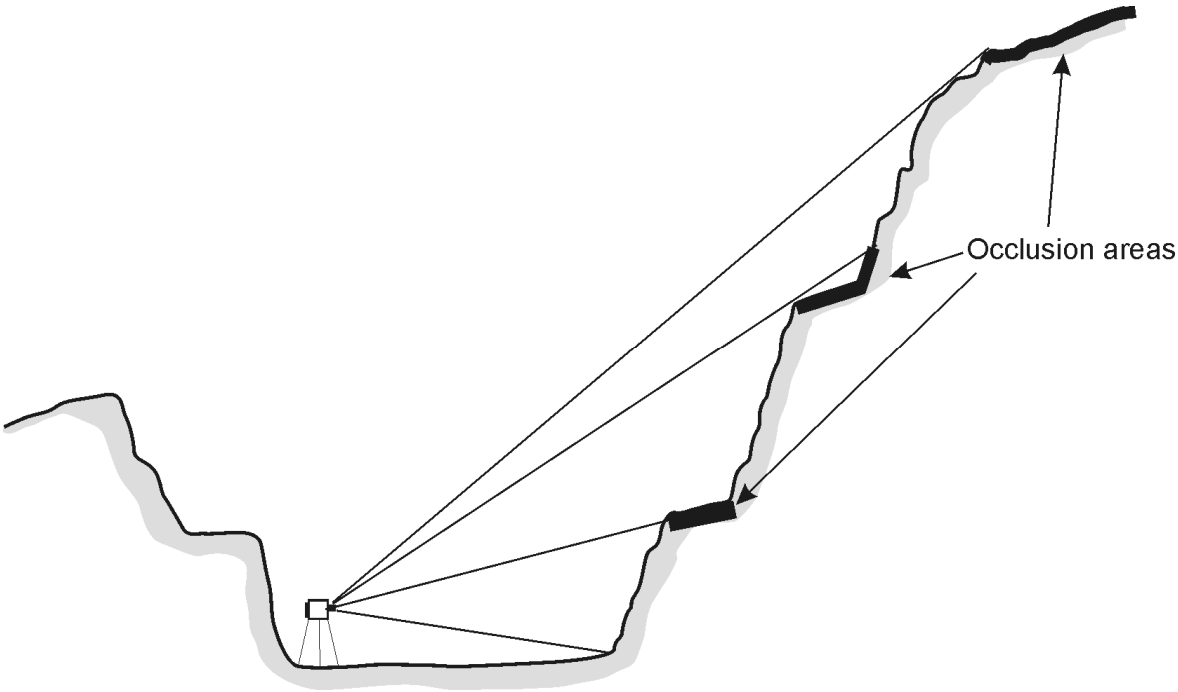

Figure 4.4. Vertical sampling bias due to occlusion. The amount of occlusion is smaller than the situation in Figure 4.3 due to an increase in scanning distance.

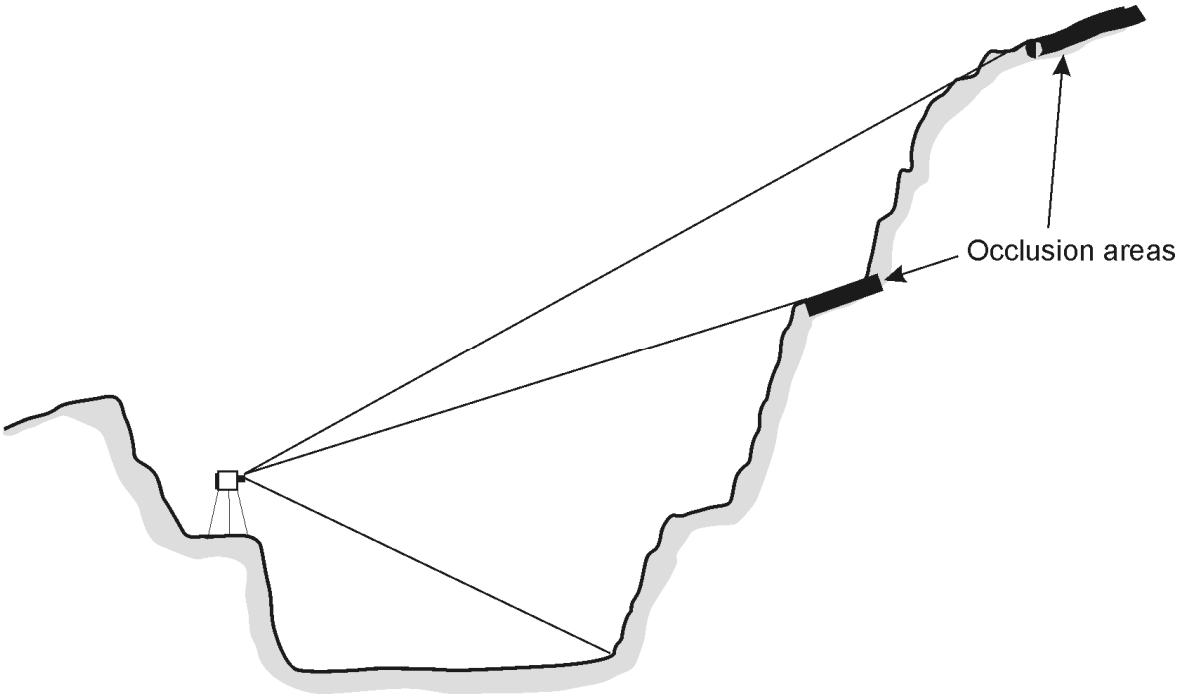

Figure 4.5. Vertical sampling bias due to occlusion. The amount of occlusion is minimised due to an improved scanning location: higher platform placement and larger survey distance. In practise it is often hard to find such an optimal survey location without the use of scaffolding or cradle elevators.

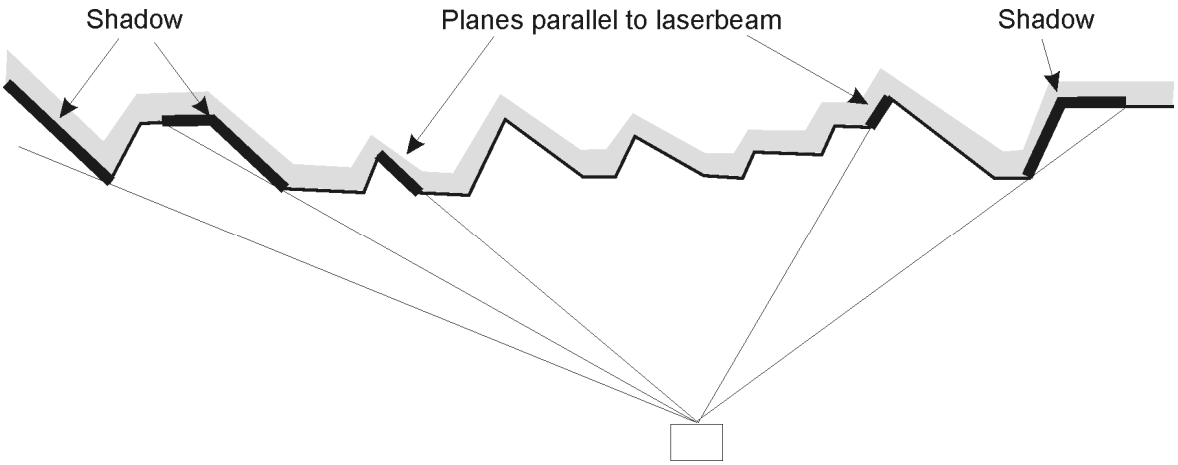

Figure 4.6. Illustration of the horizontal sampling bias due to the effects of shadowing and the presence of (semi-) parallel surfaces.

The conventional registration described above is reliable, but not very efficient, since the markers have to be manually placed in the scene and if a global registration is required, the markers have to be surveyed as well. Particularly with inaccessible and unstable rock faces, the installation of markers becomes very difficult and hazardous, and in many instances will be impossible to realise. Fortunately, much effort is currently put into the search of registration methods of multiple and single point clouds that work without the use of markers. Some examples are given in the following section.

4.6.7.2 Registration methods of multiple and single scans without the use of targets

A frequently used algorithm for the registration of multiple point clouds is the Iterative Closest Point (ICP) algorithm. In short, the ICP method determines iteratively the correspondence between different (overlapping) point clouds on a point-to-point basis using the minimum Euclidean distance (Besl and McKay, 1992). A more recently developed alternative is the Least Squares 3-D Surface Matching (LS3-D) which matches one ore more 3-D search surfaces to a 3-D template surface, while minimising the sum of squares of the Euclidean distances between the surfaces (Gruen and Akca, 2005). Another approach is to make use of the a-priori knowledge of the geometry and location of specific objects in the scanned scene, which are often present, particularly in scans of industrial objects (Rabbani et al, 2007). This method can also be used to register individual scans. The problem with natural scenes, such as rock faces, is that they mostly do not contain any regular geometric shapes. Again, it is an option to place geometric objects in the scene, such as like large planar boards, but this again complicates the operations and if the slope access is very poor, this can also be hard to achieve. It falls outside the scope of this research to explore the various alternative registration methods in more detail. However, it is is expected that in the near future these research efforts may prove to be very useful in resolving the problem of registration, particularly for multiple scans of large and inaccessible rock faces where registration information is scarce.

4.6.7.3 Rotation matrix

In order to register a point cloud it will in most cases be necessary to re-orient the data through a number of rotations along the main coordinate axes. In order to register to a reference grid, an additional translation is also required to get the absolute coordinates right. In order to perform the rotations, the *rotation matrix (R)* must be defined. This rotation matrix is the resultant of three rotations along the main coordinate axes. The first rotation is by an angle about the Z-axis, the second is by an angle about the X-axis and the third rotation is by an angle about the Z-axis again. The three angles giving the three rotation matrices are also called *Euler angles* (Goldstein, 1980).

The final transformed data set will have the Z axis as the vertical axis and the Y axis as the North-South oriented axis, with the positive Y axis oriented northward and the positive X axis oriented eastward. The decision on the orientation of the X- and Y-axes is arbitrary. In this study it was considered logical to define them in this manner. The selection of the positive Y axis as the North axis is maintained throughout this study to avoid confusion.

As explained above, the rotation matrix is the combined effect of three rotations. The various steps to construct the rotation matrix are given below and are illustrated in Figure 4.7. The construction of the rotation matrix is following a reverse order, i.e. the three rotation steps are described starting from the final correct orientation of the axes to arrive in three rotations at the uncorrected system of axes. The reasoning behind this is that the resultant rotation matrix (based on the three Euler angles) merely needs to be multiplied with the uncorrected dataset to compute the re-oriented dataset. All rotations are counter-clockwise and follow the right-hand rule (mathematically positive).

First a rotation is needed along the vertical Z-axis by Euler angle *α* (see Figure 4.7)

$$R_z(\alpha) = \begin{pmatrix} \cos\alpha & \sin\alpha & 0 \\ -\sin\alpha & \cos\alpha & 0 \\ 0 & 0 & 1 \end{pmatrix} \quad [34]$$

Where:

– $0^\circ \leq \alpha \leq 360^\circ$

The second step is to rotate along the (new) X-axis (X') to correct for the tilt angle *β* (see Figure 4.7).

$$R_x(\beta) = \begin{pmatrix} 1 & 0 & 0 \\ 0 & \cos\beta & \sin\beta \\ 0 & -\sin\beta & \cos\beta \end{pmatrix} \quad [35]$$

Where:

– $0^\circ \leq \beta \leq 180^\circ$

The final rotation is along the (new) Z-axis (Z'') with angle γ, which result in the original uncorrected system of the laser scanner's coordinate axes (See Figure 4.7).

$$R_z(\gamma) = \begin{pmatrix} \cos\gamma & \sin\gamma & 0 \\ -\sin\gamma & \cos\gamma & 0 \\ 0 & 0 & 1 \end{pmatrix} \quad [36]$$

Where:

– $0^\circ \leq \gamma \leq 360^\circ$

The combined effect of these three rotations is given by the rotation matrix R:

$$R(\alpha,\beta,\gamma) = \begin{pmatrix} \cos\alpha\cos\gamma - \sin\alpha\cos\beta\sin\gamma & \cos\alpha\sin\gamma + \sin\alpha\cos\beta\cos\gamma & \sin\alpha\sin\beta \\ -\sin\alpha\cos\gamma - \cos\alpha\cos\beta\sin\gamma & \cos\alpha\cos\beta - \sin\alpha\sin\gamma & \cos\alpha\sin\beta \\ \sin\beta\sin\gamma & -\sin\beta\cos\gamma & \cos\beta \end{pmatrix} \quad [37]$$

The rotated coordinates (x_r, y_r, z_r) can be computed accordingly:

$$\begin{pmatrix} x_r \\ y_r \\ z_r \end{pmatrix} = R \begin{pmatrix} x \\ y \\ z \end{pmatrix} \quad [38]$$

Let A be the (n x 3) matrix containing the uncorrected 3-D point cloud coordinates with n points, then the re-oriented matrix B can be computed accordingly:

$$B = R\ A \quad [39]$$

4.6.7.4 Registration of point clouds for rock mass discontinuity analysis

For characterising discontinuities within a rock mass, it is not always necessary to register the entire point cloud to a local or global coordinate system. Technically, it is not required to register to a real reference coordinate system, unless the point cloud data needs to be merged with other point cloud or CAD data for example. The strictly geometric measurements, such as spacing and roughness, do actually not require any registration. For an accurate computation of orientations, the main requirement is that the Cartesian coordinate system is aligned with the true North and with the

horizontal levelling plane. This means, for example, that the positive X-axis points should be pointed toward the real East, the positive Y-axis points towards the real North and the positive Z-axis is pointing perfectly vertically upwards. In this way the dip direction and dip angles will have a physical meaning and the orientation calculations can be compared with conventional (manual) compass measurements. Referencing the data set in this way will also make it possible to carry out analytical and kinematical stability analyses.

In practice, three methods can be identified to register a single point cloud to prepare for further discontinuity analysis. All methods essentially boil down to determining the three Euler rotation angles to define the rotation matrix *R*. Only the georeferencing to an absolute reference coordinate system will involve an additional translation, which is a simple addition and subtraction of all three coordinates with three X, Y and Z constants. It is assumed here that the data is from a single scan. If multiple scans are involved, these need to be merged first.

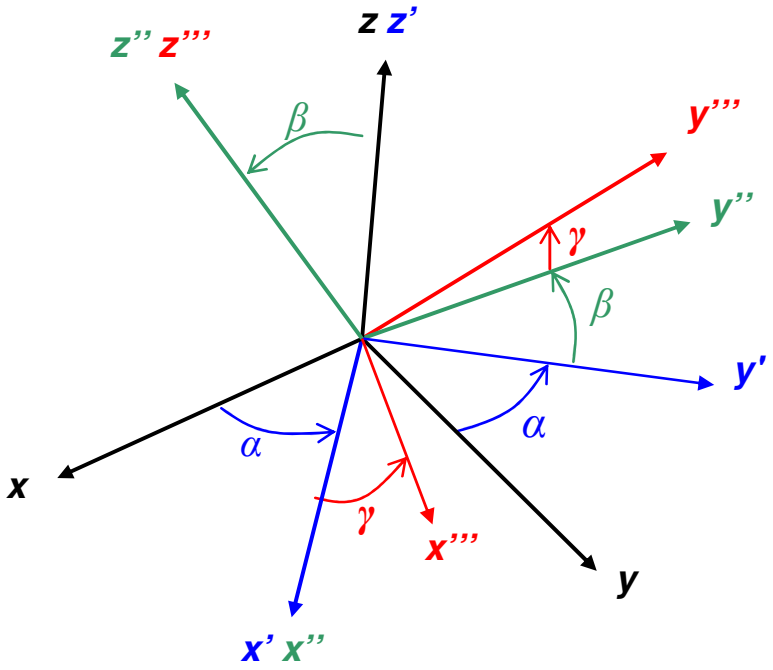

Figure 4.7. Illustration of the three rotations and Euler angles included in the rotation matrix R.

The first option is to measure, using conventional methods, several (at least 4) control points or targets with known Northings, Eastings and Elevation and compare these with the scanner coordinates of the matching points in the point cloud. As previously explained, these targets must be clearly recognised in the scanned scene. Placing reflectors (e.g. reflecting cylinders or spheres) that can easily be recognised by their particular shape and strong reflection intensity can assist in the accurate measurement of targets. It has to be emphasized that the reference coordinate system should consist of real Northings and Eastings, and not have x and y coordinates with respect to an arbitrary or other local coordinate system, otherwise the orientation calculations cannot be related to compass measurements[10]. Also the markers should be distributed evenly over the scanned scene. It goes beyond the scope of this thesis to elaborate in detail on how the rotation and translation parameters are exactly computed. It suffices here to mention that that computation of the rotation matrix involves finding the least-squares solution to a system of (at least) four equations with the three unknowns (the three Euler angles) based on Equation [37]. This is the reason why four markers are needed.

[10] Naturally, the geologic compass needs to be compensated for the local and current magnetic declination so that the observations are in correspondence with the geographic North and not the magnetic North.

A simpler solution, compared to the georeferencing with targets, is to make use of geometric objects in the scene that have known orientations. For example, (flat) boards can be placed in the scene before the scanning. The orientations of the boards (dip direction and dip angle) can simply be measured using a geological compass, in the same way that orientations of discontinuities are measured. By comparing the orientations of these boards, obtained from evaluating the trend in the points from the scanner's point cloud that represent the board, it is possible to derive the rotation matrix and thus rotate the point cloud to fit the orientation of the reference boards. The computation of the orientation of the points that represent the board can be done by a principal component analysis (see Section 6.6.6). It should be noted that this is not a very accurate georeferencing. The entire georeferencing is based on a single compass measurement with respect to a relative small area of the scan. The compass measurement itself is only precise to 1 to 2 degrees or less. The accuracy of the rotation can be checked if multiple reference boards are placed in the scene. The rotation matrix is relatively simple to construct once the orientations are known. The construction of the rotation matrix follows the same order as described in the Section 4.6.7.3 above, i.e. the rotations are described in a reverse order, starting with the final correctly oriented point cloud:

1. The first rotation with angle α is along the Z-axis through the azimuth of the pole of the measured reference board (same as the dip direction). This rotation will orient the point cloud such that the pole with point towards the north, so that a rotation along the X-axis can correct for the difference in dip angle.
2. The second rotation with angle β is along the X-axis through the difference in dip angle of the poles of both the measured board and the calculated dip angle of the points representing the board.
3. The third and final rotation with angle γ is again along the Z-axis through 360 degrees minus the azimuth of the laser-derived pole of the board. The intermediate point cloud after step 1 and 2 is still oriented towards the North. Because a positive angle rotates counter clockwise it is necessary to subtract the azimuth from 360 degrees. (a negative azimuth as rotation angle would give the same result.

A third and more straightforward option is to make sure that the scanner itself is level. Some laser scanners have a small bubble levelling device build in, so that by carefully adjusting the base of the scanner and the tripod the scanner can be levelled. If this levelling is sufficiently accurate, only a single (horizontal) rotation along the Z-axis of the scanner's coordinates will be sufficient to re-orient the entire point cloud data towards the North. If the (initial) position of the laser scanner is measured in term of bearing, then this horizontal rotation angle is equal to the bearing of the scanner. However, it has to be confirmed that the internal X or Y axis is parallel to the scanner bearing. Mostly the laser beam with 0° azimuth and 0° zenith corresponds to the bearing and level of the scanner (resulting in an x-coordinate = 0 and z-coordinate = 0; the y-coordinate is in this case the horizontal distance from the scanner's origin). It depends on the type of scanner how simple it is to determine the bearing of the 0° azimuth and 0° zenith beam. With the fixed Optech Ilris 3-D laser scanner (see Figure 4.2), the (square) side of the casing was used as a reference plane to get the bearing with a compass. The Riegl LMS Z420i for example, also has a base with square sides that could be used as a reference (see Figure 4.1). However, the Riegl scanner itself is round and has a rotating head so it has to be made sure that the head is facing forward, parallel to the base, at the start of the scan, if this base is used as a reference for the bearing. The advantage of the Riegl scanner is that is has the ability to pitch the scanner forward or backward and this is done over a calibrated tilt scale, so that this measured angle can in turn be used in the rotation of the point cloud.

The measurement error of the bearing of the scanner will result in the same orientation error, irrespective of the distance. For instance, a discontinuity plane that is oriented perpendicular to the laser beam should be result in a dip angle computation of 90°. If the scanner was not perfectly levelled, but was slightly pitched downward by an angle of 2°, then the dip angle should actually be

88°. It is advisable to keep reference boards in the scene, so the result of the transformation can be verified and (small) adjustments can still be made.

4.7 Comparison with 3-D photogrammetry

Terrestrial photogrammetry has proven to be a good way of obtaining remotely sensed information from exposed rock faces. Since the digital camera revolution and the development of image processing techniques of the past decade, the technique has become very attractive compared to the previous analogue and analytical techniques. Nowadays, with relative inexpensive equipment and the greater computing power available on personal computers, it is possible to realise accurate 3-D models based on photogrammetric principles.

4.7.1 Principles of 3-D photogrammetry

Photogrammetry is a measurement technology in which the three-dimensional coordinates of points on an object are determined by measurements made in two or more photographic images taken from different positions. Common points are identified on each image, which is nowadays done with image matching techniques on digital imagery. Subsequently, a line of sight (or ray) can be re-constructed from each camera location to the target point based on the camera properties and the baseline between the two images. Next, triangulation is carried out, which is the intersection of these rays from both photos, in order to determine the three-dimensional location of the point. Three-dimensional coordinates are computed for each point in the image, and this result in a point cloud of the target, similar to laser scanning. Therefore, the higher the resolution of the image, the denser the point cloud and more detailed the model of the target.

The accuracy of photogrammetry depends heavily on the quality of the image. Particularly image resolution plays an important role, as well as environmental factors (haze, dust, heat shimmer, etc). In addition, the camera's internal properties and calibration parameters need to be known in detail to create an accurate and precise 3-D model stereoscopic model. If those parameters are not known, which is often the case with the non-professional digital cameras, the three-dimensional coordinates of several ground control points need to be measured within the target scene.

4.7.2 Accuracy and precision of 3-D photogrammetry

Much research has been done over the past to determine the accuracy and precision of airborne and terrestrial photogrammetric techniques. It falls outside the scope of this research to evaluate carefully all of the published results of calibration studies. Specific references to benchmarks tests for evaluation of quality of photogrammetric survey of rock slopes are scarce, just as is the case with laser scanning. The main reason is that benchmark data, due to the irregular structure of exposed rock faces, is very difficult to create. Most of the terrestrial benchmark tests are carried out at close-ranges for well-defined objects like buildings or bridges. Again, as is the case with laser scanning, it is impossible to provide a generalised value for target geometry accuracy and precision. The reason is that the position error of photogrammetric 3-D models depends on different factors, such as camera type, focal length of the camera, baseline, range to the target and size and geometry of the target object.

Rengers et al. (1988) computed the accuracy of an analogue photogrammetric survey of terrestrial images made using professional cameras. For a 40 m high slope, a survey distance has to be observed between 50 and 100 metres. For this distance, 3-D coordinate accuracy is in the order of 15 to 30 cm. According to Maas and Hampel (2006), the precision of photogrammetric techniques will usually show a linear dependency on the object dimension. A realistic and typical value for the coordinate standard deviation measured under controlled conditions is in the order of 1:100,000 of the object dimension. Theoretically, typical and well-calibrated modern photogrammetric systems may achieve range measurement accuracy of the order of 1:10,000 in terms of distance to the object. This means for example that at a distance of 100 metres, the measured position of a single point on this object will be within 1 cm of its actual position. According to Poropat (2006), robust,

accurate image matching algorithms and appropriate calibration enable modern CCD[11] cameras to achieve precision from 1 to 10 centimetres at distances of the order of 100 metres with moderate focal length lenses. The accuracy of such systems varies linearly with the focal length or pixel size and varies non-linearly with other parameters such as the camera baseline. Typically, when using for example a Nikon D200 with a 50 mm focal length lens the resolution of the range measurement at 150 metres is 15 cm for a displacement within the 2-D image of 1 pixel if the baseline is 25 metres. The corresponding precision of the range measurement is approximately 7 cm.

From this we can conclude that, theoretically, high spatial accuracies can be achieved with photogrammetry that is comparable to three-dimensional laser scanning. However, the final accuracy that defines the physical shape of the target object can vary significantly (Krosley, 2003). It is difficult to quantify this variation in accuracy since it relates to human error and lack of experience with the photogrammetric techniques and software that were used.

4.7.3 Advantages of 3-D photogrammetry compared to 3-D laser scanning

4.7.3.1 Equipment cost

The biggest advantage of 3-D photogrammetry is that stereoscopic measurements can be done with photographic equipment that are widely available. With a high-end good quality consumer digital camera, one can create reasonably accurate three-dimensional models. The cost of a high-end professional digital camera is in the order of 20-30 K Euros. The high-end consumer digital cameras with 10 Megapixel are only around 1-3 K Euros and these prices are expected to go down in the near future. The method is therefore considered very low-priced compared to 3-D terrestrial laser scanning that require the use of laser scanners, which cost in the order of 100 K Euros.

4.7.3.2 Photographic (ortho-rectified) documentation

Another advantage of 3-D photogrammetry is that one has instant photographed documentation of the surveyed target. With the 3-D stereoscopic model that is generated, the photographs can be corrected for geometric distortions, so-called ortho-correction. This means that the picture can be projected to a single vertical reference plane which can then be used as a base for engineering drawing, since all measurement on this *ortho-photo* are to scale. Many of the older generation terrestrial laser scanners do not include photo cameras. However, most of the current 3-D terrestrial laser scanners have the possibility of attaching a high-end digital camera to it, which allows for the concurrent capture of photographic images.

4.7.4 Disadvantages of 3-D photogrammetry compared to 3-D laser scanning

4.7.4.1 Increased complexity of survey

Inherent to the photogrammetric principle, two (stereoscopic) photographic images of the rock face have to be taken from different angles and standpoints. An appropriate baseline is important to achieve sufficient stereo overlap. As a rule-of-thumb, the distance between the two camera standpoints in relation to the distance to the rock face should be around 1/5 (Gaich et al., 2004). This does complicate the operational aspects of a survey. If for example the rock face is at 20 metres distance, the baseline between the two camera standpoints should be around 4 metres. Often this is not a problem, but there may be situations in complex surroundings with difficult access, where it is hard to find even a single camera standpoint, let alone two or more. Particularly with a long rock face, several stereo pairs are needed, requiring multiple standpoints.

In order to do the triangulation, it is necessary to know the mathematical camera model as well as interior camera orientation (Gaich et al., 2004). The mathematical camera model describes how theoretically a 3-D scene is being projected on a 2-D image sensor or film for a particular camera.

[11] CCD is abbreviation for Charge-Coupled Devices. Image sensors are devices that are usually made up of arrays of CCD's. The image sensor converts reflected electromagnetic energy, e.g. light, that falls on the CCD's to an electric signal.

Since the mathematical model always differs from the actual projection the camera needs to be calibrated. The interior camera orientation includes the focal length, the axis of rotation, the principal point and the correction of the lens distortions. The information on both the mathematical model as well as the interior camera orientation is only available for the very professional photographic equipment. This equipment is again much more costly than even the high-end consumer cameras. Therefore, in order to carry out a triangulation with the simpler consumer-type cameras, it is always necessary to have a number of non co-planar *ground control points* (at least 6) within the target scene. The three-dimensional metric coordinates of these ground control points need to be known precisely, which can only be achieved with a professional geodetic survey. In any case, the ground control points are required to register or geo-reference the generated points from the arbitrary camera-based coordinate system to a regional coordinate system or local grid.

The advantage of laser scanning is that single survey point is normally sufficient, where at least two standpoints are needed for photogrammetry. Of course, similar to stereo photography, if the target is partly obscured because it is out of the line-of-sight of the laser scanner, multiple scans are needed to measure the geometry of the hidden portions. But this is the same for stereo photogrammetry. Multiple scans that are generated by a laser scanner, need however to include several reflectors, that act as reference or ground-control points, otherwise the point clouds cannot be merged. This is not required with photogrammetry, since the process uses image matching. However, there are currently methods being developed that allow the merging of points clouds without the use of targets (see Section 4.6.7.2).

4.7.4.2 Increased data processing time

In the past, the processing of analogue stereo imagery to create the 3-D geometric model was time consuming. Several processing steps were needed. The film first had to be developed and printed, and then the resulting image had to be scanned if it was to be used in digital image processing. Digital cameras can obviously skip this step. Modern digital methods have thus reduced both time and cost. However, digital photogrammetric methods also require investments of time and costs. Even with the latest software and hardware capabilities, the digital image matching process is computationally expensive when applied to very high-resolution imagery, sometimes taking several hours or more to generate a 3-D model (Kadobayashi et al., 2004). In many cases the image matching will not find an unambiguous result and may require some user interaction to arrive at a solution, which also increases the processing time and introduces bias.

The advantage of laser scanning is that in real-time unambiguous and geometrically correct measurements are generated. Since the three parameters – range, vertical angle and horizontal azimuth – are instantaneously recorded, the metric x,y,z coordinates can be computed immediately. These coordinates are still in the laser scanner's internal coordinate system. However, with a number of ground control points within the measured scene, of which the coordinates are known, the local or regional coordinates can also be computed immediately. This gives the capability of integrating the measurements in real-time, on-site, with existing data. It also allows immediate data analysis, which photogrammetry cannot achieve.

4.7.4.3 Limited field-of-view

Most of the consumer and professional photo cameras have a limited field-of-view. A full 360 degree single panoramic survey that most of the current laser scanners are capable of is therefore impossible to realise with cameras. However, a special type of panoramic camera has been developed by 3G Software & Measurement GmbH (n.d.) that can generate 100 Megapixel-resolution imagery. An example of the capabilities is given in Gaich et al. (2004): The resolution of the panoramic camera results in geometric resolution of 5 cm per pixel of a rock face of 200 m. height and 400 m. width. This type of highly specialised equipment is more costly than the high-end professional digital cameras used for "normal" photography. It also takes more time to register an image, since the camera is using a "scanning" mode, rather than an instant capture mode that regular cameras use. For single rock exposures with limited width, a panoramic survey is not

required. For larger exposures of quarries or underground excavations, panoramic capability is very valuable, since it reduces the survey time and the complexity of having to make multiple scans or photos.

4.7.4.4 Influence of vegetation and dynamic disturbances

On a typical natural rock face or exposure there is always a certain degree of vegetation present in the form of grass, bushes or even small trees. In (digital) photogrammetry, it is very hard to perform image matching for areas with vegetation on or in front of the exposure. One reason is that between the two stereoscopic images it is difficult to find corresponding points in the vegetated areas because some parts are obscured which may be visible in the other image due to the different camera angle. The other reason is that vegetation is generally dynamic (leaves and grass can be moved by the wind) since both images are often taken at different moments, the coherence between the two images will be lost, which makes it more difficult to find corresponding image points or pixels.
The vegetation will also cause 'noise' in a point cloud that is generated by a laser scanner (see Section 0). If a laser beam 'hits' part of the vegetation, that piece of grass, branch or leaf will generate a reflection, resulting in a point. However, there are always a number of nearby laser beams, particularly if the scan resolution is chosen to be very high, which are able to penetrate the vegetation and hit the target behind the vegetation. The laser beam may be only partly reflected by the vegetation, allowing the remaining beam energy to continue and hit the target behind it still. Most laser scanners allow the operator to record either or both 'first' and 'last' arrivals separately. By selecting the 'last arrival' option, some of the negative influence of vegetation, dust or dynamic disturbances can be eliminated.

4.7.4.5 Fixed resolution

Another disadvantage of photogrammetry is that the resolution of the imagery is rather fixed. Of course the resolution of the imagery can be lowered, but this will result in a great loss of quality. The resolution of the imagery determines the amount of target points that can be measured and ultimately the density of the generated three-dimensional point cloud. The resolution of analogue professional film is still higher than the resolution of the best digital camera, although developments in image sensors are such that the resolution is quickly approaching the quality of analogue imagery. However, in order to carry out digital photogrammetry, the analogue film or photo still has to be scanned to a digital image in order to process it. The resolution of the scanning is limited though, determined by the size of the images that can reasonably be handled by the available software and hardware.

One of the advantages of 3-D terrestrial laser scanning is that the scanning resolution can interactively be changed, depending on the objective of the survey and the characteristics of the target. Of course, there is also an upper physical limit in the scanning resolution of a laser scanner, just as is the case with digital photography. However, it will hardly ever be needed to scan an entire target at the highest possible resolution. However, the advantage of the interactive selection of resolution is that it is also possible to scan part of the target in a higher resolution in order to study a particular part of the target in higher detail. For example, this could be relevant in studying the roughness of a particular discontinuity in an exposed rock face.

4.7.4.6 Sufficient image contrast needed

The digital image matching process works in an optimal way if there is good contrast in the images. The image matching algorithm searches for similar patterns of pixel values in both images. If all pixel values are very similar, which is more likely when there is very little contrast in the image, it becomes very hard to find patterns of similar pixel values. This may also be the case of smooth rock faces, or along rock surfaces that have an even colour. Mostly, when dealing with exposed rock faces where the discontinuities are well exposed, there is sufficient contrast to make the image matching techniques work. The constraint of sufficient contrast is not an issue with 3-D terrestrial laser scanning, since the method is not image-based.

4.8 Discussion and conclusions

At present, terrestrial digital photogrammetry and three-dimensional terrestrial laser scanning both offer logical solutions for remote sensing of the three-dimensional geometry of exposed rock slopes and faces. Both laser scanning and photogrammetry are capable of generating a dense three-dimensional point cloud of the rock mass exposure. The differences in accuracy and precision between laser scanning and photogrammetry are difficult to compare since it depends on a number of parameters, such as: the hardware used, the range to the target and the dimensions, geometry, and reflective properties of the target. No standardised benchmarks tests have to date been carried out to compare the performance of the various terrestrial remote sensing techniques. Particularly in the field of the terrestrial remote sensing of exposed rock faces, proper calibrations and comparison studies have not yet been carried out. Nevertheless, both terrestrial laser scanning and photogrammetry have successfully been used for a variety of applications, and the accuracy and precision of both methods are generally considered sufficient to allow detailed modelling of rock exposures and the subsequent derivation of geometric discontinuity properties.

The greatest advantages of digital photogrammetry are the cost of the equipment and the accurate photographic documentation of the site. With high-end consumer-type, off-the-shelf digital cameras it is already possible to create good quality digital imagery on the basis of which good three-dimensional stereoscopic models can be made. Nevertheless, terrestrial laser scanning has a number of important advantages over photogrammetry. The most important advantage is that instantaneously a geometrically correct three-dimensional point cloud can be generated. This is not possible with photogrammetry. Only laser scanning provides the user with the ability to carry out real-time on-site analyses. The operational set-up is also much simpler with the latest types of laser scanners, only a single survey point is generally needed to create a full 360-degree panoramic survey. A simple operational setup is much preferred, particularly in a complex survey environment, such as are common along highways and railway lines, or in quarries, open pit mines, and underground excavations,. Specifically for the survey of natural rock exposures, that contain vegetation, terrestrial laser scanning is preferred, since the point cloud data is less influenced by the presence of vegetation. Most of the more recent laser scanners include the possibility of attaching a high-resolution calibrated digital camera that allows the concurrent photographic documentation of the scanned target object or scene. This removes the advantage of having photographic documentation of the site that is often presented as the major advantage of the digital photogrammetry approach.

Although the equipment investment costs are higher, terrestrial laser scanning is considered a better method to terrestrial photogrammetry for surveying exposed rock masses. Laser scanning is a relative new technology, but is experiencing currently a rapid development. As with many new technologies, the initial costs are relatively high, but as the technology becomes more widely applied and further developed, prices will go down, while the functionalities and data quality continue to improve. On the other hand, the much shorter data processing time and the operational advantages make the operational costs lower.

That is the main reason why terrestrial laser scanning has been selected in this research as the method for the acquisition of remotely sensed geometric point cloud data of exposed rock masses. There are two main types of laser scanners; time-based and pulse-based. The key differences between the two main types are related to range and rate. Time-based scanners, can measure much longer distances than phase-based systems, sometimes up to a kilometre. They typically capture data at a rate of between hundreds and thousands of points per second. The phase-based systems have a much more limited range, usually measuring at distances less than 25 metres. However, their rate of capture is more than 100 times faster than time-based scanners (Greaves, 2004). Time-based scanners obviously have the advantage in longer-range applications even though their rate of capture is slower. If capture time and density of data were important considerations then a phase-based system would be the sensible approach to adopt (Greaves,

2004). Phase-based laser scanners are capable of generating higher resolution point clouds with higher accuracy and precision. The question is whether this is strictly required for characterisation of rock masses. This will be useful only if the discontinuities are not well exposed, with small surface areas, At this time, time-based laser scanners are more widely used and available than phase-based laser scanners. Because the time-based scanners can be used for larger ranges, there are more applications for this type of scanner.

Both photogrammetry and laser scanning methods generate a point cloud describing the three-dimensional geometry of an exposed rock mass. The data analysis methods developed by this research for deriving geometric properties are based on any point cloud data. So whether the data is generated with photogrammetry or laser scanning will not make any difference to the processing methods. The differences in resolution, accuracy and precision, however, will undoubtedly influence of the quality of the final results.

5 Field data acquisition

5.1 Introduction

The previous chapters show laser scanning to be a potential and probably optimal remote sensing method to survey rock faces. To investigate the potential of laser scanning for obtaining geometric discontinuity properties, two field data acquisitions have been carried out. One field campaign was conducted at three sites around Namur, Belgium with a Riegl LMS-Z420i time-based scanner and one campaign was conducted at 12 sites in the Baix Camp region in Spain (Catalonia Province) with an Optech Ilris-3-D time-based scanner. The sites in Spain were scanned over 10 days and information on the properties of the rock masses, such as orientation, spacing and roughness was obtained. In contrast, no reference information in the form of scanline surveys or compass measurements were made for the sites in Belgium. The three sites in Belgium were scanned in one day, without the possibility of obtaining detailed ground control data, as the field time was limited and physical access at two sites was difficult with scanning restricted to high parts of the slope. The objective of the surveys in Belgium was to demonstrate the capabilities of laser scanner manufactured by a different vendor that included advanced control features.

5.2 Data acquisition methodology

Time-based laser scanning is already widely applied and can be used in a wide range of situations. Particularly for scanning larger rock faces, at various distances, the time-based laser scanning method is suitable. The resolution, precision, and spatial accuracy of phase-based laser data is better; however phase-based scanners have a more limited maximum surveying range. This study used time-based laser scanners. The reasoning behind this is twofold. First, there is a pragmatic reason, which is that time-based laser scanners were at the time more available with service providers and survey companies. Secondly, if the method that is developed in this research works well with time-based laser scanner data, it should certainly work even better with the higher quality (higher resolution and precision) data from the phase-based scanners.

The surveys in Belgium and Spain generated large amounts of data. However, only the data from two rock exposures in Spain, scanned with the Optech Ilris 3-D scanner, were used to test the 4 different data processing and analysis methods that are worked out in Chapters 7 and 8. These two sites were selected because they had well-developed discontinuities. To use more sites in this thesis for testing the methodology would result in a much too large and bulky document that would not further clarify the merits of the alternative methods.

5.3 Field methods

The field sites were described following the British Standard BS5930 (1999) and the ISRM “Suggested Methods” (ISRM, 1981). The rock mass characterizations were performed according to the methodology developed by Hack (1996) and formalised in the SSPC system (Hack, et al., 2003). The identification of discontinuity sets and the measurement of the discontinuity orientations of the various sets in the SSPC method are based on the rapid face mapping approach (see Section 3.5.3). The scan line mapping or line surveys were conducted according to the method suggested by Priest and Hudson (1981) (see Section 3.5.1). The main purpose of the SSPC-based characterisation and scan line mapping is to gather information on the number of sets, average spacing per set, the discontinuity set spacing, and the discontinuity characteristics such as roughness. The SSPC method provides a generalised value for the geotechnical unit in the rock

exposure, while the scanline mapping method results in a statistically sounder underpinning of these values in the same unit.

The advantage of the scanline survey is that orientation and, in particular, spacing data are gathered systematically. The main objective of all the manual survey data is to provide a basis for comparison with the information that result from analysis of the laser-based survey data. The scanline and SSPC data only provide statistical information on the discontinuities and it is therefore not possible to verify the orientations of individual discontinuities. Therefore additional orientation measurements of individual discontinuities were made using a type of cell-mapping approach. A specific part of the slope was selected where certain (well recognisable) discontinuities were marked on a photograph. The orientations of the marked discontinuities were subsequently measured in the field. In this way individual orientations can be compared on a plane-to-plane basis, which helps to determine to what extent the computed orientations from the laser-based survey match the actual measured orientation of individual discontinuities.

5.4 Laser scan survey and fieldwork Spain

Twelve rock exposures in the Baix Camp region of Catalonia, Spain, were scanned with the Optech Ilris 3-D laser scanner (Figure 20). This laser scanning field campaign was carried out in the period between 2 and 10 June 2004. The sites are located on the map in Figure 21. The registration of the point clouds was done with the method described in the final part of Section 4.6.7.4. The registration simply consisted of levelling the laser scanner with a bubble levelling device such that the scanner was horizontal, while the bearing of the scanner was measured with the geological compass. The registration of the point cloud prior to the further data processing then merely required a rotation about the z-axis to account for the bearing, such that the positive y-axis of the point cloud is oriented north.

Engineering geological investigations were carried out before, during, and after the laser scanning survey to obtain rock mass descriptions, scanline surveys and cell-mapping of selected sections of the rock exposures were performed to obtain additional orientation data. As explained in the Introduction to this Chapter, two rock exposures were later selected to demonstrate the various data processing and analysis methods,. Both exposures consist of rocks of Carboniferous age. The characteristics of the Carboniferous rocks in the Baix Camp region are summarized in Section 5.4.1. Sections 5.4.2 and 5.4.3, respectively, provide detailed descriptions of the two specific rock exposures (Sites 1 and 2) that are used in the analysis.

5.4.1 Description of the Carboniferous rock mass units

The following brief geological description is largely derived and assembled from the geological explanations accompanying the older 1:50,000 geological map sheet series of the IGME (Instituto Geologico Y Minero de España), in particular the following map sheets:

- 472-33-18 Reus (Colodron et al., 1976)
- 471-32-18 Mora de Ebro (Orche et al., 1977)
- 444-32-17 Flix (Orche and Colodron, 1977)

The Carboniferous rocks in the Baix Camp region are typical basin deposits, mainly composed of shales and sandstones. The shales and sandstones are often interbedded, resembling flysch[12] deposits. Most of the rocks have undergone some degree of metamorphism, resulting in the presence of slates, metasandstones, micaceous sandstones and greywackes. The earliest

[12] Flysch is a sedimentary facies of mountain belts. The deposits were formed during the early stages of orogenesis in which the first relief forms yielded unsorted sediments in deeper waters. Flysch deposits are characterized by a thick series of thinly bedded mainly argillaceous beds, usually with intercalations of arenaceous turbidites (Encyclopædia Britannica, 2007). The term flysch is attributed to the geologist B. Studer (Studer, 1853) and it comes from the German word “fliessen” which means “to flow,” probably in reference to the frequent landslides that can occur in these formations.

sediments to be deposited were predominantly argillaceous. Towards the upper part of the sedimentary sequence the sediments became coarser. The total thickness of the Carboniferous sequence in the area is estimated to be up to 2000 metres. During the Hercynian orogeny in the Carboniferous and Permian periods, these sediments were folded in two phases, and slatey cleavage developed in the Carboniferous sedimentary rocks due to low-grade regional metamorphism. Later intrusions of mainly granodioritic composition within these metamorphosed sedimentary rocks resulted in additional contact metamorphism at some locations. The contact metamorphic rocks often contain “spotted” slates. The intrusions probably took place during the Late Carboniferous and Early Permian times.. The contact metamorphism was followed by pneumatolytic[13] events that resulted in the formation of white mica and tourmaline. A period of region erosion followed, forming an erosional surface across the Palaeozoic rocks. Above this erosional surface the red clastic materials of the Buntsandstein were deposited during the Triassic Period. The rock masses from the Carboniferous contain more than three sets of discontinuities, and these discontinuities are well developed, which makes exposures of these rocks well suited to demonstrate the methodologies presented in this thesis.

Figure 5.1. Typical laser scanning field survey setup during the field campaign in Spain in June 2004. The laser scanner is an Optech Ilris 3-D type. This laser scanner has an external battery pack (on the ground), while the point cloud data is stored on a removable media. The scanner is controlled through the infrared port of a handheld PDA. The umbrella is used to keep the scanner cool and to allow better readings of the LCD control screen on the scanner’s back.

[13] Pneumatolysis is a metamorphic process caused by action of hot vapours or superheated liquids under pressure that are emitted from solidifying magma (Pneumatolysis, n.d.).

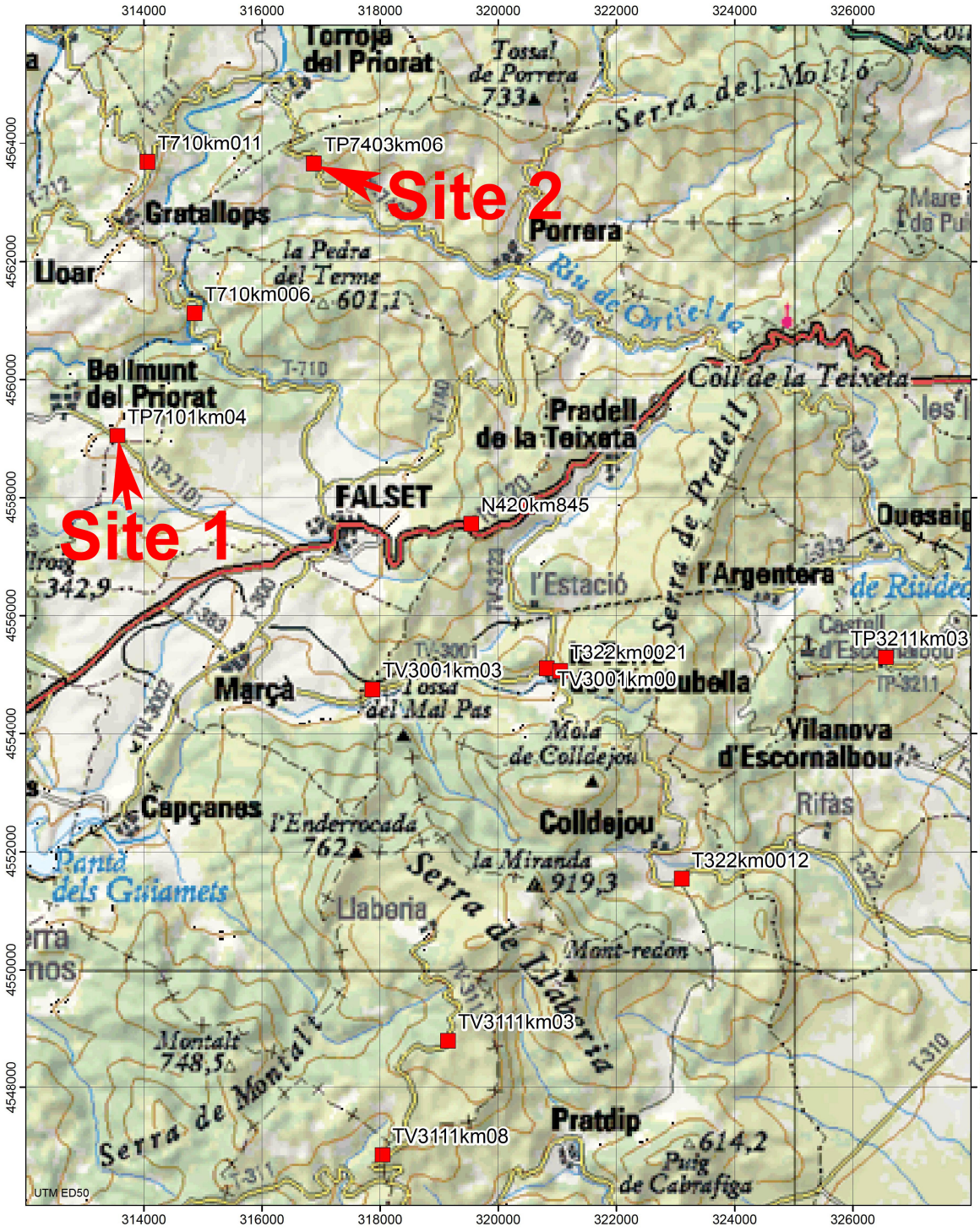

Figure 5.2. Map of the fieldwork area in the Baix Camp region in Catalonia, Spain. The 12 survey sites are marked with red squares. The two test sites that are used in this study (Site 1 and Site 2) are also indicated. The coordinates are in metres, projection UTM, zone 31, European Datum 1950.

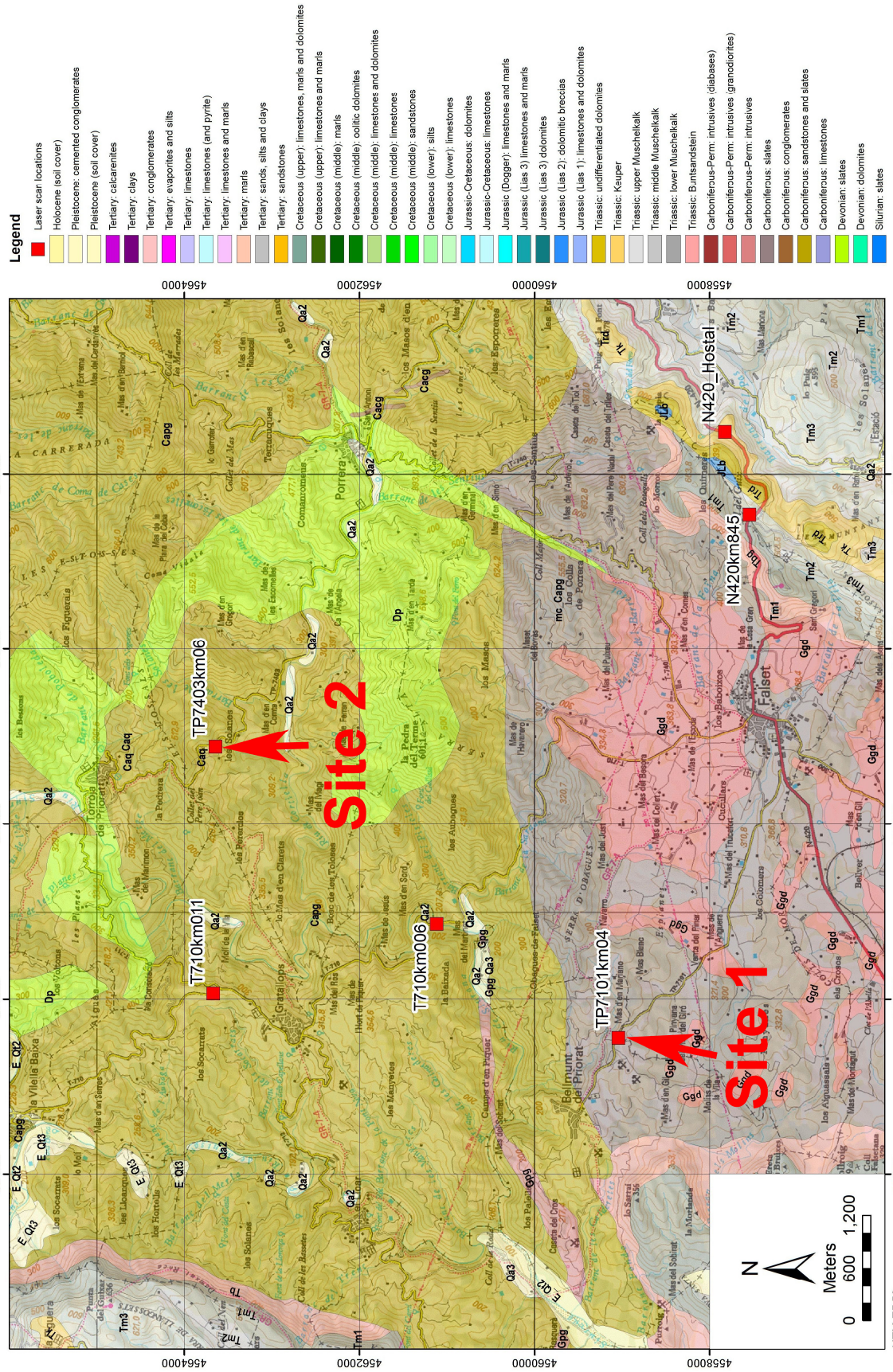

Figure 5.3. Geological map of the area in which six of the laser scan surveys have been carried out. The two sites that are described in this Chapter in detail (Site 1 and Site 2) are the locations TP701km04 and TP7403km06, respectively. The map is created in ESRI ArcMap® 9.0. The source of the topographic GIS data is ICC (2007) and the source of the geological data is IGC (2007).

5.4.2 Site 1 – Along Road TP7101 Falset to Bellmunt del Priorat

The rock exposure defined as Site 1 is located about 4 km west of Falset along road TP7101 and is near the western edge of the Baix Camp region illustrated in Figure 5.2. Figure 5.4 provides an overall view of the rock exposure and illustrates the use of two 60 x 60 cm white boards with measured orientations that act as additional scale and orientation reference markers during the analysis of the laser scanned point cloud data.

Figure 5.5 illustrates part of the 3-D point cloud data obtained at Site 1. The reflected intensity values have been assigned grey-scale values to create this visualisation. The average distance from the scanner to the exposure was quite short, only about 11.3 m. Thus the spatial resolution, the typical distance between adjacent scanned points, is about 5 mm. The point cloud contains 1.9 million points.

5.4.2.1 General rock mass characterisation and rapid face mapping data

The exposed rock mass was initially systematically described using the SSPC system (Hack, 1996). The results are given in "Appendix A. Field observations Site 1 – Bellmunt (Table 11.1)". According to the British Standard BS 5930 (1999) the exposed rock mass can be described as:

- "Dark Grey to Black, Silt-Clay size, Small tabular, Slightly weathered META-SILTSTONE and SLATE".

According to the 1:25000 scale geological map shown in Figure 5.3 (ICG, 2007), the exposure is located in a geological unit of Carboniferous age. The legend of the geological map gives the following description for this geological unit:

- Carboniferous: Slates – The geological code for the unit is *mc_Capg*. This gives some additional information, i.e.: In this Carboniferous unit contact metamorphism (mc) may occur due to porphyritic granites (pg) that intruded during the late Carboniferous or during the early Permian.

The SPCC characterisation, based on the rapid face mapping approach explained in Section 3.5.3, resulted in the identification of eight discontinuity sets (see Table 5.1 below). However, it should be noted that the identification of the sets by this method may be biased. Subsequent scanline analysis and/or plotting of the orientations in a stereo polar plot will reveal whether the initially identified sets are truly independent discontinuity sets. This is discussed in the following Section. The rapid face mapping approach was considered to be an essential first step in the entire rock mass characterisation process, even if it may result in some bias in identifying joint sets.

Table 5.1. Identified and characterised discontinuity sets in the Bellmunt rock exposure (Site 1), based on a rapid face mapping approach. Data are from the SSPC form table in Appendix A, Table 11.1.

	C1	J2	J3	J4	J5	J6	J7	J8
Mean dip direction (°)	344	328	147	263	240	054	268	265
Mean dip angle (°)	44	85	58	90	64	80	58	42
Mean normal set spacing (m)	0.01	0.60	0.40	0.60	1.80	1.20	0.80	0.20

5.4.2.2 *Scanline survey and cell mapping data*

Two scanline surveys were conducted on the rock exposure at Site 1:

- one horizontal scanline, and
- one vertical scanline (see Appendix A, Figure 11.3).

Additional, more detailed, orientation measurements (20 in total) were made for a specific part of the exposure in an area of around 2 m. x 1.5 m. around the start of the horizontal scanline (see Appendix A, Figure 11.6). By plotting all the orientations in a polar plot, five discontinuity sets can be recognised (see Figure 5.6 and Figure 5.7). The number of sets is thus fewer than the eight sets that were previously identified in the rapid face mapping and shown in Table 5.1.

In order to calculate the spherical statistics on the sets that are identified in the polar plot, every observation has been assigned to one of the five recognised sets. The average orientation, the resultant *R*, Fisher's *K*-value and spherical variance *s* can be calculated based on the methods described in Section 3.7.3. The discontinuity set spacing is computed through sorting of the intersection distances in the scanline data (see Appendix A, Table 11.2 and Table 11.3) for all observations from each set. A list of set spacings is derived by subtracting subsequent intersection distances. The list of set spacings must be corrected to get the normal set spacings. This is accomplished by multiplying each set spacing along the scanlines with the cosine of the acute angle between the normal corresponding to the mean orientation and the bearing of the specific scanline. These methods are described previously in Section 3.5.1). Table 5.2 provides the results of the spherical statistics and the spacing calculations for Site 1.

Table 5.2. Summary statistics of the scanline surveys done on the Bellmunt exposure (Site 1). In order to increase the number of observations, the data from the additional survey on individual discontinuities (listed in Appendix A, Table 11.4) are added to the scanline data. Since the additional survey data do not contain data on spacings, the Mean normal set spacing is solely based on the scanline data.

	Set 1	Set 2	Set 3	Set 4	Set 5
Mean dip direction (°)	341.1	71.8	172.6	335.0	267.0
Mean dip angle (°)	41.3	84.5	56.0	78.8	56.2
Number of observations N	38	37	12	7	6
Resultant R	37.82	36.06	11.90	6.94	5.95
Fisher's K	199.38	37.06	104.86	77.44*	83.63*
Spherical variance s	0.069	0.160	0.089	0.096	0.089
Mean normal set spacing (m)	0.10	0.17	0.60	0.29	0.77
Stand. dev. NS spacing (m)	0.17	0.13	0.60	0.31	0.63
Max. normal set spacing (m)	0.58	0.46	1.71	0.87	1.45

*) Remark: these Fisher's K constants are not valid, because the number of observations (N) are smaller than 10.

5.4.2.3 *Discussion of the results for Site 1*

From the stereo plots shown in Figure 5.6 and Figure 5.7, it is obvious that not more than five discontinuity sets can be recognised. However, the rapid face mapping resulted in the identification of eight sets. It is possible that both the scanline survey as well as the cell mapping overlooked some important sets, since both methods are constrained to a specific part of the exposure, while the rapid face mapping is supposed to consider the entire exposure. On the other hand, there is also the option that the rapid face mapping identified some sets as separate discontinuity sets, which, based on subsequent analysis, do not form multiple sets, are possibly part of a set that exhibits large spherical variance. Since the polar plots show such distinct sets, it is assumed that the latter option is the case. This is investigated below.

In order to determine which of the sets identified in the rapid face mapping may be redundant, the sets from Table 5.1 and Table 5.2 were compared and paired where possible. To avoid confusion, the sets from the rapid face mapping (Table 5.1) and the scanline and cell mapping survey (Table 5.2) are deliberately named and numbered differently.

- The most obvious sets that are identical are C1 in Table 5.1 and Set 1 Table 5.2. Both have very similar orientations and they correspond to the slatey cleavage and bedding in the meta-siltstones and the slates. This set forms in the polar plot the very well identified set with the strong (circular) Fisher distribution, having a relative high K-value. However, the observed mean normal set spacing differs strongly by a factor 10 (0.001 versus 0.10). This discrepancy is most likely because in the rapid face mapping the distance of the slatey cleavage itself was measured. In the scanline survey only the exposed cleavage planes are measured, which do not necessarily correspond to the actual cleavage distance. The size of the rock blocks that are generated from this slope are also not tabular and typically “slatey” but are much thicker, tending more towards decimetre size than centimetre size as suggested by the rapid face mapping. The thickness of the blocks is about 5 cm, which is the approximately the spacing between the two cleavages.
- Both sets J4 and J6 in Table 5.1 are similar (almost vertical, thus the dip direction can suddenly change to the opposite direction) and most likely related to the oval-shaped discontinuity Set 2 in Table 5.2. The oval shape of Set 2 in Figure 5.6 and Figure 5.7 is typical for a Bingham distribution, which corresponds to curved or wavy discontinuity surfaces. This can be confirmed by the observation made in the SSPC form for set J4 (see Appendix A, Table 11.1) which is characterised as having “Curved” large-scale roughness, more curved than any of the other sets.. Set J6 has been identified having “Slightly curved” large-scale roughness and which is therefore not very evident. The observed mean normal set spacings of J4 and J6 (0.6 and 1.2 m., respectively) are much larger than the mean normal set spacing computed for Set 2 (0.17 m). However, considering the fact that both sets J4 and J6 were treated separately already means that there is an overestimation of the normal set spacing. It seems that the 1.2 m spacing of J6 is cut in half by the set J4 (with spacing 0.6 m), probably due to the fact that the planes of J6 are also used in the estimation of the spacing of J4.
- Joint set J3 in Table 5.1 corresponds to Set 3 in Table 5.2. Although the difference in dip direction is quite large, orientation of set J3 still falls within the range of orientations identified as Set 3. The observed mean normal set spacings are similar.
- Joint set J2 in Table 5.1 corresponds to Set 4 in Table 5.2. The dip direction is similar although the dip angle differs by almost 20 degrees from the average dip of Set 4, but this falls still into the range of orientations within this set. However, Set 4 is not a very distinct joint set and only seven observations can be attributed to this set. This set appears to be an “intermediate” set of the more obvious Set 1 (Slatey cleavage) and Set 3 with about the same strike but with varying dip angle. The mean normal set spacing differs by a factor 2.
- The joint sets J7 and J8 are very similar in orientation and can therefore be combined. Also joint set J5 in Table 5.1 does also not differ much from joint sets J7 and J8. All three sets plot fall well within the identified Set 5 in Table 5.2. Set 5 is also not a very distinct discontinuity set, much like Set4, with only six observations. This is due to the combination of having a relative large normal set spacing compared to the other sets (0.77 m) and the fact that this set is oriented almost parallel to the exposed slope, which has an orientation of 208/62.

In conclusion, it appears that the eight sets recognised by the rapid face mapping survey and summarised in Table 5.1 can be reduced and attributed to the five discontinuity sets identified in the polar plots of the scanline and the cell mapping data and defined in Table 5.2. The mean normal set spacing observed by the rapid face mapping is in most cases several times larger than the spacing calculated with the scanline survey. In some instances this is due to the fact that multiple sets recognised in the rapid face mapping should have actually been assigned to a single set, which results in an overestimation of the spacing. The small (1 cm) slatey cleavage as observed with the

rapid face mapping procedure does not result in the thin blocks, small tabular size (according to the BS5930:1999), and thus underestimates the typical size of the blocks that are currently falling out of the slope. However, if the weathering processes on the slope increase (for example due to increased groundwater flow, surface runoff and/or wetting and drying processes), increased fracturing along the slatey cleavage and bedding planes is likely to develop within an engineering lifetime (perhaps 50 years). In turn, this would indeed result in the development of smaller, thinner block sizes (Huisman, 2006).

Figure 5.4. Photograph of the surveyed and scanned rock exposure at Site 1. The two white boards act as scale and orientation reference: the left white board has an orientation of 024/40 and the right one 022/39. Both white boards are 60 x 60 cm in dimension. View direction is SSW.

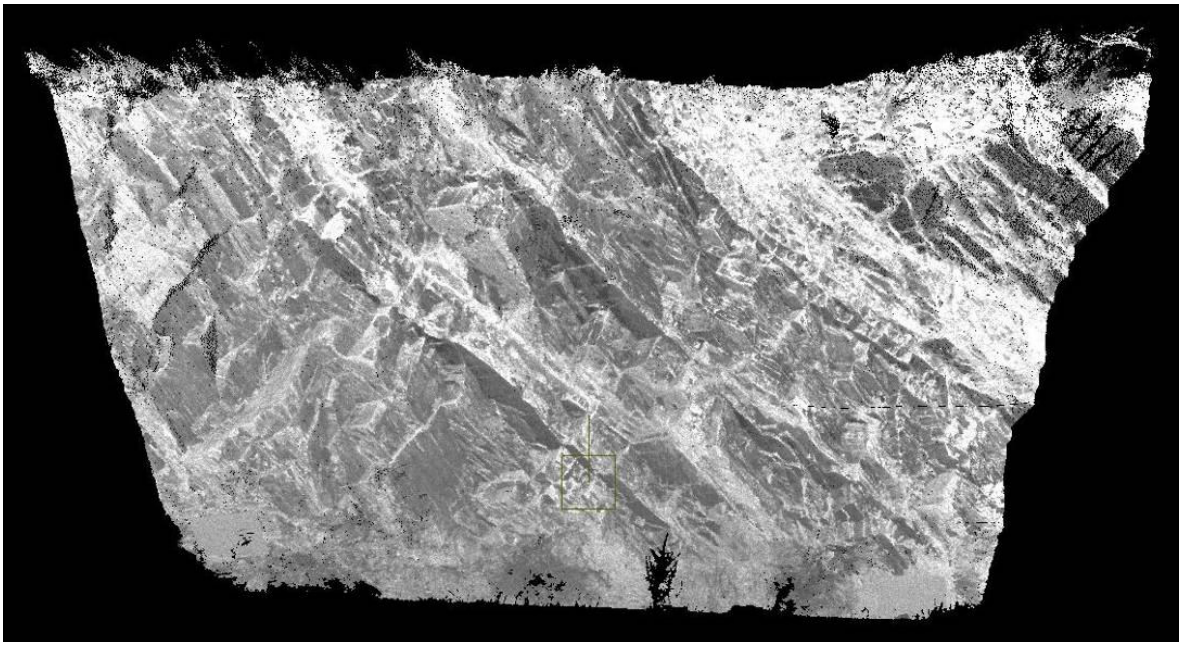

Figure 5.5. Part of the 3-D point cloud generated for Site 1 rock exposure. For visualisation purposes, the points in the point cloud have been assigned a grey-scale value, based on the reflected intensity. The original raw point cloud consists of 1.9 million points, with a spatial resolution of about 5x5 mm. The average distance of the laser scanner was 11.3 m and the bearing of the scanner was 204 degrees. For more details, please refer to Appendix C. Optech laser scanner survey details Site 1 (Bellmunt, Spain)

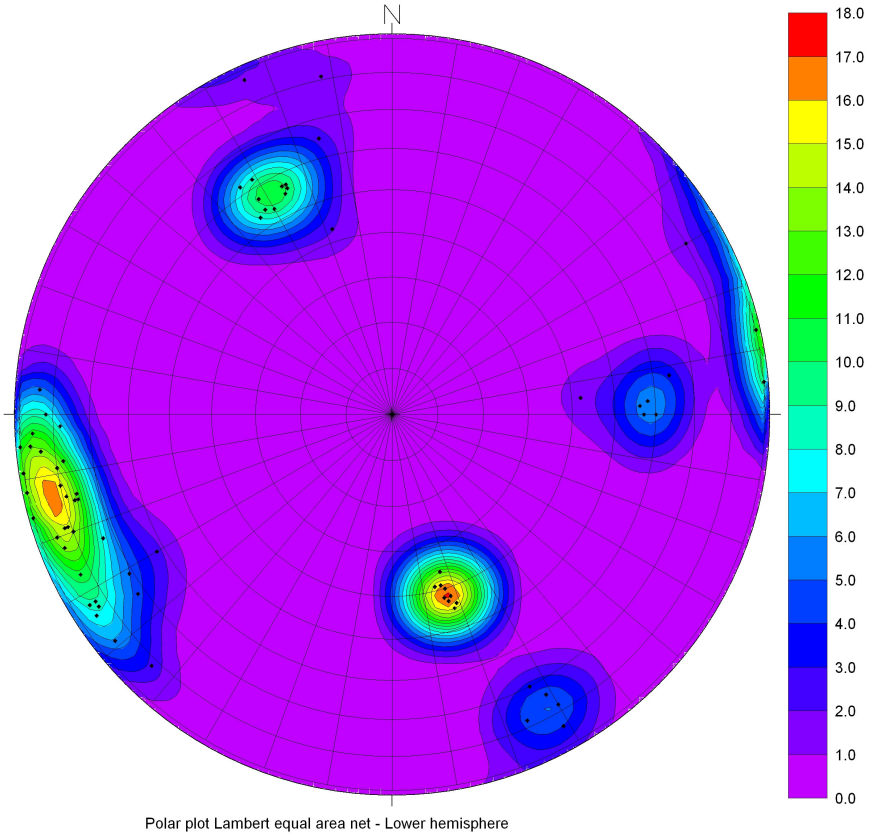

Figure 5.6. Site 1 (Bellmunt) stereo polar density plot of scanline observations. Five discontinuity sets can be distinguished of which three have many observations and although the other two sets have fewer observations, they still show distinct set separation.

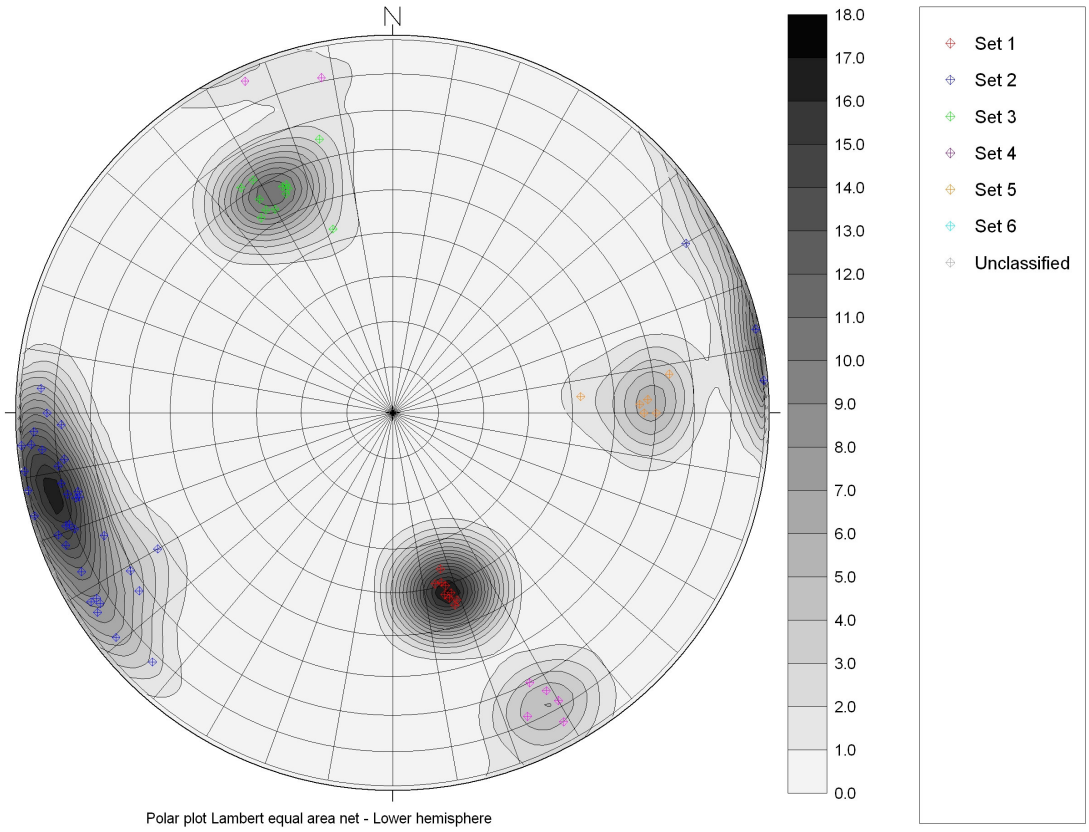

Figure 5.7. Site 1 (Bellmunt) stereo polar density plot of scanline observations. The individual observations are classified into five sets, and are coloured accordingly. Remark: the legend gives by default six sets, but only five sets are plotted. (Set 1 = red, Set 2 = blue, Set 3 = green, Set 4 = purple, Set 5 = orange dots).

5.4.3 Site 2 – Along Road TP7403 from Porrera to Torroja del Priorat

The rock exposure defined as Site 2 is located about 1.6 km south of the village of Torroja del Priorat along road TP7403 and is near the northern limit of the Baix Camp region illustrated in Figure 5.2. Figure 5.8 provides an overall view of the rock exposure and illustrates the use of two 60 x 60 cm white boards with measured orientations that act as additional scale and orientation reference markers during the analysis of the laser scanned point cloud data.

5.4.3.1 Site 2 Rock mass characterisation

The exposed rock mass was initially systematically described using the SSPC system (Hack, 1996). The results are given in Appendix B. According to the British Standard BS 5930 (1999) the exposed rock mass can be described as:

- "Mottled light brown, Arenaceous, Medium Blocky, Slightly weathered, META-SANDSTONE."

According to the 1:25000 scale geological map as shown in Figure 5.3 (ICG, 2007) the exposure is located in a geological unit of Carboniferous age. The legend of the geological map gives the following description for this geological unit:

- Carboniferous: Sandstones and Slates - The geological code for the unit is *Capg*. This gives some additional information, i.e.: In this Carboniferous porphyritic granites (pg) intruded during the late Carboniferous or during the early Permian.

The SPCC characterisation, based on the rapid face mapping approach explained in Section 3.5.3, resulted in the identification of four discontinuity sets (see Table 7 below) As was described in the analysis for Site 1, subsequent scanline analysis and/or plotting of the orientations in a stereoplot may reveal whether these initially identified sets are truly independent discontinuity sets.

Table 5.3. Identified and characterised discontinuity sets in the Torroja rock exposure (Site 2), based on a rapid face mapping approach. Data are from the SSPC form table in Appendix B, Table 11.5.

	J1	J2	J3	J4
Mean dip direction (°)	209	135	279	086
Mean dip angle (°)	90	54	24	63
Mean normal set spacing (m)	0.50	0.30	0.50	0.25

5.4.3.2 Scanline survey

Three scanline surveys were done on the rock exposure at Site 2:

- one horizontal scanline and
- two vertical scanlines (see Appendix B, Figure 11.9 to Figure 11.11).

Additional more detailed orientation measurements (26 in total) were made for a specific part of the exposure in an area of around 4 x 2 m. covering the first part of the horizontal scanline and the area where the two vertical scanlines are located (see Appendix B, Figure 11.12). By plotting all the orientations a polar plot, six discontinuity sets can be recognised (see Figure 5.10 and Figure 5.11). Three sets are very distinct with many observations, but the other three sets have fewer observations and show more scatter. It should be noted that the total number of sets thus identified on the polar plots is higher than the four sets that were identified in the rapid face mapping (see Table 5.3). This is different from the situation at Site 1, where more sets were observed with the rapid face mapping method compared to the scanline surveys.

In order to calculate the spherical statistics on the sets identified in the polar plot, every observation was assigned to one of the six recognised sets. The average orientation, the resultant *R*, Fisher's *K*-value and spherical variance *s* can be calculated based on the method described in Section 3.7.3. The discontinuity set spacing is computed through sorting of the intersection distances in the scanline data (see Appendix B, Table 11.6 to Table 11.8) for all observations from each set. A list of set spacings is derived by subtracting subsequent intersection distances. The list of set spacings must be corrected to get the normal set spacings. This accomplished by multiplication of each set spacing along the scanlines with the cosine of the acute angle between the normal corresponding to the mean orientation and the bearing of the specific scanline. These methods are described previously in Section 3.5.1. Table 5.4 provides the results of the spherical statistics and the spacing calculations for Site 2. In order to increase the number of observations, the data from an additional survey of individual discontinuities (listed in Appendix B, Table 11.9) were added to the scanline data. Since the additional survey data do not contain data on spacings, the value of the mean normal set spacing is solely based on the scanline data.

Table 5.4. Summary statistics of the scanline surveys done on the Torroja exposure (Site 2).

	Set 1	Set 2	Set 3	Set 4	Set 5	Set 6
Mean dip direction (°)	213.5	133.4	287.9	219.9	246.3	087.8
Mean dip angle (°)	83.6	49.0	37.2	73.5	69.8	53.4
Number of observations N	36	20	21	8	4	4
Resultant R	35.53	19.78	20.70	7.81	3.87	3.85
Fisher's K	72.36	82.50	64.21	31.47*	15.05*	12.98*
Spherical variance s	0.114	0.104	0.119	0.154	0.182	0.196
Mean normal set spacing (m)	0.18	0.60	0.21	0.28	0.44	0.04
Stand. dev. NS spacing (m)	0.18	0.50	0.12	0.12	n.a.	n.a.
Max. normal set spacing (m)	0.81	1.41	0.53	0.46	0.75	0.37

*) Remark: these Fisher's K constants are not valid, because the number of observations (N) is smaller than 10.

5.4.3.3 Discussion of the results for Site 2

Distinct bedding structures are absent in the exposed coarse (sedimentary) sandstone,. The apparent lack of bedding structures can be explained by the possibility that this particular sandstone unit has been deposited by a turbidity current in a single event. The subsequent formation of joint patterns within the rock mass will likely follow some internal deposition structure, but it is not possible to identify any of the joint systems as bedding orientations.

The polar plots (Figure 5.10 and Figure 5.11) show three very distinct joint sets: Set 1, Set 2 and Set 3. All three sets have a relatively large number of observations with K-values and spherical variances that are similar. The remaining sets, Set 4, Set 5 and Set 6 are less pronounced due to fewer observations and larger scatter. Set 4 especially shows a large scatter and appears to be an "intermediate" joint set between Set 2 and Set 3. A similar situation was observed at Site 1 (the "Bellmunt" site) where the joint Set 4 was the intermediate set of Set 1 (the Slatey Cleavage) and Set 3 (see Section 5.4.2.3).

In comparison with the sets recognised in the rapid face mapping survey and summarised in Table 5.3, Set 1 (Table 5.4) can be linked to the set J1 (in Table 5.3). Set 2 can be linked to set J2, Set 3 to set J3, and Set 6 to set J4. Set 4 and Set 5, which are identified on the polar plots, have not been identified in the rapid face mapping. This is not very surprising, since both sets consist of relatively few observations. Further, the joint planes in both sets are almost parallel to the general trend of the slope (276/75), which makes these sets hard to recognise unless a systematic analysis of the joints is done by scanline surveys.

The spacing estimations from the rapid face mapping survey are also difficult to relate to the normal set spacing calculations that are based on the scanline survey. The sets J1 and J3 overestimate the spacing by more than a factor 2 compared to the spacings of Set 1 and Set 2. The spacing of joint

set J2 is underestimated though, by a factor 0.5 as compared to the spacing of Set 2. Only Set 6 and the set J4 have a mean normal set spacing that is comparable. However, the spacing computation is based on merely four observations along the scanlines and is therefore far less reliable as the spacing computations of Set 1, Set 2 and Set 3 are based on more observations.

Figure 5.8. Photograph of the surveyed and scanned rock exposure at Site 2. The two white boards act as scale and orientation reference: the left white board has an orientation of 262/70 and the right one 266/70. Both white boards are 60 x 60 cm in dimension. View direction is towards the East.

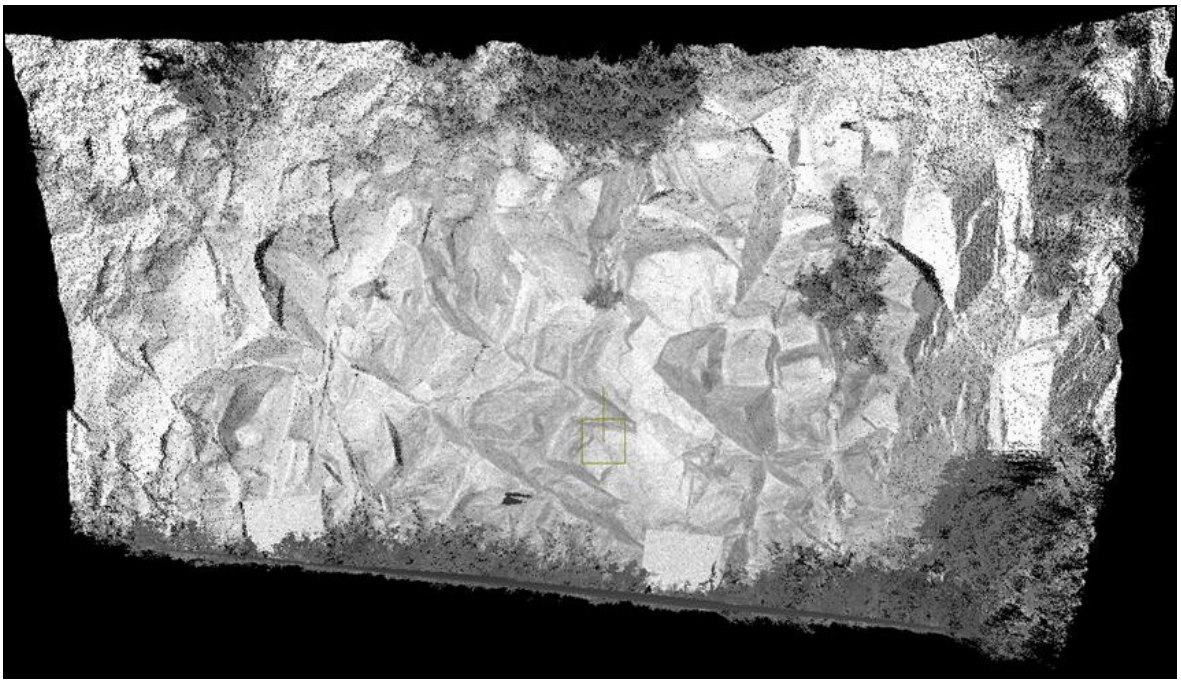

Figure 5.9. Part of the 3-D point cloud generated of rock exposure 2. For visualisation purposes, the points in the point cloud have been assigned a grey-scale value, based on the reflected intensity. The original raw point cloud consists of 1.7 million points, with a spatial resolution of about 6 x 6 mm. The average distance of the laser scanner was 15 m and the bearing of the scanner was 084 degrees. For more details, please refer to Appendix D. Optech laser scanner survey details Site 2 (Toroja, Spain)

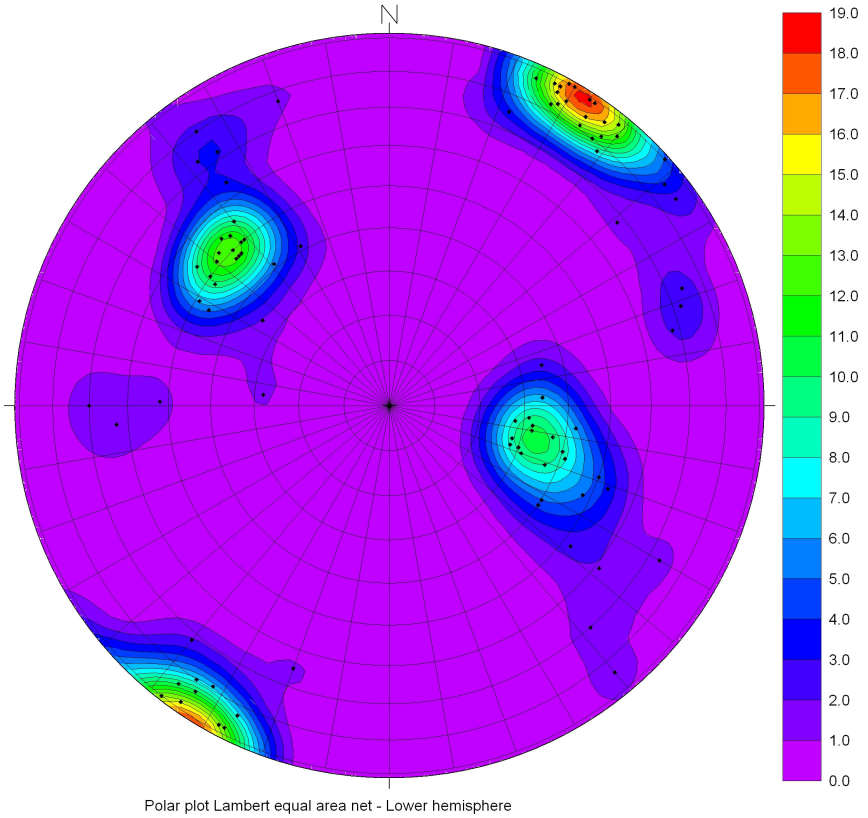

Figure 5.10. Site 2 (Torroja) stereo polar density plot of the scanline observations. Six discontinuity sets can be distinguished. Three are distinct, with many observations, while the other three are less obvious. See also Figure 5.11 below.

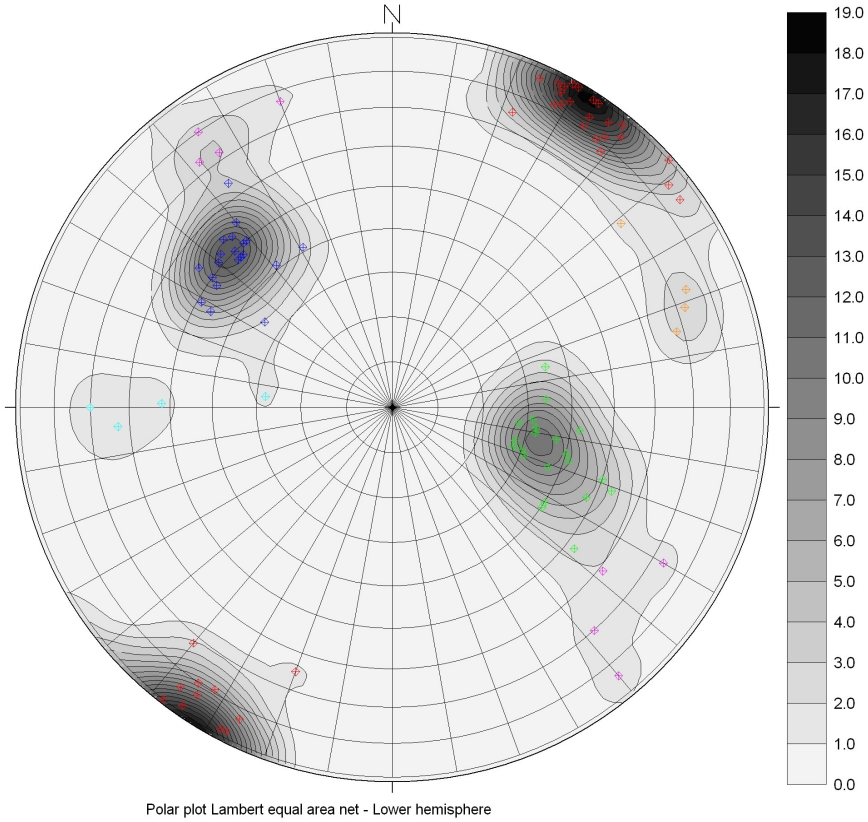

Figure 5.11. Site 2 (Torroja) stereo polar density plot of the scanline observations. The individual observations are classified into six sets, and are coloured accordingly. (Set 1 = red, Set 2 = blue, Set 3 = green, Set 4 = purple, Set 5 = orange and Set 6 = cyan coloured dots).

5.5 Laser scan survey Belgium

A field campaign was conducted at three sites around the city of Namur in Belgium, with a Riegl LMS-Z420i time-based scanner. The features of this particular laser scanner are discussed in Section 4.4. The objective of the surveys in Belgium was to demonstrate the capabilities of laser scanner manufactured by a different vendor that included advanced control features. In contrast to the field survey conducted in Spain no reference information in the form of scanline surveys or compass measurements were made for the sites in Belgium. The reason is that the three sites were scanned in one day, without the possibility of obtaining detailed ground control data, as the field time was limited. The physical access at the two sites was also difficult with scanning restricted to the higher parts of the slope. However, the quality of the scan data and the capabilities of the scanner are relevant to be discussed here.

5.5.1 Laser scan survey of a rock face near Thon, Belgium

The first survey was conducted on a well-exposed large rock face near the town of Thon consisting of Carboniferous (Upper Visean) limestones. The site is assumed to be an abandoned quarry. The scanned rock face is showing almost horizontal bedding planes. The rock face was scanned from one position and the field setup is shown in Figure 5.12.

The rock face is first surveyed with a quick scan at a high speed-low resolution mode (scanning at 11000 points per second, with an oscillating mirror), in order to get a general overview of the scene in the form of a point cloud. Subsequently, in the software that controls the scanner (which runs on the attached laptop PC), the area can be specified which needs to be surveyed. Then the scanning resolution is defined after which the survey starts.

Parts of the rock face were scanned at two different resolutions:

1. a high resolution scan of a smaller section of the rock face: approximately 2.2 million points (900 horizontal x 2459 vertical) at an angular resolution of 0.018 degrees, and
2. a medium resolution scan of the entire rock face: approximately 1.8 million points (2015 horizontal X 910 vertical) at an angular resolution of 0.05 degrees.

With the 8000 points per second measurement rate, both scans took approximately 4 minutes. The Riegl scanner rotates the scanner head around its vertical axis and can perform a full 360 degrees rotation. In contrast, the Optech scanner (used during the Spain survey) has a fixed scanner head.

During the survey, while the Riegl's scanner head is rotating, the mounted digital photo camera is taking a number of overlapping photographic images of the scanned scene. The camera is fully calibrated to the scanner and the imagery is co-registered to the point cloud data. The geometric information from the point cloud data can therefore be used to create an ortho-rectified image.

Concurrently, the image colour information can be used to add Red, Green and Blue Digital Number (DN[14]) values to the (X, Y, Z, and Intensity) data already generated by the scanner. This allows the user to show the point cloud data as coloured points, an example of which is show in Figure 5.13. The advantage of showing the points with colour instead of intensity is that is becomes easier for the user to relate the data with the actual situation and with acquired field measurements. Details of the scans are given in Appendix E.

[14] A Digital Number or DN is the value stored within a pixel or cell of an image.

Figure 5.12. Field setup of the Riegl LMS-Z420i at the Thon site. A digital camera is connected with a mount on top of the laser scanner. The camera is geometrically and optically calibrated. This allows the colour information from the digital camera to be added to the point cloud data. The laser scanner is operated by the attached laptop computer.

Figure 5.13. Visualisation of the point cloud of the Thon site. Information from the digital camera is used to add colour to the points.

5.5.2 Laser scan survey of a rock face near Dave, Belgium

The second survey was conducted on a steep rock face along the Meuse river. referred to locally as “Rochers de Néviaux”, just north of the town of Dave. The rock face is popular for rock climbing. The rock mass consist of limestones that are of Carboniferous age. The bedding planes of the scanned rock face are oriented nearly vertical. The rock face was scanned from one position and the field setup is shown in Figure 5.14. The scanner and camera were tilted from the vertical to obtain an optimal field of view of the high rock face. The whole scanner and camera combination can be tilted in steps of 5 or 10 degree to a maximum of 90 degrees. The tilt positions are calibrated so that the point cloud data registration is not affected.

Parts of the rock face were scanned at two different resolutions:

1. a high resolution scan of a smaller section of the rock face: approximately 3.0 million points (1818 horizontal x 1672 vertical) at an angular resolution of 0.026 degrees, and
2. a medium resolution scan of the entire rock face: approximately 1.8 million points (947 horizontal X 1889 vertical) at an angular resolution of 0.06 degrees.

With the 8000 points per second measurement rate, the first (high resolution scan) took approximately 6 minutes and the medium resolution scan took approximately 4 minutes.

Details of the scan are given in Appendix F.

Figure 5.14. Field setup of the Riegl LMS-Z420i at the Dave site. It can be seen that the laser scanner has been tilted backward to obtain an optimal field of view of the upper part of the slope.

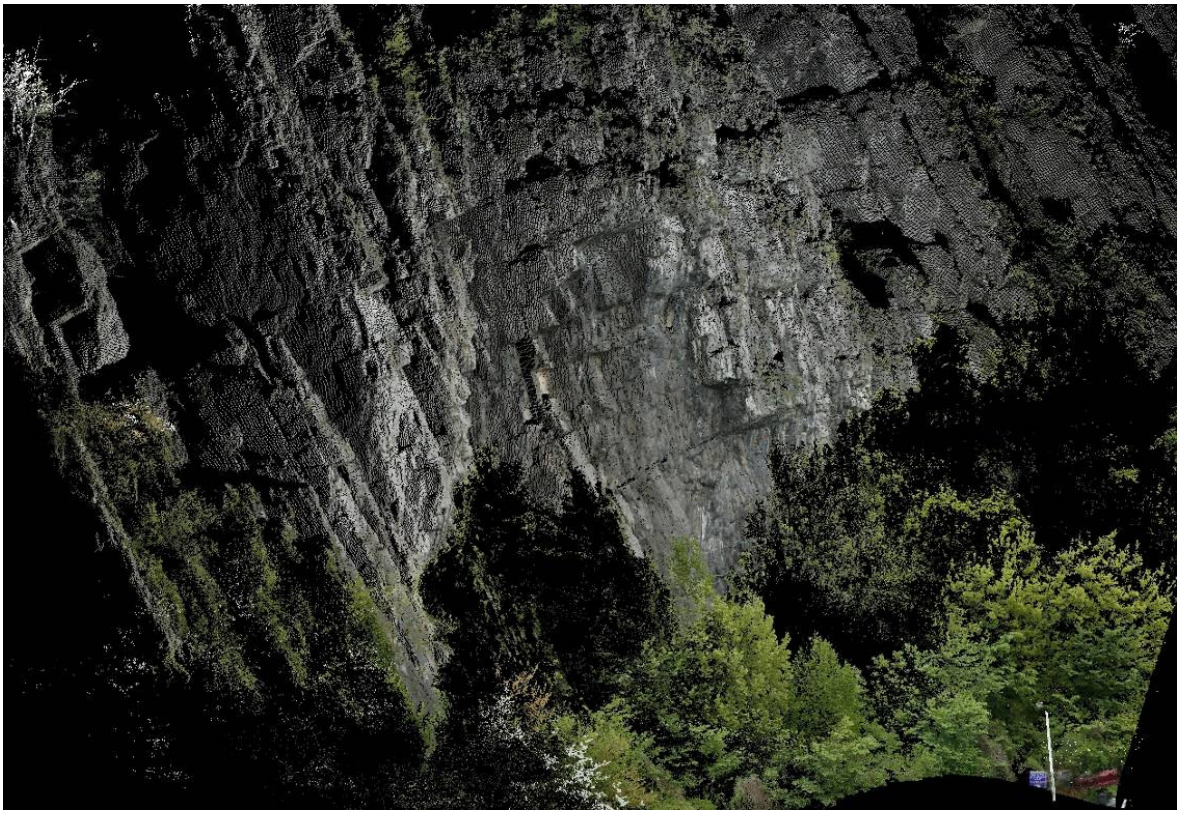

Figure 5.15. Visualisation of lower part of the point cloud of the Dave site. Information from the digital camera is used to add colour to the points.

6 Methods for analysing point cloud data

6.1 Introduction

The application of terrestrial three-dimensional laser scanners in all kinds of fields has resulted in the demand for very specific data handling and processing techniques. Before, laser scanners were merely used by geodetic engineering experts as an additional survey tool. Geodesists are used to dealing with this kind of data and these experts know well how to integrate the data with their own applications. However, as other applications fields discover the potential benefits of 3-D laser scanners, many of these individuals have difficulties handling and processing the laser scanner data. The point cloud is, by definition, 'just' data and therefore does not provide instantaneous useful information to the user. Point cloud data can be intuitively interpreted from a visual point of view, thus many users find it sufficient to keep the data as it is. However, in order to use the data to its full potential and derive more useful information from it, preferably in an efficient (automated) manner, it is necessary to process and analyse the point cloud data further. This chapter first discusses the typical character of laser-scanner derived point cloud data, then defines the most important data analysis techniques.

6.2 Methodologies

The data generated by three-dimensional terrestrial laser scanners have a number of very specific characteristics. While this data is, by definition, three-dimensional, unorganised, and noisy; it is also, in general, very dense, but can contain regions with lower point density or areas without data points. These areas of lower point density are "shadowing" effects related to the inherent inability of a light beam from a single source to illuminate all portions of an irregular surface. These specific characteristics, in turn, require very specific data handling and processing techniques. Regular 2-D GIS or CAD systems, which most of the data users are familiar with are generally not well-suited to process to handle the often very large point cloud data sets. Most of the commercially available laser scanners come with their own software; however, this software is mostly only designed to operate the scanner and to store and export the point cloud data. Some more advanced scanner-specific software may be capable of georeferencing the locations of the data points, merging successive scans, and co-registering digital photographs with the point-cloud data points.

Specific software for the automated processing of terrestrial laserscan data to support rock mechanics evaluations by analysing discontinuity geometries is still very rare and development of such software is still in its infancy. The only such software known to exist presently by the author is called "Split-FX", developed by Split Engineering (Split Engineering, 2004). This software is still only available as a beta version but is expected to soon become commercially available. This research used the beta version of the Split-FX software and the results are described in Section 7.5.

However, other disciplines, in particular those that are supporting automotive and aerospace design, the medical professions, and the gaming and entertainment industry, have spend much effort into the development of software to automate the analysis of point cloud data in order to reconstruct surfaces from unorganised point clouds. These applications have the potential to be used for the analysis of discontinuities. Specifically, much research has been done on the recognition of specific geometric shapes, such as planes, spheres, or cylinders from point cloud data, often based on so-called point cloud segmentation methodology. The field of geodetic

engineering has focussed on the processing of airborne lidar point cloud data for detailed topographic surface modelling and for the removal of surface objects such as buildings and vegetation to create so-called “bare-earth” topographic models. Additional geodetic engineering research focuses on the recognition of specific geometric shapes from airborne laser scan data, especially for building and structure detection. Vosselman (n.d.) developed software called PCM (Point Cloud Mapper), which performs point-cloud segmentation based on Hough transformation. PCM was originally designed to interactively model buildings in 3-D. The PCM software is used in this study and the results are described in Section 8.5. Although designed for airborne lidar data, the PCM methodology has proved to be useful for the detection of discontinuity planes from terrestrial laser scan data as well. PCM is also not yet commercially available and is primarily intended for use in support of internal research and education within ITC and TU Delft.

From these various developments it can be concluded that there are basically two possible methodologies to analyse point clouds in order to derive geometric properties of rock mass discontinuities:

1. By structuring of the point cloud through point interpolation or surface reconstruction, a surface mesh is generated that can be used as input to the geometric analysis. Within this methodology, surface reconstruction can be undertaken by 2-D or 3-D approaches.
2. By structuring of the point cloud through a tree-structuring procedure, the original point cloud may then be segmented or classified into subsets that belong to the same geometric shape. For identifying planar discontinuities, the appropriate geometric shape is a plane. This procedure is generally called point cloud segmentation.

These two methodologies are further analysed in this chapter. Various surface reconstruction and point cloud segmentation techniques are discussed. The characteristics of laser-generated point-cloud data sets that are important in selecting the most appropriate techniques are discussed first, in Section 6.3. Section 6.4 discusses 2-D surface reconstruction methods, while Section 6.5 discusses 3-D surface reconstruction methods. Section 6.6 discusses point-cloud segmentation methods.

6.3 Character of point cloud data

6.3.1 Introduction

The laser scan-derived data set is by definition, a dense, three-dimensional, unorganised and noisy point cloud. The fact that the data is three-dimensional and dense makes it very hard to handle with conventional geographic software packages such as 2-D GIS (for instance ArcGIS, Ilwis or MapInfo). The standard 2-D point interpolation and gridding may also not readily work on 3-D point cloud data, although with some modifications, these principles can still be applied (Section 6.4). However, some of the more advanced CAD packages like AutoCAD are already fully three-dimensional and they do allow the integration of 3-D point cloud data. Handling of the point cloud data is generally memory-intensive, since much of the point cloud data need to be loaded in the computer’s RAM or into the memory of the graphics card, for proper visualisation and handling. However, new PC’s with a RAM of 2 Gigabyte and a good graphics card will have no major difficulties handling an average point cloud data set.

6.3.2 Three-dimensionality

The laser scan point cloud data is by-definition three-dimensional. In terms of three-dimensional coordinates this means that it is theoretically possible that there are several points in the point cloud that have similar coordinate pairs, but with a third coordinate that is different. For a single laser scan of a more or less vertical and straight rock face, it is quite likely that a series of point-cloud data points may have very similar x and y coordinates, but a series of changing z coordinates as the data points range from the top to the bottom of the rock face. On the other hand, two-dimensional

geometric or topographic point data typically have a single third coordinate value defining the "z" or "elevation" found at every unique x and y coordinate pair[15]. However, in contrast, every point in the point-cloud data is uniquely defined by the measured azimuth, angle and distance, which translates in a unique x, y and z coordinate in the scanner's coordinate system.

In particular, if the point-cloud data representing a more or less vertical rock face is rotated or geo-referenced to an absolute reference grid that is oriented with its principal axes N-S, E-W and vertical, the relative original scanner coordinate system is likely be transformed such that in the new coordinate system similar coordinate pairs in the x and y directions do have different third coordinates in the vertical direction. Also if scans of the same object or scene, obtained from different scanner locations, are merged, after geo-referencing, into a single data set, the three-dimensionality of the dataset will play an even more important role.

6.3.3 Spatial data structure

6.3.3.1 Data organisation

The raw point-cloud data is "unorganised", which means that there is no spatial structure in the data. In other words, the points are spatially uncorrelated. The data is stored serially, which means that each point is stored sequentially in the order in which the measurements are made. Usually, the laser beam rotates first along the (vertical) angle, producing a vertical profile series of data points, and subsequently moves incrementally horizontally along the azimuth, and the vertical scan process is repeated. This data gathering sequence causes the first vertical line scan or column to be stored as the first sequence of points. The second vertical line (column) is then appended to the data set as the next sequence of points and this process is repeated for the entire area scan.

In theory, the fact that data is stored sequentially can be used to organise the data. Take point $P_{(i,j)}$ for example, in column *i* and row *j*. The points in the previous and next row in the same data column (points $P_{(i,j-1)}$ and $P_{(i,j+1)}$) are the neighbours. The points in the next and previous column (points $P_{(i-1,j)}$ and $P_{(i+1,j)}$) are also the neighbours of point $P_{(i,j)}$. However, in case of a complex geometric shape of the scanned object, this criterion may not necessary be valid. Especially in the case of noise or objects in front of other objects, sequential points may be large distances from each other. In addition, from a programming point-of-view, this method of searching the dataset is computationally expensive, since it requires searching the entire point list for the neighbours based on their column and row indices.

The greatest disadvantage of having no spatial structure in the data is that it is computationally expensive to carry out any spatial analysis or, for example, specification of the neighbourhood. In order to find the nearest neighbour of a given point, the entire dataset has to be searched in order to find the point or set of points that fulfil the specific coordinate requirements. A spatial data structure makes this search more efficient. There are two strategies to create (spatial) structure in the unorganised point cloud data:

1. Through surface reconstruction, using either a 2-D or 3-D approach, and
2. by tree-structuring.

These approaches are discussed in Sections 6.4, 6.5 and 6.6.

6.3.3.2 Neighourhood specification

The purpose of having a spatial datastructure is that neighbourhood functions can more efficiently be carried out. The use of neighbourhood functions are essential in point cloud segmentation, which

[15] This (often topographic) data can be referred to as 2.5 D data, since it is used for "three-dimensional" visualisation and topographic modelling based on 2-D data. Many make the mistake of referring to this as "3-D modelling" which is fundamentally incorrect.

is described in Section 6.6. The neighbourhood to any given point can be specified in two different methods.

- K-Nearest-Neighbours (KNN): In this method for a given point, the closest k-points from the point cloud are selected. As the number of points (k) is fixed, the method adapts the Area Of Interest (AOI) according to the point density. Assuming that the point density is an indicator of the measurement noise (which is usually the case as for a given laser scanner the density declines with distance and angle of incidence), this results in a better sample of points for subsequent estimation of the seed surface as a bigger AOI is used in the areas of lower point density. Moreover, this method always uses the defined number of points and avoids degenerate cases (e.g. a point having no neighbours). (Arya, et al., 1998).
- Fixed-Distance-Neighbours (FDN): This method uses a given fixed AOI, and for each query point, selects all the points within this area. FDN results in different numbers of points according to the density of the point cloud, and so this method does not have the adaptive behaviour of KNN. This method is more suitable if the density of the points does not change much throughout the point cloud.

6.3.4 Areas of sparse or absent data

Point-cloud data often contains areas where data are sparse or absent. In the case of scans of rock exposures, this may result from occlusion of parts of the rock exposure that are almost parallel to the incoming laser beam (see section 4.6.4). Vegetation in front of the rock face will also create shadows on the rock face, resulting in areas where data is sparse or non-existent. Dynamic disturbances (see section 4.6.6) may obscure (small) parts of the scanned object and may also obscure (small) parts of the scanned rock face. Some of the surface reconstruction methods that are discussed in Sections 6.4 and 6.5 allow the interpolation and continuation of the surface over the data-sparse areas. It has to be considered whether this is actually desired or not. The fact that there is sparse data in certain areas means that the uncertainty of the shape of the surface in these areas is probably high as well. It is sometimes appropriate that these areas should be omitted from the analysis since the lack of data will affect the accuracy of the overall results. On the other hand, even the smaller number of data points in a particular area may still be sufficient to model the geometry of a discontinuity plane that happens to be in that area; for instance, an important discontinuity that would otherwise be omitted from analysis.

6.3.5 Noise and data error

Point-cloud data is also noisy. This is partly due to range measurement and instrument errors (see Section 4.5); such noise is inherent in the laser scanning process and cannot be avoided. The instrument error noise is an issue that will limit the accuracy of the surface reconstruction, particularly in the 3-D Delaunay interpolation (see Section 6.5.4). Laser scan surveys conducted to define rock faces in the open field also encounter noise in the data due to dust, vegetation, and dynamic disturbances in the scene, such as passing vehicles or persons. The locations of points representing dust or dynamic objects are mostly at some distance away from the rock face. Therefore, a simple spatial selection of the points in front of the face can remove this noise. The noise caused by vegetation near or on the rock face is difficult to remove. A manual selection of the noisy (vegetation) areas is not only very labour-intensive, but there is also the chance that parts of important rock features in the vicinity or behind the vegetation are removed as well. From an operational point of view, it is unfavourable to have to remove the noise from the data before processing and analysis, since this would require much manual editing that is time-consuming and prohibits a real-time operation. Instead, data analysis techniques should be used that can handle the noise in the data in an optimal and automated manner.

6.4 2-D gridding as a surface reconstruction technique

6.4.1 Introduction

2-D gridding is a standard technique used by GIS software, such as ArcGIS (ESRI) or other frequently employed point-interpolation software, such as Surfer (Golden Software). 2-D gridding is, in principle, not suitable for analysing 3-D point-cloud data and standard GIS and regular point-interpolation packages have difficulties handling and displaying the large volumes of dense point-cloud data that are typically associated with 3-D terrestrial laser scanners, and are therefore not suited to handle and grid laser-scanned data (see Section 6.3.1). The principle of 2-D gridding can nevertheless still be applied to analysing point cloud data, but with some modifications. The Split-FX software, the only available dedicated software for processing laser scan data for the purpose of rock mass characterisation, successfully uses the 2-D gridding approach. In the Split-FX implementation, as discussed in Section 7.5, 2-D gridding has a number of advantages over 3-D surface reconstruction.

6.4.2 Grid cell size and number of cells

2-D gridding is used by many GIS for terrain evaluation to produce a regularly spaced array of Z values from irregularly spaced (X, Y, Z) point data. Terrain data is in most cases relatively sparse; the distances between the data points are generally larger than the resulting grid size. The Z-values are therefore interpolated using various data interpolation techniques, such as inverse distance, nearest neighbour, Kriging or linear interpolation with triangulation. The interpolated elevation values are subsequently returned as a gridded array of Z-values. However, point cloud data generated by a 3-D terrestrial laser scanner is, contrary to most terrain data, spatially very dense. Interpolating between these already very dense data points will produce large numbers of very small grid cells that results in extremely large data storage and computer memory requirements. Instead of interpolating the values, the resulting grid data density may be reduced by averaging the multiple values contained within a single grid cell to each grid cell, although this leads to data loss.

6.4.3 Interpolation parallel to the rock face

Another issue with point cloud data is that it may not necessarily be the vertical Z-axis value that needs gridding. Particularly when dealing with scans of (near) vertical rock faces, the vertical Z-axis should be one of the two coordinate axes. This issue can thus be resolved by simple interchanging the Y and Z coordinates, but only if the X-axis runs (near) parallel to the face. When the laser scanner is directed towards the rock exposure, the resulting (non-georeferenced) point cloud data has generally the X-coordinate as the horizontal axis parallel to the general trend of the rock face, while the Y-coordinate is in fact the value that needs gridding since this value determines the surface variation of the (near) vertical rock face. The simple solution of interchanging Y and Z values will not work if the point cloud data is georeferenced. Even if the rock face is vertical, the georeferenced X and Y coordinate axes are unlikely to be orthogonal to the general trend of the rock face, unless the rock face runs North-South or East-West.

The appropriate solution to overcome this problem is to drape a 2-D grid onto the point cloud so that the two coordinate axes are not simply the standard georeferenced X and Y-axes, but are chosen such that they accommodate the largest variation in coordinates in two orthogonal directions. In other words, the gridding should be done parallel to the general trend of the rock face. The third orthogonal dimension with the smallest spatial variation can subsequently be used as the value for gridding, similar to “normal” 2-D surface interpolation. The Split-FX software package utilizes this modified 2-D gridding approach (Split Engineering, 2007). A regular grid is placed parallel to the general trend surface of the selected rock face. Furthermore, as discussed in Section 6.4.5, the total volume of the gridded data is reduced because the grid-cell size is interactively adjusted, based on the average amount of point cloud sampling points that fall within a grid cell. The average orthogonal distance of the points to the grid is then returned as the gridded value.

These gridded values are then used to create a triangulated mesh, and this mesh is in turn used as input for the geometric analysis.

6.4.4 Three-dimensionality

Section 6.3.2 explained that, because the point-cloud data is, by definition, three-dimensional, similar coordinate-pairs may have different third coordinates. In practice this does not occur, if a single point cloud scan is used that is not rotated or georeferenced. In addition, even if the data is rotated or georeferenced, 2-D gridding methods with axes aligned parallel to the general trend of the rock face may work satisfactorily with three-dimensional point-cloud data (see Section 6.4.3). There are some instances however where the three-dimensionality of the data creates problems in the surface reconstruction with 2-D gridding.

Vegetation and dynamic disturbances in front of the rock face may cause such instances. If this noise is not removed, the surface gridding will result in erroneous and “spiked” surfaces. Also a highly curved rock face, scanned by multiple scans that are subsequently merged, cannot be satisfactorily analysed by 2-D gridding methods for surface reconstruction.

6.4.5 Data reduction

As explained before, instead of interpolating the point data, it will be more advantageous, from a computational and data storage point-of-view, to chose a grid size larger than the mean spatial resolution of the points and to average the gridded point values over each grid cell. The disadvantage is that the high data density is reduced and some detail will be lost. The grid cell size should be varied according to density of the point cloud data and the requirements of the user.

6.5 3-D surface reconstruction techniques

6.5.1 Introduction

3-D surface reconstruction techniques have been applied to data gathered by close range digital photogrammetry and 3-D laser scanning to create realistic computer-based polygonal or mathematical models, while also providing improved data handling and visual rendering. The first and most important step in the creation of the models is to reconstruct the original surfaces of the objects and scenes represented by the point-cloud. However, the reconstruction of surfaces is a complex problem and has been a challenge for the wide array of disciplines that deal with this data. The following difficulties with the reconstruction of surfaces are generally identified:

1. The measured points are usually unorganised, often noisy and can contain sparse data and gaps as discussed in Section 6.3.
2. The surface is in general arbitrary, with a known topological type and with sharp features. (Fabio, 2003).

These problems have been addressed in many disciplines, ranging from reverse engineering[16], virtual reality, and architecture modelling to the medical and entertainment (gaming and movie) industry. The solutions and methodologies that have been developed, and continue to be developed, are now available for use in other applications.

6.5.2 Free-form surfaces versus closed surfaces

The techniques to reconstruct free-form surfaces are called surface-oriented algorithms, while the techniques that reconstruct volumes or closed surfaces are classified as volume-oriented algorithms. Volume-oriented algorithms are only used in reconstruction of closed surfaces of individual objects. Examples of volume-oriented algorithms are Delaunay or Voronoi tetrahedrisation, such as the Quickhull algorithm (Bradford Barber et al., 1996) and Alpha-Shapes

[16] Reverse engineering is the process of reconstructing a 3-D model from an existing physical (engineered) object.

(Edelsbrunner, 1994). Surface-oriented algorithms do not distinguish between open and closed surfaces. Scanned rock exposures are typically open surfaces and the focus in this research will therefore be on surface-oriented algorithms that support free-form surface reconstruction techniques.

6.5.3 Free-form surface reconstruction techniques

6.5.3.1 Introduction

Free-form surface reconstruction techniques may be classified based on the on the type of representation that is used; with distinctions being made between parametric and simplicial representations. Parametric representations define the surface according to a series of surface "patches," each patch described by a parametric equation. A simplicial representation makes use of points, edges, and triangles to represent a surface.

Reconstruction techniques can also be classified as either interpolation or approximation techniques. A surface interpolation is used when an accurate model is required that fits all the data points exactly. The model is said to "honour all data points. In a surface approximation, the represented surface does not necessarily fit all the data points, but the points of the reconstruction are as close to the input points as possible. Different examples are discussed below.

6.5.3.2 Surface approximation with a parametric representation

In surface approximation with a parametric representation, the surface is represented by a number of parametric surface patches, described by parametric equations. A continuous surface is subsequently created by joining the individual patches. A parametric surface reconstruction method, which is well-suited for modelling geological surfaces, uses *NURBS*, which is an abbreviation from *Non-Uniform Rational B-splines* (Girod et al., 2000; Zhong, et al., 2006. The first publication on NURBS was by K.J. Versprille (1975). NURBS were developed from the mathematics on Bézier curves and B-splines[17]. Since there were numerous algorithms that had to be developed, it took about a decade for NURBS to catch on. However, by the late 1980's they were emerging in the CAD/CAM and CAE (Computer Aided Engineering) industry and by the 1990's they have become the defacto standard (pers. comment: C.J. Turner.)

The generation and visualisation of NURBS are computationally demanding processes, which before could only be handled well by high-performance (Unix) workstations like the Silicon Graphics. Silicon Graphics also developed the well known OpenGL[18] standard for three-dimensional visualisation. However, the advent of powerful PC's with high-performance graphics cards in the last decade diminished the need for specialised graphics workstations, such as the ones developed by Silicon Graphics.

6.5.3.3 Surface approximation with an implicit representation

With implicit representation, a single function is found that passes through all points where the implicit function evaluates to a specified value (often zero). The advantage is that this technique offers the possibility to interpolate across holes with sparse or missing data. In contrast to traditional parametric surfaces, implicit methods can easily describe smooth, intricate and manifold[19] shapes. An example of an implicit method is *Radial Basis Functions* (RBF's) (Carr et al., 2001 and 2003). RBF's have also been used in 3-D geological modelling software (Cowan et al., 2002). RBF's are

[17] A B-spline is a generalisation of a Bézier curve, while Bézier curves and B-splines are generalised to Non-Uniform Rational B-splines or NURBS (Weisstein, 2009).

[18] OpenGL (Open Graphics Library) is a computer standard that provides a programming language and platform-independent API (Application Programming Interface) for applications that generate 3-D graphics. Source: OpenGL (n.d.)

[19] A manifold is a shape that on a small scale looks like the Euclidean space of a specific dimension, which is the dimension of the manifold. For instance a line and a circle are one-dimensional manifolds, a plane and sphere are two-dimensional manifolds. A rock surface is typically a two-dimensional manifold with an edge, i.e. it does not contain a volume.

discussed further in Section 6.5.5 and are used as one of the surface reconstruction techniques in Section 7.2.

6.5.3.4 Surface interpolation with a simplicial representation

An interpolated surface with a simplicial representation makes use of points, edges and triangles to represent the surface (for example, "triangulated irregular network – TIN" representation). This is a standard method in traditional GIS, CAD and some 3-D (Geological) modelling programs (Houlding, 1994). There are many examples of surface interpolation techniques that directly result in a simplicial representation. Three-dimensional Delaunay triangulation is the 3-D variant of the well-known 2.5D Delaunay triangulation functionally utilized by most GIS and CAD/CAM packages. Other interpolation methods make use of the creation of Voronoi or Thiessen polygons. The Delaunay and Voronoi algorithms are often used for the generation of 3-D closed surfaces or volumes, where the surface is represented by 3-D polyhedra and as such not applicable to this research. Examples of 3-D interpolated open-surface-generation applications are the non-commercial software Cocone (Dey et al., 2001; Amenta et al., 2000 and Cocone, 2009) and the commercial software by Metris (Metris, 2006). Examples in the field of the geosciences are the modeling of ore-bodies or volumes of groundwater contaminant

6.5.3.5 Topological algorithms

Surface reconstruction with topological algorithms assumes that the topological type of surface is known beforehand. For instance, if there is a-priori knowledge of the presence of planes, cylinders, spheres or cones, the algorithm can start searching for these surfaces or objects. This is also used by several point-cloud segmentation techniques designed for use by architectural or mechanical engineering applications; the point-cloud is segmented or grouped into subsets that represent a surface with a specific shape. This approach is further discussed in Section 6.6.

6.5.4 3-D Delaunay triangulation

3-D Delaunay triangulation links three points (P_1, P_2 and P_3) from the point cloud by a single triangle (T_1). The triangulation is accomplished on the basis of the 3-D Delaunay criterion, which is that any set of three points are only linked by a triangular facet if a sphere can be drawn through these three points that does not contain any other point. The 3-D Delaunay criterion is the three-dimensional extension of the 2-D criterion that, obviously, uses a circle in a similar way to interpolate linearly between the three nearest points (Delaunay, 1934). This triangulation maximises the minimum angle between all the angles of the triangles, which results in equivalent shaped triangles, avoiding the generation of elongated or "sliver" triangles. Normally, a 3-D Delaunay interpolation is referred to as closed surface interpolation, resulting in a 3-D volume model, composed of tetrahedra[20]. In this study, the objective is to model free-from surface, rather than closed surfaces or volume models (see Section 6.5.1). Therefore, only the free-surface variant of the 3-D Delaunay triangulation is applicable.

In a completed 3-D Triangulated Interpolated Network (TIN), each triangle is listed with its three nodes. Once the TIN is created and stored, it is relatively easy to determine for each point the nearest neighbours. For a given point P_1 the TIN list is searched for the triangles that have P_1 as a node. All other nodes of the found triangles are thus the nearest neighbours of point P_1. The search can be extended by finding all triangles that contain these nearest neighbour points as nodes. A TIN data structure not only defines a 3-D surface, it also readily permits visualisation and 3-D digital rendering[21], and the local surface gradient can be computed easily from the orientation of each individual triangular facet.

[20] A tetrahedron is 3-D object that is composed of four triangular faces. Three faces meet at each of the four corners of the tetrahedron.

[21] 3-D digital rendering is the process of creating an image (for instance on a computer screen) from a 3-D digital model. Various techniques exist to enhance the quality and realism of the rendering, for instance: illumination techniques to create shading, texture mapping (draping of images on the 3-D model) and the introduction of transparency to the surface.

However, the Delaunay triangulation is strongly influenced by the local noise in the data, since it does not take into account the regional surface variation. Especially if the resolution of the data is comparable to the noise (for instance if the distance between the points is around 1 cm, while the noise (error) is around 1 cm as well), then the computed orientations of the triangles are more a function of the frequency introduced by the noise than of the actual surface gradient. The visualisation will be affected as well, since the resulting surface is likely to look like a “spiked” surface due to the noise in the data (see Figure 6.1). Under-sampling of the data, or scanning at lower resolutions, may eliminate this problem, but this approach retains the disadvantage, of course, that the high-information-density also disappears, thus eliminating one of the main benefits of using 3-D laser scanning.

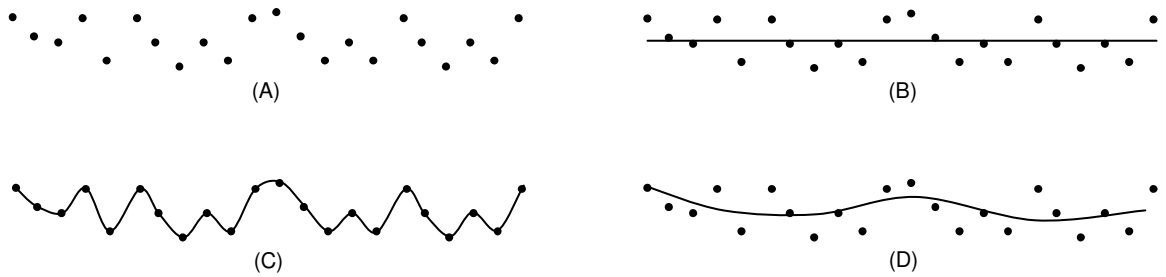

Figure 6.1. These four diagrams illustrate the influence of the noise on the surface reconstruction. Shown in (A) is a sample of laser points of a flat surface (in sideview) where the spatial resolution is larger than the laser range error. Instead of an equally elevated set of points along a (straight) trend line (B), the added noise is linearly interpolated with Delaunay based interpolation (C). A parametric interpolation (in this case as an example a first-degree polynomial) will give a more realistic result (D). After: Van Knapen (2005).

6.5.5 Radial Basis Functions

Polyharmonic Radial Basis Functions (RBF’s) are a means for an implicit surface interpolation that can be used to reconstruct smooth, manifold surfaces from (noisy) point cloud data. Any surface reconstructed is defined implicitly as the zero-set of an RBF to the given surface data (Carr et al., 2001 and 2003). Surface data can be represented with a single 3-D Radial Basis Function. This spatial function represents a signed distance from the object's surface. Points inside the object have a negative distance while points outside are positive. The object's surface is defined implicitly as the zero set of this function. A Radial Basis Function (RBF) is a function of the form:

$$s(x) = p(x) + \sum_{i=1}^{N} \lambda_i \phi\left(\left|x - x_i\right|\right) \qquad [40]$$

Where:

- s is the Radial Basis Function (RBF)
- p is low degree polynomial, typically linear or quadratic
- λ_i are the RBF coefficients
- φ is a real valued function called the basic function
- x_i are the RBF centres
- $|x - x_i|$ is simply a distance, i.e. how far is x from x_i

The RBF is continuous and smooth and can be as smooth as is required by selecting the appropriate basic function φ. The basic function φ is a real function of a positive real r where r is the distance or radius from the origin. For fitting functions of the three variables (x, y, z) good choices of basic functions are the bi-harmonic and tri-harmonic as given below. These poly-harmonic splines (which include the thin-plate spline) minimise certain energy semi-norms and are therefore the “smoothest" interpolators.

Bi-harmonic (spline + linear polynomial)I: $\varphi(r) = r$ [41]

Tri-harmonic (spline + quadratic polynomial): $\varphi(r) = r^3$ [42]

During evaluation of the RBF, smoothing of the data can easily be established by substituting the basic function with a smoother function. Smoothing of the surface can also be achieved by low pass filtering of the point cloud data (Carr et al. 2001 and 2003) or simply by under sampling of the point cloud. It is not always desirable to interpolate scattered data exactly when a data set contains noise. A smooth approximation is often more useful. Smoothing can also be desirable (even in data without noise) to remove unwanted detail or to avoid aliasing when evaluating an RBF on a mesh or grid which is coarse compared to the detail present in the input data. In this last case, a low pass (i.e. anti-aliasing) filter can be used to prevent artefacts due to sub-sampling.

The program used for implicit surface reconstruction in this study is the FastRBF software (Farfield technology, 2004). FastRBF is well-suited to interpolating large scattered point cloud datasets that may be non-uniformly sampled or contain large regions of missing data. The equation that defines an RBF (see Equation [40]) imply that the number of terms in the RBF equals the number of data points. Particularly with the very large point data densities typically associated with terrestrial laser scan data, it becomes computationally very expensive to include all data points to create the interpolation. The FastRBF software provides a so-called “greedy algorithm” in the fitting process that starts with a small number of data points. The algorithm will iteratively add more data points to the RBF until the desired accuracy is reached. This approach increases the processing time dramatically.

An implicit surface model that is generated with the RBF method cannot directly be used in existing visualisation or other 3-D software. For this, it is necessary to create an explicit surface representation in the form of polygonal meshes from the RBF representation. Because the RBF is a continuous smooth 3-D solid model the surface model can be generated as a smooth continuum. Because the functional representation is, in effect, a solid model, gradients and surface normals can be determined analytically. This helps to generate uniform and continuous meshes even in areas with sparse or non-existent data.

6.5.6 Errors in the surface reconstruction by RBF or TIN methods

As mentioned, sparse and noisy regions in the point cloud can be caused by the laser settings or due to the position of the laser scanner with respect to the rock face. In addition, the presence of unwanted phenomena in the laser scan window will also affect the topological correctness of the reconstructed surface by making the point cloud noisy. Such features include foreign objects on the rock surface, vegetation, and dynamic disturbances at the time of a scan.

Application of simplicial surface reconstruction with such noisy data will lead to holes in areas where the method could not create a proper interpolation, whereas a surface reconstruction using RBF will give ‘blobby’ shapes in such data-sparse regions. In both cases, these are not representations of the true rock surface and should be disregarded. Also, smoothed RBF surfaces will have rounded edges at locations defined by discontinuity intersections that are sharp in nature. Such surface areas ought to be disregarded as well.

Sparse point cloud regions are also introduced when the scanned rock surface is parallel to the laser beam, resulting in very few measuring points. The surface reconstruction will be less accurate with RBF, and contains holes when 3-D Delaunay triangulation is applied.

A high spatial resolution of the laser scanner leads to a high frequency of points or dense point cloud regions. As long as the range resolution (also: noise or error) introduced by the laser remains

relatively small compared to the spatial resolution, this will cause no problem. In all other cases, the Delaunay interpolation gives poor results (see Figure 6.1).

6.6 Point cloud segmentation techniques

6.6.1 Introduction

The application of point-cloud segmentation techniques offers another approach to the analysis of point-cloud data. These techniques start with the assumption that certain pre-defined geometric shapes (such as cylinders, spheres or planes) are represented by the point-cloud data. By careful analysis of the point-cloud data points, these shapes are recognised and defined. The point cloud is classified, or 'segmented', into subsets of points that match a particular geometric object, e.g. a single cylinder; sphere or, in the case of recognising discontinuities, a plane. The advantage of point-cloud segmentation is that the analysis can be done on the raw point cloud, without the need of prior surface reconstruction. In a way, point-cloud segmentation is also a kind of surface-reconstruction technique, since the points are segmented into clusters with similar shape, which can again be simplified into surfaces. Another advantage is that it the method not affected by noise due to vegetation or dynamic disturbances, since this noise is not recognised as being part of any pre-defined geometric object and therefore is ignored. Before the segmentation can be carried out, the data need is stuctured using a tree-structuring strategy.

6.6.2 Tree-structuring of the unorganised point cloud data

A common strategy for spatially partitioning unorganised point cloud is tree-structuring (Preparata and Shamos, 1985). Binary search tree data structures, such as *K-dimensional tree* (Bentley, 1975) or *Octree* (Yerry and Shephard, 1984) are commonly used for structuring unorganised point-cloud data. A K-dimensional (K-D) tree is a space-partitioning data structure for organizing points in a multi-dimensional - in this case three-dimensional - space. A K-D tree recursively subdivides a space into balanced subcells, which means that each subcell contains more or less the same number of points and there are no subcells, or "leaves," in the final tree that contain no points.

An Octree partitions three-dimensional space by recursively subdividing the space into eight octants or subcells, irrespective of the number of points in each subcell. The subdivision stops if there are no more, or very few, points found in each Octree subcell. Unlike the K-D tree structuring, an Octree is not balanced, which means that there are subcells that do not contain any points or just very few. An Octree structure can be built faster than a K-D tree, because no decision has to be made where to place the subdivision. However, the Octree method suffers from the disadvantage of having large empty cells in the tree when the data contains areas with sparse data.

When dealing with terrestrial laser-scan data defining rock faces, the largest part of the volume occupied by the rock face contains sparse or even no data, only the surface area of the actual rock surface has points. In this case, it is therefore more advantageous to use the balanced K-D tree structuring. Octree structures are more advantageous to use in the case of compact volume-based datasets.

The 3-dimensional K-D tree method uses splitting planes that are perpendicular to the three coordinate axes. The entire 3-D space (or root cell) occupied by the point cloud is recursively split by planes in increasingly smaller spaces or subcells. Each subsequent splitting plane splits an un-partitioned portion of the space in two subcells containing points left and right of this plane. Splitting planes are selected along each coordinate axis in an alternating way; i.e.: first the root cell is divided along a single splitting plane perpendicular to the x-axis, then the two subcells thus created are split by two splitting planes along the z-axis, then the four spaces are then split by four splitting planes perpendicular to the y-axis, and so forth (see Figure 6.2). This process is continued until each subcell contains only a limited number of points, which are relatively simple to handle. The final subcells are called leaf cells. The position of the next splitting plane is chosen such that it intersects

a point in the subcell with a coordinate corresponding to the median value of this cell on the axis that the splitting plane intersects. This point in the point-cloud data is stored as a node or leaf in the K-D tree. Four vertices spatially define each cell.

The advantage of using a K-D tree is that, when performing a nearest neighbour search, large portions of the data can be quickly be discarded by performing a simple test. Once the tree is built, the nearest neighbour search for a specific seed point starts at the root of the tree. Each leaf of the tree contains information about the nodes and the splitting plane. By comparing the coordinates of the seed point with the dimensions of the left and right subcells created by the splitting plane, the search knows which of the two branches of the tree it needs to follow. In this way, the search moves up the tree very quickly and reaches the final leaf cells to which the seed point belongs. It is possible that the nearest points are located outside the leaf cell. It is then necessary to backtrack the search through the tree to find the points within a given search radius or an orthogonal range search (search box).

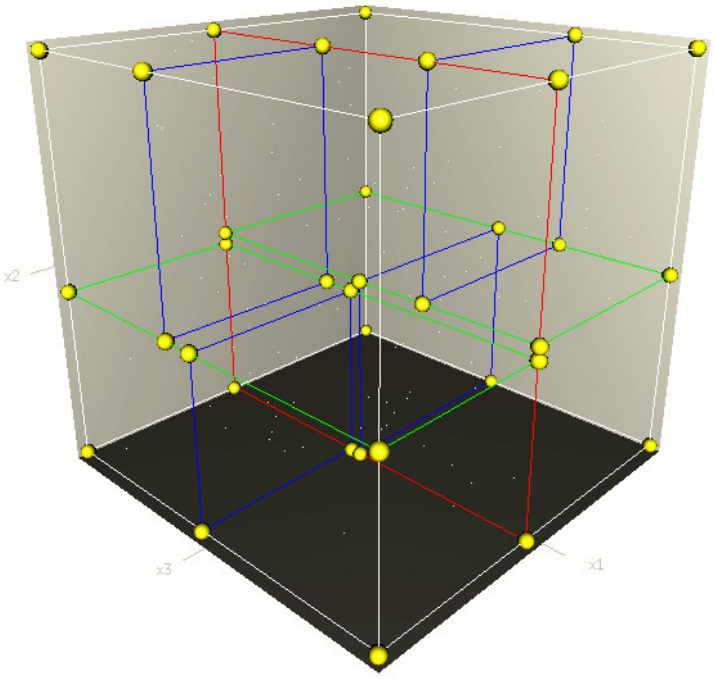

Figure 6.2. Illustration of the (3-D) K-D tree splitting tree (Tyner, 2007).

6.6.3 Region-growing as a segmentation strategy

Point-cloud segmentation has some similarities with surface reconstruction. During segmentation, points are also analysed spatially because the neighbours of points have to be found in order to undertake the point-cloud segmentation. Instead of attempting to connect the neighbouring points, the neighbouring points are analysed to determine whether they are part of the same object. When planar discontinuities are being searched for, this object should be a plane. Similar methods exist to recognise other geometric shapes such as spheres or cylinders.

A method that is often applied is called ‘region-growing’. A random seed point is selected and a certain pre-defined number of points, or points within a pre-defined search area around the seed point, are chosen. Then, the K-D-tree structuring becomes important, since repetitive spatial searches must be carried out. The neighbouring points of the seed point, including the seed point itself, can be tested against a specific algorithm to verify whether they are part of a particular geometric shape, such as a plane. Various algorithms exist, but those most frequently encountered in the literature are: Hough transformations, Principal Component Analyses (PCA), Random Sample Consensus (RANSAC), and the Least-Squares Method. These methods are discussed in the following paragraphs. The most promising techniques: Hough transformations, PCA and Least-Squares Methods are discussed in the Sections 6.6.4, 6.6.5 and 6.6.6 below.

The region-growing strategy use the following definition as basis: all points that are identified as being part of a single plane are labelled with an identifier, which is a unique label representing an independent plane. A distinction is made between points that are “inliers” or “outliers.” Since very few points will in an absolute sense fall on a plane, certain threshold criteria have to be defined to determine which points are “inliers,” members of a planar surface, and which points are “outliers,” points that are not part of this planar surface. If a sufficient number of inliers is found, as defined by the user, the seed is considered successful, the inliers are labelled as members of the plane, and subsequently these labelled points are used as new seed points. This process is repeated until all points are classified or *segmented* to individual and independent planes.

This discussion has demonstrated that there are several user-defined threshold values that must be defined in order for the region-growing and segmentation process to run in an optimal way. These operational aspects are discussed in more detail in Chapter 8.

6.6.4 3-D Hough transformation

To solve complex mathematical problems, it is often useful to transform the data to another domain. Once the problem is solved in the other domain, the data is transformed back to the original domain. A good example of such a process is the Fourier transform that solves problems by transforming the data from a time domain to a frequency domain and vice-versa. The similar concept can be applied to the analysis of point-cloud data: we have a large number of point coordinates but we only need to identify a relatively small number of planar objects, each of which can be described by only a few parameters. It may therefore be advantageous to transform the coordinates from 3-D Cartesian space to a 3-D parametric space. This is explained further below.

The Hough transformation algorithm was originally developed for the recognition of patterns, such as lines, in 2-D images (Hough, 1962). The three-dimensional Hough transformation is an extension to this algorithm in order to recognise planes and other pre-defined geometric objects, such as cylinders and spheres, in 3-D unorganised point clouds (Maas and Vosselman, 1999; Vosselman et al., 2005). This technique has been used successfully to analyse high-density airborne Lidar data in order to define planar objects such as roofs and bridges. Sarti and Tubaro (2002) used the 3-D Hough transform to detect micro-fractures in rock from X-ray/NMR tomography data.

The principle of the Hough transformation in 2-D is that there are an infinite number of theoretical lines with different orientations that pass through any point. The transformation is made to determine which of these potential lines pass through most of the features in an image. In the standard Hough transform, each line is represented by a line equation, which consists of two parameters:

1. The angle (θ) of its normal, and
2. The (perpendicular) distance (d) of the line to the origin:

$$d(\theta) = \cos\theta\, x + \sin\theta\, y \qquad [43]$$

Each point in the image is plotted as a sinusoidal curve in the parameter or Hough space. If for example three image points fall on the same line, then in parameter space this line is represented as the point where all three lines cross (see Figure 6.3 and Figure 6.4). In reality the lines in parameter space do not cross exactly through a single point, since the points in 2-D space may also not be perfectly aligned. For this reason, the parameter space has to be rasterised (binned) and the number of lines passing through each accumulator cell or bin is counted. The highest local counts (maxima) are then potential lines in the image. The variables that have to be set by the user are the raster or bin size and the threshold counting accumulator value, in order to define the minimum amount of points that form a line.

This principle in two dimensions can be extended to three dimensions to find planes that pass through points in the point-cloud data. In this case, each laser-scan point in 3-D space is transformed to a sinusoidal curved surface in the 3-D Hough or parameter space. In order to do this a parameterisation of planes in 3-D space has to be defined. The parameterisation of planes can be done in various ways. One method, employed by (Maas and Vosselman (1999), uses the slope parameters of the plane in x and y direction and the distance (*d*) of the plane to the origin:

$$d(s_x, s_y) = s_x\ x + s_y\ y + z \qquad [44]$$

Where:

- s_x is the plane gradient in x direction
- s_y is the plane gradient in y direction

The only problem with this parameterisation method is that vertical instances of planes cannot be transformed because there are multiple z values for every unique x and y combination. Another method of parameterisation that avoids this problem with vertical planes is to use polar coordinates of the normal to the plane (Overby et al, 2004). This results in the plane equation discussed in Section 3.7.1 (please refer to Equations [11] and [13]). The three polar coordinates that form this parameterisation are the azimuth and angle of the normal, and the perpendicular distance (*d*) of the plane to the origin:

$$d(\theta, \gamma) = \sin(\theta)\cos(\gamma)\ x + \cos(\theta)\cos(\gamma)\ y + \sin(\gamma)\ z \qquad [45]$$

Where:

- θ is the azimuth (similar to the dip direction of the plane) of the normal to the plane (from 0 to 2π). In this case the azimuth is measured in a clockwise manner, from the positive y-axis, assuming the normal is directed upwards.
- γ is the angle of the normal to the plane (from 0 to $½\pi$) with the horizontal

This parameterisation is also similar to the hemispherical or stereographic projection of orientation data that is previously discussed in section 3.7.2.1. However, in the Hough transform, an extra third distance parameter (*s*) is used to separate planes that have a similar orientation but with a different location in 3-D space. In (2-D) stereographic projections, different planes with similar orientation are not differentiated, because the aim is to identify sets, not planes.

To determine which points fall on the same plane, points from the 3-D point cloud are transformed as sinusoidal curved surfaces in the 3-D Hough or parameter space. The location in Hough space where most of the curved surfaces intersect is forming the combination of parameters that uniquely define the plane in Cartesian space. Similar to the 2-D Hough transform, the parameter space needs to be discretised to accumulator cells or bins with a user-specified size, because the surfaces will never cross exactly in the same point, since the laser-scanner points never perfectly match a single plane.

The discretisation also allows a more efficient implementation in a computer algorithm. Initially, all accumulator cells are set to a count value of *0*. Every laser-scanned point is transformed to a curved surface in the Hough space that intersects the accumulator cells. Each time a cell is intersected, the accumulator is increased. By counting the number of times that a bin is intersected, potential planes in the point cloud data can be identified. The bin with (locally) the highest number of points is a potential plane in the point cloud. The points that are mapped within this bin, fall on a plane with the parameters of the bin and can subsequently be segmented or classified as belonging to the same plane.

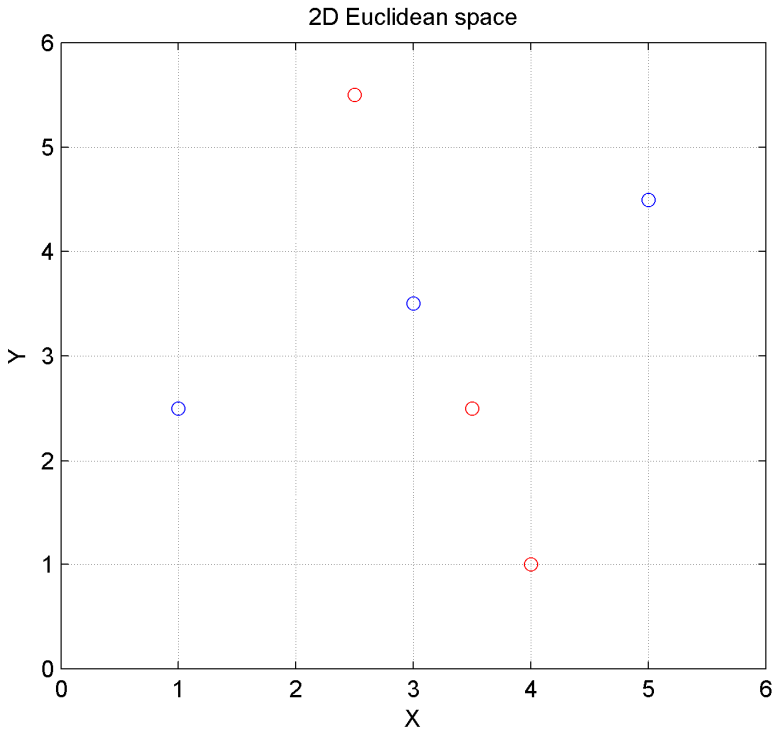

Figure 6.3. This graph Illustrates the principle of 2-D Hough transform. Shown here are 6 points in 2-D Euclidean space. Through each point pass an infinite number of straight lines that can uniquely be defined by their perpendicular distance to origin and the angle that this line makes with the X axis. There is only one straight line through each point that intersects with any other point. In this example it is easy to see that the three blue points and the three red points can be aligned by a straight line.

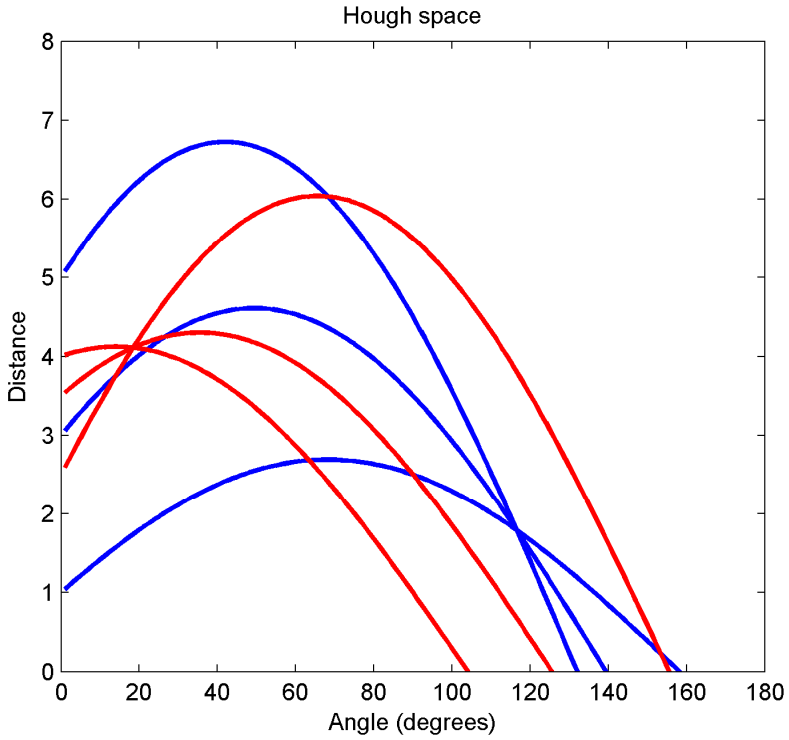

Figure 6.4. The points in 2-D Euclidean space are transformed to curves in 2-D Hough space. It is clear to see that the three blue curves intersect in one point (distance 2 and angle 120) and the three red curves intersect in another point (distance 4 and angle 20). The distance and angle combination define the intersection line uniquely in 2-D Euclidean space.

The user needs to define a number of variables. These variables are the bin size and the threshold value for the count. The counting threshold specifies the minimum number of points required to define a plane.

In theory, all points in the dataset could at once be transformed into the parameter space, but this is not very efficient from a computational point of view. A better tactic is to use the region-growing approach that described in Section 6.6. In this way, smaller point subsets are sampled and plotted in parameter space, allowing a quick evaluation to verify which of the sampled points potentially form the same discontinuity plane.

The 3-D Hough transform is a very robust way of finding planes through scattered and noisy point clouds, since it is not influenced much by outliers in the data, as long as the bin sizes are properly selected. A potential problem with the application of the 3-D Hough transform to point cloud data of rock faces is that it assumes the planes to be perfectly planer. For man-made objects this may be the case. For natural objects, such as discontinuity planes, this does not often correspond to reality. Strongly curved or undulating surfaces occur frequently; these become harder to recognise as a single plane with the 3-D Hough transform, particularly if the planes extend over larger distances. Undulating or curved discontinuity surfaces may thus be classified into a number of point classes that only locally are truly planar.

Another issue with the 3-D Hough transform is that points from different planes that are not directly connected, but satisfy the same transformation criteria, will be classified as belonging to the same plane. For the application to outcropping rock faces this may not necessarily pose a problem. There are instances were straight and persistent discontinuities are exposed as various (unconnected) patches. With the Hough transform, these patches can then be connected and classified as belonging to the same plane. However, there may also be other instances, especially when dealing with undulating and non-persistent discontinuities, where different exposed discontinuity planes, which coincidentally are locally similar in terms of Hough parameterisation, will be classified as the same plane, but in reality are actually two different planes. This issue can be overcome by incorporating spatial evaluation criteria to exclude some planes from a global class. For instance, a rule may be employed, such as: if some points are located at a greater than a certain specified distance from previously found points, they are not included in the class.

6.6.5 (Total) Least Squares method

The *Least Squares* method is a very common statistical method used to define (linear) regression relationships between variables. This method has been successfully used by Feng (2001) to compute plane equations defining the best-fit (discontinuity) planes through sets of sample laser-scanner point-cloud data. In the Least Squares Method it is assumed that only the response variable (for example *z*) has an error component, while the predictor values (for example *x* and *y*) are measured exactly. The errors in the response variables are computed as a squared distances from the data points along one of the axes directions, in this example the z-axis. However, laser-scanner point-cloud data contain three independent (*x,y,z*) variables that all contain errors. It is thus more logical to calculate the error as the perpendicular distance to the fitted planar function. This suggests that the *Total Least Squares Method*, which uses an orthogonal regression to the fitted planar function (Golub, and Van Loan, 1980), is a better method for analysing point-cloud data. The fitted function to the data with dimension N is always a subspace of this data (e.g. a line, plane or hyperplane) with dimension N-1.

In this case the problem is reduced to finding data in a low-dimensional space by analysing data defined in a higher-dimensional space. In other words, the problem is to find 2-dimensional planes in 3-dimensional data. In this case it would be convenient to project the 3-D data to a 2-D subspace in order to analyse it. The least-squares formulation of the problem is to find a subspace that summarises the summed squared vector lengths of the data. The axes of this sub-dimensional

space are also known as the *Principal Components* of the data. The method for finding the principal components is called *Principal Component Analysis* (PCA) and is defined in terms of *eigenvectors*.

6.6.6 Principal Component Analysis (PCA)

Through comparison of the three coordinates *x, y and z* of all points by their respective covariance properties it would in theory be possible to discover linear (planar) trends in the 3-D geometric data. A method to accomplish this is to create a covariance matrix. From this covariance matrix a transformation matrix can be derived that allows one to completely de-correlate the data or, from a different point of view, to find an optimal basis for representing the data in a compact way. This is technique is called *Principal Components Analysis* (PCA) (Jackson, 1991). PCA is a statistical technique that is frequently used in pattern recognition. PCA is very powerful at recognising patterns in data like outliers and trends and is therefore ideally suited to detect linear (planar) trends through a noisy cloud of 3-D points. PCA can be used to fit a linear regression that minimizes the perpendicular distances from the data to the fitted model. This is the linear case of what is known as orthogonal regression or Total Least Squares (see Section 6.6.5). The PCA method is appropriate for the 3-D laser scanned data where there is no distinction between predictor and response variables, and where all the variables are measured with a certain error. This method is in contrast to regression analysis, where there is a distinction between dependent and independent variables (Afifi et al., 2004).

In general terms, PCA is used for simplifying a dataset by reducing multidimensional datasets to a lower dimension. Similar to the Hough transform, PCA transforms the data to another domain, in this case the *principal component space*. In contrast to the Hough transform, the PCA transformation is done in such a way that the greatest variance of the data is mapped to the first coordinate axis (the first principal component), the second greatest variance on the second coordinate axis, and so on. The procedure for computing the principal components and mapping the points to the principal component space is described below.

6.6.6.1 Calculation of covariance matrix

First a (3x3) covariance matrix C is calculated from a sample set A (*N*x3) of the point cloud. The covariance is calculated for the three positional variables, in this case the 3-D coordinates x, y and z:

$$C = \operatorname{cov} A \qquad [46]$$

$$C = \begin{pmatrix} \operatorname{cov}(x,x) & \operatorname{cov}(x,y) & \operatorname{cov}(x,z) \\ \operatorname{cov}(y,x) & \operatorname{cov}(y,y) & \operatorname{cov}(y,z) \\ \operatorname{cov}(z,x) & \operatorname{cov}(z,y) & \operatorname{cov}(z,z) \end{pmatrix} \qquad [47]$$

Written out, this would give for the covariance matrix:

$$C = \frac{1}{(N-1)} \begin{pmatrix} \sum_{i=1}^{N}(x_i-\bar{x})^2 & \sum_{i=1}^{N}(x_i-\bar{x})(y_i-\bar{y}) & \sum_{i=1}^{N}(x_i-\bar{x})(z_i-\bar{z}) \\ \sum_{i=1}^{N}(x_i-\bar{x})(y_i-\bar{y}) & \sum_{i=1}^{N}(y_i-\bar{y})^2 & \sum_{i=1}^{N}(y_i-\bar{y})(z_i-\bar{z}) \\ \sum_{i=1}^{N}(x_i-\bar{x})(z_i-\bar{z}) & \sum_{i=1}^{N}(y_i-\bar{y})(z_i-\bar{z}) & \sum_{i=1}^{N}(z_i-\bar{z})^2 \end{pmatrix} \qquad [48]$$

Where $(\bar{x},\bar{y},\bar{z})$ is the arithmetic mean of each coordinate. The PCA becomes easier if an adjusted data set A_{adj}, which has the arithmetic means of each of the coordinate variables (*x*, *y* and *z*) subtracted from the data. In this way the mean of the new variables (*x'*, *y'* and *z'*) in matrix A_{adj}

become 0, but the sample variances between the variables remain the same. The covariance matrixes from A and A_{adj} are thus similar as well. The arithmetic means $(\overline{x},\overline{y},\overline{z})$ of A_{adj} become equal to (*0,0,0*) and, written out, the covariance matrix C becomes simplified:

$$C = \frac{1}{(N-1)} \begin{pmatrix} \sum_{i=1}^{N} x_i'^2 & \sum_{i=1}^{N} x_i' y_i' & \sum_{i=1}^{N} x_i' z_i' \\ \sum_{i=1}^{N} x_i' y_i' & \sum_{i=1}^{N} y_i'^2 & \sum_{i=1}^{N} y_i' z_i' \\ \sum_{i=1}^{N} x_i' z_i' & \sum_{i=1}^{N} y_i' z_i' & \sum_{i=1}^{N} z_i'^2 \end{pmatrix} \quad [49]$$

6.6.6.2 Calculation of the eigenvectors

The three eigenvectors are calculated from this (3x3) covariance matrix C. The eigenvector with the highest eigenvalue is the first principal component, the eigenvector with the second highest eigenvalue is the second principal component and the eigenvector with the lowest eigenvalue is the third principal component. If there is any linear trend in the point data, the first and second principal components will span the two principal directions of the hyperplane. The third and smallest eigenvalue is the third principal component and provides the direction of the variance in the data. This third principal component is the normal vector to the 2-D plane spanned by the first two eigenvectors, since all eigenvectors or principal component vectors are perpendicular to each other.

From a mathematical point of view, the principle of PCA is simply the transformation of the covariance matrix C in the following way:

$$C = P\ D\ P^{-1} \quad [50]$$

Where:
- P is containing the eigenvectors in its columns
- D is a diagonal matrix with the eigenvalues as the diagonal entries.

The eigenvalues are found by determining the characteristic polynomial $p_c(\lambda)$ of C and solving the characteristic equation $p_c(\lambda) = 0$. The characteristic polynomial of C is given below:

$$p_C(\lambda) = \det(C - \lambda I) \quad [51]$$

Where:
- $\lambda \in \mathbb{R}$

The characteristic equation is then:

$$\det(C - \lambda I) = 0 \quad [52]$$

Where:
- λ the eigenvalue and has three solutions (λ_1, λ_2 and λ_3) to the characteristic equation
- I is the identity matrix

Since C is a real symmetric 3x3 (covariance) matrix, the characteristic equation has three roots, which are the eigenvalues λ_1, λ_2 and λ_3. For a symmetric matrix the smallest eigenvalue is always equal to 0. Based on Equations [49] and [52], the characteristic equation of covariance matrix C with λ as unknown becomes therefore:

$$\left| \begin{pmatrix} \sum_{i=1}^{N} x_i'^2 - \lambda & \sum_{i=1}^{N} x_i' y_i' & \sum_{i=1}^{N} x_i' z_i' \\ \sum_{i=1}^{N} x_i' y_i' & \sum_{i=1}^{N} y_i'^2 - \lambda & \sum_{i=1}^{N} y_i' z_i' \\ \sum_{i=1}^{N} x_i' z_i' & \sum_{i=1}^{N} y_i' z_i' & \sum_{i=1}^{N} z_i'^2 - \lambda \end{pmatrix} \right| = 0 \quad [53]$$

Writing out the above determinant to solve for the characteristic equation becomes very lengthy and elaborate and is therefore omitted here. Once the eigenvalues are found, the eigenvectors are determined in the following way:

$$(C - \lambda_i I)v_i = 0 \quad [54]$$

Where:

- λ_i is the eigenvalue (i = 1-3)
- v_i is the eigenvector (1x3) (i = 1-3)

The PCA method is most easily illustrated by using an actual example. Appendix E provides such an example.

6.7 Discussion and conclusions

Point clouds are generated by 3-D laser scanning surveys, but also by 3-D photogrammetry surveys, of rock faces. The typical characteristics of point-cloud data dictate the use of very specific data-analysis techniques. The point-cloud data is, by definition, three-dimensional and noisy, and contains areas with sparse data points and areas without any data. Further, the data is unorganised, containing in many cases hundreds of thousands to even millions of points. It is essential that the point-cloud data be spatially structured in order to extract geometric information concerning discontinuities in the scanned rock face. Without the creation of a data structure, it becomes very difficult to spatially relate the points in the data set with each other. There are two principal ways of creating a suitable data structure: by reprocessing the data points through surface reconstruction techniques, or by creating a tree-based data structure, such as a K-D tree.

There are several surface reconstruction techniques, each with their own advantages and disadvantages. In many cases, a simple 2-D gridding technique can be applied, but the gridding can result in a certain degree of data loss. Since the technique is 2-D instead of 3-D, it is difficult to detect certain geometries, particularly discontinuity planes that run more or less perpendicular to the general trend of the rock face. An alternative is to use 3-D surface reconstruction techniques. A widely used 3-D method is 3-D Delaunay triangulation, but this method is strongly influenced by the noise or error in the point-cloud data, since the method connects neighbouring points. Particularly if the data density is high compared to the error, the Delaunay triangulation represents the variations due to the error more than that the actual rock surface geometry. 3-D implicit or parametric surface reconstruction techniques, on the other hand, are more appropriate for analysing such irregular and noisy point-cloud data because the underlying surface reconstruction algorithms result in more realistic-appearing surface reconstructions. Theoretically, the implicit or parametric surface reconstruction techniques would therefore form a better basis for further analysis. However, all surface reconstruction techniques result in a meshed data structure. While the meshed data structure can be used for subsequent discontinuity orientation analysis, in general, the nodes of the created meshes do not coincide with the original laser-scanner point-cloud data points. Only the 3-D Delaunay triangulation honours the original data points.

The method of point-cloud segmentation offers a completely different approach. This technique relies upon a tree-based or TIN-based point-cloud data structure to optimise the segmentation process; to accelerate the required nearest-neighbour searches. In point-cloud segmentation, the

original point-cloud data is kept completely unaltered and no surface reconstruction is carried out. Point-cloud segmentation uses a so-called region-growing strategy in order to find geometric objects. In this case, the desired objects are the (discontinuity) planes. Point-cloud segmentation evaluates, continuously and recursively during the region-growing process, whether small sub-sample sets of the point cloud are part of the same planar object. Several mathematical methods are candidates for evaluating planarity in the 3-D point-cloud data, including 3-D Hough transformation, (Total) Least Squares Analysis, and Principal Component Analysis (PCA). The result of the segmentation is essentially a classified (segmented or labelled) point cloud, where points with a similar label belong to the same discontinuity plane. As with 3-D reconstructed surfaces, point-cloud segmentation provides a basis for further analysis of discontinuity orientations.

7 Extracting discontinuity planes with surface reconstruction

7.1 Introduction

This chapter describes how to derive discontinuity orientation information on the basis of two different surface reconstruction techniques: a 3-D implicit surface modelling technique (Method 1) and a 2-D gridding technique (Method 2). The methodologies are illustrated and verified by the data from the two cases described in Chapter 4. The rationale behind both methods is that information on the geometry of the scanned rock face is determined by surface reconstruction techniques that create a spatial data structure in the point cloud data. This allows the identification of the geometry of discontinuity planes that are present in the rock surface.

The first method makes use of an implicit surface reconstruction technique known as Radial Basis Functions (RBF's). Compared to other 3-D surface reconstruction techniques, such as Delaunay triangulation, implicit surface reconstruction is much less influenced by noise in the point-cloud data and results in the most realistic-looking surface models. Through meshing of the implicitly defined surface, the rock face is represented by a network of facets that are triangular in shape. The second method uses a surface reconstruction technique that is based on 2-D gridding. The dense point cloud is structured and simplified by "draping" a 2-D mesh efficiently over the scanned rock face. The user can interactively change the mesh size to create an optimal balance between resolution and data handling capacity. Both methods ultimately yield geometrical information on each uniquely identified discontinuity plane, including: orientation, the plane equation's parameters (*a,b,c* and *d*), the centroid of the plane, and the plane dimensions.

7.2 Introduction to the surface reconstruction approach

The orientation of planar discontinuities can be automatically derived from laser-scanner point-cloud data if surface reconstruction techniques are used to impose spatial data structures onto the irregularly spaced, spatially unorganized, and noisy raw point-cloud data. This chapter discusses, applies and compares two different surface reconstruction techniques: a 3-D implicit surface modelling technique (Method 1) and a 2-D gridding technique (Method 2).

Method 1 utilizes polyharmonic Radial Basis Functions (RBF's), one type of surface interpolation method that is well suited to producing smooth surfaces from irregularly sampled and noisy data, a characteristic of many point clouds. The RBF approach retains the inherent 3-D character of the original scanned point-cloud data. However, it is computationally expensive and requires a number of specific pre- and post-processing steps to arrive at an optimal result. The RBF method used in this study was implemented with a number of Matlab-based functions contained in the FastRBF toolbox. Once the RBF surface is defined, Method 1 converts it to a 3-D mesh, represented by a network of triangular facets. Fuzzy k-means clustering automatically classifies each facet into identifiable discontinuity sets. The entire procedure produces highly realistic representations of the original rock face, yet also allows statistical and graphical analysis to identify individual planar elements and their orientations, automatically, thereby producing a list of most likely discontinuity planes exposed in the rock face.

Method 2 uses a surface reconstruction technique that is based on 2-D gridding. This approach is implemented in the existing software package Split-FX. The 2-D gridding and meshing approach

allows the mesh to be generated very quickly, since the underlying algorithms are relatively simple and require little computation time. The often very large and unorganised point-cloud data set is reduced to a much smaller dataset of organized regularly-spaced points, and these can be interpolated into a triangular mesh very rapidly, since the interpolation is only done in only two dimensions. The Split-FX software provides a very fast and intuitive way of processing the point-cloud data to extract discontinuity plane orientations from the raw point-cloud data. However, the 2-D gridding imposes some potential constraints when very irregular rock faces, or locations with complex geometries are being evaluated.

7.3 Method 1: Surface reconstruction with an implicit representation

The main objective of this method is to create a virtual surface that represents the rock surface as accurately as possible because the most accurate discontinuity information can be obtained only from such an accurate surface representation of the rock surface. This objective also poses challenges since, while the reconstruction of surfaces from noisy point-cloud data is possible, it is computationally expensive and requires a number of specific pre- and post-processing steps to arrive at an optimal result. This method makes use of an implicit surface reconstruction technique known as Radial Basis Functions, or RBF's. Compared to other 3-D surface reconstruction techniques, such as Delaunay triangulation, implicit surface reconstruction is much less influenced by noise in the point-cloud data and results in the most realistic-looking surface models.

Through meshing of the implicitly defined surface, the rock face is represented by a network of facets that are triangular. Each facet contains information on the orientation of that particular part of the (reconstructed) rock face. Subsequently, the orientations of all facets are plotted in a stereographic plot. Through statistical analysis, trends or clusters in the data can be observed in the stereographic plot, and the assumption is that they are related to the discontinuity sets present in the scanned rock mass.

Fuzzy k-means clustering is used as a method to classify each surface facet automatically, into identifiable discontinuity sets. This approach is computationally demanding since the orientation of each individual meshed facet is used in the analysis. The implicit surface reconstruction technique itself is also computationally intensive. For this research, the method is implemented in a number of Matlab-based scripts and functions, and the processing steps are implemented in the form of programming scripts in Matlab. The FastRBF toolbox used to create the 3-D surfaces also works under Matlab.

7.3.1 Radial Basis Functions (RBF) for surface reconstruction

Polyharmonic Radial Basis Functions (RBF's) are a surface interpolation method that can be formulated as an exact fitting method; thus RBF's are useful in producing smooth surfaces from irregularly sampled and noisy data, such as commonly encountered in point clouds (Carr, et al., 2001; 2003). Section 6.5.5 discusses the basic principles behind Radial Basis Functions (RBF's). This Section covers the operational issues about the actual reconstruction. The RBF method used in this study was implemented with a number of Matlab-based functions contained in the FastRBF toolbox. FastRBF is a registered trademark of Farfield Technology Inc. (Farfield Technology, 2004). The FastRBF toolbox allows scattered 2-D and 3-D data sets to be described by a single mathematical function, a Radial Basis Function (RBF), as an implicit representation of the scanned rock surface. The resulting function and its gradient can be evaluated anywhere on a grid. RBF's are a natural way to interpolate scattered data, particularly when the data samples do not lie on a regular grid and when the sampling densities vary (Farfield Technology, 2004). Therefore, RBF's are well-suited to analysing 3-D point-cloud data. Another advantage of RBF's is that the influence of the noise or precision error in the point cloud data can be reduced through various data smoothing techniques. The Matlab toolboxes also include various smoothing and anti-aliasing filters to create more realistically looking 3-D surface models, depending on the quality (density and noise level) of the input point data.

7.3.1.1 *Fitting RBF to surface point cloud data in 3-D*

The process of fitting a 3-D RBF to a set of points that lie on a surface involves a series of steps. A single 3-D RBF represents the surface data as a spatial function that represents a signed distance to the surface. Points inside the surface have a negative distance, while points outside the surface have a positive distance. For a set of *N* points, the RBF is developed so that the distances to all the points are zero ($s(x_i) = 0$, where i= 1 to *N*) and thus the surface smoothly passes through all the points. The interpolated surface is an iso-surface of the function *s* and is referred to as an *implicit surface*. The process of forming an *explicit* representation of the surface, such as a triangulated mesh, is called iso-surfacing. The advantage of explicit representations is that it is easier to render and deform these surfaces. The isosurfacing is explained in the following Section 7.3.1.2. The steps used within the FastRBF toolbox to create the implicit surface in the form a function $s(x) = 0$ are discussed in this Section. It describes the method to fit the RBF's based on centres (surface points) and density (off-surface) data that are generated from the normals to the centres.

First, the point-cloud coordinate data need to be loaded. It is advisable to first try the RBF fitting method on a smaller (cropped) subset of the data before a larger dataset is processed. The various parameters that need to be defined depend on the density and the noise (error) of the data. The *N* surface points that are selected for the RBF fitting are assigned a value 0, which will be the iso-value for the surface. However, with only the *N* surface points the function s(x) = 0 will create a trivial solution. In order to constrain the linear system of equations that define the RBF solution sufficiently, *off-surface points* need to be generated. These are new points, which are projected along the normals to each of the *N* surface points for a user-specified distance. The off-surface points are assigned distance-to-surface values, which are negative for "inside" and positive for "outside" the surface. The surface normals are estimated by fitting a plane to a subset of points in the neighbourhood of each point.

In the case of modelling a physical (real) surface, it is not necessary to fit the RBF outside a specific bandwidth around the given points, since the scanned surface will likely not be present there. The bandwidth is set by user through the maximum and minimum normal length. For the maximum normal length, a value several times larger than the average scanning resolution is usually sufficient. Therefore, if for example, the scanning resolution is in the order of 20 mm the maximum normal length can be around 60 mm. The minimum length of the normal vector should be in the same order or larger as the level of noise or precision of the data. If the minimum normal vector length is chosen smaller than the noise level, the influence of the error will become too large, resulting in "dimpling" at the surface. Subsequent surface smoothing during the iso-surfacing may not be able to remove this. For example, if the precision is in the order of 15 mm (typical for the Optech scanner) the minimum normal length might be set to 20 mm.

In the case of very complex surfaces, sharp corners, or where sub-parallel surfaces are close together, the generated normals with the defined lengths may overlap each other. This creates inconsistent distance-to-surface or density data that will result in erroneous RBF iso-surfaces. A consistency check is thus required to eliminate and correct the density data from the overlapping bandwidths in such a way that closely spaced surfaces and sharp corners remain well defined in the final iso-surfaced RBF. In order to speed the process of fitting the RBF's, a so-called centre reduction can be applied, where redundant centres (points lying more or less in the same plane between the two nearest points) are removed. However, in the case of dense and noisy laser-scanner data, a centre reduction is generally not applied, since it becomes hard to determine what the redundant centres are. Another way to increase the processing speed is by a creating a (smaller) selection of the density data. Instead of using the density points on both sides of the surface, only points on one side of the surface (either just the positive, or just the negative, points) can be used. Another way is to create density points from the normal of only every other surface point, omitting intermediate points. Of course, a combination of both data reduction strategies can be used.

7.3.1.2 Isosurfacing

A meshed surface needs to be generated for the final stage of the surface reconstruction after the RBF has been fitted. The process of meshing a RBF is called iso-surfacing, since the mesh follows a pre-defined value (*a*), which is a set of points where $s(x) = a$. If the input data does not relate to a physical surface, but consists of (3-D) density such as concentration of pollutants or ore grade, the mesh can follow any iso-value (*a*) of the continuous RBF. In that case, a full grid evaluation needs to be carried out, using a *marching cubes* algorithm. In this study, the data represents a physical 3-D surface and a full-grid evaluation is therefore not necessary. The meshed surface in this case follows the points where the RBF function $s(x) = 0$. For iso-surfacing of signed-distance-to-real-surface data, the *surface-following* algorithm is used. This algorithm uses a tetrahedral sampling lattice to ensure an even sampling. Seed points that are close to the iso-surface are required to begin the surface-following process. In the case of a single continuous (rock face) surface, the selection of a single seed point should be sufficient.
The input laser scanned points are noisy. Therefore, the resulting iso-surface will reflect the spatial error if all points are exactly fitted by the RBF and/or the iso-surfacing. As mentioned previously, this can result in a 'dimpled' surface. There are two ways in FastRBF to filter out the noise and create a smoother iso-surface. Smoothing techniques can be applied during the RBF fitting, or during the iso-surfacing process.

Smoothing during the RBF fitting can be done with *spline smoothing* (also known as *ρ smoothing*), or by using the *smoothest restricted range approximation* (also referred to as *error-bar fitting*). The two methods optimise different smoothness criteria, and these are discussed in detail in the Fast RBF User Manuals (FastRBF, 2004). Smoothing during the iso-surfacing is referred to as low-pass filtering. This has an advantage because the RBF is fitted only once, with the highest possible accuracy, and the filtering is carried out afterwards with the required smoothing parameters. This will save computation time and allows the user to view much more quickly the results of different smoothing settings. The main result of the low-pass filtering is that high frequencies, irrespective of origin and magnitude, are globally reduced. In this study, low pass filtering during the iso-surfacing is carried out on an exactly fitted RBF. The low-pass filtering and meshing parameters depend on the scanning resolution and the data error.

Figure 7.1 to Figure 7.6 provide an example of the iso-surfacing process and the result of different smoothing distances. The 3-D surfaces have been rendered using artificial shading to enhance the surface features. The example is a subset from the point cloud data of Site 1 (For details, refer to Appendix C), the location is indicated by the box on the photograph in Figure 7.7. The scanned area is about 20 by 20 cm, perpendicular to the viewing direction. The actual surface area is larger, due to the irregularity of the surface. The meshing distance is chosen to be the same as the scanning resolution (5 mm). This will reveal the optimal amount of detail in the data. The RBF was fitted with an accuracy of 2 mm. Figure 7.2 shows the result of the iso-surfacing without any smoothing. Much surface detail can be observed that is the combined result of small-scale surface roughness, small irregularities and data noise. The small-scale detail can be filtered out with a 1 cm and 2 cm low pass smoothing filter, as illustrated in Figure 7.3 and Figure 7.4. The result is that details smaller than 1 and 2 cm are removed. The meshing distance of 5 mm has been maintained for comparison. When smoothing is performed, a larger mesh size can be selected without significant information loss, as illustrated in Figure 7.5 and Figure 7.6. The mesh size can be smaller or equal to the smoothing distance. The selection of a mesh size that is much smaller than the smoothing distance will create redundant information since the meshing algorithm will merely sub-sample the data.

7.3.2 Stereographic analysis of the reconstructed surface mesh

After the reconstruction of the rock surface in a 3-D mesh, the surface mesh itself can be analysed. The surface mesh consists of triangles, also called *facets*. Each facet has three corner points or *vertices*, which are no longer the original laser scan points, but the interpolated points. These three

corner points uniquely define the orientation of the facet, similar to the way orientations of discontinuity planes are defined.

The meshed surface has a straightforward data structure. The surface is stored as a list of vertices and a list of facets. The vertex list contains the *x*, *y* and *z* coordinates of all the corner points of the facets. The facet list contains, for each facet, a record of the three vertex numbers, which correspond to the record numbers of each point in the vertex list. In this way the coordinates of the corners of each facet can be retrieved and used to compute the normal vector and corresponding orientation of the planar facet, according to the method described in Section 3.7.1.

Subsequent plotting of all facets in a stereographic plot allows the orientations of the surface to be visualised in detail. The sets in which the discontinuities are clustered should thus become visible, but only if the geometry of the rock surface is largely due to the discontinuities present within the rock mass. With this method, the amount of orientation data is equivalent to the number of facets present in the 3-D surface mesh and typically, this will be a very large number. For example, a rock face that measures about 25 m^2, and represented by a 3-D meshed surface with a 2 cm mesh size, contains about 450 000 facets and, therefore, the same number of orientation measurements. Most of the available stereographic plotting programs developed for geological applications do not support such large orientation data sets. Therefore, the data is plotted with a special script in Matlab. The results of the stereographic plotting of the orientations of all surface facets of the rock faces at Site 1 are provided in Figure 7.24, and for Site 2 in Figure 7.40. Apparent trends in the data can be observed in both cases, despite the large amount of noise. The hypothesis is that these trends relate to the presence of discontinuity sets. Another observation is that these detailed stereographic plots show a distinct and unique picture of the rock face, which is in direct relation to the geometry of the rock face. However, the typical patterns in the stereographic plots are also a function of the surface reconstruction and meshing parameters that are used. The mesh spacing and smoothing parameters that are applied will influence the amount of scatter shown in the stereographic plot. Figure 7.8 to Figure 7.12 illustrate this effect. These figures show the stereographic plots that refer to the meshed surfaces shown in Figure 7.2 to Figure 7.6. The unsmoothed surface shows a much larger scatter and number of poles (due to the larger number of facets) than the smoothed surfaces. The smoothing removes much of the scatter in the stereographic plot, but the main trends in the data are preserved and even enhanced. A larger mesh size does therefore not necessarily result in loss of information, since the main trends can still be observed.

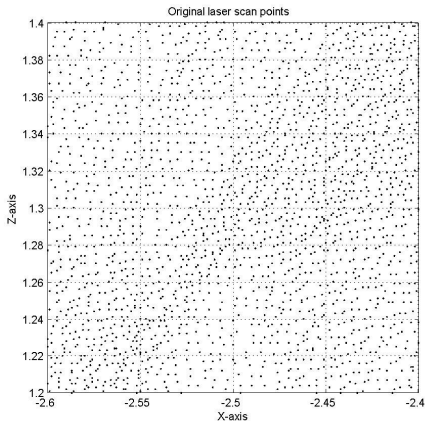

Figure 7.1. Original laser scan points. The scanning resolution is about 5 mm

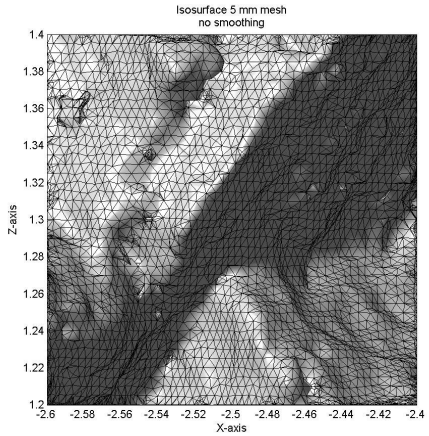

Figure 7.2. Isosurface without smoothing and a 5 mm mesh size

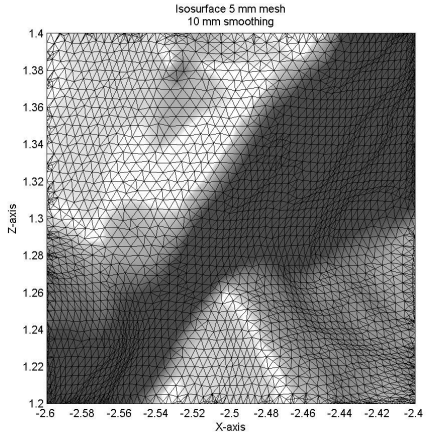

Figure 7.3. Isosurface with 1 cm smoothing and a 5 mm mesh size

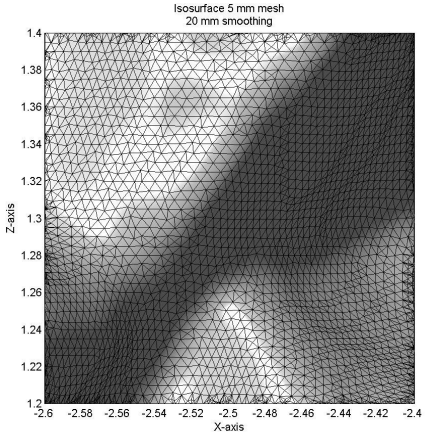

Figure 7.4. Isosurface with 2 cm smoothing and a 5 mm mesh size

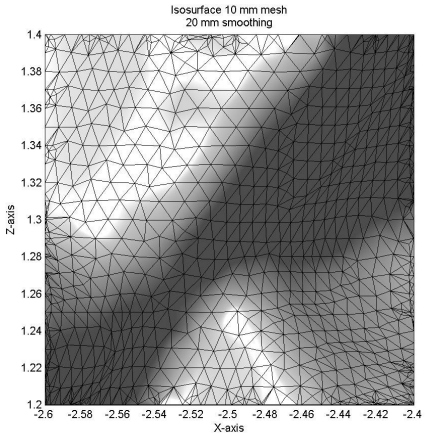

Figure 7.5. Isosurface with 2 cm smoothing and a 1 cm mesh size

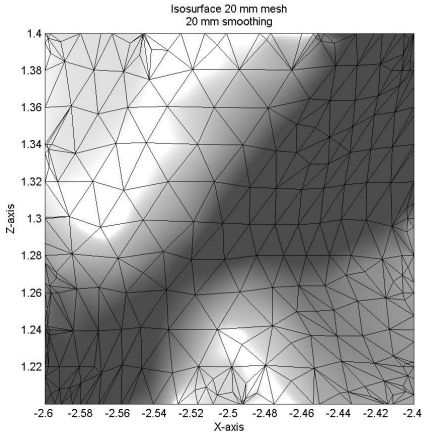

Figure 7.6. Isosurface with 2 cm smoothing and a 2 cm mesh size

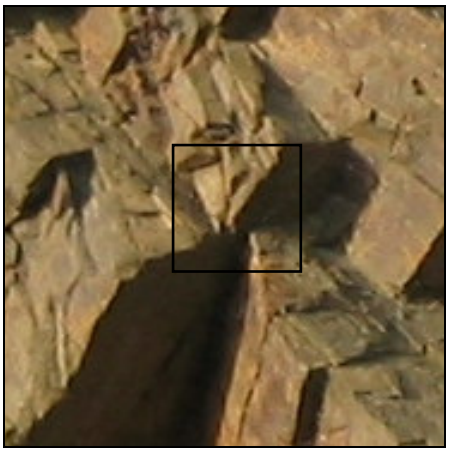

Figure 7.7. The box in this photo shows the location of the isosurfacing example given on the previous page (Site 1)

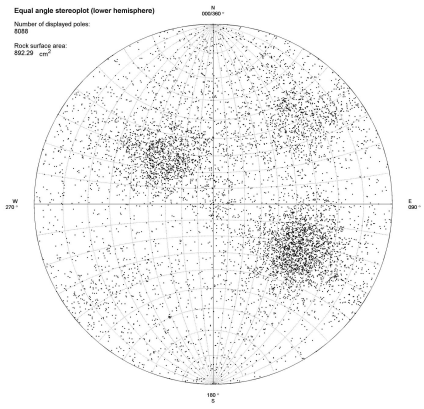

Figure 7.8. Polar plot of the facets of the unsmoothed surface shown in Figure 7.2

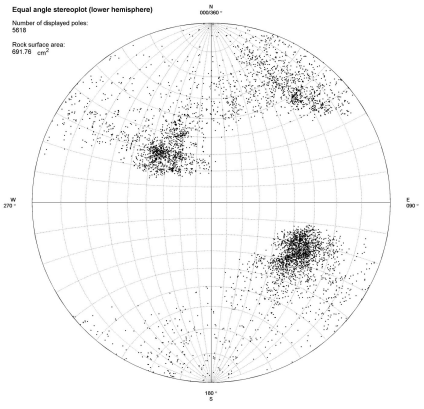

Figure 7.9. Polar plot of the facets of the smoothed surface shown in Figure 7.3.

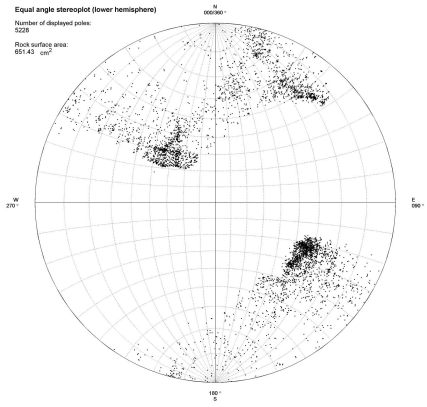

Figure 7.10. Polar plot of the facets of the smoothed surface shown in Figure 7.4.

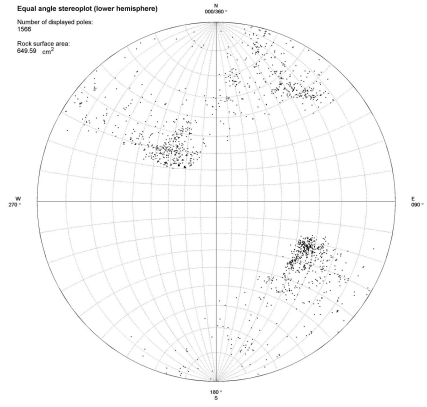

Figure 7.11. Polar plot of the facets of the smoothed surface shown in Figure 7.5

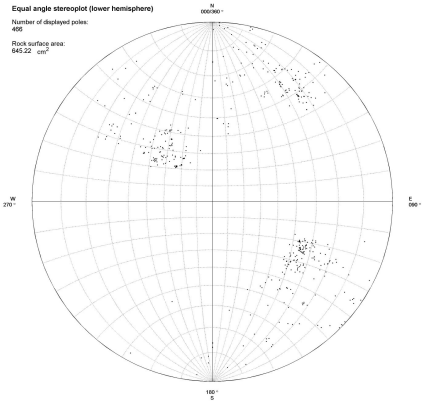

Figure 7.12. Polar plot of the facets of the smoothed surface shown in Figure 7.6

7.3.3 Fuzzy k-means clustering of the facet orientation data

The detailed stereographic plots of the facet orientation data must be clustered in order to derive information on the various identified discontinuity sets. Considering the large number of discontinuity measurements, the most appropriate method is fuzzy k-means clustering, as described in detail in Section 3.7.4. This method requires the user to enter the number of independent discontinuity sets that are believed to exist (*k*). The fuzzy k-means clustering classifies each of the orientation measurements (and thus all facets) to the one of these sets. At the same time, the mean orientation, Fisher's *K* values and various other cluster statistics are determined for each discontinuity set. The classification results can also be used to colour all facets in the original 3-D surface according to the set number (see Figure 7.16 for Site 1 and Figure 7.32 for Site 2). This allows the resulting classification to be inspected. If the result is not in accordance to what is expected, or gives unrealistic results, the fuzzy k-means clustering can be repeated with a different number of sets. It should be noted that all facets are clustered. Therefore, facets from parts of the surface that are not necessarily part of any discontinuity plane are also included in the classification.

7.3.4 Outlier removal

Cluster outlier removal (see Section 3.7.5) restricts the orientation data to "real" clusters. The outliers in the data can be removed interactively, or according to user-defined constraints to specific parameters, such as a Fisher's *K* value, eigenvalue ratio, or spherical variance. If the results plotted in the stereographic plots (see Figures 60 and 76) are judged to be satisfactory, the classification results can be projected onto the original 3-D surface, with only the surfaces belonging to the designated discontinuity sets being coloured (see Figure 7.17 and Figure 7.33).

It proved to be difficult to define standard rules to control the removal of cluster outliers. The number of iterations needed to remove the outliers depends strongly on the number of poles and the scatter of the plotted poles in each set. In practice, the best way to determine the optimal outlier removal appears to involve running the iterative outlier removal algorithm with a fixed distance step for a (large) number of times, for example for 200 steps. In most case this results in a very small remaining cluster with a circular (Fisher) pattern. By plotting on stereographic plots, and then visually inspecting, the poles retained during selected intermediate steps, it is possible determine when the optimal cluster delineation is achieved. For instance if, for a specific iteration step, the cluster shows a "nice" circular and dense Fisher's distribution, then that is used as the final number of iterations needed to delineate the cluster. By visualising the results projected onto the original 3-D surface, as explained above, the results can always be verified and adjusted as needed.

Still, the decision as to where to place the delineation boundary of each cluster is a subjective one. It proved necessary to rely mainly on a "visual" check by the user. Thus, use of the delineated data set may introduce bias and comparison of the results obtained from this method with those attained by the other three methods becomes more difficult. The other methods do not require cluster outlier removal because the resultant orientation data does not contain so many noisy outliers as with this method. Therefore, the outlier removal process is not used in the final discussions of data analysis and comparison among the methods. It is merely shown here as a demonstration of how it can be applied to large orientation data sets that contain considerable scatter and noise.

7.3.5 Classification of facets and vertices to planes

After the fuzzy k-means classification of the facets, and the optional application of outlier removal procedures, the facets remain classified as belonging only to the defined discontinuity sets. Yet, a single discontinuity set may contain several distinct and individual discontinuity planes. A re-classification of facets into discontinuity planes is essential if discontinuity spacing is to be computed, as this requires the separation of planes within a set. The re-classification into planes will also simplify the data significantly, since a large number of facet orientations will be transformed into a (much smaller) number of discontinuity planes.

Discontinuity planes within each set are found by connecting neighbouring facets of the same set. It can be assumed that connecting facets belonging to the same discontinuity set form part of a single discontinuity plane. Connecting facets are defined as two facets that share two vertices. Two facets that share only one vertex are not considered “connecting” facets. The procedure is as follows: a random (seed) facet is chosen. All neighbouring facets are quickly found through the mesh data structure described in Section 7.3.2. Next, the neighbours of these neighbours are in turn found until all connecting facets are joined into a single plane. This process is repeated for each set until all facets are re-classified into planes. Thus every facet finally gets two labels assigned: one for the set number and one for the plane number. In addition, the three vertices that make the facets get both labels assigned. Every single vertex belongs in general to more than one facet. Therefore, it is logical to expect that all or some of the facets that are “attached” to that vertex have different planes or set labels. In order to keep a unique classification of the vertices, the last assigned label is the one that is kept. It should be noted here that the vertices are not the original laser scan points, but the interpolated points that form the nodes in the mesh.

The result is thus a classified set of vertices that make the reconstructed (interpolated and meshed) surface of the rock face. The classification is a unique combination of set- and plane number. The result is similar to the results that will be obtained with the two other (segmentation) techniques that are discussed in Chapter 8. The main difference is that the point-cloud segmentation methods use the original point-cloud data while this method uses the vertices from the meshed surface.

The next step, after the classification of vertices to planes, is to obtain the geometric information for each plane by computation of plane equation parameters of the individual discontinuity planes. The other three methods require subsequent processing by fuzzy k-means clustering to classify the individual discontinuity planes into discontinuity sets. This is opposite to the sequence to that is required for this method, since the fuzzy k-means clustering has already determined the discontinuity set membership for each surface facet before the plane identification step.

Once the set number is known for each discontinuity plane, one can immediately proceed to the computation of the normal for each discontinuity set, as well as the calculation of other discontinuity set statistics, such as Fisher’s K value and spherical variance. These values can then be used to compute discontinuity spacing statistics. This post-processing step is identical for the other three methods. Thus, the post-processing procedures for Method 1 are described in Chapter 9 together with those of the other methods. The results are also provided in Chapter 9 so that a better comparison between the various methods can be made. Section 7.4 that follows, concentrates on the presentation and evaluation of the results of the plane extraction.

7.4 Results of applying surface reconstruction with an implicit representation (Method 1)

On the following pages, the results of Method 1 are presented with a number of illustrations. For convenience, the figures are all presented together. The results are presented for both rock exposure test sites in four steps:

1. Visualisations of the point cloud data input and the resulting 3-D rock surfaces
2. Stereographic polar plots of the surface facets of the meshed surfaces
3. The fuzzy k-means clustering results of the stereographic polar plots
4. Visualisation of the effect of the fuzzy k-means clustering on the 3-D surface

The specifics with regard to the data processing and the results are summarised in the next two sections for each test site individually.

7.4.1 General processing remarks

7.4.1.1 Surface reconstruction steps

The 3-D surface reconstruction was done with the FastRBF method in Matlab. The parameters for the density data generation and the RBF fitting are constrained by the inherent noise level of the point cloud data and the data density. Therefore, by varying the mesh size and the smoothing distance, the user can influence the final quality of the generated surface. For both sites the best results (the most realistic representation of the actual rock face) was delivered with a meshing distance of 1 cm together with a smoothing distance of 2 cm. A smaller smoothing and meshing distance resulted in a surface with a low signal-to-noise ratio, while a larger meshing and smoothing distance removed too much detail. The precise surface reconstruction processing steps and the processing parameters that were used for reconstructing the surfaces of both test sites are the following:

1. First the normals are estimated from the original laser scan points
2. Density data are created from the normals with a minimum projection distance of 1 cm and a maximum projection distance of 3 cm
3. The FastRBF fitted a RBF to the surface based on the density data with an accuracy of 3 mm.
4. Finally, a mesh is created from the RBF with a mesh size of 1 cm and a smoothing distance of 2 cm. The mesh can be exported to several formats. In this case, an ASCII *Wavefront* 3-D file format (with an *.obj* file extension) was used.

7.4.1.2 Cluster outlier removal

An attempt was made to perform cluster outlier removal. Figure 7.26 and Figure 7.27 show the remaining and the removed as stereographic plots for Site 1, while and Figure 7.42 and Figure 7.43 show the equivalent stereographic plots for Site 2. The poles that remain after the outlier removal can again be linked to the respective facets of the 3-D surface. Figure 7.17 (for Site 1) and and Figure 7.33 (for Site 2) show the surfaces belonging to the designated discontinuity sets in various colours, while the facets designated as outliers remain grey. Since it is very difficult to determine the right threshold values to limit the cluster removal, it boiled down to a trial-and-error, visually oriented process (defined in Section 7.3.4) that resulted in an “optimal” outlier removal. This introduces some bias into the analysis, making it difficult to compare the results with the other methods that do not include a similar outlier removal step. Therefore all facets are included in the further analyses and thus all planes that can be identified in the 3-D surface are used.

7.4.2 Results of Method 1 for Site 1 (Bellmunt)

The input data consist of a cropped portion of a single laser scan survey with the Optech scanner. The details of this particular survey are given in Appendix C; Figure 7.13 shows the outline of the cropped data portion on a photograph of the outcrop. The input data set consists of 616300 points that have an average scan resolution of 5 mm (Figure 7.14).

The parameters used to perform the RBF fitting and the subsequent surface meshing are given in Section 7.4.1.1. More details can be found in the Matlab scripts that are given in Appendix F. Figure 7.15 provides a digital rendering of the resulting 3-D surface. This 3-D digital surface appears to be a most “realistically looking” representation of the rock face. However, small “blobby” artefacts are clearly seen all over the slope, mainly caused by vegetation on the slope. The final meshed surface consists of 457213 facets. The orientations of the facets are plotted in a stereographic plot (Figure 7.24). A fuzzy k-means clustering into 5 sets gave the best results; these are shown in the stereographic polar plot (Figure 7.25). The facets of the 3-D surface can in turn be coloured according to their discontinuity set number; Figure 7.15 provides a digital rendering. The cluster statistics are computed based on all cluster poles and are summarised in Table 7.1.

Table 7.1. Statistics for the clustered polar plot of the facets of the FastRBF surface of Site 1 (Bellmunt).

	Set 1 (blue)	Set 2 (red)	Set 3 (yellow)	Set 4 (magenta)	Set 5 (cyan)
Dip (degr.)	87	63	53	43	72
Dipdir (degr.)	75	153	24	344	53
N (no. of poles)	106258	61125	64309	128168	97352
K (Fisher const.)	6.141	2.794	16.72	10.95	19.83

From observation of the 3-D coloured surface view shown in Figure 7.16, it is clear that the visually most “obvious” sets are the blue, red and magenta sets, or: sets 1, 2 and 4, respectively. The magenta set (set 4) is the bedding. The cyan set (set 5) seems in the 3-D view to be closely related to the blue set (set 1). The yellow set (set 3) does not appear to be a “real” discontinuity set due to the fuzzy character of the clustered facet poles. It may thus be possible that the surfaces that are classified as the yellow set 3 results from the fracturing of intact rock caused by the excavation process or due to failure after the excavation through rock bridges[22] (see Section 2.5.8). The dislodging of the rock blocks during or after the excavation would have been controlled by the sets 1 and 5 (blue and cyan) on the one hand and the orthogonal (bedding) set 4 (in magenta) on the other hand. The bedding set is fully persistent. If the other sets 1 and 5 are not persistent, the only way to be able to remove the blocks, is through failure of the rock bridges between the joint planes of set 1 or 5 and the bedding set 4. The failure of these rock bridges could have thus resulted in fracture surfaces with a general orientation corresponding to set 3.

By studying the stereographic plots in Figure 7.24 and Figure 7.25, it is possible to distinguish 3 or 4 sub-clusters within the blue set (set 1). However, the fuzzy k-mean clustering method was not able to separate these sub-clusters. When the fuzzy k-mean clustering was re-computed using 6 clusters, the result was another set located between the yellow and cyan sets (sets 3 and 5), while the blue set (set 1) was more or less maintained, including the apparent sub-clusters. Therefore, it is assumed that the apparent sub-clusters within set 1 result from orientations of the poles from facets that are contained within the relatively extensive discontinuity planes present in set 1. Figure 7.18 and Figure 7.21 show that set 1 contains a few relatively large surfaces that vary somewhat in general orientation, thus creating the apparent sub-clusters.

The individual planes within each discontinuity set were subsequently identified using the method described in Section 7.3.5. The geometry of each individual discontinuity plane is characterised by orientation (dip direction and dip angle), the parameters (a, b, c and d) defining the individual plane equation, the coordinates of the centre of the plane, and the planar extent expressed as minimum and maximum coordinates. This geometric information can then be used to visualise the individual planes in 3-D, as shown in Figure 7.18 to Figure 7.23. These figures demonstrate how the surfaces for each set can be separately visualised, together with their corresponding planar representations in 3-D. In total, 403 individual discontinuity planes have been identified. In order to keep the number of planes manageable, very small planes were removed; i.e., individual planes containing less than 100 vertices.

[22] A rock bridge is the intact piece of rock that exists between two coplanar or non-coplanar discontinuities. At least one of the two discontinuities is a non-persistent plane.

Figure 7.13. Photograph of the scanned exposure at Site 1 (Bellmunt). The box indicates the extent of the cropped point-cloud data area that is used for the processing (see Figure 7.14). The circle indicates the approximate location of the example of smoothing effects given in Figure 7.1 to Figure 7.12 and described in Section 7.3.1.2

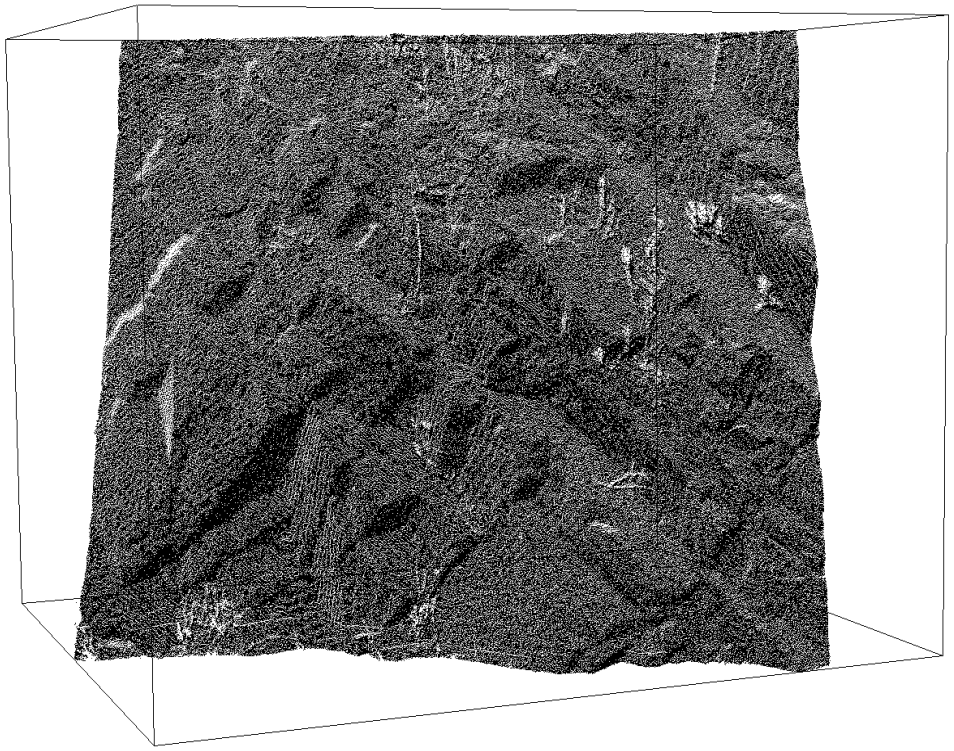

Figure 7.14. 3-D view of the selected input point cloud data of the Bellmunt slope. For the outlined area on the exposure refer to Figure 7.13. Note the presence of small pockets of vegetation on the slope. The size of this part of the slope is about 5 meters wide and 4 metres high. The 3-D box shows the maximum data extend in x, y and z direction

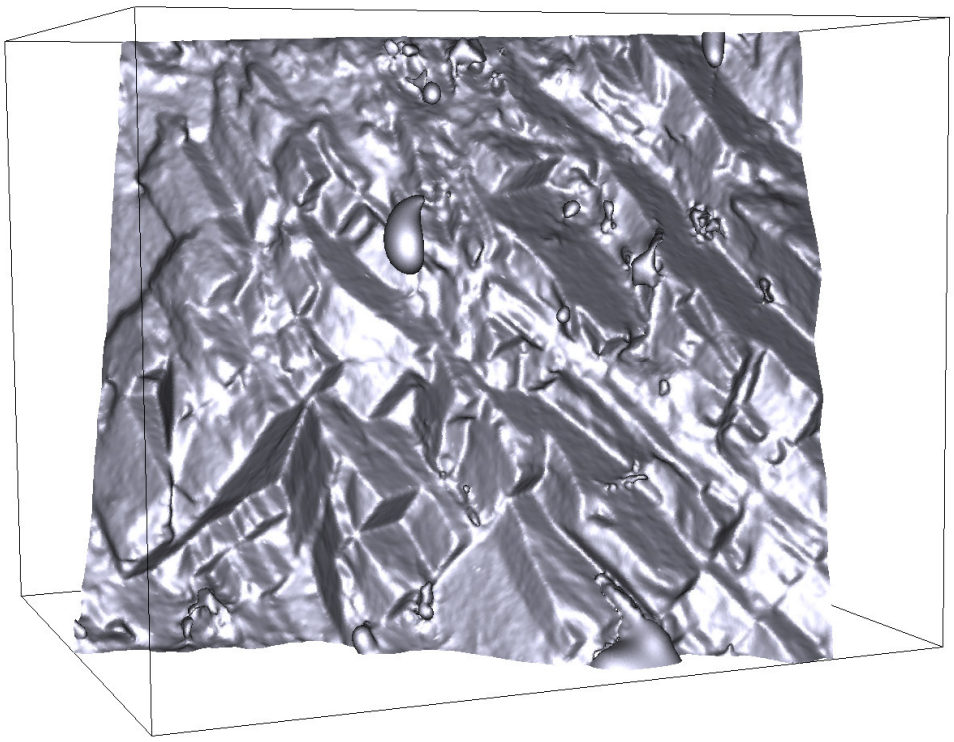

Figure 7.15. 3-D digital rendering of the interpolated and meshed surface that was created with FastRBF. Artificial lighting has been applied to enhance the surface features. The mesh size is 1 cm and the smoothing distance is 2 cm. Note the “blobby” parts, due to the noisy points caused by vegetation.

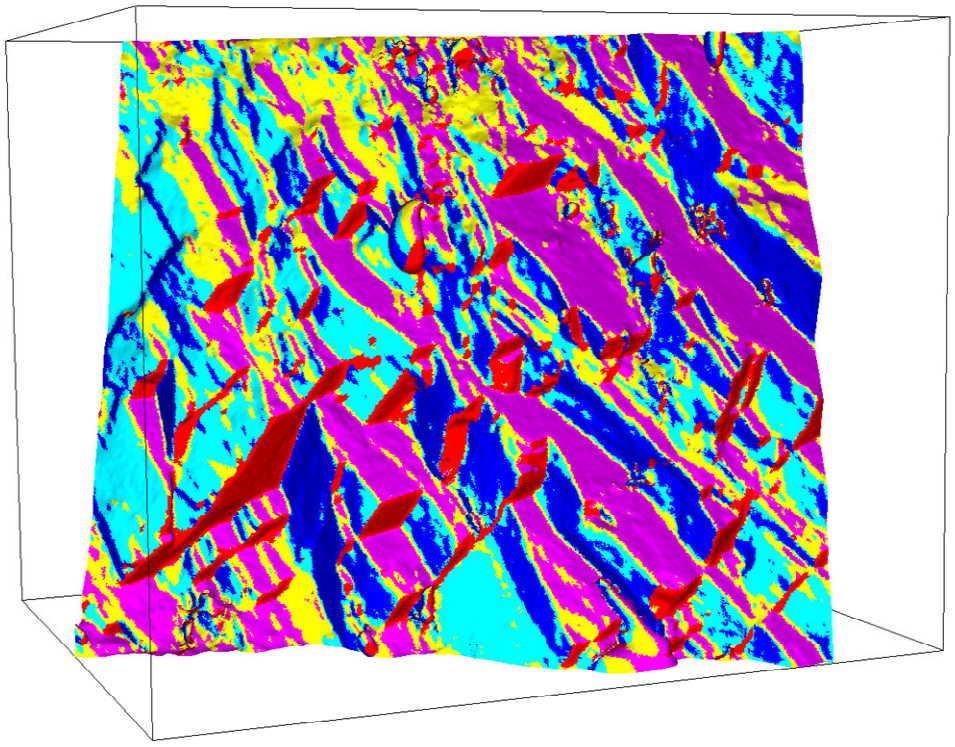

Figure 7.16. 3-D digital rendering of the interpolated and meshed surface of Site 1, where the colours refer to the 5 different discontinuity sets to which all facets have been clustered. The colours are the same as the colours used in the clustered polar plot of Figure 7.25.

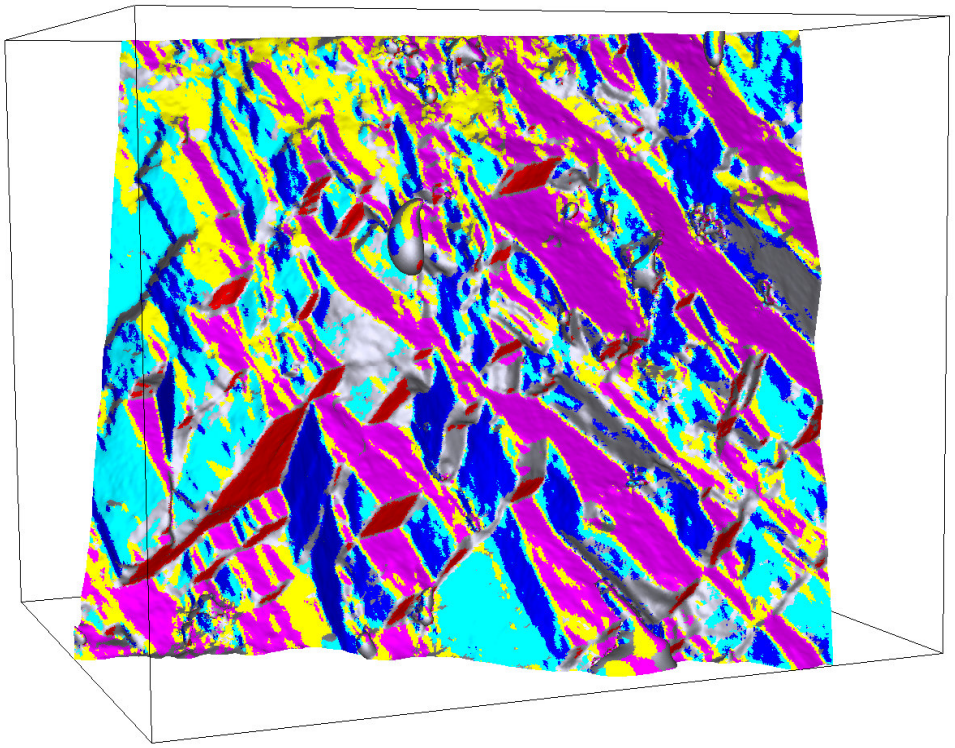

Figure 7.17. Same rendering as in the Figure 7.16, only in this view the facets that have been removed with cluster outlier removal are not coloured (shown in grey). The coloured surfaces belong to the facets that remained. Please refer to Figure 7.26 and Figure 7.27 for the corresponding stereographic polar plots.

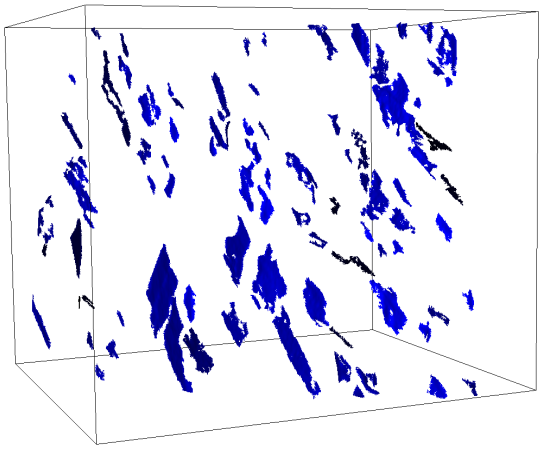

Figure 7.18. 3-D view showing only the rock surface classified to Set 1

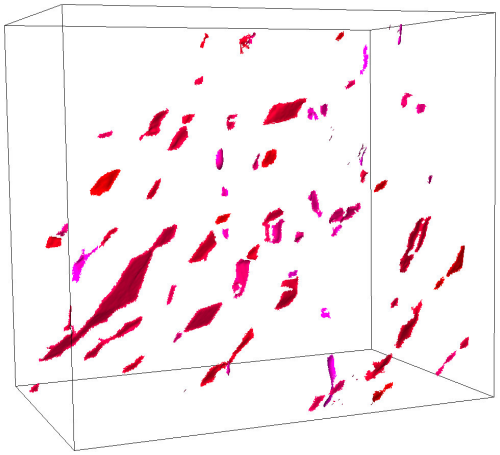

Figure 7.19. 3-D view showing only the rock surface classified to Set 2

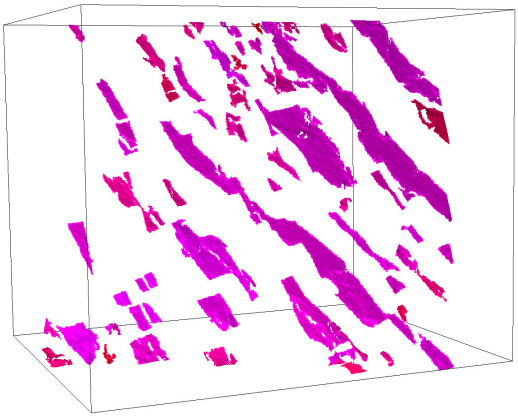

Figure 7.20. 3-D view showing only the rock surface classified to Set 4

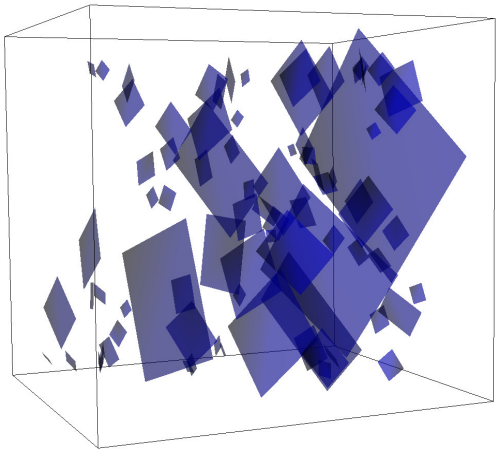

Figure 7.21. Rock surfaces of set 1 simplified to planar objects

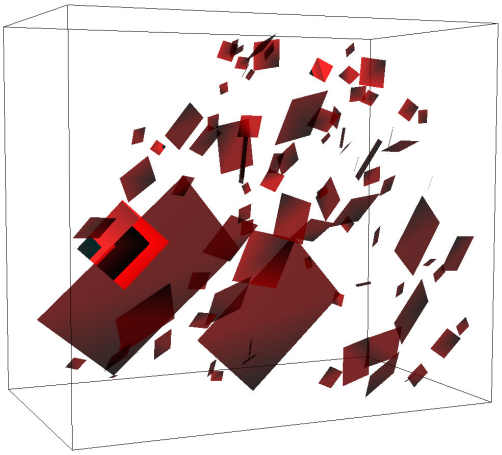

Figure 7.22. Rock surfaces of set 2 simplified to planar objects

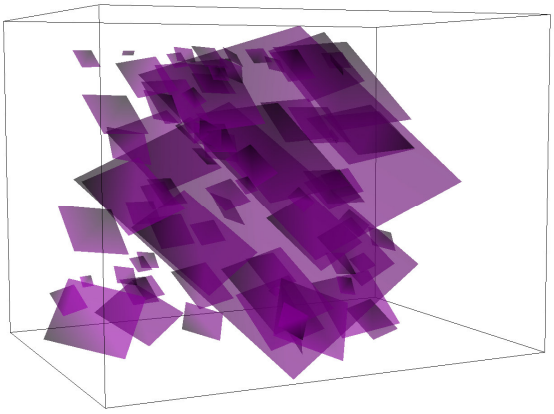

Figure 7.23. Rock surfaces of set 4 simplified to planar objects

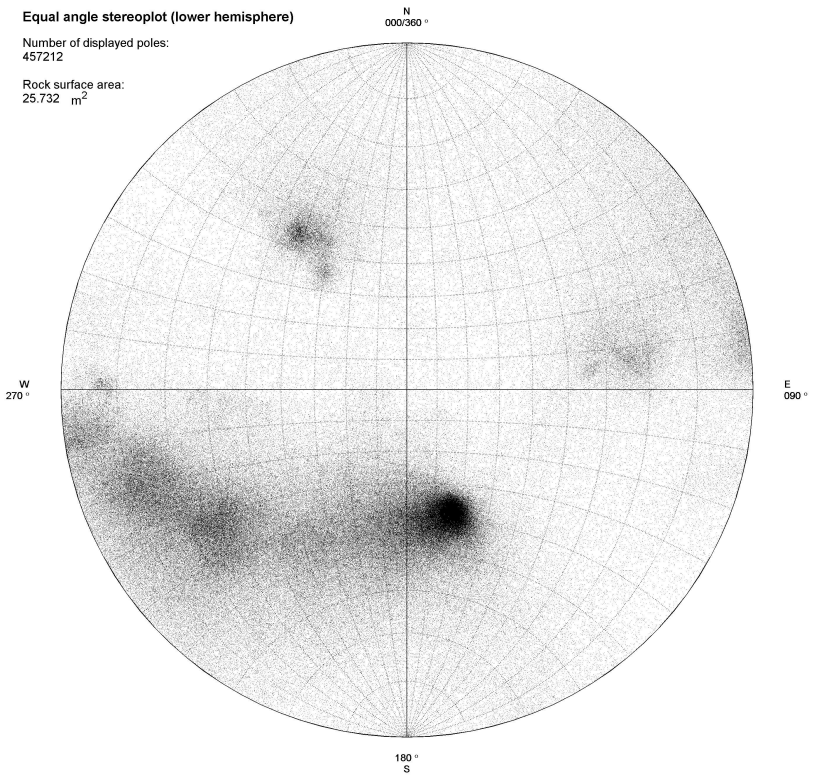

Figure 7.24. Equal angle stereonet plot (lower hemisphere) of all facet poles (457213 poles) of the interpolated and meshed surface of the laser scan data from Site 1. The entire interpolated surface area (the combined surface of all facets) is about 26 m^2.

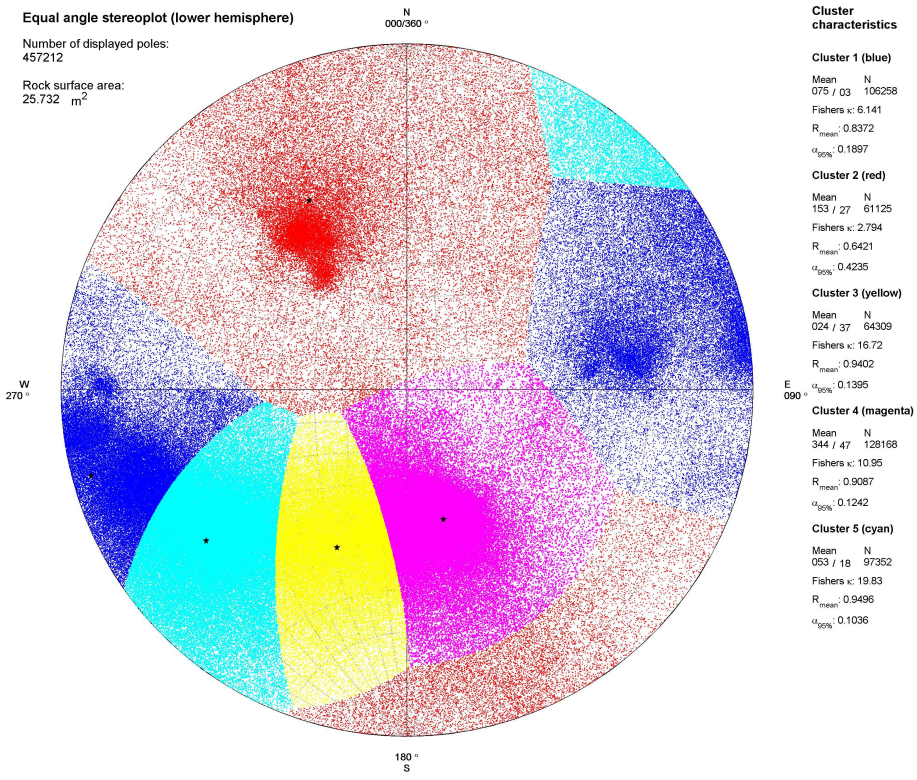

Figure 7.25. Equal angle stereonet plot (lower hemisphere) of all facet poles of Site 1, but now classified and coloured according to a fuzzy k-means clustering with 5 discontinuity sets. The blue colour is for set (cluster) 1, red is for set 2, yellow is for set 3, magenta is for (bedding) set 4 (the bedding) and cyan is for set 5.

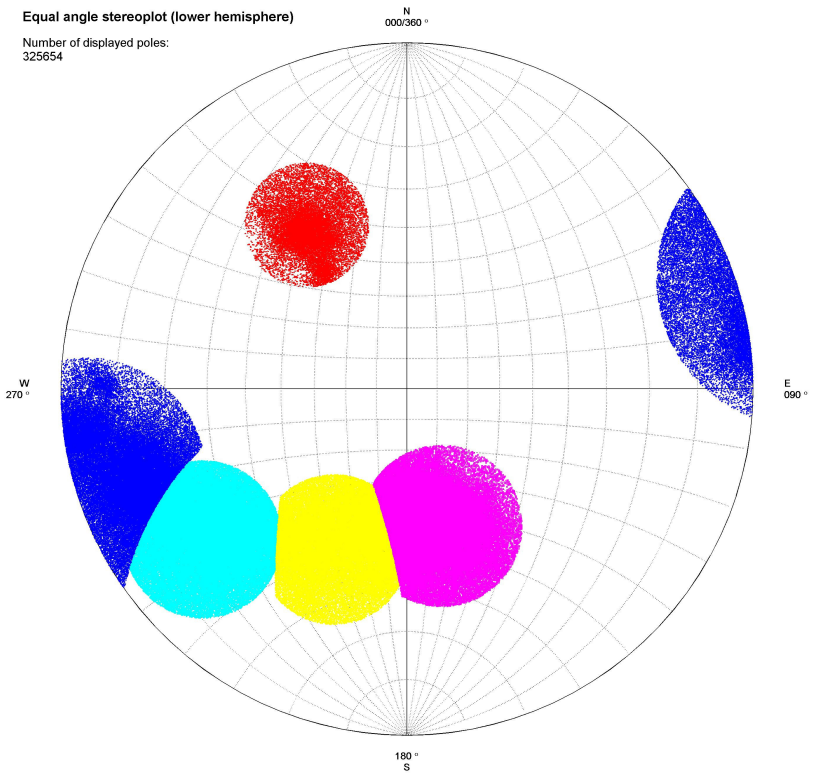

Figure 7.26. Equal angle stereonet plot (lower hemisphere) of the remaining facet poles of Site 1 after the cluster outlier removal.

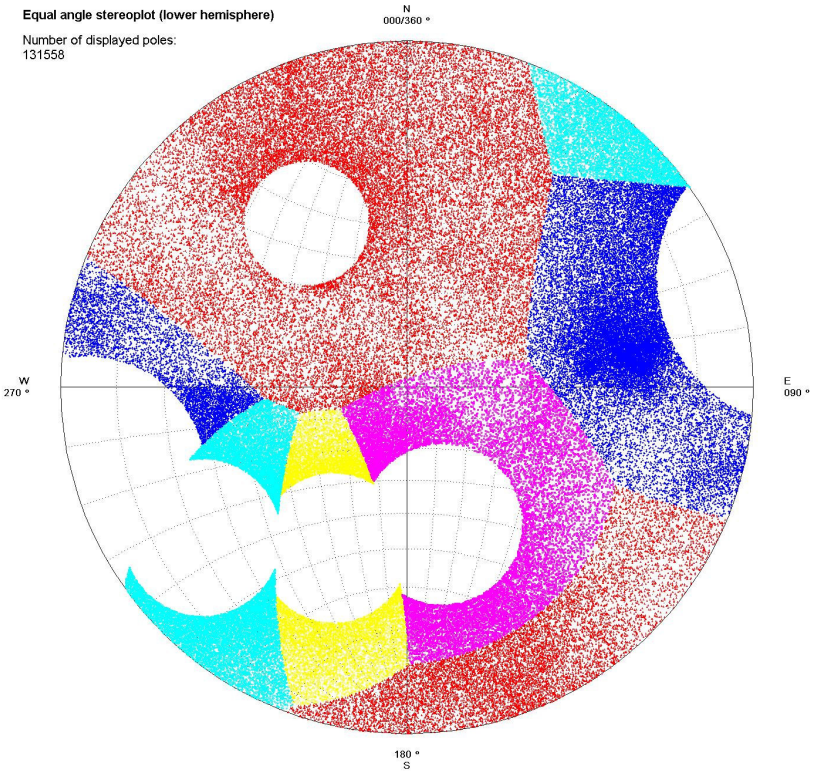

Figure 7.27. Equal angle stereonet plot (lower hemisphere) of the outlier facet poles of Site 1 that are removed (see also Section 7.4.1.2).

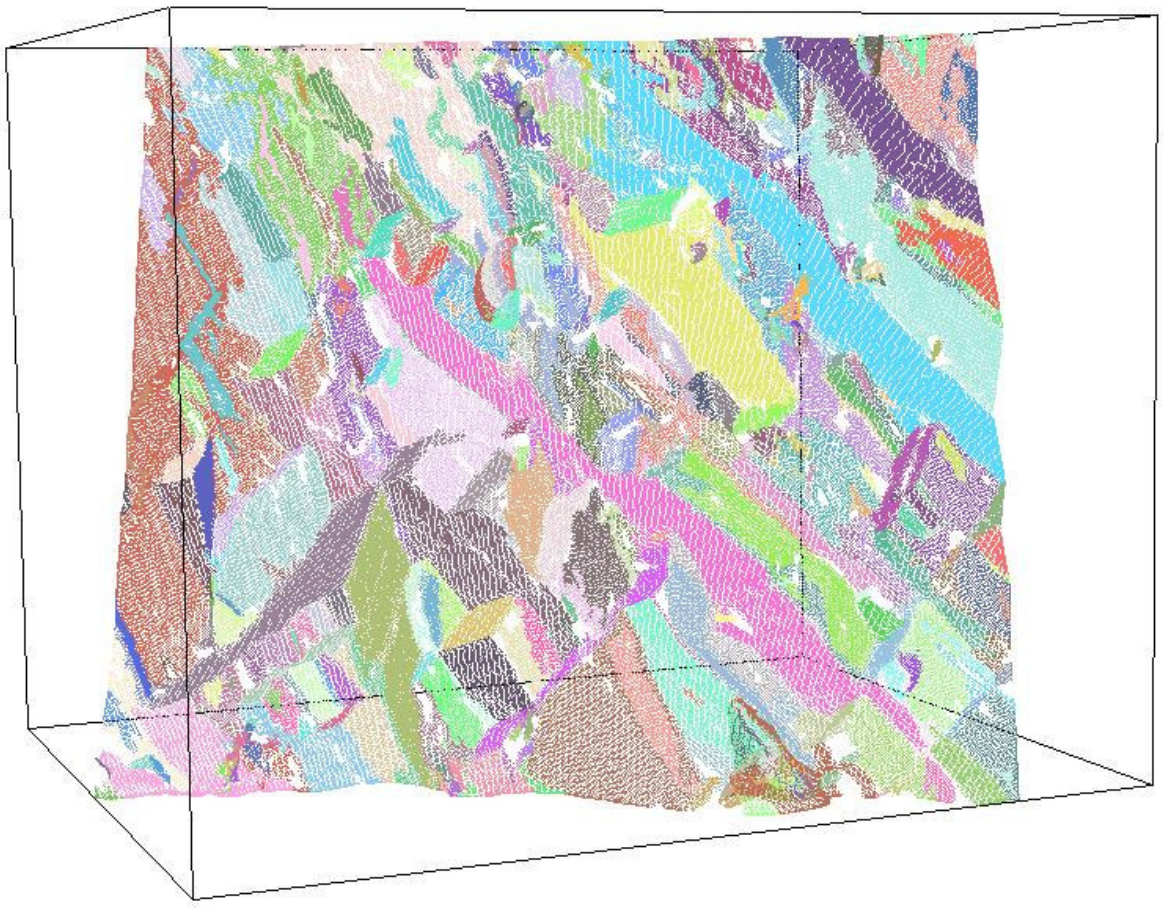

Figure 7.28. This illustration shows the 3-D view of the vertices of the facets from the meshed 3-D surface of Site 1. Note that this is *not* the laser scan point cloud. Points (vertices) with similar colour represent a single discontinuity plane that is identified with method 1, i.e. planes that fall in the same cluster and which are connected are classified to the same plane and receive in this view the same (random) colour.

7.4.3 Results of Method 1 for Site 2 (Torroja)

The input data consist of a cropped portion of a single laser scan survey with the Optech scanner. The details of this particular survey are given in Appendix D; Figure 7.29 shows the outline of the cropped data portion on a photograph of the site. The input data set consists of 480,942 points that have an average scan resolution of 6 mm (Figure 7.30).

The parameters used to perform the RBF fitting and the subsequent surface meshing are given in Section 7.3.1. More details can be found in the Matlab scripts that are given in Appendix F. Figure 7.31 provides a digital rendering of the resulting 3-D surface. This 3-D digital surface appears to be a most “realistic” representation of the rock face. However, the area of “blobby” artefacts clearly seen in the upper right part of the slope is caused by vegetation. A large single artefact is present in the upper left part of the slope. It is probably the result of some noisy data in combination with an edge effect, caused by an attempt by FastRBF to create a locally continuous surface. A little noise (points in front of the actual surface) does generally not affect the surface reconstruction. However, the FastRBF reference manual (Farfield, 2001) indicates that these undesirable blobs may be caused by inconsistent distance-to-surface data that is generated during the creation of density data from the normals. The reference manual suggests repeating the creation of density data from the normals but with a shorter normal projection length. This was tried, but it did not solve the problem. This artefact can clearly be recognised as a small heart-shaped region in the northeast section of the stereographic plot (Figure 7.40). In the clustered stereographic plot (Figure 7.41) the artefact is situated right at the boundary between cluster 1 (blue) and cluster 2 (red). A smaller portion of the

artefact is also plotted in the northeast section of the polar plot, in cluster 3 (yellow). These artefacts could not be removed from the surface and thus are included in the analysis.

The final meshed surface (including artefacts) consists of 383 344 facets. The orientations of the facets are defined in a stereographic polar plot (Figure 7.40). A fuzzy k-means clustering into 4 sets gave the best results; these are shown in the stereographic polar plot (Figure 7.41). The facets of the 3-D surface can in turn be coloured according to the set number; Figure 7.32 provides a digital rendering. The cluster statistics computed based on all cluster poles are summarised in Table 7.2.

Table 7.2. Statistics for the clustered polar plot of the facets of the FastRBF surface of Site 2 (Torroja).

	Set 1 (blue)	Set 2 (red)	Set 3 (yellow)	Set 4 (magenta)
Dip (degr.)	75	89	57	44
Dipdir (degr.)	253	34	128	289
N (no. of poles)	59014	112747	98896	112687
K (Fisher const)	6.788	4.187	3.208	4.342

From observation of the 3-D coloured surface view shown in Figure 7.32, it is clear that the visually most “obvious” sets are the red, yellow and magenta sets, or: sets 2, 3 and 4, respectively. The blue set (set 1) consists of one large surface and several smaller and indistinct surfaces. It can also be seen that many facets that are coloured blue are actually forming the edges made between the red and magenta surfaces. This can also be confirmed by the clustered stereographic polar plot (Figure 7.41). The poles that are clustered to the blue set (set 1) are located between the red and magenta sets (sets 2 and 4). The poles in the blue set (set 1) do also not have a distinct cluster centre. Thus, it is possible that set 1 is composed of fractures that are caused by the breaking of rock bridges during or after the excavation of the slope. The occurrence of a set of non-distinct fracture surfaces, possible caused by rock bridge fractures, was also observed in the data for Site 1 (the Site 1 yellow set, or set 3, see Section 6.3.2). Fractures caused by failing rock bridges have been discussed in Section 2.5.8.

The individual discontinuity planes within each discontinuity set were subsequently identified using the method described in Section 7.3.5. The geometry of each individual discontinuity plane is characterised by orientation (dip direction and dip angle), the parameters (a, b, c and d) defining the individual plane equation, the coordinates of the centre of the plane, and the planar extent expressed as minimum and maximum coordinates. This geometric information can then be used to visualise the individual planes in 3-D, as shown in Figure 7.34 to Figure 7.39. These figures demonstrate how the surfaces for each set can be separately visualised in 3-D, together with their corresponding planar representations. In total, 265 individual discontinuity planes have been identified. In order to keep the number of planes manageable, very small planes were removed; i.e., individual planes containing less then 100 vertices.

Figure 7.29. Photograph of the scanned exposure at Site 2 (Torroja). The box indicates the cropped point cloud data area that is used for the processing (see Figure 7.30).

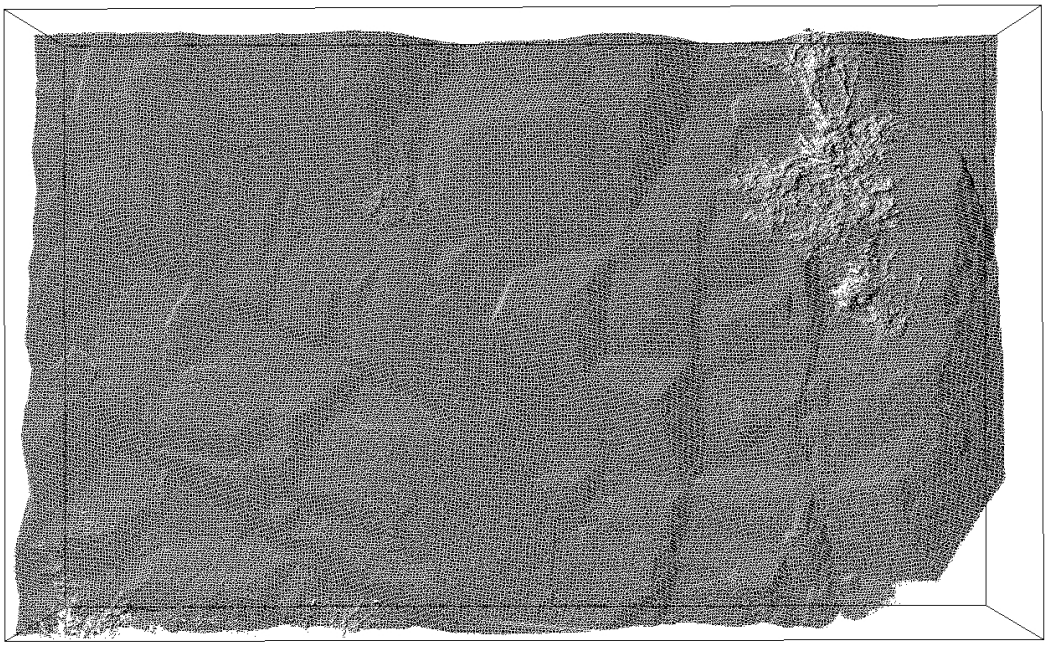

Figure 7.30. 3-D view of the selected input point cloud data of the Torroja slope. Note the presence of vegetation in the upper right and lower left part of the slope. The size of this part of the slope is about 5.5 meters wide and 3 metres high. The 3-D box shows the maximum data extend in x, y and z direction

Figure 7.31. 3-D digital rendering of the interpolated and meshed surface that was created with FastRBF. Artificial lighting has been applied to enhance the surface features. The mesh size is 1 cm and the smoothing distance is 2 cm. Note the “blobby” surface in the upper right part of the slope that is caused by vegetation. A large “blob” also appeared in the upper left. This is probably due to a combined noise and edge effect.

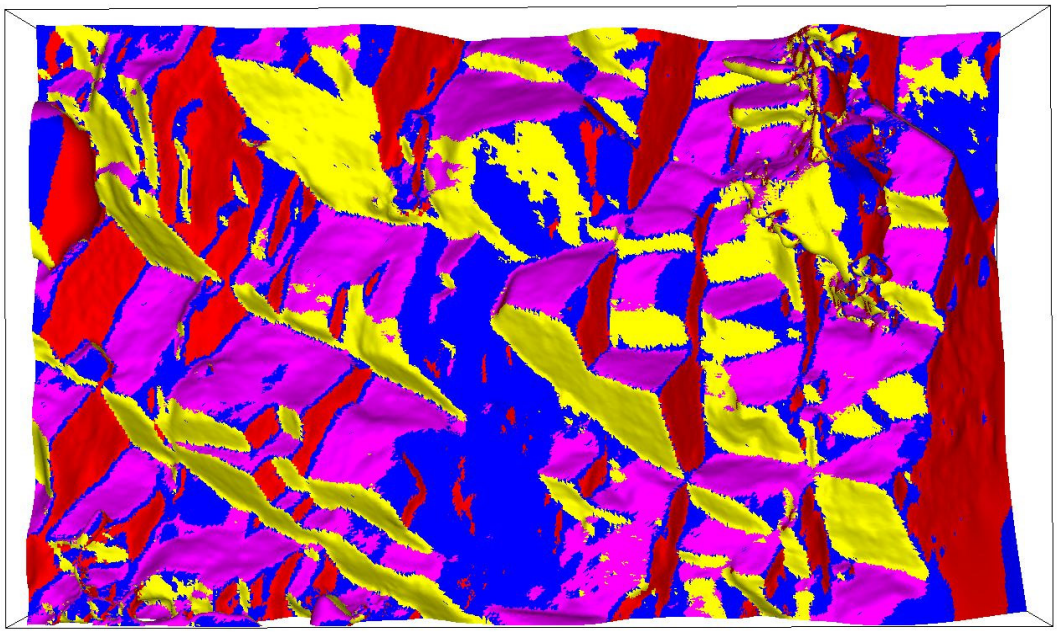

Figure 7.32. 3-D digital rendering of the interpolated and meshed surface of Site 2, where the colours refer to the 5 different discontinuity sets to which all facets have been clustered. The colours are the same as the colours used in the clustered stereographic polar plot of Figure 7.41.

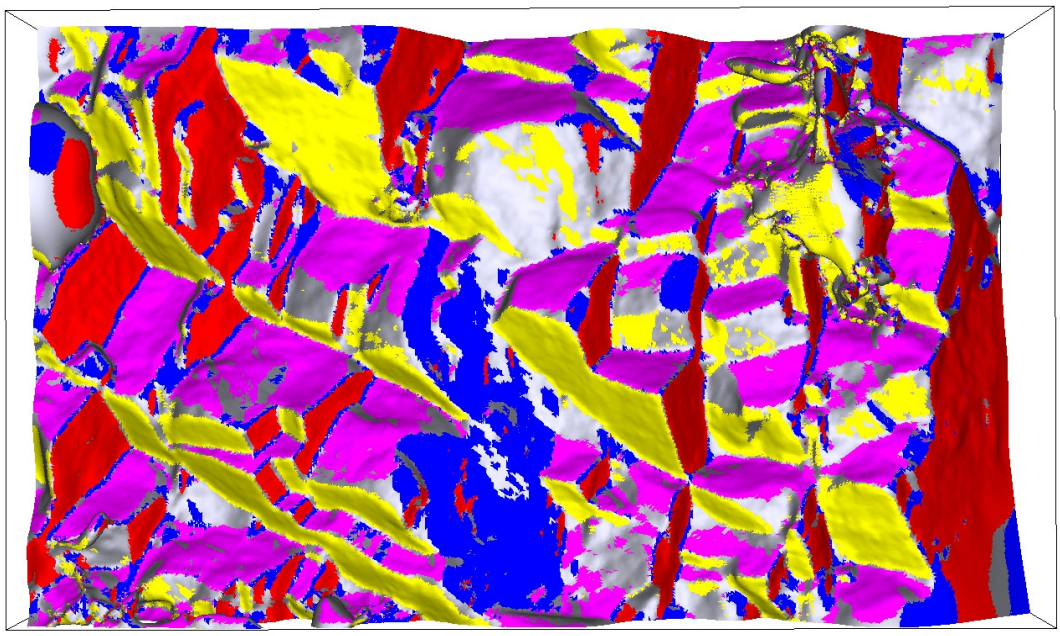

Figure 7.33. Same rendering as in Figure 7.32, only in this view the facets that have been removed with cluster outlier removal are not coloured and are shown in grey. The coloured surfaces belong to the facets that remained. Please refer to Figure 7.42 and Figure 7.43 for the corresponding stereographic polar plots.

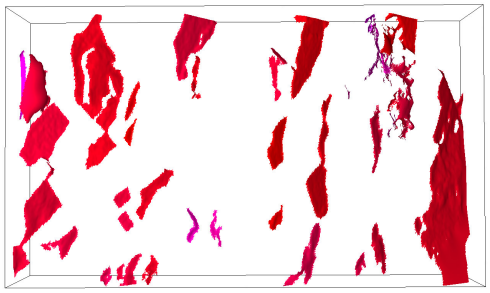

Figure 7.34. 3-D view showing only the rock surface classified to Set 2

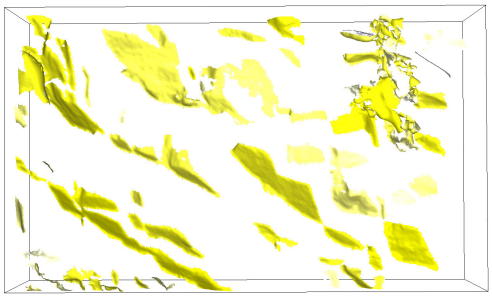

Figure 7.35. 3-D view showing only the rock surface classified to Set 3

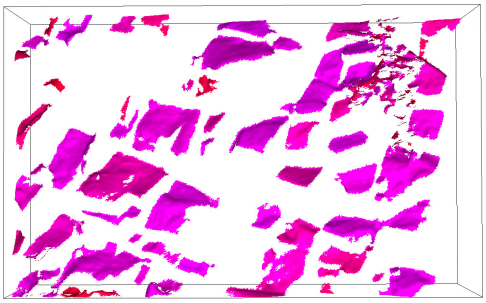

Figure 7.36. 3-D view showing only the rock surface classified to Set 4

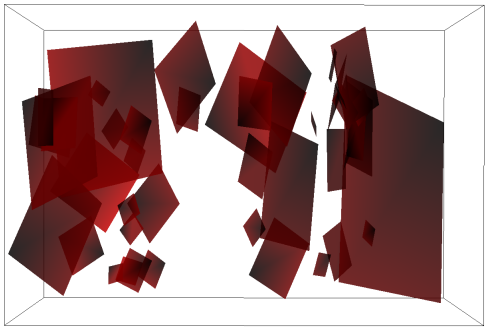

Figure 7.37. Rock surfaces of set 2 simplified to planar objects

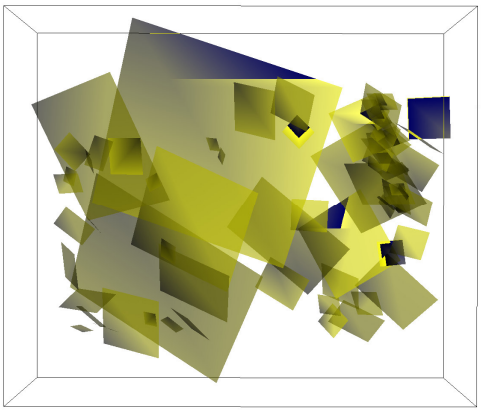

Figure 7.38. Rock surfaces of set 3 simplified to planar objects

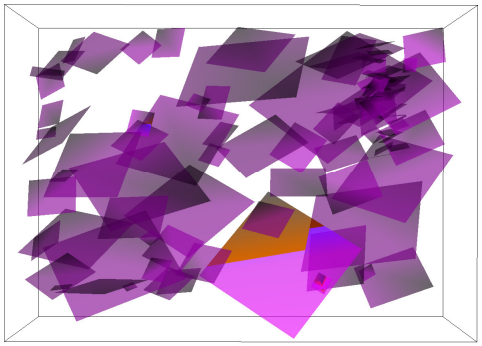

Figure 7.39. Rock surfaces of set 4 simplified to planar objects

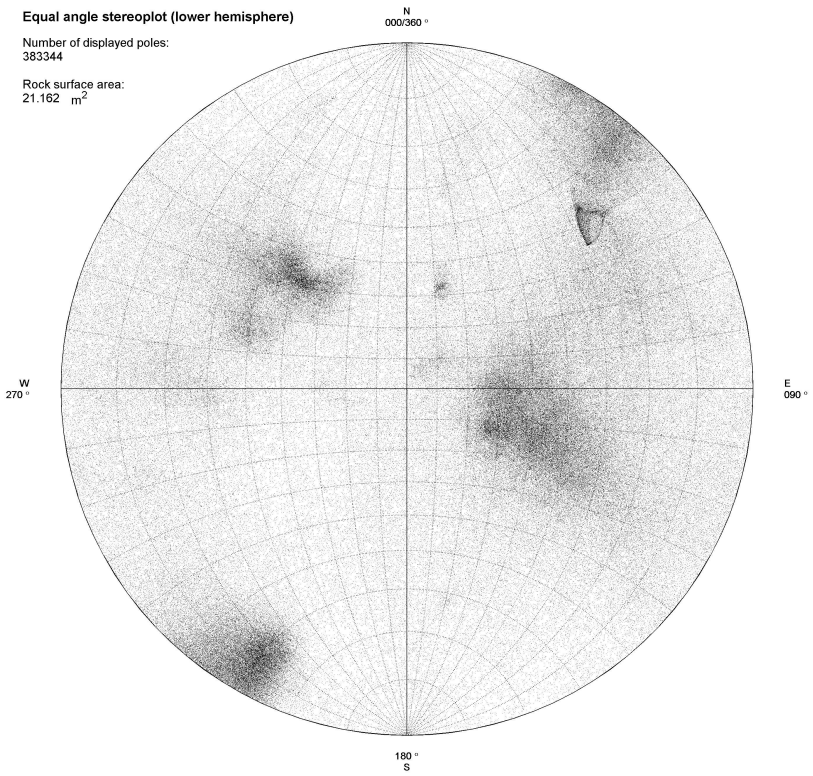

Figure 7.40. Equal angle stereonet plot (lower hemisphere) of all facet poles (383344 poles) of the interpolated and meshed surface of the laser scanner data from Site 2. The entire interpolated surface area is about 21 m2. Note the triangular-shaped artefact in the northeast section.

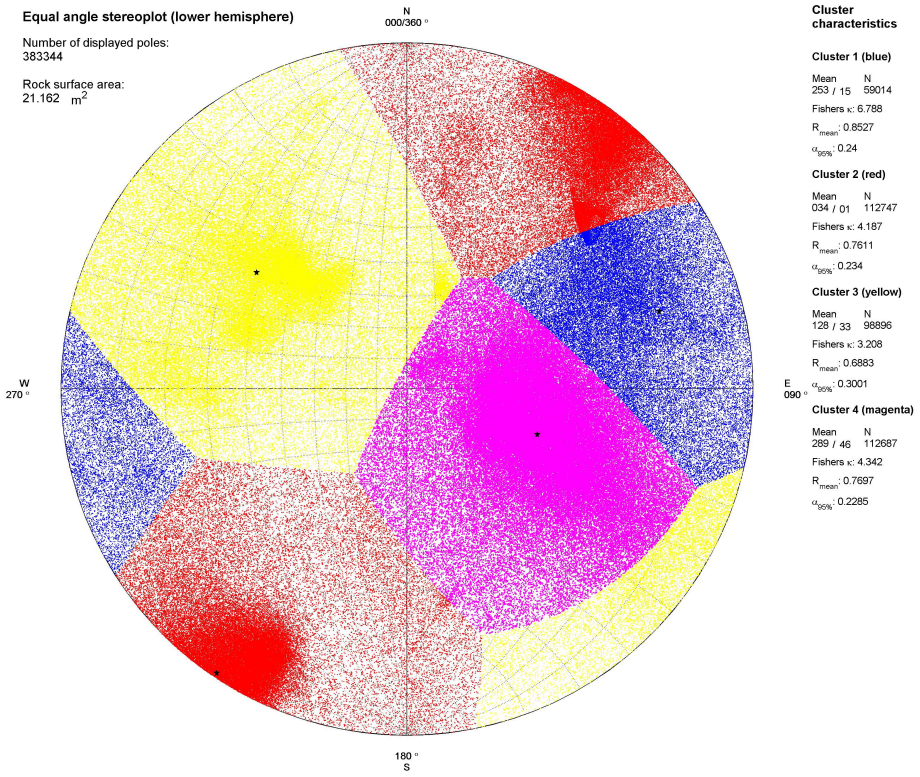

Figure 7.41. Equal angle stereonet plot (lower hemisphere) of all facet poles of Site 2, but now classified and coloured according to a fuzzy k-means clustering with 4 discontinuity sets. The blue colour is for set (cluster) 1, red is for set 2, yellow is for set 3 and magenta is for set 4.

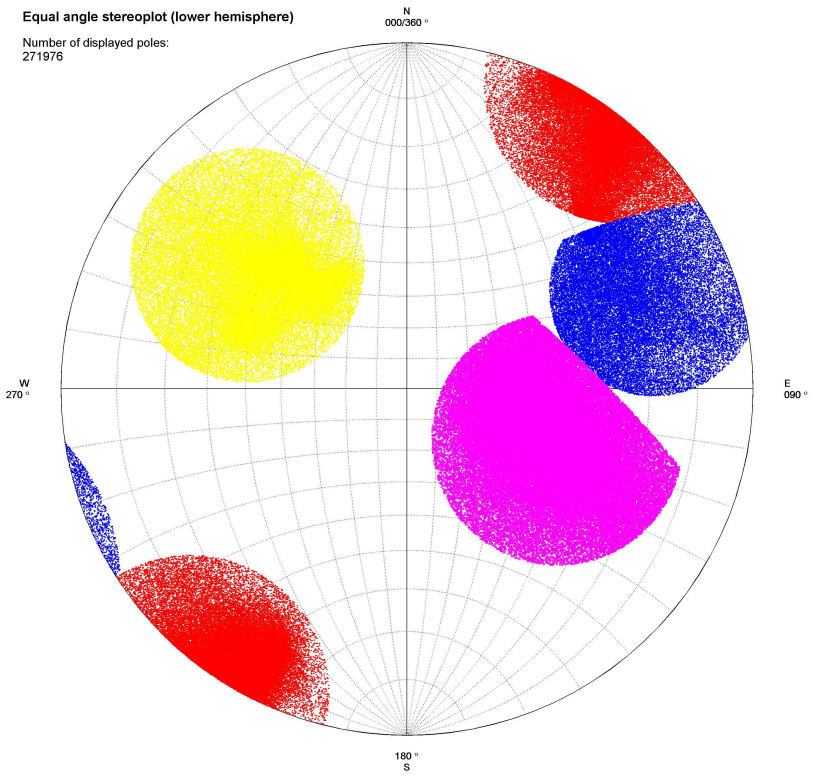

Figure 7.42. Equal angle stereonet plot (lower hemisphere) of the remaining facet poles of Site 2 after the cluster outlier removal.

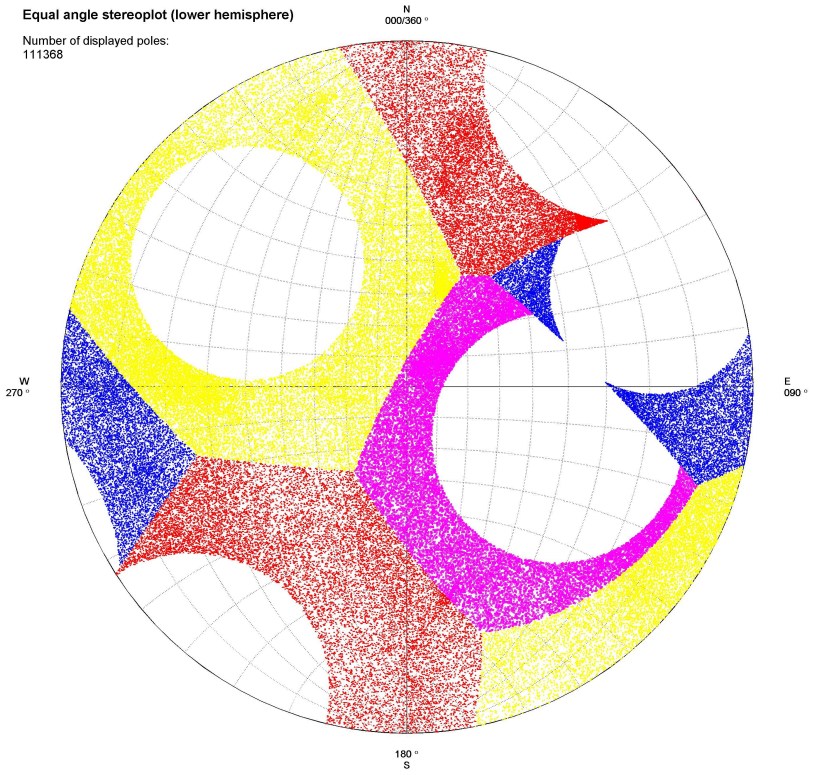

Figure 7.43. Equal angle stereonet plot (lower hemisphere) of the outlier facet poles of Site 2 that are removed. (see also Section 7.4.1.2).

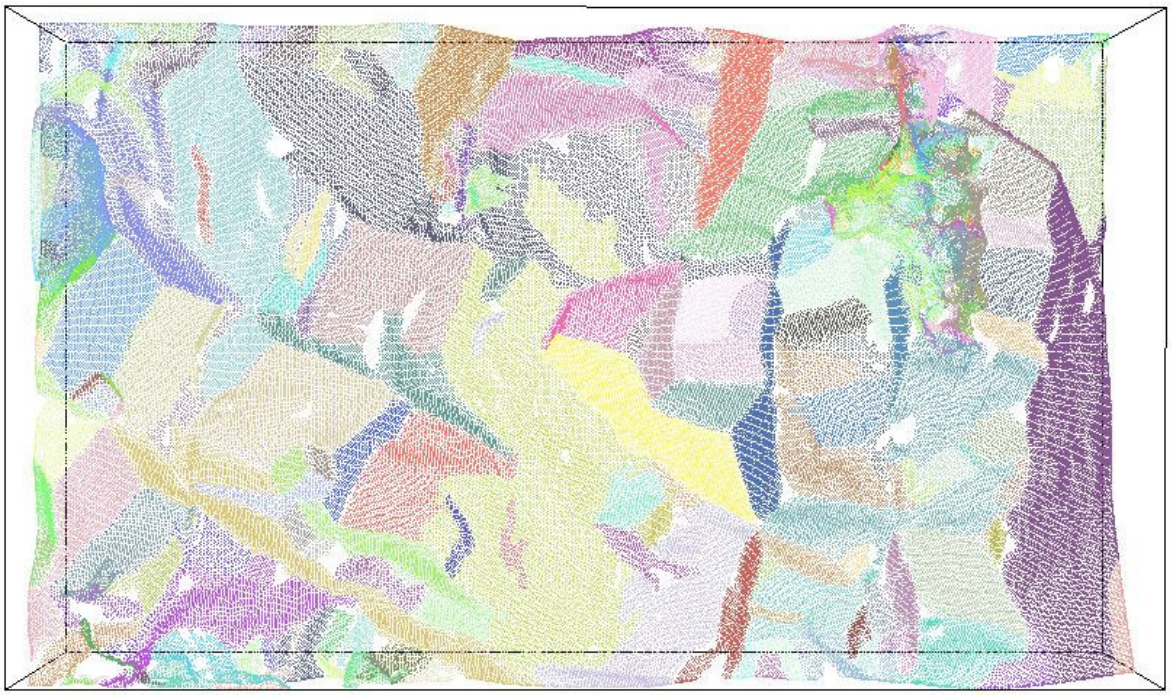

Figure 7.44. This illustration shows the 3-D view of the vertices of the facets from the meshed 3-D surface of Site 2. Note that this is *not* the laser scan point cloud. Points (vertices) with similar colour represent a single discontinuity plane that is identified with Method 1 (I.e., planes that fall in the same cluster and which are connected are classified to the same plane and receive in this view the same (random) colour).

7.5 Method 2: Surface reconstruction with 2-D gridding using Split-FX software

7.5.1 Introduction

Method 2 uses a surface reconstruction technique that is based on 2-D gridding. The dense point cloud is structured and simplified by "draping" a 2-D mesh most efficiently over the scanned rock face. The user can change the mesh size interactively to create an optimal balance between resolution and data handling capacity. This approach is implemented in the existing software package Split-FX of which a beta version was made available by Split Engineering LLC (Split Engineering, 2007). The generated 2-D mesh is analysed and clustered into so-called "patches". In brief, this is accomplished by comparing the orientation of each mesh facet (having a triangular shape) with those of its neighbouring facets. If the angular difference between neighbouring facets does not exceed a user-defined threshold, the facets are combined into individual larger patches, which represent discontinuity planes. The average orientations of these patches are then plotted in a stereographic plot. In this way, discontinuity sets can be recognised and discontinuity planes belonging to the same set can be clustered.

7.5.2 Description of the Split-FX software

This method is carried out with the software Split-FX (Split Engineering, 2007). The software was made available as a beta trial version, while Version 1.0 has recently been released as fully functioning commercial software product for automated rock-mass fracture characterisation. A recently published project report by Kemeny and Turner (2008) discusses the Split-FX approach, provides examples of applications to rock slope mitigations issues and recommends procedures for field data acquisition.

The Split-FX software was developed for use with laser-scanner-derived point-cloud data. The basis for the rock mass fracture characterisation is a 2-D surface gridding of this point cloud data. Subsequent analysis of the meshed grid delivers discontinuity orientation data. Since the source code of the software was not provided, it was not possible to evaluate the exact data processing

and analysis features of the program. The following sections briefly describe the software processing sequence. These descriptions are solely based on the experience gained in using the program and from analysing information provided by the developers on the Split Engineering website (http://www.spliteng.com/).

7.5.2.1 Data input and point cloud visualisation

Point-cloud data can be imported into the Split-FX program as an ASCII data file. The file needs to have the *x*, *y*, and *z* coordinates, and *intensity* data, organised in columns, with each laser-scanned point as an individual record (or row). The imported data can be stored as an internal binary data format to save disk space. Images, for instance photographs, scanned maps and reports, can be opened and viewed within the program as well. This image information can be associated with the point cloud and stored with the binary point data as what is called in the program a 'region'. The point-cloud data are visualised in 3-D as a projection on the screen where the intensity range is used to add (monochromatic) colour. Various stretching colour schemes can be applied to emphasize certain high or low intensity features. It is also possible to reverse the monochromatic range so that low intensity gets a "high" monochromatic colour. The program has rotation, zooming, and panning functions to examine the point cloud. It also makes optimal use of the RAM and video memory of the PC so that the visualisation can be done interactively and in real-time, even with very large point clouds of more than a million points.

7.5.2.2 Data registration

By default, the Split-FX software considers the positive X-axis as East, the positive Y-axis as North and positive Z-axis as the vertical axis. The Split-FX software does not have extensive registration functionality. However, if the point cloud has not been registered into a real-world coordinate system, a simple re-orientation can be done based on the scanner orientation, similar to the procedure described in Section 4.6.7.4. If the scanner is not level, but the forward- and sideway tilt of the scanner is known, the point cloud can also be re-oriented to match the actual North, East and vertical axes. In this way, the discontinuity orientations are computed correctly and no additional re-computations are necessary.

7.5.2.3 Data editing and processing

The first data-processing step is the extraction of discontinuity information through gridding and subsequent meshing of the point cloud. Before this is done, it is important to edit the point cloud to remove outlier points. The Split-FX software allows the user to interactively select points and delete them. Often there are dynamic disturbances in-between the scanner and the rock face (passing vehicles, individuals, bugs, or dust in the air) that result in points located significantly in front of the rock face. Points representing vegetation on the rock face or in the background do not have to be removed from the data, since the analysis will not mistake them for discontinuity surfaces. However, it is better to remove points that represent trees, bushes, or other objects in front of the rock face, since they will result in an erroneously meshed surface that does not accurately represent the rock face.

After the point cloud has been edited, the mesh can be generated. It is possible to create a mesh of only a portion of the point cloud. The meshing is based on a 2-D gridding approach (see Section 6.4). The orientation of the 2-D grid is based on the general trend of the rock face. This is determined by examining the overall spatial extents of the point cloud (or portion of the point cloud, if that is what is being analysed). For instance, if the general trend of the rock face is East-West, a 2-D grid is generated based on the X and Z-axes; i.e. by using the X and Z coordinates as the spatial variable. The Y coordinate in this case becomes the "elevation" variable. The user should define the appropriate grid size. The size is defined in "point cloud units", or fractions of the overall point cloud lateral extent. The grid size can be adjusted subsequently. Once the grid size is selected, the Split-FX software provides the user with the number of grid cells and the average number of original scanned point-cloud points will be found within each grid cell. These values depend upon the dimensions of the rock face that is to be gridded and the density of the point cloud

data. Typically, a grid size should be chosen such that each cell contains between 10 and 20 points (pers. comment J. Kemeny). Based on such a “rule-of-thumb” and the provided data, the user can either re-define the proposed grid size choice, or continue with the gridding and meshing process.

The Split-FX software computes an average “elevation” for the centre of each grid cell, based on the average “elevation of the original scanned point-cloud points contained within the grid cell. These elevations are then used to compute elevations for the corners of each grid cell, based an interpolation of adjacent grid cells. The result is a number of regularly gridded points, which are subsequently connected through a 2-D linear triangulation to a regular 2-D mesh (each grid cell is divided into two triangles by passing a diagonal though the cell). This procedure is very similar to the generation of topographic surfaces in GIS or gridding packages, such as Surfer (Golden Software, 2007).

7.5.2.4 Generation of surface patches

As described above, the mesh consists of a series of triangular facets. The orientation of each triangle is defined by the elevations of its three corner nodes; the normal orientation of each triangle in the mesh can thus be readily computed. Neighbouring triangles that have similar orientations can be combined into so-called “patches” to form discontinuity surfaces. The outlines of the patches, which are formed by the outer triangles, are immediately shown in the 3-D view (see Figure 7.49 and Figure 7.52). It is possible that there are “holes” inside a patch; these are formed by triangles that do not fulfil the patch-creation criteria. The user can set a number of parameters for joining adjacent triangles into patches. These main parameters are:

- Minimum patch size (defined as a minimum number of constituent triangles). This will avoid the creation of very small patches that may not represent a real discontinuity surface
- Maximum neighbour angle (in degrees). This defines degree of dispersion of orientation among adjacent triangles. If this is set to a small value, very few patches will be found, but they will be highly planar (or smooth). If this angle is set to a larger value, many patches will be created, but they may include very irregular surfaces.

There are no standard values suggested for these parameters. Which parameters work best depend on the data, the mesh size, and the character of the rock face. Experience shows that the maximum angle of adjacent triangles should be between 5 and 20 degrees. The minimum patch size should be in the range of 5 and 15 triangles.

7.5.2.5 Stereo plotting and interactive set selection

The orientation of the various patches that were found in the previous step can be plotted in a stereographic plot. The Split-FX program has the ability to use the information on the size of the patches to create and display appropriately sized circles located to show the central orientations of the patches. In this way the smaller patches can be differentiated from the larger patches, which may possibly represent more important discontinuity surfaces. The user can select patches in the stereographic plot that are considered to belong to a single discontinuity set, and the corresponding patches are at the same time highlighted in the 3-D view of the gridded rock-face mesh. Hence, the user has immediate visual control over the value of the selection. If the selection is satisfactory, the discontinuity set can be named and the patches forming the discontinuity set are classified as individual discontinuity surfaces belonging to that discontinuity set. Spherical statistics, such as mean orientation, Fisher’s k-value, and spherical variance, are also calculated for each discontinuity set.

The Split-FX software also has the ability to allow the user to manually select points in the point cloud that have somehow not been converted into patches. Usually these are located in the occlusion areas of the rock face that lack data, or in areas with noisy data due to vegetation. In some cases, discontinuity surfaces may be oriented semi-parallel to the incoming laser beam and therefore are represented by fewer points. In such a situation, the 2-D gridding technique and the

subsequent meshing creates larger and more elongated triangles than in the parts of the rock face with denser points (see Figure 7.46). The parameters used in the patch generation step may, therefore, omit these triangles and not create patches. By manual selection of these points, the patch creation criteria may be overruled and the patch can still be created and plotted as additional data in the stereographic plot.

7.5.2.6 Data export

The information concerning the patches can also be exported as an ASCII file. Information that can be exported include: dip direction, dip, plane equation parameters (a, b, c, d), and the mean coordinate (patch centroid). The ASCII data is in turn used as input for post-processing: including the automatic clustering of the patches into discontinuity sets and the computation of discontinuity set statistics and spacing distributions (see Chapter 9).

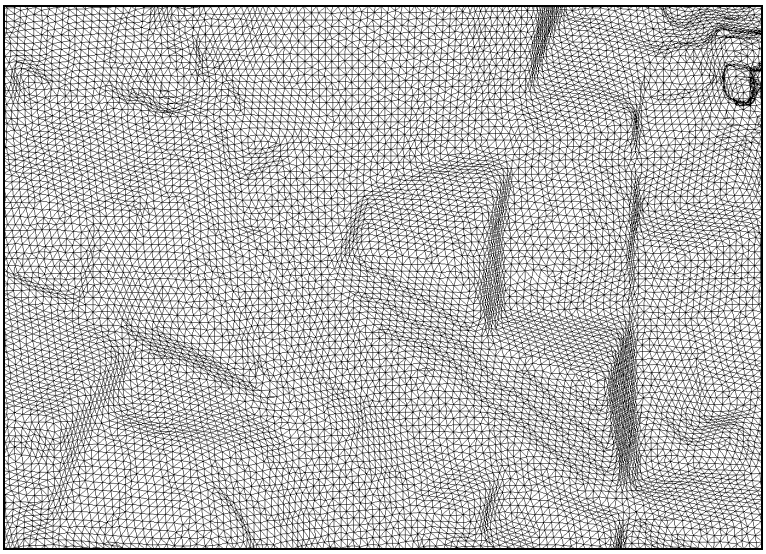

Figure 7.45. Detail of the mesh of the rock face of Site 2 generated from the 3-D surface made with FastRBF (Method 1). The mesh size of this mesh is 1 cm with a smoothing distance of 2 cm. Note the regular facet size of the mesh. Compare with Figure 7.46 below, which shows a more irregular facet size.

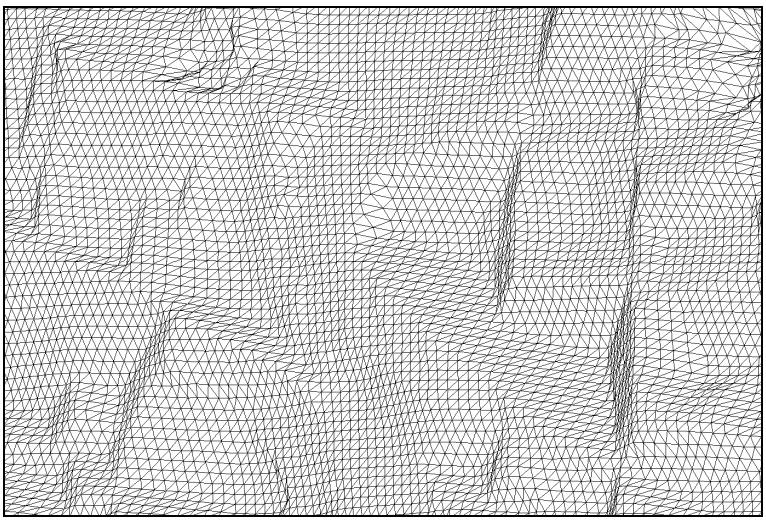

Figure 7.46. Detail of the mesh file of the rock face of Site 2 generated using the 2-D gridded-surface approach employed by the Split FX software (Method 2). Note the irregular facet size of the mesh. Planes perpendicular to the general orientation of the slope get larger facets, based on fewer points. Sharp corners and edges are also rounded off. It should be noted that a slightly larger mesh size is shown here than in the Figure 7.45 above. A gridding size of about 1.5 cm was used.

7.6 Results of surface reconstruction with 2-D gridding using Split-FX software (Method 2)

On the following pages the results of Method 2 are presented as a number of illustrations. For convenience, the figures are all presented together. The results are presented for both rock exposure test sites in three steps:

1. Visualisations of the point cloud data input
2. Illustrations showing the gridded and meshed 3-D rock surface
3. Illustrations of the identified planar patches that represent discontinuity planes

The specifics with regard to the data processing and the results are summarised in the next two sections for each test site individually. In order to be able to compare the results, the input data analysed by the Split-FX software are the same as by Method 1 – cropped sections of the laser-scanned data obtained at each site (see Appendix C for Site 1 and Appendix D for Site 2).

7.6.1 Results of Method 2 for Site 1 (Bellmunt)

The input data consists of 616 300 points (5 mm scan resolution). Figure 7.47 visualises the point cloud data using the intensity as a reversed grey scale.

The mesh was subsequently generated with a mesh size of 0.02 point-cloud-units (2 cm). This resulted in a 230 x 180 grid, with 41 400 grid cells. Each grid cell contains on average 14.9 original scanned point-cloud points. Figure 7.48 shows the gridded and meshed surface. The 2-D grid approach visually provides a very good representation of the actual rock surface. It does not contain as much detail as the 3-D surface generated with the FastRBF interpolation (please refer back to Figure 7.15), but the meshed surface is less influenced by the noisy points produced by vegetation on the slope.

The generation of the surface patches requires the user to visually inspect the results of various parameter combinations and then use the combination of parameters that give the best results. In this instance, the following patch generation parameters were used: minimum patch size was 15 mesh triangles; maximum neighbour angle was 15 degrees. The results are shown in Figure 7.49. The geometric information for each patch; i.e., its orientation, plane equation parameters, centroid coordinates, and size, were exported as an ASCII data file. This output file was further processed according to the methods that will be discussed in Chapter 9.

7.6.2 Results of Method 2 for Site 2 (Torroja)

The input data consists of 480 942 points (6 mm scan resolution). Figure 7.50 visualises the point cloud data the intensity as a reversed grey scale.

The mesh was subsequently generated with a mesh size of 0.01 point cloud units (1 cm). This resulted in a 145 x 264 grid, with 38 280 grid cells. Each grid cell contains on average 12.6 original scanned point-cloud points. Figure 7.51 shows the gridded and meshed surface. The 2-D grid approach visually provides a very good representation of the actual rock surface. It does not contain as much detail as the 3-D surface generated with the FastRBF interpolation (Method 1, see Figure 7.31), but the meshed surface is less influenced by the noisy points produced by the vegetation in the upper right part of the slope. One advantage of the gridding method used in the Split-FX software is that if there are not enough points, it will not create a mesh. Thus low-resolution areas, or areas with large noise and scatter, will not be interpolated. For example, the Split-FX software did not generate a grid in the triangular lower-right area of the slope, simply because there was insufficient point-cloud data presenting this section. The FastRBF method however, did interpolate in this area and was able to create a surface mesh in this area with little or no data (compare Figure 7.31 and Figure 7.51).

Generation of the surface patches followed the meshing interpolation process. The selection of the combination of processing parameters is similar to the method described for Site 1. In this instance the following patch generation parameters were used: minimum patch size was 15 mesh triangles; maximum neighbour angle was 10 degrees. The results are shown in Figure 7.52. The geometric information for each patch; i.e., its orientation, plane equation parameters, centroid coordinates, and size, were exported as an ASCII data file. This output file was further processed according to the methods that will be discussed in Chapter 9.

7.7 Discussion and conclusions

In this chapter two methods are described that extract discontinuity planes from point-cloud data. Both methods rely on surface reconstruction techniques to structure the irregular and noisy point cloud data. Although the subsequent analyses are fundamentally different, the resulting products are similar. Both methods produce a list of most likely discontinuity planes defined according to their average orientation, plane equation, and dimensions. The main difference is that Method 1 has already classified the discontinuity planes into discontinuity sets, while Method 2 does not. The following two sections summarise the main features of both methods and discuss the advantages and disadvantages of each method.

7.7.1 Method 1

The surface reconstruction method used in Method 1 (the implicit representation with Radial Basis Functions) is a technique that results in the most realistic-appearing representation of the original object. The user can use various mesh sizes and smoothing distances to filter out or enhance smaller details of the surface and remove the influence of the inherent error in the point-cloud data. The facet orientation plots of the reconstructed and meshed 3-D rock surface give the user a large amount of detail on the trends in the orientations, and thus provide a good basis for visually determining the number of potential discontinuity sets present in the scanned rock mass.

The fuzzy k-means technique provides the most objective way of clustering large numbers of (facet) orientations into distinct discontinuity sets. It is one of the few automated methods of accomplishing this task. The only input that is needed from the user is the number of sets that are present. The subsequent colouring of the mesh facets according to their membership in the discontinuity sets, allows a visual inspection of the quality of the clustering. If needed, multiple fuzzy k-means classifications can be carried out using different numbers of sets and the results can be compared and evaluated.

Outlier removal can be carried out as an additional technique to remove those facets that have an orientation differing greatly from the average orientation of a discontinuity set. By removing these “outlier facets”, the remaining facets will more likely represent “real” discontinuity planes and thus this process reduces variability of the discontinuity orientations and improves the results. The absence of standard criteria for defining the outlier removal procedure is a problem. Without such standards, the ad hoc removal of outliers will introduce bias into the entire process. The other techniques do not use any outlier removal strategy. In order to compare the results from this method with those of the other methods, the outlier removal was demonstrated, but not used.

Another problem with Method 1 is the generation of “blobs” in the 3-D surface. This is inherent to the use of laser-scanner point-cloud data from rock exposures. Rock exposures are not “clean” man-made objects, but natural surfaces that contain also points representing vegetation, rubble, and other objects that are not part of the actual rock surface. To a large extent, the point-cloud data can be “cleaned” by the user to remove dynamic disturbances and parts of the scan that are of no interest. However, the vegetation that is growing on the slope is difficult to remove. It is possible, but it requires much (manual) editing. However, this surface reconstruction method will interpolate across many of the gaps in the point-cloud data created by removing undesired points. This process effectively creates false surface information.

Figure 7.47. The selected point cloud data of Site 1, visualised in a reversed grey-scale based on laser scan intensity. Please refer back to Figure 7.13 for a photograph of the slope where the exact location of this point cloud dataset is outlined.

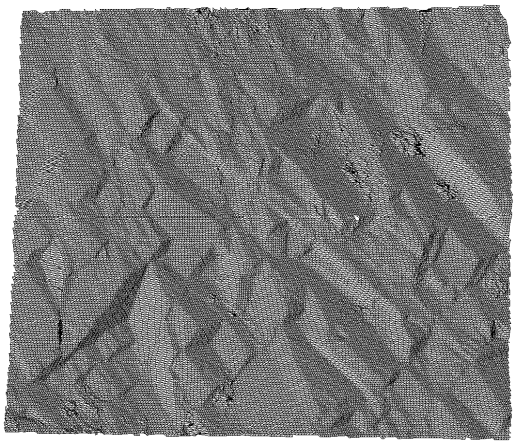

Figure 7.48. The gridded and meshed surface, based on the point cloud data depicted in the previous figure. The mesh spacing is 2 cm, resulting in an average of about 15 point cloud points per grid cell.

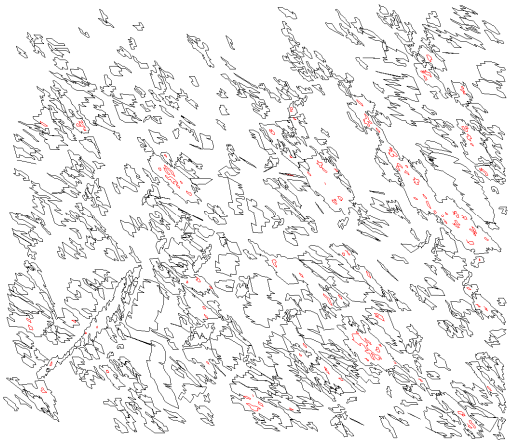

Figure 7.49. The identified planar "patches". The minimum patch size contains 15 mesh triangles, while the maximum pole vector difference between neighbouring triangles is set at 15 degrees. The black lines give the patch outlines, while the red lines outline the “holes” within a patch outlining areas where triangles do not fulfil the patch-criteria.

Figure 7.50. The selected point cloud data of Site 2, visualised in a reversed grey-scale based on laser scan intensity. Please refer back to Figure 7.29 for a photograph of the slope where the exact location of this point cloud dataset is outlined.

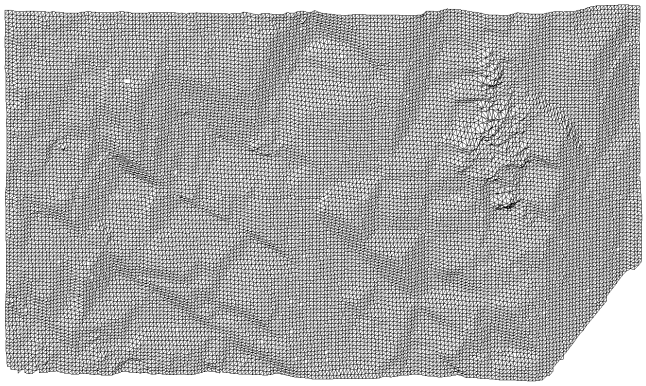

Figure 7.51. The gridded and meshed surface, based on the point cloud data depicted in the previous figure. The mesh spacing is 1.0 cm, resulting in an average of about 13 point cloud points per grid cell.

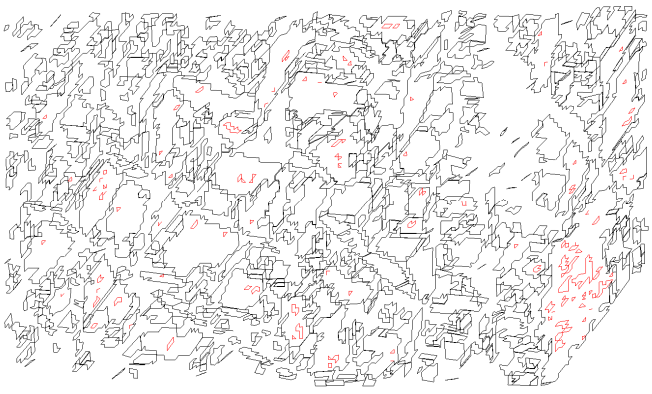

Figure 7.52. The identified planar "patches". The minimum patch size contains 15 mesh triangles, while the maximum pole vector difference between neighbouring triangles is set at 10 degrees. The black lines give the patch outlines, while the red lines outline the “holes” within a patch outlining areas where triangles do not fulfil the patch-criteria.

The point-cloud data of the two test sites used in this study contain some points that represent vegetation. Because the vegetation grows in front of the rock surface, it produces “noisy” points in front of the general trend of the slope. The RBF surface reconstruction method creates “blobby” objects from these noisy vegetation points. Nevertheless, the influence of the blobby objects on results is considered negligible for two reasons:

1. In the stereographic plot of facet orientations, only some of the larger blobby objects can be recognised, but they do not appear to have any influence on the cluster segmentation. The overall influence of the discontinuity surfaces and their trends are considered much more dominant.
2. After the fuzzy k-means clustering, all facets are separated into the defined number of discontinuity sets and subsequently into individual discontinuity planes. The blobby surfaces fall into these discontinuity sets, but only as very small planes. Most of these small planes are easily removed and thus excluded from further analysis.

7.7.2 Method 2

The Split-FX software provides a very fast and intuitive way of processing the point-cloud data to extract discontinuity plane orientations from the raw point-cloud data. The user only needs to define the size of the mesh and set the threshold parameters for the “patch” detection. The patches are immediately shown in a 3-D view, with or without the mesh and original point cloud information. In this way the results can be verified directly. The patch orientations are also shown in a stereographic plot. When clusters of patches are interactively selected in the stereographic plot, the corresponding patches are highlighted in the 3-D view of the rock-face mesh, giving the user an immediate insight into the possible presence of discontinuity sets.

The advantage of the 2-D gridding and meshing approach is that the mesh can be generated very quickly. The underlying algorithms are relatively simple and require little computation time. By gridding the point cloud, the often very large and unorganised point-cloud data set is reduced to a much smaller (10 to 20 times smaller) dataset of organised (regularly spaced) points. This reduced set of gridded points can thus be interpolated into a triangular mesh very rapidly, since the interpolation is only done in only two dimensions. Another advantage of the Split-FX software is the interactive selection of patches in the stereographic plot and the ability to view simultaneously the corresponding patches in the 3-D gridded mesh view. This gives the user a very powerful tool to (visually) validate the selection of discontinuity sets. The possibility of manually adding omitted patches from the original point-cloud points is also an added advantage, although it reflects an undesirable aspect of the 2-D gridding (see below).

The largest disadvantage of the Split-FX approach is that it relies on 2-D gridding and meshing, while the point-cloud data is inherently 3-D. When dealing with single scans of relatively straight rock faces, this will not give many problems. However, very irregular rock faces or rock faces that show strong curvatures will result in a mesh whose triangles vary in size and shape all over the rock face. Small and regular triangles will occur in areas that are semi-perpendicular to the scan direction, while large and elongated triangles will form on surfaces that are semi-parallel to the scan direction, as the scanned points are much less dense in these areas. The patch generation will be influenced strongly by this, and therefore different results may be obtained for different parts of the slope. This can be improved by manually selecting scanned points in areas where the mesh evaluation did not automatically create patches.

Therefore, because of the required manual intervention, this method does not permit an fully automated process to analyse entire or merged point clouds from different parts of rock faces, or single scans of rock faces with strong curvatures, such as in tunnels or caverns, unless parts of the rock face with different characteristics, or individual scans, are analysed separately. Before the gridding, the point cloud also needs to be manually “cleaned” to remove points that are in front of

the rock faces, especially those caused by dynamic disturbances. If these points are not removed, they usually produce large protruding “spiky” features in the surface mesh.

The gridding process, by definition, also means that the data is averaged within each grid cell. If there are sharp edges or corners in the rock face, the gridding will average (soften) these sharp features. Also roughness or other geometric details on discontinuity planes are lost due to the gridding. Discontinuity planes that have fewer points, due to the fact that they are oriented more or less parallel to the incoming laser beam, are often not turned automatically into patches, although it is possible to manually correct for this (see Section 7.5.2.5 and the last few paragraphs above). Discontinuity planes that are perpendicular to the general trend of the rock face will similarly contain less points, but, more importantly, are difficult to grid in 2-D (due to the large variation in “elevation”). For these planes, the 2-D gridding process typically results in large and strongly elongated triangles in the mesh (see Figure 7.46). These triangles are often not converted to patches since they show a larger variation in orientation than triangles created in areas with higher point densities.

The main consequence of the selection and use of a 2-D gridding approach is that there will be a strong over-emphasis of discontinuities that are parallel to the general trend of the slope, or perpendicular to the bearing of the scanner. Discontinuity planes that are perpendicular to the general trend of the slope, or sub-parallel to the incoming laser beams, will be under-represented, even if they are well-exposed.

8 Extracting discontinuity planes with direct segmentation

8.1 Introduction

This chapter discusses two direct segmentation methods for the mathematical recognition of planes in the original point cloud data:

- A method that uses a Principal Component Analysis (PCA).
- A method based on the Hough transformation and least-squares regression.

The approach that is based on PCA is implemented in a Matlab-based computer code. The procedure using the Hough transformation and least-squares regression has been previously implemented in a software package called “Point Cloud Mapper” (Vosselman, n.d.).

Both procedures yield a segmented (classified) point cloud where each segmented set of points represents a unique, individual, potential discontinuity plane. Both methods are illustrated with the laser scan data from the two test sites in Spain; the same data that is used to illustrate the surface reconstruction methods discussed in Chapter 7.

Chapter 9 further discusses the subsequent analysis of the segmented point cloud data containing these individual potential discontinuity planes to evaluate statistically their orientations, to derive distinct discontinuity sets, and to evaluate the spacings of these sets.

8.2 Introduction to the direct segmentation approach

8.2.1 Introduction

Segmentation is the process of labelling each measurement in a point cloud, so that the points belonging to the same surface or region are given the same label (Rabbani, et al., 2006). Various approaches for segmentation have been suggested in the literature. They differ mainly in the method or criterion used to measure the similarity between a given set of points and hence for making the grouping decisions. Once such a similarity measure has been defined, segments can be obtained by grouping together the points whose similarity measure is within given thresholds and which are spatially connected.

8.2.2 Previous research concerning direct segmentation

Most reported segmentation methods have been developed for image-analysis applications and assume that the data are partially structured within a 2.5D environment. They are thus termed “range segmentation algorithms” and three main varieties can be identified (Rabbani, et al., 2006):

- Edge-based segmentation algorithms have two main stages: edge detection, which outlines the borders of different regions, followed by grouping of the points inside the boundaries to define the final segments. Edges in a given depth map are defined where changes in the local surface properties exceed a given threshold (Sappa & Devy, 2001).

- Scanline-based segmentation methods are based on the principle that a scan line on any 3-D plane makes a 3-D line. Planar segments are formed by grouping adjacent lines that have

similar properties. Sithole and Vosselman (2003; 2004; 2005) used profiles in different directions for the segmentation of air-borne laser scanner data to define planar elements. Hoover, et al. (1996) provides a definitive comparison of scanline-based methods for finding planar segments in range-based images. However, all these applications have been with 2.5D data, and Rabbani, et al. (2006) point out that the extension of this scanline-based approach to 3-D point clouds would require choosing a few preferred directions for scan-lines, making the results of segmentation orientation dependent.

- Surface-based segmentation methods use local surface properties as a similarity measure and merge the points that are spatially close and have similar surface properties. These methods are relatively less sensitive to the noise in the data, and usually perform better when compared to edge based methods. Two approaches are possible: bottom-up and top-down. Bottom up approaches start from some seed-points and grow the segments from this seed-segment based on the given similarity criterion. The final segmentation results depend greatly upon the selection of the seed points. Top-down methods start by assigning all the points to a single group and fitting a single surface to it. They then continue subdividing this region until a given threshold criterion is met. Most of the reported methods use a bottom-up strategy (Rabbani, et al., 2006).

The top-down surface-based method is in fact similar to the surface reconstruction approach from Chapter 7 and according to this definition, therefore also a segmentation method. In this study this definition is not followed; the bottom-up segmentation method is defined as “the segmentation method”, while the top-down segmentation in the definition of Rabbani (2006) is defined as “the surface reconstruction method”. However, the short “top-down” approach for the surface reconstruction and the “bottom-up” appraoch for the segmentation, are appropriate terms and used interchangeably.

Because of the noisy and unstructured nature of the 3-D point clouds, both segmentation methods that are described in this study use a surface-based segmentation incorporating a bottom-up strategy. Rabbani, et al. (2006) note that this is the most successful approach to the segmentation of unstructured 3-D point clouds. However, they also suggest that many proposed methods involve considerable numbers of parameters and frequently result in “over-segmentation,” the creation of large numbers of individual segments. They propose a method of segmentation of point clouds using a “smoothness constraint,” which finds smoothly connected areas in the point cloud. Because the algorithm uses only local surface normals and point connectivity, defined by either k-nearest or fixed-distance neighbours, they suggest their method uses only a small number of intuitive parameters, while providing a trade-off between under- and over-segmentation. They demonstrate the effective application of their algorithm to the assessment of point clouds imaging industrial facilities.

8.2.3 Direct segmentation of unstructured 3-D point clouds

The direct segmentation approach directly analyses the raw point cloud data and does not require prior surface reconstruction. The spatial structure of the point cloud data is provided through a (K-D) tree-based structure. This tree structure speeds up the spatial searches within the point cloud, and is the principal factor that determines the efficiency of the direct segmentation approach.

The process of direct segmentation of unstructured 3-D point clouds is fully analysed by Vosselman, et al. (2004) and by Rabbani, et al. (2006). These two publications represent two stages in a long-term research program by a single research team. Their research has focused on the development of efficient algorithms to segment unstructured 3-D point clouds based upon surface-based segmentation methods incorporating bottom-up strategies (see also 8.2.2).

The basis of the segmentation method is relatively simple: it starts with the selection of a seed point around which the nearest neighbouring points are selected, providing they occur within a specified search distance. If it can be mathematically verified that most of the neighbouring points are located

close to the same flat plane, they are all provided with the same identification (or code) label. This forms the seed surface. In turn, the neighbouring points to these labelled points are selected and it is again determined whether these points are located close to the previously defined plane. This process is repeated, and the extent of the defined plane increases, until no new points are found that are located on the defined plane. This demarcates the spatial extent of this individual discontinuity plane. Then a new random (unlabelled) seed point is selected and the process of planar demarcation is repeated until all points in the data set are classified. This approach involves two steps: (1) identification of seed surfaces and (2) extension (growing) of these surfaces to include all appropriate adjacent points.

8.2.3.1 Identification of seed surfaces

An initial seeds point is randomly selected from the point cloud, and then a local neighbourhood is defined around this point. This neighbourhood should contain a minimum number of nearby points and these will form a "seed surface" which will be evaluated to see if it meets a planar condition. As was explained in Section 6.3.3.2, this neighbourhood can be specified in two different methods.

- K-Nearest-Neighbours (KNN): In this method for a given point, the closest k-points from the point cloud is selected. As the number of points (k) is fixed, the method adapts the area of interest (AOI) according to the point density.
- Fixed-Distance-Neighbours (FDN): This method uses a given fixed AOI, and for each query point, selects all the points within this area.

These seed points can then be assessed to see if they define a planar element, within the specified tolerances. Planarity can be evaluated by least-squares regression, or by utilizing Hough transform approaches. Additional criteria may also be used to assess the suitability of this "seed surface," such as the degree of local connectivity exhibited by the points (an evaluation of their local spatial distribution) or the surface smoothness.

8.2.3.2 Extension (growing) of these surfaces

Once a "seed surface" has been found, the area surrounding it needs to be examined so determine if this surface extends further. Application of KNN or FDN criteria can be used to identify additional points lying near the borders of the seed surface. Computational efficiency requires that the seed points for these analyses lie at or near the borders of the existing surface. In addition, these repeated searches within the unstructured 3-D point cloud can only be efficiently handled if space-partitioning strategies, such as K-D trees (Arya, et al., 1998), are used. One or more of the following criteria can control the extent of growth of surfaces:

- *Proximity of points:* Only points that are near one of the surface points can be added to the surface. Proximity can be evaluated by applying any of several thresholding parameters that define distances within the planar orientation and deviations from it. Application of too strict criteria may lead to fragmented surfaces.
- *Locally planar:* For this criterion, a plane equation is determined for each surface point by fitting a plane through all surface points within some radius around that point. A candidate point is only accepted if the orthogonal distance of the candidate point to this plane is below some threshold. This threshold and the size of the neighbourhood used in the estimation of the plane equation determine the smoothness of the resulting surface.
- *Smooth normal vector field:* Another criterion to ensure a smooth surface is to estimate a local surface normal for each point in the point cloud and only accept a candidate point if the angle between its surface normal and the normal at the nearest point of the surface to be grown is below some threshold.

The above growth process is continued until all the points forming a single unique planar element are found. The two-step procedure is then recursively applied until the entire point cloud has been

examined. This will result in a number of unique individual planar surfaces (segments) being identified. There may be some points within the point cloud that do not define any planar element, at least any planar element that meets the specified shape and size criteria defined by the thresholds and parameters controlling the process.

Rabbani, et al. (2006) note that individual planar elements may be separated by two types of discontinuities, or edges:

- *Step edge:* A step edge is defined by two planes with the same orientation but with a different offset from the origin. The segmentation algorithm leads to their separation provided the offset between planes is greater than the AOI for the neighbourhood search. For KNN this depends both on the value k and point density, while for FDN it is equal to the fixed distance specified by the user.
- *Intersection edge:* An intersection edge is defined by the intersection of two surfaces, where they make an angle greater than the given threshold. An example is the intersection of the two planar sides of a box. The two box surfaces would be segmented because of they meet the smoothness constraint.

Additional points forming irregular, or noisy, rough zones may be marked unsuitable for inclusion in the next generation seeds, and thus are not assigned to any planar element, because they have residuals with all their neighbours that are greater than a specified threshold.

8.2.4 Further analysis of segmented planar elements

Since all points having the same unique identifying label form a single discontinuity plane, they may be used to determine the mathematical expression, in the form of a plane equation, which gives the geometric information of this discontinuity. The poles or normals to these planes can also be plotted as orientations in a stereographic plot, in exactly the same way as is done with regular orientation data obtained in a conventional way with a geologic compass.

As will be discussed in Chapter 9, further analysis allows these individual planar elements to be grouped or clustered, to identify and outline discrete discontinuity sets. The poles of the planes that are part of the same cluster are subsequently re-classified as belonging to the same discontinuity set. In the end, the entire dataset can be simplified in this way as containing a number of distinct discontinuity sets, and the statistical descriptions of the set orientations, such as their averages and variabilities, can be determined. Since the plane equation of each plane in a set is known, and this defines the position of this discontinuity plane uniquely in 3-D space, the calculation of discontinuity set spacing becomes possible as well.

8.3 Method 3: Segmentation based on Principal Component Analysis and implemented in Matlab

8.3.1 Data import and registration

The data are converted into a comma-delimited ASCII format that can be directly imported into Matlab using the *load* function. Only the x, y, z values are used in this analysis. Any additional data values, such as reflected intensity and/or Red, Green, Blue values from digital camera images, that are present in the dataset are not used and must be either removed from the data set, or ignored when using the *load* function. Thus Matlab stores the entire point cloud as a single 3 x n size matrix (called matrix A), where n is the total number of points and the three columns in the matrix hold the x, y and z coordinates.

The segmentation analysis involves the sequential analysis of all the points within the point-cloud, and their classification according to their membership within individual planar elements or as random points within rough non-planar sections. This classification process requires each point to

be given a “label”. The label information is stored in a separate label matrix *L* (n x 1), which is arranged in the same order as the points in the point cloud matrix *A*. Initially all points are provided with label *0*. Depending on the threshold values and other parameters set by the user prior to the analysis, points that do not belong to any of the segmented discontinuity planes and can therefore be considered as lying within non-planar rough areas or representing noise, are labelled with a default value of *-999*. All the points lying within identified planar elements are labelled with integer values ranging from *1* to the maximum number of planes that are found. The segmentation process stops when no points remain with an initial label *0*.

As discussed in Section 4.6.7.3, the analysis computations assume the x-y plane to be truly horizontal (without any tilt), so that the z-axis is vertical, and the y-axis of the data is oriented to the North. Accordingly, if the point cloud is not georeferenced, or if the point cloud is not levelled or oriented to the North, the data must be adjusted. During the fieldwork (as described in Chapter 5) two simple registration methods were used in order to level and re-orient the point cloud data to meet these minimum orientation requirements. These two methods are: (1) the measurement of the orientation of the scanner (tilt and bearing), and (2) the placement and measurement of the orientation of reference boards in the scanned scene. These methods allow for three options for computing the correct orientation for the data. These options are, in order of increasing computational complexity:

1. Assume the scanner is level (no tilt), but use the bearing of the scanner to align the y-axis of the data to North. This involves just a single rotation along the (vertical) Z-axis of the point cloud data until the y-axis is aligned to the North.
2. Use the bearing and the tilt angle of the scanner to correctly orient the data in both the horizontal plane and make the y-axis point to the North. This involves three rotations to re-orient and to level the point cloud data.
3. Use the known orientations of reference board(s) to re-orient the point-cloud data. This involves: (a) selection of the sample subset of the point cloud representing the board; (b) computing the initial orientation of this point-cloud subset with PCA; (d) comparing the computed orientation with the measured orientation; and (e) undertaking three rotations of the full point-cloud data set to make the computed orientation match the measured orientation. If more than one reference board is visible within the point-cloud data set, then internal accuracy checks on these computations are possible because the orientations of each reference board can be evaluated.

The options 2 and 3 above require the computation of the three rotation (Euler) angles that define the rotation matrix R (as discussed previously in Section 4.6.7.3). When this rotation matrix is determined, the inverse of the input matrix A is simply multiplied by the (3 x 3) rotation matrix R to compute the 3 x n matrix B that holds the correctly oriented data (see Equation 34).

8.3.2 Structuring of the data

In order to speed up the search for nearest neighbours and before the actual point cloud segmentation is carried out, a spatial data structure needs to be created from the unorganised point cloud data (Section 6.6.2). Since the entire segmentation approach is based on a recursive search for neighbours of seed points, it is essential that a tree-based structure be implemented before further data analysis is attempted. The method used in this research is based on the K-D tree-structuring algorithm. Because the point-cloud data is 3-dimensional, the term “3-D-tree structure” is more accurate but, in practice, the term "3-dimensional K-D tree" is more commonly used.

The creation of the 3-dimensional K-D tree from the registered point-cloud matrix (defined as matrix B in the previous section) is implemented using a number of Matlab functions based on a K-D tree search algorithm. Three principal Matlab functions were developed by Michael (2005) and are largely based on the theory provided in Berg et al (2000). These functions are written and compiled

in C++ code and can be used freely since they are provided through the Matlab Central website, which is an open exchange forum for the Matlab and *Simulink* user community. The three main functions are:

- Kdtree — tree class creation
- Kdtree_range — return all points within a range
- Kdtree_closestpoint — return array of closest points to a corresponding array of input points

The function *Kdtree* is used only once, prior to the segmentation process, to create the tree structure. The function *kdtree_range* is used within the segmentation procedure for finding points within the specified search range, and employs a FNN (Fixed Nearest Neighbour search, see Sections 6.3.3.2 and 8.2.3.1). The user specifies the ranges beforehand. They define the search distances in x-, y- and z-directions and thus define a (square) search box around a (seed) point. As was explained, this (FNN) method is not the optimal method for a point cloud with varying data density. However, for a near vertical rock face at even distance from the scanner, the data density does not vary significantly. However, the method may experience problems in finding neighbours in occlusion areas with (locally) a lower density (see Section 4.6.4).

8.3.3 Segmentation procedure

After the spatial data structure has been created, the segmentation procedure can start. It may be defined as a “region-growing” procedure because the points that form a single planar feature are found through a gradual searching algorithm that starts with a single, so-called seed-point. The criteria to define which points form a plane are based on Principal Component Analysis, discussed further in Section 8.3.3.1. As more points defining the plane are found in the searching process, the plane increases (grows) in size, until no more points belonging to the plane can be found. The selection of an appropriate first seed point is relatively simple. Technically, this can be any random point in the point cloud that has not been segmented (classified) yet. The selection of subsequent seed points to continue the region-growing process should be done more intelligently to ensure a steady and fast “growth” of the plane. The selection of subsequent seed points is explained further in Section 8.3.3.2.

8.3.3.1 Outlining planes through Principal Component Analysis

This step is the most essential part of the entire point-cloud segmentation strategy. The use of a Hough transform (see Section 6.6.4) provides an alternative method for defining planes in the 3-D point data, and this method is described in Section 8.6. Principal Component Analysis of subsets of the point cloud determines whether a potential (discontinuity) plane is defined by the data subset. The theory behind the recognition of planes with Principal Component Analysis is explained in Section 6.6.6. The implementation is discussed here in some more detail.

At this stage in the analysis, a first sub-sample of the point cloud is made, based on the selection of a seed point and a user-specified spatial search range around this point. In Matlab this subset is a matrix of size 3 x m, where m is the number of sample points. In Matlab the computation of the principal component can be carried out the same way as explained in the theory, i.e: first by computing the covariance matrix, subsequently by computing the eigenvalues, etc. Fortunately, the entire principal component analysis procedure is simplified in the Statistics Toolbox of Matlab with the function *Princomp* (Mathworks, n.d.). The function *Princomp* returns several results on the basis of analysing a (subset) matrix with the selected points. The matrix containing the-principal component vectors, also known as *loadings,* is the most important result that is used further in the analysis. These are in fact the eigenvectors of the covariance matrix of the input data points. The third principal component or eigenvector is the normal to the orthogonal regression plane that defines the orientation of the planar surface that passes through the selected points.

8.3.3.2 *Selection of subsequent seed points*

The points that form the plane may be defined as “inlier” points and any of these can be used as new seed points in the region-growing process. However, from a computational point of view, it would not be very efficient to use all these inlier points as new seed points. Only the points at the edge of the newly found plane should be used as new seed points. In particular, the points that form the extremes of the plane can efficiently serve as the optimal seed points, since these are the most likely places from which the plane will “grow” further. In order to find the optimal seed points at the perimeter of the growing plane the *Qhull* algorithm is used (Barber et al., 1996). *Qhull* is a small, but widely-used freeware program that has been implemented in Matlab as function *Convhull* (Mathworks, n.d.). This function computes in 3-D a *convex hull* around a selection of (three-dimensional) points. Formally, a convex hull is the smallest convex set of points that contains the entire selection. In two-dimensions, the analogous principle, known as a *convex envelope*, is easily visualised as an elastic-band that is stretched to include a number of given points on a plane. When this elastic band is released, it will follow the shape of the convex envelope. The points that the envelope touches are the points at the outer rim of the selected points (Figure 8.1).

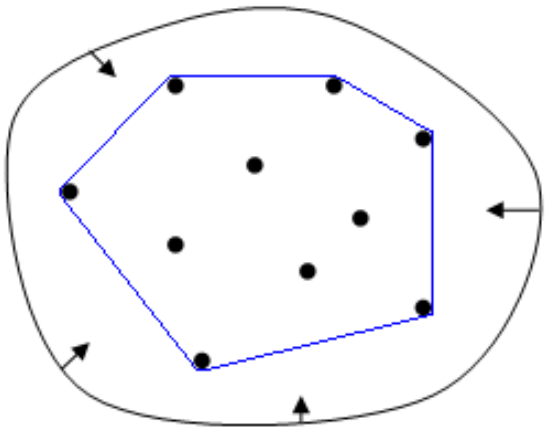

Figure 8.1. This diagram illustrates the convex hull analogy: an elastic band that contracts to form the convex envelope in 2-D. The points that the envelope touches are the optimum new seed points in the next step of the region-growing process.

Since the point cloud data is three-dimensional, the resultant is not an envelope but a hull around the outermost points (a volume). However, the data on which the convex hull is based are the inliers to the previously found (discontinuity) plane. The resulting hull will thus be very thin and the shape will be dominated by the outer points at the rim of the plane. There will be a few points that form the top and bottom of the hull that fall within the area of the (growing) plane. These are therefore not good seed points and if these points are used it will slow down the region-growing process. However, these seed points will quickly be discarded subsequently in the process, since very few unlabelled new points are likely to be found in the search box around these “improper” seed points.

8.3.4 Implementation in Matlab

This method is implemented in Matlab code. Matlab is a high-level interpreted programming language for numerical computations. A great advantage over the use of (compiled) programming languages like C or FORTRAN is that is relatively easy to develop code in the form of scripts. This is because of the user-friendly interface and the many build-in functions and visualisation tools. Another advantage in this particular study is the ease with which Matlab allows to compute and manipulate vectors and matrices. The point cloud data, for example, is simply read into the Matlab environment and stored as a single matrix in the Matlab workspace. On this point cloud matrix, all the manipulations and calculations can be carried out to derive the required information. The main disadvantage of Matlab is that it is an interpreted language. This means that every time a script is run, Matlab has to interpret the script line-by-line. This makes data processing slow, particularly if

the programming is not done efficiently. Also in computations that deal with large data sets, many of the intermediate results are stored as matrices, which can thus quickly fill in the workspace, which will result in loss of memory and the computations will slow down or even halt.

8.3.5 Program structure

The methodology that is implemented in the form of Matlab scripts and functions is explained below. It explains step-by-step in general terminology, what the various processing steps are. It is for the general reader easier to understand than the actual Matlab code. In some instances, the processing steps require some additional explanation. This is also provided in the following paragraphs.

8.3.5.1 Definition of constants and threshold values

Prior to the data processing, the user has to define the following constants and threshold values:

a. Definition of search box size. This has mainly an influence on the processing time. There is an optimum box size, a box size that is too small, will take too long to process, while the same is true for a box size that is too large.
b. Definition of threshold value for the number of points within the search box. The threshold depends on the local data density and the scanning spatial resolution.
c. Definition of the threshold value for the orthogonal distance of each point (in metres) to the plane found. This threshold value depends on the precision (noise) of the point cloud data and is important, since it defines which of the points are the inliers and outliers to the plane.
d. Define the threshold value in percentage of inliers compared to all points within the search box. Inliers are considered the points located at a perpendicular distance to the found plane that is below the average error and the outliers are considered points with a distance larger than the mean error.
e. Define the threshold pole-vector difference angle to exclude neighbouring points that form planes with a different orientation.
f. Define the minimum amount of points a segmented plane should contain. This can be used to remove very small planes. The choice to remove small planes from the result has consequences for the end results. This will be discussed further in Section 8.7.1.

8.3.5.2 Data processing

After the constants and threshold values have been defined, that data is imported, structure is created in the data and data is initialised. After this step the data processing is done in two programming loops: the first loop finds an appropriate seed point for a new plane and the second (nested) loop grows the plane from the newly found seed point. The entire list of processing steps that are carried out is given below:

Data import and initialisation

- Import the raw point cloud data, entirely or as a subset. The (N) points of the stored in a matrix. Here the x, y, z values are used (not the intensity and/or colour data), thus resulting in an Nx3-sized matrix.
- Create a structure in the raw point cloud (x, y, z) data with K-D tree structuring.
- Add a label (attribute) to each point, with default value of 0 for example. The label is used as an identifier for the segmented discontinuity plane. The labels are stored in a separate label list which is an Nx1-sized matrix.
- At the start of the processing, use label number 0. All found planes are numbered sequentially, thus when the processing moves to the next level to find another plane the label number is increased by 1.

Start of Loop 1 (Seed point selection for new plane) - Repeat this loop until there are no more points left that are unlabelled (i.e. there are no more points left with label 0)

–

- Selection of a random seed point, which should not have been labelled before, thus with the default label value 0.
- Find neighbouring points within the search volume with specified size around the seed point
- If a sufficient number of (unlabelled) points are found within the search volume, proceed with the next step, otherwise, select a new seed point return to the start of Loop 1.
- Determine the best-fitting plane through the selected points using the Principal Component Analysis and store the third principal component vector (the normal to the plane) in a separate plane matrix.
- Determine the points that are inliers and outliers to the computed plane using the specified threshold distance. If there are a sufficient percentage of inliers, proceed to the next step, if not, then select a new seed point by going back to the start of Loop 1.
- Increase the label number with 1
- Label all inliers with the current label, which is valid for the presently found plane. Label all outliers with a default label (e.g. -999)
- Find new seed points at the edges of the newly found plane.
- Add these new seed points to a newly created seed point list for this plane with the current label.

Start of nested Loop 2 (Plane growing) - Repeat this loop until all seed points in the seed point list are used and no more new seed points can be found

- Go sequentially through the entire seed point list and select the first unused seed point
- Find neighbouring points within the search volume with specified size around the seed point
- If a sufficient number of unlabelled points is within the search volume, proceed to the next step, otherwise select the next seed point from the seed point list
- From the points found within the search volume, use only the unlabelled points to determine the best-fitting plane using a Principal Component Analysis, store the third principal component vector (the normal to this plane).
- Determine the difference in acute angle between the newly found normal and the normal of the plane through the previously found and labelled points (with same label). If the difference is too large, then go back to the start of Loop 2 and select a new seed point from the seed point list.
- Determine the points that are inliers and outliers to the computed plane using with the specified threshold distance. Only if there is a sufficiently large percentage of inliers (d), then proceed to the next step, if not, then go back to the start of Loop 2 and select a new seed point from the seed point list
- Label all inliers with the current label, which is valid for the presently found plane. Label all outliers with a default label (e.g. -999)[23]
- Compute for all presently found and labelled points the third principal component with PCA and store this as the normal.
- Find new seed points at the edges of the points forming the plane that is found so far. Only add the newly found seed points to the seed point list, but only if they do not yet exist in the seed point list
- Return to the start of Loop 2

End of nested Loop 2

End of loop 1

[23] The outlier point with label -999 is re-tested if it falls within the search distance (box) of a new seed point in a subsequent loop. If it passed the PCA test (i.e. if it is an inlier to the plane), it is re-labelled with the plane number. This can occur with intersecting planes at rockblock corners and edges.

8.3.6 Data output and visualisation of the segmentation results.

The data analysis stops when all points have been evaluated and received a label with the default value of *–999*, or with an integer value ranging from *1* to the maximum number of planes that have been identified, and corresponding to the individual planar element to which the point belongs. The label information is stored in a separate label matrix *L* (n x 1), which is labelled in the same order as the points in the correctly oriented point-cloud matrix *B*. Both matrices *B* and *L* will be used further in the post-processing.

Matlab has built-in visualisation routines for plotting point data, but the number of data points forming a point cloud is generally too high for a fast visualisation. Therefore, in order to visualise the results, the point cloud matrix *B* and the labels from matrix *L* are converted into a VRML[24] file. Although the VRML file format is bulky, since it is in text (ASCII) format, the data structure of a VRML file is very simple. Once the data is loaded in the graphics memory, the interactive visualisation is fast and of high quality. In this case, the basic objective was to colour the point cloud according to the label number in a random manner. The VRML format is suitable for this purpose. Moreover, various freeware applications and freely available web-browser plug-ins exist to view the VRML format, which makes it easier to exchange the results with other individuals.

A visual inspection is very important to verify whether the segmentation generated the correct and expected results. In the visual inspection, it is important to check whether the discontinuity planes are correctly recognised. For instance, depending on specified threshold levels, two or more clearly distinct and separate discontinuity planes may be classified as forming a single planar element. On the other hand, it is also possible that a clear and distinct single discontinuity plane is segmented into several sub-planes. These problems generally occur when the threshold angle (e) is set too large (in the first case) or too small (in the latter case) (see also Section 8.3.5.1). It may also be due to a critically low threshold value for the number of inliers, see below.

If the spatial threshold values are selected to tightly or too broadly, many of the points may remain un-labelled. The threshold value defining the minimum percentage of inliers (*d*) in each region-growing step is especially important here (see also Section 8.3.5.1). A small threshold value may cause the region-growing process to ‘jump’ to a different discontinuity plane and continue there. Particularly, if there is a gradual change from one plane to another and if the threshold angle (*e*) is large, this may occur. On the other hand, when the threshold value for the minimum percentage of inliers is too high, then only the very smooth and ‘planar’ discontinuities are identified, while the points of the rougher and more undulating planes will be rejected.

A number of iterative “trial-and-error” steps are often required to determine the optimal combination of parameters that result in the best segmentation. It is difficult to determine the optimal combination beforehand, because it depends primarily on the scanning resolution and the error (noise), which can change from scan to scan and will depend on the type of laser scanner that is used.

[24] VRML is an abbreviation for Virtual Reality Model Language. It is a standardised text-based file formation for representing 3-D vector graphics with the main objective of visualisation over the internet. The VRML format is now superseded by the X3-D format (web3-D, n.d.).

8.4 Results of applying Principal Component Analysis segmentation (Method 3)

The Principal Component Analysis segmentation method just described was applied to two field sites in Spain, namely:

- Site 1 (Bellmunt) located 5 km west of Falset along road TP7101 and described in Section 5.4.2 and illustrated by Figure 5.4 and Figure 5.5.
- Site 2 (Torroja) located 2.5 km south of the village of Torroja del Priorat along road TP7403 and described in Section 5.4.3 and illustrated by Figure 5.8 and Figure 5.9.

The final processing parameters for both data sets have been kept the same, although there is a slight difference in data density between the two data sets. Please refer to Section 8.3.5.1 for a detailed description of the parameters. The processing parameters that were used, which had the best results are given in Appendix I.

a. Box size = 0.06. The dimensions of the search box (in metres)
b. Minimum points boxed = 10. The minimum number of points found in the search box)
c. Threshold distance = 0.0050.This is the maximum perpendicular distance (in m.) of a point to the plane, which strongly depends on the noise level. This threshold distance is in the final analysis not used. Instead, the parameter (*d*) is used (see below).
d. Percentage inliers = 0.5. With the percentage of inliers, it is not required to know the noise level of the data. Here, inliers are defined as points that are located closer to the local calculated plane than the mean orthogonal distance level of all points within the search box together.
e. Orientation threshold = 0.3. Neighbouring points that form a local plane that has a pole-vector difference larger than this threshold value (in degrees) are rejected. This parameter makes sure that the region-growing stops when it hits another plane
f. Minimum points in plane = 200. After the segmentation, points that form small planes (containing less than 200 points in this case) are removed.

8.4.1 Results of Method 3 for Site 1 (Bellmunt)

The input point cloud data set for site 1 contains 616300 points. This is the same dataset that is used for the other processing methods 1, 2 and 4. After the processing, 360404 points were segmented, while 255896 points remained un-segmented. Hence, 59 percent of the points have been segmented. The points that are not segmented represent noise or points in low data density areas, which, according to the criteria defined above, are not part of a (discontinuity) plane. In total 603 segments that represent individual planar elements, or potential discontinuity planes, have been recognised. Figure 8.2 illustrates results from this segmentation. Each individually identified planar element is shown by a randomly applied colour.

8.4.2 Results of Method 3 for Site 2 (Torroja)

The input point cloud data set for site 2 contains 480942 points. This is the same dataset that is used for the other processing methods 1, 2 and 4. After the processing, 259796 points were segmented, while 221146 points remained un-segmented. This means that 54 percent of the points have been segmented. The points that are not segmented represent noise or points in low data density areas, which, according to the criteria defined above, are not part of a (discontinuity) plane. In total 216 segments that represent individual planar elements, or potential discontinuity planes, have been recognised. Figure 8.3 illustrates the results from this segmentation. Each individually identified planar element is shown by a randomly applied colour.

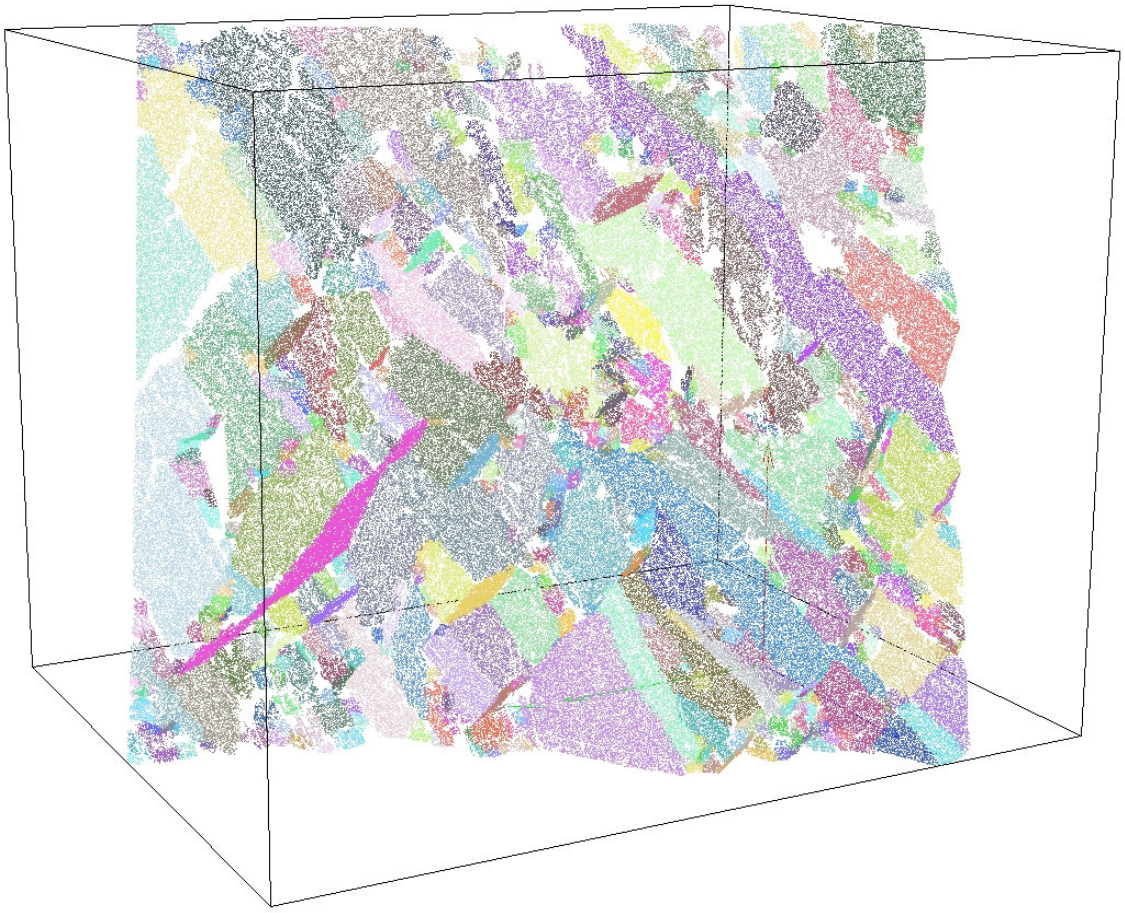

Figure 8.2. This illustration is the pointcloud coloured based on the segmentation that is carried out using Method 3 (Matlab; PCA). Points belonging to a single plane received a similar colour. The point cloud is segmented into 603 planes. It concerns the dataset from Site 1.

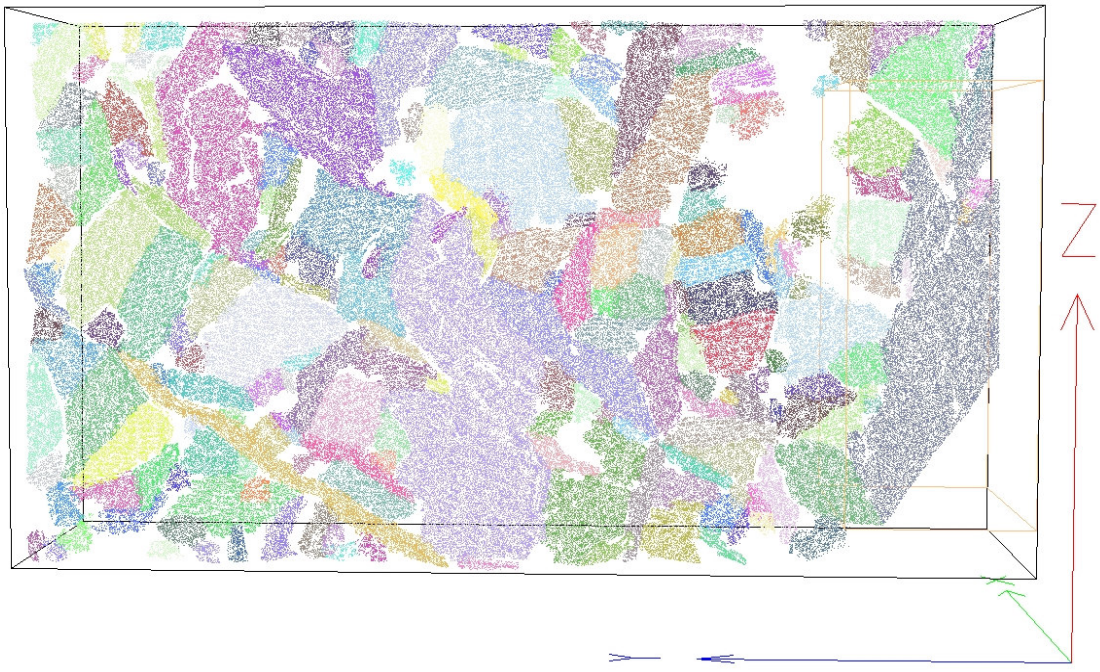

Figure 8.3. This illustration is the pointcloud coloured based on the segmentation that is carried out using Method 3 (Matlab; PCA). Points belonging to a single plane received a similar colour. The point cloud is segmented into 216 planes. It concerns the dataset from Site 2.

8.5 Method 4: Segmentation based on Hough transformation and Least-Squares regression and implemented in Point Cloud Mapper (Method 4)

8.5.1 Implementation

Vosselman (2004) implemented this segmentation method in the software *Point Cloud Mapper* (PCM). At this time, the PCM software is not commercially available and so far, it has mainly been used for research and educational purposes. The program was initially developed to process air-borne laser scanner data, in order to detect roofs of buildings, bridges and other planar geometric features from the point cloud. However, the method works equally well on point cloud data from terrestrial laser scanners. The PCM software uses the principle of region- or plane-growing and the data can be partitioned with a K-D tree structure, similar to Method 3.

The main difference between Methods 3 and 4 lies in the approach employed in recognising planar features in the data. While Method 3 applied Principal Component Analysis (PCA), Method 4 employs a 3-D Hough transformation to identify and select an appropriate number of "seed points" from the point cloud that form part of a planar element, and these are then evaluated by a least-squares regression to determine their planarity. If these points define a planar element within pre-defined tolerances, then this "seed surface" plane is then "grown" step-by-step using a spatial search and the new plane is repeatedly optimised with least-squares estimation. For the background on 3-D Hough transformation and least-squares estimation, refer to Sections 6.6.4 and 6.6.5.

Method 4, as implemented by the PCM software, follows the general processing sequence described in Section 8.2.3 and defined by Vosselman, et al. (2004) and Rabbani, et al. (2006). The PCM software requires the user to specify several parameters and thresholds that control the segmentation process. Some of these parameters and thresholds affect the Hough transformation; additional parameters are required to control the efficient selection of initial "seed points," to ensure that the planar elements grow efficiently as the segmentation process progresses, and that "noisy" (non-planar) areas are avoided. These specifications, and the various processing steps, are discussed in greater detail in the following sections.

8.5.2 Data importation, registration, and structuring

As with the Method 3, the PCM software accepts the comma-delimited ASCII format to define the x, y, z values of each point in the point cloud. Any additional data values, such as reflected intensity and/or Red, Green, Blue values from digital camera images, that are present in the dataset can also be used.

The segmentation analysis involves the sequential analysis of all the points within the point-cloud, and their classification according to their membership within individual planar elements or as random points within rough non-planar sections. This classification process requires each point to be given a "label". The label information is stored as a point attribute. Initially all points are provided with label *0*. Points that have not been segmented keep the label *0*. There is another attribute that keeps track of whether a point has been evaluated. All the points lying within identified planar elements are labelled with integer values ranging from *1* to the maximum number of planes that are found. The segmentation process stops when all points have been evaluated.

In order to speed up the search for nearest neighbours and before the actual point cloud segmentation is carried out, a spatial data structure needs to be created from the unorganised point cloud data (Section 6.6.2). Since the entire segmentation approach is based on a recursive search for neighbours of seed points, it is essential that a tree-based structure be implemented before further data analysis is attempted. The PCM software provides three options for this spatial portioning. In the software, these options are referred to as "Storage models" and they include:

- K-D tree
- Delaunay TIN
- Octree

As discussed previously in Section 6.6.2, K-D tree partitioning is the optimal method for segmentation of laser scan point cloud data, and accordingly was the option selected for this research. The creation of a Delaunay TIN structure is not recommended, because of the noisy and unorganised nature of the point cloud data. The Octree storage model is unbalanced compared to the K-D tree model; the Octree model will contain cells with varying numbers of points, while with K-D tree partitioning the cells contain more or less the same number of points.

8.5.3 Definition of constants and threshold values

The PCM software requires the user to define several parameters and thresholds to control the segmentation process. These parameters and thresholds can be grouped into several categories and are discussed accordingly in the following sections.

8.5.3.1 Connected component parameters

The following parameters are defined to ensure that points found during each seed selection step and after each plane-growing step are sufficiently "dense" in a spatial sense; that is, they are closely spaced. Areas with noisy and scattered points (at the edges of the point cloud or in occlusion areas) are thus avoided:

- Maximum distance between points: This option is not used with the segmentation into planar surfaces. It is only used in connected component analysis where only the distance between points is evaluated. Whether these points form a plane or not is not considered.
- Minimum number of points: The minimum number of points depends strongly on the dimensions of the scanned rock face and the resolution of the point cloud data. Again, using on an average resolution of 5 mm, it means that planes with less than 100 points (for example) are smaller than 25 cm^2. Setting an appropriate threshold value for this parameter will ensure that only the larger planes will be identified for use in subsequent analyses. However, the decision to remove small planes from the result has consequences for the results. This will be discussed further in Section 8.7.2.

8.5.3.2 Seed selection parameters

There are two options to select a number of potential seed points from a randomly selected point from the point cloud:

- Direct neighbours option: This option selects a fixed number (k) of nearest neighbouring points to the selected random point. The number (k) corresponds to the minimum number of points defined above as one of the connected components parameters. This option corresponds to the K-Nearest-Neighbour (KNN) definition discussed in Sections 6.3.3.2 and should be used when the point cloud data density varies much throughout the scene.
- All within radius option: The second option is to use a specific search radius from the random point. The user has to define the radius of the neighbourhood to be searched. This option corresponds to the Fixed-Distance-Neighbours (FDN) definition described in Section 6.3.3.2. This option can be used if the data density of the point cloud does not vary a great deal throughout the scene.

8.5.3.3 Seed point selection thresholds

The following are threshold values that have to be set to limit the number of seed points and to filter out "noisy" seed points:

- Minimum number of seed points: If too few seed points are found, the seeds do not form a significant planar area and the process is aborted. A minimum of around 10 seed points appear to be an appropriate threshold value to ensure proper plane growth. If this threshold value is set too high, no seed points will be found and the point cloud remains un-segmented.
- Maximum distance to plane: This parameter results in the selection of seed points that are only within a specified orthogonal distance from the found plane. This excludes the use of noisy points as additional seed points. The appropriate distance depends again on the precision of the data. All points within the precision are proper seed points. The threshold value should be smaller than the bin size distance (see Section 8.5.3.4 below), but larger or equal to the precision. If this value is too small, a large portion of the point cloud data will remain un-segmented, although obvious planar surfaces are present.

8.5.3.4 Hough transform parameters

Once the potential seed points are selected, these are transformed to the Hough parameter space in which there are three parameter axes: (a) the slope angle of the plane along the X-axis, (b) the slope angle of the plane along the Y-axis, and (c) the (perpendicular) distance of the plane to the origin. Section 6.6.4 also explains that, because the data points are usually not perfectly aligned, precise intersections in the parameter space will not occur, and thus these three parameter axes need to be rasterised (*binned*) in order to create the accumulator cells. The selection of the bin size is very important. If the chosen bin size is too small, the accumulator cell will find too few intersections. If the chosen bin size is too large, points that belong to different planes (co-planar) will be classified similarly. The following parameters define the 3-D Hough transformation parameters:

- Maximum slope angle: This parameter can be used to exclude certain (more steeply dipping) planes. If all slope angles are to be used, the maximum angle should be 90 degrees.
- Bin size slope angle: This parameter divides the two parameter axes that define both X and Y slope angles into equal bins. A bin size of 3 degrees for example, discretises both parameter axes into 60 bins. Experience shows that the selection of the optimal bin size requires some "trial and error".
- Bin size distance: This parameter divides the distance parameter axis in Hough space into equal bins. The selected bin size depends strongly on the precision of the data. For instance, if the data points have a precision of about 1 cm, the distance bin size should not be made smaller than 1 cm, otherwise only very few points are classified to the same plane. If the bin size is chosen much larger than the error, then points from a nearby parallel plane will be classified together. For instance, a 2-cm bin size for a 1-cm precision will be a good choice.

8.5.3.5 Plane growing parameters

- Surface growing neighbourhood definition: There are two options: "direct neighbours" or "all within radius". As with the potential seed selection in the previous step, new (potential) plane points are found by selecting points around previously classified points. Once again, this can be done based on a minimum number of direct neighbours or by defining a specific search radius.
- Surface growing radius: This refers to the previous parameter for both options "direct neighbours" as well as "all within radius" (see above). Direct neighbours at a distance further than the indicated radius are thus ignored. It is advisable to select a radius similar to the seed selection radius (see above). If this value (surface growing radius) is chosen too large, the calculation time will increase significantly.
- Maximum distance to surface: This parameter defines the maximum distance value of the found points to the re-computed plane. A distance should be used that is slightly larger than the average precision of the value that is used as "maximum distance to plane" in the Hough-based seed selection step. If this value is too large, too many noisy points[25] will be included in the growing plane. This results in an under-segmentation of the point cloud. If the value is set at the

[25] Here, noisy points refer to points that can not be part of the found mathematical expression of the plane, because they are farther away from the plane than the precision of the laser data.

noise level or even smaller, it is too much of a constraint and the plane-growing will stop too early. This results in an over-segmentation of the point cloud.

- Competing surfaces: In the PCM software, it is optional to select this parameter, although for this study this option should always be selected. This option detects whether the points that are found in the surface growing process have been labelled (segmented) before. If this is the case, the program will re-evaluate the previously segmented points and determine if they fit better to the new plane. The points will be included in the new class if the fit is better. It is therefore important to select this option, because it results in an improved delineation of the planes, especially at the edges and corners. Without the use of this option the surface growing process may result in segmented points that have "grown" over an edge onto the adjacent parts of another (obviously different) plane. Usually only small linear sections of the plane are chosen, because only these meet the other criteria. These erroneously segmented points are thus kept, since subsequent plane-growing steps will not include the already segmented points.

8.5.4 Sensitivity analysis

After much trial-and-error, it was concluded that the entire segmentation process with the PCM programme is very sensitive to the following parameters:

In the seed selection phase:
- Minimum number of seed points
- Maximum distance to plane

In the plane-growing phase:
- Maximum distance to surface
- Competing surfaces: this option needs to be selected.

As explained previously, the choice of the appropriate values depends entirely on the precision (or noise) of the point cloud data. If the precision is unknown, the correct parameter values are quickly found by entering some sample values for a small test area. The precision can range between 0.5 and 2 cm for time-based laser-scanners.

Also data density plays a role in the selection neighbourhood definition of the surface growing radius and the seed selection radius. If the data density is not known it is better to choose the *direct neighbour* option. This avoids the need for defining an absolute search radius by the user.

8.5.5 Program structure

The methodology employed within the Point Cloud Mapper (PCM) software (Vosselman, n.d.) is summarized in the following sections so that the general reader can appreciate the sequence of analysis steps conducted by PCM.

8.5.5.1 Data processing

After the constants and threshold values have been defined, the data is imported, and georeferenced if required. A spatial data structure is created from the unorganised point cloud data by applying a K-D tree-building option, as defined in Section 7.4.2. The data is initialised so that each point has a dummy label.

The segmentation process is accomplished by two programming loops: the first loop undertakes the selection and identification of "seed surfaces." The second (nested) loop grows these seed surfaces. The entire list of processing steps that are carried is given below:

Data import and initialisation

- The PCM software has various data import facilities and is also able to import additional information such as intensity and colour information

Start loop 1 - Seed selection with Hough transform: repeat until no more planes are found

- Increase label number
- Select a random start (seed) point, assign the new segment label number if it has a dummy label
- Find all points within specific radius from the random start seed point or select the nearest neighbours from this point (with a specified minimum number).
- Transform the found points to the 3-D Hough discretised parameter space. The Hough transform is a very robust algorithm that is not influenced by noise and outliers (see Section 6.6.3).
- The points that fall in the discretised Hough space within the bin (accumulator cell) with the highest count form a plane.
- If the number of points that form a plane is smaller than a specified threshold value, then skip this seed point, select a new random seed point and start again.
- Make a sub-selection of the Hough points that are closer than a specified threshold distance value to the plane, label those points with the present segment label and use those points as seed points or seed plane for the subsequent plane growing .

Start of nested loop 2 - Plane growing with Least-squares estimation: repeat until the plane does not grow anymore

- The plane is grown by selecting neighbouring points of the seed points on the basis of a specified radius or by selecting a nearest number of neighbours. To determine which of the new points lie on the previously found plane the entire plane is re-computed with Least-squares estimation. This step can also be done with the Hough transform that is used to find the first seed points. However, the Least-squares estimation algorithm is faster although it is more influenced by outliers. It is sufficient to start with a good set of seed points that are found with the robust Hough method, and continue the plane growing with a less robust method like Least-squares.
- The Least-squares estimation gives a new set of plane equation parameters for the plane. The inliers and outlier points to this plane are identified based on a user-specified threshold distance value. Only the inliers, the points within this orthogonal distance to the plane, are labelled
- The plane is grown further by selecting the neighbouring points of the newly labelled points and the previous two steps are repeated. Now, instead of using the seed points that were selected with the Hough transform, the newly found point in the plane growing step are used to find neighbouring points. This loop is repeated until no more new inliers are labelled. If the plane growing halts, return to the start of Loop 1
- It is likely to find points during the plane growing that are already labelled. This means that the points belong to another plane, which can occur at rock edges and corners. In the software, this is referred to as “competing surfaces”. The PCM software allows the re-evaluation of these points based on the new plane parameters.

- **End of nested loop 2**

- **End of Loop 1**

8.5.6 Data viewing and data export

The result of the segmentation can be viewed in 3-D within the PCM program. Points that belong to the same plane receive a similar colour. If the results look satisfactory the segmented point cloud data can be exported.

The segmented point cloud is exported as ASCII data. Apart from the x, y, z coordinates, and extra fourth data column is added with the segmentation label, which refers to the plane number. The data shoulde be further processed to derive the discontinuity information. This is explained further in Chapter 9.
Small segments, i.e. segments containing less than a user-specified number of points can be removed prior to the data export. In this study, segments smaller than 200 points are removed. This amount is similar to the threshold value set with method 3.

8.6 Results of applying Hough transformation and Least-Squares regression segmentation (Method 4)

The Hough transformation and Least-Squares regression (using the PCM software) segmentation method (Method 4) previously described was applied to two field sites in Spain, namely:

- Site 1 (Bellmunt) located 5 km west of Falset along road TP7101 and described in Section 5.4.2 and illustrated by Figure 5.4 and Figure 5.5.
- Site 2 (Torroja) located 2.5 km south of the village of Torroja del Priorat along road TP7403 and described in Section 5.4.3 and illustrated by Figure 5.8 and Figure 5.9.

The parameters of Method 4 for processing the two data sets of Site 1 and Site 2 have been kept the same, although there is a slight difference in data density between the two data sets. Please refer to Section 8.5.3 for a detailed description of the parameters. The processing parameters that showed the best results are given in Appendix I.

8.6.1 Results of Method 4 for Site 1 (Bellmunt)

The input point cloud data set for site 1 contains 616300 points. This same dataset is used for the other processing methods 1, 2 and 3. After the processing, 611157 points were segmented, while 5143 points remained un-segmented. This means that more than 99 percent of the points have been segmented. The points that are not segmented represent noise or points in low data density areas, which, according to the criteria defined above, are not part of a (discontinuity) plane. In total 407 segments that represent individual planar elements, or potential discontinuity planes, have been recognised. Figure 8.4 illustrates the results from this segmentation. Each individually identified planar element is shown by a randomly applied colour.

8.6.2 Results of Method 4 for Site 2 (Torroja)

The input point cloud data set for site 1 contains 480942 points. This same dataset is used for the other processing methods 1, 2 and 3. After the processing, 467378 points were segmented, while 13564 points remained un-segmented. This means that more than 97 percent of the points have been segmented. The points that are not segmented represent noise or points in low data density areas, which, according to the criteria defined above, are not part of a (discontinuity) plane. In total 332 segments that represent individual planar elements, or potential discontinuity planes, have been recognised. Figure 8.5 illustrates the results from this segmentation. Each individually identified planar element is shown by a randomly applied colour.

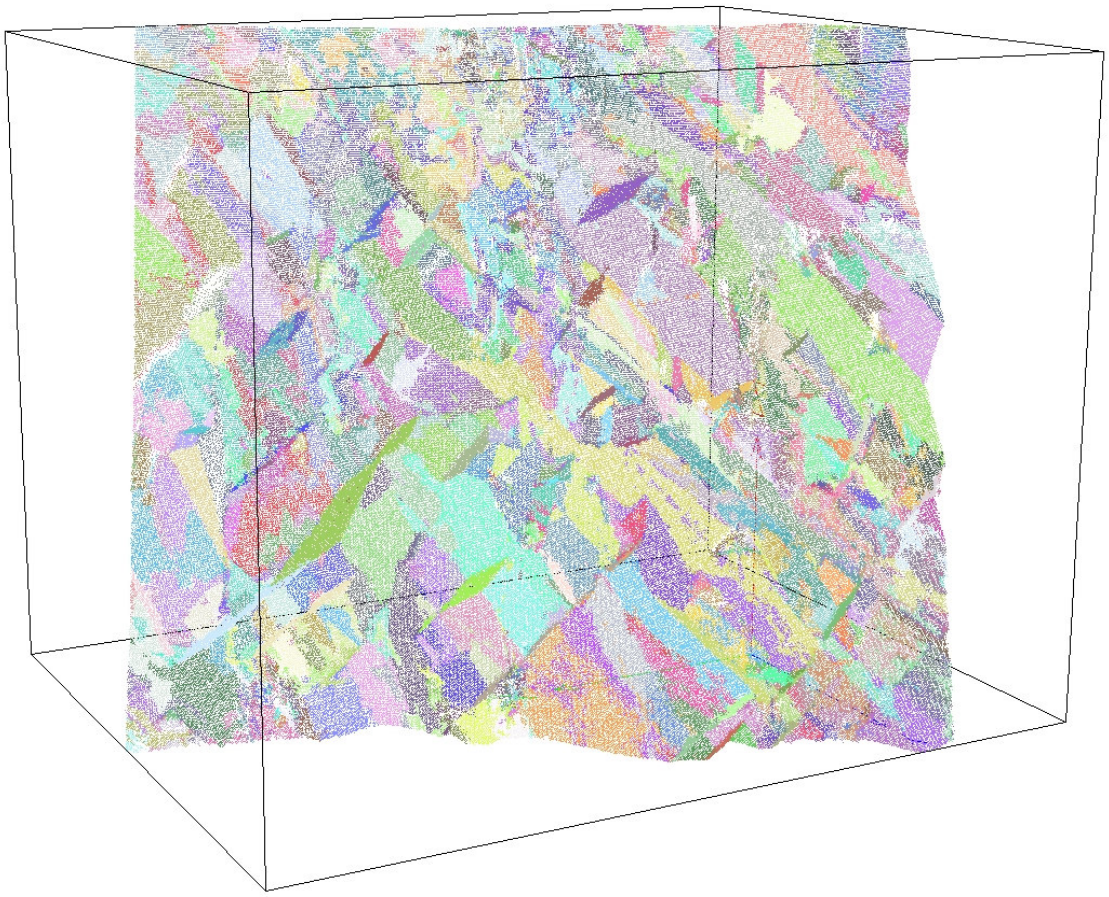

Figure 8.4. This illustration is the pointcloud of Site 1 coloured based on the segmentation that is carried out using Method 4 (PCM; Hough). Points belonging to a single plane received a similar colour. The point cloud is segmented to 407 planes.

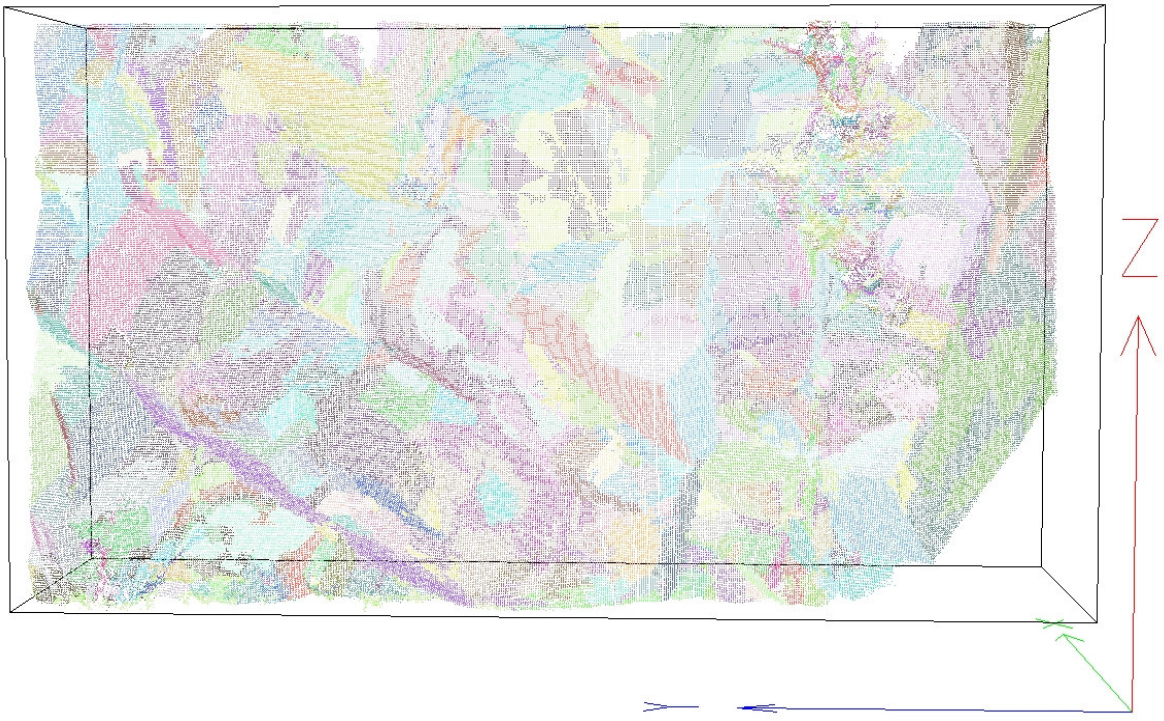

Figure 8.5. This illustration is the pointcloud of Site 2 coloured based on the segmentation that is carried out using Method 4 (PCM; Hough). Points belonging to a single plane received a similar colour. The point cloud is segmented to 332 planes.

8.7 Discussion and conclusions

This chapter introduces and applies two methods that rely on point cloud segmentation techniques to structure the irregular and noisy point cloud data and then to extract discontinuity planes. Method 3 uses a Principal Component Analysis to detect seed points and to grow the planes, while Method 4 uses a Hough transform to find suitable initial seed points and a Least-Squares estimation to grow the planes. Although the two methods employ different approaches, they both produce similar results, i.e.: a segmented point cloud. Both methods were applied to the same two data sets, and thus produce results involving the same original point cloud data (the *x*, *y*, *z* coordinates) but with different classification labels for each point record. The sections below evaluate the results of both methods in more detail.

8.7.1 Discussion and conclusions concerning Method 3

Figure 8.2 shows the results of Method 3 applied to the data for Site 1, while Figure 8.3 shows the results of Method 3 applied to the data for Site 2. In each case, the points from the original point cloud are coloured according to the segment (discontinuity plane) they belong to. Although a different colour is assigned to each individual plane, the number of colours is much less than the number of individual planes. Thus the same colour can be applied to multiple planes. The colours are merely intended to discriminate the various identified planes. In this way, one can directly visually verify the quality of the segmentation.

The un-segmented points are not shown. In both cases several white “gaps” in the data are observed, where the un-segmented points used to be. Most of the times, these white gaps are the areas with vegetation. For instance, in the upper right part of Site 2 (Figure 8.3), there is a large white (gap) area, which is caused by the presence of noisy points due to vegetation. Please also refer to the original point cloud data illustrated in Figure 7.47 (Site 1) and Figure 7.50 (Site 2) and the photographs of the two sites (Figure 5.4 and Figure 5.8). Other gaps are associated with occlusion, including discontinuity planes that contain very few points or lie with shadow zones. For instance, in the left-centre part of the slope of Site 1 (Figure 8.2), it can be seen that there are two larger gaps, one triangular and one elongated in shape above it. These are clearly associated with two planar surfaces, lacking in data points.

The segmentation process does not yield segmented points in the noisy vegetated areas, which is, of course, a positive result. The segmentation procedures of Method 3 ignore the vegetation data, because in these locations there is generally a lower data density and more plane outliers than inliers are likely to be found in these noisy data areas. A negative consequence of the implemented Method 3 is that points that do form a plane, but contain fewer points (due to a lower point density) are also ignored. This includes, not only occlusion areas, but also any planar elements that are oriented perpendicular to the slope or parallel to the incoming laser beam. In contrast, planes that are parallel to the slope or perpendicular to the laser beam are readily identified. Consequently, Method 3 tends to over-emphasize planes that are parallel to the slope or perpendicular to the laser beam, while the planes that run perpendicular to the slope or parallel to the incoming laser beam are mostly not detected.

Chapter 9 discusses the further data processing steps required to evaluate the geometric information describing these identified individual planar elements, the subsequent detection and selection of discontinuity sets, and the computation of the normal set spacings.

8.7.2 Discussion and conclusions concerning Method 4

Figure 8.4 shows the results of Method 4 applied to the data for Site 1, while Figure 8.5 shows the results of Method 4 applied to the data for Site 2. As described in the discussion of Method 3 above, the points from the original point-cloud data set are coloured according to the segment

(discontinuity plane) they belong to. In this way, one can directly verify visually the quality of the segmentation.

Compared to Method 3 where only half of the points are classified as belonging to individual planar elements, with Method 4 almost all the points classify into planar elements. This means that areas containing points from vegetation have been included within some planar elements. In fact, the vegetation areas do contain many small planes, some of these can be observed in the top right part of the slope in Figure 8.5. These segments are relatively small, but large enough to pass the applied threshold value of 200 points (see also Section 8.7.3). The main reason that part of the vegetation is still segmented is that the Hough transform still finds good seed point planes in the noisy vegetation data. If the Hough transformation parameters are further constrained, particularly the “maximum distance to plane” (which has been set to 0.01 m), many of the points that form proper seed points on actual discontinuity planes, will also be omitted, yielding unsatisfactory results. Method 4 thus finds in the vegetation areas, points with sufficient density that, from an algebraic point of view, form planes.

The advantage of Method 4 compared to Method 3 is that the points in the occlusion areas have not been removed and are actually properly segmented to planes. Please compare Figure 8.4 with Figure 8.2: here one can observe that the points forming the triangular shaped plane and the elongated plane above it in the left-central part of the slope has been segmented with Method 4, but not with Method 3.

Method 4, and the parameters that were used in this application, also resulted in a more precise result with regards to the planarity of the segmented points. Small changes in the orientation within a plane result in a sub-segmentation. A good example is the large, steeply dipping discontinuity also in the central left portion of the slope of Site 1 (see Figure 8.2 and Figure 8.4). Method 4 segments this plane into two separate planes, since there is an obvious change in dip (Figure 8.7), while Method 3 segments the entire plane to a single plane (Figure 8.6)

8.7.3 Issues concerning the selection of processing parameters

Both segmentation methods require the user to make important decisions concerning the selection of the processing parameters. An inappropriate selection or the wrong combination of processing parameters will result either in an over- or in an under-segmentation of the point cloud. However, if the point cloud data precision and resolution is known, it is not difficult to find the most appropriate parameters by some trial-and-error and small adjustments of the parameters. The evaluation of what constitutes a properly segmented point cloud is only based on a visual inspection of the results and can thus introduce bias. This study did not explore the effects of different (combinations) of processing parameters on the result. In this study, it was assumed that the best point-cloud segmentation should yield the optimal geometric discontinuity information.

8.7.4 Issues concerning the removal of small segments

In both methods, small segments are removed, i.e. planes containing less than the (arbitrary) 200 points. This is mainly done to simplify the subsequent data processing by removing large numbers of very small planes that may negatively influence the clustering process that will be conducted subsequently (see Chapter 9). The underlying assumption here is that these small planes do not actually represent a sufficiently significant discontinuity plane. However, an important consequence of this action is that discontinuities from a discontinuity set that happens to be poorly exposed are thus omitted from the analysis and the entire discontinuity (or joint) set may be missed in the clustering analysis. An example is horizontal cleavage or bedding with a small to very small spacing that will be poorly exposed in a steep exposure. Although some of the bedding or cleavage, surfaces may be detected by either segmentation method from the laser data, the arbitrary removal of the smaller and noisy segments results in the removal of these few important discontinuity surfaces as well. A conventional survey would most likely not overlook such an important discontinuity set. If such a situation is identified, (part of) the rock face could then be scanned with a

higher resolution and/or with a difference angle of incidence, so that the small, poorly exposed discontinuity surfaces can be detected from the laser data.

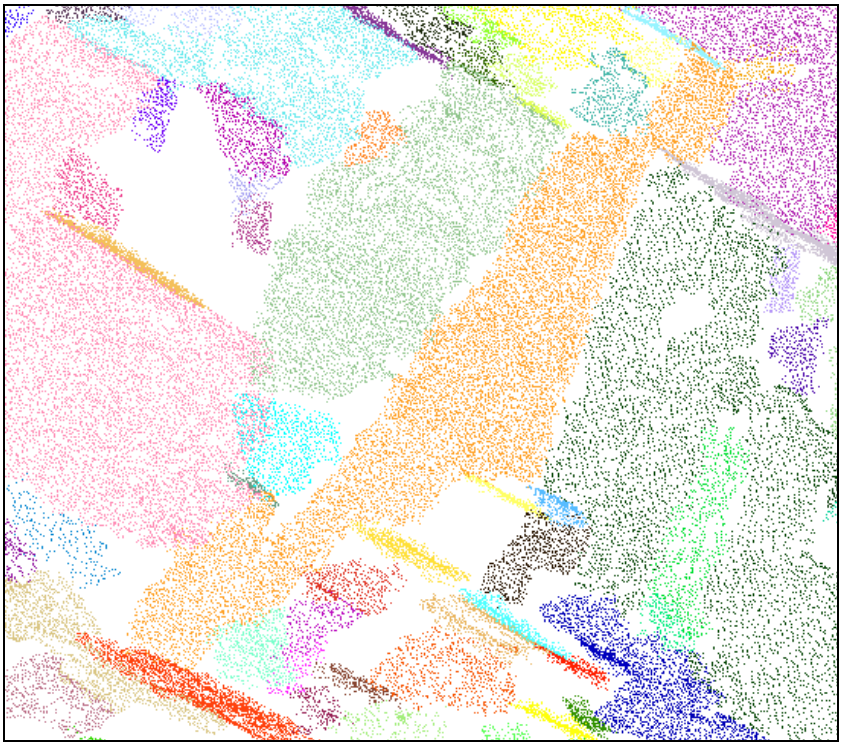

Figure 8.6. Detail of the segmented point cloud of Site 1, generated with Method 3. One clearly observes the large dipping discontinuity plane that has been segmented to a single (orange) plane. Also, note the un-segmented parts (the white gap) of the discontinuity plane that contain less dense points because it is semi-parallel to the incoming laser beam. Please compare with Figure 8.7 below.

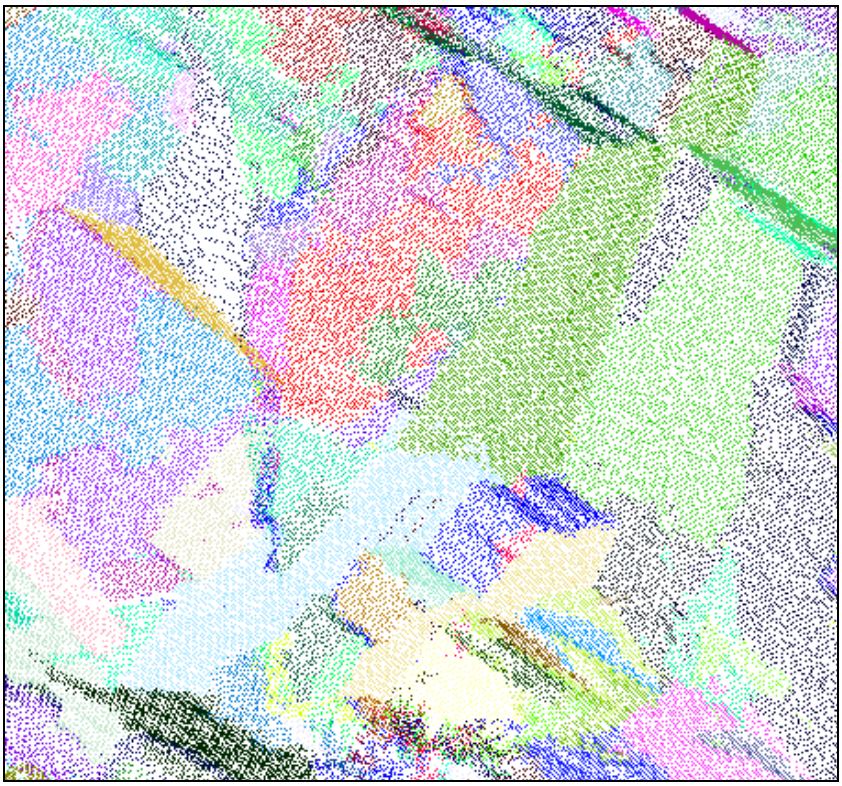

Figure 8.7. Detail of the segmented point cloud of Site 1, generated with Method 4. Once clearly observes the large dipping plane that has been segmented here into two different planes (dark green and cyan) with a clear demarcation at the change in dip. Also note the segmented occlusion areas, containing points which are less densely spaced. Please compare with Figure 8.6 above.

9 Deriving discontinuity information

9.1 Introduction

Chapters 7 and 8 discuss four different methods that create structure to the laser scan point cloud data and thus allow the delineation of discontinuity planes. Chapter 7 covers the surface reconstruction, or, “Top-down” approach, while Chapter 8 covers the segmentation, or, “Bottom-up” approach. The delineation of discontinuity planes is an essential first step to the derivation of information on discontinuity sets, including their orientations and spacings.

This chapter discusses the various post-processing steps that are required to extract and evaluate the discontinuity information defining the discontinuity sets, their constituent individual discontinuity planes, and the spacing distribution of discontinuities within each discontinuity set. The results of the application of these additional processing procedures for the two test sites in Spain are provided for all four methods. The results produced by all four methods are compared with each other and with the data gathered in the field using conventional methods.

9.2 Methodology

The two surface reconstruction methods (Methods 1 and 2) provide the average orientation (dip direction and dip angle) and the plane equation parameters for each identified discontinuity plane. They also provide additional information, including the mean coordinates (centroid) and dimensions (extent) of each discontinuity plane. In contrast, the two segmentation methods (Methods 3 and 4) only yield a classified point cloud where individual points representing a single discontinuity plane are given a unique identifier label. These segmented point clouds must be further analysed in order to derive the orientation, the plane equation, and the centroid coordinates for each individual discontinuity plane. This analysis process reduces the original (segmented) point-cloud data to a table that lists these location and orientation characteristics for each of the recognised individual discontinuity planes. By using these orientation data, the poles for these discontinuity planes are plotted on a stereographic plot, allowing the user to visually identify concentrations of similarly oriented planes, and thus determine the appropriate number of discontinuity sets. Fuzzy k-means clustering allows for the automatic assignment of similarly oriented discontinuity planes into one of the identified discontinuity sets. This allows the computation of spatial statistics, such as mean orientation, Fisher’s K value, and spherical variance (s), for each discontinuity set. The plane equation for each individual discontinuity plane and the discontinuity set information may then be used to calculate the normal set spacing distribution within each discontinuity set.

9.3 Computation of plane geometry for each discontinuity

The point-cloud structuring obtained either with the 3-D surface reconstruction (Method 1, see Section 7.2) or with the two point-cloud direct segmentation methods (Methods 3 and 4, see Sections 8.2 and 8.5), yield a labelled point cloud that defines the presence of unique individual discontinuity planes. Methods 3 and 4 retain the original point-cloud points, while Method 1 provides coordinates related to the vertices of the triangular facets of the interpolated 3-D surface mesh. In contrast, Method 2, utilizing the Split-FX software (Split Engineering 2007), generates a triangulated mesh by evaluating the point-cloud data with a 2-D gridding approach, and analyses the orientations of the individual triangular facets to define surface “patches,” composed of adjacent triangular facets that meet user-specified planarity and size criteria (Section 7.5). The Split-FX software then assists the user in classifying these patches into discontinuity sets. Thus, Method 2

develops a triangulated mesh with individual planar surfaces identified, and in this respect is similar to Method 1, but it also groups patches with similar orientations into larger individual surfaces and/or discontinuity sets.

The procedure required to derive the orientations and plane parameters are however exactly the same for all methods. In order to establish the appropriate number of discontinuity sets, and the membership of the individual discontinuity planes within these sets, the labelled point-cloud points, or the coordinates of the triangular facets, are imported into Matlab. In Matlab, this information is stored in the form of two matrices: a (N x 3) matrix B that contains the coordinates and a (N x 1) matrix L that contains the label (plane) numbers. Further processing is done according to the following steps:

1. First the number of labels is determined, which is equivalent to the number of individual discontinuity planes that have been recognised by each of the different methods.
2. Then, for each label, a subset matrix C of the matrix B is created that contains all the coordinates that belong to that particular individual discontinuity plane.
3. Some simple statistics of matrix C can then be computed, such as the number of points, the mean coordinates (the centroid of the plane) and the minimum and maximum extents in terms of x, y and z coordinates.
4. Principal component analysis identifies the normal vector n to the points in matrix C. The orientation of this normal defines the orientation of the plane. These orientations can be plotted as poles in a stereographic plot. Clusters of these poles within the stereographic plot allow the identification of discontinuity sets (See Section 9.4).
5. At the same time, the three (normalised) vector components of the pole to the plane form the parameters a, b and c of the plane equation ($ax + by + cz + d = 0$).
6. The parameter d of the plane equations is found by substituting the mean coordinate into the plane equation. In fact, the parameter d is the orthogonal distance of the plane to the origin of the point cloud coordinates. This parameter will become important later; in the computation of the normal set spacings (see Section 9.5).

The results of this procedure for computation of plane geometry are stored as a text file that can easily be imported in Excel for further manipulation. Table 9.1 provides an example of some of the results

Table 9.1. Example of the results obtained by the computation of the plane geometry. These show, for each individual discontinuity plane, those geometric properties that are important in determining the discontinuity sets and set spacing. Other dimensional properties, such as mean coordinate (centroid), and minimum and maximum extent of the plane, are not shown in this example.

Plane numb.	Number of points	Dip direction (°)	Dip angle (°)	Plane equation parameters			
				a	b	c	d (m)
1	7079	341.2	41.6	-0.2143	0.6282	0.7480	4.5531
2	1144	62.4	64.7	0.4186	0.8012	0.4277	9.9420
3	247	325.9	64.5	-0.5063	0.7476	0.4299	5.2673
4	3925	40.8	71.4	0.7181	0.6188	0.3183	8.1410
5	4610	33.6	74.4	0.8022	0.5333	0.2685	7.2198
6	260	223.4	82.1	-0.6802	-0.7201	0.1371	-9.7602
7	705	345.1	43.1	-0.1755	0.6606	0.7300	7.0136
8	2985	34.0	69.6	0.7767	0.5243	0.3490	7.2144
9	1519	33.0	71.7	0.7957	0.5175	0.3147	7.8357
10	11741	31.7	65.3	0.7731	0.4774	0.4176	7.3486

9.4 Classification into discontinuity sets

The processing procedures described in Section 8.2 generate the main geometric properties of each discontinuity plane. The next step is to plot the orientation of each discontinuity plane in a stereographic projection. As discussed in Section 2.2, discontinuity planes generally do not occur with random orientations, but belong to different discontinuity sets. By plotting of the orientations of discontinuity planes in a stereographic plot makes it possible to identify discontinuity sets. In addition, these stereographic plots allow for easy comparisons with stereographic plots representing discontinuities measured by conventional (manual) field methods (see Chapter 5).

After the plotting of the orientations in a stereographic plot, the next step is to classify the individual discontinuity planes into an appropriate number of discontinuity sets. Initially a decision has to be made on the number of discontinuity sets. In most of the cases, where distinct discontinuity sets are present in the scan, this will be straightforward. In other cases, with less distinct sets and/or insufficient observations, the decision on the appropriate number of discontinuity sets becomes more difficult.

9.4.1 Automated fuzzy k-mean clustering

Once the number of discontinuity sets has been established, the individual discontinuity planes can be assigned as members of the appropriate discontinuity set. When there are very few (e.g. in the order of 20 to 30) discontinuity planes, this process can be done manually. In case of a much larger data set, or when an objective clustering evaluation is required, the classification of individual discontinuity planes to discontinuity sets can be done with the fuzzy k-mean clustering method (see Section 3.7.4).

The results of the clustering should still be verified visually, to check whether the results are according to expectations. It may happen that the initial decision on the number of discontinuity sets has to be adjusted, based on the results, and the fuzzy k-means clustering can be repeated until the results are satisfactory.
For instance, if two distinctly different sets remain clustered to a single set, one may have to increase the number of sets to have these two sets clustered as well. On the other hand, if a distinct set is clustered to two sub-sets, the number of sets may be too high and the clustering can be repeated with one set less.

After this classification into discontinuity sets is completed, each of the original points in the point-cloud data can also be defined by an additional label that identifies its membership in a discontinuity set. This new discontinuity set label can in turn be used in the 3-D visualisation through colouring of the points by discontinuity set. This provides a final visual check to verify whether the individual points that form discontinuity planes are indeed classified properly into the correct discontinuity sets.[26]

Finally, for each discontinuity set, the following descriptive orientation statistics are computed based on the orientations of all the individual discontinuity planes within the set (see also section 3.7.3):

- Mean set orientation (dip direction and dip angle in degrees)
- Number of orientations (number of planes)
- The (normalised) resultant vector *R*
- Fisher's constant (*K,* a dimensionless constant)
- Spherical variance (*s*, dimensionless)

[26] This re-colouring of the point cloud according to set number is not possible with Method 2. The Fx software of Method 2 has however the possibility to manually select potential sets in the polar plot after which the corresponding patches in the 3-D view are highlighted. In Method 1 it is not the original point cloud but the vertices of the mesh that are used for the 3-D colouring.

9.4.2 User-specified identification and delineation of discontinuity sets

An alternative way of classifying the discontinuity planes to discontinuity sets is through manual or user-specified delineation of the normals of each individual discontinuity plane, plotted as poles on a stereographic polar plot. Depending of the software used, this can be done interactively on the computer-screen display by manually drawing a circle around a certain cluster, as may be done using the Split-FX software (Split Engineering 2007), or by entering a range in dip angle and dip direction around a chosen cluster centre, as provided by the Dips software (Rocscience 2007). This study implemented the manual delineation method in Matlab. The orientations of the cluster centres were entered and the corresponding threshold angle that determines the cluster size was specified. The location of the cluster centre was simply determined through visual inspection of the stereographic polar plot. Since the locations of the greatest pole densities typically indicate the various cluster centres, a stereographic plot with contour lines of pole density assists in determining the exact location of each set centre.

Once the cluster centres are determined, the orientations of the individual discontinuity planes are compared. The orientation of the normal of each of the discontinuity planes forming the specified discontinuity set may be determined by calculating the dihedral angle (or pole-vector difference - see Equation [18]) between the individual poles and the normal defining the mean orientation of the discontinuity set, i.e.: the centre of the cluster. If the dihedral angle is smaller than the specified threshold angle, the plane belongs to that particular discontinuity set. In this analysis, a circular (Fisher) distribution is assumed. Subsequently, after the classification is complete, several statistics for each discontinuity set are computed, including: the number of planes that belong to the set, Fisher's K value, and spherical variance (s). If the K value is too small, indicating a very large range in orientations of the constituent discontinuity planes, or if the number of discontinuity planes belonging to a single discontinuity set is rather low, the cluster threshold angle can be changed until a more optimal result is achieved.

9.4.3 User-specified versus fuzzy k-means classification

The user-specified delineation method is subjective, compared to the more objective fuzzy k-means clustering. The choice of the cluster centre and threshold angle guiding the manual delineation is merely based on a visual inspection of the stereographic plot. Another issue is that the manual delineation method does not classify all discontinuity planes, while the fuzzy k-means clustering does classify all discontinuity planes into one of the discontinuity sets. With manual delineation, only those discontinuity planes whose normals fall within a circular area around a defined cluster centre are classified, and the unclassified planes will not be considered in the subsequent discontinuity set spacing calculations.

An argument in favour of applying the user-specified delineation method is that there are always some random fractures that do not follow any systematic orientation and can thus be considered 'noise'. Arguably, by excluding these (seemingly) non-systematic fracture planes, the resulting discontinuity model is improved. However, there is no way to determine accurately that these seemingly non-systematic fractures are truly random. In fact, as stated in Section 2.2, no fracture is truly random, but usually follows a preferred direction, caused by the inherent planes of weakness, the discontinuities. Therefore, ideally none of the identified planes in the rock face should therefore be excluded from the analysis.

However, this user-specified delineation method does not allow for a fully automated approach of the processing of the orientation data. The fuzzy k-means clustering only requires the user to enter the number of discontinuity sets to be considered, and then classifies all discontinuity planes in an objective way. The fuzzy k-means clustering is therefore the method that is used in all of the subsequent analyses.

9.5 Calculating normal set spacing

After the clustering of the individual discontinuity planes into discontinuity sets, each individual discontinuity plane is identified with both its individual plane number and its discontinuity set number. The computation of the plane geometry described in Section 9.2 determined the plane equation parameters (*a*, *b*, *c* and *d*) for each discontinuity plane (see Table 9.1). Since each discontinuity plane within each discontinuity set is thus uniquely defined in 3-D space, it becomes relatively easy to compute the normal set spacing values. The normal set spacing is usually computed based on scanline survey data, which is, by definition, measured along an intersecting line that is parallel to the mean orientation of the particular set (see Section 3.2.2). However, data generated by laser-scanning procedures is not restricted to a line, but is distributed in 3-D space. This provides additional ways for computing normal set spacing. The derivation of total spacing and set spacing is not considered, since these are specific for scanline data and typically are converted into normal set spacing in any case. To compute the normal set spacing, two methods were developed, which are described in Sections 9.5.1 and 9.5.2.

9.5.1 Calculation of normal set spacing by using a virtual scanline

This method is based on adapting the "conventional" method of determining normal set spacing, following the definition given by Priest (1993). The first step is to define a "virtual scanline", which is oriented parallel to the mean orientation of the discontinuity set. This virtual scanline can be placed at any position in the surveyed 3-D volume occupied by point-cloud data of the scanned rock face. However, in order to obtain an optimum result, the virtual scanline is located such that it intersects with the coordinate that is the exact centre of all the discontinuity planes in the discontinuity set being evaluated (see Figure 9.1). The virtual scanline can thus be represented by the following (line) equation:

$$\begin{pmatrix} x \\ y \\ z \end{pmatrix} = \begin{pmatrix} x_0 \\ y_0 \\ z_0 \end{pmatrix} + t \begin{pmatrix} a_n \\ b_n \\ c_n \end{pmatrix} \quad [55]$$

Where:

- x_0, y_0 and z_0 are the coordinates of the centre of all the discontinuity planes forming the discontinuity set (in metres)
- a_n, b_n and z_0 are the parameters of the discontinuity set mean normal (pole) vector, whose (normalised) length is 1 meter. The set's mean normal vector is derived from the mean discontinuity set orientation.
- t is a multiplication factor that defines each point on the virtual scanline.

The problem is now reduced to finding the intersection point of the virtual scanline with the various discontinuity planes in the discontinuity set. Since the equations for individual planes are known, the intersection point along the virtual scanline is found by substituting the plane equation with the equation of the virtual scanline (Equation [55]). This gives the value for *t* for each intersection. The normal set spacings are computed by sorting the values of *t* in an ascending or descending order, and then by subtracting adjacent *t* values. Because the line equation is based on the normalised vector of the pole to the mean set orientation, the *t* values, and thus the spacings, are in metres. By plotting the found spacings in a histogram, the spacing distribution can be visualised (see Figure 9.3 to Figure 9.6).

This method will be affected by the choice of the location of the virtual scanline. The most logical and objective location choice, adopted by this research, is to make the virtual scanline go through the centre of all the discontinuity planes in the discontinuity set. However, another location would be equally correct, according to the definition by Priest (1993), yet it will yield different results. The reason for this is that the individual discontinuity planes within a defined discontinuity set are never

perfectly parallel and will vary in orientation within the set. This variability is expressed by the spherical variance (*s*) or the Fisher's constant *K*). Different planes within a set with a large difference in orientation can even cross each other when they are projected over larger distances. This is also possible in reality. In addition, individual discontinuity planes are never perfectly planar, while a (virtual) projection of these planes assumes that this is the case. In addition, the spacings between the intersection points along the virtual scanline will vary, depending on the choice of the location of the virtual scanline (see planes P1 and P2 in Figure 9.1, for example). Therefore, the choice of the placement of the virtual scanline influences the outcome. On the other hand, this is also the case for a real scanline in the field, so this method agrees with the conventional approach.

Another problem with this method results from the projection of several (smaller) planes that are actually part of the same discontinuity plane. This is a common situation when a single discontinuity plane is not continuously exposed in the rock face. The various exposed patches of the same plane are thus segmented as individual planes and, when projected to the virtual scanline, these small planar patches belonging to the same discontinuity plane will intersect the virtual scanline at different points. Minor differences in orientation make this result a rather common occurrence. In these cases, clusters of closely spaced intersection points on the virtual scanline will occur. It may be possible to visually examine the sequence of intersection values, and replace these clusters with a single intersection point. However, such a manual re-evaluation is neither simple nor without potential bias. It should be noted that the Hough-transform-based method (Method 4, see Section 8.5) is able to segment the points from different patches to the same plane, but only if the plane is (perfectly) planar. If this is the case, the problem is eliminated.

9.5.2 Calculation of "equivalent" normal set spacing by using the plane equations

A second method of determining the spacing values between individual discontinuity planes within a discontinuity set is to use the distance parameter *d* of the available plane equations representing each individual plane. The distance parameter *d* is the perpendicular distance of the plane to the origin of the point-cloud coordinates. Thus, if the distances *d* of all planes are simply sorted in an ascending or descending order, the differences between subsequent values are then the discontinuity spacing values. These values are referred to as "equivalent" normal set spacing values. The distance value *d* depends on the choice of the origin.

Ideally, the origin should be chosen similar to the choice of the location of the virtual scanline in the previously described method, i.e. through the centre of all the planes defining the discontinuity set. Thus, the values of *d* are recomputed from the centre of the entire point cloud to the centre of all the planes belonging to the discontinuity set. In this way, the spacing values will be most similar with the conventional normal set computation. However, these discontinuity spacing values will still differ from the conventional normal set spacing values as defined by Priest (1993). In the conventional calculation of normal set spacing values, the planes are projected linearly to intersect a selected virtual scanline (see Section 9.5.1). However, this equivalent normal set spacing method can be visualised as the projection of circles from selected origin. Each circle is expanded until it touches the plane in a single point. The radius of each projected circle is thus the perpendicular distance of the plane to the selected origin, and this is the distance represented by parameter *d* (see Figure 9.2). Thus, although the same origin is used by both methods (the centre of all the planes defining the discontinuity set), the distance values *d*, and the equivalent normal spacing values derived from them, will not be exactly the same as the normal spacing values computed from the linear projection method used to identify the intersections along the virtual scanline.

Although both methods yield results that vary with the choice of the origin, a closer similarity can be expected if a common origin is used. This second method has an advantage because the calculation is more straightforward, since determination of the mean normal set orientation (to define the virtual scanline orientation) is not required. Only the computation of the set coordinate centre is necessary and the re-computation of the distance *d* values based on this new origin. The same issues remain concerning the management of multiple planes that are actually part of the

same discontinuity plane. Once again, this method results in (very) small spacings that do not exist in reality (see S6 - spacing 6 - between the planes P6 and P7 in Figure 9.2).

9.5.3 Calculation of set spacing statistics

After computation of the list of normal set spacing values and/or equivalent normal set spacing values, the results can be visualised in a histogram, as described in Section 3.7.2.4. As discussed in the previous sections, the methods to compute spacing distances introduce (erroneously) small spacing values that are not representative for the actual rock mass. However, the frequency of occurrence of the very small spacing values is generally very small. The influence on the computation of the average normal and equivalent normal set spacing is therefore very small as well. An example is given in Figure 9.3 and Figure 9.5, where the histograms of, respectively, the normal and equivalent normal set spacing values are shown. Both histograms show a strong negative exponential or lognormal distribution, which is common for discontinuity spacing data. The first bin probably contains all the small spacing values that are introduced by the computation. In order to obtain a better view of the distribution in the smaller and higher spacing regions, the data should be transformed and shown in a logarithmic frequency distribution instead. The logarithmic frequency distribution then shows a distribution that more closely resembles a normal distribution.

Figure 9.4 and Figure 9.6 provide examples of the converted logarithmic frequency distributions for the normal and equivalent normal set spacing values. Appendix J contains similar histograms illustrating the normal and equivalent normal spacing values for all discontinuity sets for Site 1 (Bellmunt) and Site 2 (Toroja), as defined by all four point-cloud data analysis methods.

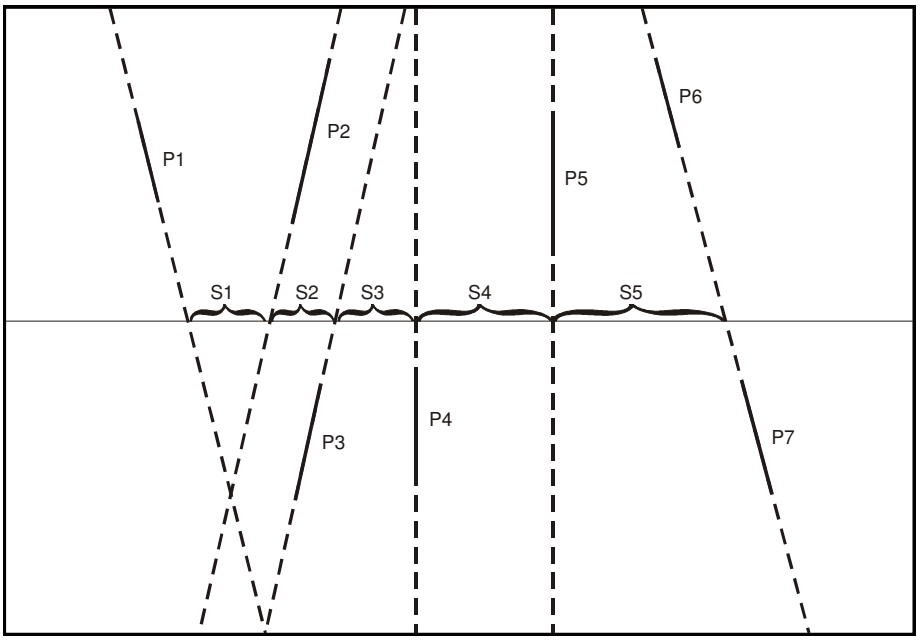

Figure 9.1. This diagram illustrates the principle of deriving normal set spacing with a virtual scanline. The virtual scanline is oriented parallel to the mean set orientation, but can in theory be placed anywhere. Here, the virtual scanline is chosen such that it intersects the point that is the spatial mean of the centre points of all planes. In this illustration, the planes are the lines annotated with P1, P2, etc. The dashed lines are the projected parts of the planes that show how they intersect the virtual scanline.

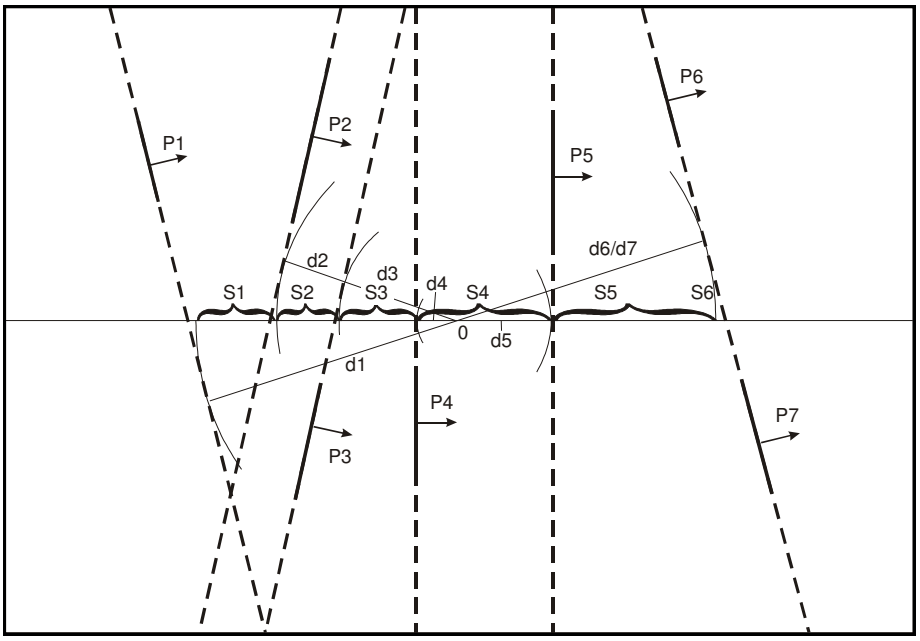

Figure 9.2. This diagram illustrates the principle of deriving the "equivalent" normal set spacing based on the re-computation of the distance d values of the planes equations which depend on the selection of the set origin (O)

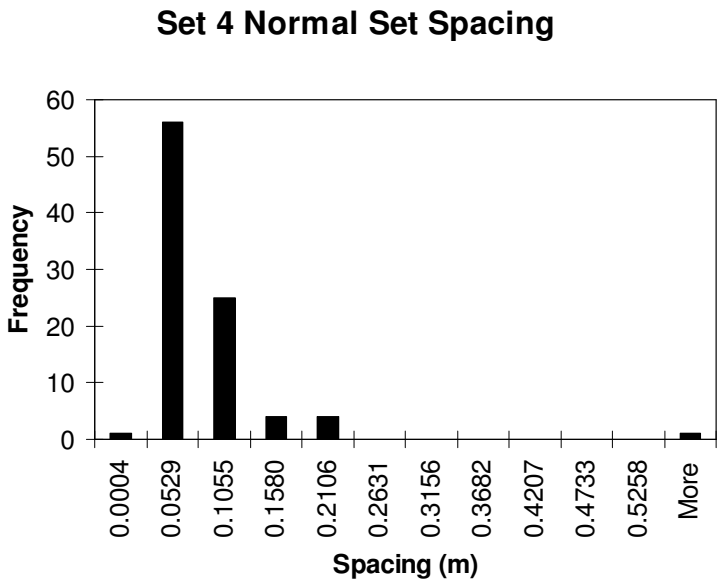

Figure 9.3. Histogram showing the frequency distribution of the normal set spacing values for Set 4 (bedding or cleavage) of Site 1, calculated with Method 1. This representation does not properly show the importance of the very small discontinuity set spacing values, which have a large influence on the average spacing value. The arithmetic mean of the spacing values is 0.051 m (see also Table 9.2).

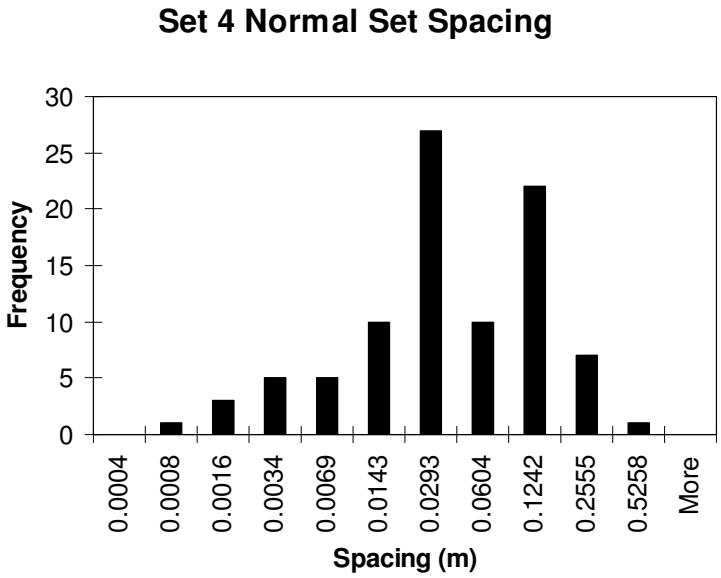

Figure 9.4. Histogram showing the logarithmic frequency distribution of the normal set spacing values for set 4 (bedding or cleavage) of Site 1, calculated with Method 1. This distribution more clearly shows the variation in spacing (the geometric mean spacing = 0.0251 m).

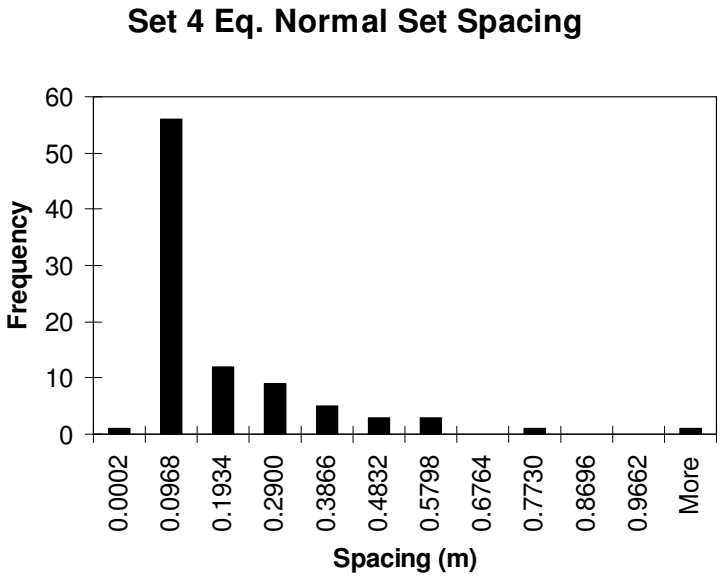

Figure 9.5. Histogram showing the frequency distribution of the *equivalent* normal set spacing values for Set 4 (bedding or cleavage) of Site 1, calculated with Method 1. The arithmetic mean of the spacing values is 0.135 m (see also Table 9.2).

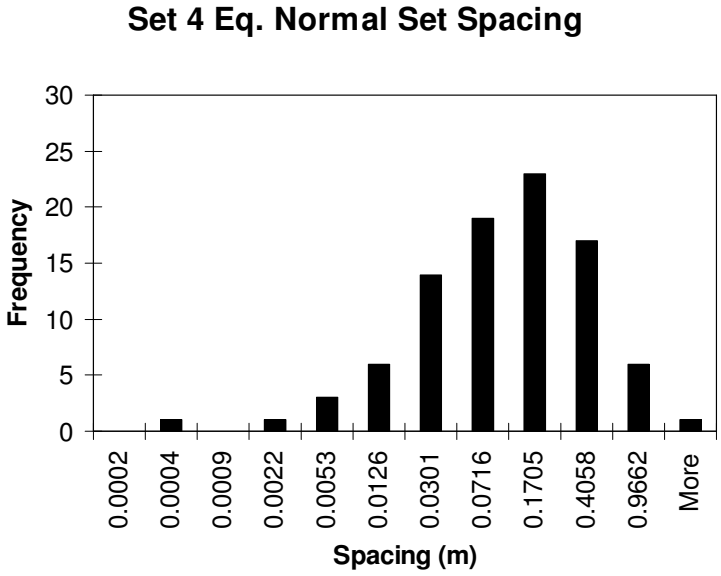

Figure 9.6. Histogram showing the logarithmic frequency distribution of the *equivalent* normal set spacing values for set 4 (bedding or cleavage) of Site 1, calculated with Method 1. Similar to Figure 9.4 this representation shows that very small discontinuity spacing values (smaller than 1 cm) do not have a very large influence on the mean equivalent normal spacing value.

9.6 Computed discontinuity set properties for Site 1: Bellmunt

This section provides the results of the geometric discontinuity property derivations for Site 1. These analyses utilise the discontinuity planes generated by the point cloud data processing Methods 1 to 4, that were discussed in the Chapters 7 and 8. The results for each Method are described in separate Sections. For Site 1, the orientations of the discontinuity planes produced by each Method 2, 3 and 4 are clustered using fuzzy k-means clustering procedures into five clusters. Each cluster corresponds to a discontinuity set.

As discussed in the Section 7.3.3, Method 1 creates discontinuity sets during the point-cloud processing phase, which are subsequently subdivided into individual discontinuity planes. Hence, the list of discontinuity planes generated by Method 1 already identifies the discontinuity set number to which each individual discontinuity plane belongs. The actual plane lists are not included in this thesis. The following sections provide these results:

- The discontinuity set statistics (in table form)
- A 3-D illustration of the defined discontinuity sets: for Method 1, the vertices of the fitted 3-D mesh are coloured to show discontinuity sets; Method 2 does not allow production of a similar coloured view of discontinuity sets; for Methods 3 and 4, the point-cloud is coloured to show discontinuity sets.
- Stereographic polar plot of all the discontinuity planes extracted with each point-cloud processing method. Pole density is shown in colour and individual poles are plotted as black dots
- Stereographic polar plot of all the discontinuity planes, similar to the previous illustration, but now the poles are coloured according to their discontinuity set membership, while the pole density is shown in grey scale

9.6.1 Site 1 Method 1: Surface reconstruction with implicit representation

The point cloud processing by method 1 for the data from Site 1 gives the following results:

- Table 9.2: containing the discontinuity set statistics for all 5 discontinuity sets;
- Figure 9.8: the vertices of the fitted 3-D mesh, coloured by discontinuity set;
- Figure 9.9: stereographic polar plot showing coloured pole density plot for all discontinuity planes;
- Figure 9.10: stereographic polar plot of all the discontinuity planes with the poles coloured according to their discontinuity set membership and with the pole density shown in grey-scale

Table 9.2. Results of discontinuity set calculations for site 1 with method 1.

	Set 1	Set 2	Set 3	Set 4	Set 5
Dip angle (°)	43.79	62.74	53.73	71.94	79.98
Dip direction (°)	345.85	153.64	24.55	55.27	255.43
R (norm. result. vector)	0.98	0.92	0.98	0.98	0.98
N (# of poles)	83	92	80	64	84
K (Fisher's constant)	55.17	12.42	50.26	52.68	56.32
s (spherical variance)	0.1330	0.2807	0.1393	0.1356	0.1317
Mean normal spacing (m)	0.039	0.025	0.041	0.021	0.020
Mean eq. nrml. spacing (m)	0.114	0.095	0.107	0.106	0.050
Std.dev. normal spacing (m)	0.046	0.038	0.060	0.036	0.034
Std.dev. eq.nrml. spacing (m)	0.164	0.193	0.114	0.134	0.097
Max. normal spacing (m)	0.287	0.275	0.288	0.275	0.312
Max. eq. nrml. spacing (m)	1.080	1.630	0.581	0.906	0.549

Total number of discontinuity planes: 403

Figure 9.7. This photo shows the section of the rock face at Site 1 that corresponds with the outline of the coloured point cloud shown in Figure 9.8 below.

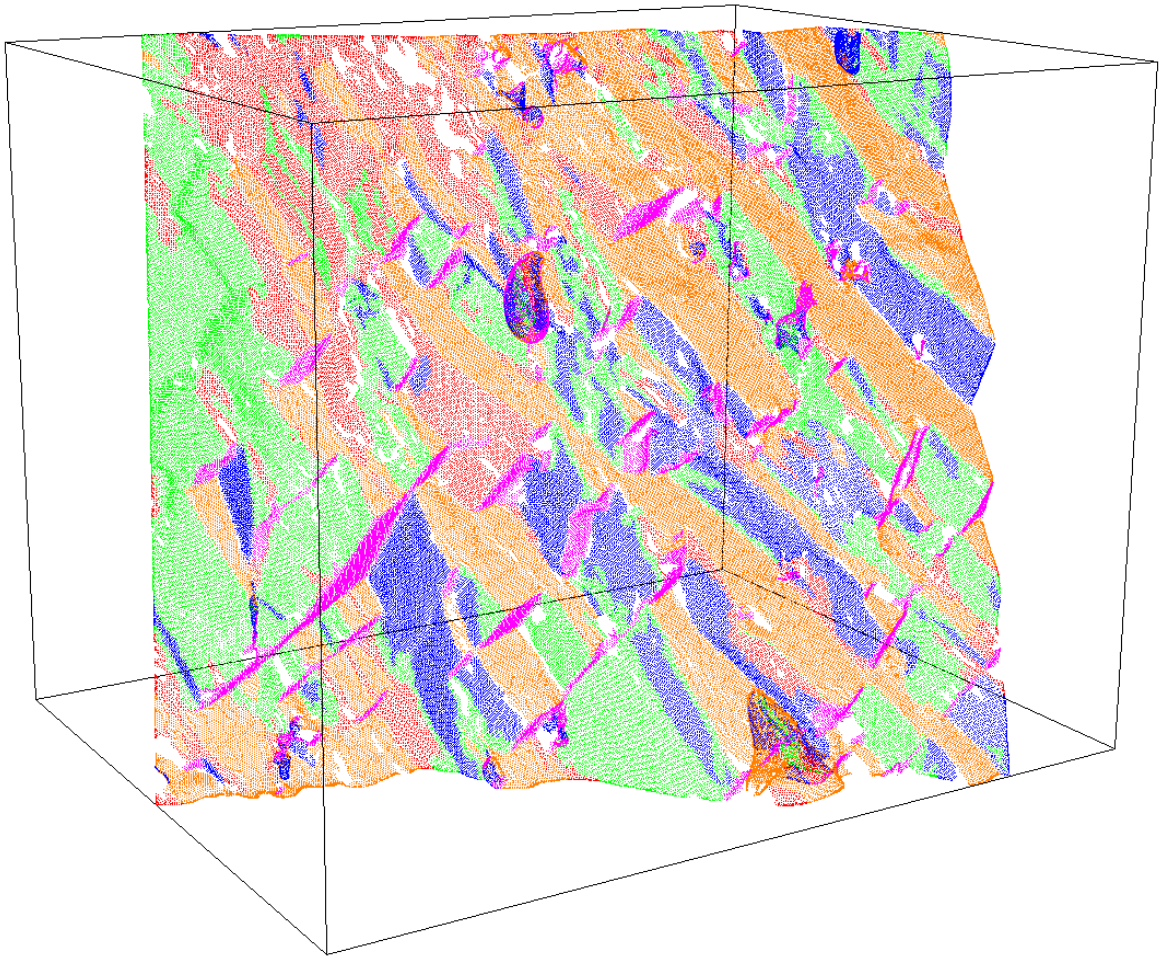

Figure 9.8. The vertices of the of the 3-D meshed surface (not the original point cloud) coloured according to their membership in the 5 identified discontinuity sets. Points belonging to the same discontinuity set, receive the same colour. The colours are similar to the colours used in the stereographic plot (see Figure 9.10).

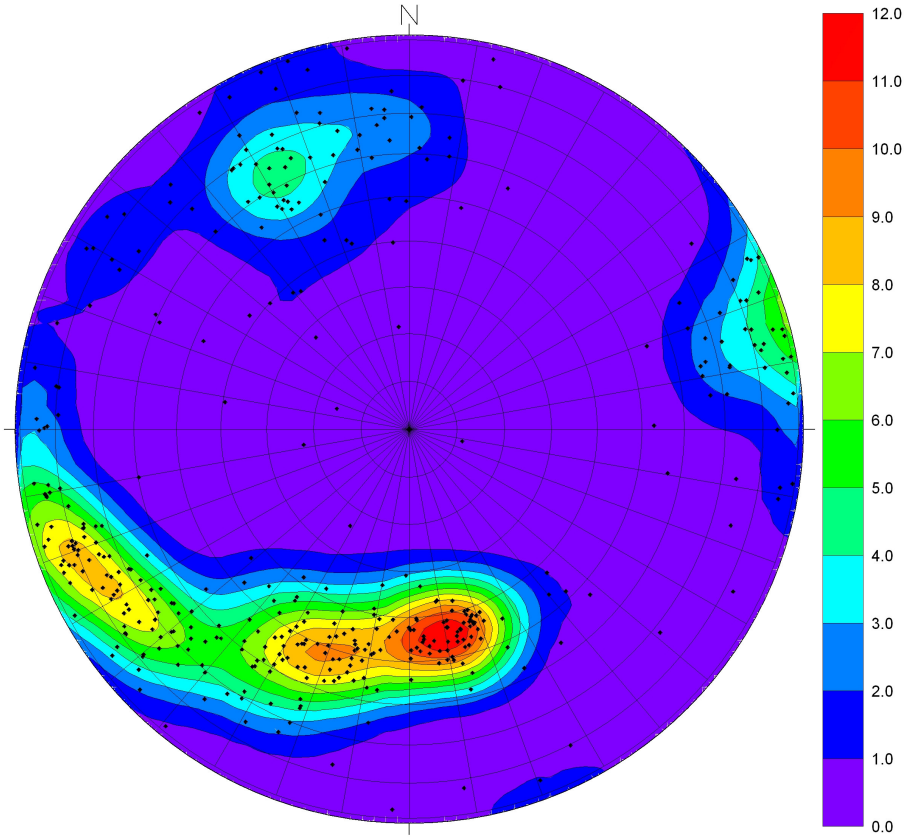

Figure 9.9. Stereographic polar plot of all the individual planes found with segmentation Method 1 at Site 1. 403 planes were found. The colour contours reflect pole densities.

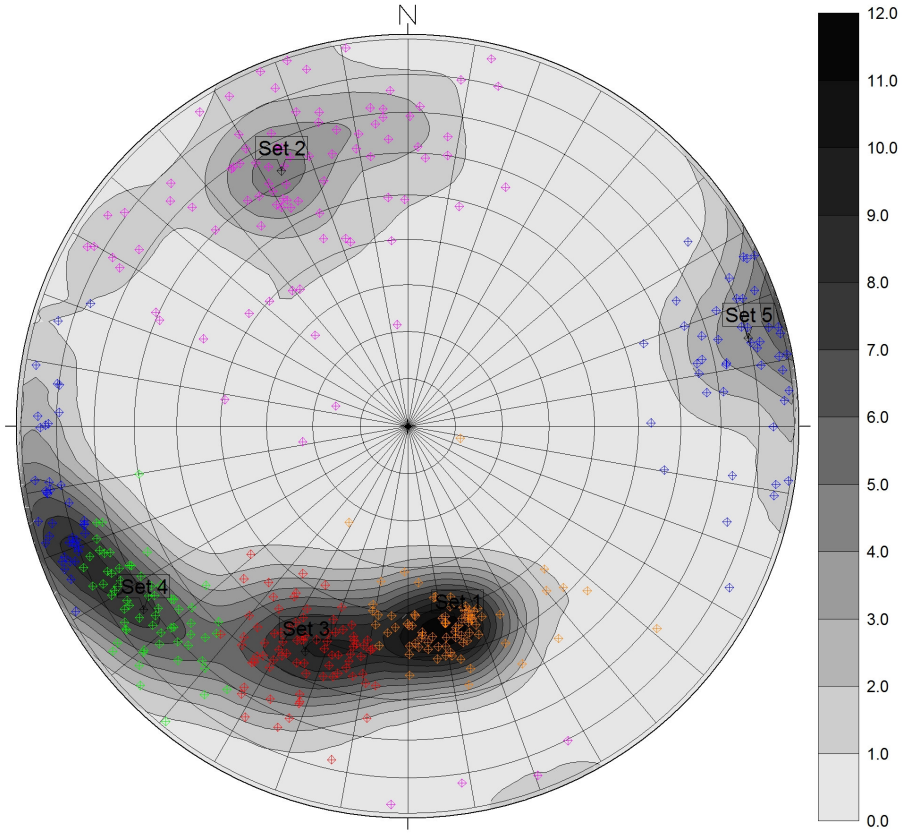

Figure 9.10. Stereographic polar plot with the poles for the discontinuity planes classified into 5 discontinuity sets using fuzzy k-means clustering. The grey-scaled contours correspond to pole densities.

9.6.2 Site 1 Method 2: Surface reconstruction with 2-D gridding (Split-FX)

The point cloud processing by Method 2 for the data from Site 1 gives the following results:

- Table 9.3: containing the discontinuity set statistics for all 5 discontinuity sets;
- Figure 9.11: stereographic polar plot showing coloured pole density for all discontinuity planes;
- Figure 9.12: stereographic polar plot of all the discontinuity planes with the poles coloured according to their discontinuity set membership and with the pole density shown in grey scale.

Table 9.3. Results of discontinuity set calculations for site 1 with method 2.

	Set 1	Set 2	Set 3	Set 4	Set 5
Dip angle (°)	39.25	50.01	44.88	62.95	48.53
Dip direction (°)	342.00	145.29	18.31	55.64	257.02
R (norm. result. vector)	0.98	0.92	0.98	0.97	0.95
N (# of poles)	72	45	44	55	25
K (Fisher's constant)	52.00	11.29	40.63	29.18	16.64
s (spherical variance)	0.1365	0.2909	0.1533	0.1817	0.2351
Mean normal spacing (m)	0.049	0.084	0.043	0.052	0.154
Mean eq. nrml. spacing (m)	0.102	0.537	0.164	0.171	0.929
Std.dev. normal spacing (m)	0.065	0.092	0.069	0.077	0.193
Std.dev. eq.nrml. spacing (m)	0.157	1.366	0.239	0.313	1.822
Max. normal spacing (m)	0.398	0.336	0.384	0.472	0.863
Max. eq. nrml. spacing (m)	0.948	8.269	1.393	1.591	8.998

Total number of discontinuity planes: 241

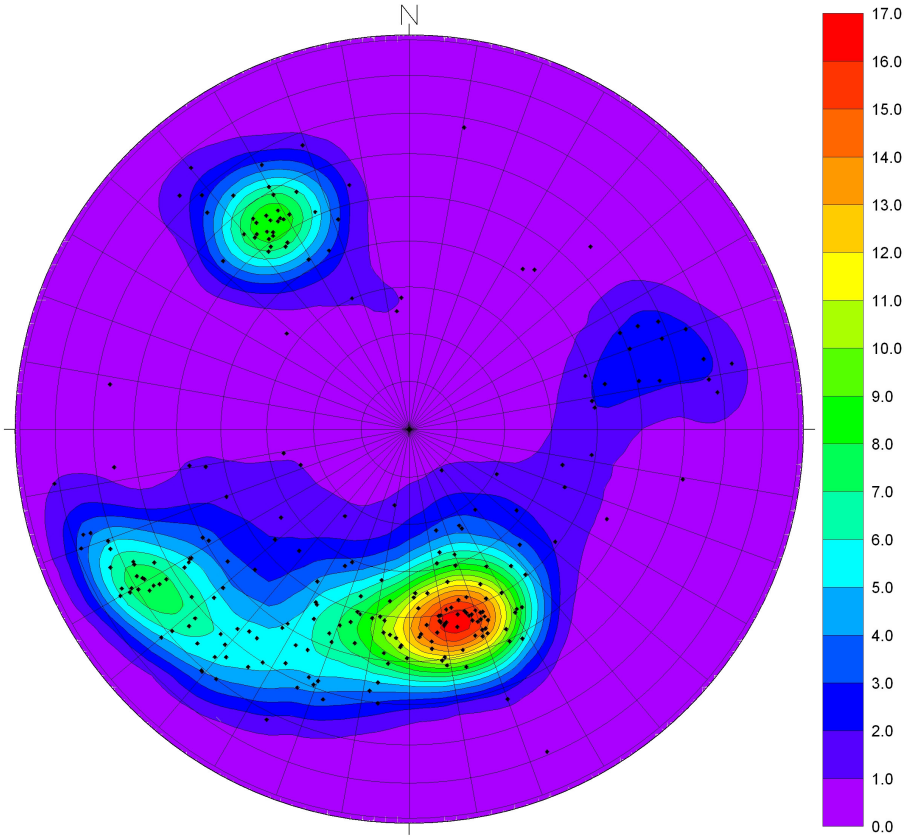

Figure 9.11. Stereographic polar plot of all the individual planes found with segmentation Method 2 at Site 1. In total 241 planes were found. The colour contours reflect pole densities.

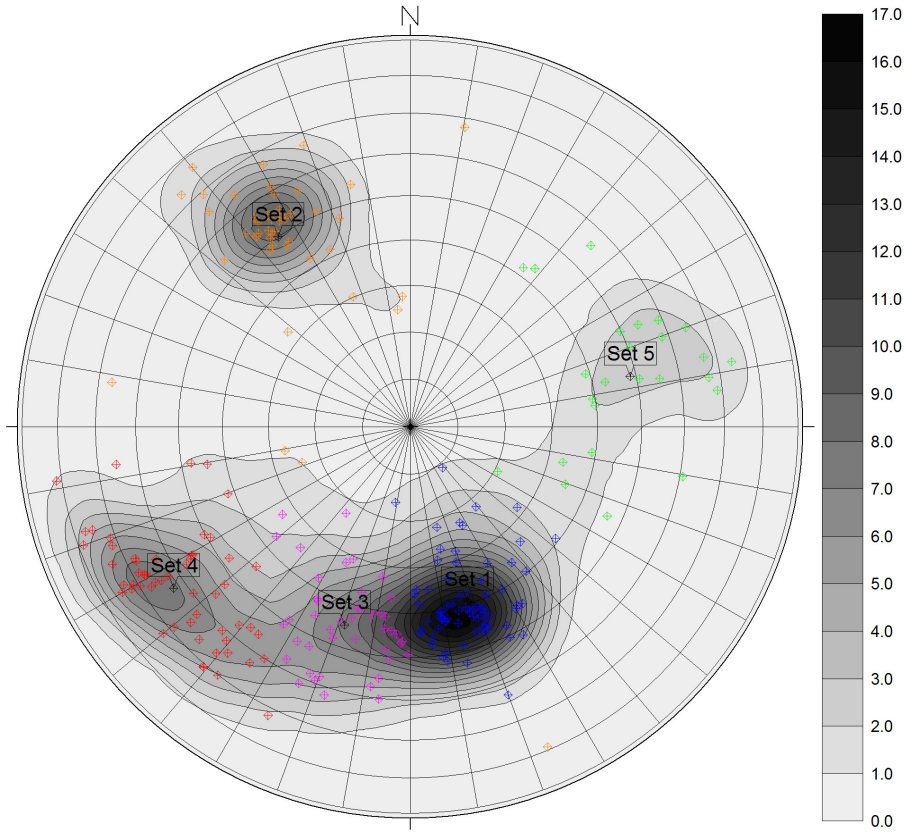

Figure 9.12. Stereographic polar plot with the poles for the discontinuity planes classified into 5 discontinuity sets using fuzzy k-means clustering. The grey-scaled contours correspond to pole densities.

9.6.3 Site 1 Method 3 – Segmentation with PCA (Matlab)

The point cloud processing method 3 for the data from site 1 gives the following results:

- Table 9.4: containing the discontinuity set statistics for all 5 discontinuity sets;
- Figure 9.14: the point cloud points, coloured by discontinuity set;
- Figure 9.15: stereographic polar plot showing coloured pole density for all discontinuity planes;
- Figure 9.16: stereographic polar plot of all the discontinuity planes with the poles coloured according to their discontinuity set membership and with the pole density shown in grey scale.

Table 9.4. Results of discontinuity set calculations for site 1 with method 3.

	Set 1	Set 2	Set 3	Set 4	Set 5
Dip angle (°)	46.87	68.31	63.30	73.38	71.62
Dip direction (°)	346.82	156.66	20.27	57.29	227.23
R (norm. result. vector)	0.98	0.96	0.97	0.96	0.94
N (# of poles)	188	102	91	119	103
K (Fisher's constant)	59.36	24.63	33.33	26.75	17.05
s (spherical variance)	0.1291	0.1995	0.1713	0.1917	0.2399
Mean normal spacing (m)	0.020	0.039	0.021	0.025	0.041
Mean eq. nrml. spacing (m)	0.050	0.114	0.106	0.095	0.107
Std.dev. normal spacing (m)	0.034	0.046	0.036	0.038	0.060
Std.dev. eq.nrml. spacing (m)	0.097	0.164	0.134	0.193	0.114
Max. normal spacing (m)	0.312	0.287	0.275	0.275	0.288
Max. eq. nrml. spacing (m)	0.549	1.080	0.906	1.630	0.581

Total number of discontinuity planes: 603

Figure 9.13. This photo shows the section of the rock face at Site 1 that corresponds with outline of the coloured point cloud shown in Figure 9.14 below.

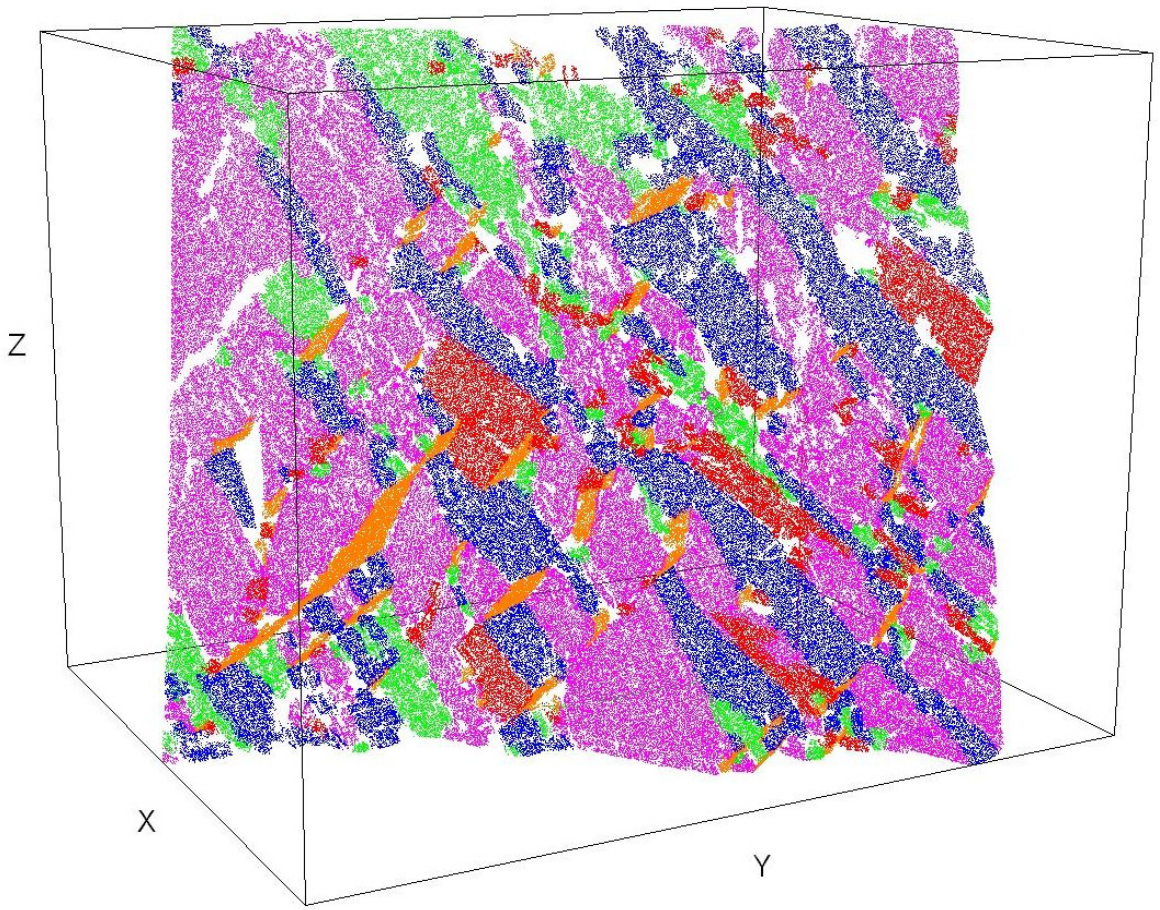

Figure 9.14. The point cloud points are coloured according to their membership in the 5 identified discontinuity sets. Points belonging to the same discontinuity set, receive the same colour. The colours are equivalent to the colours used in the stereographic plot (see Figure 9.16).

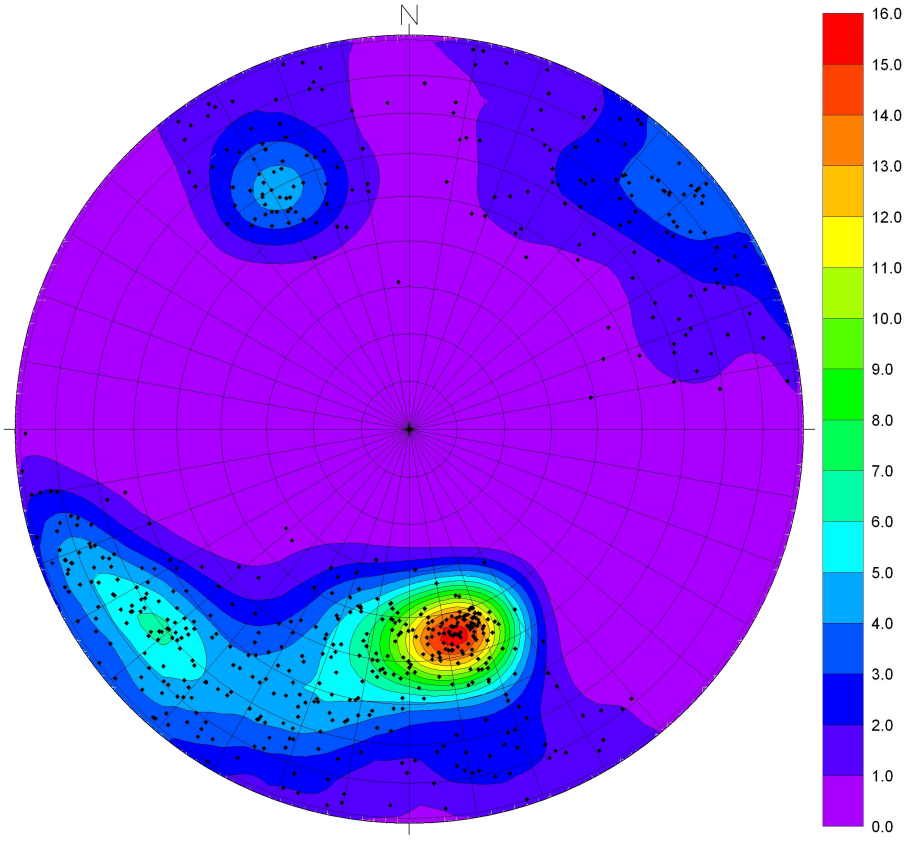

Figure 9.15. Stereographic polar plot of all the individual discontinuity planes found with segmentation Method 3 at Site 1. In total 603 planes were found. The colour contours reflect pole densities.

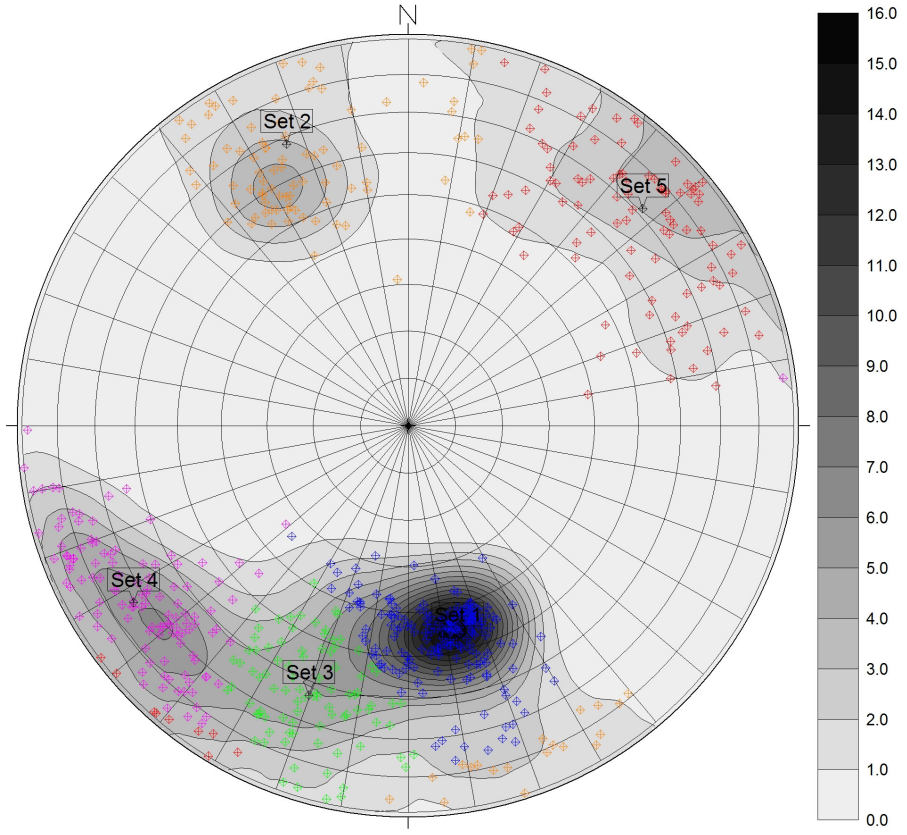

Figure 9.16. Stereographic polar plot with the poles for the discontinuity planes classified into 5 sets using fuzzy k-means clustering. The grey-scaled contours correspond to pole densities. The colours are equivalent to the colours used in Figure 9.14. The grey-scaled contours are pole densities

9.6.4 Site 1 Method 4: Segmentation with PCM

The point cloud processing by Method 4 for the data from Site 1 gives the following results:

- Table 9.5: containing the discontinuity set statistics for all 5 discontinuity sets;
- Figure 9.18: the point-cloud points, coloured by discontinuity set;
- Figure 9.19: stereographic polar plot showing coloured pole density for all discontinuity planes;
- Figure 9.20: stereographic polar plot of all the discontinuity planes with the poles coloured according to their discontinuity set membership and with the pole density shown in grey scale.

Table 9.5. Results of discontinuity set calculations for site 1 with method 4.

	Set 1	Set 2	Set 3	Set 4	Set 5
Dip angle (°)	43.46	61.06	56.76	76.63	76.09
Dip direction (°)	342.67	145.39	23.24	45.48	72.15
R (norm. result. vector)	0.96	0.91	0.96	0.98	0.98
N (# of poles)	128	92	64	86	123
K (Fisher's constant)	23.32	10.78	25.20	38.38	42.00
s (spherical variance)	0.2054	0.3012	0.1961	0.1595	0.1527
Mean normal spacing (m)	0.040	0.076	0.047	0.032	0.041
Mean eq. nrml. spacing (m)	0.085	0.146	0.153	0.096	0.087
Std.dev. normal spacing (m)	0.069	0.191	0.106	0.045	0.068
Std.dev. eq.nrml. spacing (m)	0.182	0.166	0.198	0.108	0.123
Max. normal spacing (m)	0.507	1.611	0.742	0.318	0.422
Max. eq. nrml. spacing (m)	1.435	1.002	1.287	0.668	0.987

Total number of discontinuity planes: 493

Figure 9.17. This photo shows part of the rock face of Site 1 that corresponds with the outline of the coloured point cloud shown in Figure 9.18 below.

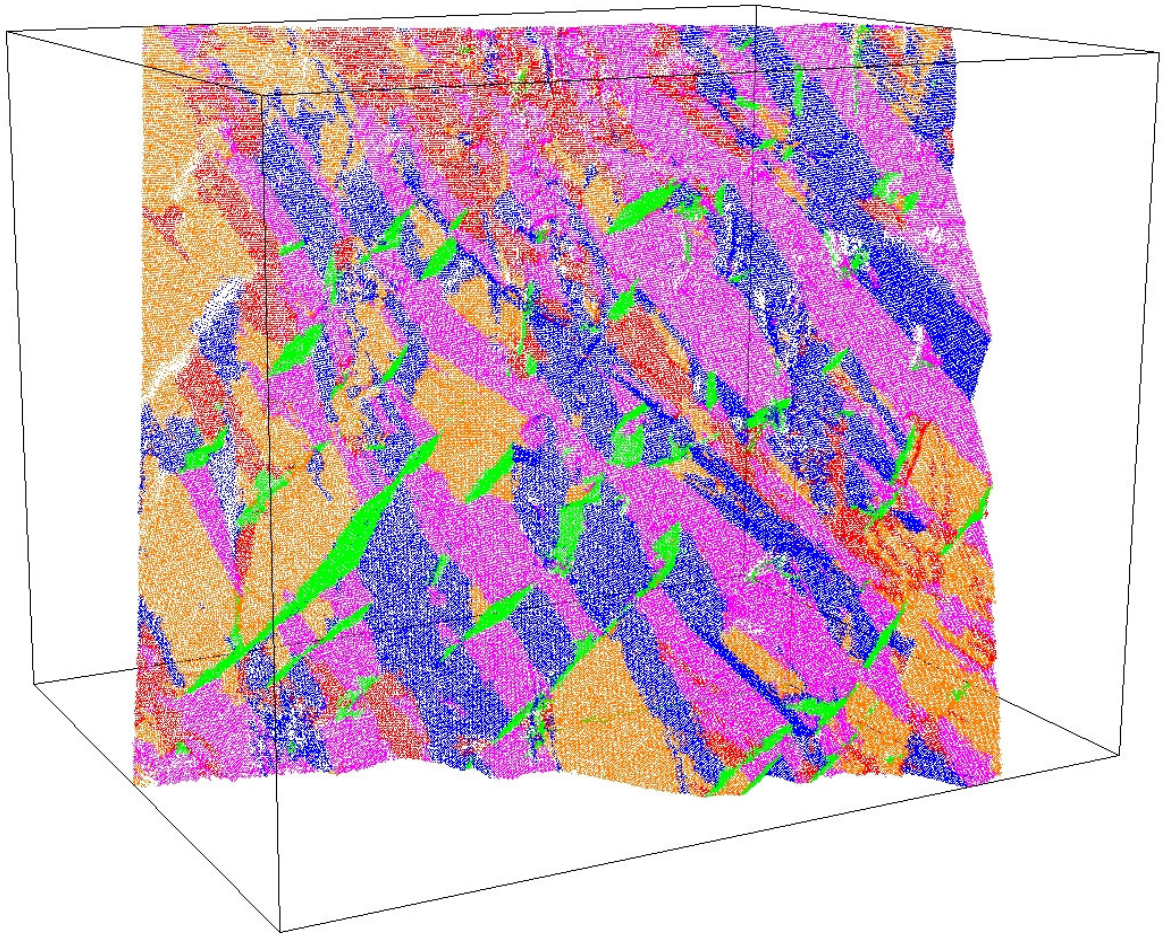

Figure 9.18. The point-cloud points are coloured according to their membership in the 5 identified discontinuity sets. Points belonging to the same discontinuity set, receive the same colour. The colours are equivalent to the colours used in the stereographic plot (see Figure 9.20).

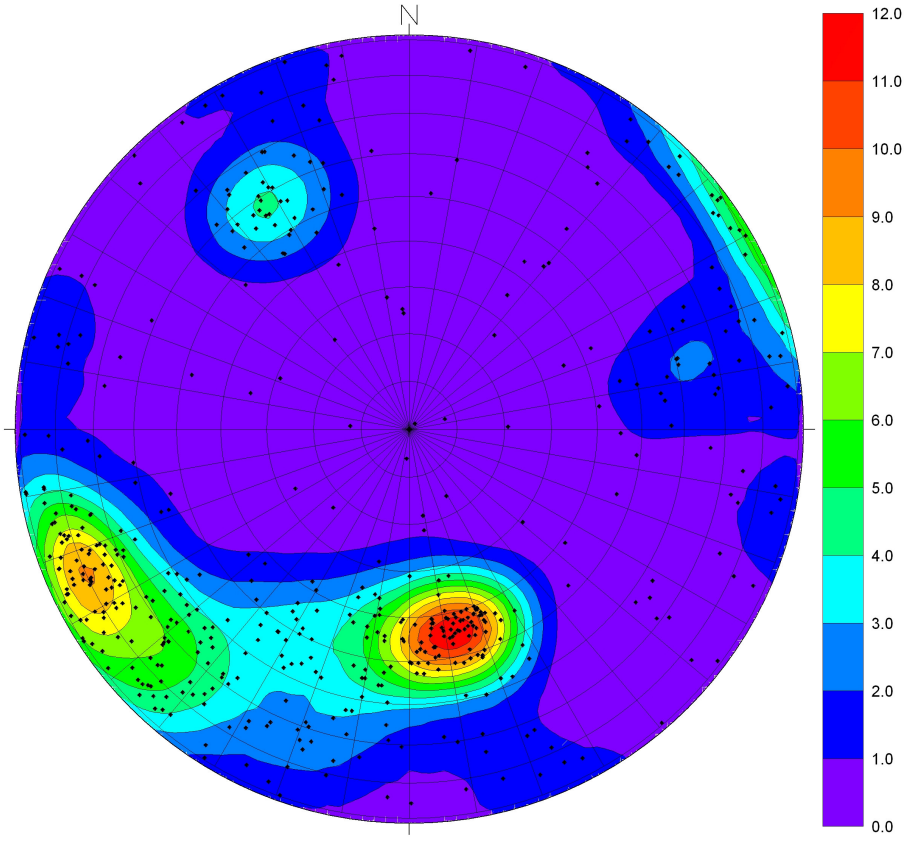

Figure 9.19. Stereographic polar plot of all the individual discontinuity planes found with segmentation Method 4 on Site 1. In total 493 planes were found. The colour contours reflect pole densities.

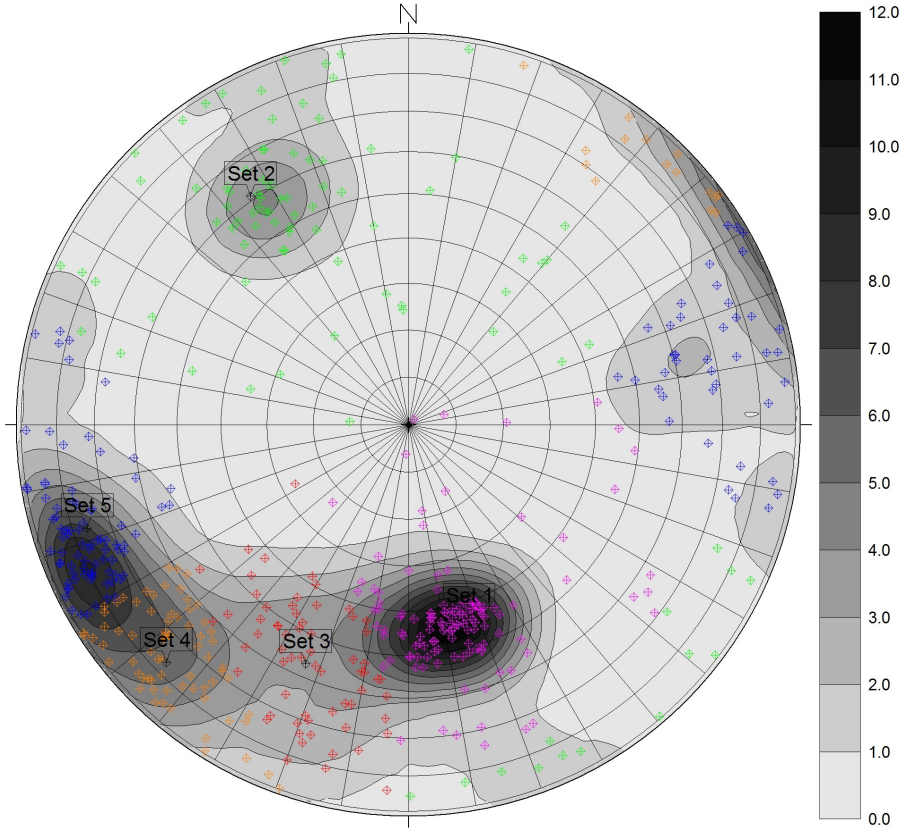

Figure 9.20. Stereographic polar plot with the poles for the discontinuity planes classified into discontinuity 5 sets using fuzzy k-means clustering. The grey-scaled contours correspond to pole densities.

9.7 Computed discontinuity set properties for Site 2: Torroja

This section provides the results of the geometric discontinuity property derivations for Site 2. These analyses utilize the discontinuity planes generated by the point-cloud data processing Methods 1 to 4 discussed in Chapters 7 and 8. The results for each Method are described in separate Sections. For Site 2, the orientations of the discontinuity planes produced by each Method 2, 3, and 4 are clustered using fuzzy k-means clustering procedures into four clusters. Each cluster corresponds to a discontinuity set.

As discussed in the Section 7.3.3, Method 1 creates discontinuity sets during the point-cloud processing phase, and these are subsequently subdivided into individual discontinuity planes. Hence, the list of discontinuity planes generated by Method 1 already identifies the discontinuity set number to which each individual discontinuity plane belongs. The actual plane lists are not included in this thesis.

The following sections provide these results:

- The discontinuity set statistics (in table form)
- A 3-D illustration of the defined discontinuity sets: for Method 1, the vertices of the fitted 3-D mesh are coloured to show discontinuity sets; Method 2 does not allow production of a similar coloured view of discontinuity sets; for Methods 3 and 4, the point-cloud is coloured to show discontinuity sets.
- Stereographic polar plot of all the discontinuity planes extracted with each point-cloud processing method. Pole density is shown in colour and individual poles are plotted as black dots.
- Stereographic polar plot of all the discontinuity planes, similar to the previous illustration, but now the poles are coloured according to their discontinuity set membership, while the pole density is shown in grey scale.

9.7.1 Site 2 Method 1: Surface reconstruction with implicit representation

The point cloud processing Method 1 for the data from Site 2 gives the following results:

- Table 9.6: containing the discontinuity set statistics for all 4 discontinuity sets;
- Figure 9.22: the vertices of the fitted 3-D mesh, coloured by discontinuity set;
- Figure 9.23: stereographic polar plot showing coloured pole density for all discontinuity planes;
- Figure 9.24: stereographic polar plot of all the discontinuity planes with the poles coloured according to their discontinuity set membership and with the pole density shown in grey scale.

Table 9.6. Results of discontinuity set calculations for site 2 with method 1.

	Set 1	Set 2	Set 3	Set 4
Dip angle (°)	82.92	70.87	56.38	39.28
Dip direction (°)	30.91	249.68	132.64	298.29
R (norm. result. vector)	0.97	0.97	0.92	0.93
N (# of poles)	47	47	74	97
K (Fisher's constant)	32.46	31.52	12.31	14.58
s (spherical variance)	0.1718	0.1743	0.2811	0.2591
Mean normal spacing (m)	0.098	0.055	0.066	0.041
Mean eq. nrml. spacing (m)	0.087	0.053	0.054	0.033
Std.dev. normal spacing (m)	0.149	0.070	0.084	0.095
Std.dev. eq.nrml. spacing (m)	0.112	0.073	0.063	0.060
Max. normal spacing (m)	0.655	0.381	0.490	0.855
Max. eq. nrml. spacing (m)	0.438	0.447	0.362	0.473

Total number of discontinuity planes: 265

Figure 9.21. This photo shows part of the rock face of Site 2 that corresponds with the outline of the coloured point cloud shown in Figure 9.22 below.

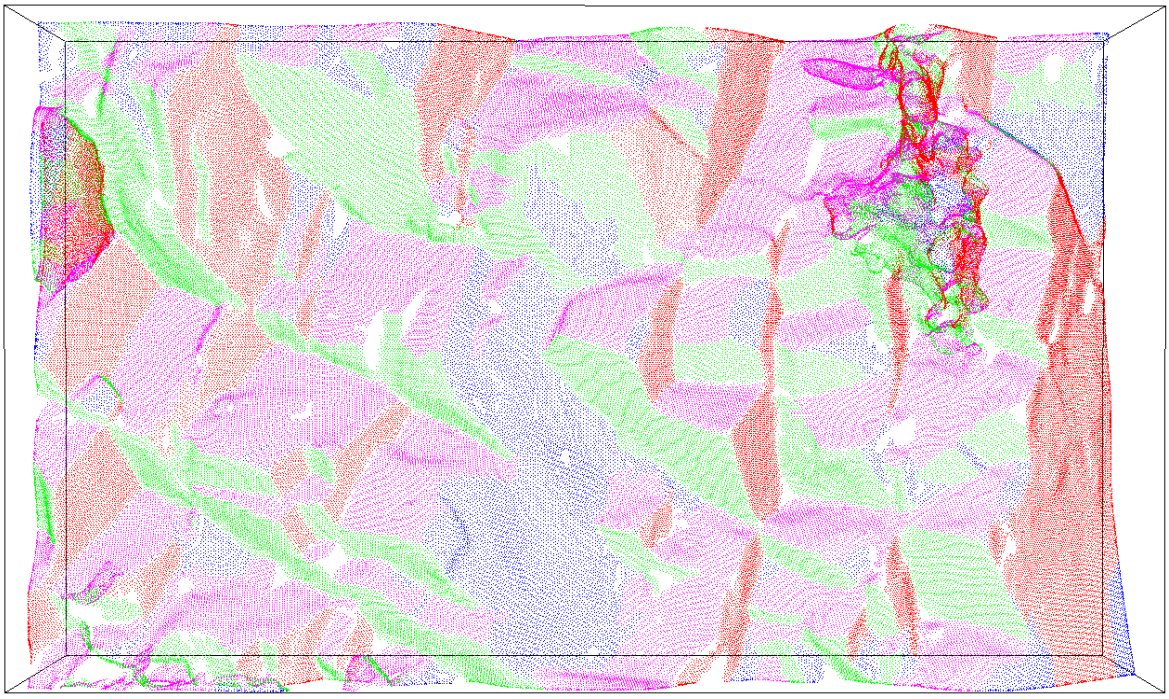

Figure 9.22. The vertices of the of the 3-D meshed surface (not the original point cloud) coloured according to their membership in the four identified discontinuity sets. Points belonging to the same discontinuity set, receive the same colour. The colours are equivalent to the colours used in the stereographic plot (see Figure 9.24)

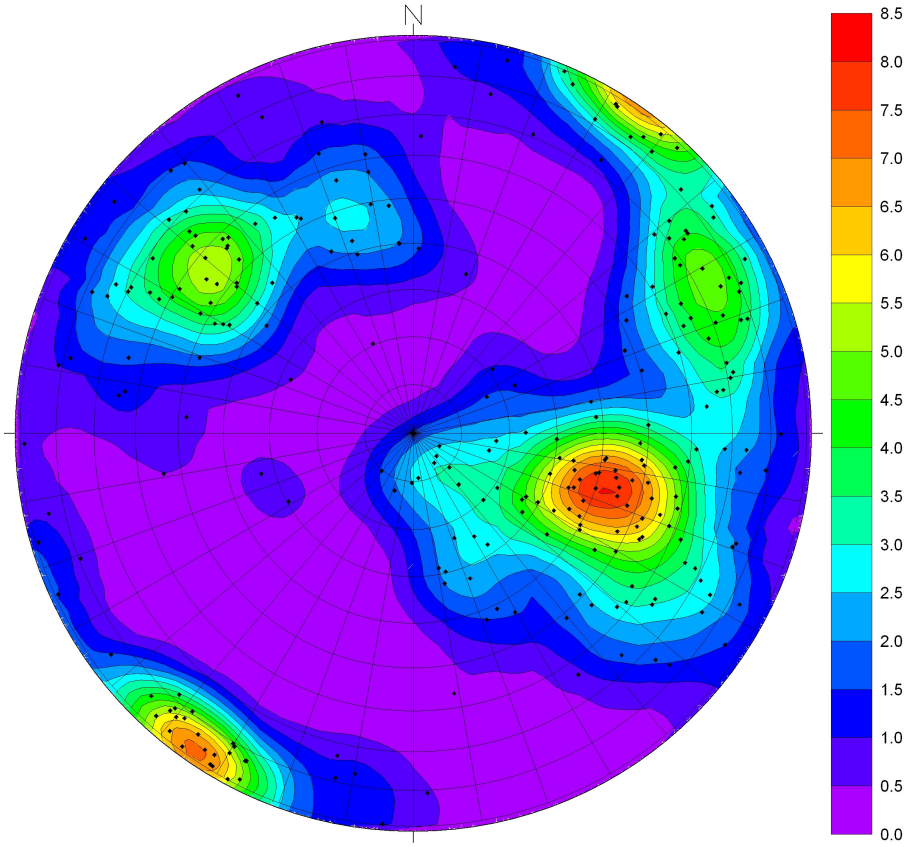

Figure 9.23. Stereographic polar plot of all the individual discontinuity planes found with Method 1 at Site 2. In total 265 planes were found. The colour contours reflect pole densities.

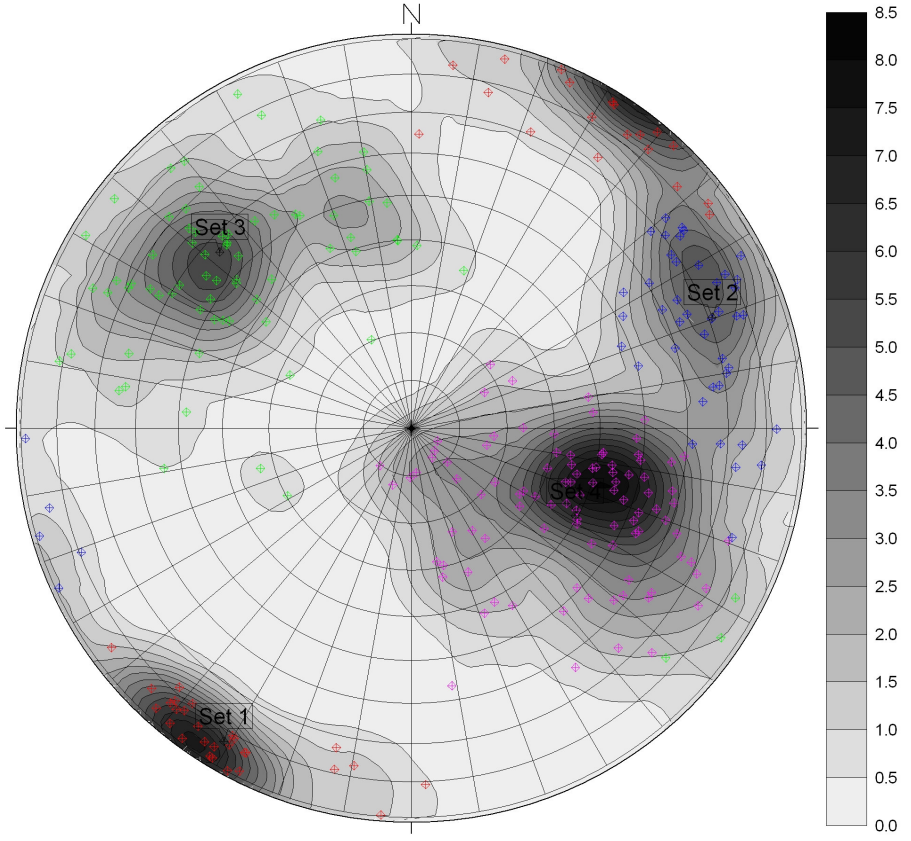

Figure 9.24. Stereographic polar plot with the poles for the discontinuity planes classified into four discontinuity sets using fuzzy k-means clustering. The colours are equivalent to the colours used in Figure 9.22. The grey-scaled contours correspond to pole densities.

9.7.2 Site 2 Method 2: Surface reconstruction with 2-D gridding (FX)

The point cloud processing by Method 2 for the data from Site 2 gives the following results:

- Table 9.7: containing the discontinuity set statistics for all 4 discontinuity sets;
- Figure 9.25: stereographic polar plot showing coloured pole density for all discontinuity planes;
- Figure 9.26: stereographic polar plot of all the discontinuity planes with the poles coloured according to their discontinuity set membership and with the pole density shown in grey scale.

Table 9.7. Results of discontinuity set calculations for site 2 with method 2.

	Set 1	Set 2	Set 3	Set 4
Dip angle (°)	62.89	51.21	53.26	51.19
Dip direction (°)	34.68	259.56	117.86	303.63
R (norm. result. vector)	0.57	0.94	0.92	0.96
N (# of poles)	59	60	66	96
K (Fisher's constant)	2.25	18.00	12.27	22.65
s (spherical variance)	0.6551	0.2319	0.2811	0.2079
Mean normal spacing (m)	0.099	0.054	0.059	0.056
Mean eq. nrml. spacing (m)	0.241	0.160	0.138	0.100
Std.dev. normal spacing (m)	0.129	0.075	0.115	0.135
Std.dev. eq.nrml. spacing (m)	0.363	0.192	0.215	0.132
Max. normal spacing (m)	0.628	0.397	0.837	0.906
Max. eq. nrml. spacing (m)	1.621	1.114	1.262	1.008

Total number of discontinuity planes: 281

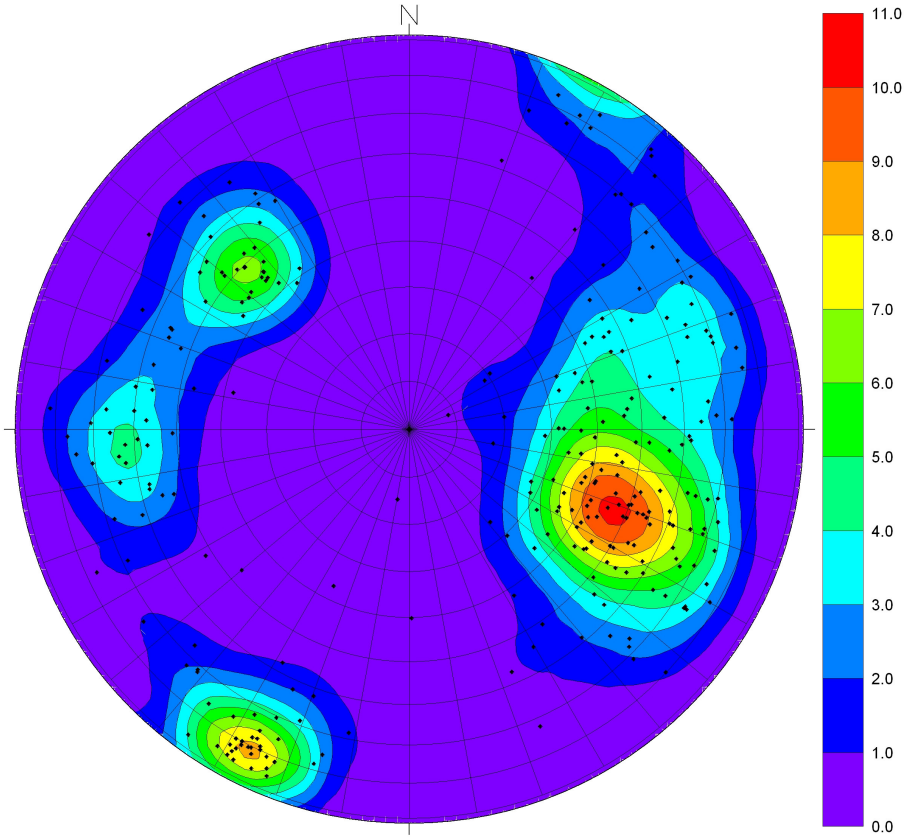

Figure 9.25. Stereographic polar plot of all the individual discontinuity planes found with Method 2 at Site 2. In total 281 planes were found. The colour contours reflect pole densities.

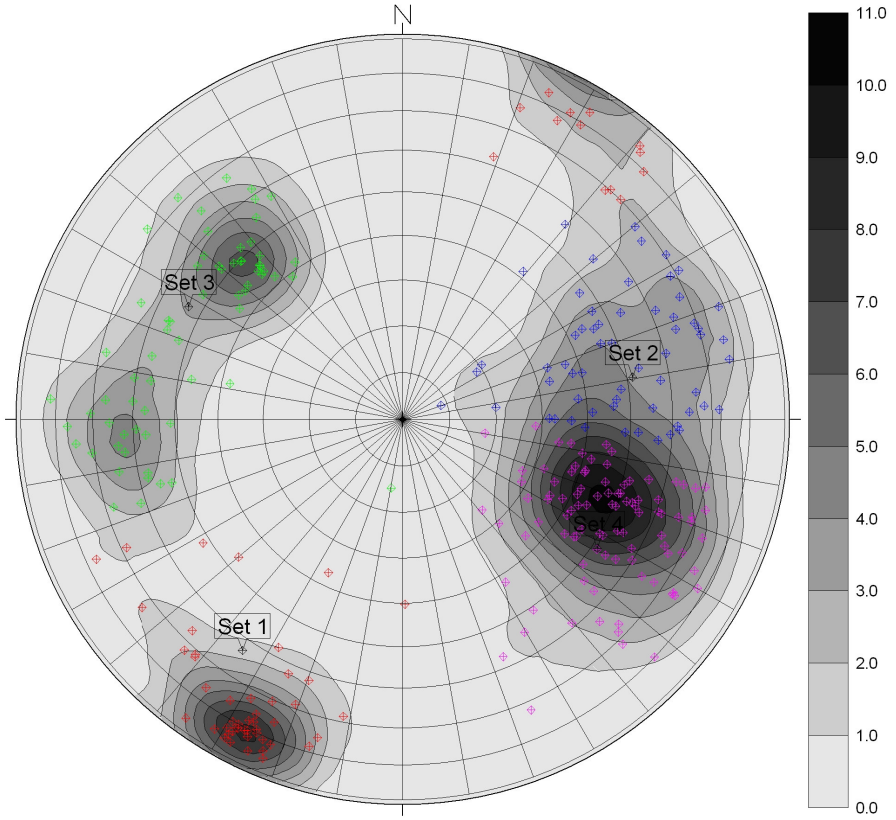

Figure 9.26. Stereographic polar plot with the poles for the discontinuity planes classified into 4 discontinuity sets using fuzzy k-means clustering. The grey-scaled contours correspond to pole densities

9.7.3 Site 2 Method 3: Segmentation with Matlab (PCA)

The point cloud processing by Method 3 for the data from Site 2 gives the following results:

- Table 9.8: containing the discontinuity set statistics for all 4 discontinuity sets;
- Figure 9.28: the point-cloud points, coloured by discontinuity set;
- Figure 9.29: stereographic polar plot showing coloured pole density for all discontinuity planes;
- Figure 9.30: stereographic polar plot of all the discontinuity planes with the poles coloured according to their discontinuity set membership and with the pole density shown in grey scale.

Table 9.8. Results of discontinuity set calculations for site 2 with method 3.

	Set 1	Set 2	Set 3	Set 4
Dip angle (°)	82.42	60.53	60.72	53.15
Dip direction (°)	40.12	254.41	121.65	292.68
R (norm. result. vector)	0.97	0.96	0.89	0.95
N (# of poles)	48	40	61	67
K (Fisher's constant)	31.58	26.21	16.72	20.87
s (spherical variance)	0.1742	0.1904	0.2405	0.2156
Mean normal spacing (m)	0.079	0.062	0.046	0.045
Mean eq. nrml. spacing (m)	0.086	0.059	0.045	0.042
Std.dev. normal spacing (m)	0.105	0.089	0.047	0.066
Std.dev. eq.nrml. spacing (m)	0.101	0.096	0.048	0.052
Max. normal spacing (m)	0.375	0.421	0.194	0.371
Max. eq. nrml. spacing (m)	0.481	0.530	0.218	0.234

Total number of discontinuity planes: 216

Figure 9.27. This photo shows part of the rock face of Site 2 that corresponds with the outline of the coloured point cloud shown in Figure 9.28 below.

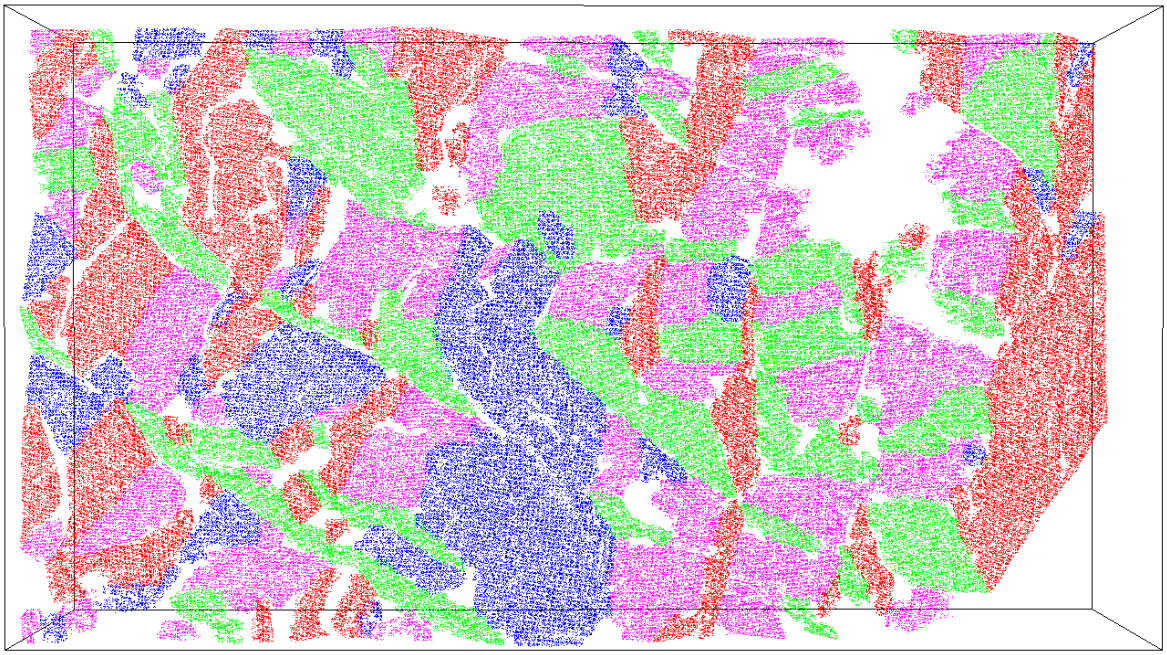

Figure 9.28. The point cloud points are coloured according to their membership in the four identified discontinuity sets. Points belonging to the same discontinuity set, receive the same colour. The colours are equivalent to the colours used in the stereographic plot (see Figure 9.30)

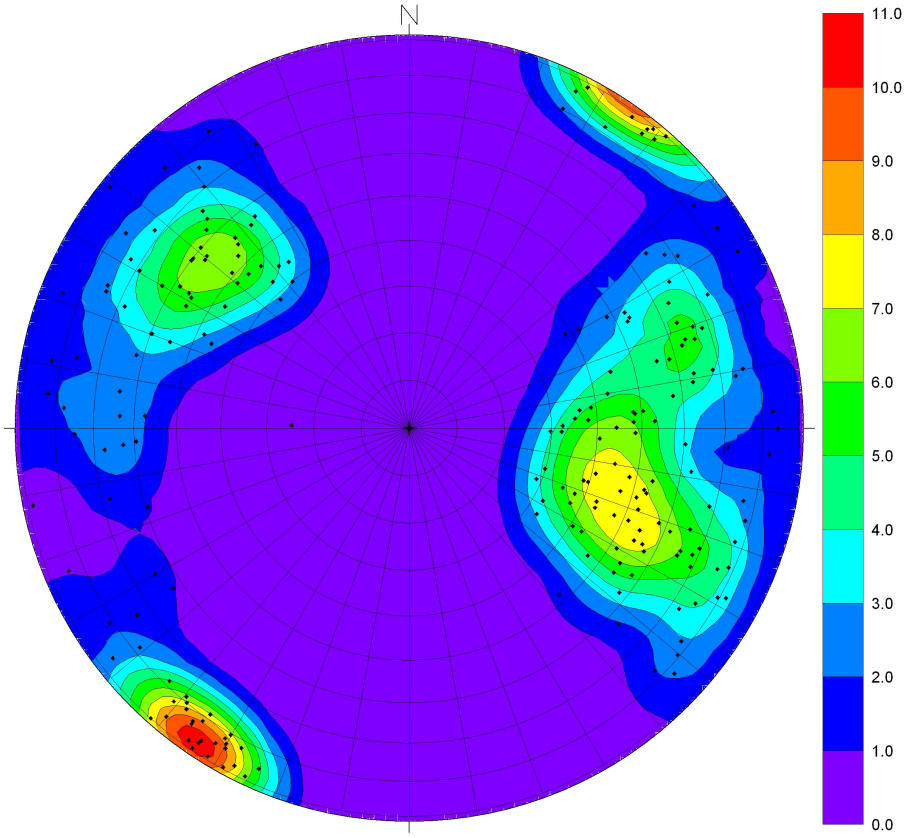

Figure 9.29. Stereographic polar plot of all the individual discontinuity planes found with Method 3 at Site 2. In total 216 planes were found. The colour contours reflect pole densities.

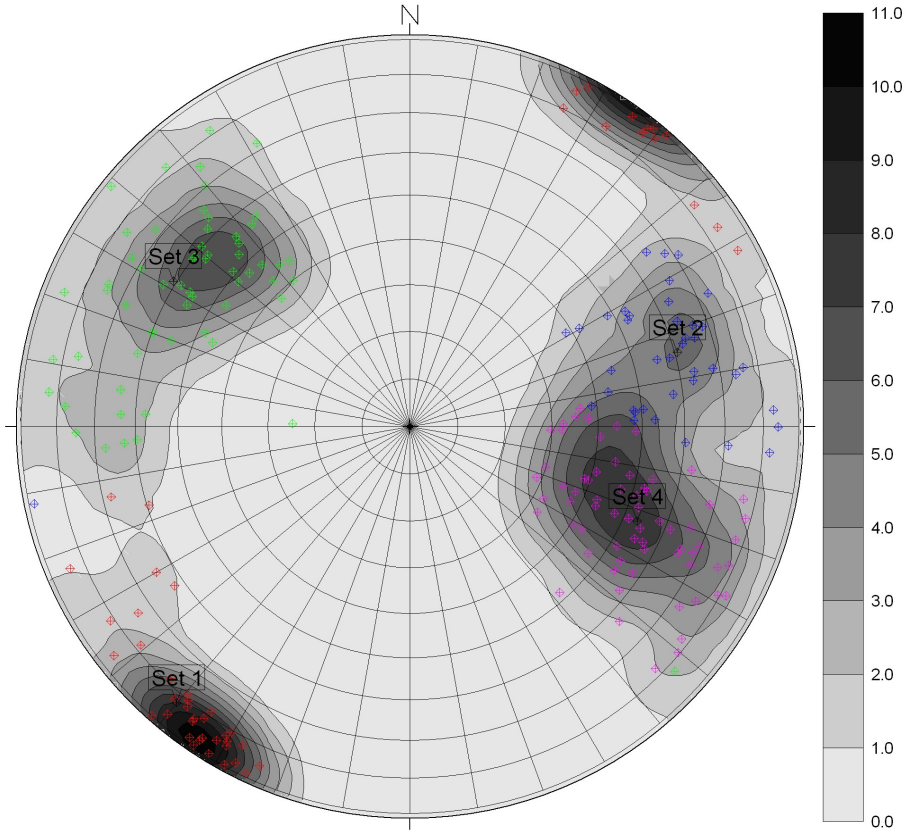

Figure 9.30. Stereographic polar plot with the poles for the discontinuity planes classified into 4 discontinuity sets using fuzzy k-means clustering. The colours are equivalent to the colours used in Figure 9.28. The grey-scaled contours correspond to pole densities.

9.7.4 Site 2 Method 4: Segmentation with PCM (Hough and TLS)

The point cloud processing Method 4 for the data from Site 2 gives the following results:

- Table 9.9: containing the discontinuity set statistics for all 4 discontinuity sets;
- Figure 9.32: the point cloud points, coloured by discontinuity set;
- Figure 9.33: stereographic polar plot showing coloured pole density for all discontinuity planes;
- Figure 9.34: stereographic polar plot of all the discontinuity planes with the poles coloured according to their discontinuity set membership and with the pole density shown in grey scale.

Table 9.9. Results of discontinuity set calculations for site 2 with method 4.

	Set 1	Set 2	Set 3	Set 4
Dip angle (°)	78.16	74.22	57.08	38.40
Dip direction (°)	39.51	289.60	128.04	291.82
R (norm. result. vector)	0.94	0.96	0.91	0.96
N (# of poles)	97	67	75	93
K (Fisher's constant)	17.19	26.00	11.37	26.14
s (spherical variance)	0.2387	0.1924	0.2926	0.1935
Mean normal spacing (m)	3.248	0.040	0.078	0.036
Mean eq. nrml. spacing (m)	0.040	0.036	0.052	0.031
Std.dev. normal spacing (m)	16.993	0.058	0.098	0.064
Std.dev. eq.nrml. spacing (m)	0.046	0.047	0.059	0.042
Max. normal spacing (m)	138.640	0.339	0.488	0.468
Max. eq. nrml. spacing (m)	0.223	0.241	0.307	0.210

Total number of discontinuity planes: 332

Figure 9.31. This photo shows part of the rock face of Site 2 that corresponds with the outline of the coloured point cloud shown in Figure 9.32 below.

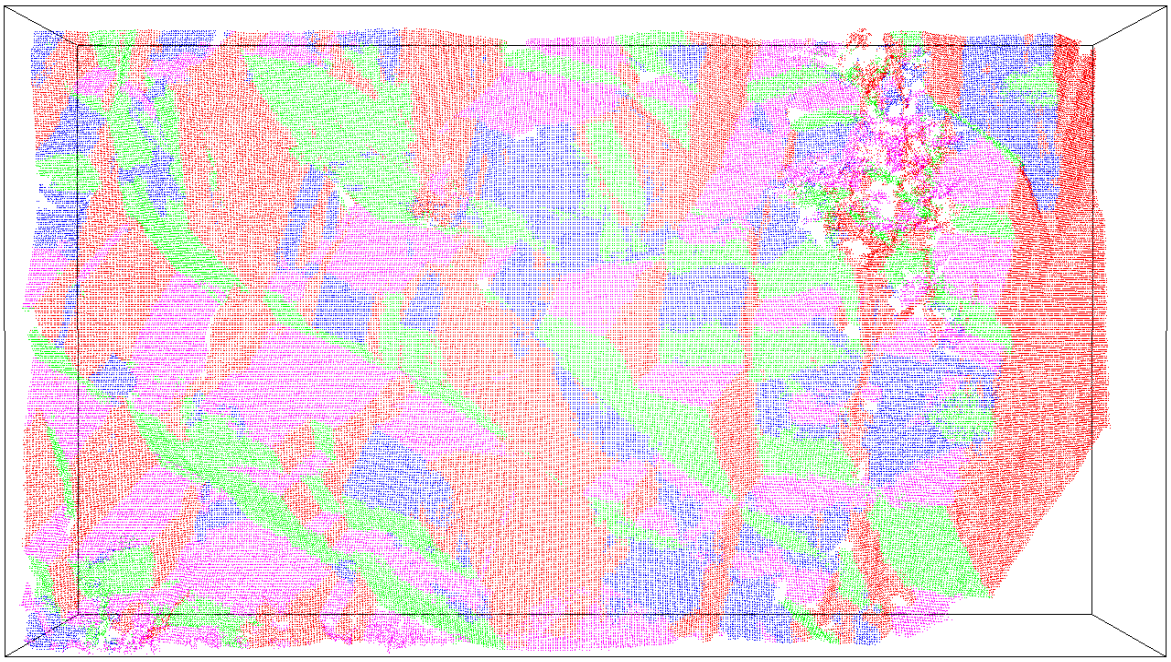

Figure 9.32. The point-cloud points are coloured according to their membership in the 4 identified discontinuity sets. Points belonging to the same discontinuity set, receive the same colour. The colours are similar to the colours used in the stereographic plot (see Figure 9.34).

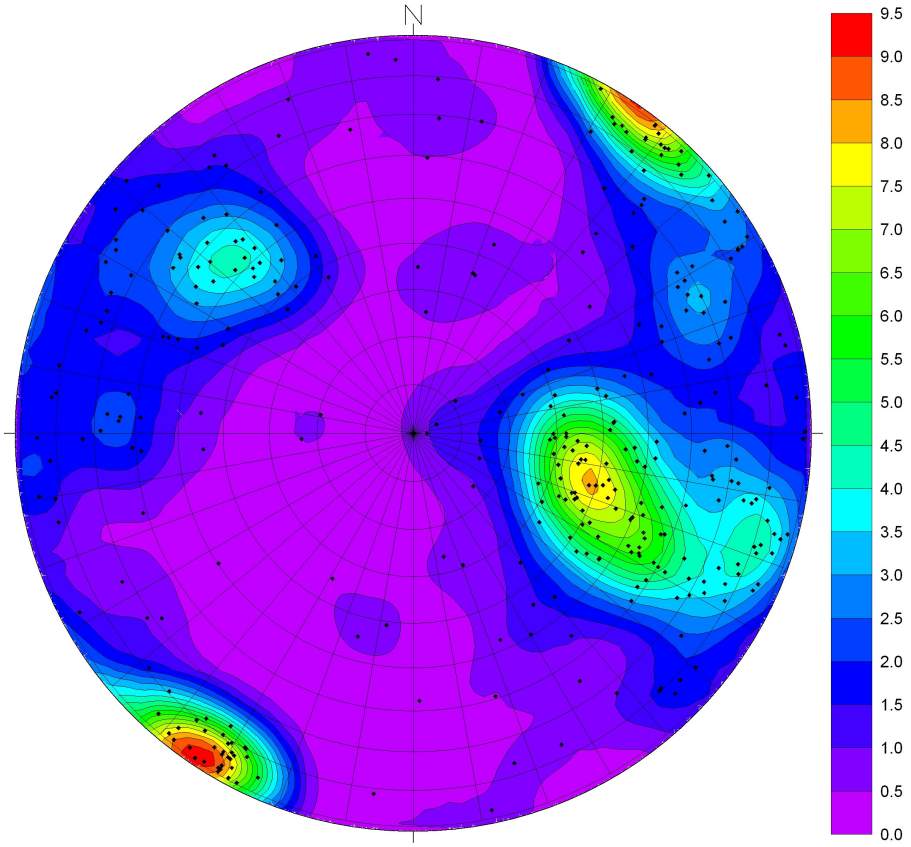

Figure 9.33. Stereographic polar plot of all the individual discontinuity planes found with Method 4 at Site 2. In total 332 planes were found. The colour contours reflect pole densities.

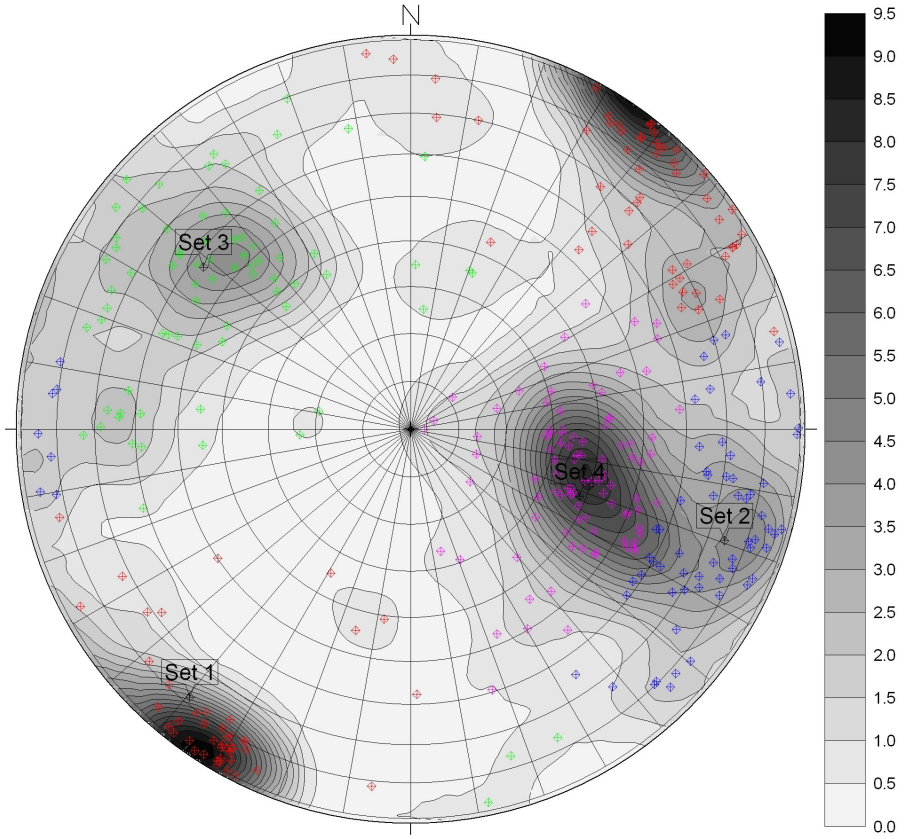

Figure 9.34. Stereographic polar plot with the poles for the discontinuity planes classified into 4 discontinuity sets using fuzzy k-means clustering. The colours are equivalent to the colours used in Figure 9.32. The grey-scaled contours correspond to pole densities.

9.8 Evaluation of the results

The computed discontinuity orientation and spacing information presented in Sections 9.6 and 9.7 is evaluated in three stages:

- a quantitative comparison between the computed and measured orientations of a number of specific discontinuity planes (see Section 9.8.1);
- a qualitative comparison between the computed discontinuity sets and discontinuity sets identified by conventional field survey methods (see Section 9.8.2); and
- a comparison between the computed normal set spacing values and normal set spacing data derived from traditional field-based scanline methods (see Section 9.8.3).

9.8.1 Plane-by-plane comparison

Verification of the accuracy of the orientations of individual discontinuity planes defined by analysing the point-cloud data by each of the four methods was undertaken at each site. At Site 1 (Bellmunt) the orientations of 20 discontinuity planes were measured in the field using a geologic compass. At Site 2 (Toroja) the orientations of 26 discontinuity planes were measured in the field. In each case, the planes were selected from identifiable planes that exhibited a high degree of planarity. The results of these surveys are shown in Appendix A for Site 1 (Figure 11.6 and Table 11.4) and for Site 2 in Appendix B (Figure 11.12 and Table 11.9).

Methods 1, 3 and 4 allow for the relatively straightforward retrieval of computed orientations for individual discontinuity planes. Each of these three methods yield a classified or segmented point cloud, although Methods 3 and 4 use the original point-cloud points while Method 1 uses vertex points of the interpolated mesh surface. With these Methods, the classified points are converted to a VRML file for 3-D visualisation. In these visualisations each individual discontinuity plane receives a randomly assigned colour (Figure 7.28 and Figure 7.44 illustrate these visualizations of individual discontinuity planes produced by Method 1 for Sites 1 and 2, respectively; while Figure 8.2 to Figure 8.5 illustrate the individual discontinuity planes produced by Methods 3 and 4 for Sites 1 and 2). By visually comparing these 3-D VRML representations with the marked planes identified in the photographs of the appropriate Site (Figures 130 and 136), the appropriate computed discontinuity plane was easily cross-referenced to the equivalent plane measured by the field survey. The identification number of each discontinuity plane is provided when this plane is identified by moving the cursor onto its image in the VRML view and “clicking” on the mouse. By referencing this identifier number, the computed orientations of the discontinuity planes are retrieved from the tabulated plane list generated by each method..

With Method 2 based on the Split-FX software (Split Engineering 2007), the retrieval of the orientations of individual planes is more cumbersome, since the tabulated plane list cannot be directly linked by visually querying the resulting 3-D patches or the original point cloud. In order to cross-reference the orientations with Method 2, the outline of the selected individual discontinuity plane has to be manually selected from the original point cloud displayed by the Split-FX program. Subsequently the software then generates a grid and patch for this selection, using the same parameter criteria used for the original analysis (please refer to Section 7.6). The orientation and other parameters for this identified single plane are then exported to a text file, and thus the correct orientation is retrieved.

Subsequently, all computed orientations are compared with the compass orientation measurements. The difference in orientation is computed in terms of pole-vector difference, or dihedral angle, following Equation [18]. The results of these comparisons are summarised in Table 11.12 for Site 1 and in Table 11.13 for Site 2 (please refer to Appendix K.). Several conclusions can be drawn from these comparisons:

1. Method 1 results in the least accurate orientation computation.
2. Methods 2, 3 and 4 show similar average and standard deviations of the pole-vector differences at Site 2,
3. At Site 1, Method 2 produces differences about twice as large as those for Methods 3 and 4.
4. The pole-vector differences are similar for Methods 3 and 4, which is expected, since these are comparable methods.

Two questions remain:

1. Why are the pole-vector differences for Method 1 so much larger than for the other methods?
2. What are the reasons of the pole-vector differences between the point cloud processing methods and the manual method?

The surface reconstruction process used by Method 1 does not appear to cause the larger pole-vector difference. The calculation of the plane orientation is based on the meshed surface, but this appears to be best possible representation of the actual rock surface. The main reason for the large pole-vector difference is the manner in which the planes are constructed with Method 1. In Method 1 a plane is constructed by joining facets that have orientations that are clustered to the same discontinuity set. If the set has a small Fisher-K value and the set is not constrained, there will be a large variation in orientation. If this is the case, facets that statistically belong to the same surface may actually represent multiple planes having a large variation in orientation. The calculated average orientation of such a composite plane may differ significantly from the measured orientation. In these situations, the way the planes are constructed in Method 2 would therefore be a better option: i.e. to join facets to form a plane only if they fulfil a specified dihedral-angle-difference criterion.

Both the computational and field-measurement methods have their own error sources, and these may be the cause of the remaining pole-vector differences between the point-cloud processing methods and the manual measurements. As explained previously (in Chapter 2), the manual compass measurements introduce several errors. First of all, the dip direction and dip angle can only be measured with a compass with a precision no better than a single degree. In this survey, the compass is also placed on a single spot of the plane. Orientation variations within the plane, particularly if it is a larger discontinuity, are thus not incorporated. The various computational methods measure the orientation of the entire plane, although the size of the plane can differ depending on the selected method. Another source of error can be the point cloud registration. As is explained in Section 5.4, the registration of the point clouds used in this study was quite elementary. The registration consisted of levelling of the scanner with a bubble level and measurement of the scanner's bearing with a geological compass. Both the levelling and the bearing measurement may result in measurement errors of several degrees. The error caused by the point cloud processing method is considered several scales smaller than the combined manual measurement and data registration error. Those point-cloud segmentation methods (Methods 3 and 4) that make use of the original point-cloud data result in the most accurate orientation calculation possible. Although the point-cloud data contain a positional imprecision (noise) that is around 1.5 cm (for the Optech scanner), the PCA approach (Method 3) or the Hough transform and least squares approach (Method 4) calculate a best fitting plane that is not significantly influenced by this noise.

9.8.2 Qualitative comparison between the computed discontinuity sets and discontinuity sets identified by conventional field survey methods

The number of discontinuity sets identified by the four different point-cloud processing Methods was kept the same for each site: Site 1 was evaluated according to five discontinuity sets, while Site 2 was evaluated according to four discontinuity sets. Sections 8.4 and 8.5 describe the computed discontinuity set properties, on a method-by-method basis, for Site 1 (Bellmunt) and Site 2 (Toroja).

Thus, the first step in undertaking a qualitative comparison of the results obtained by the various Methods required the creation of tables summarising these results. Three summary tables for each Site were used for this qualitative comparison:

- A table comparing the average dip angles, average dip directions, and Fishers-K values for each discontinuity set, computed by each method;
- A table comparing the numbers, and percentages of the total numbers, of individual discontinuity planes included within each discontinuity set, as defined by each Method; and
- Since Method 1 procedures allow for an additional comparison; a table comparing these discontinuity set orientation characteristics defined by individual triangular facets with those defined by the individual discontinuity planes composed of groups of facets.

While related only to Method 1, this third comparison summary table provides an opportunity to assess the consequences resulting from the use of average orientation statistics related to individual discontinuity planes to define discontinuity set orientations. When average planar orientations are used, information on internal variations, or roughness, of the planar elements is ignored. One additional assessment is also possible during this comparison. Since the triangular facets are relatively small and uniform in size, they can be considered as elemental areas. Thus, the number of facets per planar element provides an estimate of the average size of individual discontinuity planes within each discontinuity set.

After these comparisons were concluded, an additional qualitative comparison was undertaken between the orientations of the computed discontinuity sets and the orientations of discontinuity sets identified by traditional field survey methods. While the number of discontinuity sets computed for each site was kept consistent (five sets for Site 1, and four sets for Site 2), the number of discontinuity sets determined by the conventional field analysis methods may differ, depending on the method used. For example, the SSPC system utilizes visually identified discontinuity sets, while the analysis of scanline data relies on the identification of discontinuity clusters. The easiest way to determine which discontinuity sets are identical is by plotting the poles of the average orientation of all discontinuity sets on a single stereographic plot. Pole-density values are computed and shown as a grey-scale behind the poles on the stereographic plot. Although this is a pseudo density, because the poles are not individual measurements but average discontinuity-set orientations, density concentrations allow the rapid observance of differences and similarities between the computed discontinuity sets defined by the four computational Methods and the discontinuity sets identified by traditional field methods.

This visual evaluation of stereographic polar plots allowed the identification of “generic” discontinuity sets for each Site. Each generic discontinuity set was typically related to several discontinuity sets determined by the point-cloud analyses or by the traditional field data analyses. Site 1 has seven generic discontinuity sets (labelled ‘A’ through ‘G’), while Site 2 has five generic discontinuity sets (labelled ‘A’ through ‘E’). These generic discontinuity sets form the basis of the qualitative comparison between the various computational point-cloud processing methods and the results of traditional field data analyses.

These comparisons made it possible to verify the results of the new proposed point-cloud analysis approaches with those results obtained by conventional field data acquisition methods. These comparisons for Sites 1 and 2 are discussed in the following two sections.

9.8.2.1 Comparisons of discontinuity sets identified at Site 1

Table 9.10 provides comparison data for the orientations of the five discontinuity sets defined for Site 1 by Methods 1-4. Average dip angles, average dip directions, and Fishers-K values allow for the comparison of the orientations of each discontinuity set, as computed by each Method. In the table, entries shown in bold format are values that are larger than comparable entries, while italic entries indicate values that are smaller than comparable entries.

An examination of Table 20 reveals that there is a high consistency in orientations of a defined discontinuity set as computed by the four Methods. One departure from this consistency is the much smaller dip angle values computed for all discontinuity sets by Method 2. In contrast, the dip direction values for Method 2 are comparable to those of the other Methods. There is no obvious explanation for this result. It apparently is the result of the gridding method applied by the Split-FX software. Method 3 produces somewhat larger dip angles than the other Methods, but only the dip angle for discontinuity set 3 (by Method 3) appears unusually large.

Fishers-K values are used to demonstrate the variability in orientation of individual discontinuity planes within a discontinuity set. However, the Fisher-K is an awkward statistic to accomplish this task. The Fisher-K value is zero for a uniform spherical distribution, but is infinity for a directed distribution with no variation. Thus, the numbers shown (ranging from about 10 to almost 60) in reality all represent tightly oriented clusters. In spite of these limitations, it is obvious that each of the defined discontinuity sets is distinct, and represents a strongly co-planar set of discontinuity planes.

Table 9.11 provides comparison data defining the numbers, and percentages of the total numbers, of individual discontinuity planes included within each of the five discontinuity sets defined for Site 1 by Methods 1-4. Each Method produced rather different numbers of individual discontinuity planes, ranging from 241 planes identified by Method 2 to 603 planes identified by Method 3. Thus, the numbers of planes comprising each discontinuity set for each Method were converted to percentages of the total number of planes identified by that Method. This allows a comparison of the relative frequencies of each discontinuity set as identified by each Method. Although there is some fluctuation in frequency by Method there appears to be a general consistency in the frequency of occurrence of each discontinuity set by each Method.

Since Method 1 procedures allow for additional comparisons, Table 9.12 was created to compare the discontinuity set orientation characteristics defined by individual triangular facets, as reported in Table 7.1, with those defined by the individual discontinuity planes composed of groups of facets, and reported in Table 9.2. This comparison yield several interesting and useful observations. First, there is a very strong similarity between the average dip angles and average dip directions computed by facets with the equivalent measurements made using individual planar elements within each discontinuity set. This shows that orientation bias has not been introduced when characterising the discontinuity set orientations by using the orientations of individual discontinuity planes belonging to the set.

Second, the increase in Fishers-K values for those discontinuity sets defined by planes, as compared to those defined by facets, shows the greater uniformity in orientation introduced by the use of the average orientations defining individual planar elements. In other words, these comparisons show the consequence of ignoring the variability or roughness of the individual planar elements. However, as noted above, the differences in Fishers-K values (ranging between about 3 and 56) is actually rather small in terms of spherical variation; in reality, each discontinuity set represents a fairly tightly oriented cluster of planar elements.

Finally, Table 9.12 allows for the evaluation of the average size of planar elements making up each discontinuity set - based on the ratio of number of facets to number planes. Since each facet is more or less an equal size, then the average number of facets in a plane provides an estimate of average size of a planar element. This computation shows that discontinuity set 1 is composed of the largest planar elements and discontinuity set 2 is composed of the smallest planar elements.

Figure 9.35 is a stereographic polar plot of all identified discontinuity sets for Site 1. To assist the qualitative comparison, pole-density values are computed and shown in grey-scale behind the poles. This is a pseudo density, because the poles are not individual measurements, but average discontinuity set orientations.

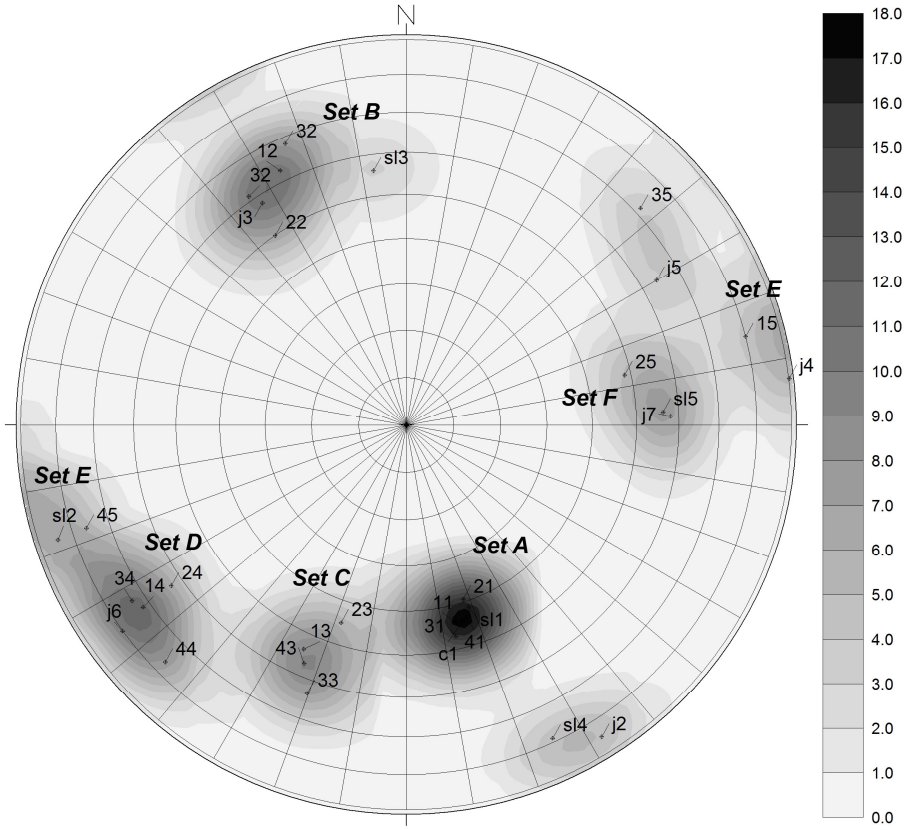

Figure 9.35. This illustration shows a generic polar plot with all identified sets of Site 1, with (pseudo) density values in grey-scale. The numbered labels refer to the Method and discontinuity set number (e.g. label 35 refers to Method 3, Set 5). The labels with sl in front (e.g. sl2) refer to the set number identified in the scanline survey (see Appendix A). The other labels (e.g. c1 or j2) refer to the corresponding sets identified in the SSPC survey data in Appendix A (c refers to cleavage and j refers to joint set).

Evaluation of Figure 9.35 allowed seven generic sets to be recognised, and these are termed 'Set A' through 'Set G'. Table 11.14 in Appendix L contains the numerical values for each generic set, but a brief summary of each set follows:

- **Set A**: The most unambiguous discontinuity set is the day-lighting bedding or slatey cleavage that dips towards the NNW at about 45 degrees. All four point-cloud processing methods recognised this discontinuity set, which is labelled as 'Set 1' by all Methods (see Tables 12-15 and Tables 20-21). As noted above, the orientations are relatively consistent. The scanline field survey (set sl1) and the SSPC field survey (set C1) recognised this set with similar orientation values.
- **Set B**: The second-most unambiguous discontinuity set is the joint set that is almost orthogonal to the bedding, and dips into the slope (dip direction SE, with a dip angle of about 60 degrees). All four point-cloud processing methods recognised this discontinuity set, which is labelled as 'Set 2' by all Methods (see Tables 12-15 and Tables 20-21). The orientations are relatively consistent, but not as tight as with the bedding set. The SSPC field survey (set J3) provides estimates that correspond well with the average orientations derived from the point cloud data. However, the discontinuity set identified in the scanline survey (set sl3) is oriented about 25 degrees more towards the South, but has a similar dip angle.
- **Set C**: The third discontinuity set is an intermediate set between Set A and Set D. It is recognised by all four point-cloud processing methods as 'Set 3' (see Tables 12-15 and Tables 20-21). However, neither the SSPC nor the scanline field surveys identified discontinuity planes with these orientations as a distinct discontinuity set.
- **Set D**: The fourth discontinuity set is the joint set that is dipping steeply and perpendicular to the rock face. It is identified by all four point-cloud processing methods as 'Set 4' (see Tables 12-15

and Tables 20-21). This joint set has a general dip direction towards the NE and a dip angle of about 75 degrees. It is also recognised in the SSPC survey (set J6). The scanline survey is more ambiguous; discontinuity set 2 (sl2) shows a significantly greater Eastward trend , and although it has a similar dip angle, it appears more likely to be part of the Set E, and is so tabulated in Table 39 (Appendix L).

- **Set E**: The fifth discontinuity set is less distinct than the previous sets. It is almost vertical, thus dip orientations are evenly divided between East and West. The set is identified by three point-cloud processing methods ('Set 5' in Methods 1, 3 and 4 – see Tables 12, 14-15 and Tables 20-21). Both the SSPC and the scanline survey identified this set. The SSPC classified it as joint set 4 (J4), while the scanline survey classified it as joint set 2 (sl2).
- **Set F**: The sixth discontinuity set was recognised as Set 5 by point-cloud processing Method 2 (see Table 13 and Tables 20-21). The SSPC survey recognised this discontinuity set as joint set 7 (J7), while the scanline survey classified it as set 5 (sl5).
- **Set G**: This discontinuity set is not recognised by any of the point cloud processing methods. As shown in Table 39 (Appendix L), the scanline survey identified it as set 4 (sl4) and the SSPC survey as joint set 2 (J2). However, the two discontinuities show considerable differences in orientation, so it is doubtful whether both discontinuity sets can indeed be classified together.

The only discontinuity set that cannot clearly be identified with any other discontinuity set is the joint set 5 (J5) of the SSPC survey. Accordingly, it is listed separately in Table 11.14 of Appendix L.

9.8.2.2 Comparisons of discontinuity sets identified at Site 2

Table 9.13 provides comparison data for the orientations of the four discontinuity sets defined for Site 2 by Methods 1-4. Average dip angles, average dip directions, and Fishers-K values allow for the comparison of the orientations of each discontinuity set, as computed by each Method. In the table, entries shown in bold format are values that are larger than comparable entries, while italic entries indicate values that are smaller than comparable entries.

An examination of Table 9.13 reveals that there is a high consistency in orientations of a defined discontinuity set as computed by the four Methods. Method 2 produces much smaller dip angle values for discontinuity sets 1 and 2, and a markedly larger dip angle for discontinuity set 4. The dip angle for discontinuity set 1 is about 20 degrees less than values produced by the other three Methods. There is no obvious explanation for this result. It apparently is the result of the gridding method applied by the Split-FX software.

Discontinuity set 4 shows two very different estimates of dip angles – Methods 1 and 4 produce dip angles of around 39 degrees, while Methods 2 and 3 produce dip angles of slightly more than 50 degrees.

As with Site 1, Fishers-K values are used to demonstrate the variability in orientation of individual discontinuity planes within a discontinuity set. The values (ranging from about 2 to about 32) all represent fairly tightly oriented clusters. The differences are actually rather small in terms of spherical variation. Method 2 often shows lower values and thus slightly greater variability in orientation, than the other Methods. In spite of these limitations, it is obvious that each of the defined discontinuity sets is distinct, and represents a strongly co-planar set of discontinuity planes.

Table 9.14 provides comparison data defining the numbers, and percentages of the total numbers, of individual discontinuity planes included within each of the four discontinuity sets defined for Site 2 by Methods 1-4. Each Method produced different numbers of individual discontinuity planes, ranging from 216 planes identified by Method 3 to 332 planes identified by Method 4. The variation in total numbers of planes was much less than for Site 1. Comparison of the relative frequencies of discontinuity sets identified by each Method revealed a general consistency, although there is some fluctuation in the frequency of occurrence of each discontinuity set defined by each Method.

Table 9.10. Comparison of Orientations of Discontinuity Sets for Site 1 by Methods 1-4

		Set 1	Set 2	Set 3	Set 4	Set 5
METHOD 1 (Table 12)	Dip (deg)	43.79	62.74	53.73	71.94	79.98
	Dip Direction (deg)	345.85	153.64	24.55	55.27	255.43
	Fisher's K	55.17	12.42	50.26	**52.68**	**56.32**
METHOD 2 (Table 13)	Dip (deg)	*39.35*	*50.01*	44.88	*62.95*	*48.53*
	Dip Direction (deg)	342.00	145.29	18.31	55.64	257.02
	Fisher's K	52.00	11.29	40.63	29.18	16.64
METHOD 3 (Table 14)	Dip (deg)	46.87	68.31	**63.30**	73.38	71.62
	Dip Direction (deg)	346.82	156.66	20.27	57.29	227.23
	Fisher's K	59.36	**24.63**	33.33	26.75	*17.05*
METHOD 4 (Table 15)	Dip (deg)	43.46	61.06	56.76	76.63	76.09
	Dip Direction (deg)	342.67	145.39	23.24	45.48	72.15*
	Fisher's K	*23.32*	10.78	*25.20*	38.38	42.00

Remarks:

Bold Values are unusually large; *Italic* values are unusually small

*) This value is 180 degrees opposite direction to other values

Table 9.11. Comparison of Numbers (and Percentages) of Planes in Discontinuity Sets for Site 1 Identified by Methods 1-4

		Set 1	Set 2	Set 3	Set 4	Set 5	Total Number of Planes
METHOD 1 (Table 12)	Number of Planes	83	92	80	64	84	403
	Percent of Total	21%	23%	20%	16%	21%	
METHOD 2 (Table 13)	Number of Planes	72	45	44	55	25	241
	Percent of Total	30%	19%	18%	23%	10%	
METHOD 3 (Table 14)	Number of Planes	188	102	91	119	103	603
	Percent of Total	31%	17%	15%	20%	17%	
METHOD 4 (Table 15)	Number of Planes	128	92	64	86	123	493
	Percent of Total	26%	19%	13%	17%	25%	

Table 9.12. of Orientations of Facets (Table 9) and Orientations of Individual Planar Elements (Table 12) for Site 1 Method 1

	Set 1		Set 2		Set 3		Set 4		Set 5	
	Facets Table 7.1	Planes Table 9.2	Facets Table 7.1	Planes Table 9.2	Facets Table 7.1	Planes Table 9.2	Facets Table 7.1	Planes Table 9.2	Facets Table 7.1	Planes Table 9.2
Dip (deg)	43	44	63	63	53	54	72	72	87	80
Dip Direction (deg)	344	346	153	154	24	25	53	55	75	255
Fisher's K	10.95	55.17	2.79	12.42	16.72	50.26	19.83	52.68	6.14	56.32
Number	128168	83	61125	92	64309	80	97352	64	106258	84
% Total	28	21	13	23	14	20	21	16	23	21
Avg. Size (#Facets/ Plane)	1544		657		804		1521		1265	

Remark:
Total Number Facets: 457212
Total Number Planes: 403

Table 9.15 shows the additional comparisons possible with the Method 1 procedures, including the discontinuity set orientation characteristics defined by individual triangular facets, as reported in Table 7.2, with those defined by the individual discontinuity planes composed of groups of facets, and reported in Table 16. These comparisons yield results very similar to those found for Site 1. First, there is a very strong similarity between the average dip angles and average dip directions computed by facets with the equivalent measurements made using individual planar elements within each discontinuity set. This shows that orientation bias has not been introduced when characterising the discontinuity set orientations by using orientations of individual discontinuity planes belonging to the set.

Second, the increase in Fishers-K values for those discontinuity sets defined by planes, as compared to those defined by facets, shows the greater uniformity in orientation introduced by the use of the average orientations defining individual planar elements. In other words, these comparisons show the consequence of ignoring the variability or roughness of the individual planar elements. However, as noted above, the differences in Fishers-K values (ranging between about 3 and 33) is actually rather small in terms of spherical variation; in reality, each discontinuity set represents a fairly tightly oriented cluster of planar elements.

Finally, Table 9.15 allows for the evaluation of the average size of planar elements making up each discontinuity set - based on the ratio of number of facets to number planes. Since each facet is more or less an equal size, then the average number of facets in a plane provides an estimate of average size of a planar element. This computation shows that discontinuity set 1 is composed of the largest planar elements; these are almost twice the size of those contained in the other three discontinuity sets which are all composed of planar elements with about the same average size.

Table 9.13. Comparison of Orientations of Discontinuity Sets for Site 2 by Methods 1-4

		Set 1	Set 2	Set 3	Set 4
METHOD 1 (Table 16)	Dip Angle (deg)	82.92	70.87	56.38	*39.28*
	Dip Direction (deg)	30.91	249.68	132.64	298.29
	Fisher's K	32.46	31.52	12.31	14.58
METHOD 2 (Table 17)	Dip Angle (deg)	*62.89*	*51.21*	53.26	**51.19**
	Dip Direction (deg)	34.68	259.56	117.86	303.63
	Fisher's K	*2.25*	18.00	12.27	22.65
METHOD 3 (Table 18)	Dip Angle (deg)	82.42	60.53	60.72	**53.15**
	Dip Direction (deg)	40.12	254.41	121.65	292.68
	Fisher's K	31.58	26.21	16.72	20.87
METHOD 4 (Table 19)	Dip Angle (deg)	78.16	74.22	57.08	*38.40*
	Dip Direction (deg)	39.51	289.60	128.04	291.82
	Fisher's K	17.19	26.00	11.37	26.14

Remarks:
Bold Values are unusually large; *Italic* values are unusually small

Table 9.14. Comparison of Numbers (and Percentages) of Planes in Discontinuity Sets for Site 2 Identified by Methods 1-4

		Set 1	Set 2	Set 3	Set 4	Total Number of Planes
METHOD 1 (Table 16)	Number of Planes	47	47	74	97	265
	Percent of Total	*18%*	18%	28%	**37%**	
METHOD 2 (Table 17)	Number of Planes	59	60	66	96	281
	Percent of Total	21%	21%	24%	34%	
METHOD 3 (Table 18)	Number of Planes	48	40	61	67	216
	Percent of Total	22%	19%	28%	31%	
METHOD 4 (Table 19)	Number of Planes	97	67	75	93	332
	Percent of Total	**29%**	20%	23%	28%	

Remarks:
Bold Values are unusually large; *Italic* values are unusually small

Table 9.15. Comparison of Orientations of Facets (Table 7.2) and Orientations of Individual Planar Elements (Table 9.6) for Site 2 Method 1

	Set 1		Set 2		Set 3		Set 4	
	Facets Table 7.2	Planes Table 9.6	Facets Table 7.2	Planes Table 9.6	Facets Table 7.2	Planes Table 9.6	Facets Table 7.2	Planes Table 9.6
Dip (deg)	89	82.92	75	70.87	57	56.38	44	39.28
Dip Direction (deg)	34	30.91	253	249.68	128	132.64	289	298.29
Fisher's K	4.19	32.46	6.79	31.52	3.21	12.31	4.34	14.58
Number	112747	47	59014	47	98896	74	112687	97
% Total	29	18	15	18	26	28	29	37
Avg. Size #Facets/Plane	2399		1256		1336		1162	

Remarks:
Total Number Facets: 383344
Total Number Planes: 265

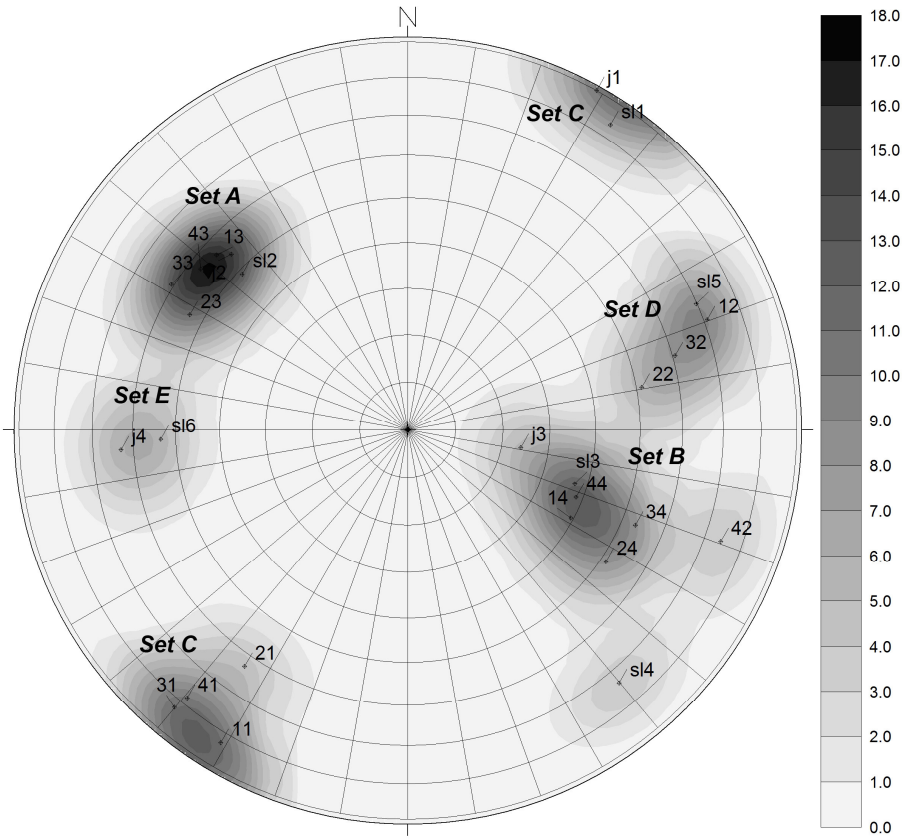

Figure 9.36. This illustration shows a generic polar plot with all identified sets of Site 2, with (pseudo) density values in grey-scale. The numbered labels refer to the Method and discontinuity set number (e.g., label 35 refers to Method 3, set 5). The labels with sl in front (e.g. sl2) refer to the set number identified in the scanline survey (see Appendix B). The other labels (e.g. c1 or j2) refer to the corresponding sets identified in the SSPC survey data in Appendix B (c refers to cleavage and j refers to joint set).

Figure 9.36 is a stereographic polar plot of all identified discontinuity sets for Site 2. To assist the qualitative comparison, pole-density values are computed and shown in grey-scale behind the poles. This is a pseudo density, because the poles are not individual measurements, but average discontinuity set orientations. Evaluation of Figure 9.36 allowed five generic sets to be recognised, and these are termed ‘Set A’ through ‘Set E’. Table 11.15 in Appendix L contains the numerical values for each generic set, but a brief summary of each set follows:

- **Set A**: The most unambiguous discontinuity set dips steeply into the slope with a dip between 50 and 60 degrees. All four point-cloud processing methods recognise this discontinuity set (identified as ‘Set 3’ for Methods 1-4; see Table 9.6 to Table 9.9, and Table 9.13 to Table 9.14). As noted above, the orientations are relatively consistent. The scanline field survey (set sl2) and the SSPC field survey (set J2) recognised this set with similar orientation values. It is not clear if this discontinuity set represents bedding. Field surveys did not describe this discontinuity set as being bedding planes. The most likely reason for this is that the sandstone has undergone a low grade of metamorphism that erased any of the original bedding structures. However, the consistent orientations of the discontinuity planes within the discontinuity set make it very likely that this set reflects the original sandstone bedding planes.
- **Set B**: The second-most unambiguous discontinuity set is the joint set that day-lights from the slope and is almost orthogonal to the previous discontinuity set. It has a dip angle of about 45 degrees. All four point-cloud processing methods recognise this discontinuity set (identified as ‘Set 4’ for Methods 1-4; see Tables 16-19, and Tables 23-24). The variation in orientations is consistent, but not as tight as with Set A. The scanline field survey set 3 (sl3) corresponds well with the average orientations derived from the point-cloud data. The SSPC survey set 3 (J3) is

identified as belonging to this discontinuity set, as it has a similar dip direction, but a significantly smaller dip angle (about 20 degrees less steep).

- **Set C**: The third discontinuity set dips vertically and is oriented perpendicular to the previous sets A and B, with a dip direction either NE or SW. All four point-cloud processing methods recognise this as a distinct discontinuity set (identified as 'Set 1' for Methods 1-4; see Table 9.6 to Table 9.9, and Table 9.13 to Table 9.14). The orientation of Set 1 of Method 2 shows the largest deviation from the general orientation of the other sets. Both field surveys also yield a discontinuity set that corresponds with this orientation: the Scanline survey set 1 (sl1) and the SSPC survey (J1). The fact that all methods define these discontinuity sets as "set 1" is mere coincidence.
- **Set D**: This fourth discontinuity set is recognised only by three of the point cloud processing methods (identified as 'Set 2' for Methods 1-3; see Table 9.6 to Table 9.8, and Tables 23-24). The scanline survey identified discontinuity set (set sl5) that has a similar orientation. The SSPC survey did not recognise this as a separate discontinuity set.
- **Set E**: The orientation of this discontinuity set is due East with a dip angle of about 60 degrees. This set is only recognised by the field surveys. The scanline survey identified this discontinuity set as set 6 (sl6), while the SSPC identified joint set 4 (J4). Very few planes identified with the point cloud processing methods plotted in this region, and so they did not identify this discontinuity set.

Two sets cannot clearly be identified as belonging to any of the above generic discontinuity sets. These are discontinuity set 2 defined by Method 4 and scanline survey set 4. Accordingly, they are listed separately in Table 11.15 of Appendix L.

9.8.3 Spacing comparison

In Table 11.14 and Table 11.15 of Appendix L, the set spacing statistics are also listed for each point-cloud processing method and for each field-survey method. The data are presented according to the generic discontinuity set classifications for the two Sites described in the previous two sections. Appendix J contains all the histograms showing the equivalent normal and normal discontinuity set spacing distributions for Site 1 and Site 2, computed for each discontinuity set and for each point-cloud processing method. The following general observations can be made concerning these discontinuity set spacing distributions:

1. The computed mean normal set spacing and the mean equivalent normal set spacing distances for all four point-cloud processing methods are comparable. The standard deviations of these distances are also similar for the four Methods. Only Method 2 results in some instances in spacing distances, which are significantly larger than those computed by the other three Methods are.
2. However, the mean spacing distances computed by the point-cloud processing methods are generally smaller than the measured spacing distances produced by the SSPC and scanline methods. The reason for this has been explained in Section 0. In short, the four point-cloud processing methods may find different planes that may actually be part of the same discontinuity plane. Since these methods do not incorporate the joining of potentially similar planes into a single plane, the separate planes create additional small spacing distances that may not exist in reality. The generation of these small spacing distances obviously affects the computed average spacing values for both the normal set spacing as well as the equivalent normal set spacing. The point cloud processing methods therefore underestimate the mean normal and mean equivalent normal set spacing. It will therefore be important to look at the standard deviation values, the maximum spacing values as well as the spacing histograms, to get a better idea of the variation in the computed spacing values.
3. The SSPC survey generates larger spacing distances for each set than the scanline survey. In contrast to the point cloud processing methods, the SSPC survey may overestimate the larger spacing distances; this is inherent to the approach. The SSPC survey methodology suggests

using plain ‘engineering judgment’ to select the seemingly most appropriate set spacing for the particular discontinuity set, and use this value as the normal set spacing. If in doubt, the method suggests the estimation of a number of spacing values, and then to calculate the mean from those. Intuitively, the largest spacing values are selected and the smaller values that may exist are omitted or overlooked.

4. In one instance however, the SSPC method results in a much smaller spacing. This is the case with the cleavage or bedding exposed at Site 1. This has been observed by the SSPC method as 1 cm, while the scanline survey resulted in a 10-cm spacing for the cleavage or bedding. In the intact rock, a spacing of 1 cm can indeed be observed, but in the exposure not all the cleavage or bedding planes are actually exposed and the rock mass breakage results in about a 10-cm spacing. According to the SSPC survey, the size of block that may fall from the slope indicates a “small tabular” structure (see Appendix A) which, according to the relevant British Standard code of practice for site investigation (BS 5930:1999), suggests a thickness of 6- to 20–cm. This is in conflict with the 1-cm that was recorded in the field.
5. Another observation from the data recorded at Site 1 is that the mean equivalent normal (EN) set spacing values computed with the four point-cloud processing methods are generally 2 to 3 times larger than the mean normal (N) set spacing values. In Site 2 this is not the case, here the EN set spacing values are comparable to the mean N set spacing values.
6. Only the EN set spacing computed with Method 2 appears to have a vague correlation with the normal set spacing computed by the scanline survey. The mean EN spacing that is computed with other three Methods is several orders of magnitude smaller than the matching scanline spacing values and does not appear to be correlated with the scanline-derived normal set spacing values.
7. In some instances, the calculated *maximum* N set spacing or the calculated *maximum* EN set spacing appears to be more closely related to the measured scanline or SSPC normal set spacing values. This may correspond to the second and third observations (see above), which state that the conventional surveys tend to overestimate the larger discontinuity spacing distances.

In conclusion, it appears that there is that there no good correlation between the spacing values computed from the point-cloud survey procedures and those measured by traditional field-survey methods. The main reason for this is that the point-cloud processing methods on the one hand and the conventional field-survey methods on the other hand are fundamentally different in nature. The scanline survey concentrates on acquiring spacing data along a single specific line across the rock face, while the spacing computations from the point-cloud processing methods use the discontinuity plane data from the entire rock face. The SSPC survey normal set spacing estimations do incorporate the entire rock exposure. However, the correlation with the SSPC survey data is even more difficult to make than with the scanline survey data, because the SSPC survey tends to overestimate the spacings.

9.9 Discussion and conclusions

Although all four point-cloud processing methods differ fundamentally in their approach to finding discontinuity planes in the point-cloud data, they all find a series of planar elements and yield a list of geometric information on the individual planes that are found. The geometric data include the plane’s centroid and plane equation. From the plane equation, the plane’s orientation can be derived. The plane orientations can then be displayed in a stereographic plot from which the number of discontinuity sets can be determined by visual examination. Fuzzy k-means clustering subsequently classifies each discontinuity plane into a specific discontinuity set. Discontinuity set statistics such as mean set spacing and Fisher-K values defining the spatial dispersion of the planar elements within discontinuity sets can be computed as well. Since all discontinuity planes are classified into discontinuity sets, the normal set spacing can be determined by using the plane equation and the plane centroid. A new way of calculating normal set spacing is introduced: *equivalent normal set spacing*. Equivalent normal set spacing uses the distance of the plane to a

chosen set centre point. It is relatively easy to compute, since it only depends on the parameter *d* of the plane equation, which is already computed. The computation of the conventional *normal set spacing* using the laser-derived data is more cumbersome and the result depends strongly on the choice for the location of the virtual scanline.

In order to allow a proper comparison between the different point cloud data processing methods, the plane orientations are clustered with the fuzzy k-means method to the same number of clusters at each site. At Site 1, the data is clustered to a total of five clusters and at Site 2 to four clusters. The choice for the number of clusters was based on the visual observation of the stereographic polar plots of the point cloud-derived orientations. Several trial runs with different numbers of clusters were made, but this did not result in an improved clustering. For example, a test with large number of clusters merely resulted in a subdivision of a previously clustered poles and a test with a smaller number of clusters resulted in a fusion of previously clustered poles. Each cluster corresponds to a discontinuity set.

The data from the field surveys however, did not always result in the same number of discontinuity sets as were derived from the analysis of the laser-derived point-cloud data. At Site 1 the scanline survey yielded the same number of discontinuity sets (five) as had been established from the point-cloud data processing, but the SSPC survey estimated a total of seven discontinuity sets. At Site 2 the scanline survey yielded more discontinuity sets (six) than had been established from the point-cloud data processing (four sets), but the SSPC survey estimated the same number of discontinuity sets (four) as had been established by the point-cloud data processing.

In order to compare the results of the various methods for establishing and characterising discontinuity sets, the poles representing the average orientations of all planar elements within each identified discontinuity set at each Site were plotted on a single stereographic plot. Figure 9.26 shows these poles for Site 1, and Figure 9.30 shows these poles for Site 2. In these plots, pole-density values are displayed in grey-scale behind the actual poles. These allowed the rapid observance of differences and similarities between the computed discontinuity sets defined by the four computational methods and the discontinuity sets identified by traditional field methods. These observations in turn allowed the identification of “generic” discontinuity sets for each Site.

Site 1 has seven generic discontinuity sets (labelled ‘A’ through ‘G’). Four genereic discontinuity sets (Sets ‘A’, ‘B’, ‘C’, and ‘D’) were identified as equivalent by all four point-cloud processing Methods. The fifth generic discontinuity set (set E) is more variable in orientation and was identified as similar by only three of the four point-cloud processing Methods. Point-cloud processing Method 2 identified a discontinuity set (Set 3) that deviates strongly from any discontinuity set identified by the other Methods, but can be identified with two sets from the scanline survey and the SSPC survey. This was therefore classified as generic discontinuity set F. Discontinuity sets from both the scanline survey and SSPC survey coincide with only three out of the first four generic discontinuity sets identified by the point-cloud processing Methods (Sets ‘A’, ‘B’, and ‘D’). Generic discontinuity set ‘C’ was identified by all four point-cloud processing Methods but by none of the field methods. On the other hand, generic discontinuity set ’G’ is identified by both field methods, but by none of the point-cloud processing Methods.

Site 2 has five generic discontinuity sets (labelled ‘A’ through ‘E’), but in other respects Site 2 results are similar to those observed at Site 1. Three generic discontinuity sets (Sets ‘A’, ‘B’, and ‘C’) are identified as equivalent by all four point-cloud processing Methods, as well as by both field survey methods. The fourth generic discontinuity set (Set D) is more variable in orientation and was identified by Methods 1-3. Method 4 identified a discontinuity set (Set 2) that deviates strongly from any discontinuity set identified by the other Methods, and it also does not coincide with any discontinuity set identified by any of the field methods. Similar to the observations for Site 1, there is one generic discontinuity set (Set E) that is identified by both field methods, but by none of the point-cloud processing Methods.

The generic sets that are only identified by the field methods do not coincide with orientations that are perpendicular to the slope, which should be expected. Rather, both these sets are oriented almost parallel to the slope. Thus, it would seem that they should be readily identified by the laser-scanning methods. Since they are not, and yet it is assumed that the field measurements that discovered these “unidentified” discontinuity sets have been properly undertaken, an explanation is that they are not sufficiently large or exposed to be spatially significant, and thus cannot be classified as a discontinuity set by point-cloud processing procedures. Another explanation is that these are measurements outside the scanned area, which may have identified another set.

In this chapter a comparison is also made between the computed orientations of specific discontinuity planes and actual measured orientations obtained by geologic compass in the field. The computed orientations from Methods 2, 3 and 4 tally well with the measured orientations, with an average pole-vector difference or dihedral angle ranging between 3 and 7 degrees. The mean pole-vector differences between the computed orientations from Method 1 and the measured orientations are larger, ranging between 8 and 11 degrees. As explained in Section 9.8.1, the remaining error has several components and can mainly be attributed to:

- The (manual) compass orientation measurement error.
- The choice of location on the discontinuity plane where a representative orientation measurement was made with the geologic compass.
- The registration error caused by an inaccurate levelling of the laser scanner and/or measurement of the bearing of laser scanner.
- The plane outlining criteria employed during data processing to define planar elements, since the orientation of the planar element is calculated as the average orientation of the entire selected plane.

The error caused by the noise in the laser data should be considered negligible to the other errors. The larger mean pole-vector difference with Method 1 should be attributed to the method employed for assembling the discontinuity planes into discontinuity sets by evaluating the orientations of the surface reconstruction facets. The adopted method may result in the assembly of larger (virtual) discontinuity planes that are actually composed of multiple planes that may have a significant difference in orientation, although they still fall within the same set. The subsequent computation of the average discontinuity plane orientation may therefore differ significantly from a geologic compass measurement that only represents a small portion of this larger virtual plane.

The computed values of normal set spacing and the introduced “equivalent” normal set spacing statistics show strong similarities among the four point-cloud processing methods. However, the comparison between the spacing distributions computed by the point-cloud processing methods with those measurements produced by convential (field) methods did not show any clear correlation. The mean spacing computations based on the point-cloud data are strongly affected by the large number of redundant and small spacing values generated by individual discontinuity planes that may actually be part of the same discontinuity plane. One can imagine three individual planar surfaces exposed on the rock face, and thus recognised by any of the four point-cloud processing methods, will create two small and redundant normal or equivalent normal spacing distances where there should be only a single observation point. One the other hand, there is also no good correlation between the two different field survey methods. The SSPC method tends to over-estimate the normal set spacing values, since an observer tend to focus on the larger spacing distances rather than on the smaller ones. In general, it is very hard to make a proper comparison between the spacing estimates produced by computational methods and the field methods, since they are fundamentally different in nature.

10 Conclusions

10.1 Introduction

Terrestrial laser scanning is a state-of-the-art mapping technology that can rapidly acquire accurate three-dimensional spatial data. Over the past decade it has experienced very fast growth as it has been found useful in many engineering and surveying applications.

Laser scanners emit and detect the reflection of a very narrow light beam in order to determine distance to a reflected object. The beam is progressively shifted using rotating mirrors, so that millions of measurements are made over an entire scene in a short period. The distance and bearing values for each of the resulting extremely large number of reflected points are converted into x, y, and z coordinates, producing a “point cloud” that accurately defines the geometric details of all objects located within the scene being scanned.

The primary focus of this research project is the development and use of automated or semi-automated procedures to extract the geometric properties of discontinuities encountered in rock exposures by analysis of point-cloud datasets. The point-cloud datasets offer opportunities to obtain much-improved geometric characterisations of discontinuities within a rock mass, compared to discontinuity characterisations resulting from conventional field mapping methods. Yet the characteristics of the point-cloud datasets, including their relatively large size and lack of spatial organisation, present difficulties in efficiently analysing them and extracting the desired geometric information.

The following sections discuss and summarise several important conclusions resulting from this research. The discussions begin with a summary comparison of the conventional field methods of rock face mapping and the new remote sensing methods of obtaining similar information, including both photogrammetry and laser scanning. Then there is a review of the research hypothesis and the project objectives and methodology, including a summary of the four point-cloud data processing methods developed and evaluated in this study. These discussions are concluded by a summary of the steps taken to verify the accuracy of the results achieved by the new analysis methods, compared to results that may be obtained by traditional methods. A brief assessment of the potential applications of these proposed new analysis methods, and their limitations, is followed by some concluding remarks.

10.2 Conventional rock face mapping versus remote sensing

The conventional method of mapping the geometric properties of discontinuities in rock exposures is based on manual survey with compass-clinometer and measuring tape. This method, although simple and effective, can be biased, is often inaccurate, and usually is dangerous and time-consuming. Nevertheless, discontinuities play a major role in controlling the geomechanical characteristics of a rock mass and thus a comprehensive assessment of their properties is crucial to the design of civil engineering works.

Remote sensing techniques offer an alternative to conventional manual surveys for assessing discontinuities in rock exposures. The obvious operational advantage is that a rock face can be mapped from a distance without the need for physical contact. Analogue and digital terrestrial photogrammetry has already been used successfully to determine discontinuity orientations, although usually not in a fully automated way. 3-D terrestrial laser scanning is a relative new remote

sensing technique that has several operational advantages over photogrammetry. Although the equipment costs are higher, 3-D terrestrial laser scanning gives the user more control over the resolution and accuracy of the survey data and is able to deliver the survey data in near real-time. Both laser scanning and digital photogrammetry generate survey data as a point cloud that describes the geometry of surveyed rock face with a high amount of detail and precision.

10.3 Hypothesis, objectives and methodology

The point-cloud data can subsequently be visualised using a computer; the data can be rotated and assessed from a variety of viewpoints, and can be enhanced with reflected laser intensity information or with colour imagery obtained with a digital camera. The scanned rock face can thus be inspected in detail from all directions at any time and place. Discontinuity planes and discontinuity sets are easily recognised, often better than in the field. Experience has demonstrated that this new visual perspective allows access to and the use of a great amount of discontinuity information hidden in this data. Consequently, this has triggered the formulation of the hypothesis for this research, which is the following:

"Information on the geometric properties of the discontinuities that are visible in an exposed discontinuous rock mass can be extracted from a 3-D point cloud data set. The extraction of information can be carried out in a fully automated way."

As a result, the main objective of this study became the development of computer-based methods to extract the geometric properties of discontinuities within rock masses from the point-cloud data. The formalisation of this derivation process should eventually lead to the development of an automated or semi-automated system based on a combination of hardware and software procedures. The principal advantage of the automation of the entire process is that the human bias will be eliminated as much as possible. Automated processing of the data will also reduce the operational costs and may permit a near real-time processing of the data on-site.

This research investigated two different point-cloud data processing approaches: a top-down and bottom-up approach. The first (top-down) approach uses surface reconstruction methods to create a mesh representing the 3-D surface of the rock exposure from the point-cloud data. Discontinuity planes are then identified by evaluating this 3-D mesh. The second (bottom-up) approach is called point-cloud segmentation. This approach directly evaluates the original point-cloud data using various plane-finding algorithms to detect planar features. Both approaches create a spatial data structure that allows the efficient analysis of the spatially unorganised and noisy point-cloud data. The common goal of both approaches is to find planar features in the point-cloud data and evaluate their geometric discontinuity properties. This evaluation include the computation of orientations of individual planar features, the classification of these planar features into a series of identifiable discontinuity sets, and by further analysis of these discontinuity sets, to provide statistical descriptions of these discontinuity sets and to compute their set spacing distributions.

At the beginning of the research, no software was available. This required the development and implementation of data processing methods through programming, which was accomplished using Matlab. However, in the course of the research two suitable (beta) software methods were made available by their developers to support the purposes of this study. One of the software methods (called Split-FX) uses the surface reconstruction approach, while the other software method (called PCM) uses the point-cloud segmentation approach. Therefore, in total four different methods were applied to derive the geometric discontinuity properties: two methods used surface reconstruction and two methods used point-cloud segmentation. The methods were tested using datasets from two rock exposures located in northeastern Spain. Both rock exposures consisted of Carboniferous sedimentary rocks containing well-developed discontinuities forming more than three discontinuity sets.

10.4 The point cloud processing methods

The first method was developed in Matlab and makes use of an implicit surface representation with Radial Basis Functions. This technique yields a truly 3-D surface reconstruction of the original scanned object. The surface can be represented by a meshed surface composed of triangular facets, with each facet having a specific orientation. By plotting and analysing all the facet orientations, the user can identify possible discontinuity sets from the surface data. Through fuzzy k-means clustering, facet orientations can subsequently be classified into distinct discontinuity sets. Subsequent joining of connecting facets that form individual planar elements or features within each discontinuity set allows for the identification of individual discontinuity planes within each discontinuity set. Geometric information on these discontinuity planes, and on their membership within discontinuity sets, can be saved for further analysis.

The second method is implemented in the software Split-Fx, and makes use of a 2-D gridding surface reconstruction approach. The user merely defines the grid size and the software subsequently simplifies the point-cloud data and represents the rock exposure face by a gridded surface, defined by a triangulated mesh. Discontinuity planes are found by joining adjacent mesh facets whose orientation differences are below a user-specified angular dispersion threshold. The surface patches defined by this process can be plotted directly on a stereographic plot and the plane information can be exported for further analysis.

The third method was developed in Matlab and makes use of a direct point-cloud segmentation approach. The method starts by creating a kd-tree data structure in the point cloud data. This allows rapid spatial searches through the previously unorganised point-cloud data. A seed point is then selected that has a sufficient number of neighbouring points to represent a (user-defined) plane. Principal Component Analysis (PCA) is used to determine the best fitting plane through a selection of neighbouring points and which of these points define this plane. Through the repeated selection of seed points, their neighbouring points, and subsequent evaluation of the outliers and inliers to the defined plane, the plane is “grown” with new points until no additional points fulfil the plane definition. This process is repeated until all points in the point cloud capable of belonging to planar features are classified (segmented) to individual planes. There will remain certain number of outliers or noisy points that do not belong to any discontinuity plane.

The fourth method is implemented in the software PCM and also uses a point-cloud segmentation approach. Similar to the third method, it starts by creating a kd-tree structure in the data. The difference is that seed points are selected with a 3-D Hough transform. The points that form a cluster in 3-D Hough space define a plane and are used as seed points. These seeds points are then spatially “grown” as newly found points are evaluated by least-squares estimation to determine whether they fall on the previously found plane.

Although they utilise fundamentally different approaches, all four methods yield a discontinuity plane list for the surveyed rock face that describes the geometry of each recognized discontinuity plane in terms of its plane equation and other properties such as the plane centroid and maximum and minimum spatial extents. These values are used in further processing steps to derive average discontinuity set orientations, to compute discontinuity set statistics such as Fisher’s-k measurement of dispersion of spatial orientations, and to analyse discontinuity set spacing distributions by computing values of normal set spacing and equivalent normal set spacing. This allows objective comparisons to be made among the four different point-cloud data processing methods and a verification of these new methods by comparisons of their results with the results obtained by conventional manual field survey methods.

10.5 Verification of the results

There is a good correlation, on a plane-by-plane basis, between the measured orientations obtained by conventional manual field surveys and the computed orientations obtained by the four point-

cloud data processing methods. The computed orientations produced by methods 2, 3 and 4, when compared to the measured field orientations, have an average pole-vector difference or dihedral angle ranging between 3 and 7 degrees. The mean pole-vector differences between the computed orientations of method 1 and the measured orientations are larger, ranging between 8 and 11 degrees. These differences are considered acceptable, considering the many factors that influence both the manual orientation measurements and the computed orientation measurements with the laser scan data.

Clear relationships between the discontinuity sets found with the four data processing methods and the field surveys were more difficult to establish. In order to compare the set statistics between the data processing methods, the plane orientations were clustered with fuzzy k-means clustering to the same number of discontinuity sets. Based on the results obtained for the two test sites, one can conclude that in both cases the three most prominent and orthogonal discontinuity sets are recognised by all point cloud data processing sets as well as by the field surveys. The remaining discontinuity sets were more ambiguous; some were only recognised by some (or all) of the point-cloud processing methods, while other discontinuity sets were only clearly recognised by the conventional field survey methods. It should be mentioned that the conventional field survey methods did not always produce consistent results; some scanline surveys detected discontinuity sets that were not recognised by the SSPC survey and vice versa. In one instance, the point-cloud processing method clearly recognised a discontinuity set, probably a set of rock bridge fractures that was not recognised by conventional field methods.

Where the discontinuity sets of the four point cloud processing methods matched, there was a good correlation between the computed values describing the set spacing values. However, no good correlations could be established between the computed spacing values and the measured spacing values. The main reason for this is that the point-cloud processing methods and the conventional field survey methods are fundamentally different in nature. Scanline surveys concentrate on acquiring spacing data along a single specific line along the rock face, while the spacing computations from the point-cloud processing methods use discontinuity plane data from the entire rock face. Another reason is that the computed spacing values based on the laser-derived point-cloud data were considerably smaller than the measured spacing values obtained from the field data. This is caused by the fact that individual planes found with any of the four methods may actually be part of the same discontinuity plane. These separate planar elemental definitions create additional small spaces that may not exist in reality.

10.6 Applications and limitations

This research demonstrated that it is possible to automate to a great extent the entire procedure for using point-cloud data to generate discontinuity information. Some user interaction will still be required, for instance to define the number of sets and to establish the processing parameters. However, manual outlining of discontinuity planes and discontinuity sets has been replaced with fully automated procedures. This manual outlining process is still required in most of the available software and methods, and especially by those procedures currently supporting many close-range digital photogrammetry applications.

The unbiased extraction of discontinuity information provides an important initial step for various applications where the modelling of a discontinuous rock-mass structure is vital, for instance:

- 2-D and 3-D numerical (discrete element) rock mass models.
- Rock mass slope stability analysis and support design
- Rock mass classification systems
- Support design for underground excavations and tunnels
- Block size distribution analysis, particularly for quarrying operations
- Blast design for quarrying, mining and tunnel operations

- Structural geological analysis
- Permeability assessment of rock masses (especially secondary, or fracture permeability)

The fact that the entire process can be automated has several advantages. For time-critical applications, such as slope stability design and blast design (Kemeny and Handy, 2004) for quarrying or mining operations, the rapid generation of key discontinuity information can have important economic and operational advantages. During the design of tunnel support for instance, the design of support measures (rockbolts or shotcrete) can be verified or adjusted, based on the locally scanned and derived assessment of discontinuity conditions directly behind or in the tunnel face. For scientific applications, such as structural geological studies, the on-site generation of discontinuity information can assist in the understanding of the structures in the field.

There are a number of limitations to the methodologies described in this study. Some limitations are related to the inherent restrictions of the laser scan data, while other limitations are related to the data processing methods.

The most important limitation is due to the geometric approach of the methodologies, i.e. a discontinuity plane can only recognised if it is exposed. From a practical point-of-view, a discontinuity plane can be measured if one can put a hand on its surface. Discontinuities that are only shown as traces in the rock face are therefore not distinguished by the methods developed and assessed during this research. However, other researchers are currently evaluating accurate 3-D digital images of rock exposure faces created by combining point-cloud data produced from terrestrial laser scanners with high-resolution digital images. Under at least some circumstances, the extraction and analysis of useful geometrical discontinuity information may be possible by analysing discontinuities that can be seen only as traces on the exposed rock face.

The occlusion or shadowing of areas during a single scan may result in further important limitations in the application of the laser-scan-derived point-cloud data. This effect can be eliminated by scanning from different locations. In practice, occlusion areas that are located higher on a rock face are difficult to remove.

What has not been done yet is to carry out comprehensive testing, for the specific purpose of scanning of rock faces, to select the optimal laser scanning system and configuration. This should be investigated for different scanning distances, exposure dimensions and even rock types, since these factors all have influence on the final data quality. Also the scanning environment, for instance operations at various temperatures or under dusty conditions should be incorporated.

At present, data registrations of laser-scan-derived point clouds remain an operational challenge. Laser-scanners are generic surveying tools and of not specifically designed for rock face surveying. Nevertheless, the addition to the laser scanner hardware of a relative simple levelling device, combined with a calibrated compass, would allow a simple but adequate data registration for many rock-surveying purposes.

The data processing and data visualisation tools that have been created and used in this study have not been developed into complete software packages. To see the methods become operational data-processing tools that can be used in the field remains, up to this point, an uncompleted ambition.

10.7 Concluding remarks

This thesis described four point cloud processing methods that allow the automated extraction of the geometric discontinuity information: orientation, plane geometry, discontinuity set statistics and normal set spacing values based on 3-D laser scanner data. In terms of accuracy of the derived information compared to the manual field measurements, all four methods performed equally well.

The main problem was that a comprehensive statistical comparison with the conventional methods was very difficult to make, since these methods are so fundamentally different in nature. The only good quantitative comparison that could be made was between the individual computed orientations and the measured orientations. Here, all four point-cloud-based methods showed a good correlation with those obtained by manual surveys; however, method 1 gave the least-accurate result. Experience gained with the two data-processing approaches suggests that point-cloud segmentation is the most promising in terms of future software implementation. Point-cloud segmentation has the great advantage that no prior surface reconstruction is required. This not only saves processing time; it also keeps the original point-cloud data in its original state, and this will have additional advantages if for example, in the future, discontinuity surface roughness has to be determined. Another advantage of point-cloud segmentation is that the processing algorithms are not affected by vegetation or other noise in the point-cloud data. This also saves valuable time since the point-cloud data set does not require any prior data cleanup.

Although tested on point cloud data that was derived from a 3-D terrestrial laser scanner, the point cloud processing methods that are proposed here should work equally well on point-cloud data derived from a 3-D photogrammetric survey. However, 3-D terrestrial laser scanning has several operational advantages as well as advantages in terms of data quality. A system is therefore envisioned where hardware in the form of a 3-D terrestrial laser scanner, combined with a laptop with dedicated point-cloud-processing software (based on the point-cloud segmentation principle), delivers discontinuity information in near real-time, in the field, to the operator. It will remain essential however, to review the results critically by a geological or engineering geological expert and where possible, complement the survey with conventional measurements. The efficient employment of any laser-scanning survey, and especially the selection of appropriate processing parameters, requires an adequate knowledge of the geological site characteristics, the specifications and capabilities of the laser scanner, and experience with the characteristics of point-cloud data and with the procedures for processing and analysing the data.

References

3G Software and Measurement GmbH., n.d. Contact free acquisition and assessment of rock and terrain surfaces by metric 3-D images, from: http://www.3gsm.at.

Afifi, A., Clar, V.A. and May, S., 2004. Computer Aided Multivariate Analysis. Texts in Statistical Science. Chapman and Hall/CRC.

Amenta, N, Choi, S., Dey, T. K. and Leekha, N., 2000. A simple algorithm for homeomorphic surface reconstruction. Proc. 16th. ACM Sympos. Comput. Geom, pp. 213-222.

Anderson, E.M., 1951. The Dynamics of Faulting, Oliver and Boyd, Edinburgh, 206 pp.

Arya, S., Mount, D.M., Netanyahu, N.S., Silverman, R. and A.Y. Wu., 1998. An optimal algorithm for approximate nearest neighbour searching fixed dimensions. Journal of ACM, Vol. 45(6), pp. 891-923.

Balk, R., 1938. Structural Behaviour of Igneous Rocks, Geological Society of America Memoir 6, xxp.

Baroudi, H., Piguet, J.P., Chambon, C. and Asof, M., 1990. Utilization of the block generator 'Resoblok' to complex geological conditions in an open pit mine. In: Mechanics of jointed and faulted rock, Rossmanith (editor), Balkema, Rotterdam, pp. 529-535.

Barton, N. and Choubey, V., 1977. The shear strength of rock joints in theory and practice. Rock Mechanics, 10, pp.1-54.

Barton, N. R.; Lien, R. and Lunde, J., 1974. Engineering classification of rock masses for the design of tunnel support. Rock Mechanics, 6, pp.189-236.

Barton, N., 1973. Review of a new shear strength criterion for rock joints. Engineering Geology, **7**, pp. 287-332.

Barton, N., 1978. Suggested methods for the Quantitative Description of Discontinuities in Rock Masses, Intl. Journal Rock Mech. Min. Sci. & Geomech. Abstr., Vol.15, pp. 319-368.

Bell, F.G., 1983. Fundamentals of Engineering Geology, Butterworths, London, 648 pp.

Beraldin, J.A., Blais, F., Boulanger, P., Cournoyer, L., Domey, J., El-Hakim, F., Godin, G., Rioux, M and Taylor, J., 2000. Real world monitoring through high resolution digital 3-D imaging of objects and structures. ISPRS Journal of Photogrammetry and Remote Sensing, 55: pp 230-250.

Berg, M. de., Kreveld, M. van, Overmars, M, and Schwarzkopf, O., 2000. Computational Geometry: Algorithms and Applications", Springer-Verlag, 386 pp.

Besl, P.J. and McKay, N.D., 1992. A method for registration of 3-D shapes, IEEE Transactions on Pattern Analysis and Machine Intelligence, 14 (2), pp. 239-256.

Bezdek, J.C., 1981. Pattern recognition with fuzzy objective function algorithms. Plenum, New York.

Bieniawski, Z.T., 1976. Rock mass classification in rock engineering. In: Proceedings of the Symposium On Exploration for Rock Engineering, Johannesburg, ed. Bieniawski. Balkema, Rotterdam, pp. 97-106.

Bieniawski, Z.T., 1989. Engineering Rock Mass Classification. Wiley, New York, USA, 251 pp.

Bingham, C., 1964. Distributions on the sphere and on the projective plane. PhD Thesis, Yale University, New Haven, Connecticut.

Borradaile, G., 2003. Statistics of Earth Science Data. Springer-Verlag, Berlin, 351 pp.

Bracco Gartner, G.L. and Schlager, W., 1997. Quantification of topography using a laser-transit system. Journal of Sedimentary Research, 67, pp. 987-989.

Bradford Barber, C.B., Dobkin, D.P., and Huhdanpaa, H.T., 1995. The Quickhull algorithm for convex hulls. ACM Trans. on Mathematical Software, 22(4), pp 469-483.

BS 5930:1999. Code of practice for site investigations. British Standard. British Standard Institution, London. BSI 10-1999. 192 pp.

Budynas, R.G., 1977. Advanced Strength and Applied Stress Analysis, McGraw-Hill, 508 pp.

Carr, J.C., Beatson, R.K., Cherrie, J.B. Mitchell, T.J., Fright, W.R., McCallum, B.C. and Evans, T.R., 2003. Smooth surface reconstruction from noisy range data. ACM GRAPHITE 2003, Melbourne, Australia, pp 119-126, 11-19 February 2003.

Carr, J.C., Beatson, R.K., Cherrie, J.B., Mitchell, T.J., Fright, W.R., McCallum, B.C. and Evans, T.R. 2001. Reconstruction and Representation of 3-D Objects with Radial Basis Functions. ACM SIGGRAPH 2001, Los Angeles, CA, pp. 67-76, 12-17 August 2001.

Clayton C. R. I., Matthews M.C., Simons N.E., 1995. Site Investigation. Second Edition. Blackwell Science, Oxford. 584 pp.

Cloos, H., 1923. Das batholithenproblem, Fortschr. Geologie und Palaeontologie, HT, 1.

Cocone, 2009. Cocone Softwares for surface reconstruction and medial axis. From: http://www.cis.ohio-state.edu/~tamaldey/cocone.html.

Colodron, I., Nuñez, A. and Ruiz, V., 1976. Memoria y Hoja Geológica número 472 (Reus). Mapa Geológica de España E: 1:50.000 (Segunda Serie). IGME, Madrid.

Cowan, E.J., Beatson, R.K., Fright, W.R., McLennan, T.J. and Mitchell, T.J., 2002. Rapid geological modeling. In: Applied Structural Geology for Mineral Exploration and Mining, International Symposium, Australian Institute of Geologists, International Structural Conference, Kalgoorlie, WA, Australia, 23-25 September 2002.

Davis, J.C., 2002. Statistics and Data Analysis in Geology. John Wiley and Sons, 2nd edition, Singapore, 646 pp.

Deere, D.U., 1964. Technical description of cores for engineering purposes. Rock mechanics and rock engineering, Vol.1, pp. 17-22.

Delaunay, B., 1934. Sur la sphère vide. Izvestia Akademii Nauk SSSR, Otdelenie Matematicheskikh I Estestvennykh Nauk, 7:739-800, 1934.

Dey, T.K., Giesen, J. and Hudson, J., 2001. Delaunay Based Shape Reconstruction from Large Data. Proc. IEEE Symposium in Parallel and Large Data Visualisation and Graphics (PVG2001), pp. 19-27.

Edelsbrunner H., Mucke, E., 1994. Three dimensional alpha shapes. ACM Transactions on Graphics, Vol. 13 (1), pp. 43-72.

Ehlen, J., 2000. Fractal Analysis of Joint Patterns in Granite, International Journal of Rock Mechanics and Mining Sciences., 37(6), pp 909-922

Einstein, H., 1993. Modern developments in discontinuity analysis- the persistence-connectivity problem. In: J.A. Hudson (Ed.) Comprehensive rock engineering, principles, practice, and projects, Vol. 3: Rock testing and site characterization, pp. 193-213. Oxford: Pergamon Press.

Einstein, H., Veneziano, D., Baecher, G. and O'Reilly, K., 1983. The effect of discontinuity persistence on rock slope stability. International Journal of Rock Mechanics and Mining Sciences, 20(5), pp. 227-236.

Engelder, T. and Geiser, P., 1980. On the use of regional joint sets as trajectories of paleostress fields during development of the Appalachian Plateau, New York, Journal of Geophysical Research, Vol.85, B11, pp. 6319-6341.

Fabio, R., 2003. From point cloud to surface: the modeling and visualization problem, Int. Arch. Photogrammetry, Remote Sensing, Information Sciences, Vol. XXXIV-5/W10.

Fardin, N., Feng, Q. and Stephansson O., 2004. Application of a new in situ 3-D laser scanner to study the scale effect on the rock joint surface roughness. International Journal of Rock Mechanics and Mining Sciences, Vol. 41, pp. 329-335.

Farfield Technology, 2004. FastRBF Toolbox, v.1.4 [computer software], FarField Technology, New Zealand. Website: http://www.farfieldtechnology.com/

Fasching, A., Gaich, A. and Schubert, W. 2001. Data acquisition in Engineering Geology. An improvement of Acquisition Methods for Geotechnical Rock Mass Parameters. Felsbau 19 (2001) Nr. 5., pp. 93-101.

Fecker, E. and Rengers, N.F., 1971. Measurement of large-scale roughness of rock planes by means of profilograh and geological compass. First International Symposium on Rock Mechanics, Nancy, I-18.

Feng, Q., Sjögren, P., Stephansson, O. and Jing, L., 2001. Measuring fracture orientation at exposed rock faces by using a non-reflector total station. Engineering Geology, 59, pp. 133-146.

Feng, Q., Fardin, N., Jing, L. and Stephansson, O., 2003, A new method for in situ non-contact roughness measurement of large rock fracture surfaces. Rock Mechanics and Rock Engineering, 36(1), pp. 3-25.

Feng, Q.H. and Röshoff, K., 2004. In-situ mapping and documentation of rock faces using a full-coverage 3-D laser scanning technique, Int. J. Rock Mech. Min. Sci., Vol 41 (3), Paper 1A, 23 Sinorock 2004 symposium.

Fisher, N.I., Lewis, T. and Embleton, B.J. 1987. Statistical analysis of spherical data. Cambridge university Press, New York, 329 pp.

Fisher, R., 1953. Dispersion on a sphere. Proceedings Royal Society London A217, pp. 295-305.

Franklin, J.A, Maerz, N.H. and Bennett, C.P., 1988. Rock mass characterisation using photoanalysis. International Journal of Mining and Geological Engineering, 6(2), pp. 97-111. Presented at the 28th US Rock Mechanics Symposium, Tucson, Arizona, 29 June-1 July 1987.

Fröhlich, C. and Mettenleiter, M., 2004. Terrestrial Laser Scanning - New Perspectives in 3-D Surveying. International Archives of Photogrammetry, Remote Sensing and Spatial Information Sciences, Vol XXXVI, Part 8/W2, October 2004.

Fukuyama, Y. and Sugeno, T., 1993. A new method for choosing the number of clusters for the fuzzy c-means method. In: Proc. 5th Fuzzy Syst. Symp., 1989, pp. 247-250 (In Japanese).

Gaich, A., Pötsch, M., Fasching, A. and Schubert, W., 2004. Contact-free measurement of rock mass structures using the jointmetrix3-D system. International Journal of Rock Mechanics and Mining Sciences, Vol. 41 (3), Paper 1B 18 Sinorock 2004 symposium.

Galante, G.; Piacentini, M. and Ruisi, V. F., 1991. Surface roughness detection by image processing tool. Wear 148 (2), pp. 211-220.

Gath, I. and Geva, A.B., 1989. Unsupervised optimal fuzzy clustering. IEEE Transactions on Pattern Analysis and Machine Intelligence. 11(7), pp. 773-781.

Girod, B., Greiner, G. and Niemann, H., 2000 (eds.). Principles of 3-D Image Analysis and Synthesis, Kluwer Academic Publishers, Boston, 466 pp.

Glaesner, R and Cap, R. 2004. Ground-based laser positioning. In: Proceedings of the ISPRS working group VIII/2 'Laser-Scanners for Forest and Landscape Assessment'. Freiburg, Germany 03-06 October 2004. International archives of photogrammetry, remote sensing and spatial information sciences. Volume 36, Part 8/W2. Eds: Thies, M. Koch, B., Spiecker, H. and Weinacker, H.

Golder Associates Inc., 2004. FracWorks XP - Discrete Feature Simulator [software]. User documentation V 4.0. Golder Associates Inc. Seattle, Washington. August 2004. 88 pp. Website: http://www.fracman.com/

Goldstein, H. 1980. Classical Mechanics. Second edition. Reading, MA. Addison-Wesley.

Golub, G.H. and Van Loan, C.F., 1980. An analysis of the total least squares problem. SIAM Journal on Numerical Analysis, 17 (6), pp. 883- 893.

Goodman, R.E, Kieffer, S., 2000. Behavior of rock in slopes. Journal of Geotechnical and Geoenvironmental Engineering. 126(8), pp 675-684.

Goodman, R.E. and Shi, G., 1985. Block Theory and Its Application to Rock Engineering, Prentice-Hall, New Jersey, 1985.

Goodman. R.E., 1989. Introduction to rock mechanics. Second edition. New York, Wiley and Sons, 1989, 562 pp.

Grasselli, G. and Egger, P., 2000. 3-D surface characterization for the prediction of the shear strength of rough joints. In: Proceedings of EUROCK 2000, 14th Nationales Symposium für Felsmechanik und Tunnelbau, Aachen, Germany, pp.281-286.

Greaves, T., 2004. Inside Laser Scanners. Position. October/November 2004. South Pacific Science Press International, Alexandria, N.S.W, Australia. Issue 3, pp 50-52.

Griffith, A.A., 1920. The Phenomenon of Rupture and Flow in Solids, Philosophical Transactions of the Royal Society, Vol.A221 pp. 163-198

Griggs, D. and Handin, J., 1960. Observations on Fracture and a Hypothesis on Earthquakes, In: Rock Deformation (D. Griggs and Handin, J., eds.), Geological Society of America Memoir 79, pp. 347-364.

Grima, M.A., 1994. Scale effect on shear strength behaviour of ISRM roughness profile. MSc Thesis, ITC Delft, Kanaalweg 3, 2628 EB Deft, The Netherlands, 200 pp.

Gruen, A. and Akca, D., 2005. Least squares 3-D surface and curve matching. ISPRS Journal of Photogrammetry and Remote Sensing. Volume 59, Issue 3, May 2005, pp. 151-174.

Hack R., Price, D. and Rengers N., 2003. A new approach to rock slope stability - a probability classification (SSPC). Bulletin of Engineering Geology and the Environment. Springer Verlag. Vol. 62: article: DOI 10.1007/s10064-002-0155-4. pp. 167-184 and erratum: DOI 10.1007/s10064-002-0171-4. pp 185-185.

Hack, H. R. G. K., 1998. Slope stability probability classification (2nd edition). International Institute for Aerospace Survey and Earth Sciences (ITC), No. 43, Enschede, The Netherlands, 258 pp.

Hack, H. R. G. K., 2003. Discontinuous rock mechanics. Lecture notes, version 2 (unpublished), International Institute for Aerospace Survey and Earth Sciences (ITC), Enschede, The Netherlands.

Hack, H.R.G.K. and Price, D.G., 1995. Determination of discontinuity friction by rock mass classification. Proc. 8th ISRM congress. Tokyo. Publ. Balkema, Rotterdam. pp. 23-27.

Hadjigeorgiou, J. and Poulin, R., 1998. Assessment of ease of excavation of surface mines. Journal of Terramechanics, 35, pp. 137-153.

Hagan, T.O., 1980. A case for terrestrial photogrammetry in deep-mine rock structure studies. International Journal of Rock Mechanics and Mining sciences, 17, pp. 191-198.

Hammah, R.E. and Curran, J.H., 1999. On distance measures for the fuzzy k-means algorithm for joint data. Rock Mechanics and Rock Engineering, Springer-Verlag. Vol. (1), pp. 1-27.

Hammah, R.E. and Curran, J.H., 2000. Validity Measures for the Fuzzy Cluster Analysis of Orientations. IEEE Trans. on pattern analysis and machine intelligence, Vol. 22 (12), pp. 1467-1472.

Hammah, R.E. and Curran, J.H.,1998. Fuzzy cluster algorithm for the automatic identification of joint sets. International Journal of Rock Mechanics and Mining Sciences, Vol. 35 (7), pp. 889-905.

Haneberg, W.C., 2007. Directional roughness profiles from three-dimensional photogrammetric or laser scanner point clouds. In: Eberhardt, E., Stead, D. and Morrison, T. (Editors), Rock Mechanics: Meeting Society's Challenges and Demands: Proceedings, 1st Canada-U.S. Rock Mechanics Symposium, Vancouver, May 27-31, 2007, p.101-106.

Haneberg, W.C., 2008. Using close range terrestrial digital photogrammetry for 3-D rock slope modelling and discontinuity mapping in the United States. Bulletin of Engineering Geology and the Environment, The official journal of the IAEG, Springer Verlag.

Haneberg, W.C., Norrish, N.I. and Findley, D.P. 2006. Digital Outcrop Characterization for 3-D Structural Mapping and Rock Slope Design Along Interstate 90 Near Snoqualmie Pass, Washington. In: Proceedings of the 57th Highway Geology Symposium, Breckenridge, Co., Sept. 26-29, 2006. Hosted by the Colorado Geological Survey and the Colorado Department of Transportation.

Harrison, J.P. and Rasouli,V., 2001. In-plane analysis of fracture surface roughness: anisotropy and scale effect in anisotropy, Proceedings of the 38th US rock mechanics symposium, Washington DC, USA, 7 - 10 July 2001, In: Tinucci,J.P., Heasley,K.A., Elsworth,D., editor, Lisse, Netherlands, Swets & Zeitlinger Publishers, pp 777-783.

Harrison, J.P., 1992, Fuzzy objective functions applied to the analysis of discontinuity orientation data. In: Eurock'92, pp. 25-30.

Hobbie, D., 1979. The Zeiss G-2 Stereocord: A simple stereoplotter for computer supported plotting. The Photogrammetric Record, 8(47), pp. 563-582

Hobbs, B.E., 1993. The Significance of Structural Geology in Rock Mechanics, in: Comprehensive Rock Engineering (Ed. Hudson), Vol. 1, pp. 25-62.

Hobbs, B.E., Means, W.D. and Williams, P.F., 1976. An Outline of Structural Geology, J. Wiley & Sons, New York, 571 pp.

Hoek, E. and Bray, J.W.,1981. Rock slope engineering. Revised third edition, The Institution of Mining and Metallurgy, London, pp 358.

Hong, E., Lee, I. and Lee, J., 2006. Measurement of Rock Joint Roughness by 3-D Scanner. Geotechnical Testing Journal, 29 (6), 8 pp.

Hoover, A., Jean-Baptiste, G., Jiang, X., Flynn, P.J., Bunke, H., Goldgof, D.B., Bowyer, K.K., Eggert, D.W., Fitzgibbon, A.W. and Fisher, R.B., 1996. An experimental comparison of range image segmentation algorithms. IEEE Transactions on Pattern Analysis and Machine Intelligence (PAMI), Vol. 18(7), pp. 673-689.

Hough, P.V.C., 1962. Method and means for recognizing complex patterns. U.S. Patent 3069654.

Houlding, S.W. 1994. 3-D geoscience modeling - Computer techniques for geological characterization. Springer-Verlag. pp. 131-135.

Huisman, M. 2006. Assessment of rock mass decay in artificial slopes. ITC dissertation number 137. 283 pp.

ICC, 2007. Base topogràfica 1:5000 v2.0 and Ortofoto 1:5000 v5.0. Digital Version. Generalitat de Catalunya, Institut Cartográfic de Catalunya. Retrieved from: www.icc.cat

ICG, 2007. Mapa Geològic de Catalunya 1:25000 v1. Digital Version. Generalitat de Catalunya, Institut Geològic de Catalunya. Retrieved from: www.icg.cat

Ilsley, R.C., 1994. Engineering geological mapping of rock slopes using a laser-transit. In: Proceedings of the 7th International congress of the International Association of Engineering Geology (IAEG). 5-9 September, Lisbon, Portugal.

ISRM, 1978(a). Barton, N., Rengers, N., et al.: Suggested Methods For the Quantitative Description of Discontinuities, International Society for Rock Mechanics, Int. J. Rock Mech. Sci. and Geomech. Abstr., Vol. 17, pp. 69-76.

ISRM, 1978(b). Suggested methods for the quantitative description of discontinuities in rock masses. Int. J. Rock Mech. Min. Sci. Geomech. Abstr., 15, pp. 319-368.

ISRM, 1981. Rock characterization, testing and monitoring, ISRM suggested methods. Editor: Brown, E.R. Pergamon Press, Oxford. 211 pp.

Jackson, J. E., 1991. A User's Guide to Principal Components, John Wiley and Sons, Inc., 592 pp.

Kadobayashi, R, Kochi, N., Otani, H. and Furukawa, R., 2004. Comparison and evaluation of laser scanning and photogrammetry and their combined use for digital recording of cultural heritage. The International Archives of the Photogrammetry, Remote Sensing and Spatial Information Sciences, Vol. XXXV, part B5.

Kalenchuk, K.S., Diederichs, M.S. and McKinnon, S., 2006. Characterizing Block Geometry in Jointed Rockmasses. International Journal of Rock Mechanics and Mining Sciences, Vol. 43, pp 1212-1225.

Kemeny, J. and Handy, J., 2004. Improving blast fragmentation prediction with new technologies for rock mass characterization, Proceedings of the 30th Annual Conference on Explosives and Blasting Technique, International Society of Explosive Engineers, New Orleans, LA.

Kemeny, J. and Post, R., 2003. Estimating three-dimensional rock discontinuity orientation from digital images of fracture traces. Computers and Geosciences, Vol. 29, pp. 65-77.

Kemeny, J. and Turner, A.K., 2008. Ground-Based LiDAR: Rock Slope Mapping and Assessment. Federal Highway Administration, Publication No. FHWA-CFL/TD-08-006, September 2008, Central Federal Lands Highway Division, Lakewood, CO 80228, 103p. Retrieved from: http://www.cflhd.gov

Kemeny, J., 2003. The time-dependent reduction of sliding cohesion due to rock bridges along discontinuities: A fracture mechanics approach. Rock mechanics and rock engineering. Springer, Wien. Vol. 36, Number 1, pp. 27-38. January 2003.

Kemeny, J., 2005. Time-dependent drift degradation due to the progressive failure of rock bridges along discontinuities. International Journal of Rock Mechanics and Mining Sciences. Vol. 42, pp 35-46.

Kemeny, J., Monte, J., Handy, J. and Thiam, S., 2003. The use of digital imaging and laser scanning technologies in rock engineering. International Symposium on the Fusion Technology of Geosystem engineering, Rock engineering, and Geophysical exploration, Seoul, Korea.

Kent, J.T., 1982. The Fisher-Bingham distribution on the sphere. Journal of the Royal Statistical Society. Series B (Methodological), Vol. 44, No. 1 (1982), pp. 71-80.

Kerstiens, C.M.D., 1999. A Generic UDEC model for rock joint shear tests, including roughness characterisation MSc Thesis, TU Delft, The Netherlands, 211 pp.

Krosley, L., 2003. An evaluation of using digital photogrammetry to obtain geotechnical data. Unpublished internal report, Colorado School of Mines.

Kulatilake, P. H. S. W., 1993. Application of probability and statistics in joint network modeling in three dimensions. In: Probabilistics methods in geotechnical engineering, Li and Lo (eds), Balkema, Rotterdam, pp. 63-87.

La Pointe, P.R. and Hudson, J.A., 1985. Characterisation and Interpretation of Rock Mass Joint Patterns, Special Paper 199, The Geological Society of America.

Ladeira, F.L. and Price, N.J., 1981. Relationship between fracture spacing and bed thickness, Journal of Structural Geology, Vol.3, pp. 179-183

Laubscher, D. H., 1990. A geomechanics classification system for rating of rock mass in mine design. Journal of the South African Institute Of Mining and Metallurgy, 90 (10), pp. 257-273.

Lemmon, T. and Biddiscombe, P., 2007. Trimble White Paper: Trimble 3-D scanning for surveyors. Trimble Survey, Westminster, Colorado, USA. Retrieved from: http://www.trimble.com.

Lemy, F. and Hadjigeorgiou, J., 2004. A field application of laser scanning technology to quantify rock fracture orientation. In: Proceedings of the ISRM regional symposium EUROCK 2004 and 53rd geomechanics colloquy, pp. 435-438.

Lichti, D. D., Stewart, M. P., Tsakiri, M. and Snow, T., 2000. Benchmark tests on a three -dimensional laser scanning system. Geomatics Research Australasia, 72, pp. 1-24.

Lichti, D.D., 2004. A resolution measure for terrestrial laser scanners. The International Archives of the Photogrammetry, Remote Sensing and Spatial Information Sciences, Vol. 34, Part XXX, pp. 6.

Lichti, D.D., Gordon, S.J. and Stewart, M.P., 2002. Ground-based laser scanners: operation, systems and applications. Geomatica, Vol. 56 (1), pp. 22-33.

Linkwitz, K., 1963. Terrestrisch-Photogrammetrische Kluftmessung. Rock Mechanics and Engineering Geology V I, pp 153-159.

Lu, P. and Latham, J.P., 1998. A model for the transition of block sizes during fragmentation blasting of rock masses, FRAGBLAST - International Journal of Blasting and Fragmentation 2 , pp. 341-368, 1998.

Lu, P. and Latham, J.P., 1999a. Developments in the Assessment of In-situ Block Size Distributions of Rock Masses, Rock Mech. Eng. 32 (1), pp. 29-49, 1999.

Lu, P. and Latham, J.P., 1999b. Development of an assessment system for the blastability of rock masses, Int. J. Rock Mech. Min. Sc. 36, pp. 41-55, 1999.

Lu, P. and Latham, J.P., 1999c. Investigation into the relationship between fractal dimension and the blastability of rock masses, Fragblast 1999 Symposium Proceedings, South African Institute of Mining and Metallurgy, Johannesburg, 1999.

Lu, P., 1997. The characterisation and analysis of in-situ and blasted block size distributions and the blastability of rock masses, Thesis of PhD, Queen Mary and Westfield College, University of London, 1997.

Lu., P. and Latham, J.P., 1996. In-situ Block Size Distribution Prediction with special reference to discontinuities with fractal spacing distributions. In: Eurock '96 Symposium Proceedings.

Maas, H.-G. and Hampel, U., 2006. Photogrammetric Techniques in Civil Engineering Material Testing and Structure Monitoring. Photogrammetric Engineering and Remote Sensing, Vol. 72, No. 1, pp. 39-45.

Maerz, N.H. and Germain, P., 1996. Block size determination around underground openings using simulations. Proceedings of the FRAGBLAST 5 Workshop on Measurement of Blast Fragmentation, Montreal, Quebec, Canada, 23-24 Aug. 1996, pp. 215-223.

Maerz, N.H., 1996. Reconstructing 3-D Block Size Distributions from 2-D Measurements on Sections, Proceedings of the FRAGBLAST 5 Workshop on Measurement of Blast Fragmentation, Montreal, Quebec, Canada, pp. 39-43.

Maerz, N.H., Franklin, J.A., Bennett, C.P., 1990. Joint roughness measurement using shadow profilometry. International Journal of Rock Mechanics, Mining Sciences and Geomechanical Abstracts. Vol. 27, pp. 329-343.

Mardia, K.W., 1972. Statistics of directional data. Academic Press, New York/London. 357 pp.

Markland, J., 1974. The analysis of principal components of orientation data. International Journal of Rock Mechanics, Mining Sciences and Geomechanical Abstracts. Vol. 11 (3), pp 157-163.

Matherson, G.D., 1983. Rock stability assessment in preliminary site investigations - graphical methods, TRRL Report LR 1039, Transport Research Laboratory, Crowthorne, Berks.

Mathworks, n.d. Matlab, The language of Technical Computing. Version 6.5, Release 13 [software]. From http://www.mathworks.com

Mekel, J.F.M., Savage, J.F. and Zorn, H.C., 1964. Slope Measurements and estimates from aerial photographs. ITC Publication, Serie B, No. 26, 1964.

Michael, S., 2005. K-D tree range and nearest neighbor search. Matlab Central - an open exchange for the Matlab and Simulink user community. Retrieved 24 April 2007 from www.mathworks.com/matlabcentral/fileexchange

Optech, n.d. Optech-ILRIS-3-D features and benefits. Retrieved April 2009, from http://www.optech.ca.

OpenGL, n.d. OpenGL website @

Orche, E. and Colodron, I., 1977. Memoria y Hoja Geológica número 444 (Flix). Mapa Geológico de España E: 1:50.000 (Segunda Serie). IGME, Madrid.

Orche, E., Robles, S. and Rosell, J., 1976. Memoria y Hoja Geológica número 471 (Mora de Ebro). Mapa Geológico de España E: 1:50.000 (Segunda Serie). IGME, Madrid.

Pal, N.R. and Bezdek, J.C., 1995. On Clustering Validity for the Fuzzy C-MeansModel, IEEE Trans. Fuzzy Systems, vol. 3 (3), pp. 370-379.

Papaliangas, T, Hencher, S.R., Lumsden, A.C. and Manolopoulou, S., 1993. The effect of frictional fill thickness on the shear strength of rock discontinuities. International Journal of Rock Mechanics and Mining Sciences & Geomechanics Abstracts. V30-2, April 1993, pp 81-91.

Patterson, M.S. and Wong, T-F., 2005. Experimental Rock Deformation- The Brittle Field, Springer-Verlag, Berlin, 347 pp.

Patton, F. D., 1966. Multiple modes of shear failure in rock. Proc. 1st Cong. on Rock Mechanics, ISRM, Lisbon, Portugal, 1. ed. Rocha M. pp. 509-513.

Pneumatolysis, n.d. In: Science and Technology Dictionary. McGraw-Hill Dictionary of Scientific and Technical Terms, 6th edition, published by The McGraw-Hill Companies, Inc. Retrieved April 2009, from http://www.accessscience.com

Poropat, G.V., 2001. New methods for mapping the structure of rock masses. CSIRO Exploration and Mining, paper submitted for Explo 2001. Retrieved december 2004 from http://www.sirovision.com

Poropat, G.V., 2006. Remote 3-D Mapping Of Rock Mass Structure. In: Laser and Photogrammetric Methods for Rock Face Characterization. Eds: Tonon, F. and Kottenstette, J., ARMA, Golden, Colorado, June 17-18, 2006.

Post, R., 2001. Characterization of joints and fractures in a rock mass using digital image processing. MSc. Thesis, University of Arizona, Tucson, AZ, 105 pp.

Post, R., Kemeny, J., Murphy, R., 2001. Image processing for automatic extraction of rock joint orientation data from digital images. Proceedings of the 38th US Rock Mechanics Symposium, Washington, DC. A.A. Balkema, Rotterdam, pp. 877-884.

Preparata, F.P. and Shamos, M.I., 1985. Computational Geometry - An Introduction. Texts and monographs in computer science. Springer Verlag, NY, 1985. 398 pp.

Price, N.J., 1966. Fault and Joint Development in Brittle and Semi-brittle Rock, Pergamon Press, London, 1966.

Priest, S.D. and Hudson, J.A., 1981. Estimation of discontinuity spacing and trace length using scanline surveys. Int. J. Rock Mech. Min. Sci. and Geomech. Abstr. Vol 18, pp. 183-197.

Priest, S.D., 1980. The use of inclined hemisphere projection methods for the determination of kinematic feasibility, slide direction and volume of rock blocks, Int. J. Rock Mech. Mi Sci. and Geomech. Abstr., 17, pp. 1-23.

Priest, S.D., 1985. Hemispherical projection methods in rock mechanics. George Allen and Unwin Ltd, London, 124 pp.

Priest, S.D., 1993. Discontinuity Analysis for Rock Engineering, Chapman and Hall, London, 473 pp.

Priest, S.D., Hudson, J.A., 1976. Discontinuity Spacings In Rock, International Journal of Rock Mechanics, Mining Sciences and Geomechanical Abstracts, Vol. 13, pp 135-148, 1976.

Rabbani, T., Dijkman, S., Van den Heuvel. F. and Vosselman, G., 2007. An integrated approach for modelling and global registration of point clouds. ISPRS Journal of Photogrammetry and Remote Sensing. Volume 61, Issue 6, February 2007, pp. 355-370.

Rabbani, T., Heuvel, F.A. van den and G. Vosselman., 2006. Segmentation of point clouds using smoothness constraints. International Archives of Photogrammetry, Remote Sensing and Spatial Information Sciences, Vol. 36, part 5, Dresden, Germany, September 25-27, pp. 248-253.

Rahman, Z., Slob, S. and Hack, H.R.G.K., 2006. Deriving roughness characteristics of rock mass discontinuities from terrestrial laser scan data. Proc. Engineering geology for tomorrow's cities. 10th IAEG Congress, Nottingham, United Kingdom, 6-10 September 2006.

Rasouli, V. and Harrison, J. P., 2001a. Is observational method of roughness determination trustworthy? In: Särkkä and Eloranta (eds.), Rock Mechanics- a challenge for Society. Swets and Zeitlinger Lisse, pp. 277-282.

Rasouli, V. and Harrison, J. P., 2001b. In plane analysis of fracture surface roughness: anisotropy and scale effect in anisotropy. In: Elsworth, Tinucci and Heasley (eds.), Rock Mechanics in the national interest. Swets and Zeitlinger Lisse, pp. 277-282.

Rawnsley, K.D.,. Hencher, S.R and Lumsden, A.C., 1990. Joint origin as a predictive tool for the estimation of geotechnical properties. In: Barton, N. and Stephansson, O. (eds.). Rock Joints. International Society for Rock Mechanics, Norwegian Rock Mechanics Group, Norges geotekniske institutt, pp 91-96.

Reid T.R., 1998. A methodology for the detection of discontinuity traces in digital images of rock mass exposures. Ph.D. thesis, Imperial College, London, UK, 1998.

Reid, T.R. and Harrison, J.P., 2000. A semi-automated methodology for discontinuity trace detection in digital images of rock mass exposures. . International Journal of Rock Mechcanics and Mining Sciences. Vol. 37 pp. 1073-1089.

Rengers, N, Berghuis, R. and Rösingh, J.W., 1988. Recent developments in the preparation of maps and plans of steep rockslopes with help of stereophotogrammetry, Delft University of Technology, Delft Progress Report, 13 (1988/1989) pp. 297-306.

Rengers, N., 1967. Terrestrial photogrammetry: a valuable tool for engineering geological purposes. Rock Mechanics and Engineering Geology. Vol. V/2-3, pp. 150-154.

Rengers, N., 1970. Influence of surface roughness on the friction properties of rock planes. Proc. 2nd Int. Cong. on Rock Mechanics. ISRM. Belgrade. 1. pp. 229-234.

Rengers, N., 1971. Unebenheit und Reibungswiederstand von Gesteinstrennflächen. Dr. Ing. Dissertation. Fakultät für Baueringennieur- und Vermessungswesen, Universität Karlsruhe. Veroffentlichungen des Institutes fur Bodenmechanic und Felsmechanik der Universitat Fridericiana in Karsruhe. (47). 129 pp.

Reshetyuk, Y., 2006. Investigation and calibration of pulsed time-of-flight terrestrial laser scanners. Licentiate thesis in Geodesy. Royal Institute of Technology (KTH). Department of Transport and Economics. Division of Geodesy. 100 44 Stockholm. October 2006.

Riegl, n.d. Riegl Laser Measurement Systems. From: http://www.riegl.com

Roberts, G. and Poropat, G., 2000. Highwall joint mapping in 3-D at the Moura mine using using SIROJOINT. Bowen Basin Symposium, 2000 Coal and Mining The New Millennium, Rockhampton, Oct. 2000.

Robertson, A.M., 1970. The interpretation of geological factors for use in slope theory. Planning of Open Pit Mines, Proceedings, Johannesburg, pp. 55-71.

Rocscience, 2009. Rocscience website: http://www.rocscience.com/. Last accessed: march 2009.

Romana, M., 1985. New adjustment ratings for application of Bieniawski classification to slopes. In: Proceedings International Symposium On the Role of Rock Mech., pp 49-53. Zacatecas.

Roncella, R. and Forlani, G., 2005. Extraction of planar patches from point clouds to retrieve dip and dip direction of rock discontinuities. ISPRS WG III/4, V/3 Workshop “Laser scanning 2005”, Enschede, The Netherlands, September 12-14, 2005.

Sappa, A.D. and Devy. M., 2001. Fast range image segmentation by an edge detection strategy. In: Proceedings, Third International Conference on 3-D Digital Imaging and Modeling, pp.292-299.

Sarti, A. and Tubaro, S., 2002. Detection and characterisation of planar fractures using a 3-D Hough transform. Signal Processing 83, pp 1269-1282.

Savage, J.F., 1965. Terrestrial photogrammetry for geological purposes. ITC Publication, Serie B, No. 33, 1965, pp. 41-53.

Shen, B., 1993. Mechanics of fractures and intervening bridges in hard rock. Doctoral thesis, Royal Institute of Technology, Stockholm, Division of Engineering Geology.

Sithole, G. and Vosselman, G., 2003. Automatic Structure Detection in a Point-Cloud of an Urban Landscape. 2nd Joint Workshop on Remote Sensing and Data Fusion over Urban Areas (URBAN2003), May 22-23, Berlin, Germany, [CD-ROM], 5 p.

Sithole, G. and Vosselman, G., 2004. Experimental Comparison of Filter Algorithms for Bare Earth Extraction From Airborne Laser Scanning Point Clouds. ISPRS Journal of Photogrammetry and Remote Sensing, Vol.59 (1-2), pp.85-101.

Sithole, G. and Vosselman, G., 2005. Filtering of airborne laser scanner data based on segmented point clouds. International Archives of Photogrammetry, Remote Sensing and Spatial Information Sciences, Vol.36, part 3/W19, Enschede, The Netherlands, September 12-14, pp. 66-71.

Sjoberg J., 1996. Large scale slope stability in open pit mining—a review. Technical Report 1996:10T, Lulea University of Technology, Division of Rock Mechanics, Lulea, Sweden; 1996. p. 229.

Slob, S., Hack, H.R.G.K. and Turner, A.K., 2002. An approach to automate discontinuity measurements of rock faces using lasers scanning techniques. In: Proceedings of ISRM International Symposium on Rock Engineering for Mountainous Regions - Eurock 2002, Funchal, 2002 November 25-28th, pp. 87-94.

Slob, S., Hack, H.R.G.K., van Knapen, B., Turner, K. and Kemeny, J., 2005. A method for automated discontinuity analysis of rock slopes with three - dimensional laser scanning. In: Transportation Research Record: Journal of the Transportation Research Board (USA), 1913, pp. 187-194.

Slob, S.; Hack, H. R. G. K.; Van Knapen, B. and Kemeny, J., 2004. Automated identification and characterization of discontinuity sets in outcropping rock masses using 3-D terrestrial laser scan survey techniques. In: Proceedings of the ISRM regional symposium EUROCK 2004 and 53rd geomechanics colloquy, pp. 439-443.

Split Engineering, 2009. Split Engineering LLC. March 2009, from http://www.spliteng.com.

Stimpson, B., 1982. A rapid field method for recording joint roughness profiles. International Journal of Rock Mechanics and Mining Science and Geomechanics Abstracts, 19(6): pp. 345-346.

Surpac, 2006. Surpac Minex Group home page. Software products, Sirovision. Website. http://www.surpac.com. Last accessed 19-12-2006.

Terzaghi, R., 1965. Sources of error in joint surveys. Geotechnique, 15, pp. 287-304.

Tyner, B., 2007. Packages: K-D trees. http://www.stat.purdue.edu/~btyner/packages.hml

Versprille, K.J., 1975. Computer-aided design applications of the rational b-spline approximation form. PhD dissertation, published by Syracuse University, Syracuse, NY, USA. 123 pp.

Villaescusa, E., 1992. A review and analysis of rock discontinuity mapping methods. Proc. 6th ANZ Conf. on Geomechanics, Christchurch, New Zealand, pp. 274-279.

Vos, B., 2002. In-situ block size distribution (IBSD) analysis to determine the variation in rock mass properties and the relationship of ISBD with rippability of rock masses. M.Sc. Thesis, TUDelft.

Vosselman, n.d. PCM – Point Cloud Mapper. Point cloud processing software. Initially developed within TU Delft and further developed within ITC.

Vosselman, G., 1999. Building reconstruction using planar faces in very high density height data. In: Proceedings of the ISPRS conference on automatic extraction of GIS objects from digital imagery, Munich, pp. 87-92.

Vosselman, G., Gorte, B.G.H., Sithole, G. and Rabbani, T., 2005. Recognising structure in laser scanner point clouds. The International Archives of the Photogrammetry, Remote Sensing and Spatial Information Sciences. ISPRS WG III/4, V/3 Workshop “Laser scanning 2005”, Enschede, The Netherlands, September 12-14, 2005.

Vosselman, G., Gorte, B.G.H., Sithole, G. and T. Rabbani., 2004. Recognising structure in laser scanner point clouds. International Archives of Photogrammetry, Remote Sensing and Spatial Information Sciences, Vol.46, part 8/W2, Freiburg, Germany, October 4-6, pp.33-38.

Wang, H., Latham J.-P., Poole, A. B., 1990. In-situ block size assessment from discontinuity spacing data. In: Price, D. G. (ed.), Proc., 6th Int. IAGE Cong., Balkema, Rotterdam, pp. 117-127.

Wang, H., Latham, J.-P., Poole, A.B., 1991. Predictions Of Block Size Distribution For Quarrying, Quarterly Journal of Engineering Geology, 24.

Wang, L.G., Yamashita, S., Sugimoto, F., Pan, C. and Tan, G, 2003. A methodology for predicting the in situ size and shape distribution of rock blocks, Rock Mech. and Rock Eng. Vol. 36 (2), pp. 121-142.

Wavefront Technologies, n.d. In: Wavefront OBJ File Format Summary. http://www.fileformat.info/format/wavefrontobj/egff.htm. Last accessed May 2009.

Web3-D, n.d. Web3-D Consortium web site. www.web3-D.org. Last accessed April 2007.

Wehr, A., 2005., Laser scanning and its potential to support 3-D panoramic recording. In: Proceedings of the ISPRS working group V/5. Panoramic Photogrammetry Workshop. Berlin, Germany 24-25 February 2005. Eds. Reulke, R. and Knauer, U. International Archives of Photogrammetry, Remote Sensing and Spatial Informations Sciences. Vol. XXXVI-5/W8.

Weissbach, G., 1978. A new method for the determination of the roughness of rock joints in the laboratory. Int. J. Rock Mech. Min. Sci. Geomech. Abstr., 15, pp. 131-133.

Wickens, E. H. and Barton, N. R., 1971. Application of photogrammetry to the stability of the excavated rock slopes. Photogrammetric Record 7, pp. 46-54.

Windsor, C.R., Robertson, W.V., 1994. Rock Reinforcement Practice, Volume 1: Rock Mass Model Formulation, Publisher unknown.

Woodcock, N.H., 1977. Specification of fabric shapes using an eigenvalue method, Geol. Soc. America Bulletin, Vol. 88, pp. 1231-1236.

Xie, X.L. and Beni, G.A., 1991. A validity measure for fuzzy clustering. IEEE Trans. Pattern Anal. Machine Intell., 13(8), pp. 841-847.

Xu, J. and Cojean, R., 1988. Three-dimensional simulation of natural block granulometry (in French), In: Price, D.G. (ed.), Proc., 6th Int. Cong. IAEG, Balkema, Rotterdam, pp. 797-802.

Yerry, M.A. and Shephard, M.S., 1984. Automatic three-dimensional mesh generation by the modified Octree technique. International Journal for Numerical Methods in Engineering. John Wiley, 20, pp 1965-1990.

Yilbas, B. S. and Hashmi, M. S. J., 1998. An optical method and neural network for surface roughness measurement. Optics and lasers in Engineering 29, pp. 1-15.

Zadeh, L.A., 1965. Fuzzy sets. Information Control Vol. 8 (3), pp. 338-353.

Zhang, Z, Zhenga, S and Zhana., 2004. Z. Digital terrestrial photogrammetry with photo total station. The International Archives of the Photogrammetry, Remote Sensing and Spatial Information Sciences, Vol. XXXV, part B5.

Zhong, D H., Li, M. C., Song, L G. and Wang, G., 2006. Enhanced NURBS modelling and visualization for large 3-D geoengineering applications: An example from the Jinping first level hydropower engineering project, China. Computers and Geosciences, Vol.32, pp.1270 1282.

Zhou, W. and Maerz, N.H., 2002. Implementation of multivariate clustering methods for characterizing discontinuities data from scanlines and oriented boreholes. Computers and Geosciences, Vol. 28, pp. 827-839.

Curriculum Vitae

Siefko Slob was born on December 31, 1969 in Nickerie, Surinam. From 1982 to 1988 he attended highschool at VWO-B level at the Rijksscholengemeenschap Ooststellingwerf in Oosterwolde. In 1988 he started studying at the Faculty of Mining and Petroleum Engineering of the Delft University of Techology, where he graduated in 1994 as Mining Engineer with a specialisation in Engineering Geology.

After his graduation in 1994 he worked at ITC in Delft and in early 1996 he was given the opportunity to work for the GIS and remote sensing laboratory of the Royal Museum for Central Africa in Tervuren, Belgium. From his base in Belgium he worked on research projects in The Philippines and Uganda.

In 1999 he joined ITC again as an assistant professor at the section Engineering Geology in Delft. Here he worked on various consulting projects, delivered courses on GIS and remote sensing and has also been teaching and supervising MSc students from both TU Delft and ITC. Next to his work at ITC he carried out a PhD research that has culminated in this thesis.

From 2008 onward he has been employed with Witteveen+Bos Consulting Engineers. He is currently working as engineering geological advisor at the department Subsurface Infrastructure in the Amsterdam office of Witteveen+Bos. Siefko Slob is married to Malou Prestado and they have one daughter, Francesca. They live in Amersfoort, The Netherlands.

List of abbreviations

ASCII	American Standard Code for Information Interchange
AOI	Area Of Interest
BS	British Standard
CAD	Computer Aided Design
CAE	Computer Aided Engineering
CAM	Computer Aided Manufacturing
CCD	Charge Coupled Device
DEM	Digital Elevation Model
DGPS	Differential Global Positioning Systems
FDN	Fixed-Distance-Neighbours
GIS	Geographical Information Systems
GPS	Global Positioning Systems
IAEG	International Association of Engineering Geology and the Environment
ICC	Istitut Cartographic de Catalunya
IGC	Istitut Geologic de Catalunya
ISRM	International Society of Rock Mechanics
ITC	International Institute for Geo-Information Science and Earth Observation
JRC	Joint Roughness Coefficient
KNN	K-Nearest-Neighbour
LCD	Liquid Crystal Display
LIDAR	Light Detection and Ranging
NURBS	Non-Uniform Rational B-Splines
OBJ	Filename extension for the Wavefront 3-D geometry definition file format
PC	Personal Computer
PCA	Principal Component Analysis
PCM	Point Cloud Mapper (Software)
PDA	Personal Digital Assistant
PTTS	Photo Total Station System
RAM	Random Access Memory
RANSAC	Random Sample Consensus
RBF	Radial Basis Functions
RMR	Rock Mass Rating
RQD	Rock Quality Designation
SSPC	Slope Stability Probability Classification
TIN	Triangulated Interpolation Network
TLS	Total Least-Squares
VRML	Virtual Reality Modelling Language
WRL	Filename extension for the VRML 3-D geometry definition file format

Appendices

Appendix A. Field observations Site 1 – Bellmunt, Spain

SPPC Form data

Table 11.1. SSPC Form data, Bellmunt, Site 1.

ITC/TUD ENGINEERING GEOLOGY			Exposure characterization							SSPC - SYSTEM
LOGGED BY: **B.v.Knapen & H.R.G.K. Hack**	DATE: **07/06/04**		TIME: **12:22** hr							exposure no: **TP7101km04**
WEATHER CONDITIONS		LOCATION	map no: **256-137 (1:5K)**							
Sun: cloudy/fair/**bright**		Map coordinates:	northing: **4559029 (UTM)**							
Rain: **dry**/drizzle/slight/heavy			easting: **313558**							

METHOD OF EXCAVATION (**ME**)		DIMENSIONS/ACCESSIBILITY								
(tick)		Size total exposure:	(m)	l:	**50**	h:	**6**	d:	**10**
natural/hand-made	1.00	mapped on this form	(m)	l:	**6**	h:	**6**	d:	**1**
pneumatic hammer excavation	**0.76**	Accessibility:	poor/**fair**/good						
pre-splitting/smooth wall blasting	0.99								
conventional blasting with result:									
good	0.77								
open discontinuities	0.75								
dislodged blocks	0.72								
fractured intact rock	0.67								
crushed intact rock	0.62								

FORMATION NAME: **Carboniferous (mc_Capg): mainly SLATE, occurrence of porphyritic GRANITE and contact metamorphism (IGC, 2007)**

DESCRIPTION (BS 5930: 1981)

colour	grain size	structure & texture	weathering	NAME
DARK GREY - BLACK	**SILT-CLAYSIZE**	**SMALL-TABULAR**	**SLIGHTLY**	**META-SILTSTONES (+ SLATES)**

INTACT ROCK STRENGTH (**IRS**) (tick)		sample number(s):	WEATHERING (**WE**)	
< 1.25 MPa	Crumbles in hand		(tick)	
1.25 - 5 MPa	Thin slabs break easily in hand		unweathered	1.00
5 - 12.5 MPa	Thin slabs broken by heavy hand pressure	**TP7101km04_1**	slightly	**0.95**
12.5 - 50 MPa	Lumps broken by light hammer blows	**TP7101km04_2**	moderately	0.90
50 - 100 MPa	Lumps broken by heavy hammer blows (50-60 Mpa)		highly	0.62
100 - 200 MPa	Lumps only chip by heavy hammer blows (Dull ringing sound)		completely	0.35
> 200 MPa	Rocks ring on hammer blows. Sparks fly			

DISCONTINUITIES B=bedding C=Cleavage J=joint			C1	J2	J3	J4	J5	J6	J7	J8	EXISTING SLOPE?	
Dip direction		(degrees)	**344**	**328**	**147**	**263**	**240**	**054**	**268**	**265**	dip-direction/dip	
Dip		(degrees	**44**	**85**	**58**	**90**	**64**	**80**	**58**	**42**	**208/62**	
Spacing (**DS**)		(m)	**0.01**	**0.60**	**0.40**	**0.60**	**1.80**	**1.20**	**0.80**	**0.20**		
Persistence	along strike	(m)	>	**> 0.50**	**> 1.00**	**> 1.00**	**> 5.00**	**> 4.00**	**> 0.50**	**0.10**	height:	**6 m**
	along dip	(m)	>	**1.00**	**> 6.00**	**> 5.0**	**> 1.00**	**> 1.00**	**> 4.00**	**0.40**		

CONDITION OF DISCONTINUITIES												
Roughness large scale (**RI**) (on an area between 0.2 x 0.2 and 1 x 1 m2)	wavy: 1.00 slightly wavy: 0.95 curved: 0.85 slightly curved 0.80 straight 0.75		**N.A.**	**0.75**	**0.75**	**0.85**	**0.80**	**0.80?**	**0.85?**	**0.75?**	Stability (tick) stable **1** small problems 2 large problems 3	
Roughness small scale (**Rs**) (on an area of 0.2 x 0.2 m2)	rough stepped 0.95 smooth stepped 0.90 polished stepped 0.85 rough undulating 0.80 smooth undulating 0.75 polished undulating 0.70 rough planar 0.65 smooth planar 0.60 polished planar 0.55		**N.A.**	**0.60**	**0.65**	**0.95**	**0.95**	**0.95**	**0.80**	**0.65**		
Infill material (**Im**)	cemented/cemented infill 1.07 no infill - surface staining 1.00		**1.00**	**1.00**	**1.00 (clay infill by inflow)**	**1.00 (red coating)**	**1.00**	**1.00**	**1.00**	**1.00**	notes: 1) For infill 'gouge > irregularities' and 'flowing material' small scale roughness = 0.55. 2) If roughness is anisotropic (e.g. ripple marks, striation, etc.) roughness should be assessed perpendicular and parallel to the roughness and directions noted on this form. 3) Non-fitting of discontinuities should be marked in roughness columns.	
	non softening & sheared material, e.g. free of clay, talc, etc.	coarse medium fine										
	soft sheared material, e.g. clay, talc, etc.	coarse medium fine										
	gouge < irregularities 0.42 gouge > irregularities 0.17 flowing material 0.05											
Karst (**Ka**)	none 1.00 karst 0.92		**1.00**	**1.00**	**1.00**	**1.00**	**1.00**	**1.00**	**1.00**	**1.00**		

SUSCEPTIBILITY TO WEATHERING (**SW**)			remarks:
degree of weathering:	date excavation:	remarks:	All scanlines have been performed in this geotechnical unit
Slightly-moderately (definitely moderately at right side of exposure)	1990		

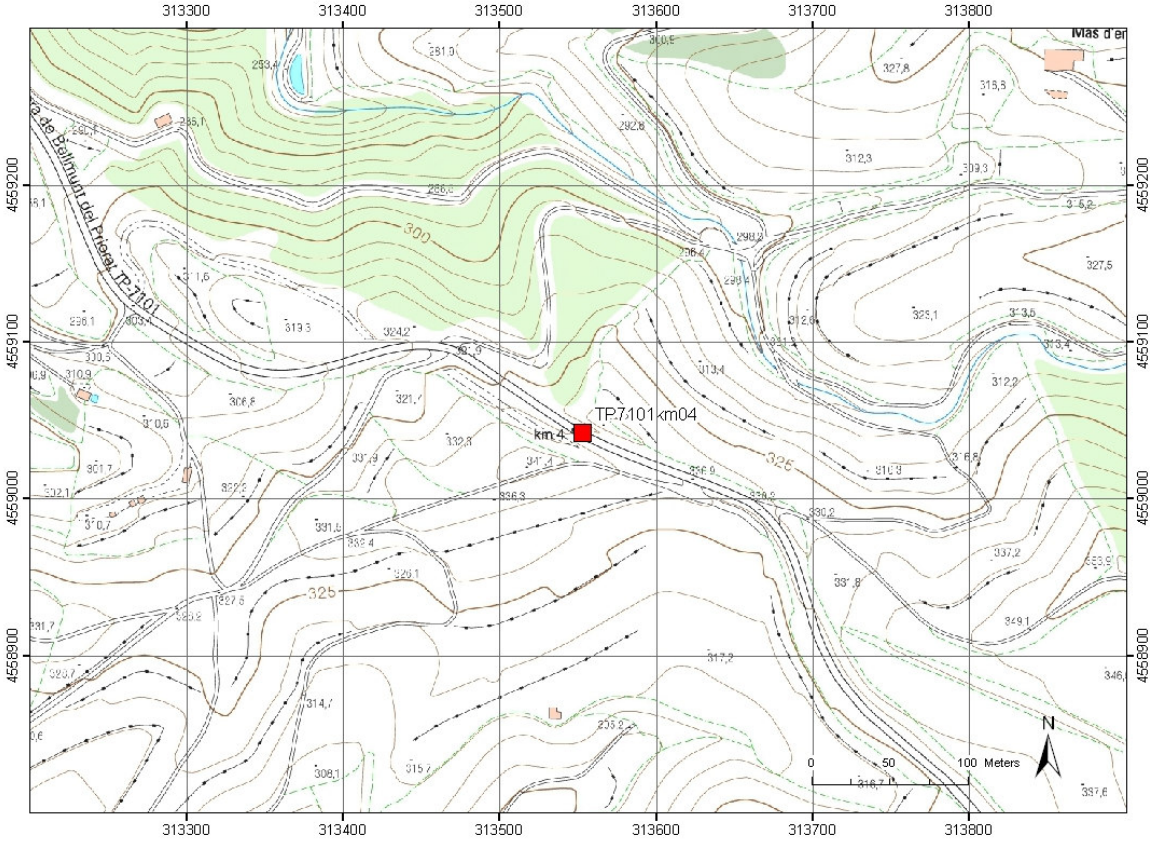

Figure 11.1. Location map Site 1 (Bellmunt site). Data source: ICC, 2007.

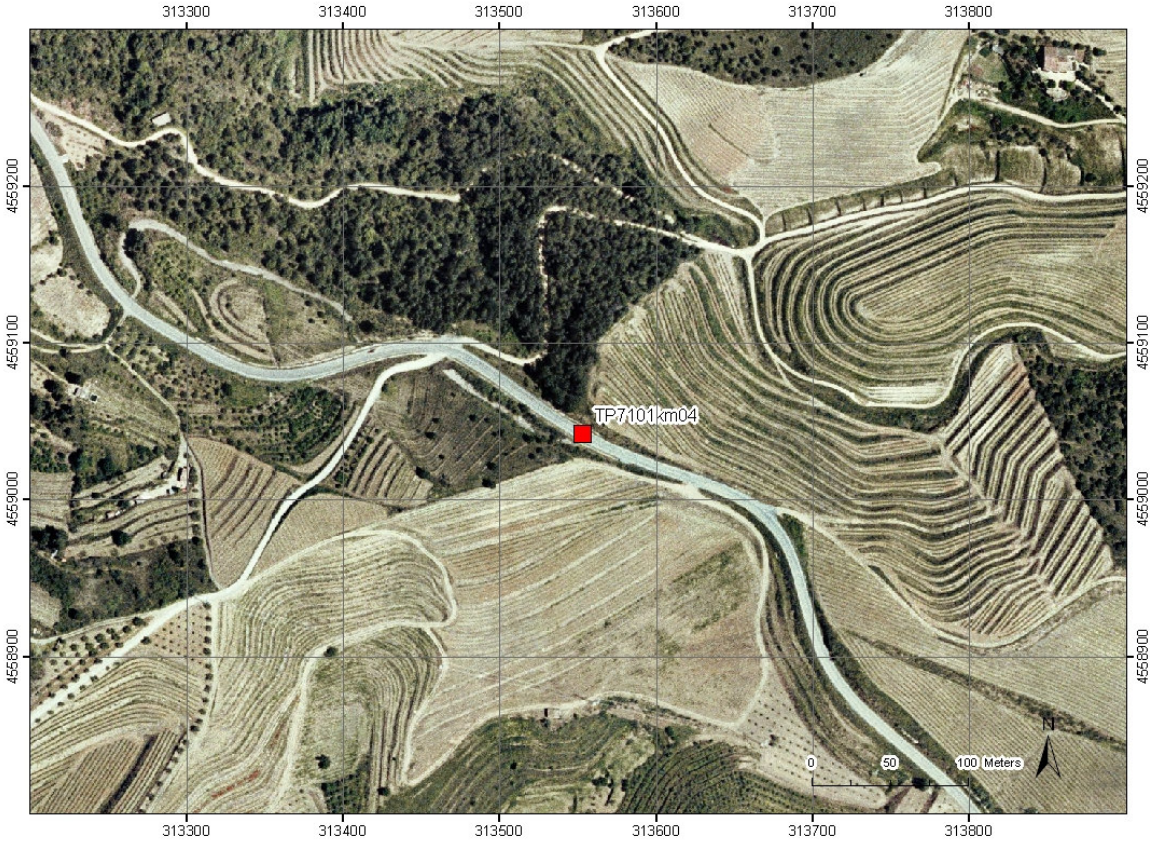

Figure 11.2. Orthophoto map of Site 1 (Bellmunt site). Data source: ICC, 2007.

Figure 11.3. Position of the horizontal (yellow tape) and vertical scanline (white ruler) at exposure of Bellmunt site. The horizontal scanline survey was done from left to right over 6.45 metres.

Figure 11.4. Detail of intersection point of horizontal and vertical scanline.

Figure 11.5. More detailed photograph of scanline intersection point, showing the slatey cleavage of the rock mass.

Scanline data

Table 11.2. Horizontal scanline (Bellmunt, Site 1)

Scanline orientation:		307/01	
Rock face orientation:		208/62	
Scanline length:		6.45 m	
Intersection distance (m)	Dip direction (°)	Dip angle (°)	Semi-trace length (m)
0.00	265	90	0.80
0.00	342	45	0.10
0.00	154	55	0.60
0.10	85	90	0.35
0.32	56	85	0.30
0.55	150	53	0.40
0.80	70	85	0.60
0.88	344	42	1.20
1.14	82	78	0.40
1.14	346	39	0.50
1.50	60	62	0.20
1.70	270	57	0.20
1.78	57	83	0.20
1.80	344	42	5.00
1.98	146	62	1.50
2.18	148	54	0.30
2.26	84	84	0.60
2.45	155	57	2.60
2.90	55	72	0.30
2.92	71	81	0.30
2.94	344	39	5.00
3.20	149	62	0.50
3.20	156	87	0.60
3.75	76	79	0.40
3.82	88	78	0.30
3.90	270	60	0.60
3.93	78	90	0.20
4.00	343	43	5.00
4.06	74	90	0.10
4.22	331	84	0.50
4.25	68	84	0.25
4.44	168	81	0.50
4.56	330	78	0.30
4.90	262	64	0.40
4.97	331	74	0.30
5.00	75	77	0.40
5.00	343	36	5.00
5.00	333	70	0.20
5.20	336	78	0.60
5.40	343	40	5.00
5.40	154	57	0.40
5.45	67	73	0.40
5.45	240	80	0.30
5.80	78	80	0.40
6.10	70	80	0.50
6.34	71	82	1.00

Table 11.3. Vertical scanline (Bellmunt, Site 1)

Scanline orientation:		030/65	
Rock face orientation:		208/62	
Scanline length:		1.44 m	
Intersect. with hor. Scanline:		1.56 m	
Intersection distance (m)	Dip direction (°)	Dip angle (°)	Semi-trace length (m)
0.05[27]	342	42	5.00
0.11	342	42	5.00
0.15	342	42	5.00
0.20	342	42	5.00
0.25	342	42	5.00
0.30	342	42	5.00
0.35	342	42	5.00
0.40	342	42	5.00
0.45	342	42	5.00
0.50	342	42	5.00
0.52	44	82	0.20
0.55	342	42	5.00
0.60	342	42	5.00
0.65	342	42	5.00
0.70	342	42	5.00
0.75	146	53	1.50
0.75	342	42	5.00
0.80	342	42	5.00
0.82	165	65	0.30
0.85	342	42	5.00
0.89	265	42	0.40
0.90	342	42	5.00
0.95	342	42	5.00
1.00	342	42	5.00
1.05	342	42	5.00
1.10	342	42	5.00
1.15	267	58	0.50
1.15	342	42	5.00
1.20	342	42	5.00
1.25	342	42	5.00
1.30	342	42	5.00
1.33	63	83	0.30
1.37	342	42	5.00
1.44	257	90	0.15

[27] This is the slatey cleavage, resulting in a dicontinuity plane occurring about every 5 cm.

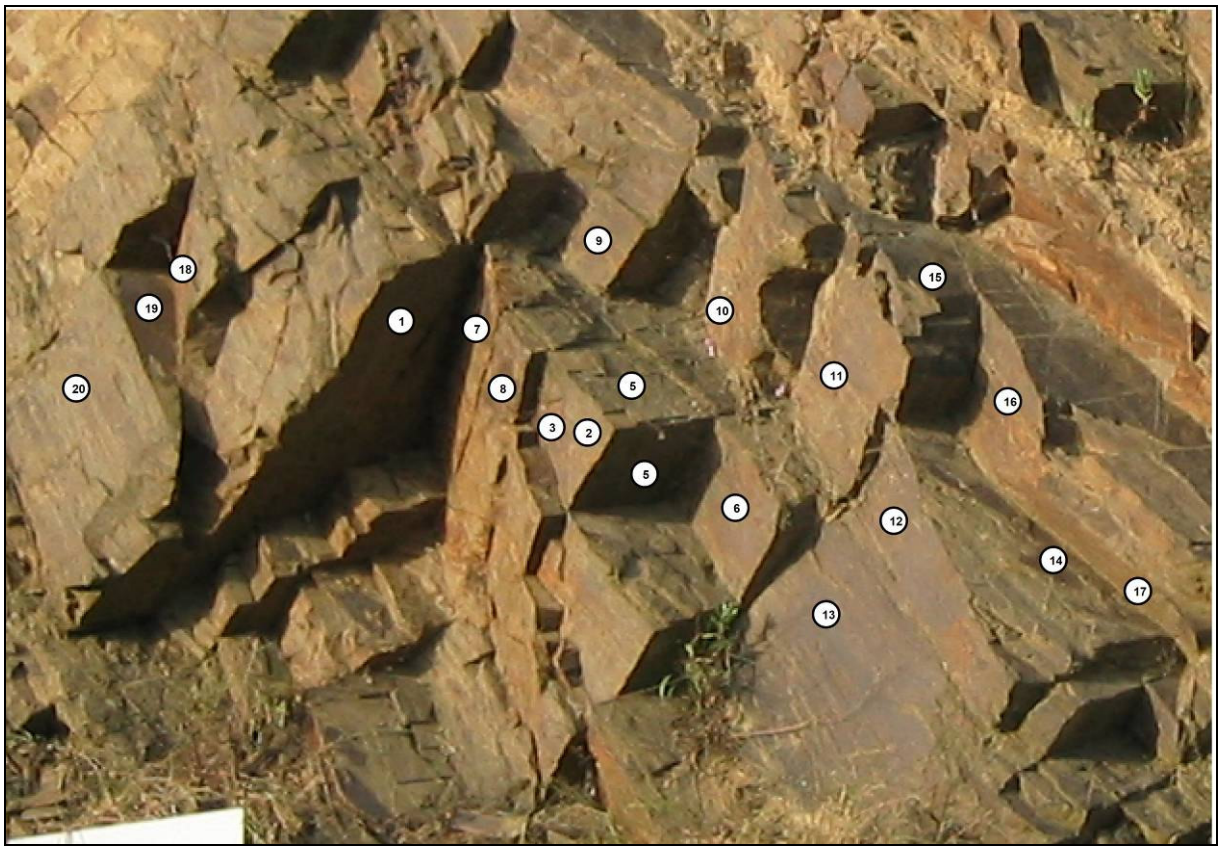

Figure 11.6. Photo of the part of the exposure at Site 2 where the orientations of individual discontinuity planes that are marked and measured. The orientations are found in the Table 11.4 below.

Table 11.4. Orientation measurements of individual discontinuities, marked in the Figure 11.6 above.

No	Dip direction (°)	Dip angle (°)
1	148	57
2	58	85
3	85	87
4	155	56
5	342	43
6	71	82
7	90	82
8	81	90
9	51	85
10	87	86
11	75	76
12	76	76
13	58	63
14	343	40
15	343	40
16	81	80
17	268	56
18	94	84
19	341	44
20	59	71

Appendix B. Field observations Site 2 – Torroja, Spain

SSPC Form data

Table 11.5. SSPC Form data, Torroja, Site 2.

ITC/TUD ENGINEERING GEOLOGY			Exposure characterization					SSPC - SYSTEM
LOGGED BY: **S. Slob**		DATE: **27/05/05**		TIME: **11:30**	hr	exposure no: **TP4703km06**		
WEATHER CONDITIONS		LOCATION		map no: **257-135 (1:5K)**				
Sun:	cloudy/fair/**bright**	Map coordinates:		northing:		**4563653 (UTM)**		
Rain:	**dry**/drizzle/slight/heavy			easting:		**316879**		

METHOD OF EXCAVATION (**ME**)		DIMENSIONS/ACCESSIBILITY							
(tick)		Size total exposure:	(m)	l:	**40**	h:	**6**	d:	**< 1**
natural/hand-made	1.00	mapped on this form	(m)	l:	**7**	h:	**6**	d:	**< 1**
pneumatic hammer excavation	**0.76**	Accessibility:		poor/fair/**good**					
pre-splitting/smooth wall blasting	0.99								
conventional blasting with result:									
good	**0.77**								
open discontinuities	0.75								
dislodged blocks	0.72								
fractured intact rock	0.67								
crushed intact rock	0.62								

FORMATION NAME: **Carboniferous (Capg): mainly SANDSTONE and SLATE, occurrence of porphyritic GRANITE (IGC, 2007)**

DESCRIPTION (BS 5930: 1981)

colour	grain size	structure & texture	weathering	NAME
MOTTLED LIGHT BROWN	**ARENACEOUS**	**MEDIUM BLOCKY**	**SLIGHTLY**	**META-SANDSTONE**

INTACT ROCK STRENGTH (**IRS**) (tick)		sample number(s):	WEATHERING (**WE**)	
< 1.25 MPa	Crumbles in hand	**TP4703km06_01**	(tick)	
1.25 - 5 MPa	Thin slabs break easily in hand		unweathered	1.00
5 - 12.5 MPa	Thin slabs broken by heavy hand pressure		slightly	**0.95**
12.5 - **50** MPa	Lumps broken by light hammer blows		moderately	0.90
50 - 100 MPa	Lumps broken by heavy hammer blows		highly	0.62
100 - 200 MPa	Lumps only chip by heavy hammer blows (Dull ringing sound)		completely	0.35
> 200 MPa	Rocks ring on hammer blows. Sparks fly			

DISCONTINUITIES B=bedding C=Cleavage J=joint				J1	J2	J 3	J4	5	EXISTING SLOPE?	
Dip direction			(degrees)	**209**	**135**	**279**	**086**		dip-direction/dip	
Dip			(degrees	**90**	**54**	**24**	**63**		**276/75**	
Spacing (**DS**)			(m)	**0.5**	**0.3**	**0.5**	**0.25**			
Persistence	along strike		(m)	**> 2**	**> 4**	**1.5**	**1**		height:	**6 m**
	along dip		(m)	**> 5**	**> 2**	**> 0.5**	**0.5**			
CONDITION OF DISCONTINUITIES									Stability (tick)	
Roughness large scale (**RI**) (on an area between 0.2 x 0.2 and 1 x 1 m2)	wavy:		1.00	**0.75**	**0.75**	**0.95**	**0.75**		stable	1
	slightly wavy:		0.95						small problems	**2**
	curved:		0.85						large problems	3
	slightly curved		0.80							
	straight		0.75							
Roughness small scale (**Rs**) (on an area of 0.2 x 0.2 m2)	rough stepped		0.95	**0.95**	**0.95**	**0.95**	**0.65**			
	smooth stepped		0.90							
	polished stepped		0.85							
	rough undulating		0.80							
	smooth undulating		0.75							
	polished undulating		0.70							
	rough planar		0.65							
	smooth planar		0.60							
	polished planar		0.55							
Infill material (**Im**)	cemented/cemented infill		1.07	**1.00**	**1.00**	**1.00**	**1.00**		notes: 1) For infill 'gouge > irregularities' and 'flowing material' small scale roughness = 0.55. 2) If roughness is anisotropic (e.g. ripple marks, striation, etc.) roughness should be assessed perpendicular and parallel to the roughness and directions noted on this form. 3) Non-fitting of discontinuities should be marked in roughness columns.	
	no infill - surface staining		1.00							
	non softening & sheared material, e.g. free of clay, talc, etc.	coarse	0.95							
		medium	0.90							
		fine	0.85							
	soft sheared material, e.g. clay, talc, etc.	coarse	0.75							
		medium	0.65							
		fine	0.55							
	gouge < irregularities		0.42							
	gouge > irregularities		0.17							
	flowing material		0.05							
Karst (**Ka**)	none		1.00	**1.00**	**1.00**	**1.00**	**1.00**			
	karst		0.92							

SUSCEPTIBILITY TO WEATHERING (**SW**)			remarks:
degree of weathering:	date excavation:	remarks:	
Surface discolouration along discontinuities to Slightly weathered	N.A.		

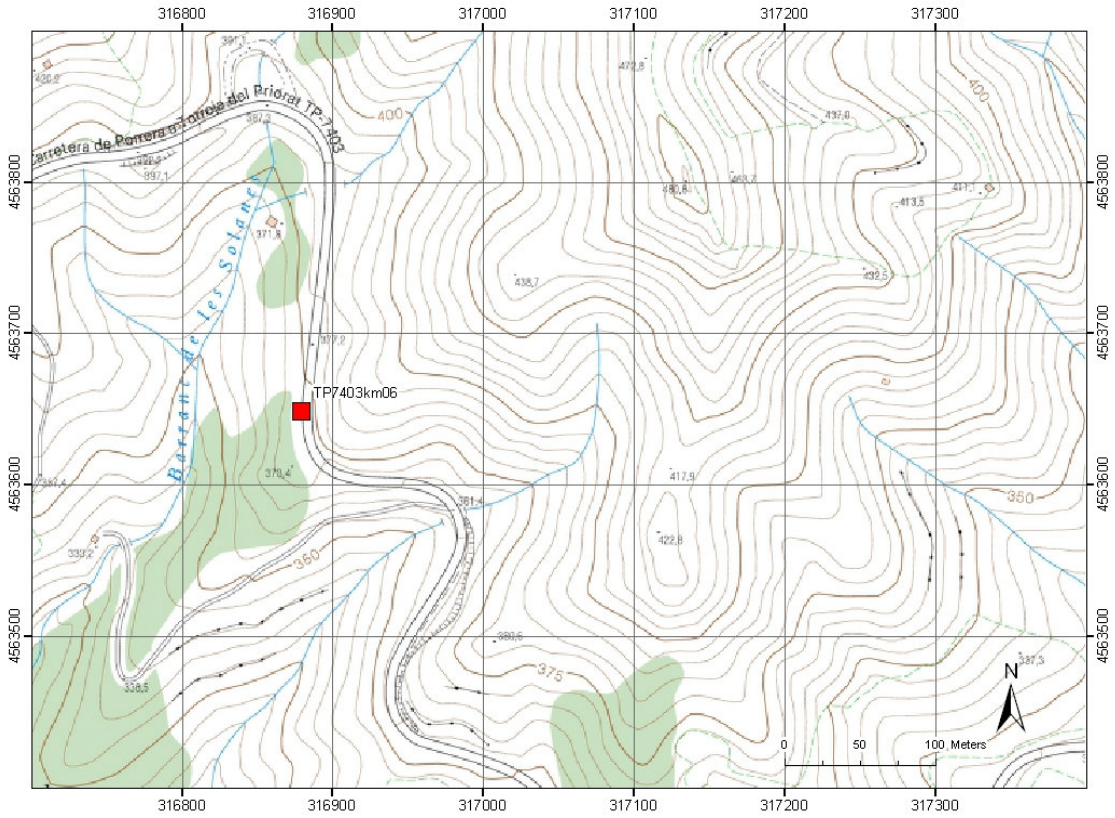

Figure 11.7. Location map Site 2 (Torroja site). Data source: ICC, 2007.

Figure 11.8. Orthophoto map Site 2 (Torroja site). Data source: ICC, 2007.

Figure 11.9. Approximate position of the horizontal scanline and the two vertical scanlines near Torroja: Site 2. Scanlines are drawn-in by hand. The horizontal scanline survey was done from left to right over 5.85 metres.

Figure 11.10. Detailed photograph of second vertical scanline (left on the overview picture above).

Figure 11.11. Detailed photograph of the first vertical scanline (right on the overview picture above).

Scanline data

Table 11.6. Horizontal scanline (Torroja, Site 2)

Scanline orientation:		360/03	
Rock face orientation:		276/75	
Scanline length:		5.85 m	
Intersection distance (m)	Dip direction (°)	Dip angle (°)	Semi-trace length (m)
0.00	202	75	0.50
0.08	202	75	0.40
0.24	295	48	0.20
0.32	231	85	infinite
0.50	207	88	0.15
0.69	144	64	2.20
0.76	20	65	0.10
0.80	285	40	0.90
0.90	208	82	0.50
1.18	308	52	0.45
1.25	234	85	0.15
1.35	204	87	0.60
1.39	209	83	0.60
1.58	217	80	0.60
1.60	217	80	0.60
1.63	228	90	infinite
1.66	231	68	0.30
1.78	208	88	infinite
1.89	300	73	0.35
1.97	291	53	0.05
2.00	255	68	0.70
2.07	214	89	0.15
2.12	213	89	infinite
2.20	219	88	0.60
2.33	160	77	0.50
2.42	208	86	1.00
2.45	277	42	0.30
2.70	218	82	0.25
2.90	38	90	infinite
3.00	320	84	0.40
3.10	135	50	2.10
3.22	125	48	0.40
3.22	145	80	infinite
3.30	255	35	0.60
3.43	34	83	1.70
3.50	318	70	0.20
3.60	40	72	0.35
3.80	308	61	0.20
3.90	251	72	0.10
4.60	214	81	0.60
4.70	126	50	2.10
5.02	210	90	2.20
5.45	140	55	1.20
5.60	210	85	infinite
5.85	288	28	0.60

Table 11.7. Vertical scanline 1 (Torroja, Site 2)

Scanline orientation:		276/73	
Rock face orientation:		276/75	
Scanline length:		1.87 m	
Intersect. with hor. Scanline:		5.20 m	
Intersection distance (m)	Dip direction (°)	Dip angle (°)	Semi-trace length (m)
0.32	304	40	0.40
0.37	124	34	2.30
0.78	302	40	0.20
1.10	288	30	0.50
1.21	139	50	1.20
1.46	95	28	0.30
1.50	287	41	0.80
1.75	280	32	0.50
1.87	91	52	0.50

Table 11.8. Vertical scanline 2 (Torroja, Site 2)

Scanline orientation:		276/81	
Rock face orientation:		276/75	
Scanline length:		1.45 m	
Intersect. with hor. Scanline:		3.33 m	
Intersection distance (m)	Dip direction (°)	Dip angle (°)	Semi-trace length (m)
0.19	275	31	0.40
0.24	219	78	0.70
0.52	142	73	0.20
0.65	277	28	0.90
0.65	214	84	Infinite (3.5)
0.90	281	37	0.15
1.04	137	53	3.20
1.19	291	37	0.80
1.21	119	49	0.70
1.24	217	86	0.20
1.38	285	28	0.50
1.45	146	72	0.15
1.45	32	79	Infinite (3.0)

Figure 11.12. Photo of the part of the exposure at Site 2 where the orientations of individual discontinuity planes that are marked and measured. The orientations are found in the Table 11.9 below.

Table 11.9. Orientation measurements of individual discontinuities, marked in the Figure 11.12 above.

No	Dip direction (°)	Dip angle (°)
1	29	90
2	135	54
3	278	32
4	132	52
5	86	63
6	141	41
7	37	84
8	126	54
9	220	85
10	138	50
11	290	31
12	27	88
13	28	88
14	90	70
15	289	50
16	136	48
17	134	48
18	118	46
19	35	80
20	267	34
21	135	48
22	26	83
23	35	88
24	151	41
25	248	74
26	130	51

Appendix C. Optech laser scanner survey details Site 1 (Bellmunt, Spain)

Scan position	TP7101km04_1 (Bellmunt, Site 1, Position 1)
Scan date	10 June 2004
Tilt of scanner	00 degrees
Bearing of scanner	204 degrees
Reference board 1 (left)	024/40
Reference board 2 (right)	022/39

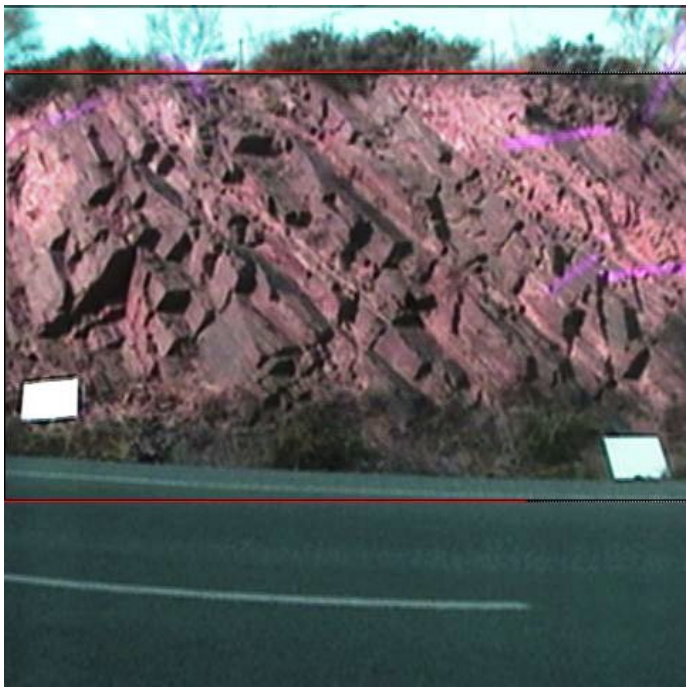

Figure 11.13. Digital image taken by the CCD camera in the laser scanner of the rock exposed at Site 1. Outlined is the scanned area, scanned from position 1. This rock face was also scanned from two other positions. The details of these scans are not included here. In the table below are the survey details of this scan.

```
         Block Header Info:
============================================================
Scan Block No.1:
Input: Number of shots:       1910564
    Number of rows:       1093
    Number of columns:      1748
    Pulse mode:          Last Pulse
    Shot type:           I3-D
    Pattern type:         Step Stare
    Box ID:           1
    Start position:       Lower Left
    Loop number:          0x01
    Average range:         11.29m
    Step stare info:
    X spot spacing(mm/integer): 5mm(/15)
    Y spot spacing(mm/integer): 5mm(/15)
    Orientation:          Horizontal
Output: Number of shots:      1855914
    Number of rows:       1093
    Number of columns:     1698
    Number of outliers removed: 624
```

Appendix D. Optech laser scanner survey details Site 2 (Toroja, Spain)

Scan position	TP7403km06_1
Date	3 June 2004
Tilt of scanner	00 degrees
Bearing of scanner	084 degrees
Reference board 1 (left)	262/70
Reference board 2 (right)	266/70

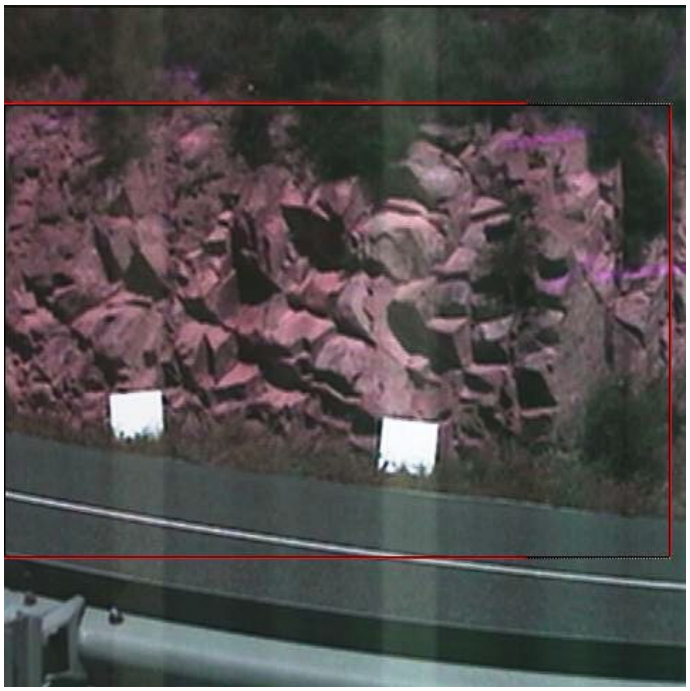

Figure 11.14. Digital image taken by the CCD camera in the laser scanner of the rock exposed at Site 2. Outlined is the scanned area, scanned from position 1. At this site one other scan was made of the adjacent rock face. The details of this scan are not included here. In the table below are the survey details of this scan.

```
         Block Header Info:
============================================================
Scan Block No.1:
Input: Number of shots:       1735428
    Number of rows:       1086
    Number of columns:      1598
    Pulse mode:          First Pulse
    Shot type:           I3-D
    Pattern type:         Step Stare
    Box ID:           1
    Start position:       Lower Left
    Loop number:          0x01
    Average range:         15.00m
    Step stare info:
    X spot spacing(mm/integer): 6mm(/16)
    Y spot spacing(mm/integer): 6mm(/16)
    Orientation:          Horizontal
Output: Number of shots:      1681128
    Number of rows:       1086
    Number of columns:     1548
    Number of outliers removed: 2263
```

Appendix E. Riegl laser scanner survey details Site Thon (Belgium)

Medium resolution scan (scan 002)

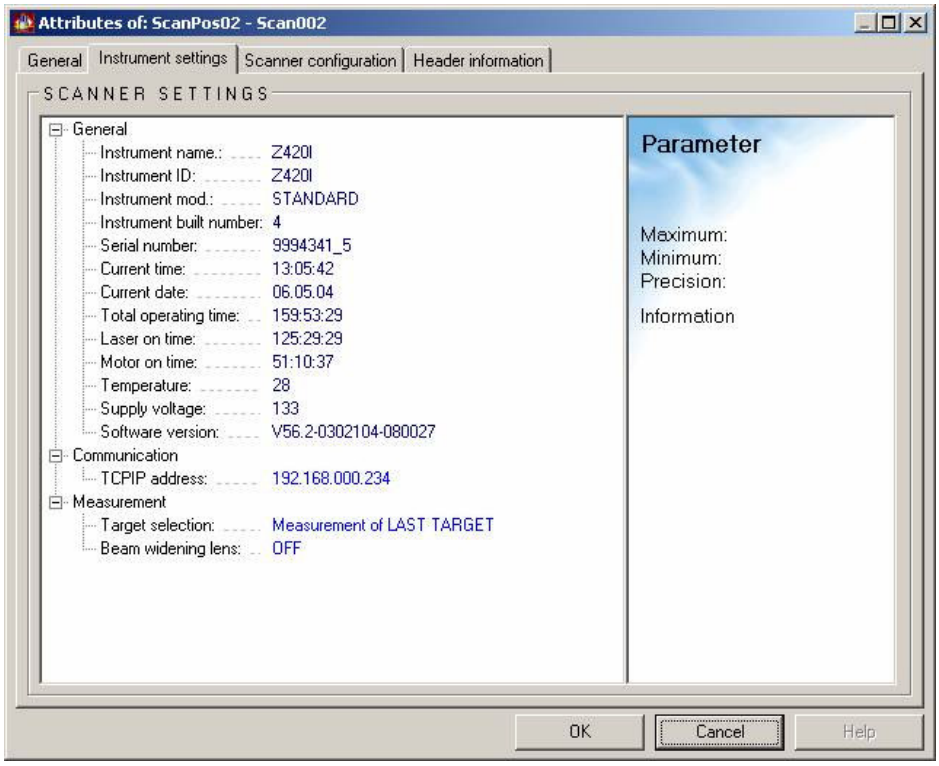

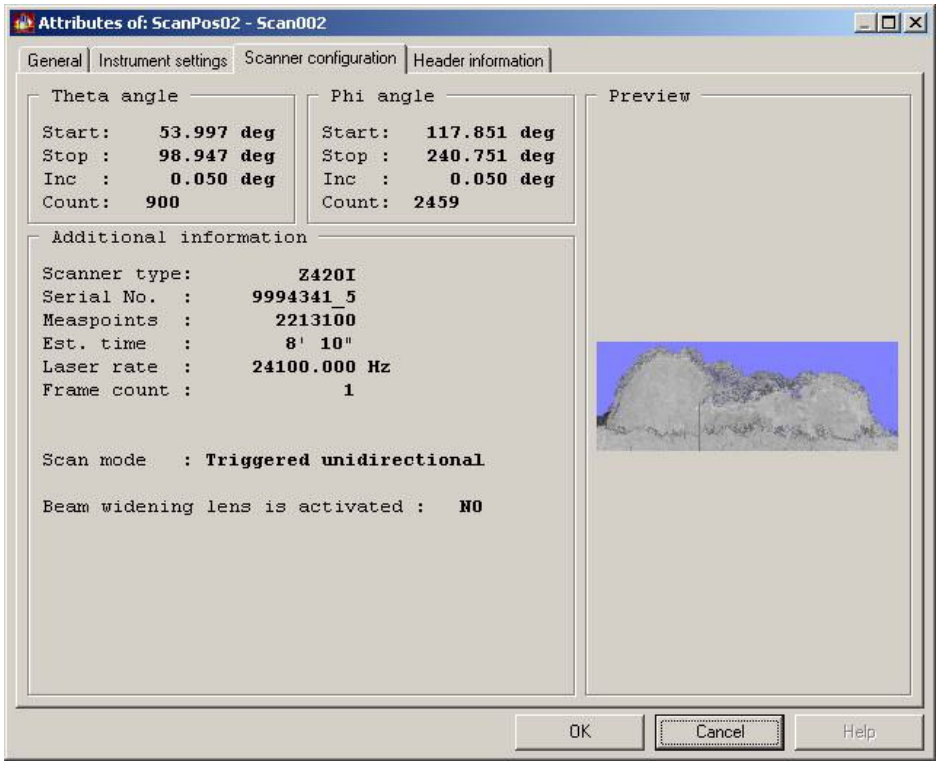

High resolution scan (scan 003)

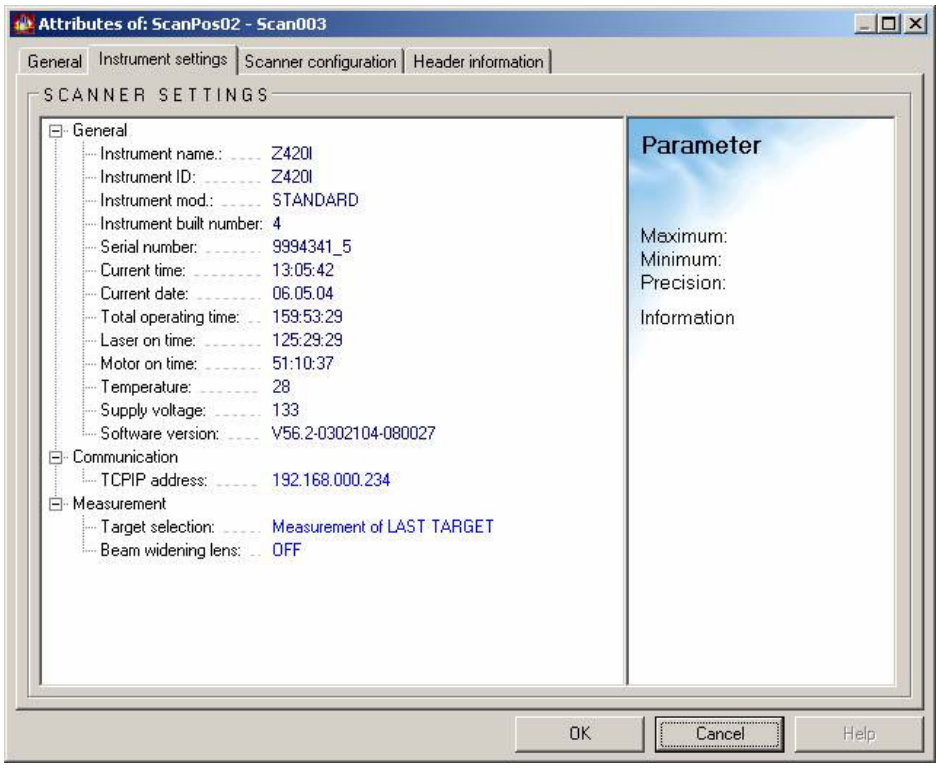

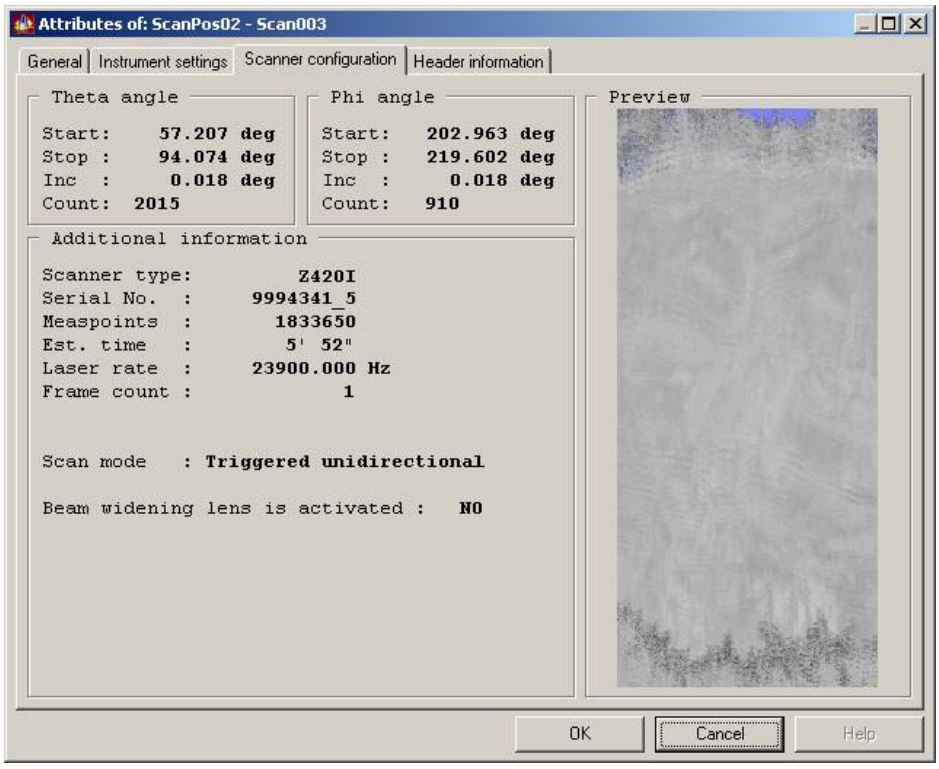

Appendix F. Riegl laser scanner survey details Site Dave (Belgium)

High resolution scan (scan 002)

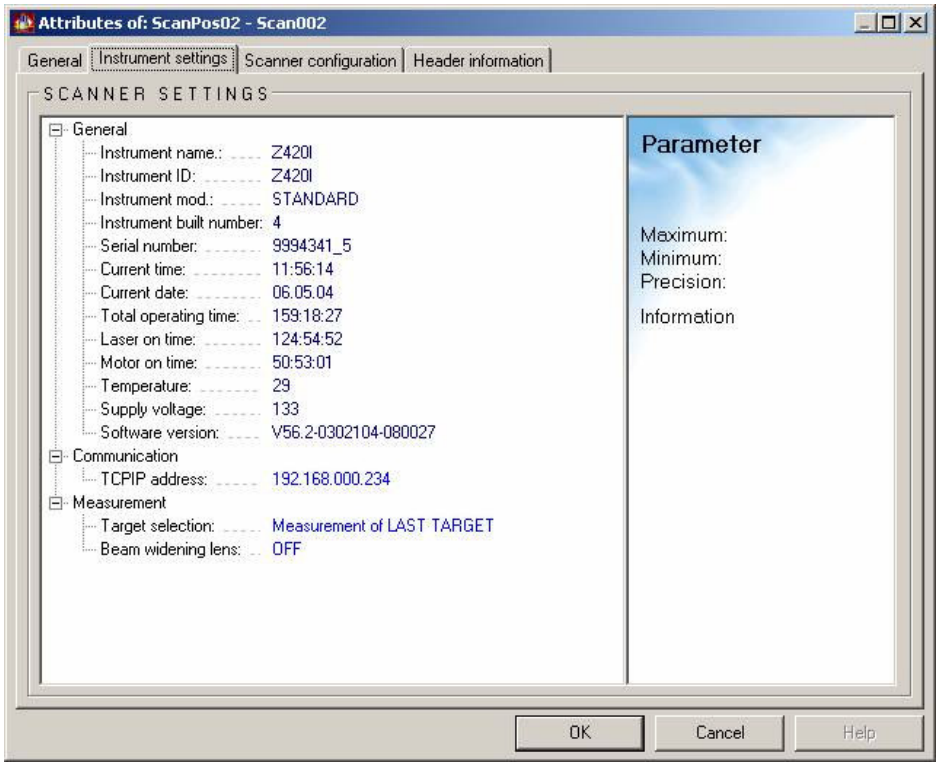

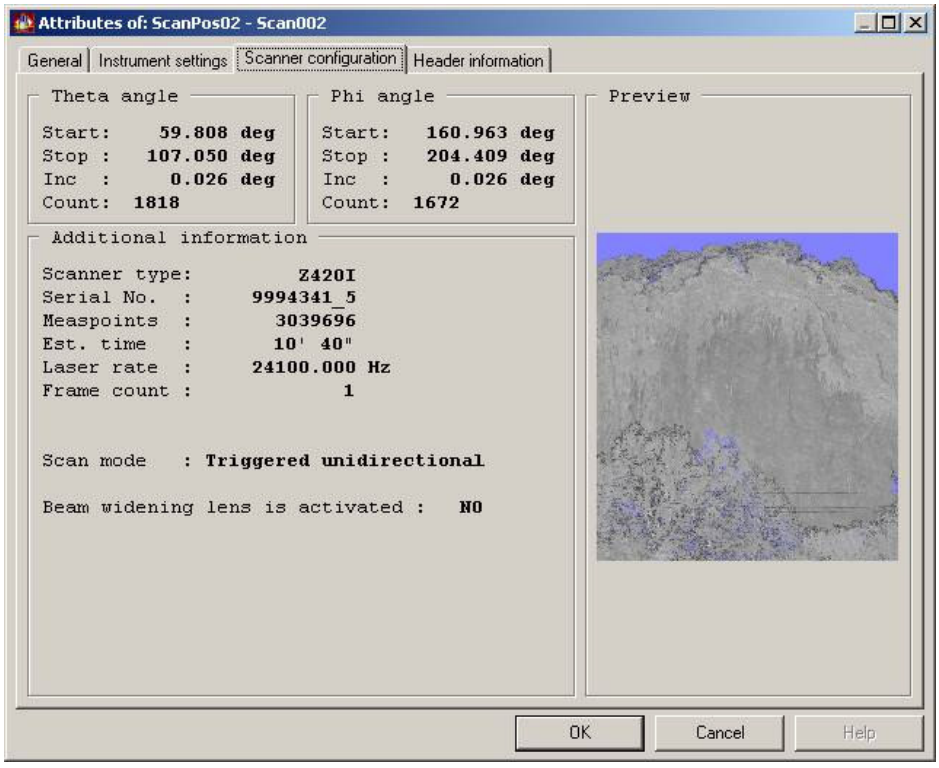

Medium resolution scan (scan 003)

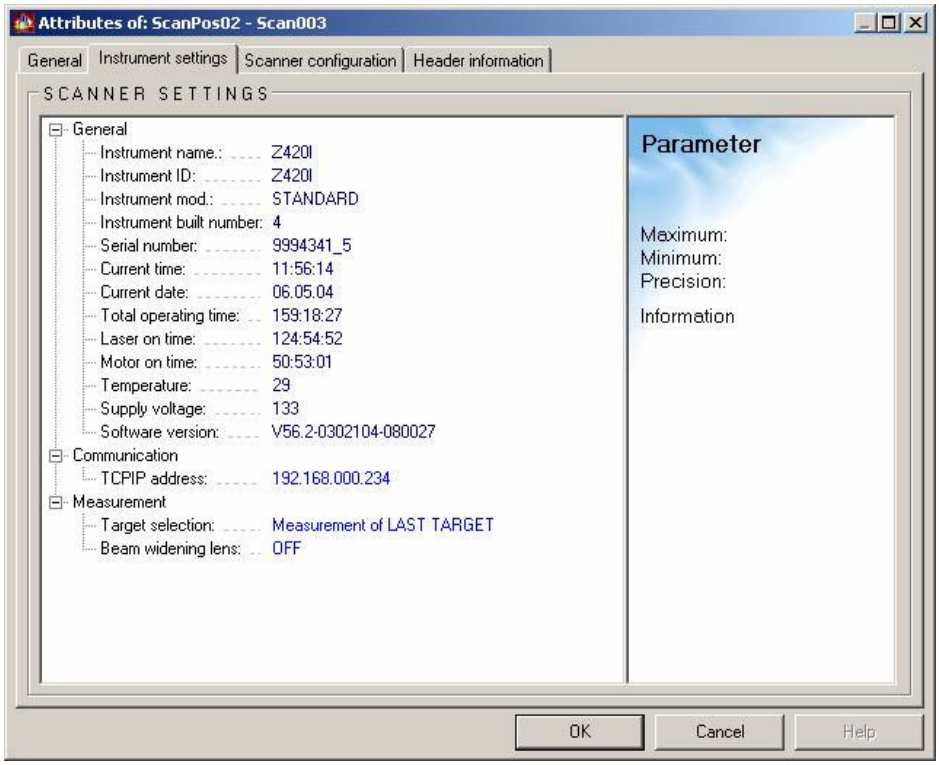

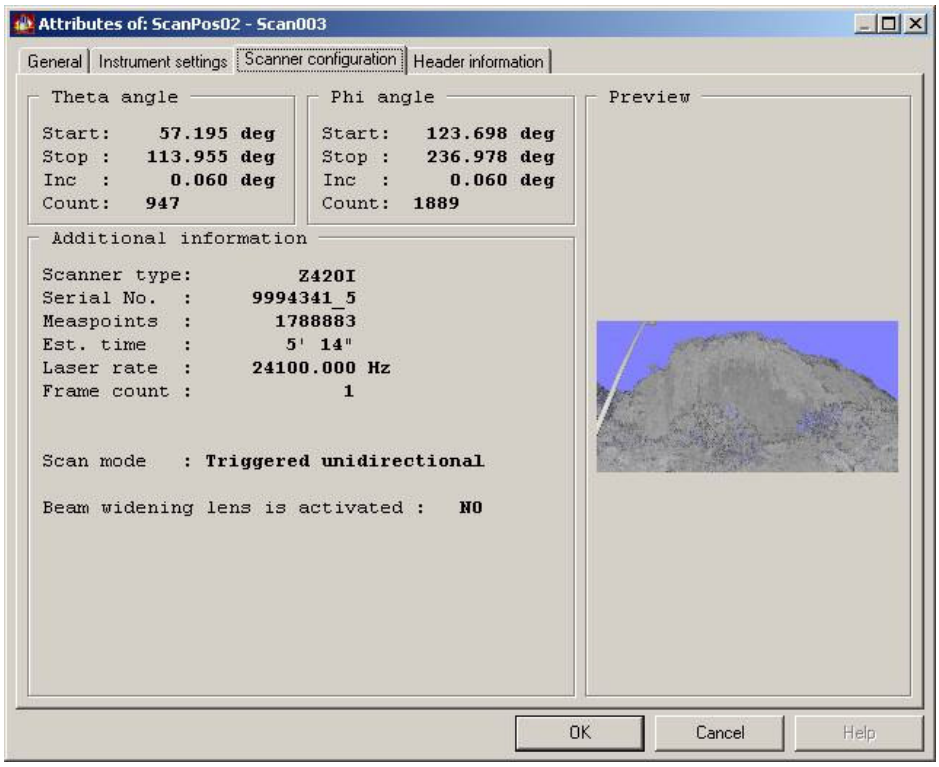

Appendix G. Example of Principal Component Analysis (PCA)

The entire PCA is best illustrated by an example. Given in Table 11.10 s an arbitrary subset A of the point cloud. The point cloud has been generated by an Optech Ilris 3-D terrestrial laser scanner. It is a very small part of the rock face of Site 1 (see 5.4.2). Matrix A consists of 939 points. The data set has been oriented towards the North, such that the positive y-axis points in the North direction and the positive x-axis points in the East direction. The data set is also levelled, such that the z-axis is the true vertical axis. The arithmetic mean of dataset A is a_{mean}:

$$a_{mean} = \begin{pmatrix} \bar{x} \\ \bar{y} \\ \bar{z} \end{pmatrix} = \begin{pmatrix} -4.474 \\ -10.349 \\ 1.655 \end{pmatrix} \quad [56]$$

Table 11.10. This table lists the example point cloud subset A, containing a total of 939 laser scan points. The points are unorganised. The adjusted coordinate values (each coordinate subtracted with its arithmetic mean), stored in Aadj, are given as well

	A			A_{adj}		
no	x (m)	y (m)	z (m)	x' (m)	y' (m)	z' (m)
1	-4.480	-10.130	1.428	-0.007	0.219	-0.227
2	-4.490	-10.122	1.427	-0.016	0.227	-0.228
3	-4.482	-10.132	1.432	-0.008	0.217	-0.223
4	-4.489	-10.125	1.431	-0.015	0.224	-0.224
5	-4.497	-10.133	1.432	-0.023	0.216	-0.223
...	...	...	...	...	...	...
...	...	...	...	...	...	...
...	...	...	...	...	...	...
935	-4.463	-10.555	1.858	0.011	-0.206	0.203
936	-4.468	-10.530	1.856	0.006	-0.181	0.201
937	-4.472	-10.519	1.855	0.002	-0.170	0.200
938	-4.472	-10.506	1.852	0.002	-0.157	0.197
939	-4.466	-10.525	1.860	0.008	-0.176	0.205

The covariance matrix C of the matrix A (or A_{adj}) is:

$$C = \mathrm{cov}(A) = \begin{pmatrix} 0.0002 & -0.0019 & 0.0012 \\ -0.0019 & 0.0214 & -0.0164 \\ 0.0012 & -0.0164 & 0.0137 \end{pmatrix} \quad [57]$$

The following step is to solve the characteristic equation for *C* that results in the eigenvalue matrix *D* and eigenvector matrix *P*. It can be proven that *P D P' = C* (see Equation [50]). The matrices *D* and *P* are for this example:

$$D = \begin{pmatrix} 0.0000 & 0 & 0 \\ 0 & 0.0008 & 0 \\ 0 & 0 & 0.0346 \end{pmatrix} \quad [58]$$

$$P = \begin{pmatrix} 0.9494 & -0.3073 & 0.0652 \\ 0.2399 & 0.5753 & -0.7820 \\ 0.2028 & 0.7580 & 0.6199 \end{pmatrix} \quad [59]$$

The principal components or eigenvectors are formed by the eigenvalues. The first principal component (v_1) is formed by the largest eigenvalue (λ_1), the second principal component (v_2) by the

second eigenvalue (λ_2). The third principal component (v_3), which is the normal vector to the plane spanned by the first two principal components, is formed by the smallest eigenvalue (λ_3), which is 0 in the case of a symmetrical matrix. Summarising, the principal components are:

$$\begin{aligned} \lambda_1 &= 0.0346 \\ \lambda_2 &= 0.0008 \\ \lambda_3 &= 0.0000 \end{aligned} \quad [60]$$

$$\bar{v}_1 = \begin{pmatrix} 0.0652 \\ -0.7820 \\ 0.6199 \end{pmatrix}, \; \bar{v}_2 = \begin{pmatrix} -0.3073 \\ 0.5753 \\ 0.7580 \end{pmatrix}, \bar{v}_3 = \bar{n} = \begin{pmatrix} 0.9494 \\ 0.2399 \\ 0.2028 \end{pmatrix} \quad [61]$$

Note that the principal component vectors are already (normalised) unit vectors, i.e. having length 1. The normal vector determines the orientation of the plane that is spanned by the first two principal components, which is in this case the orientation: 076/78. This orientation is calculated based on the Equations [16] and [17], which is explained in section 3.7.1. The data and the plane are illustrated in Figure 11.16 to Figure 11.19.

Now the principal components are known, the coordinates from A can be projected from Euclidean space onto the Principal Component space to the matrix B. For this it is important to use the points from the adjusted matrix A_{adj}, which is matrix A with the means of each coordinate subtracted from each of the coordinates. The projection to the Principal Component space is done by multiplying the inversed eigenvector matrix P (see Equation [62]) with the rows of the data matrix A in the following way:

$$B = P^{-1} A_{adj}^{\;-1} \quad [62]$$

The points of A can subsequently be projected onto the plane that is spanned by the first two principal components. The projection is perpendicular to the plane, parallel to the third principal component, the normal to the plane. The projection vector is simply the difference in position between the original data point and the projected data point. The length of the projection vector is then a measure of the error or deviation of the point from the computed principal component plane. The projected points are computed by multiplying the first two dimensions of the points projected in principal component space (so the first two dimensions of B) with the inversed first two principal component vectors in P:

$$A_{fit} = B_{1,2}^{\;-1} P_{1,2}^{\;-1} \quad [63]$$

The residuals of the points can subsequently be calculated by simply subtracting the fitted points from A_{fit} from the original (adjusted) points A_{adj}. It should be noted that if the coordinates of the fitted points in the original coordinates is required, the mean vector coordinate a_{mean} have to be added again to the points in A_{fit}. The lengths of the residual vectors are then the distance of the original point to the fitted (principal component) plane. The computation can be done in the following way:

$$\begin{aligned} R &= A_{adj} - A_{fit} \\ res_i &= \sqrt{R_{i,1}^{\;2} + R_{i,2}^{\;2} + R_{i,3}^{\;2}} \\ (i &= 1:N) \end{aligned} \quad [64]$$

For the given example of the dataset A, the results are summarised in the Table 11.11 below.

Table 11.11. Results of the PCA on the example dataset A

	A_{adj}			B			A_{fit}			res
N0	x' (m)	y' (m)	z' (m)	Pc 1	Pc 2	Pc 3	x' (m)	y' (m)	z' (m)	distance (m)
1	-0.007	0.219	-0.227	-0.3120	-0.0440	-0.0001	-0.007	0.219	-0.227	0.0001
2	-0.016	0.227	-0.228	-0.3199	-0.0370	0.0069	-0.010	0.229	-0.226	0.0069
3	-0.008	0.217	-0.223	-0.3086	-0.0412	0.0011	-0.007	0.218	-0.223	0.0011
4	-0.015	0.224	-0.224	-0.3146	-0.0362	0.0064	-0.009	0.225	-0.223	0.0064
5	-0.023	0.216	-0.223	-0.3086	-0.0374	0.0153	-0.009	0.220	-0.220	0.0153
…	…	…	…	…	…	…	…	…	…	…
…	…	…	…	…	…	…	…	…	…	…
…	…	…	…	…	…	…	…	…	…	…
935	0.011	-0.206	0.203	0.2880	0.0320	-0.0021	0.009	-0.207	0.203	0.0021
936	0.006	-0.181	0.201	0.2667	0.0466	-0.0030	0.003	-0.182	0.201	0.0030
937	0.002	-0.170	0.200	0.2568	0.0536	-0.0020	0.000	-0.170	0.199	0.0020
938	0.002	-0.157	0.197	0.2455	0.0583	-0.0042	-0.002	-0.158	0.196	0.0042
939	0.008	-0.176	0.205	0.2650	0.0521	-0.0074	0.001	-0.177	0.204	0.0074

Where:

- Pc 1, Pc 2 and Pc 3 are the representations of the points of A in the principal component space.
- x_fit, y_fit and z_fit are the points of A projected along the third principal component (the plane's normal) to the plane that is spanned by the first two principal components
- The residual is the length of the vector that is the difference between the original coordinates of A and the projected coordinates.

Again, like with the Hough transformation, a number of threshold values can be defined in order to determine the accuracy of the found plane. The larger the found distance, the less the point "belongs" to the plane. A certain threshold distance can be defined in order to classify "inliers" and "outliers" to the computed plane. In Figure 11.15 the computed residual distance values are plotted in a histogram for the example data set *A*. The threshold distance should be in the same order as the error or precision noise in the data. Points outside the noise threshold are not likely to belong to the found plane. If the number of outliers exceeds the number of inliers, the point cloud subset may include data from other discontinuity planes and the computed PCA-based plane will therefore not be representing any of the discontinuity planes. The selected subset should thus be ignored and a new subset should be selected in the region-growing process.

Ultimately, the objective is to represent the found principal component plane by its plane equation. Since the normal to the plane is known (the third principal component) the factors *a*, *b* and *c* are given. The final factor *d* is found by substituting any of the points from *A* that fall on the plane in the plane equation. Alternatively, the average coordinate a_{mean} can be used.

$$ax + by + cz + d = 0 \quad [65]$$

Where

$$d = -\overline{n} \cdot \begin{pmatrix} x \\ y \\ z \end{pmatrix} \quad [66]$$

For the sample set A, the normal (see Equation [61]) and a_{mean} (see Equation [56]) are given. By substituting these vectors in Equation [65], the plane equation becomes as follows:

$$0.9494\ x + 0.2399\ y + 0.2028\ z + 6.3944 = 0 \quad [67]$$

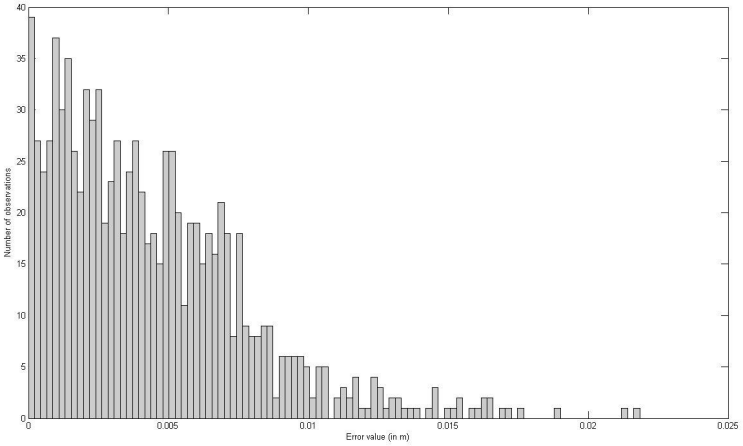

Figure 11.15. Histogram of the residual (absolute) distance (error) values (horizontal scale is in metres, vertical scale are the number of points within a bin, 100 bins, bin size 0.25 mm). Note that in this case most of the residual values fall within the 0.01 m (1 cm) range, which corresponds to the error or noise of the used Optech Ilris terrestrial laser scanner. It should be noted that the sample data set A from which this error plot is made, is chosen such that most points actually form a (discontinuity) plane.

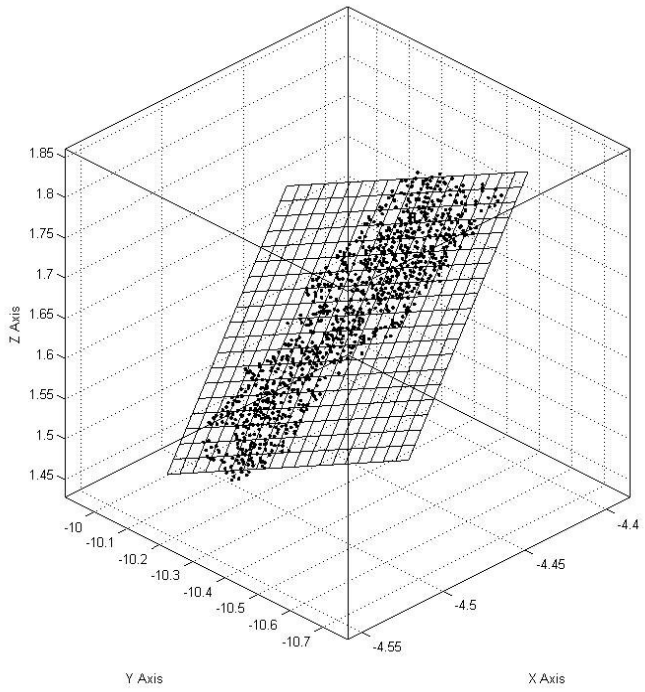

Figure 11.16. Point data set A, with the PCA plane plotted as a meshed grid.

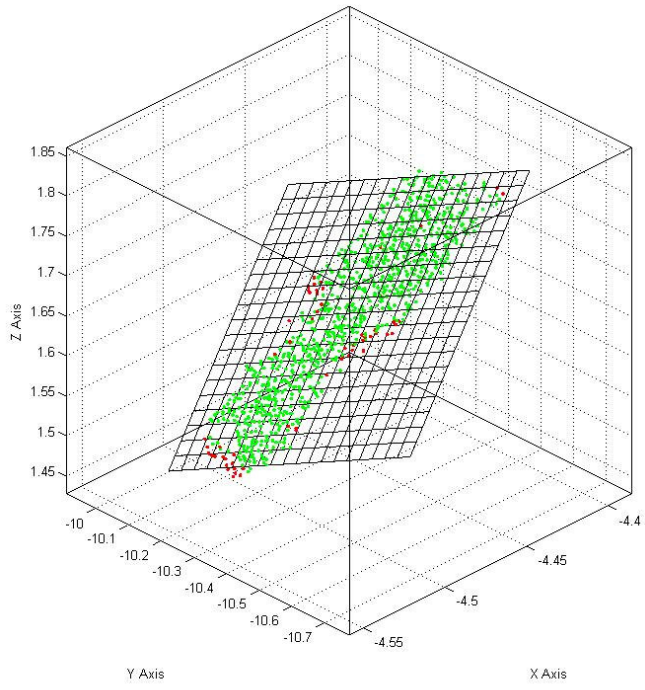

Figure 11.17. Point data set A, outlier points are coloured red and inliers are coloured green. The (arbitrary) threshold here is 1 cm.

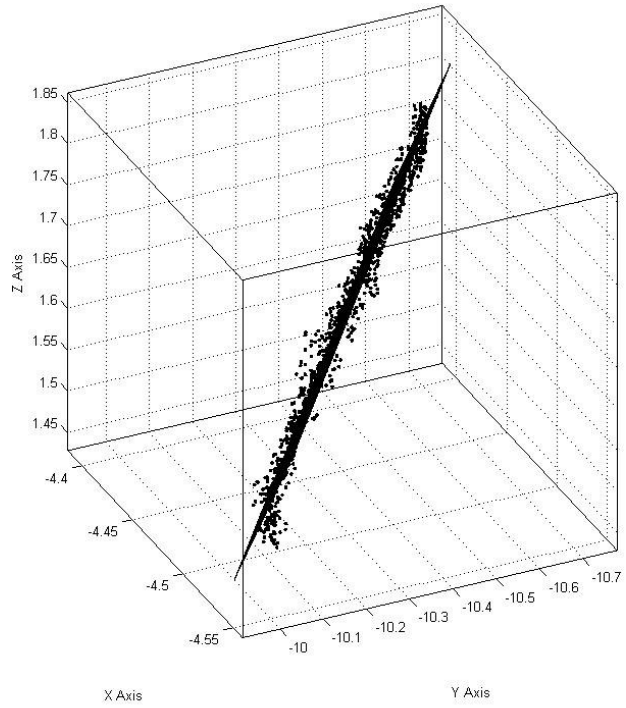

Figure 11.18. Point data set A, with the PCA plane plotted as a meshed grid. This figure shows a side view along the plane to highlight the noise.

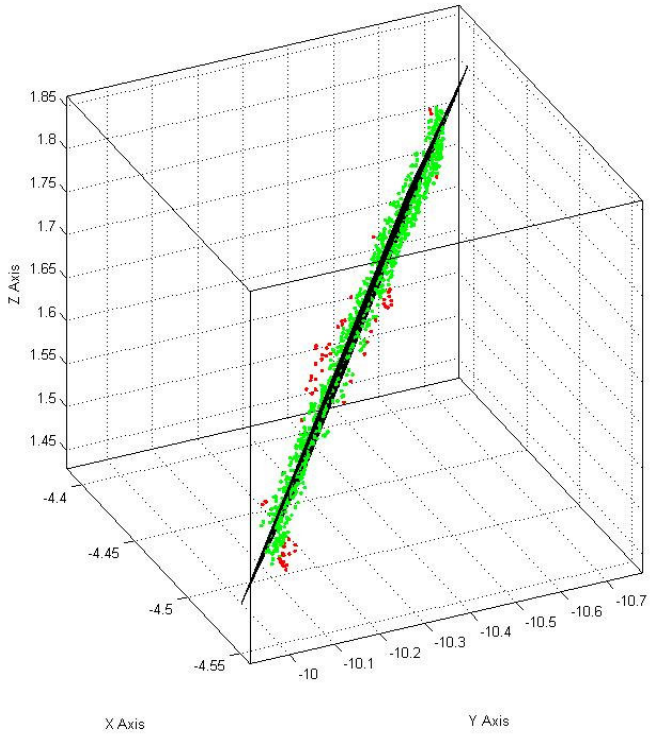

Figure 11.19. Point data set A, with the PCA plane plotted as a meshed grid. This figure shows the side view along the plane to highlight the noise. Outliers (more than 1 cm perpendicular distance from the plane) are coloured red and the inliers are coloured green.

Appendix H. Method 1 Matlab FastRBF pocessing sripts for Sites 1 and 2

Survey data of Site 1 (Bellmunt)

```
A = load('bellmunt_pointcloud.txt');

minimum = [-4.75 min(A(:,2)) min(A(:,3))];
maximum = [-1.63 max(A(:,2)) max(A(:,3))];
Points = fastrbf_crop(Points,minimum,maximum);
Points = fastrbf_import('bellmunt_pointcloud.txt','format', '%x %y %z \n')
Normals = fastrbf_normalsfrompoints(Points);
Density = fastrbf_densityfromnormals(Normals, 0.01, 0.03);
Density = fastrbf_unique(Density);
Rbf   = fastrbf_fit(Density, 0.003);
Mesh  = fastrbf_isosurf(Rbf, 0.01, 'min', minimum, 'max', maximum,
    'smooth', 0.02, 'plane', 'up', [0.4067 0.9135 0]);

fastrbf_export(Mesh, 'bellmunt_surface.obj');
```

Survey data of Site 2 (Torroja)

```
A = load('Torroja_pointcloud.txt');

minimum = [min(A(:,1)) -1.50 min(A(:,3))];
maximum = [max(A(:,1)) 2.79 max(A(:,3))];
Points = fastrbf_import('Torroja_pointcloud.txt','format', '%x %y %z \n')
Points = fastrbf_crop(Points,minimum,maximum);
Normals = fastrbf_normalsfrompoints(Points);
Density = fastrbf_densityfromnormals(Normals, 0.01, 0.03);
Density = fastrbf_unique(Density);
Rbf   = fastrbf_fit(Density, 0.003);
Mesh  = fastrbf_isosurf(Rbf, 0.01, 'min', minimum, 'max', maximum,
    'smooth', 0.02, 'plane', 'up', [0.99452 0.10453 0]);

fastrbf_export(Mesh, 'Torroja_surface.obj');
```

Appendix I. Point coud processing parameters for Methods 3 and 4.

Method 3. Processing parameters

a. Box size = 0.06. The dimensions of the search box (in metres)
b. Minimum points boxed = 10. The minimum number of points found in the search box)
c. Threshold distance = 0.0050.This is the maximum perpendicular distance (in m.) of a point to the plane, which strongly depends on the noise level. This threshold distance is in the final analysis not used. Instead, the parameter (*d*) is used (see below).
d. Percentage inliers = 0.5. With the percentage of inliers it is not required to know the noise level of the data. Here, inliers are defined as points that are located closer to the local calculated plane than the mean orthogonal distance level of all points within the search box together.
e. Orientation threshold = 0.3. Neighbouring points that form a local plane that has a pole-vector difference larger than this threshold value (in degrees) are rejected. This parameter makes sure that the region-growing stops when it hits another plane
f. Minimum points in plane = 200. After the segmentation, points that form small planes (containing less than 200 points in this case) are removed. (This can be omitted to keep the small planes in)

Method 4. Processing parameters

Neighbourhood definitions
Storage model: K-D tree (other choices: Delaunay TIN, Octree)
Octree bin maximum number of points: 100
Octree bin overlap: 1.0
Distance metric: 3-D (Other choice: 2-D)
Number of neighbours in K-D tree: 20

Connected component parameters
Maximum distance between points: 0.1
Minimum number of points: 200 (this can be omitted to keep the small planes in)

Seed selection parameters
Seed neighbourhood definition: Direct neighbours (other choice: All within radius)
Seed neighbourhood radius: 0.1
Maximum slope angle: 90
Bin size slope angle: 3.0
Bin size distance: 0.02
Maximum number of seed points: 10
Maximum distance to plane: 0.01

Surface growing parameters
Surface model: Planar (other choice: Smooth)
Surface growing neighbourhood definition: Direct neighbours (other choice: All within radius)
Surface growing radius: 0.05
Maximum distance to surface: 0.015
Competing surfaces: Yes

Appendix J. Normal Set Spacing Distributions

72 unnumbered figures showing equivalent normal and normal spacings as log-transformed histograms for 5 discontinuity sets and 4 Methods (Site 1 – 40 figs) and 4 discontinuity sets and 4 Methods (Site 2- 32 figs).

Site 1 Bellmunt – Method 1

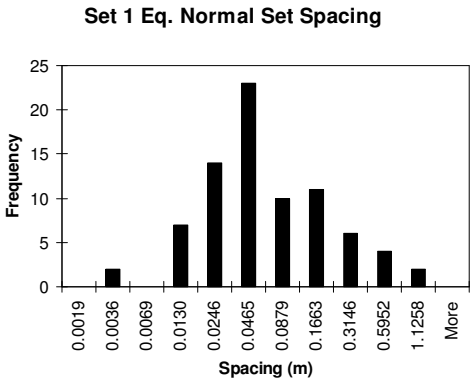

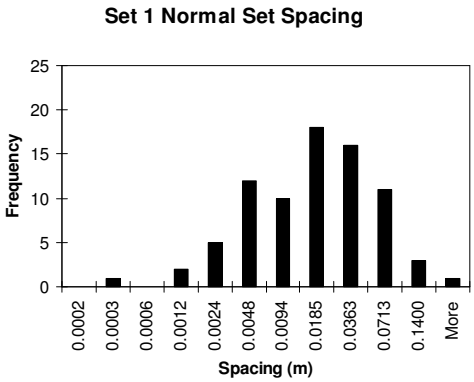

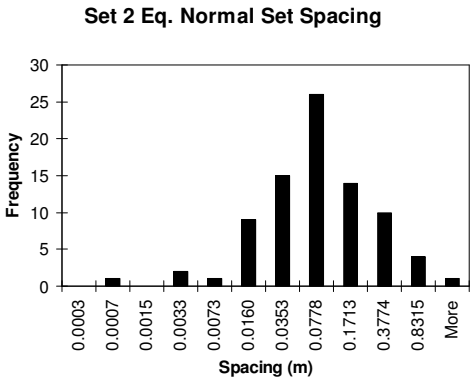

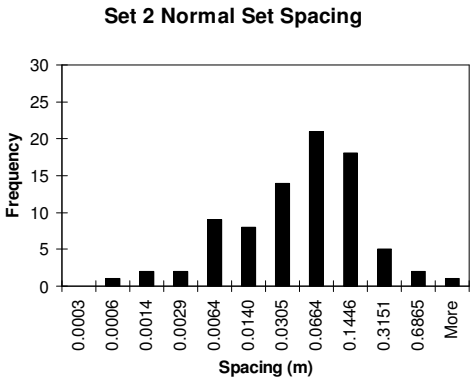

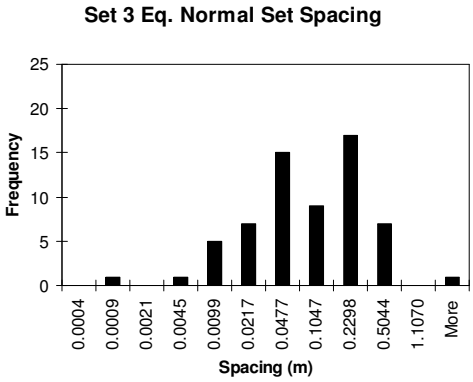

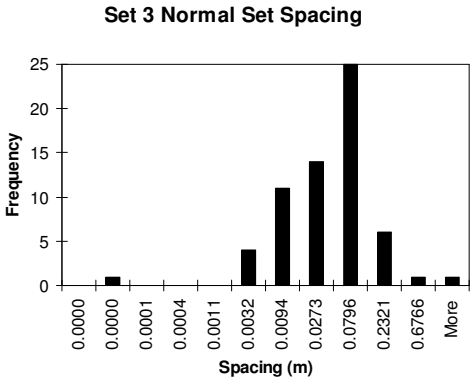

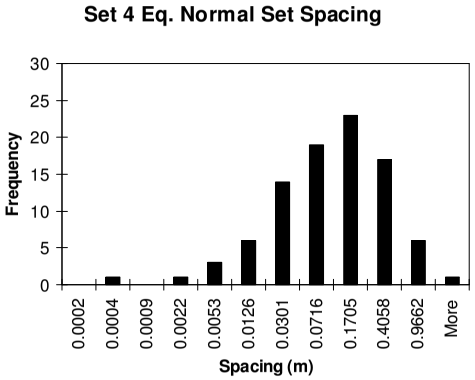

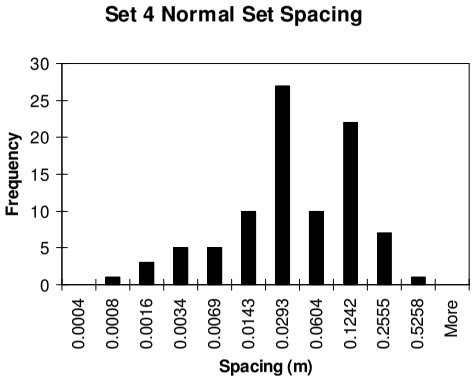

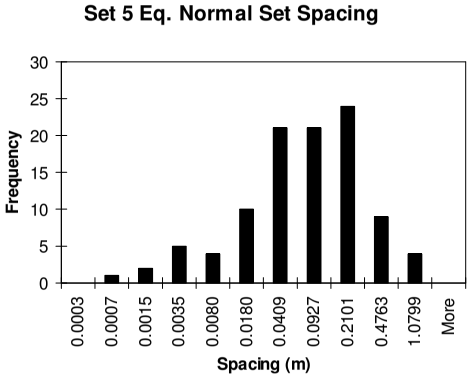

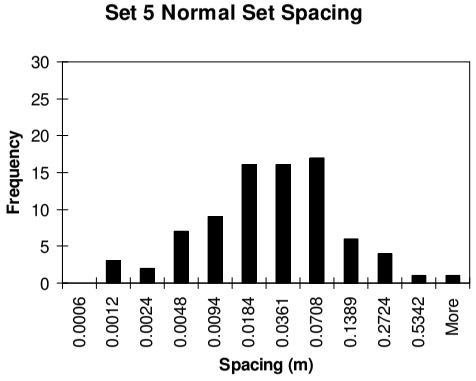

Site 1 Bellmunt – Method 2

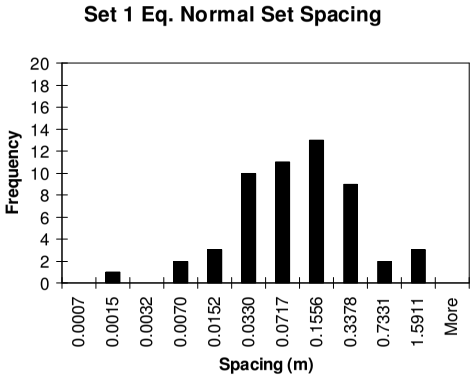

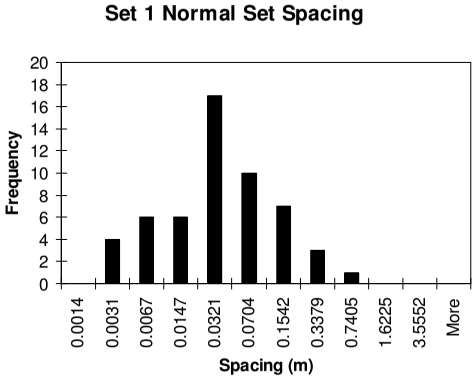

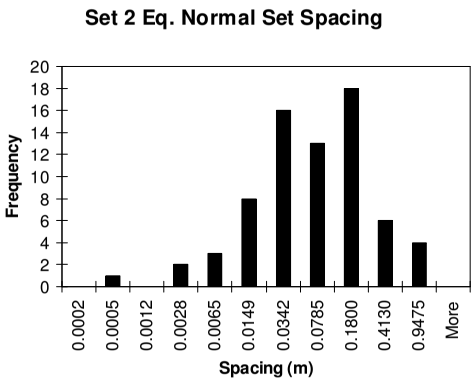

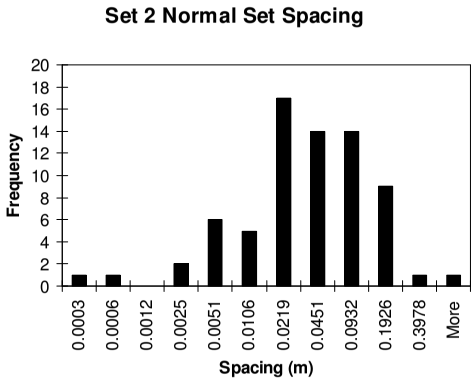

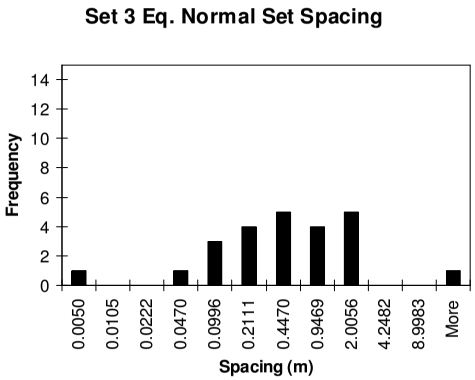

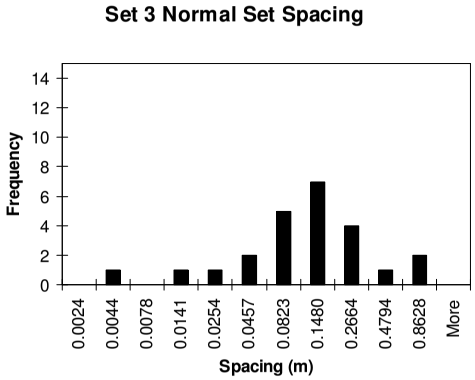

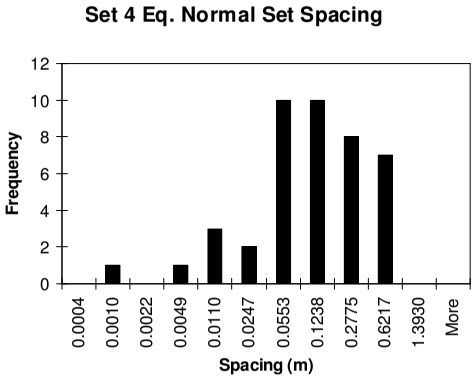

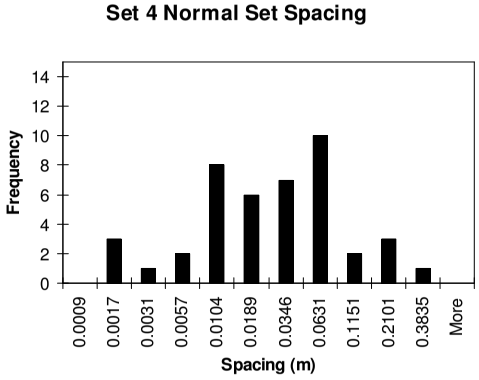

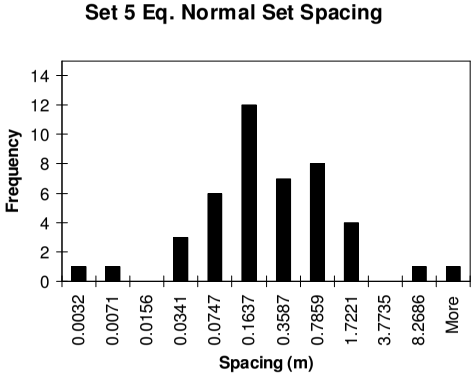

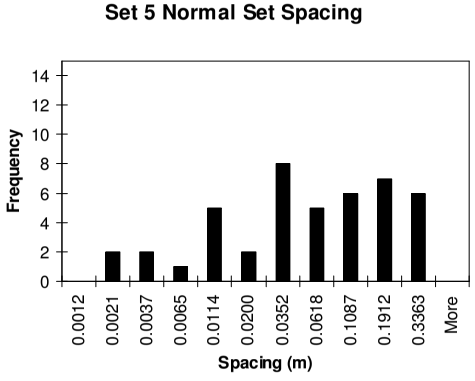

Site 1 Bellmunt – Method 3

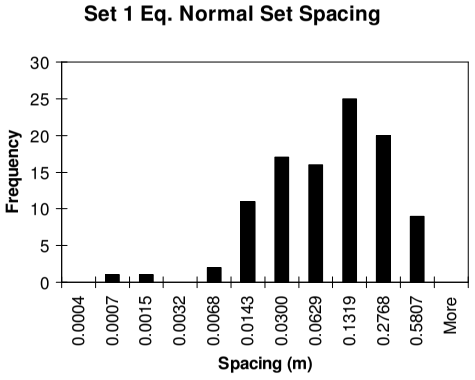

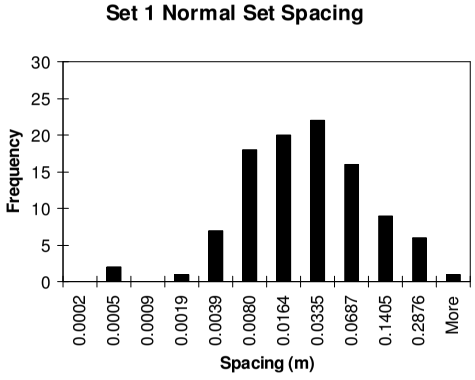

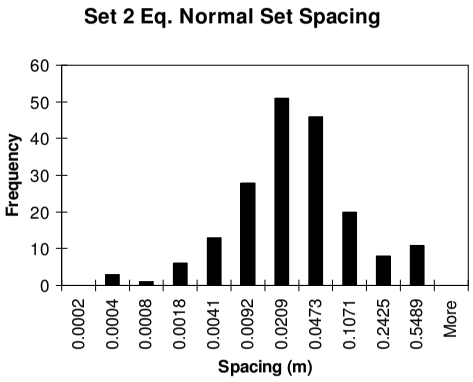
Set 2 Eq. Normal Set Spacing
Frequency
Spacing (m)
0.0002
0.0004
0.0008
0.0018
0.0041
0.0092
0.0209
0.0473
0.1071
0.2425
0.5489
More

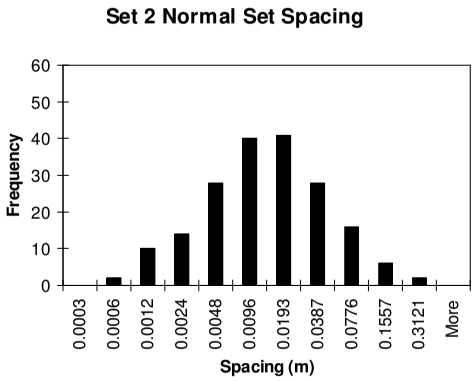
Set 2 Normal Set Spacing
Frequency
Spacing (m)
0.0003
0.0006
0.0012
0.0024
0.0048
0.0096
0.0193
0.0387
0.0776
0.1557
0.3121
More

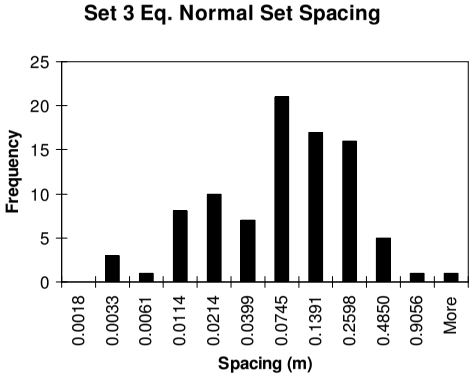
Set 3 Eq. Normal Set Spacing
Frequency
Spacing (m)
0.0018
0.0033
0.0061
0.0114
0.0214
0.0399
0.0745
0.1391
0.2598
0.4850
0.9056
More

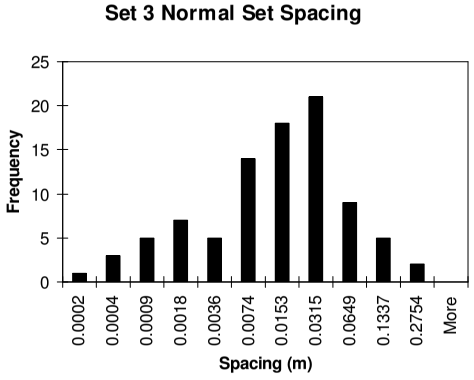
Set 3 Normal Set Spacing
Frequency
Spacing (m)
0.0002
0.0004
0.0009
0.0018
0.0036
0.0074
0.0153
0.0315
0.0649
0.1337
0.2754
More

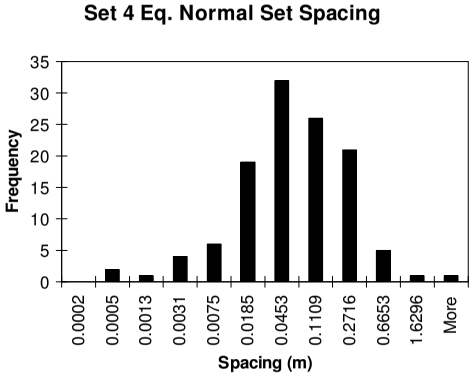
Set 4 Eq. Normal Set Spacing
Frequency
Spacing (m)
0.0002
0.0005
0.0013
0.0031
0.0075
0.0185
0.0453
0.1109
0.2716
0.6653
1.6296
More

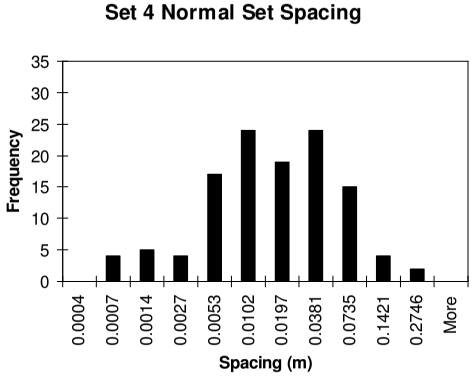
Set 4 Normal Set Spacing
Frequency
Spacing (m)
0.0004
0.0007
0.0014
0.0027
0.0053
0.0102
0.0197
0.0381
0.0735
0.1421
0.2746
More

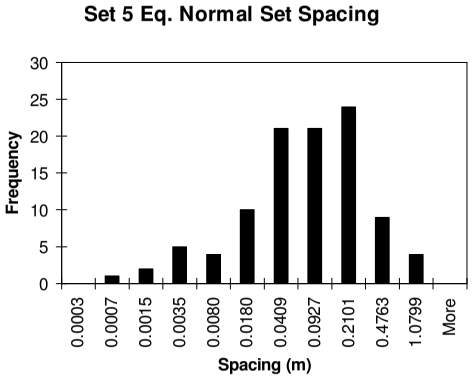
Set 5 Eq. Normal Set Spacing
Frequency
Spacing (m)
0.0003
0.0007
0.0015
0.0035
0.0080
0.0180
0.0409
0.0927
0.2101
0.4763
1.0799
More

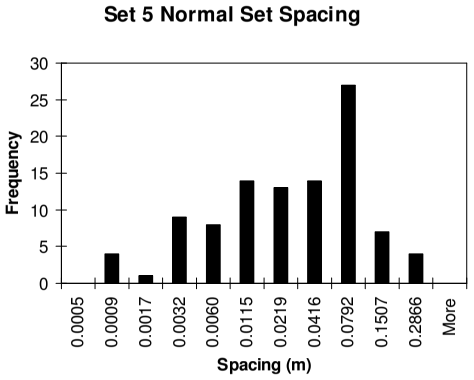
Set 5 Normal Set Spacing
Frequency
Spacing (m)
0.0005
0.0009
0.0017
0.0032
0.0060
0.0115
0.0219
0.0416
0.0792
0.1507
0.2866
More

Site 1 Bellmunt – Method 4

Set 1 Eq. Normal Set Spacing

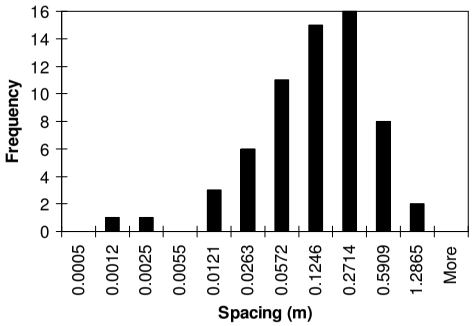

Set 1 Normal Set Spacing

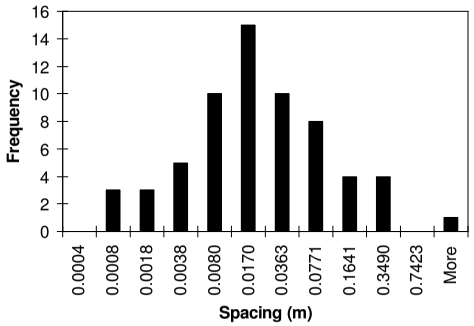

Set 2 Eq. Normal Set Spacing

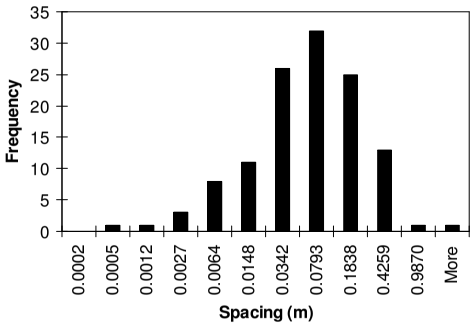

Set 2 Normal Set Spacing

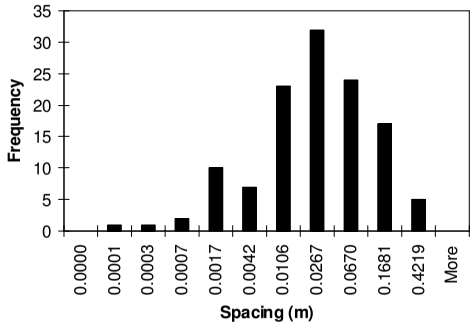

Set 3 Eq. Normal Set Spacing

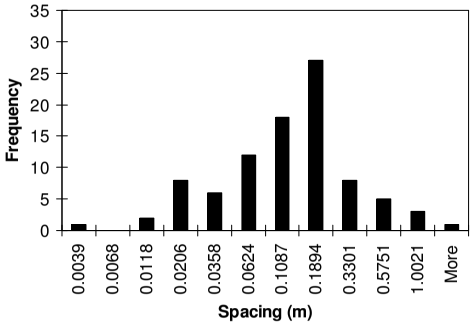

Set 3 Normal Set Spacing

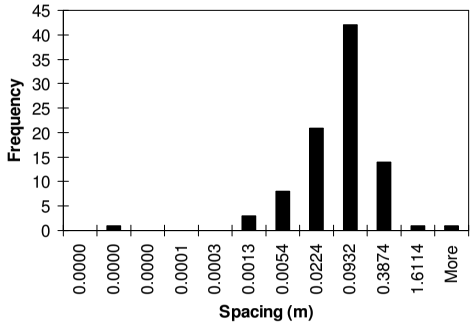

Set 4 Eq. Normal Set Spacing

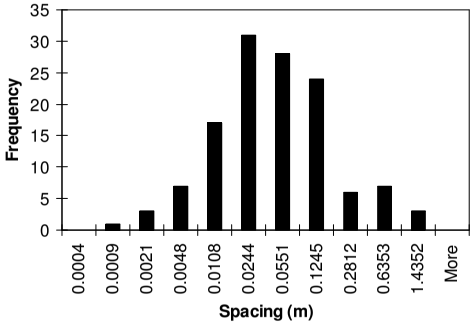

Set 4 Normal Set Spacing

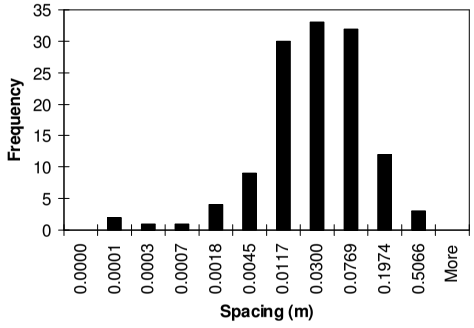

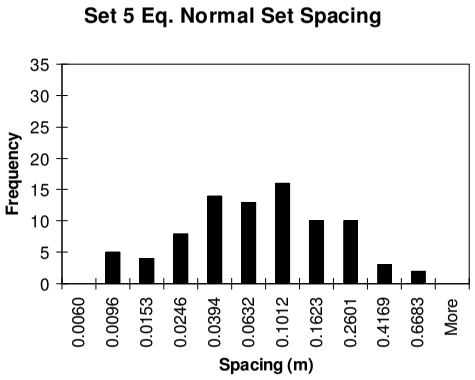

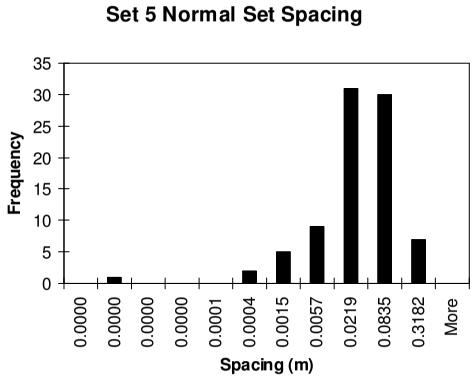

Site 2 Torroja – Method 1

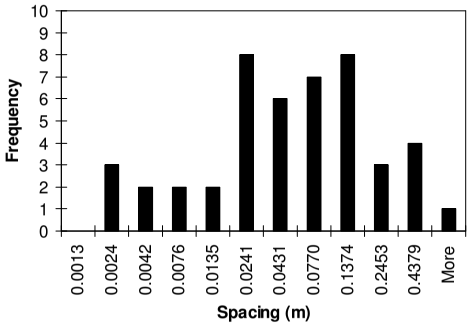

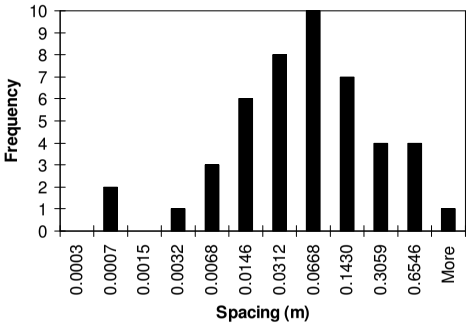

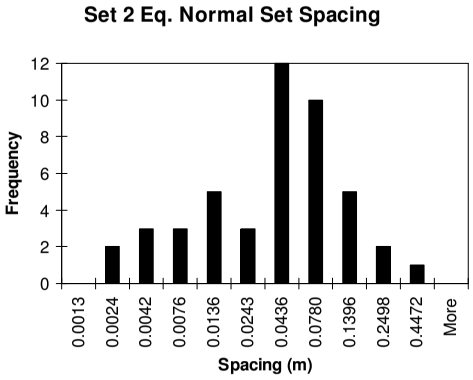

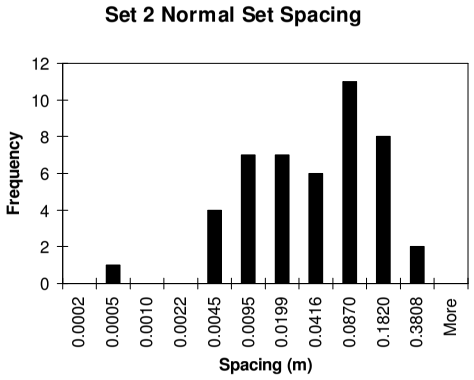

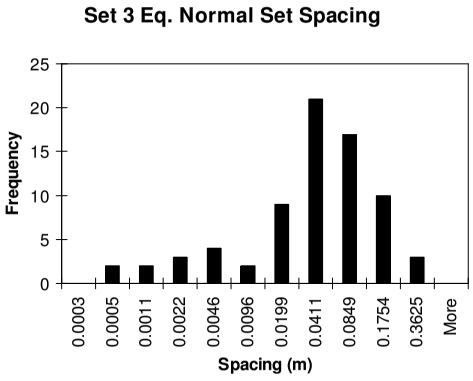

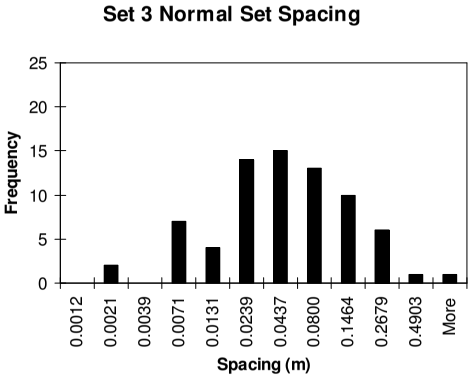

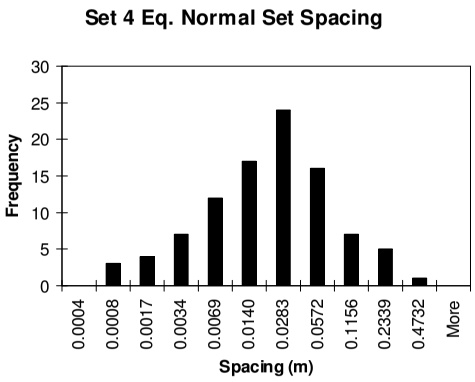
Set 4 Eq. Normal Set Spacing
Frequency
30
25
20
15
10
5
0
0.0004
0.0008
0.0017
0.0034
0.0069
0.0140
0.0283
0.0572
0.1156
0.2339
0.4732
More
Spacing (m)

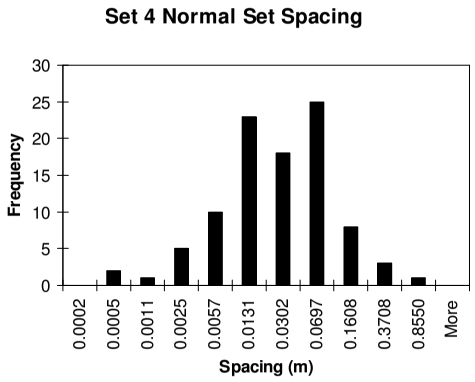
Set 4 Normal Set Spacing
Frequency
30
25
20
15
10
5
0
0.0002
0.0005
0.0011
0.0025
0.0057
0.0131
0.0302
0.0697
0.1608
0.3708
0.8550
More
Spacing (m)

Site 2 Torroja – Method 2

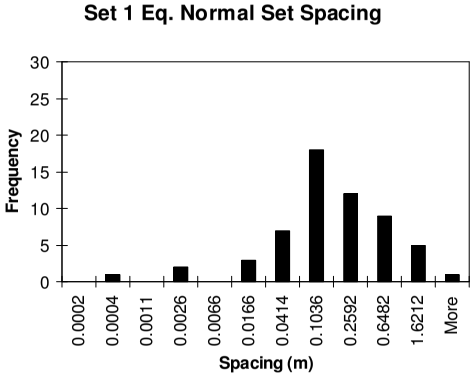

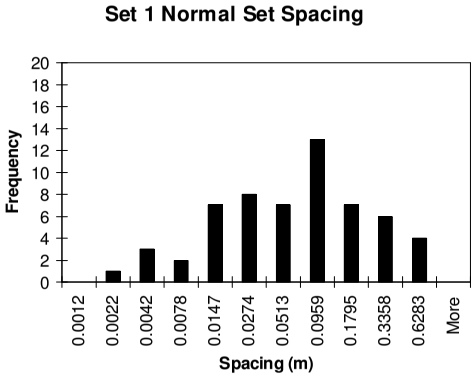

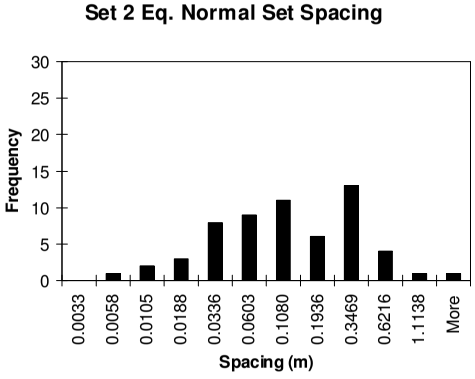

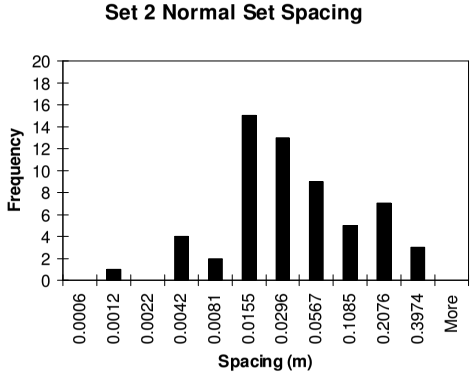

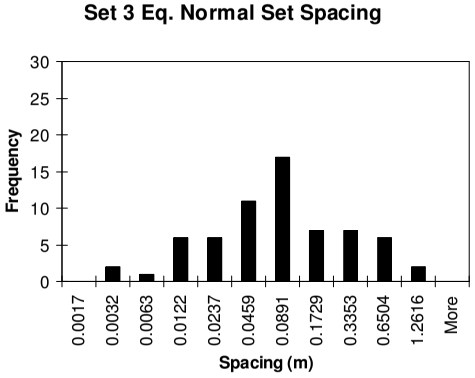

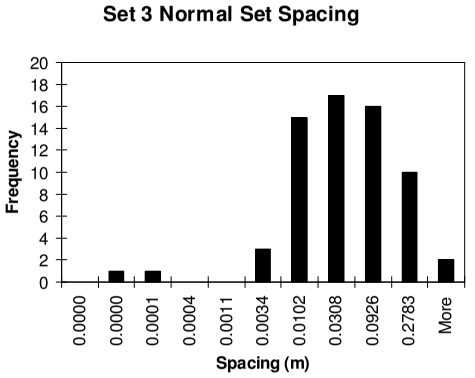

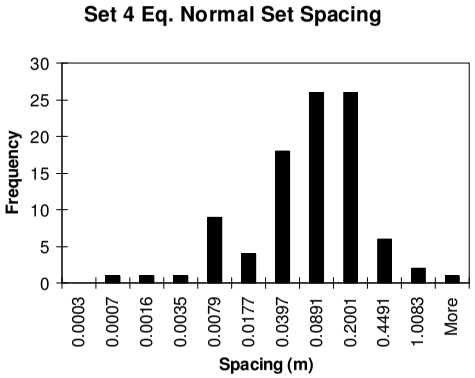

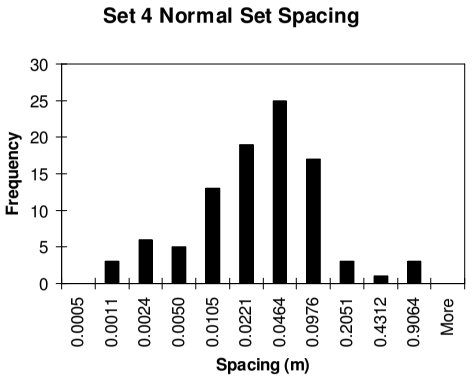

Site 2 Torroja – Method 3

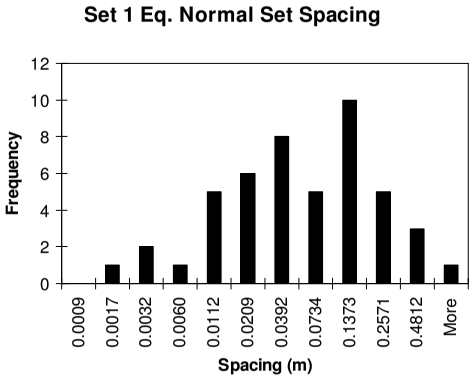

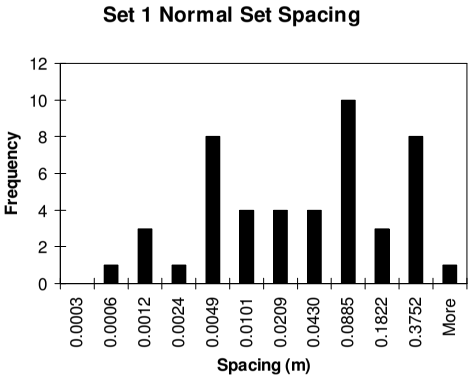

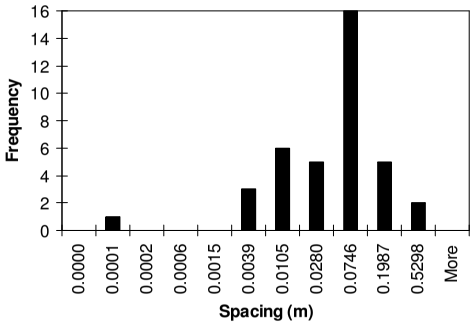

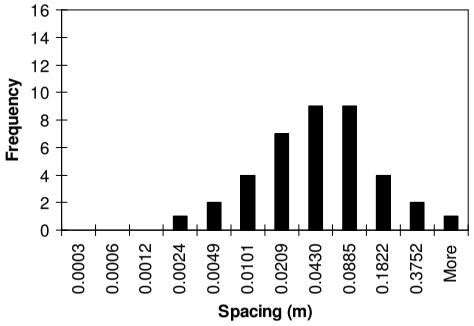

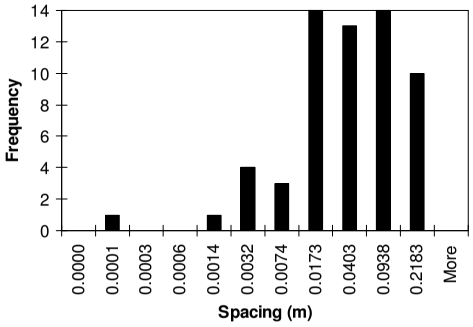

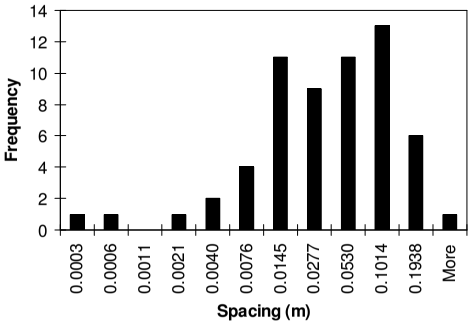

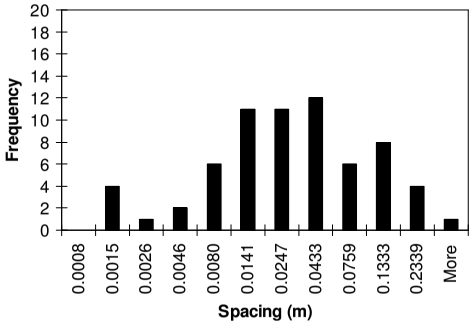

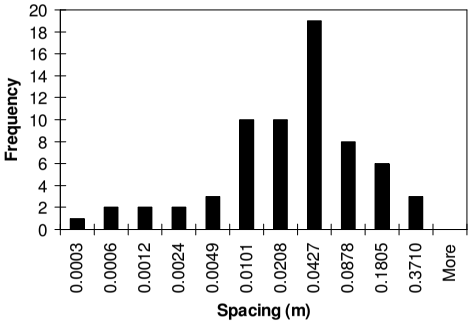

Site 2 Torroja – Method 4

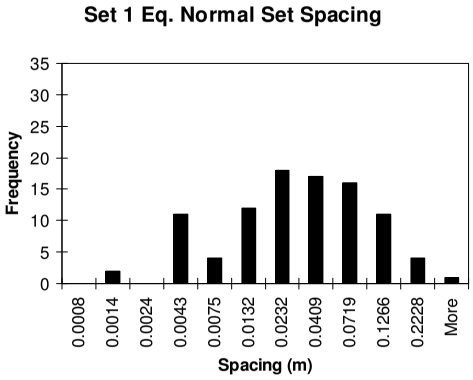

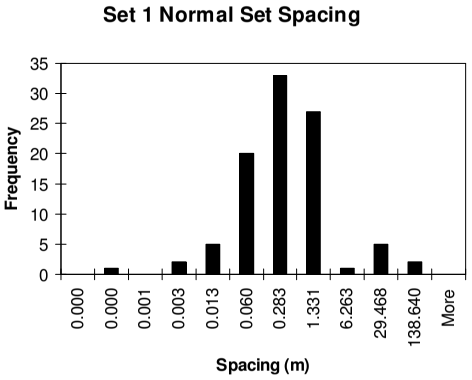

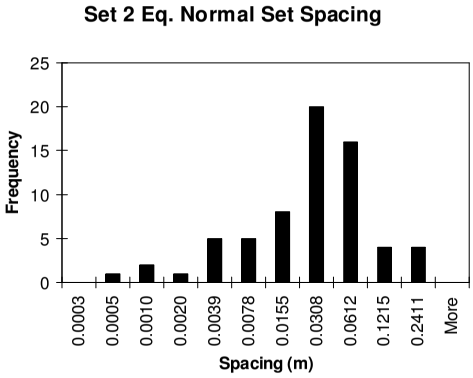

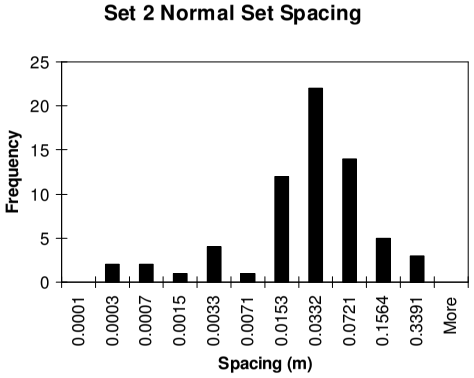

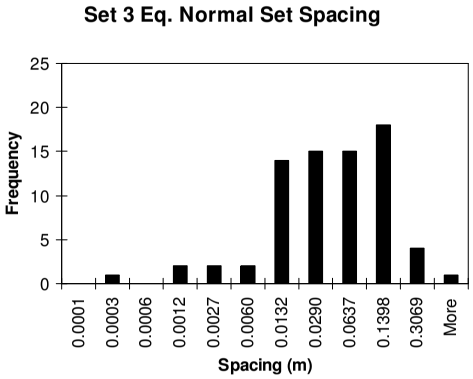

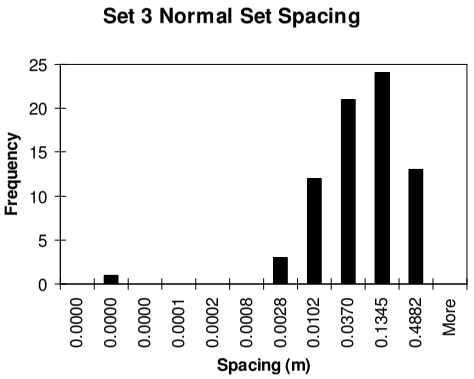

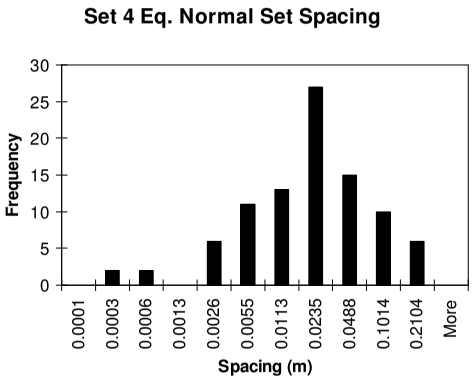

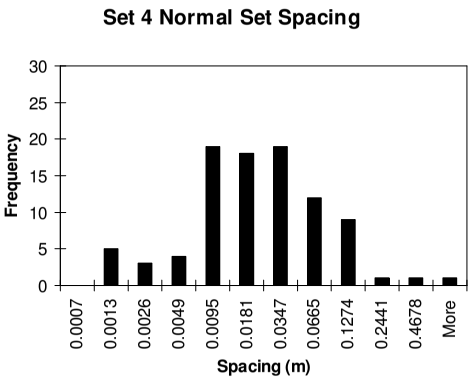

Appendix K. Comparison of Discontinuity Plane Orientations

Site 1 - Bellmunt																		
Manual readings			**Method 1**		**RBF**		**Method 2**		**Fx**		**Method 3**		**PCA**		**Method 4**		**PCM**	
No	Dip dir. (°)	Dip angle (°)	No	Dip dir. (°)	Dip angle (°)	Dihedral angle (°)	No	Dip dir. (°)	Dip angle (°)	Dihedral angle (°)	No	Dip dir. (°)	Dip angle (°)	Dihedral angle (°)	No	Dip dir. (°)	Dip angle (°)	Dihedral angle (°)
1	148	57	134	151.91	55.88	3.45	1	143.25	57.01	3.99	30	148.61	55.07	2.00	156	143.87	57.45	3.50
2	58	85	367	70.13	74.41	15.94	2	48.34	72.51	15.66	46	64.49	86.51	6.64	153	56.37	83.55	2.18
3	85	87	36	75.59	88.42	9.51	3	81.77	78.36	9.21	NA				125	70.52	87.60	14.48
4	155	56	114	151.85	53.83	3.37	4	150.72	52.53	4.91	22	151.68	54.13	3.30	132	151.48	51.79	5.08
5	342	43	300	345.91	37.48	6.07	5	339.52	41.56	2.21	96	341.87	43.59	0.59	138	344.23	42.13	1.74
6	71	82	20	66.49	80.53	4.70	6	65.49	77.84	6.84	56	64.35	79.63	6.98	104	64.82	79.68	6.53
7	90	82	37	79.22	89.66	13.19	7	85.41	83.71	4.86	17	80.17	88.17	11.57	51	80.68	89.79	12.12
8	81	90	37	79.22	89.66	1.81	*8	*85.82*	*48.62*	*41.61*	17	80.17	88.17	2.01	172	80.37	89.70	0.70
*9	*51*	*85*	370	63.14	80.40		9	50.02	75.58		91	36.43	88.54		208	41.34	85.37	
10	87	86	25	79.92	84.46	7.23	10	81.93	77.51	9.86	92	80.21	82.61	7.56	176	80.69	84.38	6.49
11	75	76	17	70.89	80.59	6.10	11	70.39	78.46	5.13	60	69.51	79.49	6.39	134	68.75	77.26	6.21
12	76	76	12	71.67	76.87	4.30	12	72.28	74.91	3.76	34	69.71	74.98	6.18	112	73.22	76.62	2.77
13	58	63	355	50.12	72.02	11.59	13	55.32	62.03	2.57	14	55.54	62.61	2.23	77	54.23	61.64	3.61
14	343	40	291	345.49	54.36	14.47	14	340.38	39.51	1.75	218	348.95	41.21	4.06	73	342.41	40.06	0.38
15	343	40	288	343.12	40.40	0.41	15	339.15	40.26	2.49	61	341.64	40.40	0.96	158	339.95	40.02	1.96
16	81	80	351	57.19	76.06	23.61	16	78.73	76.90	3.81	47	75.02	77.02	6.57	192	71.96	83.11	9.47
17	268	56	4	263.56	66.69	11.38	17	266.27	53.12	3.21	43	259.83	58.45	7.29	74	263.61	55.69	3.65
18	94	84	65	90.19	83.00	3.92		NA			NA				197	88.95	81.85	5.45
19	341	44	325	349.28	49.72	8.31	19	338.13	41.74	2.99	365	339.05	42.08	2.34	170	337.59	42.23	2.93
20	59	71	384	58.23	74.30	3.38	20	55.77	69.23	3.52	3	57.97	68.48	2.69	141	50.24	66.63	9.26
* These measurements are most likely blunders and are omitted					average	**8.04**			average	**5.10**			average	**4.67**			average	**5.18**
					stnd dev	**5.82**			stnd dev	**3.56**			stnd dev	**2.99**			stnd dev	**3.85**

Table 11.12. This table shows the measured discontinuity orientations and compares these measurements with the calculated orientations for both methods. This data is for Site 1 (Bellmunt). Please refer also to Figure 11.6 and Table 11.4 for the manual readings.

Site 2 - Toroja																			
Manual readings			**Method 1**		**RBF**			**Method 2**		**Fx**			**Method 3**		**PCA**			**Method 4**	**PCM**	
No	Dip dir. (°)	Dip angle (°)	No	Dip dir. (°)	Dip angle (°)	Dihedral angle (°)		No	Dip dir. (°)	Dip angle (°)	Dihedral angle (°)		No	Dip dir. (°)	Dip angle (°)	Dihedral angle (°)		No	Dip dir. (°)	Dip angle (°)	Dihedral angle (°)
1	29	90	55	28.22	89.74	0.82		1	34.84	85.36	7.46		84	28.72	89.44	0.63		125	28.23	89.40	0.98
2	135	54	100	134.90	52.55	1.45		2	143.46	52.27	6.98		52	135.27	52.41	1.61		121	136.14	51.90	2.29
3	278	32	179	272.30	29.90	3.60		3	278.18	29.19	2.81		154	271.36	29.69	4.11		162	272.68	28.41	4.48
4	132	52	100	134.90	52.55	2.36		4	143.17	51.07	8.79		52	135.27	52.41	2.62		121	136.14	51.90	3.26
5	86	63	107	98.26	63.13	10.93		5	104.91	58.57	17.06		30	86.67	62.68	0.68		180	87.05	60.75	2.43
6	141	41	122	116.61	73.38	37.96		6	148.47	35.58	7.12		26	141.25	44.46	3.46		155	142.67	46.10	5.23
7	37	84	74	35.58	83.41	1.53		7	37.67	78.18	5.86		24	36.33	83.73	0.72		97	35.05	81.51	3.16
8	126	54	94	130.09	58.57	5.70		8	136.37	56.50	8.88		7	130.44	57.75	5.25		56	130.16	57.07	4.60
9	220	85	52	217.80	84.80	2.20		9	226.40	82.71	6.76		16	218.23	86.04	2.05		123	219.28	88.19	3.27
10	138	50	95	135.24	56.64	7.00		10	146.87	44.67	8.42		140	137.12	54.37	4.42		95	139.37	52.07	2.33
11	290	31	172	300.17	40.42	11.11		11	299.84	28.31	5.55		85	291.87	28.74	2.45		114	291.90	28.01	3.13
12	27	88	53	44.91	83.67	18.38		12	30.85	81.61	7.46		83	31.57	84.47	5.76		23	30.77	84.48	5.15
13	28	88	60	13.26	73.11	20.78		13	31.13	84.93	4.38		70	31.51	88.87	3.61		173	29.85	88.27	1.87
14	90	70	98	120.68	86.61	34.21		14	95.25	67.68	5.41		35	88.93	74.80	4.91		175	90.45	68.47	1.59
15	289	50	176	275.87	59.48	14.28		15	295.83	51.49	5.49		6	289.59	52.33	2.37		153	288.41	43.17	6.85
16	136	48	124	119.37	52.09	13.36		16	141.08	43.96	5.45		128	131.33	50.72	4.47		79	135.79	48.87	0.89
17	134	48	114	126.65	55.26	9.26		17	143.86	45.74	7.54		33	133.84	47.75	0.28		12	134.46	47.29	0.79
18	118	46	114	126.65	55.26	11.41		18	129.70	43.13	8.69		53	123.50	47.30	4.20		106	119.35	44.98	1.40
19	35	80	80	38.77	82.19	4.32		19	42.29	74.52	8.98		114	38.36	81.39	3.59		135	37.09	80.49	2.12
20	267	34	247	279.55	30.90	7.40		20	275.54	35.21	4.99		109	267.37	37.90	3.90		92	272.67	34.35	3.20
21	135	48	114	126.65	55.26	9.76		21	143.38	45.67	6.54		33	133.84	47.75	0.90		12	134.46	47.29	0.82
22	26	83	88	27.19	82.88	1.19		22	33.93	79.30	8.67		13	27.65	82.14	1.84		104	27.20	81.71	1.75
23	35	88	89	26.99	82.76	9.54		23	36.59	82.69	5.54		61	34.11	89.27	1.55		176	33.92	89.37	1.74
24	151	41	156	132.01	65.66	28.80		24	149.64	39.24	1.97		160	141.55	39.88	6.23		227	141.40	39.46	6.38
25	248	74	15	249.90	70.64	3.82		25	258.32	65.88	12.64		113	251.05	68.36	6.33		200	253.60	69.86	6.74
26	130	51	102	117.83	62.25	15.13		26	130.17	51.21	0.24		58	120.93	54.95	8.24		96	120.91	54.03	7.82
					average	**11.01**				average	**6.91**				average	**3.31**				average	**3.24**
					stnd dev	**10.03**				stnd dev	**3.25**				stnd dev	**2.06**				stnd dev	**2.06**

Table 11.13. This table shows the measured discontinuity orientations and compares these measurements with the calculated orientations for methods 1, 3 and 4. This data is for Site 2 (Torroja). Please refer also to Figure 11.12 and Table 11.9 for the manual readings.

Appendix L. Orientation and Spacing Statistics for Discontinuity Sets at Site 1

Generic set	Site 1 - Bellmunt	Set	ID	Dip direction	Dip angle	N	Fisher K	variance s	mean N set spacing (m)	mean EN set spacing (m)	stdev N set spacing (m)	stdev EN set spacing (m)	max N set spacing (m)	max EN set spacing (m)
A	Method 1	Set 1	11	345.9	43.8	83	55	0.13	0.04	0.11	0.07	0.28	0.53	2.14
	Method 2	Set 1	21	342.0	39.3	72	52	0.14	0.05	0.10	0.07	0.16	0.40	0.95
	Method 3	Set 1	31	346.8	46.9	188	59	0.13	0.02	0.05	0.03	0.10	0.31	0.55
	Method 4	Set 1	41	342.7	43.5	128	23	0.21	0.04	0.08	0.07	0.18	0.51	1.44
	Scanline	Set 1	sl1	341.1	41.3	35	2839	0.02	0.10		0.17		0.58	
	SSPC	C1	c1	344.0	44.0				0.01					
B	Method 1	Set 2	12	153.6	62.7	92	12	0.28	0.05	0.13	0.07	0.17	0.53	0.97
	Method 2	Set 2	22	145.3	50.0	45	11	0.29	0.08	0.54	0.09	1.37	0.34	8.27
	Method 3	Set 2	32	156.7	68.3	102	25	0.20	0.04	0.11	0.05	0.16	0.29	1.08
	Method 4	Set 2	32	145.4	61.1	92	11	0.30	0.08	0.15	0.19	0.17	1.61	1.00
	Scanline	Set 3	sl3	172.6	56.0	9	125	0.08	0.60		0.60		1.71	
	SSPC	J3	j3	147.0	58.0				0.40					
C	Method 1	Set 3	13	24.6	53.7	80	50	0.14	0.02	0.10	0.02	0.18	0.14	1.13
	Method 2	Set 3	23	18.3	44.9	44	41	0.15	0.04	0.16	0.07	0.24	0.38	1.39
	Method 3	Set 3	33	20.3	63.3	91	33	0.17	0.02	0.11	0.04	0.13	0.28	0.91
	Method 4	Set 3	43	23.2	56.8	64	25	0.20	0.05	0.15	0.11	0.20	0.74	1.29
D	Method 1	Set 4	14	55.3	71.9	64	53	0.14	0.05	0.12	0.10	0.16	0.68	1.11
	Method 2	Set 4	24	55.6	63.0	55	29	0.18	0.05	0.17	0.08	0.31	0.47	1.59
	Method 3	Set 4	34	57.3	73.4	119	27	0.19	0.03	0.09	0.04	0.19	0.27	1.63
	Method 4	Set 4	44	45.5	76.6	86	38	0.16	0.03	0.10	0.05	0.11	0.32	0.67
	SSPC	J6	j6	54.0	80.0				1.20					
E	Method 1	Set 5	15	255.4	80.0	84	56	0.13	0.07	0.11	0.10	0.17	0.69	0.83
	Method 3	Set 5	35	227.2	71.6	103	17	0.24	0.04	0.11	0.06	0.11	0.29	0.58
	Method 4	Set 5	45	72.2	76.1	123	42	0.15	0.04	0.09	0.07	0.12	0.42	0.99
	Scanline	Set 2	sl2	71.8	84.5	24	3	0.52	0.17		0.13		0.46	
	SSPC	J4	j4	263.0	90.0				0.60					
F	Method 2	Set 5	25	257.0	48.5	25	17	0.24	0.15	0.93	0.19	1.82	0.86	9.00
	Scanline	Set 5	sl5	267.0	56.2	5	2	0.52	0.77		0.63		1.45	
	SSPC	J7	j7	268.0	58.0				0.80					
G	Scanline	Set 4	sl4	335.0	78.8	7	1	0.74	0.29		0.31		0.87	
	SSPC	J2	j2	328.0	85.0				0.60					

Table 11.14. This table shows the results of the set-by-set comparison for Site 1 and classification into 7 generic sets (A to G). This table is used as a basis to construct the generic polar stereo plot that is shown in Figure 9.35.

Generic set	Site 2 - Toroja	Set	ID	Dip direction	Dip angle	N	Fisher K	variance s	mean N set spacing (m)	mean EN set spacing (m)	stdev N set spacing (m)	stdev EN set spacing (m)	max N set spacing (m)	max EN set spacing (m)
A	Method 1	Set 3	13	132.6	56.4	74	12	0.28	0.07	0.05	0.08	0.06	0.49	0.36
	Method 2	Set 3	23	117.9	53.3	66	12	0.28	0.06	0.14	0.11	0.21	0.84	1.26
	Method 3	Set 3	33	121.7	60.7	61	17	0.24	0.05	0.05	0.05	0.05	0.19	0.22
	Method 4	Set 3	43	128.0	57.1	75	11	0.29	0.08	0.05	0.10	0.06	0.49	0.31
	Scanline	Set 2	sl2	133.4	49.0	20	82	0.10	0.60		0.50		1.41	
	SSPC	J2	j2	135.0	54.0				0.30					
B	Method 1	Set 4	14	298.3	39.3	97	15	0.26	0.04	0.03	0.09	0.06	0.86	0.47
	Method 2	Set 4	24	303.6	51.2	96	23	0.21	0.06	0.10	0.14	0.13	0.91	1.01
	Method 3	Set 4	34	292.7	53.2	67	21	0.22	0.04	0.04	0.07	0.05	0.37	0.23
	Method 4	Set 4	44	291.8	38.4	93	26	0.19	0.04	0.03	0.06	0.04	0.47	0.21
	Scanline	Set 3	sl3	287.9	37.2	21	64	0.12	0.21		0.12		0.53	
	SSPC	J3	j3	279.0	24.0				0.50					
C	Method 1	Set 1	11	30.9	82.9	47	32	0.17	0.10	0.09	0.15	0.11	0.65	0.44
	Method 2	Set 1	21	34.7	62.9	59	2	0.66	0.10	0.24	0.13	0.36	0.63	1.62
	Method 3	Set 1	31	40.1	82.4	48	32	0.17	0.08	0.09	0.11	0.10	0.38	0.48
	Method 4	Set 1	41	39.5	78.2	97	17	0.24	3.25	0.04	16.99	0.05	138.64	0.22
	Scanline	Set 1	sl1	213.5	83.6	36	72	0.11	0.18		0.18		0.81	
	SSPC	J1	j1	209.0	90.0				0.50					
D	Method 1	Set 2	12	249.7	70.9	47	32	0.17	0.05	0.05	0.07	0.07	0.38	0.45
	Method 2	Set 2	22	259.6	51.2	60	18	0.23	0.05	0.16	0.07	0.19	0.40	1.11
	Method 3	Set 2	32	254.4	60.5	40	26	0.19	0.06	0.06	0.09	0.10	0.42	0.53
	Scanline	Set 5	sl5	246.3	69.8	4	15	0.18	0.44		n.a.		0.75	
E	SSPC	J4	j4	86.0	63.0				0.25					
	Scanline	Set 6	sl6	87.8	53.4	4	13	0.20	0.37		n.a.		0.37	
N.A.	Scanline	Set 4	sl4	320.1	73.5	8	31	0.15	0.28		0.12		0.46	
	Method 4	Set 2	42	289.6	74.2	67	26	0.19	0.04	0.04	0.06	0.05	0.34	0.24

Table 11.15. This table shows the results of the set-by-set comparison for Site 2 and classification into 5 generic sets (A to E). This table is used as a basis to construct the generic polar stereo plot that is shown in Figure 9.36.